

2022-08-01

## **Multi-Material/Fiber/Particulate Selective Laser Sintering System Capable of Local Composition Control and Material Gradients**

Jonathan James Slager  
*University of Texas at El Paso*

Follow this and additional works at: [https://scholarworks.utep.edu/open\\_etd](https://scholarworks.utep.edu/open_etd)



Part of the [Mechanical Engineering Commons](#)

---

### **Recommended Citation**

Slager, Jonathan James, "Multi-Material/Fiber/Particulate Selective Laser Sintering System Capable of Local Composition Control and Material Gradients" (2022). *Open Access Theses & Dissertations*. 3629. [https://scholarworks.utep.edu/open\\_etd/3629](https://scholarworks.utep.edu/open_etd/3629)

This is brought to you for free and open access by ScholarWorks@UTEP. It has been accepted for inclusion in Open Access Theses & Dissertations by an authorized administrator of ScholarWorks@UTEP. For more information, please contact [lweber@utep.edu](mailto:lweber@utep.edu).

MULTI-MATERIAL/FIBER/PARTICULATE SELECTIVE LASER SINTERING SYSTEM  
CAPABLE OF LOCAL COMPOSITION CONTROL AND MATERIAL GRADIENTS

JONATHAN JAMES SLAGER

Doctoral Program in Mechanical Engineering

APPROVED:

---

Roger V. Gonzalez, Ph.D., Chair

---

Joshua T. Green, Ph.D., Co-Chair

---

Stephen W. Stafford, Ph.D.

---

Calvin M. Stewart, Ph.D.

---

C. Brandon Broome, M.D.

---

Stephen L. Crites, Jr., Ph.D.  
Dean of the Graduate School

Copyright ©

by

Jonathan James Slager

2022

## **Dedication**

This work is dedicated to my loving wife, Angel. Without her relentless dedication, steadfast love, and endless support over the last 22 years of our marriage none of this work would have been possible. However, more importantly, when I could no longer continue under my own power her faith never faltered and her prayers never ceased. It is during these times the power, guidance, and love of Jesus Christ our Savior carried us both through to the next step. All future discovery that comes from this research is dedicated to Him alone.

MULTI-MATERIAL/FIBER/PARTICULATE SELECTIVE LASER SINTERING SYSTEM  
CAPABLE OF LOCAL COMPOSITION CONTROL AND MATERIAL GRADIENTS

by

JONATHAN JAMES SLAGER, B.S, M.S.

DISSERTATION

Presented to the Faculty of the Graduate School of

The University of Texas at El Paso

in Partial Fulfillment

of the Requirements

for the Degree of

DOCTOR OF PHILOSOPHY

Department of Mechanical Engineering

THE UNIVERSITY OF TEXAS AT EL PASO

August 2022

## **Acknowledgements**

First and foremost, I would like to acknowledge the power and guidance of Jesus Christ without whom none of this research or discovery would have been possible. It is because of His miraculous direction in my life that I was brought to this University and surround by such brilliant and supportive teachers, mentors, family, and friends.

Dr. Gonzalez, Dr. Green, and my committee members never gave up on me, my vision, or work during this research. Their heartfelt mentoring, extensive knowledge, and professional guidance kept the essence of the research and reporting of the project on track from inception to completion.

Lucas, Edel, Truman, Diego, Mauricio, Daniel, Zachary, Luis, Sarahi, Ian, Ivana, Alan, Carlos, Neyda, and countless others at UTEP have poured innumerable hours into this research, but more importantly have poured their energy, expertise, and friendship into this project. Their incredible support knows no boundaries and has crossed multiple labs. PEOPLE are what make the difference in any organization, and they have certainly made the difference at UTEP!

Jeremy, Connie, Lamar, Patrick, Larry, Erika, Tom, Denise, and many others at First Baptist Church El Paso have covered me in prayer, encouragement, and solid Godly counsel with incredible fellowship throughout this journey.

Dr. G, Yvette, Lucas, and Gina Galey have always met me where I was at on any given day. Their friendship, food, listening ear, open doors, and genuine hospitality have always been there to share in laughter, frustration, and grounded advice to make it another day. They were never too busy to help me analyze one more set of data, plot one more graph, re-write one more paragraph or, bring in one more container of leftovers.

Mom, Dad, Doug, Elaine, Bennyman, SK, Uncle Dick have always supported Angel, the kids, and me every way possible. From frequent visits to the desert, camping trips, Milwaukee tools, motorcycle rides, house remodels, caverns, and campfires they have supported us every step of the way. But more importantly their love and prayers have engulfed us in such a tangible way. Family is for life and this life would not be the same without ya'll!

Lastly, my kids, Bailey, Mason, Madison, and Brodie are the real heroes. Bailey's sunshine will always light up the room, Mason's dry humor and tenacious loyalty will always put a smile on your face and ensure no task is done solo, Madison's tender selflessness will always ensure you know you are loved, and Brodie's unwavering companionship will always guarantee you are never alone on any adventure. Because of their incredible Mama they have followed me around the world over the last 17 years with a smile on their face, love in their hearts, and adventure in their soul. They have lived out Proverbs 3:16 at every turn in our journey. Thank you free range house chickens!

## Abstract

Multi-material (M2) manufacturing with functional gradients and local composition control (LCC) is an emerging technology with high demand in numerous industries. This research investigated multi-material technology that has potential impact to joint implants, synthetic joints, and damage resistant parts. Novel manufacturing subsystems within established selective laser sintering (SLS) additive manufacturing processes were pioneered to enable printing M2 parts with LCC and functionally graded materials. Powder bed fusion (PBF) material blends consisting of low temperature thermoplastics, low temperature thermoplastic elastomers (TPE), carbon fibers (CF), and hydroxyapatite (HA) particulates were explored to match the designed and tested M2 SLS prototype.

M2 sintering, material blending, and M2 parts demonstrated the feasibility of sintering material gradients using Polyamide 12 (PA12) as a matrix material mechanically blended with TPE, CF, and HA. Various PA12/CF blends were characterized via tensile tests to investigate the potential of tuning material properties based on the CF blend ratio. Printing and characterization of Single Edge Notch Tensile (SENT) specimens with binary and gradient material interfaces were performed to study the effects of functional material (fiber) gradients in polymer PBF and to validate the novel M2 SLS subsystems developed in this research. A joint implant conceptual prototype consisting of a PA12 matrix with functional binary gradients of CF and HA was printed to demonstrate the possible impact of tri-material parts.

The combination of the M2 SLS prototype, mechanical material blending, and binary gradient tests demonstrated the capability to customize and tune multiple material properties throughout a single part while increasing overall part ultimate tensile strength, yield stress, and crack energy absorption. However, the results also showed the potential to use the methods

developed in this research to stabilize and functionalize material blends (e.g., high CF or TPE blends) through M2 PBF that may otherwise be unprintable with single material PBF. However, inconsistencies between two sets of SENT tests highlighted the importance of continued research and testing under numerous environments and damaged states to fully understand sintered PA12/CF composites before “as printed” parts containing these material blends can be used in most applications. The combination of all results in this research has revealed this type of M2 manufacturing may have a broader impact in biomedical, aeronautical, and other evolving industries.

# Table of Contents

Dedication.....	iii
Acknowledgements.....	v
Abstract.....	vii
Table of Contents.....	ix
List of Tables.....	xiii
List of Figures.....	xiv
Chapter 1: Introduction.....	1
Broader Implications.....	2
Joint Implant.....	3
Synthetic Joint.....	5
Background and Scope.....	9
Limitations to Scope and Recommended Future Research.....	11
Chapter 2: Objectives.....	13
Aim 1.....	16
Aim 1 Hypothesis.....	18
Aim 2.....	19
Aim 2 Hypothesis.....	19
Aim 3.....	19
Aim 3 Hypothesis.....	20
Aim 4.....	20
Aim 4 Hypothesis.....	20
Chapter 3: Aim 1 - Design and Build Novel LCC Selective Laser System.....	21
Introduction.....	21
Background.....	21
Methods.....	24
Subsystem 1: Multi-Material Slicer.....	26
Acceptance Criteria.....	26
Subsystem 2: Multi-Material Hatch & Layer Energy Density Control.....	27

Acceptance Criteria.....	28
Subsystem 3: Multi-Material Thermal Management System .....	30
Acceptance Criteria.....	33
Subsystem 4: Multiple Reservoirs with Intra-Print Powder Extraction/Addition .....	36
Acceptance Criteria.....	36
Subsystem 5: Multi-Material Layer Application .....	38
Acceptance Criteria.....	40
Subsystem 6: Part Anchoring.....	41
Acceptance Criteria.....	42
Subsystem 7: Multi-Material SLS Host and User Interface .....	43
Acceptance Criteria.....	45
Results.....	50
Subsystems 1 & 2: Multi-Material Slicer, Hatch, & Layer Energy Density Control ..	50
Subsystem 3: Multi-Material Thermal Management System .....	51
Single Material Thermal Management: .....	51
Material Switch Thermal Management: .....	58
Subsystem 4: Multiple Reservoirs with intra-print powder extraction/addition.....	63
Subsystem 5: Multi-Material Layer Application .....	65
Subsystem 6: Part Anchoring.....	69
Subsystem 7: Multi-Material SLS Host and User Interface .....	70
Discussion .....	70
Broader Implications.....	82
Conclusion .....	83
Chapter 4: Aim 2 - SLS Material, Fiber, and Particulate Compatibility and Sintering Testing ....	84
Introduction.....	84
Background .....	85
Fiber Blend.....	89
Particulate Blend.....	90
Material Blend (Polymeric Composite) .....	90
Critical Sintering Parameters and Material Properties for Blended Polymer PBF .....	90
PBF Material Compatibility Summary .....	103
Methods.....	103

Material Preparation.....	106
Bi-Material DOE Specimen Printing .....	106
Specimen Evaluation .....	108
Single Material Evaluation .....	115
Thermoplastics.....	118
Thermoplastic Elastomers.....	119
Fibers.....	119
Particulates.....	120
Material Blend Compatibility .....	121
Thermoplastic/Fiber Blend .....	123
Thermoplastic/Particulate Blend.....	123
Thermoplastic/Thermoplastic Elastomer Blend .....	124
Results.....	125
Discussion .....	154
Broader Implications.....	160
Conclusion .....	161
Chapter 5: Aim 3 - Characterization of Stress-Strain and Fracture Data for Polyamide 12 and Carbon Fiber blends.....	162
Introduction.....	162
Background.....	163
Methods.....	170
Results.....	175
Discussion .....	186
Broader Implications.....	195
Conclusion .....	196
Chapter 6: Aim 4 - Characterization of Local Composition Control with Binary Interfaces and One-Dimensional Gradients.....	198
Introduction.....	198
Background.....	198
Methods.....	203
SENT Specimen Evaluation .....	205
Multi-Material Prototype Demonstration .....	209
Results.....	210

Discussion .....	249
Broader Implications.....	257
Conclusion .....	257
Chapter 7: Conclusion.....	259
References.....	261
Acronyms .....	277
Appendix A: UTEP Disclosure D2020-0015 .....	279
Appendix B: Alternate Hatch Patterns.....	283
Appendix C: Initial Blend Microscopy Contrast Imaging Results .....	285
Appendix D: Manufacture Material Data Sheet. ....	297
Appendix E: Industry Standard Nylon 12 Sintered Properties. ....	308
Appendix F: Differences between SENT Test 1 and Test 2.....	310
Introduction.....	310
Methods.....	310
Results.....	311
Discussion .....	311
Broader Implications.....	314
Conclusion .....	315
Vita .....	342

## List of Tables

Table 4.1: TP and TPE powder selection criteria and material brand comparison.....	116
Table 4.2: Manufacturer Data for selected TP, TPE, CF, HA (Blank Cells: data not provided). .....	117
Table 5.1: PA12/CF Buoyancy Density Results (ASTM D-792 Test Standards) .....	178
Table 5.2: PA12/CF Blend Buoyancy Density Results Compared to Calculated Theoretical Values .....	189
Table 5.3: PA12/CF Blend Ratios Comparison of Tensile Data .....	193
Table 5.4: PA12/CF Blend Ratios Comparison of Tensile Data .....	195
Table 6.1 SENT Specimen Warping Results .....	213
Table 6.2: SENT Specimen Shore D Hardness Results.....	214
Table 6.3: Test 1 SENT Analysis Data (Crack Initiation Data for Highlighted Yellow Specimens).....	215
Table 6.4: Test 1 SENT Data at Maximum Stress and Failure for Highlighted Yellow Specimens .....	216
Table F.1: Comparison of Test 1 and Test 2 Dimensions and Tensile Data .....	317
Table F.2b: Comparison of Test 1 and Test 2 Fracture Energy Data at Maximum Stress .....	319
Table F.2c: Comparison of Test 1 and Test 2 Fracture Energy Failure.....	320

## List of Figures

Figure 1.1: Benefits of a Multi-Material Tibial Orthopedic Implant Mated with a Traditional Metal Femur Implant .....	5
Figure 1.2: Synthetic Joint Prototype with LCC to Mimic Biological Material Printed on a FFF Mixing Printer (patent pending) in the Joint Laboratory at UTEP (Taylor Green & Taylor, 2018) .....	7
Figure 1.3: Possible testing process to develop more realistic synthetic joints for surgical simulation. (a) Instrument cadaver knee to quantify internal loads and load response of a human knee (Hale, 2016; Hale et al., 2018; Taylor Green & Taylor, 2018). (b) Quantify joint loadings during movement (Green et al., 2017). (c) Conceptual design implementing biological material properties with musculoskeletal based on cadaveric load response (Green, 2018; Green, Ph, et al., 2021) .....	9
Figure 1.4: Conceptual Synthetic Joint Study Showing Possible Comparison and Research Methods (Green et al., 2017; Hale et al., 2018).....	9
Figure 2.1: Multi-Material (M2) Powder Bed Fusion (PBF) printing process with associated subsystem. “Material Application and Sintering Procedure” is common to single material PBF systems. “Material Change Procedure” and procedures highlighted in blue un “Initial Print Setup” are unique to the M2 PBF design developed in this research .....	15
Figure 3.1: Block diagram depicting material flow in M2 PBF. Matrix/Infill Preparation (grey section) can be accomplished internally or externally to the system and can be automated or manual. Print control (red section) contains the hypothesized functions to incorporated M2 into PBF .....	24
Figure 3.2: Multi-material SLS operational and communication flow chart highlighting the methods to accomplish the seven critical M2 Subsystems. General (overlap exists) subsystem execution designated by color and associated subsystem number.....	25
Figure 3.3: Multi-material slicer with material designation of each part delineated based on color and defined on the right side as a different group. For clarity, the different STL files are depicted as discrete parts; however, for an M2 part the STL files would be joined into a single part .....	27
Figure 3.4: Programmed Galvanometer Speed Control.....	29
Figure 3.5: Comparison of Hatch Pattern Thermal Gradients .....	29
Figure 3.6: Proposed Hatch Pattern to Integrate Both Thermal Homogeneity and Sinter Efficiency .....	30
Figure 3.7: Thermal management subsystem heater positioning for M2 operations involving powder movement into and out of the system .....	34
Figure 3.8: M2 SLS Front Access Door with Powder Addition and Extraction Ports .....	35
Figure 3.8: Powder Extraction and Addition Flow .....	37
Figure 3.9: Proposed Methods to Switch Materials at Layer Application through Powder Isolation (a-b) and Powder Purge (c-d).....	40
Figure 3.10: Part Anchoring Depiction.....	43
Figure 3.11: Material Specific Hatch Control Interface for Subsystem 4 .....	45
Figure 3.12: Top Layer Powder Thermal Management Interface to Control Subsystem 4.....	46
Figure 3.13: Powder Exchange Interface to Control Subsystems 5-7 .....	47
Figure 3.14: Powder Exchange Interface to Control Subsystems 5-7 .....	48
(a) System Temperature feedback via top layer infrared sensor and ambient thermocouple sensor. ....	49

(b) Rake, build plate, dispensing plate, and reservoir plate movement feedback via motor status.	49
(c) Sintering health feedback via laser and layer timing	49
(d) Powder level and availability feedback through dispensing and reservoir height monitoring.	49
(e) Overall print progress through layer monitoring	49
Figure 3.16: Material Specific Hatch Example:	51
(a) 0.1 mm hatch spacing, 0 degree hatch angle for all layers, single perimeter.	51
(b) 0.1 mm hatch spacing, 45 degree hatch angle for all layers, single perimeter.	51
(c) 0.5 mm hatch spacing, 90 degree hatch angle for all layers, no perimeter.	51
(d) 1.0 mm hatch spacing, -45 degree hatch angle for all layers, no perimeter	51
Figure 3.17: Heater, PID Control, and Thermocouple and Identification Corresponding to the Temperature Profile Graphs (Figures 3.18 thru 3.20)	53
Figure 3.18: Build Area Ambient Thermocouple Data	54
Figure 3.19: Dispensing Ambient Thermocouple Data	55
Figure 3.20: Reservoir Ambient Thermocouple Data	56
Figure 3.21: Infrared Image of Build Area (Top Layer Direct Heaters set to 165° C and Bulb Weights Set To: Front = 90, Left = 65, Right = 110)	57
(a) Data for a ~120x100 mm area	57
(b) Data for a ~120x50 mm area	57
Figure 3.22: Tuned PID Setting for PA12 and PA12+CF and Internal Temperatures 13 hours and 15 Minutes into Print	58
Figure 3.23: a) Over-Sintered Top Layer and Cake After Maintaining Top Layer at Sintering Temperature for 8-10 Minutes. b) Cake Cracking Due to Being Allowed To Cool Too Much External During Material Switch	61
Figure 3.24: Temperature Profile During Powder Extraction and Addition	62
Figure 3.25: Multi-Pass Lasing with “Preheat”, “Sinter”, and “Bake” Lasing Customized for each Hatch Direction	62
Figure 3.26: Powder Addition with Copper Dispensing Tubes, Leveling Rake, and Scoop	64
Figure 3.27: Comparison of Homogeneous and Inconsistent Powder Switch and Interface	65
Figure 3.28 Layer Inconsistencies Resulting In:	66
a) Voids and low-density material at material interfaces in the build chamber	66
b) Part defects at multi-material interface	66
Figure 3.29 novel multi-pass recoating system was developed	67
Figure 3.30: Post Print Cake Showing Homogeneous Layer Application at Material Changes Novel Multi-Pass Recoating System	68
Figure 3.31: Tensile Fracture Surface of Single Material Print Demonstrating Advantages of Novel Multi-Pass Recoating System	68
Figure 3.32: PA12 Single Edge Notch Tensile Specimen without Anchoring (a) and with 10% CF anchor (b)	69
Figure 3.33: Anchoring results with 10% CF anchor (a) and PA12 anchor (b and c)	70
Figure 3.34: M2 SLS Mirrored 4 Chamber Design with Single Recoater	72
Figure 3.35: M2 SLS Removable (i.e., “Swappable”) 4 Chamber Design with Single Recoater	73
Figure 3.36: M2 SLS Linear 8 Chamber Design	74
Figure 3.37: M2 SLS Radial 8+ Chamber Design	75
Figure 3.38: M2 SLS Linear 15+ Chamber Design	76

Figure 4.1: Material properties and the effect on sintering (Adapted from Schmid, et al. (Schmid & Wegener, 2016b)) .....	86
Figure 4.2: Required material properties for sintering. (Adapted from Schmid, et al. (Schmid & Wegener, 2016b)) .....	88
Figure 4.3: Possible chain entanglement dynamics of TP and TPE hard blocks (Adapted from Auhl, et al. (Auhl et al., 2019) ) .....	89
Figure 4.4: Particle coalescence due to surface tension and decrease of viscosity at $T_m$ (image adapted from Hejmady et al., 2019).....	93
Figure 4.5: Laser/Powder Interaction (image adapter from Schmid et al. (Schmid & Wegener, 2016b)).....	98
Figure 4.6: Angle of Repose (powder image from Sinterit website).....	101
Figure 4.5: Material compatibility test methods and acceptance criteria. (a) Teat particle and fiber evaluation. (b) Neat powder evaluation. (c) Material Blend evaluation. ....	105
Figure 4.6: Bi-Material DOE reservoir preparation.....	106
Figure 4.7: Bi-Material DOE Print Planning. ....	107
Figure 4.8: Sintratec Kit build area heater modification.....	108
Figure 4.9: Primary defects that will require material and blend specific temperatures and laser parameters (adapted from Beal et al. (Beal et al., 2009)). ....	110
Figure 4.10: Hypothesized Shore Hardness Ranges for Tested Materials and Blends.....	111
Figure 4.11: Dimensional analysis measurements.....	112
Figure 4.12: Optical Microscopy analysis of printed parts and powder bed using Dino-Lite microscope .....	113
Figure 4.13: Depth of Field (DOF) capability of optical analysis with Dino-Lite AM4917MZT Equipped with DOF capability (Dino-Lite Technical Specifications, (Dino-Lite, 2022)).....	114
Figure 4.14: Porosity (estimated in red by the ImageJ program) analysis of PA12 mixed with 20% CF using ImageJ image processing program were inconclusive.....	115
Figure 4.15: Images (200x) of each powder selected for blend testing .....	118
Figure 4.14: PA12 Molecular Structure.....	118
Figure 4.16: Initial print setting for Sinterit PA12+CF blends (adapted from Espera et al. (Espera et al., 2019a)) .....	120
Figure 4.17: Mechanical tumbler used for all material blending.....	122
Figure 4.18: Laser power and wavelength unable to reach sintering window for PEEK. Laser energy is not sufficiently absorbed into the particles for affective heating and simply burns the top surface.....	127
Figure 4.19: Sinterit and Sintratec powders with the selected carbon fibers and HA particulates .....	127
Figure 4.21: Effects of energy density on PA12/TPE Blends anchored on a TPE base.....	128
Figure 4.22: Homogeneous Sinterit PA12 + CF prints with the Bi-Material DOE printed on the modified Sintratec Kit. a) Printed at 500 mm/sec, chamber 140° C, powder surface 165° C. b) Printed at 525 mm/sec, chamber 140° C, powder surface 163° C.....	129
Figure 4.24: Binary interface of Sintratec PA12+5 %vol CF and PA12+20 %vol CF sintered at constant thermal and laser settings for both blends resulting in warping, sledding and debonding at the change in blend interface. ....	130
Figure 4.25: Blend spreading difficulties at high infill percentage (a) 80% TPE – clumping of TPE due to partial sintering in high temperature chamber required to sinter PA12 (b) 50% HA –	

high agglomeration compared to 25% HA in reservoir due to spread mechanisms. (c) 60% CF – poor layer consistency and density with part sledding when compared to 40% CF..... 131

Figure 4.26: Initial PA12 + CF and PA12 + HA microscopy analysis (a) overall success with CF integration and adhesion to PA12 matrix. (b) challenges with HA spreading and adhesion..... 132

Figure 4.27: Inconclusive porosity calculation using ImageJ with Sintratec PA12 blend and 10% vol CF ..... 132

Figure 4.28: PA12/5%CF Qualitative analysis of porosity showing homogeneous CF mixture, but high porosity required sintering parameter adjustment to decrease porosity. .... 133

Figure 4.29: PA12/25%HA Qualitative printed surface analysis of porosity showing homogeneous HA mixture but extreme porosity with most of the HA not adhering to PA12 Matrix..... 133

Figure 4.30: Microscopy comparison of Sinterit and Sintratec powder and CF (10x zoom left, 200x zoom right)..... 135

Figure 4.31: Microscopy comparison of Sinterit and Sintratec powder and CF at 248x zoom.. 135

Figure 4.32: Microscopy comparison of Sinterit V2 and Sintratec PA12 layer adhesion with spreading inconsistencies during Sinterit V2 layer application..... 136

Figure 4.33: M2 SLS print setup and planning for density, hardness, and tensile testing..... 137

Figure 4.34: Buoyancy Density comparison of PA12 tensile test specimens printed at high (↑) and low (↓) densities. .... 138

Figure 4.35: 0%CF Tensile Specimen comparing sintering energy densities (Dino-Lite AM4917MZT. Zoom: 59x ..... 139

Figure 4.36: 5%CF Tensile Specimen comparing sintering energy densities (Dino-Lite AM4917MZT. Zoom: 59x Left (low density), 72x Right (high density)..... 139

Figure 4.38: 2.5%CF Final Energy Density Comparison of Dimensional and Tensile Test Data. .... 141

Figure 4.39: 5%CF Final Energy Density Comparison of Dimensional and Tensile Test Data. 142

Figure 4.40: 10%CF Final Energy Density Comparison of Dimensional and Tensile Test Data. .... 143

Figure 5.1: Loading and print orientation designations for tensile test specimens..... 164

Figure 5.2a: Sintratec reported PA12 tensile test properties based on build direction (Boxed text added) (Sintratec, 2021a). .... 166

Figure 5.2b: Sintratec reported PA12 tensile test properties based on build direction comparing layer count and loading for each print direction (Sintratec, 2021a). .... 167

Figure 5.3: Sintratec reported TPE tensile test properties based on build direction (Boxed text added) (Sintratec, 2021b)..... 168

Figure 5.4: Mode I Tensile Failure. .... 169

Figure 5.5: Lumpe et al. gradient testing Design of Experiment (DOE) with Type V test specimens additively manufactured using material jetting (Lumpe et al., 2019) ..... 170

Figure 5.6: Summary of Aim 3 methods including specimens, tests, and characterization. Specimen manufacturing was done in the order listed: neat followed by composite. Analysis was done in the order listed for each control and blend specimen: dimensional, density tensile, optical microscopy analysis. .... 171

Figure 5.7: ..... 173

a) Original tensile test specimen definitions and lengths (ASTM D638-14)..... 173

b) “3mmP” modified tensile test specimen to accommodate tri-material specimen. .... 173

Figure 5.7c: Comparison prints of standard D638 Type V tensile specimen, extended tensile specimen with reduced grip length, 3mmP specimen, and 5mmP specimen. ....	174
Figure 5.8: Proposed tensile specimen print scheme (Specimen and build area images from Sintratec Central print program). ....	174
Figure 5.10: Example of specimen condition following post print cleaning of 10% CF vertically printed tensile specimens. Some specimens broke during removal and some broke during cleaning. ....	177
Figure 5.11: 10% CF vertically printed tensile specimen failure during grip insertion and initial pulling. ....	178
Figure 5.13: 2.5% CF Vertical and Horizontal Specimen Dimensional and Tensile Test Data. ....	180
Figure 5.16: Representative 0, 2.5, 5, 10%CF Vertical and Horizontal Specimen Stress-Strain Graph.....	183
Figure 5.17: Fracture Surface of Neat PA12 (0% vol CF) Horizontally Printed 3mmP Tensile Specimen.....	184
Figure 5.18: Fracture Surface of PA12 + 5%vol Carbon Fiber Horizontally Printed 3mmP Tensile Specimen.....	184
Figure 5.19: Fracture Surface of PA12 + 10%vol Carbon Fiber Horizontally Printed 3mmP Tensile Specimen.....	185
Figure 5.20: Fracture Surface of PA12 + 10%vol Carbon Fiber Vertically Printed 3mmP Tensile Specimen.....	185
Figure 5.21: Modulus of Elasticity vs Percent CF.....	194
Figure 5.22: Ultimate Tensile Strength (UTS) and Yield Stress vs Percent CF.....	194
Figure 6.1: Stress concentration at material interface with dissimilar material properties due to differences in lateral strains between materials. (Adapted from Lumpe et a. (Lumpe et al., 2019))......	200
Figure 6.2: Material Jetting additively manufactured layout of binary material interface tensile test specimens with gradients perpendicular to build direction. (Adapted from Lumpe et al. (Lumpe et al., 2019)). ....	201
Figure 6.3: Stress concentrations reduction example using 1D gradients. Simulation with experimental results using material jetting done by Bartlett et al. (adapted from Bartlett et al. Figures 2, S2, and Table S1 (Bartlett et al., 2015a, 2015b)).....	202
Figure 6.4: Aim 4 SENT and Conceptual Prototype Print Scheme.....	204
Figure 6.5: Single Edge Notch Tensile Specimen Design and Dimensions.....	206
Figure 6.6: Single Edge Notch Tensile Specimen Print Planning (Specimens labeled 1-8 front to back to track specimen characteristics based on location in print area).....	207
Figure 6.7: SENT Specimen Post Print Machining.....	207
Figure 6.8: SENT Specimen Notching Jig.....	208
Figure 6.9: SENT Specimen Notch Analysis.....	208
Figure 6.10: SENT Specimen Warping Analysis.....	209
Figure 6.11: One-dimensional LCC joint implant conceptual prototype design.....	210
Figure 6.12: Depiction of SENT Test DIC Results Definitions and Terms:.....	217
Figure 6.12a: SENT Test DIC Results the Frame Before Specimen Failure scaled to each specimen frame with stress and energy data.....	218
Figure 6.12b: SENT Test DIC Results at the Frame of Specimen Crack Initiation (Ci) scaled to each specimen frame.....	219

Figure 6.12c: Test 1 SENT Test DIC Results at the Frame of Specimen Crack Initiation (Ci), scaled to ALL.....	220
Figure 6.12d: Test1 SENT Test DIC Results the Frame at Specimen Max Force (MF) scaled to each specimen .....	221
Figure 6.12e: SENT Test DIC Results the Frame Before Specimen Max Force (MF) scaled to ALL.....	222
Figure 6.12f: SENT Test DIC Results the Frame Before Specimen Failure scaled to each specimen frame .....	223
Figure 6.12g: SENT Test DIC Results the Frame Before Specimen Failure scaled to ALL .....	224
Figure 6.13: Comparison of 3mmP Horizontally Printed Tensile Test (Aim 3) and 30mm Extensometer SENT Stress/Strain .....	225
Figure 6.14: Single Material SENT Results Overview (T1 = Test 1, -x = Specimen Number). ..	226
Figure 6.15: Bi-Material and Binary Gradient SENT Results Overview (T1 = Test 1, -x = Specimen Number) .....	227
Figure 6.16: SENT 30mm Extensometer Stress/Strain Comparison of Representative Specimen from Each Test.....	228
Figure 6.17: SENT 30mm Extensometer Stress/Strain Comparison of Representative Specimen from Each Test with Crack Initiation Lines (dotted) for each Specimen. ....	229
Figure 6.18: Depiction of SENT Test DIC Results Energy Calculation Definitions and Terms: .....	230
Figure 6.18a: 10-0-10% CF SENT Test Results with DIC Strain Mapping and Stress-Strain Curve with Energy Data.....	231
Figure 6.18c: 5%CF Single Material SENT Energy Data. ....	232
Figure 6.18d: 10%CF Single Material SENT Energy Data. ....	233
Figure 6.18e: 0-5-0%CF Binary Material SENT Energy Data. ....	233
Figure 6.18f: 0-5-0%CF Binary Material SENT Energy Data. ....	234
Figure 6.18g: 0-10-0%CF Binary Material SENT Energy Data.....	234
Figure 6.18h: 10-0-10%CF Binary Material SENT Energy Data.....	235
Figure 6.18i: 0-5-10-5-0%CF Gradient SENT Energy Data. ....	235
Figure 6.19: 0% SENT SEM Fractography .....	236
Figure 6.20: 5% SENT SEM Fractography .....	237
Figure 6.21: 5% SENT SEM Notch Fractography .....	238
Figure 6.22: 10% SENT SEM Fractography .....	239
Figure 6.23: 0-5-0% SENT SEM Fractography .....	240
Figure 6.24: SENT SEM Fractography of CF Gradient Transitions .....	241
Figure 6.25: 0-5% SENT SEM Sanded Surface of CF Gradient Transition (estimated with 0% blue line, 5% orange line). ....	242
Figure 6.26: 0-5% SENT SEM Fractography of CF Gradient Transition (estimated with green line) .....	243
Figure 6.27: 5-10% SENT SEM Fractography of CF Ductile Gradient Transition (estimated with green line) .....	244
Figure 6.28: 10-5% SENT SEM Fractography of CF Gradient Brittle Transition (estimated with green line) .....	245
Figure 6.29: 10% SENT SEM Fractography of CF Ductile to Brittle Transition (estimated with green line) .....	246

Figure 6.30: 0%, 5%, 10%, Binary Gradient SENT SEM Fractography comparison (gradient transition estimated with green line).....	247
Figure 6.31: Joint implant conceptual prototype .....	248
Figure C1: Neat Sintratec PA12 Contrast Imaging (Porosity Calculation). .....	286
Figure C2: Neat Sinterit V1 PA12 Contrast Imaging (Porosity Calculation).....	287
Figure C3: Sintratec PA12 + 10%CF vol Contrast Imaging (Porosity Calculation). .....	288
Figure C4: Sinterit PA12 + 40%CF vol Contrast Imaging (Porosity Calculation).....	289
Figure C5: Sinterit PA12 + 40%CF vol Contrast Imaging (CF Calculation). .....	290
Figure C6: Sinterit PA12 + 5%HA vol Contrast Imaging (Porosity Calculation).....	291
Figure C7: Sinterit PA12 + 5%HA vol Contrast Imaging (HA Calculation). .....	292
Figure C8: Sintratec PA12 + 40%HA vol Contrast Imaging (Porosity Calculation). .....	293
Figure C9: Sintratec PA12 + 40%HA vol Contrast Imaging (HA Calculation).....	294
Figure C10: Sintratec PA12 + 50%TPE (Sintratec) vol Contrast Imaging (Porosity Calculation). .....	295
Figure C11: Sinterit PA12 + 50%TPE (Sinterit) vol Contrast Imaging (Porosity Calculation). .....	296
Figure D1: Sinterit PA12 Manufacturer Data Sheet. ....	298
Figure D2: Sinterit TPE Manufacturer Data Sheet. ....	299
Figure D3: Sinterit Flexa Grey Manufacturer Data Sheet. ....	300
Figure D4: Sintratec PA12 Manufacturer Data Sheet.....	301
Figure D5: Sintratec PA12 Manufacturer Tensile Data Sheet.....	302
Figure D6: Sintratec TPE Manufacturer Data Sheet.....	303
Figure D7: Sintratec TPE Manufacturer Tensile Data Sheet.....	304
Figure D8b: Carbiso MF100 CF Manufacturer Data Sheet (cont.). .....	306
Figure D8c: Carbiso MF100 CF Manufacturer Data Sheet (cont.). .....	307
Figure E1: Matweb Sintered PA12 Data on ALM PA 650 Nylon 12. ....	308
Figure E2: Materialise Manufacturing Sintered PA12 Manufacturer Data Sheet. ....	309
Figure F.1: Depiction of SENT Test DIC Results Definitions and Terms: .....	321
Figure F.1a: Test 2 Crack Initiation (Ci) scaled to each specimen frame.....	322
Figure F.1b: Test 2 Crack Initiation (Ci) scaled to ALL.....	323
Figure F.1c: Test 2 Max Force (MF) scaled to each specimen frame .....	324
Figure F.1d: Test 2 Max Force (MF) scaled to ALL .....	325
Figure F.1e: Test 2 Failure scaled to each specimen frame.....	326
Figure F.1d: Test 2 Failure scaled to ALL.....	327
Figure F.2a: Test 1 (top images) and Test 2 (bottom images) Crack Initiation (Ci) scaled to each specimen frame. ....	328
Figure F.2b: Test 1 (top images) and Test 2 (bottom images) Max Force (MF) scaled to each specimen. ....	329
Figure F.2c: Test 1 (top images) and Test 2 (bottom images) Failure scaled to each specimen frame. ....	330
Figure F.4a: Comparison Test 1 and Test 2 of 30mm Stress-Strain Curves.....	332
Figure F.5: Comparison of Wet, Dried, and Ambient Specimen 30mm Stress-Strain Curves... ..	334
Figure F.6a: 0%CF Single Material SENT 30mm Extensometer Tensile Data Comparison. ....	335
Figure F.6b: 5%CF Single Material SENT 30mm Extensometer Tensile Data Comparison.....	335
Figure F.6d: 0-5-0%CF Binary Material SENT 30mm Extensometer Tensile Data Comparison. ....	336

Figure F.6e: 0-10-0%CF Binary Material SENT 30mm Extensometer Tensile Data Comparison.	337
Figure F.6f: 10-0-10%CF Binary Material SENT 30mm Extensometer Tensile Data Comparison.	337
Figure F.6g: 0-5-10-5-0%CF Binary Gradient SENT 30mm Extensometer Tensile Data Comparison.	338
Figure F.7a: 0%CF Single Material SENT Test 2.	338
Figure F.7b: 5%CF Single Material SENT Test 2.	339
Figure F.7d: 0-5-0%CF Binary Material SENT Test 2.	340
Figure F.7e: 0-10-0%CF Binary Material SENT Test 2.	340
Figure F.7f: 10-0-10%CF Binary Material SENT Test 2.	341
Figure F.7g: 0-5-10-5-0%CF Gradient SENT Test 2.	341

## Chapter 1: Introduction

Multi-material (M2) manufacturing is a process that uses multiple materials to fabricate a single part. This specialized type of manufacturing has a high demand in numerous industries including biomedical, aerospace, automotive, and electronics (Mahamood & Akinlabi, 2017; Murr et al., 2012; NIINO et al., 1987; Saleh et al., 2020; L. J. Tan et al., 2020; X. Wang et al., 2017a; Yuan et al., 2019). M2 manufacturing is evolving as a key subprocess in Additive Manufacturing (AM). Within AM, laser sintering is one of the most likely techniques to have a future in industry producing operational plastic parts (Schmid & Wegener, 2016a).

A unique feature of M2 manufacturing is the ability to control the material in a particular location within a part. This is generally referred to as local composition control (LCC) and can be accomplished at varying levels of resolution between material types or blends and varying resolutions of dimensional accuracy. However, LCC can also be referred to changes in density or any other properties within a part. Compositions can also include one-dimensional, two-dimensional, or full three-dimensional control. Functionally graded material (FGM) manufacturing produces parts with changes in material properties throughout a part to meet specific end use requirements. FGM can include LCC but can also have gradients of other properties such as porosity, density, grain size, crystallinity, structure, etc (Saleh et al., 2020). The rise of additive manufacturing has made fine control of porosity and density relatively straightforward for many material types and structures. FGM with LCC can add incredible capability to a part and is commonplace in nature (Mahamood et al., 2012; Naebe & Shirvanimoghaddam, 2016). However, though the benefits and demands are high for LCC, it is still only an emerging capability in AM and other manufacturing techniques (*How Multi-Powder*

*Deposition Will Transform Industrial 3D Printing*, n.d.; L. Jepson et al., 1997; Saleh et al., 2020; Udupa et al., 2014).

Commonly known as 3D printing, AM is one of the primary methods for M2 part fabrication. M2 AM is rapidly advancing and has demonstrated success in direct energy deposition and PolyJet printing with limited advancements in Fused Filament Fabrication (FFF) and Powder Bed Fusion (PBF) (Bandyopadhyay & Heer, 2018; Bruck, 2017; Chianrabutra et al., 2015; Chueh et al., 2020; Greiner et al., 2017; Kennedy & Christ, 2020; Taylor Green & Taylor, 2018; Wei et al., 2019). Jepson et al. have had success in demonstrating basic LCC in polymer PBF with Nylon-11 (PA11) graded with three different concentration of glass beads and three different concentrations of silica (L. R. Jepson, 2002). This project focuses on expanding the M2 capabilities of polymer PBF by developing new Selective Laser Sintering (SLS) technologies and PBF material blends.

## **BROADER IMPLICATIONS**

This study is pertinent to numerous applications but was driven and framed by focusing on the future impact of two distinct subsets in the biomedical industry: M2 joint implants and M2 synthetic joints. Functionally graded artificial joints with LCC are poised to fill many of the voids in the current technology utilized for producing both joint implants and synthetic joints (Green, Ph, et al., 2021; Kurtz, 2011; Sola et al., 2016). LCC AM is hypothesized to increase the life, resilience, and functionality of orthopedic implants by decreasing wear and metal particles; increasing bone ingrowth and biocompatibility; and implementing patient specific isoelastic design. Additionally, customizable materials, properties, and functional gradients are hypothesized to increase the training effectiveness, value, and application of synthetic joints.

Human joint repair and joint replacement are some of the most common elective surgical procedures performed in the US (Sloan et al., 2018). Total knee and hip arthroplasty (TKA, THA) are the two most common joint repairs and are predicted to increase by over 70-100% in 2030 and again in 2040 if the current trend continues in the United States alone (Gao et al., 2020; Singh et al., 2019; Wolford et al., 2015). However, current implants are susceptible to misalignment, stress shielding, excessive wear, metallic wear particles, cement degradation, and septic loosening which result in a replacement rate of over 7% per year for all knee arthroplasty (American Joint Replacement Registry, 2019; Arnholt et al., 2019; Kurtz, 2019a; V. I. Roberts et al., 2007). This study seeks to address these issues by offering a twofold solution through functionally graded joint implants with LCC and new advancements in synthetic joints for training and research tools.

## **Joint Implant**

Functionally graded implants with LCC are a promising next step in increasing the life, resiliency, and functionality of orthopedic implants (Kurtz, 2012; Sola et al., 2016). Joint implants with binary material interfaces between multiple materials and functional coatings are currently being manufactured and used (Kurtz & Devine, 2007). However, the implementation of FGM with LCC will have distinctive benefits over the current technology. First, PBF lends itself to manufacturing dimensional patient specific implants from patient Magnetic Resonance Images (MRI) (Kang et al., 2018). Porosity and density control is also inherently built into PBF and adds significant capability for bone ingrowth through osseointegration when a lattice structure is functionalized with locally controlled embedded compositions of HA at the bone interface (Miao & Sun, 2010; Tampieri et al., 2001; Woodfield et al., 2005). LCC PBF also has the capability to

control the modulus of elasticity by manipulating the material and density at the core of the stem. There are multiple aspects that affect the elasticity throughout a bone structure making a true isoelastic implant design difficult; however, LCC PBF can adjust elasticity to approach an estimated isoelastic stem while maintaining the ability to have complex lattice structures around the stem at the bone interface. Through the isoelastic stem and functionalized lattice structures, a cementless design could be incorporated through osseointegration and bone ingrowth (Bonnheim et al., 2019; Byrne et al., 2007; Huiskes et al., 1992; Kurtz, 2019b; Pitkin, 2008). Implant wear and metallic or ultra-high-molecular-weight-polyethylene (UHMWPE) wear particles also deteriorate the life of a joint implant and can lead to septic loosening (Konttinen et al., 1997; Langton et al., 2009; Ollivere et al., 2009; Pandit et al., 2008; Pelclova et al., 2012; Revell et al., 1997; Veruva et al., 2017; Witzleb et al., 2006). Polyetheretherketone (PEEK) blended with carbon fiber (CF) has demonstrated encouraging results in decreasing wear and wear particles over UHMWPE, ceramic, or metal surfaces while increasing the longevity of the wear surface (Scholes & Unsworth, 2007, 2009; Song et al., 2018; A. Wang et al., 1999).

In total, a patient-specific functionally graded implant with an isoelastic core, a PEEK+HA latticed bone interface, and a PEEK+CF wear surface has promising potential to increasing the life expectancy, resilience, and functionality of orthopedic implants. A conceptual design of such an implant is described in Figure 1.1 below. This concept can be used for a total joint arthroplasty or can be used to replace a single side of an implant during a revision procedure.

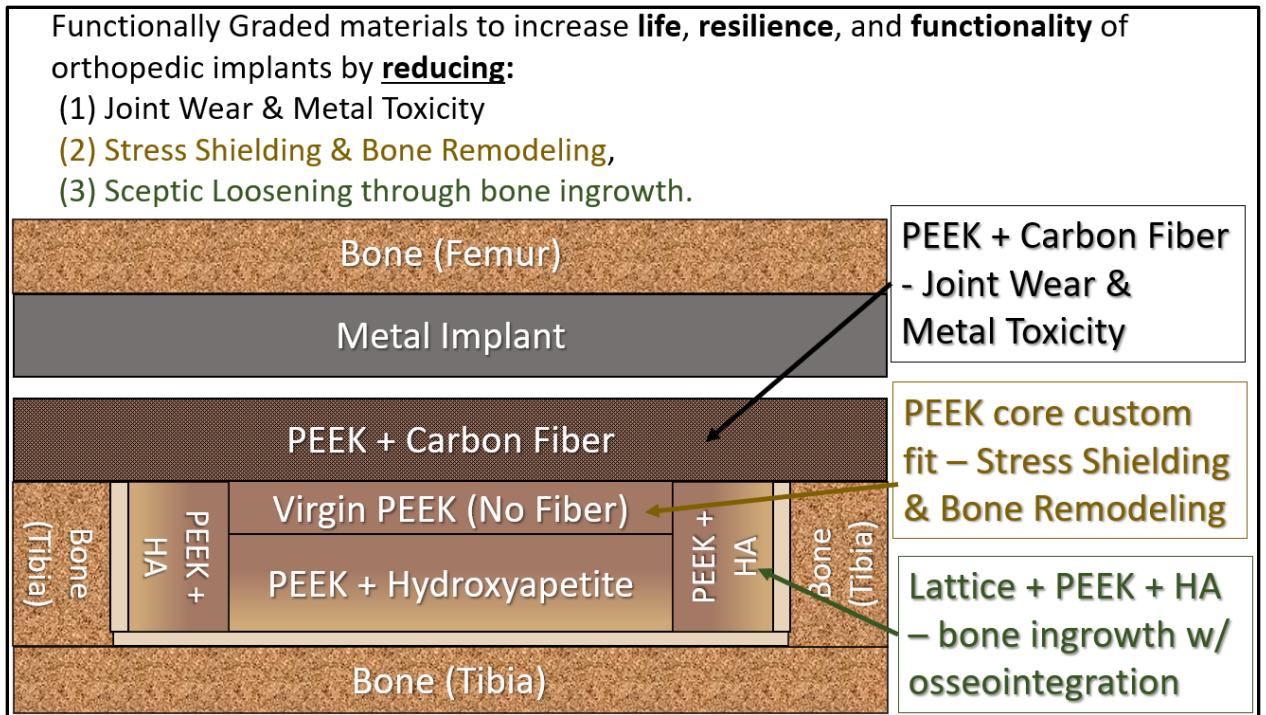


Figure 1.1: Benefits of a Multi-Material Tibial Orthopedic Implant Mated with a Traditional Metal Femur Implant

## Synthetic Joint

An equally critical element to implant design when increasing the life expectancy, resilience, and functionality of an implant is improving the surgical procedures and patient training for the implant. This component of implant life expectancy can be directly influenced through surgical training and research utilizing synthetic joints. Synthetic joints with physiological accuracy and biomimicry of both function and material properties is an emerging area of research for medical training and research. Many studies have shown 3D modeling and printing are poised to fill current technology voids in training and preoperative preparation for both the surgeons and patients (Alhonkoski et al., 2021; Jones et al., 2016; Zheng et al., 2016).

The learning curve, amount of effort verse amount of learning, is steep in surgical training. This is primarily based on the risk associated with surgery coupled with the precision

required to achieve desired patient outcomes on a spectrum from survivability to quality of life (Valsamis et al., 2018). Specific studies have already shown significant improvement in surgical training effort and results when anatomical models are used in conjunction with cadaveric materials and some limited success when used in place of cadaveric specimens (Langridge et al., 2018). Surgical training generally focuses on expert observation and repetition based on the potential high risk and precision required. However, synthetic joint training has a likely future in “error-observation” training which has been shown to improve training in novice students, especially when focusing on improving motor skills for different surgical procedures (LeBel et al., 2018). Currently the most limiting factors when using synthetic joints as opposed to cadaveric joints for training is the loss of weight, consistency, texture, color, tactile, and physical properties (Fleming et al., 2020; Lim et al., 2016). FGM synthetic joints with LCC can directly address these shortcomings while building on the success of the repeatability and quantifiability of the current 3D printed models used for training (Green, Ph, et al., 2021).

Another current shortcoming of arthroplasty that is well suited for synthetic joints is the difficulty associated with the anatomical uniqueness of each patient anatomy, injury, and/or disease. Surgical preparation for each patient’s unique anatomy is normally based on imaging such as MRI, CT, and ultrasound. The possibility of printing patient specific synthetic joints prior to a procedure based on the already existing imaging has the potential to revolutionize surgical planning and rehearsal. Some success with this technique has already been found with orthopedic surgeries and single material FFF and stereolithography (SLA) AM (Ganguli et al., 2018)(Jones et al., 2016). This type of physical modeling has not only helped the surgical team prepare for a procedure but has proven beneficial in teaching and preparing the patient (Liew et al., 2015). These same procedures can be expanded to teach both students and patients about

anatomy and different pathological diseases (Jones et al., 2016). This study looks to expand upon the initial successes of FFF, SLA and Polyjet AM synthetic joints by increasing biomimicry through LCC and FGM to bring a much broader perspective to synthetic joints as a training and preoperative planning tool. A simplified conceptional design and model of this vision is presented in Figure 1.2 below. The model was printed utilizing a FFF mixing printer (Provisional Patent 16/421,2273 (Gonzalez & Green, 2019)) capable of varying material properties by blending varying ratios of TP and TPE (Green, Slager, et al., 2021).

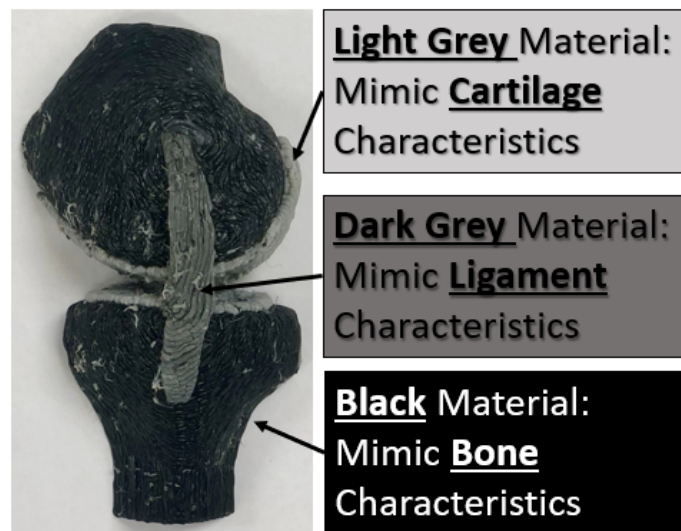


Figure 1.2: Synthetic Joint Prototype with LCC to Mimic Biological Material Printed on a FFF Mixing Printer (patent pending) in the Joint Laboratory at UTEP (Taylor Green & Taylor, 2018)

In addition, the potential research aspect of synthetic joints to influence future implant design and surgical protocols cannot be overlooked. Robust synthetic joints have the potential to open data analysis and collaboration between researchers and developers worldwide that is not currently viable with cadaveric or patient studies. Synthetic joint surgeries and testing coupled with in vitro testing can quantitatively and repeatably compare surgical techniques and implant hardware. Cadaveric studies with the University of Texas at El Paso Joint Load Simulator

(UTJLS) and testing with LCC femoral ACL tibial complex (FATC) specimens has already demonstrated future feasibility and impact of this type of research (Green et al., 2017; Green, Ph, et al., 2021; Hale et al., 2018; Leu et al., 2012). The impact of this type of research and testing using fully functional synthetic joints will ultimately increase the performance of joint implants. This project seeks to increase the capabilities of AM through LCC to overcome current limitations and work towards fully functional synthetic joints.

In summary, this study will help lay the foundation for new technology in AM required to achieve the necessary biomimicry in synthetic joints while maintaining repeatability required for quantifiable and repeatable feedback. Ultimately increasing the life expectancy, resilience, and functionality of future implants through the following three advancements. First, synthetic joints that can be used to give repeatable and quantifiable results to surgical students (Figure 1.3). Second, patient specific synthetic joints prior to surgery for training, fitting, and rehearsal that cannot be realized through imaging alone. Third, standardized synthetic joints for hardware and procedural research capable of repeatable feedback between surgical techniques and equipment (Figures 1.4).

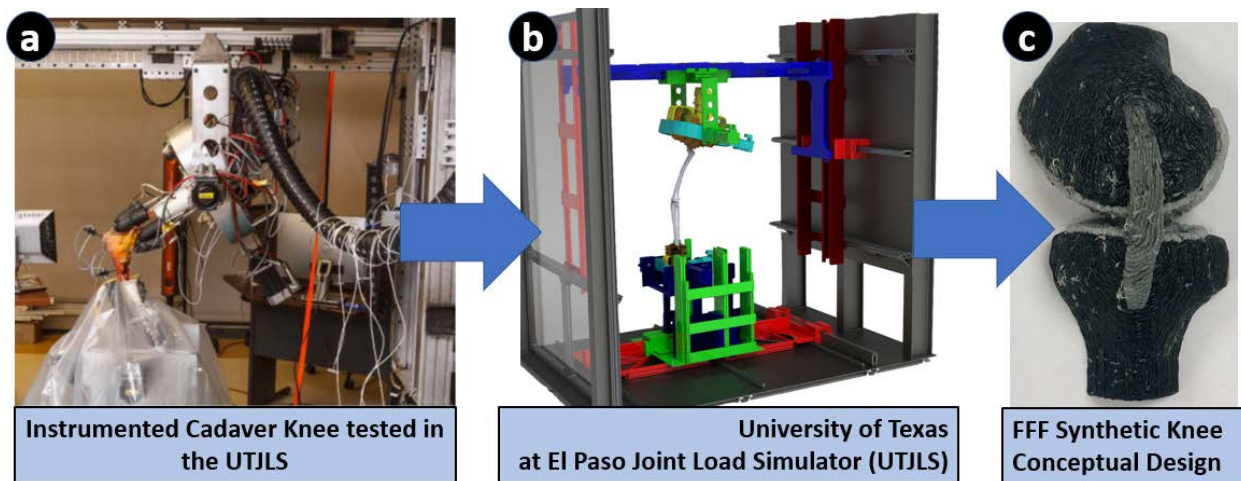


Figure 1.3: Possible testing process to develop more realistic synthetic joints for surgical simulation. (a) Instrument cadaver knee to quantify internal loads and load response of a human knee (Hale, 2016; Hale et al., 2018; Taylor Green & Taylor, 2018). (b) Quantify joint loadings during movement (Green et al., 2017). (c) Conceptual design implementing biological material properties with musculoskeletal based on cadaveric load response (Green, 2018; Green, Ph, et al., 2021)

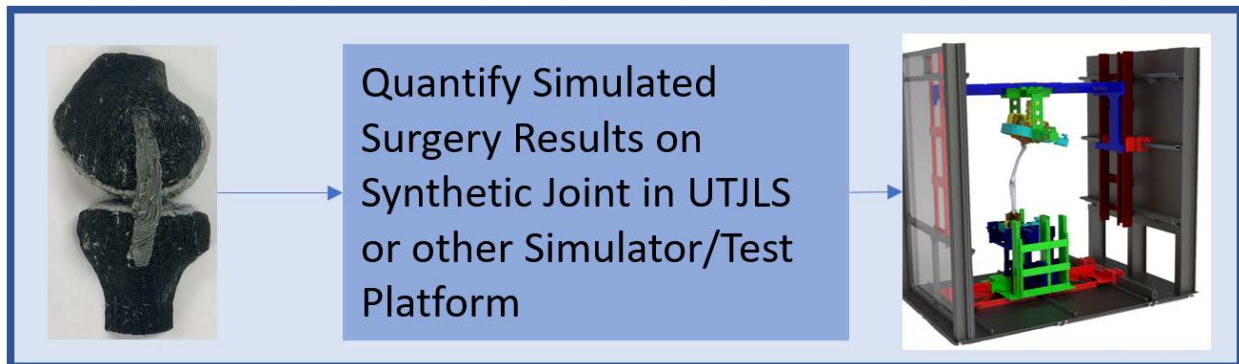


Figure 1.4: Conceptual Synthetic Joint Study Showing Possible Comparison and Research Methods (Green et al., 2017; Hale et al., 2018)

## BACKGROUND AND SCOPE

M2 SLS research has had a strong focus on multi-powder delivery systems. Small pipette hoppers have been studied as a way to selectively dispense powder but have not been operationally integrated into a Selective Laser Sintering (SLS) system (Santosa et al., n.d.). Applying multiple powders with a more traditional recoater or spreader from reservoirs on the same plane as the build area or from vertical dispensing reservoirs above the build area have also been studied but have yet to be shown operationally feasible or produced (Chivel, 2017; Forderhase & Deckard, 1993; Stucker et al., 2014). SLS design with a single chamber or reservoir on either side of the build plate has been proposed (Forderhase & Deckard, 1993; Stucker et al., 2014). However, there is no method to maintain the proper powder refresh ratio or avoiding powder cross contamination. Other approaches utilize a two-chamber recoater to dispense multiple powders on a single layer and have been more developed (Chivel, 2017; *How*

*Multi-Powder Deposition Will Transform Industrial 3D Printing*, n.d.; Laumer et al., 2016; Whitehead & Lipson, 2020).

The M2 SLS research demonstrated in this project focused on developing a novel SLS system capable of sintering a different material each layer with the future capability of sintering multiple materials in a single layer. M2 capability is introduced using multiple reservoirs with a powder extraction stage incorporated into the SLS process. The powder extraction stage is combined with a custom powder dispensing algorithm and innovative laser control with an extensive thermal management system which collectively allows multiple materials to be sequentially sintered (printed) on a single layer. Blends of thermoplastic, thermoplastic elastomer, fiber, and particulate particles were mechanically blended and tested for sinterability to facilitate M2 printing. Lastly, mechanical tensile and fracture characterization was performed on nylon-12 (PA12) + carbon fiber (CF) M2 specimens with z-axis controlled binary interfaces and gradients.

**These research goals were achieved through the following four specific aims:**

1. **AIM 1:** Design and build novel multi-material (M2) Selective Laser Sintering (SLS) system capable of Local Composition Control (LCC).
2. **AIM 2:** Investigate variations of thermoplastic (TP) powders, thermoplastic elastomer (TPE) powders, fibers, and particulates blend ratios for compatibility in low temperature and low energy density powder bed fusing (PBF) applications using a Selective Laser Sintering (SLS) System with a 455 nm, 1.8-5.1 W diode laser in an air chamber.
3. **AIM 3:** Characterize stress-strain and fracture data for novel TP/fiber blends using scaled type V tensile test specimens and Single Edge Notch Tensile (SENT) specimens additively manufactured (AM) via the M2 SLS prototype created in Aim 1.

4. **AIM 4:** Characterize stress-strain, fracture, and material interfaces using SENT specimens with one-dimensional (1D) binary material interfaces and gradients in the build direction (z-axis) using selected blend ratios of PA12/CF from Aim 3 and printed on the M2 SLS prototype created in Aim 1.

#### **LIMITATIONS TO SCOPE AND RECOMMENDED FUTURE RESEARCH**

The overall scope of this study was to characterize the feasibility of functional gradients in polymer PBF using mechanically mixed polymers, fibers, and particulates. Thus, the following items were not studied and should be considered for future investigation based on the results of this research:

1. Characterization of polymer chemical composition, chain structure, and bonding mechanisms of the materials blended and sintered.
2. Crystallization characterization of polymers due to immiscible blending of fibers and particulates
3. Compression, bending, wear, fatigue, and other mechanical testing of M2 SLS specimens.
4. Specific interface and gradient characterization such as interface bond strength, fiber orientation and density, and gradient resolution.
5. Analytical and computational analysis simulations and predict M2 SLS properties and performance based on the experimental results from this research.

Experimental materials and results were based on the developed M2 SLS prototyped and constrained by the following design characteristics of the prototype:

1. Ambient air chamber with a maximum temperature of 180 degrees Celsius

2. 90 x 90 x 90 mm cubic build area.
3. 455 nm wavelength LED laser with a maximum power output of 5.1 watts.
4. Focused laser diameter of ~0.1 mm.
5. Layer height of ~0.1 mm with material applied via a non-rotating rake.

These prototype features limited material testing to low temperature nylon matrix material for CF and HA composites or TPE blends. Material energy absorbance at 455 nm wavelength necessitated the blend be grey to black in color. Material size with a maximum single edge length of approximately 0.1 mm.

## Chapter 2: Objectives

The overall objective of the research was to add an additional user-controlled material property option to an already highly customizable SLS manufacturing method and investigate the effects of this addition on AM parts. The success of sequentially sintering or coalescing (joining and solidifying) powder by selective laser heating hinges on the varying powders having similar softening and melting temperatures and consistent thermomechanics throughout the spectrum of temperatures during the sintering process. The entire AM process is designed around the general thermodynamic flow of rapid heating, rapid cooling, remelting or sintering, and gradual cooling (Merzelis & Kruth, 2006a). This process produces the majority of both the successes and the challenges of AM and is exacerbated with varying thermomechanical properties of multiple materials. The thermal gradients produced by the laser energy or directed heat source inherently cause uneven material shrinkage resulting in residual stress, cracking, voids, and part deformation (DebRoy et al., 2018a). The uneven shrinking is intensified when multiple materials with varying thermal properties are involved. Previous experimental and analytical research has focuses on understanding and ultimately mitigating defects in single material parts by controlling the following parameters: ambient and substrate temperature; direct and indirect part heating; beam type, shape, size and speed; and post processing treatments (Anand & Gerner, 2014; Q. Chen et al., 2017a; Gusarov et al., 2011a; Merzelis & Kruth, 2006a; I. A. Roberts, 2012a; Yadroitsev et al., 2010; Y. Zhang et al., 2018). Normally any parameter that can decrease temperature gradients will decrease shrinkage, internal stresses, and final part defects. The primary objective of Aim 1 was to design a system capable of maintaining thermal consistency during material changes from both internal and external sources. Currently a 3D printing user can readily modify the geometric shape and density. The second objective of Aim 1 added an

additional user-controlled parameter to allow the user to also implement multiple materials, material interfaces, and material gradients when printing a part. Part of this implementation included M2 anchoring to allow fixing or anchoring a part to a warping resistant based material. This facilitated printing geometries and/or materials not normally possible because of warping and subsequent sledding during the recoating process. The subsystems, corresponding processes, and tunable parameters to enable the first two objectives are outlined in Figure 2.1. The single subsystem highlighted in red (Remove Unfused Powder from Current Build Layer) is included in the design but is not implemented in the prototype built and tested for this project. This inherently limited the scope of material gradient testing (Aim 4) to one dimensional material changes in the build direction.

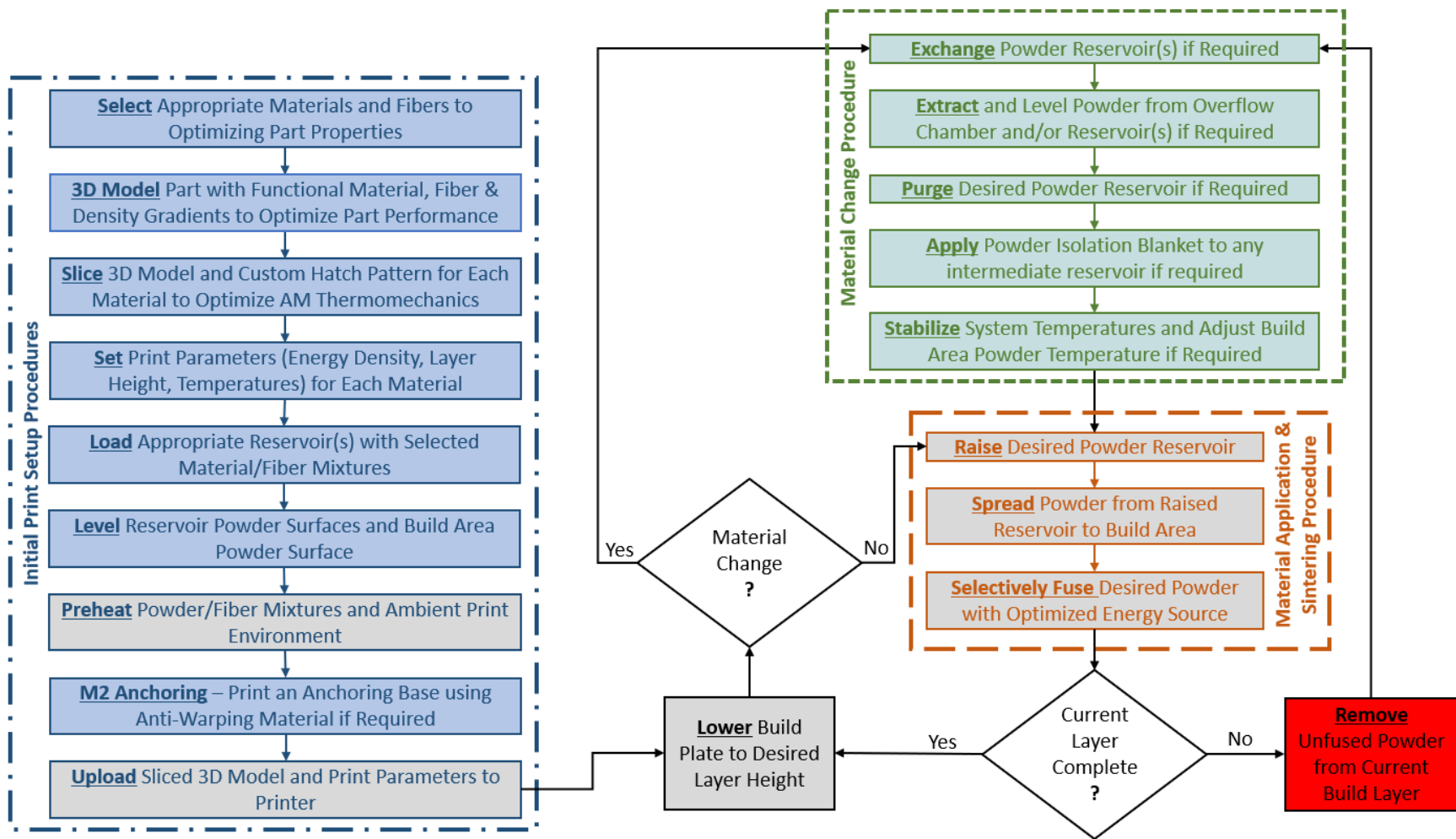


Figure 2.1: Multi-Material (M2) Powder Bed Fusion (PBF) printing process with associated subsystem. “Material Application and Sintering Procedure” is common to single material PBF systems. “Material Change Procedure” and procedures highlighted in blue un “Initial Print Setup” are unique to the M2 PBF design developed in this research

Aim 1 established a foundation to customize material properties and gradients for a specific end use when manufacturing parts via PBF. However, compatible materials with similar thermomechanical properties were critical to the success of the initial objective. The objective of Aim 2 was to find and test compatible materials and determine compatible sintering parameters across multiple blends of thermoplastics, thermoplastic elastomers, and composites with fibers or particulates mechanically blended into the powder mixture. Material blends were also specifically selected based on compatibility with the M2 SLS prototype developed in Aim 1.

Aims 3 and 4 objectives transitioned into the tensile and fracture characterization of printed parts from the first two aims. The objective of Aim 3 was to determine tensile and crack growth properties of varying PA12/CF blends established in Aim 2. Hardness and density characteristics were also evaluated to quantitatively compare properties associated with changes in CF infill volume. The objective of Aim 4 was to quantify the tensile strength and crack growth of SENT specimens to evaluate interface and gradient interactions of M2 specimens. Both binary and gradient material interfaces using select PA12/CF blends from Aim 3 printed using the M2 SLS prototype and parameters found in Aims 1 and 2 will be evaluated.

All four Aims and corresponding hypotheses of this study are outlined in the following section.

## **AIM 1**

Design and build novel multi-material (M2) Selective Laser Sintering (SLS) system capable of Local Composition Control (LCC). Characterize and tune the following novel subsystems of the M2 SLS:

1. Custom slicing program capable of the following M2 specific functions:

- a) Assign different materials to different portions of the part. (i.e., planning a M2 print).
  - b) Assign different hatch patterns to different materials to adjust energy density and maintain a uniform sintering depth and cross section area across multiple materials within a single print (i.e., sinter different materials at different temperatures to help materials bond evenly).
  - c) Assign different geometric scaling to different materials to adjust for each material's geometric shrinking when sintered. (i.e., sinter different materials at different scaling to maintain a constant overall part geometry).
2. Multiple reservoirs capable of powder extraction out of the system and powder addition into the system during a continuous print (i.e., reservoirs to add or subtract powder during print).
  3. Multi-material layer application capable of material changes within the system between internal reservoirs (i.e., switching materials internally).
  4. Thermal management system with multiple heating sources throughout the system capable of independently controlling the bulk powder temperature, top layer temperature, and ambient temperature during sintering, powder extraction, and powder addition. Thermal management system must maintain homogeneous temperatures differentials for multiple materials within a single print (i.e., temperature control capable of independently controlling different sections of the system during sintering and while exchanging material).
  5. Part anchoring capable of minimizing warping and dimensional instability between material types while maintaining printability and scalability (i.e., fixing or anchoring).

6. Control of multi-material operations from a single user interface (i.e., printing program with control interface for above items).

### **Aim 1 Hypothesis**

Aim 1 was founded by the hypothesis that a M2 SLS system could be designed and developed if the following systems are incorporated:

1. Print planning and slicing based on multiple materials capable of assigning the following unique parameters to each material as opposed to the same setting for the entire print would allow different powders and/or mixtures to coalesce into a single part:

- a) 3D models for each material allowing a single layer to be divided into multiple parts each corresponding to a user defined material.
- b) Hatch pattern that maintains consistent time between neighboring laser passes with galvanometer movements that keep laser acceleration and deceleration zero between laser on and off operations coupled with laser power changes for each different material will result in consistent sintering between each layer with material and thermomechanical changes from layer to layer.
- c) Scaling factor for each material that results in a constant sintered dimension.

2. Lowering a reservoir well below the top layer height would sufficiently isolate the print area to allow for powder exchange to and from the system while avoiding powder cross contamination.

3. Powder isolation through a powder blanket and subsequent powder purging would prevent cross contamination and thermal shock when changing intra-prints materials internal to the system.

4. Five independently controlled ambient heaters, five independent bulk powder heaters and three print area top layer heaters would be capable of maintaining sufficient thermal stability during powder extraction and addition to preventing thermal shock to the sintered part during powder exchanging.

5. Part anchoring would minimize part warping and sledding when sintering parts with varying materials and thermomechanics within a single print while allowing for large cross-section parts and scalability.

6. Printer user interface would allow user to stop print for external material changes and adjust real time parameters when switching sintering from one material to another.

## **AIM 2**

Investigate variations of thermoplastic (TP) powders, thermoplastic elastomer (TPE) powders, fibers, and particulates blend ratios for compatibility in low temperature and low energy density powder bed fusing (PBF) applications using a Selective Laser Sintering (SLS) System with a 455 nm, 1.8-5.1 W diode laser in an air chamber.

### **Aim 2 Hypothesis**

Aim 2 was founded by the hypothesis that mechanically blended TP powders with fibers, particulates and TPE could produce a homogeneous mixture capable of producing a consistent layer height when applying powder blends during PBF and the blend could be customized and additively sintered to produce parts with tailored material properties.

## **AIM 3**

Characterize stress-strain and fracture data for TP/fiber blends using scaled type V and SENT tensile test specimens additively manufactured in the M2 SLS prototype.

### **Aim 3 Hypothesis**

Aim 3 was founded by the hypothesis that hardness and tensile material properties would be enhanced (increase with CF) with the increase of blended material up to a certain blend ratio and then quickly deteriorate based on increase porosity, material clumping, and laser reflectivity with an increase of blended material. This would change based on the intended application, but the deterioration point for PA12 blends was hypothesized to be at 10% for CF additives.

### **AIM 4**

Characterize stress-strain, fracture, and material interfaces using SENT specimens with one-dimensional (1D) binary material interfaces and gradients in the build direction (z-axis) using selected blend ratios of PA12/CF from Aim 3 and printed on the M2 SLS prototype created in Aim 1.

### **Aim 4 Hypothesis**

Aim 4 was founded by the hypothesis that functionalized gradients will decrease failures and increase strength at material interfaces resulting in increased ultimate tensile strength of multi-material specimens approximately 5-30% for parts with large variations in modulus of elasticity (E) between material blends.

## **Chapter 3: Aim 1 - Design and Build Novel LCC Selective Laser System**

### **INTRODUCTION**

Aim 1 of the research designed, built, integrated, and tested required subsystems to achieve functional material gradients in Powder Bed Fusion (PBF) Additive Manufacturing (AM). The designed subsystems were integrated into a Selective Laser Sintering (SLS) system to build a low-temperature Local Composition Control (LCC) SLS prototype. The prototype was constructed to demonstrate multi-material (M2) print parameter modeling and preparation; material exchange and movement; thermal consistency and gradients; part sintering and build stability; and user interface and control. Overall, Aim 1 research proved the feasibility of this type of M2 PBF technology and provided a prototype to print specimens for the remainder of the research.

### **BACKGROUND**

Many AM techniques and processes are designed around the material thermomechanics and the general thermodynamic flow of rapid heating, rapid cooling, remelting/re-sintering, and finally gradual cooling. These processes produce the majority of both the successes and the challenges in PBF (J.-P. P. Kruth et al., 2004). Combining or mixing materials with dissimilar thermal properties in PBF generally exacerbates these challenges.

Part defects in PBF are normally due to the uneven heating and cooling of the material necessitated by the AM process. Thermal gradients inherently cause uneven material shrinkage for most metals and polymers used in PBF resulting in residual stress, cracking, voids, and deformation. Research and published literature indicate substantial work is needed to fully understand these topics with metal PBF (DebRoy et al., 2018b; Sames et al., 2016). Though most of this work focuses on metal PBF which generally require the most extreme temperature

gradients, the findings can be applied to polymer PBF or SLS. Powder Bed Fusion research has been done experimentally, analytically, and numerically to better understand and ultimately mitigate defects in the final parts primarily by controlling the following parameters: system temperatures, heating techniques, beam parameters, and post-processing treatments (I. A. Roberts, 2012b). The primary system temperature variables are ambient and substrate temperature. Primary heating techniques are direct and indirect part heating. Laser beam parameters are generally defined by type, shape, size, and speed. Post-processing treatments can reduce internal stress and provide density control. All of these parameters affect each other and are blended to melt or sinter the desired powder while simultaneously integrated to mitigate part defects.

Integrating M2 capability into PBF complicates the thermodynamics for most of the required processes. Required M2 functions such as material purging, material isolation, or material exchange by concurrently spreading relatively large volumes of powder (3-4 times the volume required to spread a single layer) creates thermal disturbances in the system. Even in an enclosed and thermally isolated system these disturbances can affect the print process, especially when the print area top layer powder temperature is inadvertently affected. However, also maintaining top layer temperature near the material's melting point (required for selective melting or sintering) for extended periods to accommodate process other than lasing or melting (i.e. M2 material exchange) can also have detrimental effects on PBF systems. Systemic thermal disturbances or delays are exacerbated when powder is removed or added from external reservoirs. M2 subsystems must be designed to mitigate the thermal disturbances, delays, and subsequent effects to minimize part defects while maximizing cross material sintering. Part defects associated with thermal disturbances and/or delays during printing generally include part

warping, dimensional inaccuracy (i.e., over sintering of surrounding powder), cracking, increased porosity, and decreased part strength.

Regulating ambient/chamber, substrate/bed, and powder temperatures have been some of the most effective methods to mitigate internal stresses (Ester et al., 2011; Gusarov et al., 2011b). An additional technique that is commonly used in metal PBF is part anchoring because of the comparatively high temperatures and thermal conductivity compared to polymer PBF. Anchoring normally involves sintering/melting a connecting lattice structure directly to the build plate and the printed part. Anchoring is not normally used in polymer PBF because of lower temperatures and insulating properties of polymer materials. Thermal control and anchoring methods are exceptionally useful because they are divorced from the primary beam adjustments used to ensure fully sintered or melted parts required for density and layer adhesion. However, cross section and total part customized hatch patterns as a supplemental method has also proven effective to minimizing thermal gradients on the sintered surface and within the part being printed (Steuben et al., 2016b)(Steuben et al., 2016a).

Based on the discussed research, seven unique functions were identified to integrate M2 functionality into PBF with over half focusing on minimizing temperatures gradients and the effects of thermal shock when switching materials. It was hypothesized that implementing the following seven functions would enable successful M2 SLS printing (see Figure 3.1 below for a block diagram depicting overall M2 print process and location of the M2 functions):

**Function 1:** Prepare a M2 print through functionally graded models by assigning specific slicing parameters to each material in the model.

**Function 2:** Tailor hatch and energy density parameters for each material during printing and adjust real time at each material change.

**Function 3:** Isolate build area and maintain strict thermal gradients during all operations.

**Function 4:** Move powder into and out of the system.

**Function 5:** Spread/coat multiple materials onto the build area.

**Function 6:** Fixate parts to stabilize part to <0.1 mm of movement during entire sintering process.

**Function 7:** Interface functions 1-6 with the end user through controls and automated algorithms.

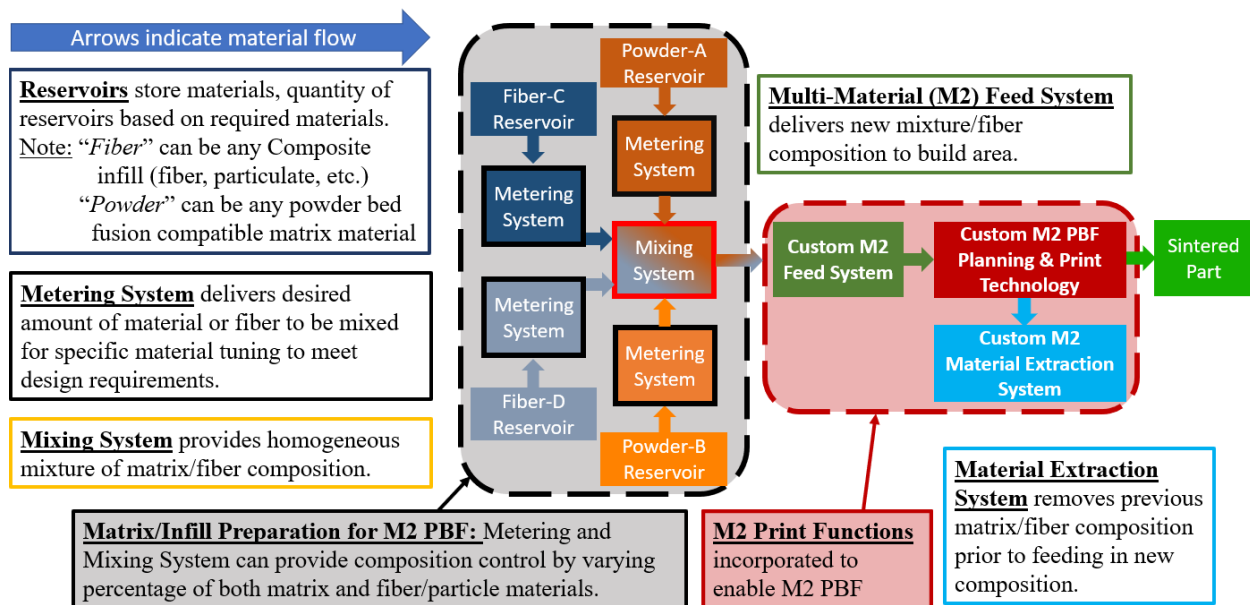


Figure 3.1: Block diagram depicting material flow in M2 PBF. Matrix/Infill Preparation (grey section) can be accomplished internally or externally to the system and can be automated or manual. Print control (red section) contains the hypothesized functions to incorporated M2 into PBF

## METHODS

The methods to integrate the seven unique M2 functions hypothesized to sinter functional material gradients were realized through seven novel subsystems. Each subsystem was tied to the method required to accomplish the corresponding M2 function identified in the previous section.

An operational and communication flow chart depicting the subsystems required to accomplish the unique M2 methods are highlighted in Figure 3:2 below.

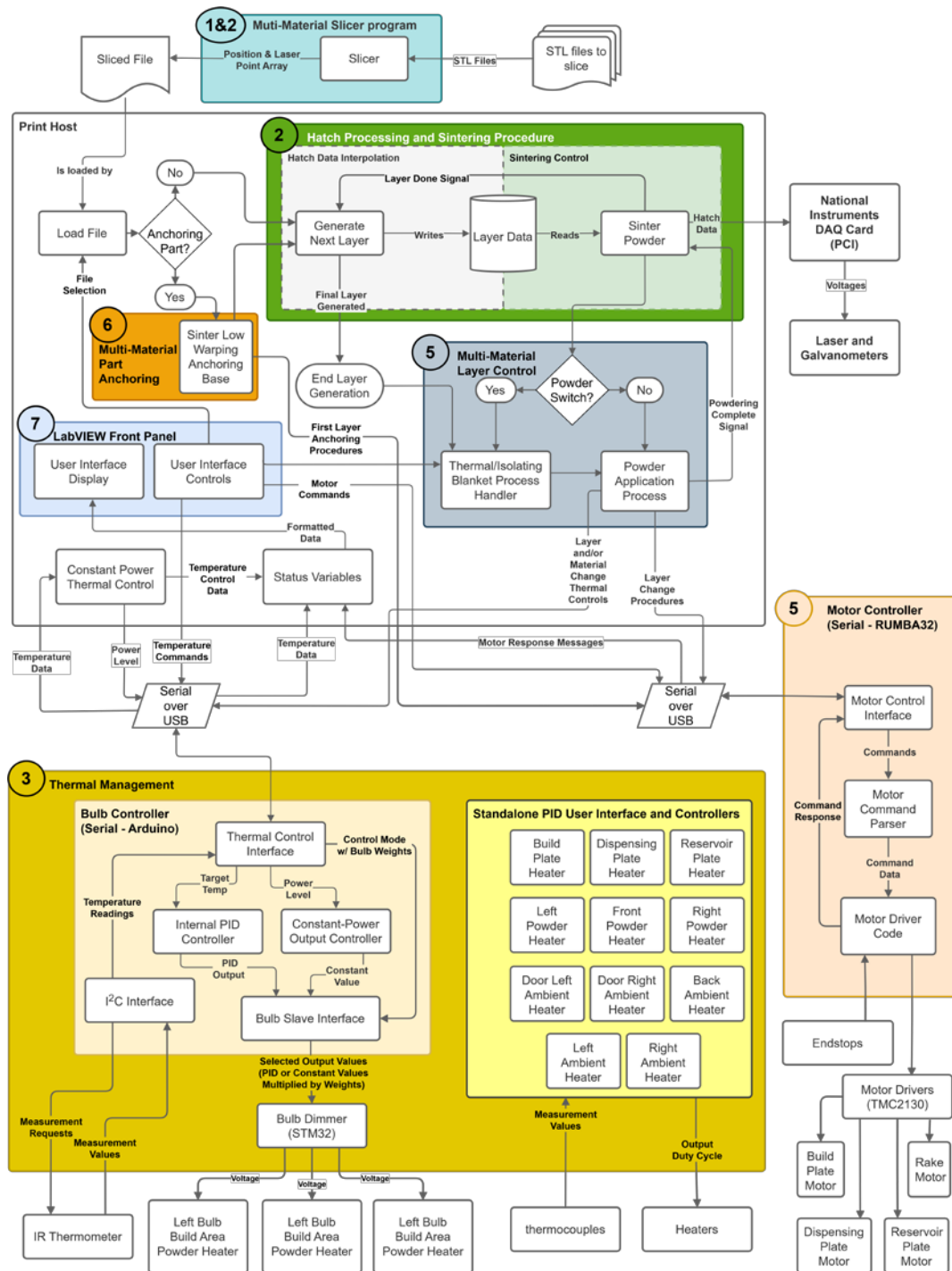


Figure 3.2: Multi-material SLS operational and communication flow chart highlighting the methods to accomplish the seven critical M2 Subsystems. General (overlap exists) subsystem execution designated by color and associated subsystem number

A description of the required tasks for each novel subsystem including hypothesized acceptance criteria are detailed below. Figure 3.2 illustrates how tightly integrated each subsystem was with the other subsystems and with the overall system. As such, acceptance criteria for each subsystem inherently depended on system integration and the simultaneous performance of multiple subsystems. Globally, all acceptance criteria were ultimately based on the ability of the system to effectively print M2 parts. Effectively printing was defined as printing without runtime errors, warping  $< 3\%$ , and dimensional accuracy  $< 3\%$ . Sintering acceptance criteria of sintered blended materials was defined as  $< 10\%$  of neat PA12 type V samples printed in a commercially available Sintratec Kit SLS printer (also inherently tied to the acceptance criteria of Aim 2). These results were also compared to published manufacturing data for neat PA12 powder. The following novel subsystems were designed to enable the hypothesized functions required to implement M2 capability into PBF:

### **Subsystem 1: Multi-Material Slicer**

Accomplishing M2 manufacturing requires a method to integrate M2 design into the manufacturing planning process. LabVIEW was used to incorporate M2 planning by developing a custom slicing program capable of accepting multiple Standard Triangle/Tessellation Language (STL) files, each of which can be assigned a different material. Each material type was loaded as a separate STL file (Figure 3.3). For clarity, the different STL files are discrete parts in Figure 3.2; however, for an M2 part the STL files are joined into a single part.

#### ***Acceptance Criteria***

1. Define individualized hatch patterns and parameters for each material type.
2. Pause sintering between defined material types when printing a M2 sliced file to allow sintering parameters and material to be autonomously or manually changed.

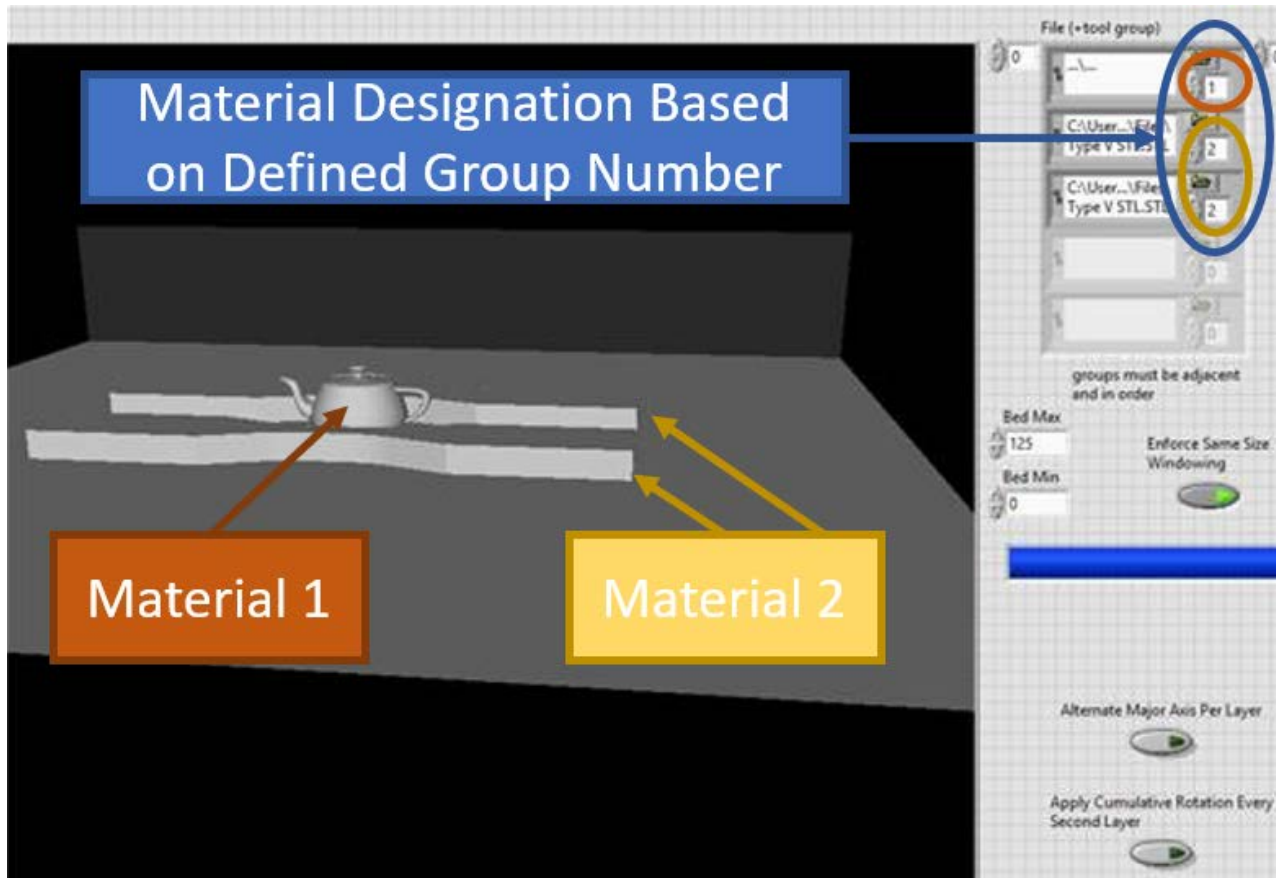


Figure 3.3: Multi-material slicer with material designation of each part delineated based on color and defined on the right side as a different group. For clarity, the different STL files are depicted as discrete parts; however, for an M2 part the STL files would be joined into a single part

### Subsystem 2: Multi-Material Hatch & Layer Energy Density Control

Hatch pattern, coupled with the laser intensity and triggering, influences the material bonding, isotropy, part defects, and density of the final part primarily due to temperature gradients during laser movements (Pinkerton, 2016; I. A. Roberts, 2012b; Steuben et al., 2016b). A system to adjust ambient, powder, and top layer temperatures coupled with laser speed, power, and pattern every time there was a material change was designed to meet each material-specific requirement to achieve effective intra-material and cross material bonding. This capability was

programmed through multiple LabVIEW subroutines. The specific capabilities and associated methods incorporated into each LabVIEW subroutine are defined below:

1. **Galvanometer speed control** that minimizes accelerations and decelerations during galvanometer movements (Figure 3.4).

2. **Hatch pattern control** that minimizes thermal gradients during laser movements.

Many available hatch patterns cause uneven thermal gradients across the part cross section based on inconsistent timing between neighboring rasters coupled with inconsistent laser velocity based on raster length (Wörz & Drummer, 2018a).

Galvanometer accelerations and decelerations were eliminated during laser triggering while maintaining constant time between individual laser rasters (Figure 3.5).

Integrating print efficiency to minimize layer sintering time and total part build time were considered to minimize the time the part and powder are at elevated temperatures to prevent excessive material degradation and preserve powder reuse options. Different proposed and tested techniques are described in Figure 3.6. Further details on alternate hatch patterns can be found in Appendix B.

3. **Intra-print sintering control** that adjusts ambient temperature, powder temperature, top layer temperature, laser speed and laser powder to match material changes.

### *Acceptance Criteria*

Overall, the completion of this subsystem was measured as part of the whole system's capability to sinter M2 parts without printing failures such as part sledding or separation between material types. Hatch patterns were assessed based on:

1. Cross section sintering completeness.
2. Energy density homogeneity.

The success of different methods were first evaluated by lasing varying mediums such as wood, cardboard, and paper. Second, subsystem were considered complete when ambient, powder, and top layer temperatures along with laser speed, power and pattern could be adjusted mid-print or intra-print when a material change was triggered.

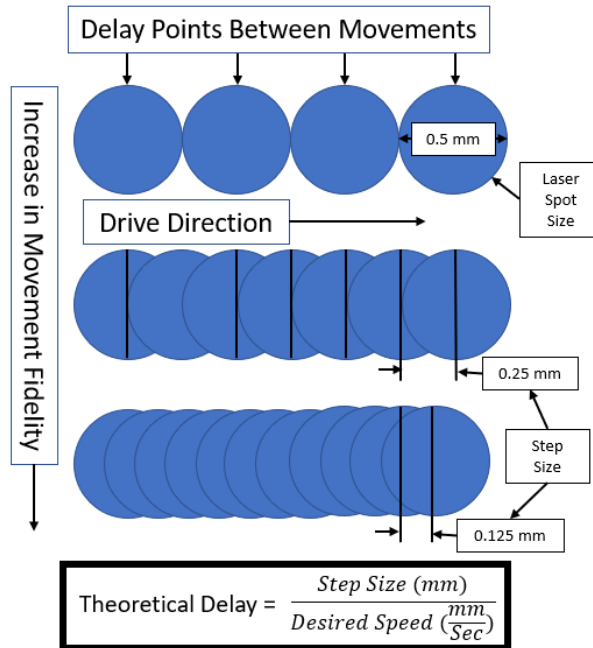


Figure 3.4: Programmed Galvanometer Speed Control

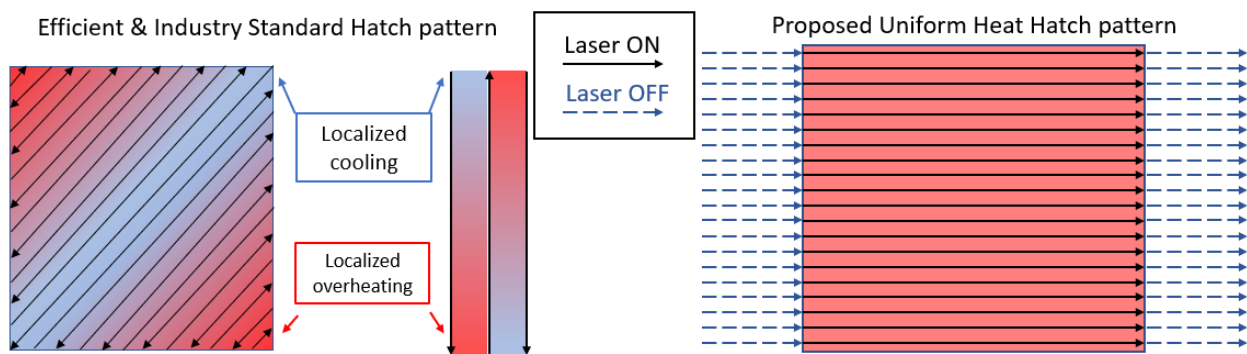


Figure 3.5: Comparison of Hatch Pattern Thermal Gradients

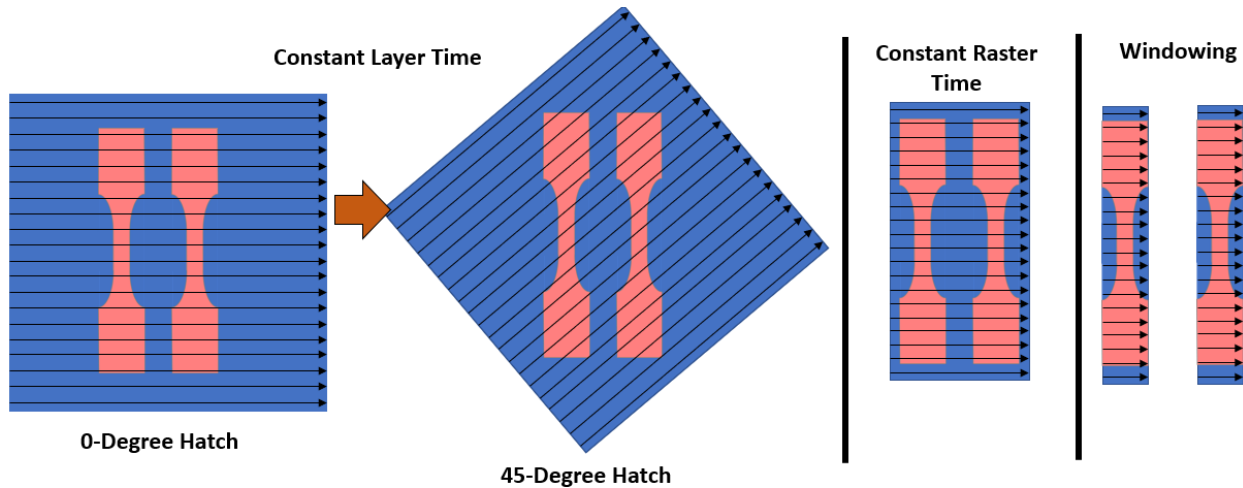


Figure 3.6: Proposed Hatch Pattern to Integrate Both Thermal Homogeneity and Sinter Efficiency

### Subsystem 3: Multi-Material Thermal Management System

Temperature gradients are critical to the SLS process; however, unintended, or inaccurate temperature gradients during the sintering process result in part defects or print failure. The methods of this subsystem specifically addressed maintaining intended and stable temperature gradients during M2 processes.

Many of the required M2 processes caused thermal and physical disturbances in the system resulting in uncontrolled temperature gradients. The primary M2 processes resulting in temperature disturbances were:

1. **Spreading more than a single layer of powder** (while isolating or purging a specific material) that moved powder below the heated top layer powder.
2. **Introducing powder into the system** that may be at a nonhomogeneous temperature or at a different temperature from the system.
3. **Removing powder from the system** that instantly decreased the volumetric heat capacity associated with the heat stability of the system.

4. **Introducing external air currents** into and out of the system that were not consistent with the temperature of the internal chamber.
5. **Creating internal air currents** within the system that mixed the intentionally maintained ambient air gradients within the system.

The methods of this subsystem directly stabilized temperatures throughout the system. Fourteen individually controlled (Proportional Integral Controller (PID)) heat sources with low thermal momentum were used to set and maintain ambient, bulk powder, and top layer temperatures. This type of system was implemented to decrease system reaction time and isolated disturbances. Fourteen heaters were used to heat specific areas while maintaining constant temperature in the remaining portions of the system during M2 operations involving powder movement into and out of the system. Three Top Layer Direct Heaters were controlled via a PID Controller within the M2 SLS Host (with individual weights for each IR heater) and all other heaters controlled via independent PID controllers. The selected location of the heaters are shown in Figure 3.7 and 3.8. Thermal gradient control specific to M2 operations for each heater location is described below:

1. **Top Layer Direct Heaters** heated the top powder layer in the build chamber via three halogen bulbs. These bulbs were independently weighted to allow thermal tuning of top layer temperatures and ensured a consistent temperature throughout the entire part cross section during sintering.
2. **Back System Ambient Heater** stabilized temperatures at the chamber linear rails along the back of the system.
3. **Build Area Ambient Heaters** maintained ambient air temperature surrounding the part just below the softening temperature of the current top layer material. These

heaters were specifically placed to allow a new ambient temperature to be set during a material change to accommodate varying softening temperatures while minimally affecting the other temperatures in the system.

4. **Dispensing and Reservoir Ambient Heaters** maintained a lower temperature than the Build Area Ambient Heaters to maintain powder granularity prior to spreading. The rake and heat deflector on the rake were positioned between the build area and dispensing plate when not spreading powder to aid in maintaining the required temperature gradient between the build area (relatively high temperature) and the rest of the internal ambient environment (relatively low temperature).
5. **Build Area Bulk Powder Heater** maintained the powder surrounding the sintered part at a constant temperature during powder extraction and addition.
6. **Dispensing and Reservoir Bulk Powder Heaters** aided in quickly stabilizing the temperature of powder added into the system.
7. **Front System Bulk Powder Heater** maintained the temperature at the front of the chambers when powder access doors were opened for powder extraction from the system or powder addition into the system.
8. **Build Plate Heater** locally maintained the temperature of the first layers of a print to facilitate part dimensional stability and reduce warping during the build process. If required, this heater also locally raised the temperature of the anchoring material.
9. **Dispensing Plate Heater** aided in quickly stabilizing temperature of powder added into the system.

### *Acceptance Criteria*

Time, location, and part cross section area all influenced this subsystem's effectiveness and thus influenced the acceptance criteria. Different areas were sensitive to different types of temperature changes and the entire system was more susceptible to print failures during the first 10 layers and with large sintered cross sections. It was hypothesized that the sintered part could tolerate a 5° C overshoot above intended temperature in the build area (both ambient and powder). However, as little as a 2° C drop for parts with large cross-sectional areas at the beginning (< ~10 layers) caused unacceptable (i.e. print failure) warping. The reservoir area was sensitive to temperature spikes and a 10° C overshoot could cause slight sintering of the powder in the reservoir or dispensing chambers which resulted in powder clumping and uneven spreading and/or print failure. It was also hypothesized a temperature drop in this powder would not affect the overall operation of the system if the powder temperature was eventually stabilized at the correct temperature prior to spreading the next layer. The following completion criteria were based on these general parameters during all operations with special attention given to M2 operations (temperatures tolerances were intended to mitigate warping affects):

1. Build bulk powder thermal fluctuations within -2 to +5° C with thermal gradients < 2° C.
2. Build area ambient thermal fluctuations within +/-5° C with thermal gradients < 5° C.
3. Build area top layer powder thermal fluctuations within -2 to +2° C with thermal gradients < 1° C.
4. Dispensing plate thermal fluctuations < +5° C during powder removal and addition and recovery temperature fluctuations after disturbance within < +/-5° C.

5. Reservoir and dispensing area thermal fluctuations  $< 5^{\circ}\text{C}$  during powder removal and addition and recovery temperature fluctuations after disturbance within  $< \pm 5^{\circ}\text{C}$ .
6. Reservoir and dispensing bulk powder thermal fluctuations  $< +5^{\circ}\text{C}$  during powder removal and addition and recovery temperature fluctuations after disturbance within  $< \pm 5^{\circ}\text{C}$ .
7. Back system ambient thermal fluctuations  $< -5$  to  $+5^{\circ}\text{C}$  with thermal gradients  $< 5^{\circ}\text{C}$ .

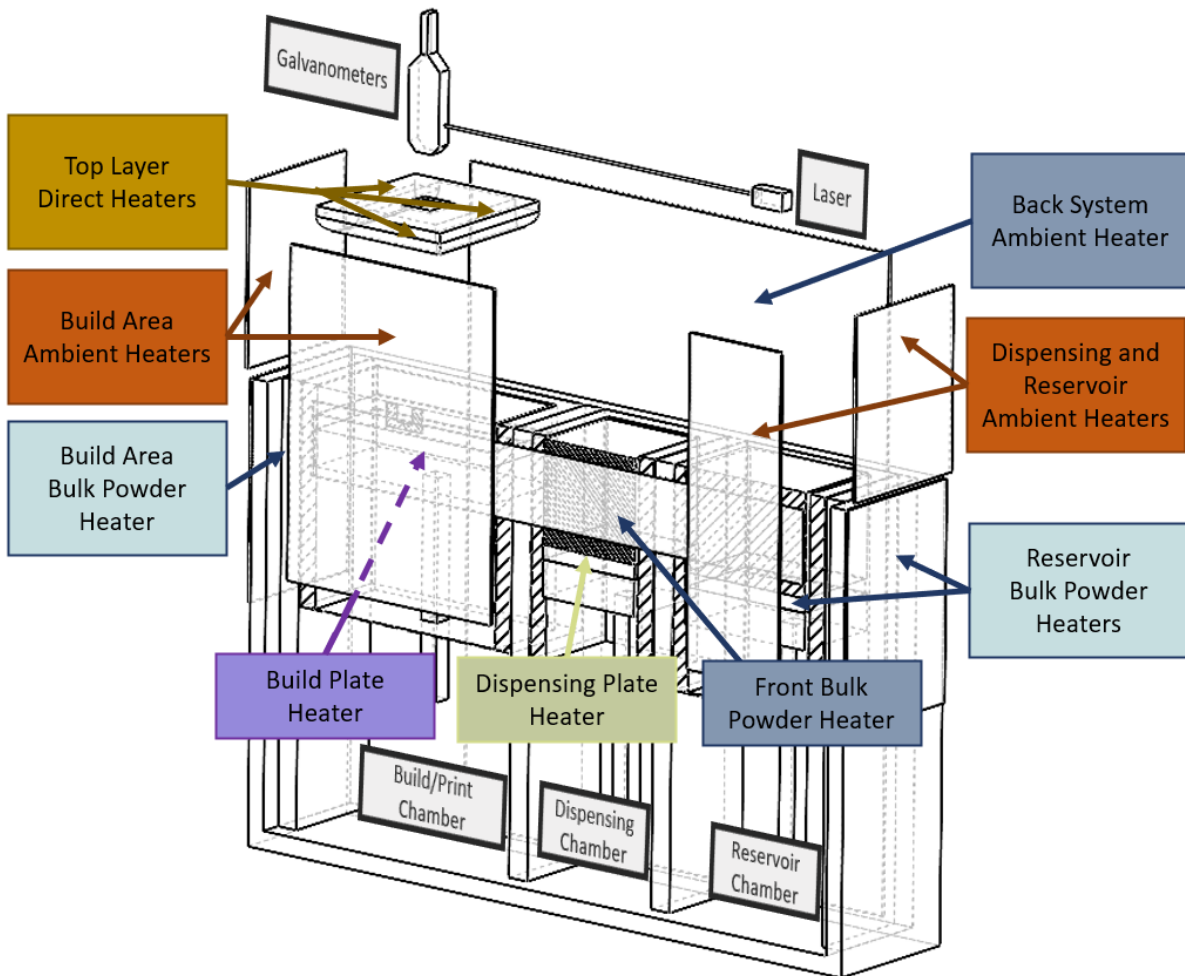


Figure 3.7: Thermal management subsystem heater positioning for M2 operations involving powder movement into and out of the system

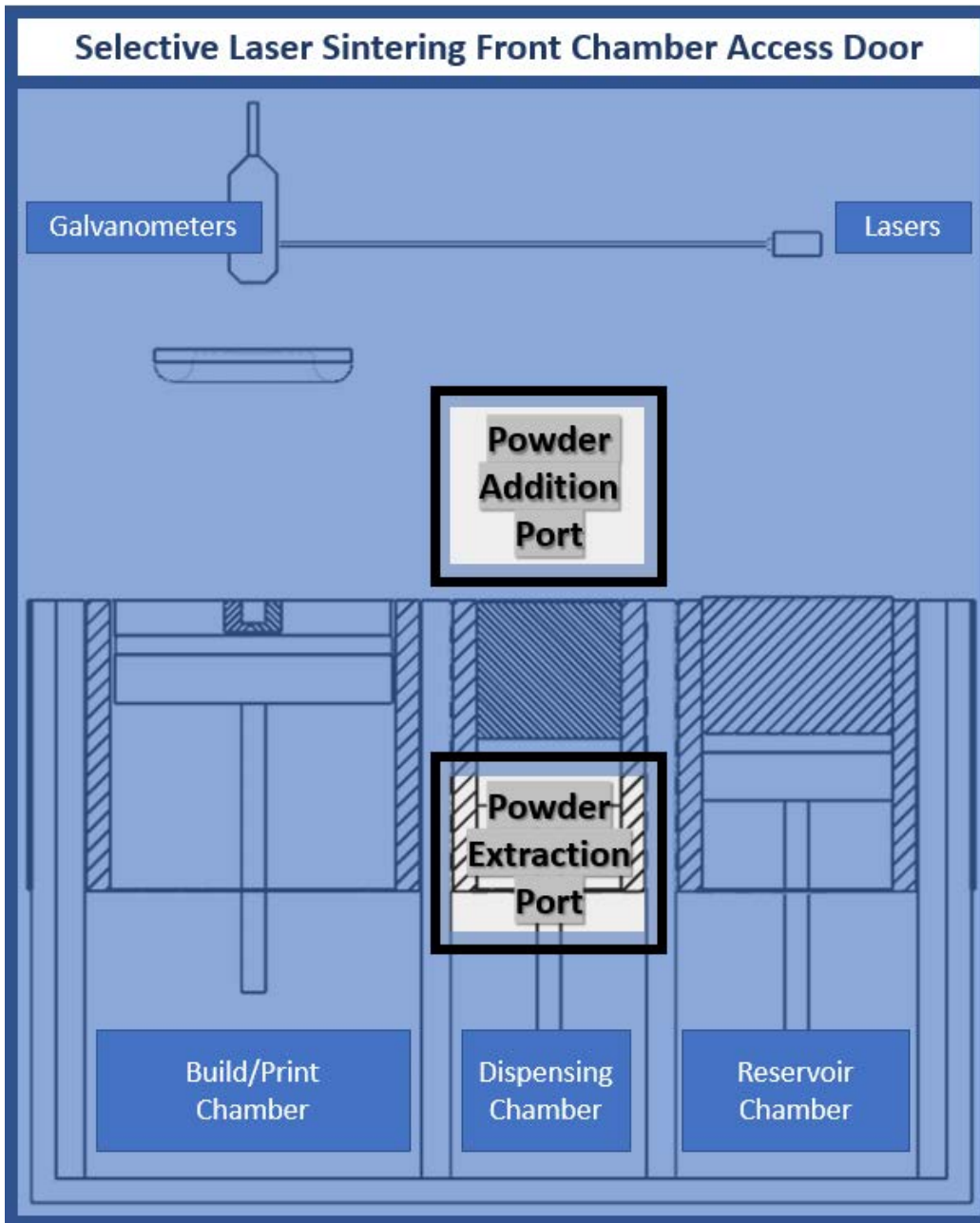


Figure 3.8: M2 SLS Front Access Door with Powder Addition and Extraction Ports

#### **Subsystem 4: Multiple Reservoirs with Intra-Print Powder Extraction/Addition**

The M2 SLS design was able to sinter any number of compatible low-temperature polymers and composite blends which required a mechanism to replace a material within the system with a different material from outside of the system. A critical aspect to integrating this subsystem into the printing routine was to minimize powder and thermal disturbance throughout the powder exchange process. Maintaining acceptable thermal stability was accomplished through synchronization of this subsystem with subsystem 3 (thermal management). The methods for intra-print powder extraction and addition were implemented through two basic procedures discussed below and depicted in Figure 3.8.

First, material was removed out of the system. To accomplish this function the dispensing plate was moved to the lowest position in line with an extraction port (Figure 3.7, 3.8a). Material was removed from the dispensing chamber via a mechanical scoop and a low flow powder extraction vacuum to avoid high air movement internal to the system which would disturb the other powder in the system and create thermal convection currents within the system.

Second, new material was added into the system. The dispensing plate was raised above the extraction port and material was added into the dispensing chamber through the upper feed port aligned with the dispensing chamber (Figure 3.7, 3.8b-c). Material was added through a dispensing powder syringe and mechanically leveled with an external rake operated in a perpendicular motion to the internal powder application rake.

#### ***Acceptance Criteria***

The following two parameters were hypothesized to be the key tolerances required to maintain print parameters during material exchange:

1. **Cross Contamination:** Less than 2% cross contamination measured via optical microscopy of powder samples from the build plate, dispensing chamber and reservoir after completing the powder exchange process.
2. **Temperature Gradients:** Temperature gradients surrounding the build area remain within 3° C of set temperature during the entire execution of powder extraction and addition. Internal temperature gradients were affected by the outside temperature and the temperature of the powder being added and so the new powder and dispensing plunger was pre-heated prior to inserting the powder. This portion of the completion criteria is the same for subsystem 5 and both subsystems were evaluated via thermocouples and infrared cameras.

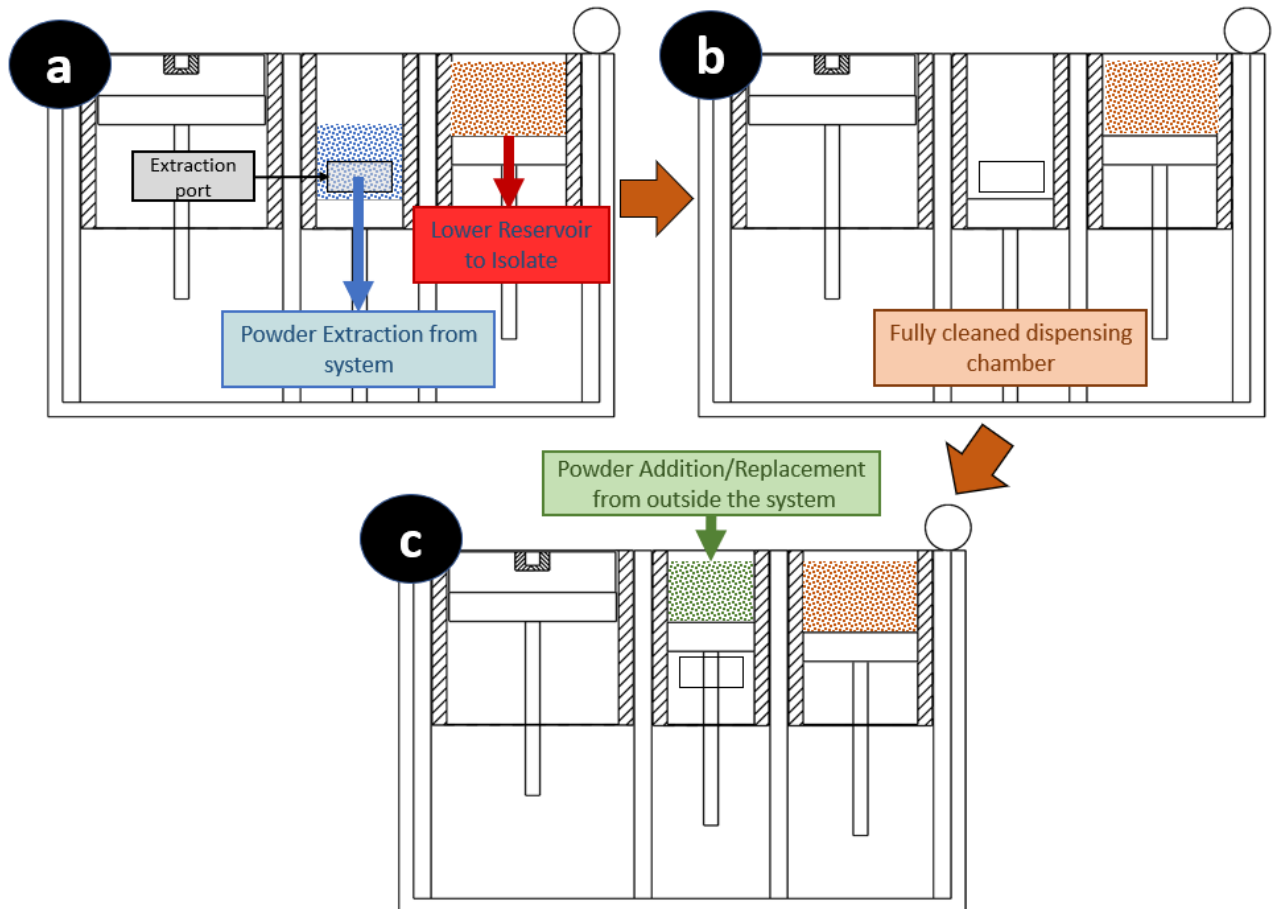


Figure 3.8: Powder Extraction and Addition Flow

## **Subsystem 5: Multi-Material Layer Application**

The M2 SLS design was also able to switch build chamber top layer materials at any time during a print. The prototype built for this research did this by spreading material from either the dispensing chamber or the reservoir chamber (each filled with different powder blends). When switching from the dispensing chamber to the reservoir an “**isolation**” layer of powder was applied to the dispensing chamber prior to spreading the first layer of the new powder (Figure 3.9b). When switching from reservoir to dispensing chamber powder the dispensing chamber was “**purged**” prior to spreading the first layer of new powder from the dispensing chamber (Figure 3.9c). These two methods are detailed below:

### **Powder Isolation Methods (Figure 3.9a-b):**

1. Reset powder spreader to the reservoir position.
2. Lower the dispensing plate until top of dispensing powder is below top of dispensing chamber. The proper depth will have to be experimentally determined for each material blend based on amount of cross contamination. For instance, CF blends cross contaminate neighboring powders significantly and so will require the dispensing plate be lowered a greater depth than most other blends. Also, if reservoir material is a higher temperature material the dispensing plate will have to be lowered to a point to also isolate the dispensing material thermally. When planning a print, the higher temperature material should be kept in the dispensing chamber to the maximum extent possible to avoid thermal mismatches during this function. A depth of 0.5-4 mm is hypothesized to be adequate for the proposed blends.
3. Raise reservoir plate to spread reservoir powder on top of the lowered dispensing powder. The reservoir will not be able to be initially raised enough to fully cover the

dispensing powder in a single pass or the powder will clump and not spread evenly and cause large temperature gradients over the build area. The amount to raise the reservoir for each pass will have to be experimentally determined for each material blend. Approximately 2-4 passes of 0.5 mm per pass is hypothesized to sufficiently isolate most blends.

4. Run the spreader each time the reservoir is raised until the dispensing powder is fully isolate and there is a homogeneous top layer of reservoir powder. The rake can move from the reservoir position to the build plate position for initial isolating spreading.

**Powder Purge Methods (Figure 3.9c-d):**

5. Reset rake to the dispensing position.
6. Raise the dispensing plate enough to expose the dispensing powder. The correct amount will be experimentally determined for each powder as raising the dispensing plate too much at a time and raking large amounts of powder can cause unacceptable thermal gradients over the build area. However, not raising the dispensing plate enough may cause the top reservoir powder to be pushed down and mixed with the underlying dispensing powder.
7. Spread the powder and return spreader to printing position if reservoir powder is sufficiently purged or return to dispensing position if multiple iterations will be required. It is hypothesized that the raised powder can be left in place until the ambient build area heat permeates the raised powder spreading can be done in 1 or 2 passes to simultaneously minimize powder mixing, cross contamination, and thermal disturbances to an acceptable level.

## Acceptance Criteria

Completion criteria was quantitatively measured through cross contamination analysis and thermal gradient analysis discussed below:

1. **Thermal gradient analysis** completion measurements will be done in accordance with completion criteria Subsystem 3 “Multi-Material Thermal Management System”.
2. **Cross contamination analysis** will be done via microscopy of powder samples from all three chambers. Less than 1% cross contamination will be considered acceptable.

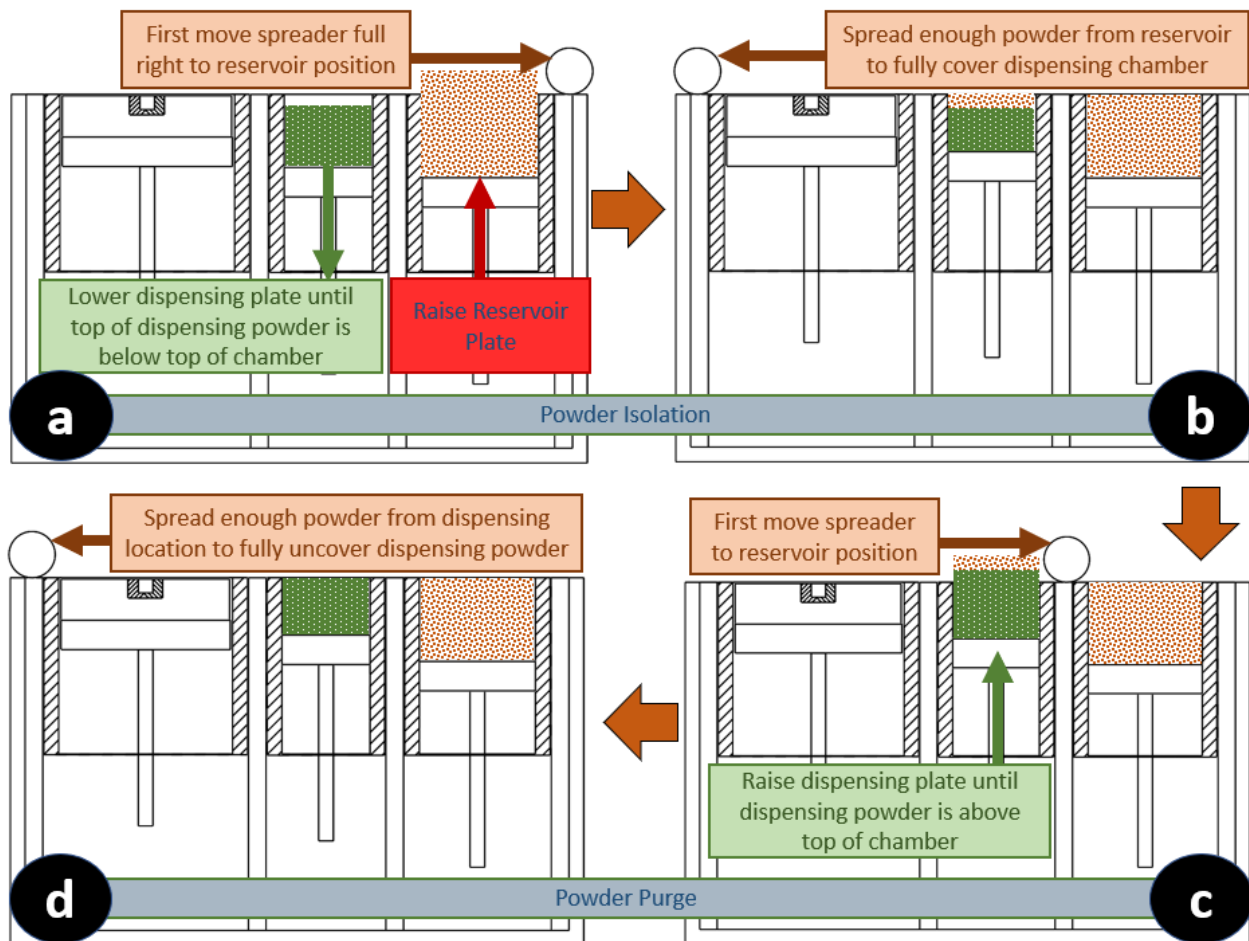


Figure 3.9: Proposed Methods to Switch Materials at Layer Application through Powder Isolation (a-b) and Powder Purge (c-d)

## **Subsystem 6: Part Anchoring**

Anchoring in metallic PBF (commonly known as Selective Laser Melting or SLM) is common but normally considered a necessary requirement to dissipate heat through conduction with numerous undesirable consequences. The conductive capacity of the anchors is required to avoid overheating due to the extreme energy (heat) required to melt and coalesce the metal particles compared to the relatively cool ambient air and insulative powder the part is immersed in during printing (C. Li et al., 2018a; I. A. Roberts, 2012b; Zaeh & Branner, 2010). Anchoring mitigates many of the impacts such as warping and residual internal stress associated with the huge temperature gradients in metallic PBF (Bartsch et al., 2019; Q. Chen et al., 2017b). However, print planning, print time, material usage all increase while part removal and post processing to remove the anchors is complicated and can damage the part. Though there are efforts to find ways to move away from anchoring in metallic PBF, anchorless printing is normally still seen as an advantage of polymer PBF (commonly known as Selective Laser Sintering or SLS) over metallic PBF (Mumtaz et al., 2011). Though the powder temperature and the sintering temperature differential is minimal during printing of polymers as opposed to metals; like metals, sintering large cross-sectional areas of a part during SLS continues to limit the process. Scalability is highly desired by many industries but quickly introduces warping, shrinking, and internal residual stress (C. Li et al., 2018b; Mercelis & Kruth, 2006b; Tofail et al., 2018; X. Wang et al., 2017b). Anchoring was hypothesized to mitigate some of these potential problems in SLS and increase the scalability of SLS printing. However, for this study anchoring was also the proposed method for stabilizing the part in the print area during material extraction and addition to prevent the part from moving when material is removed from the top layer and to prevent warping associated with thermal disturbances during M2 operations. Anchoring is

proposed as an additional method to the thermal management subsystem to mitigate part movement, warping and print defects during the material exchanges during the execution of subsystem 5 & 6 (Figure 3.10).

A novel M2 anchoring method was used for this study by incorporating the inherent M2 capabilities of the M2 SLS prototype. Traditionally SLM anchoring involve attaching “anchor points” to the build plate or a structure attached to the build plate which facilitates conductive heat flow from the part. Since this heat flow was not required for the materials utilized in this project the part was anchored to a low warping CF blend or TPE via the following methods:

1. Load the low warping material powder blend in the dispensing chamber.
2. Load the desired initial part material powder blend in the reservoir chamber.
3. Initially sinter 10-20 layers (1-2 mm) of a complete extension (footprint) of the desired first layer with the low warping material from the dispensing chamber.
4. Print the desired part with the desired material from the reservoir chamber directly on top of (adhered to) the 1-2 mm anchoring footprint.
5. Machine or cut off the anchoring footprint.

These methods were used to avoid warping but were also critical to secure the part during M2 operations.

### ***Acceptance Criteria***

While this subsystem’s completion criteria are inherently interlinked with previous subsystems at the most basic level this method was considered successful if the print did not fail due to sledding or shifting following material changes. However, this system was used to supplement all other systems to achieve the following specific completion metrics:

1. Anchor geometry and material stiffness minimized part shifting and warping during printing.
2. Anchor material remained sufficiently stable to prevent sledding.
3. Part material bonded to the anchor and remained intact during printing but facilitated removal after printing.

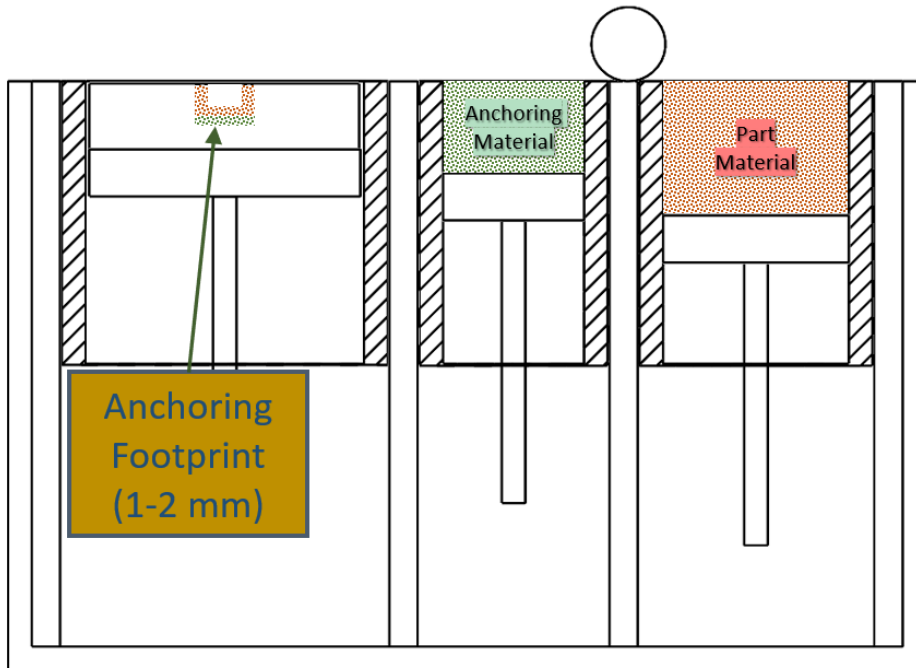


Figure 3.10: Part Anchoring Depiction

### Subsystem 7: Multi-Material SLS Host and User Interface

A user interface (“M2 Host”) was developed to execute the M2 functions and run subsystems 1-6. The only exceptions were 11 of 14 heaters in the thermal management system which were interfaced via individual external PID controllers (Figure 3.6). External PID interfaces for the majority of the heaters maintained M2 SLS prototype operational functionality while simplifying the wiring and coding for the main M2 Host. The methods for interfacing all other functions were contained in a LabVIEW host and described below:

1. M2 Slicing and hatch interface capable of setting different hatch parameters based on each material type (subsystem 1 and 2) is described in Figure 3.11. Interface allowed control of hatch geometry, perimeters and spacing to match each material type.
2. Top powder layer thermal control (subsystem 3) interface is described in Figure 3.12
3. Interface to transport multiple powders required (subsystems 4 and 5) was divided into three individual user interface tabs.
  - a. First tab (“Motor Control and Config”, Figure 3.13) allowed the user to move powder when extracting, adding, purging, or isolating powder for a material switch.
  - b. Second tab (“Print Macros”, Figure 3.13) allowed the user to change automation settings for each material type.
  - c. Third tab (“Print Controls,” Figure 3.14) allowed the user to select the proper powder chamber and rake speeds after a material switch.
4. Interface to change energy density parameters to match a new material (sintering execution of subsystems 1 and 2) was accessed on the “Print Controls” tab (Figure 3.14). Real time adjustable parameters to match material properties were laser speed, laser power, hatch density, and hatch multiplier.
5. Interface to set the first material for anchoring (subsystem 6) was inherently included in the material switching interfaces.
6. Interface to monitor print progress and overall system operation and health was presented with the following feedback mechanisms (Figure 3.15):
  - a. System Temperature feedback via top layer infrared sensor and ambient thermocouple sensor (Figure 3.15a).

- b. Mechanical movement feedback of the rake, build plate, dispensing plate, and reservoir plate via motor control status (Figure 3.15b).
- c. Sintering health feedback via laser and layer timing (Figure 3.15c).
- d. Powder level and availability feedback through dispensing and reservoir height monitoring (Figure 3.15d).
- e. Overall print progress through layer monitoring (Figure 3.15e).

**Acceptance Criteria**

Subsystem 7 was tested and considered operational upon completion of subsystems 1-6 indicating effectiveness of the respective controls interface. Results were experimentally evaluated, and interfaces changed as required to achieve completion of the respective subsystem.

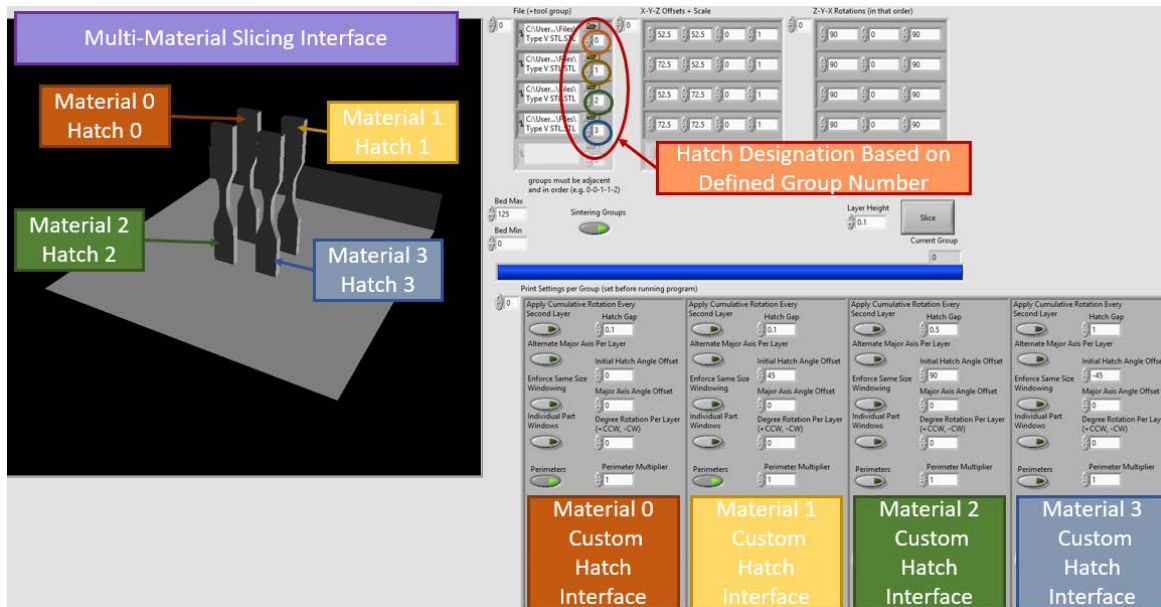


Figure 3.11: Material Specific Hatch Control Interface for Subsystem 4

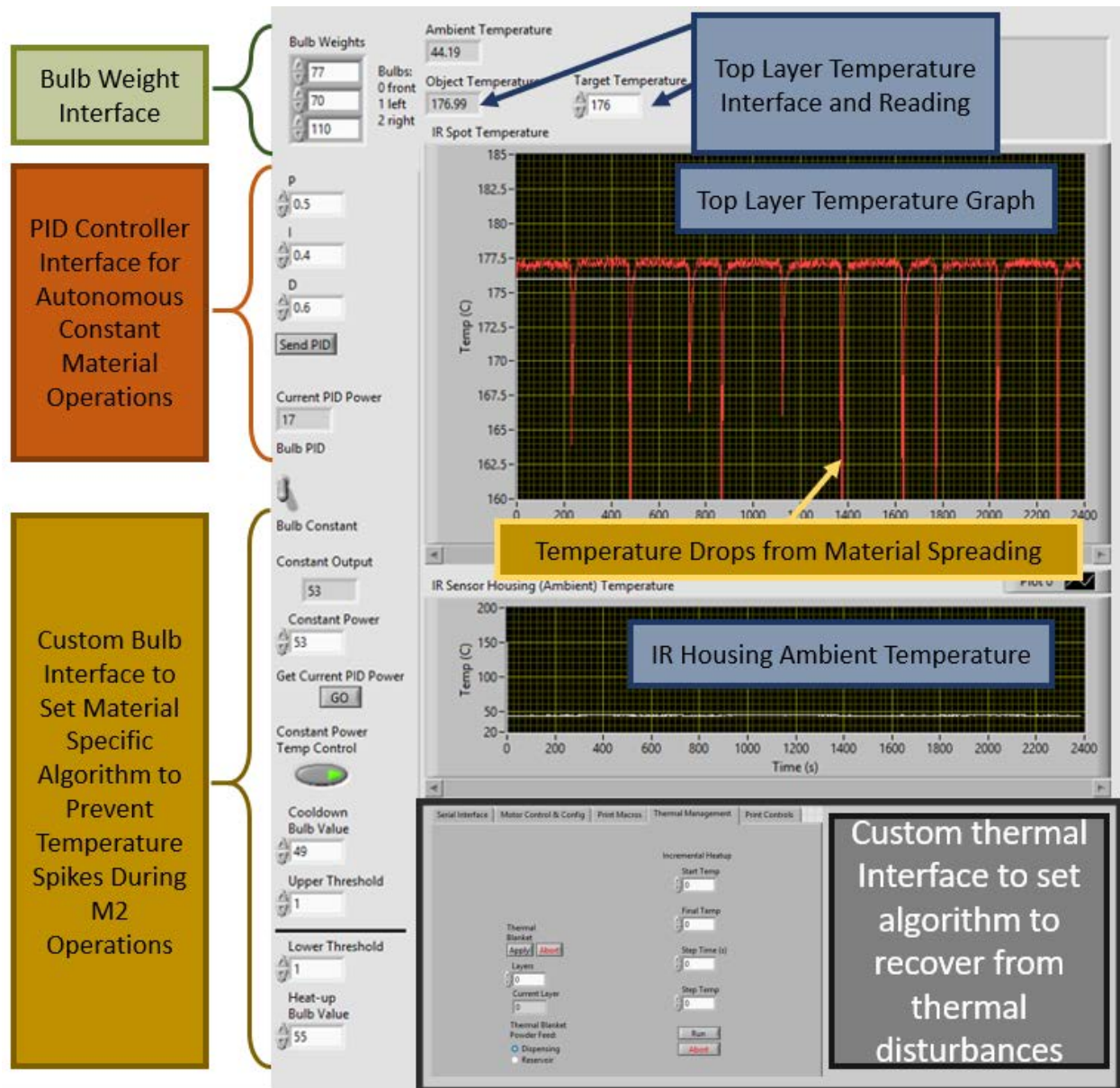


Figure 3.12: Top Layer Powder Thermal Management Interface to Control Subsystem 4

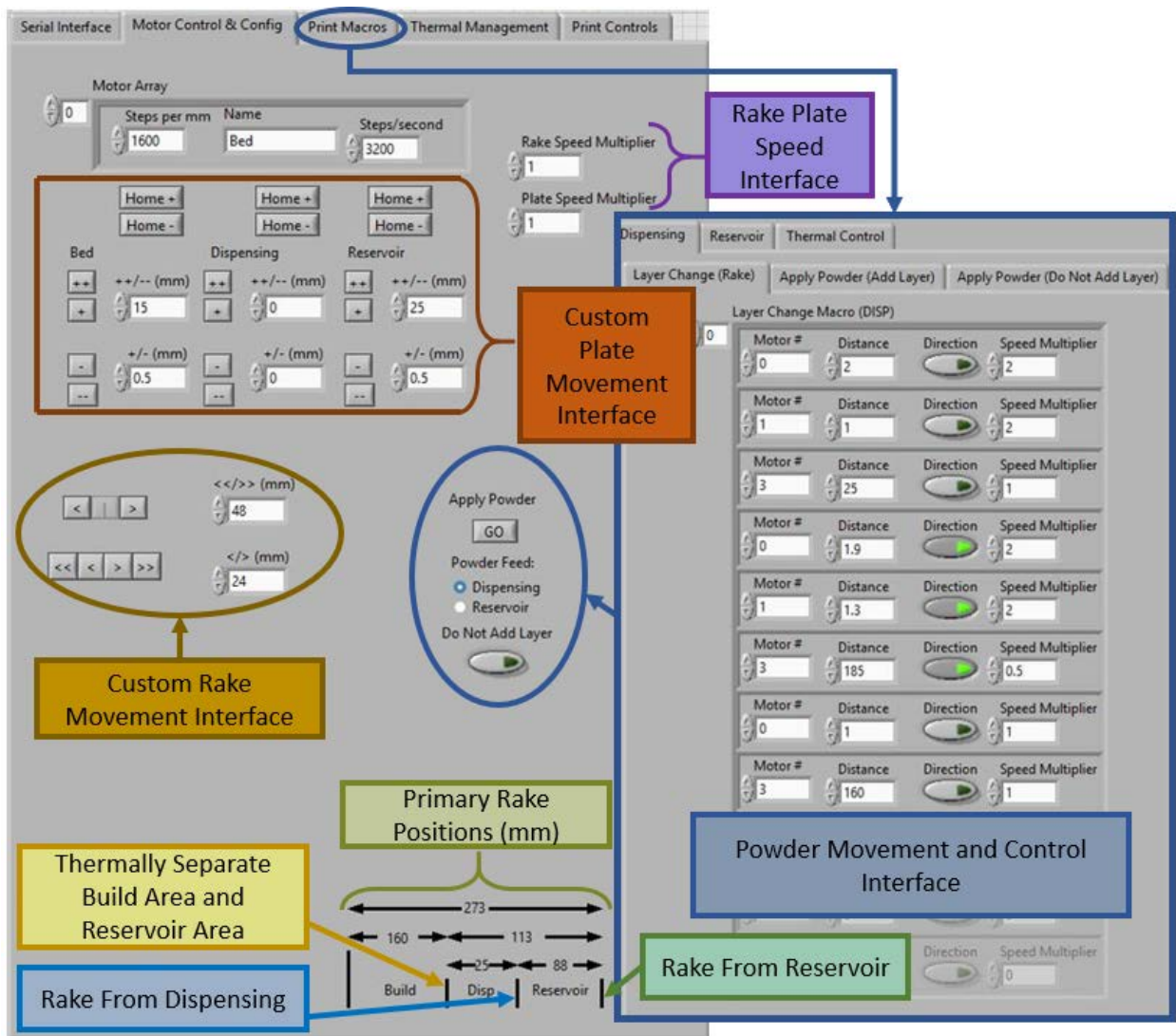


Figure 3.13: Powder Exchange Interface to Control Subsystems 5-7

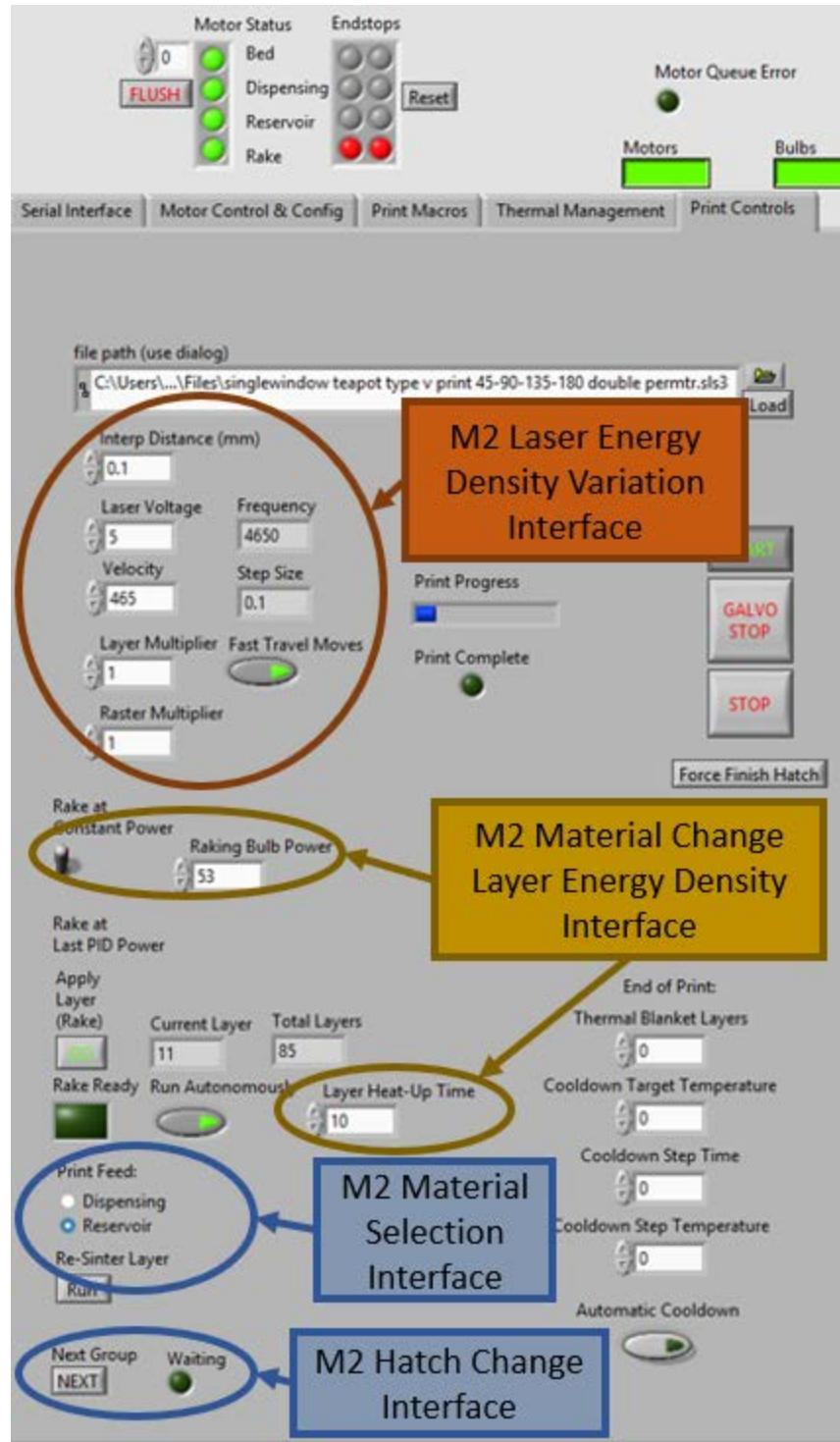


Figure 3.14: Powder Exchange Interface to Control Subsystems 5-7

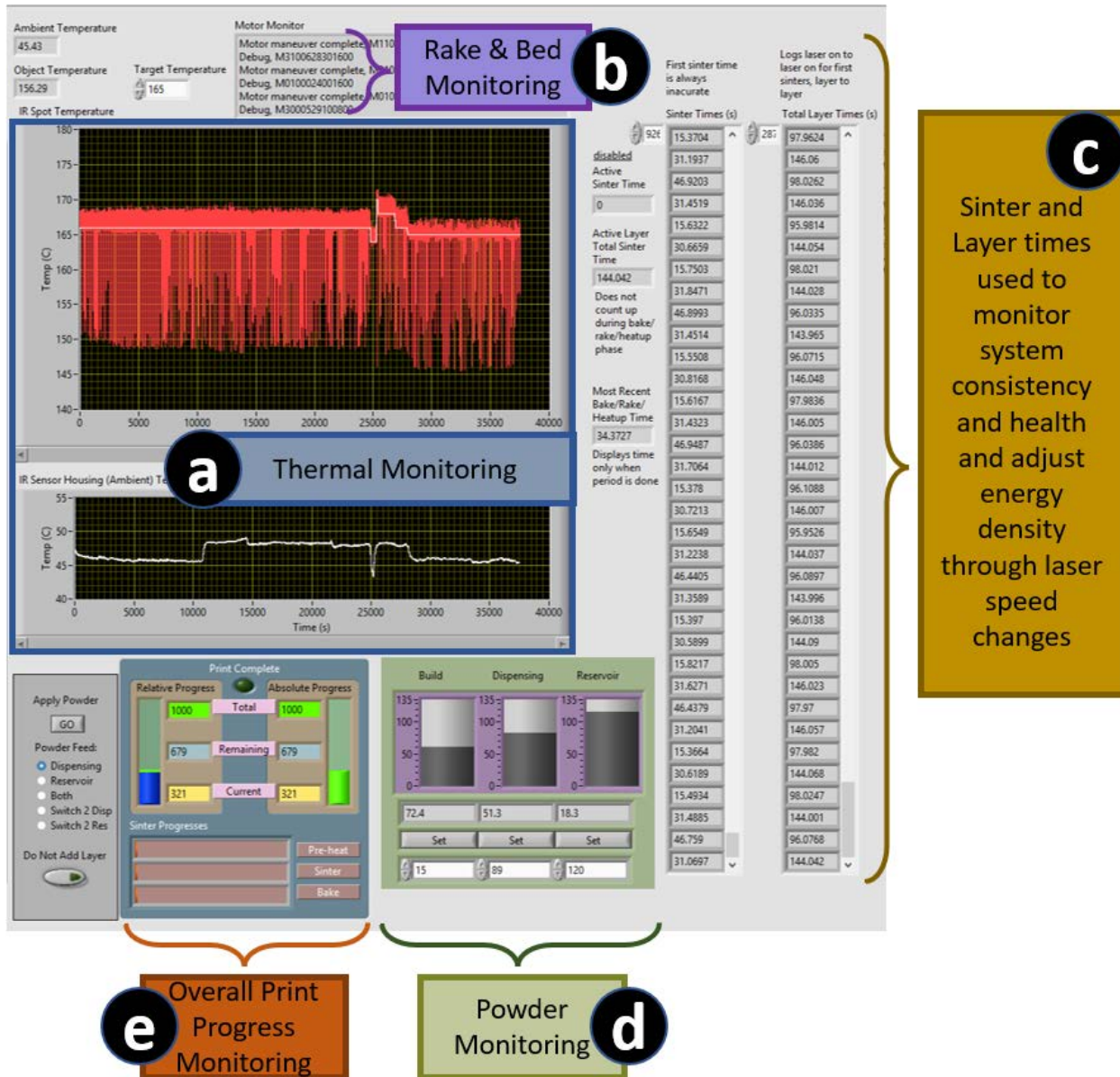


Figure 3.15: System and Print Monitoring

- (a) System Temperature feedback via top layer infrared sensor and ambient thermocouple sensor.
- (b) Rake, build plate, dispensing plate, and reservoir plate movement feedback via motor status.
- (c) Sintering health feedback via laser and layer timing.
- (d) Powder level and availability feedback through dispensing and reservoir height monitoring.
- (e) Overall print progress through layer monitoring.

## **RESULTS**

A M2 SLS prototype (Provisional Patent 63/262,580, UTEP Disclosure D2020-0015, Appendix A) was built in accordance with the methods described in this chapter. Initial sintering results have proven the ability to change material types between the two internal reservoirs and the ability to exchange powder from external sources. Printed specimens from the prototype have sintered particles across material switches and interfaces using the custom slicing, hatching, and sintering programs. Ability to sinter parts with functional gradients has been demonstrated and characterization of these gradients can be found in chapter 6 (Aim 4). Specific results for each subsystem are organized by subsystem for clarity and described in the following seven sections.

### **Subsystems 1 & 2: Multi-Material Slicer, Hatch, & Layer Energy Density Control**

Subsystems 1 and 2 were tightly integrated to produce material based sintering energy density. Both were implemented through LabVIEW by assigning hatch pattern, perimeters, laser speed, laser intensity, and number of laser passes based on material type. The hatch pattern and perimeter settings were integrated through the M2 Slicer subsystem. An example of the resulting material specific hatch pattern is depicted in Figure 3.16 with individualized hatch angle, spacing, and perimeters for each material.

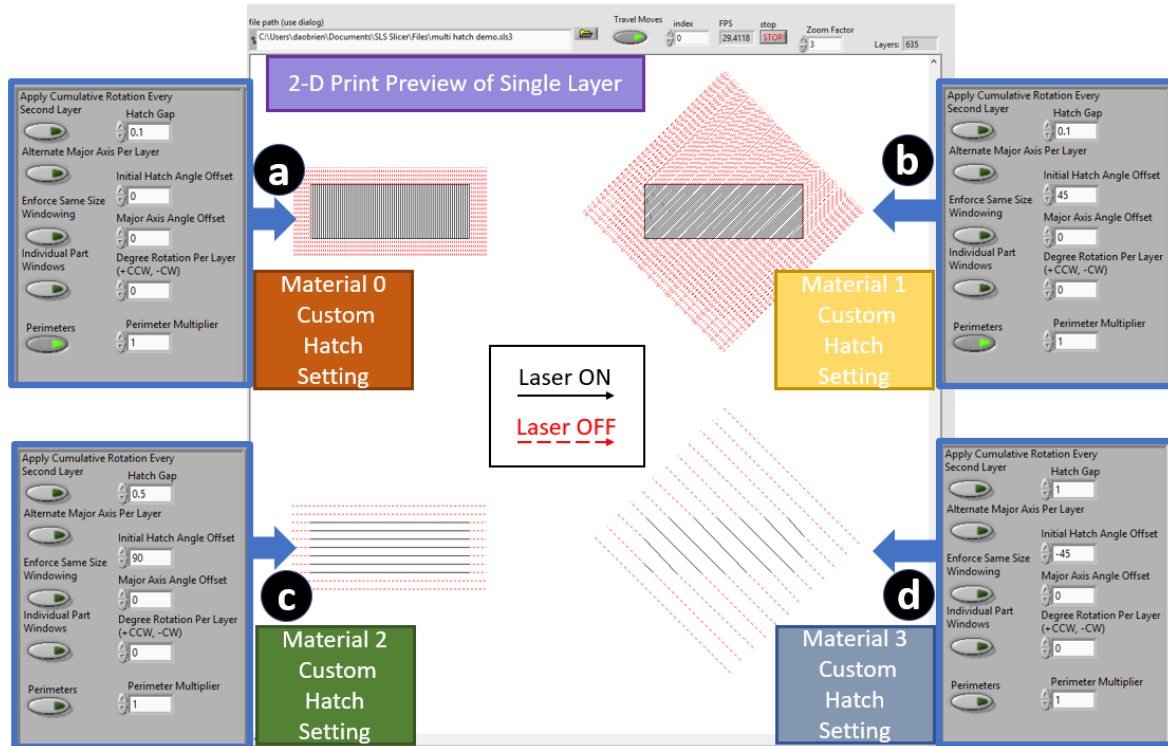


Figure 3.16: Material Specific Hatch Example:

- (a) 0.1 mm hatch spacing, 0 degree hatch angle for all layers, single perimeter.
- (b) 0.1 mm hatch spacing, 45 degree hatch angle for all layers, single perimeter.
- (c) 0.5 mm hatch spacing, 90 degree hatch angle for all layers, no perimeter.
- (d) 1.0 mm hatch spacing, -45 degree hatch angle for all layers, no perimeter

### Subsystem 3: Multi-Material Thermal Management System

The thermal management performance was evaluated and tuned for steady state operations and for material change operations. The requirements and results of each were decidedly different:

#### *Single Material Thermal Management:*

Ambient thermal testing utilized both the integrated infrared (IR) sensor and test specific thermocouples. The integrated IR sensor was located between the Top Layer Direct Heaters with an ambient thermocouple and an IR sensor focused on the build plate. Thermocouples were placed throughout the internal chambers just above leveled and raked powder on all plates. 10

mm of powder was loaded on the build plate and 60 mm of powder loaded on both the dispensing and reservoir plates. Initial testing revealed low temperature areas around the front door and access ports. This resulted in larger front ambient heaters being placed around the door and front access port. Location of the adjusted heaters, controllers, and temperature sensors for testing are labeled in Figure 3.17. Ambient testing showed thermal stability within 3.5° C for the build area (Figure 3.18) and within 1° C for the dispensing and reservoir areas (Figure 3.19 and 3.20 respectively) during the warmup period from 60-120 minutes. When the build area was brought up to a sintering temperature of 160° C and allowed to stabilize (~220 minutes of total run time) the reservoir area remained stable at 133°C ± 1° C, while the dispensing area developed a 2.9° C split between the front and back thermocouples with a temperature of 133°C ± 1.5°C (Figure 3.19 and 3.20 respectively). At the same time the build area stabilized at a thermocouple reading of 142°C ± 6°C with the front thermocouples (B7 and B8) having the lowest reading at approximately 137°C and the left middle thermocouple having the highest reading at approximately (B4) at 149°C. The middle of the print area had an average reading of approximately 142°C ± 2.5°C (Figure 3.18).

Top layer thermal testing also utilized an IR sensor (OPTXI40LTF13T090, Optris Infrared Sensing, Portsmouth, NH) and test thermocouples just below leveled powder in the build area with the same powder volume used for ambient testing. Top layer thermocouple testing indicated approximately a 7° C difference between the middle and the perimeter of the build area of the build area top layer. IR testing and bulb weight tuning were done with Top Layer Direct Heaters were set to 165° C. Bulb weights were tuned to: Front = 90, Left = 65, Right = 110 (with 120 being maximum weight) which resulted in IR readings indicated a mean of 176.2° C with a standard deviation of 1.0° C and a maximum different of 6.6° C for a ~120x100 mm area (Figure

3.21a) and a mean of 176.8° C with a standard deviation of 0.6° C and a maximum different of 3.2° C for a ~120x50 mm area (Figure 3.21b). Final tuned temperatures are given in Figure 3.22.

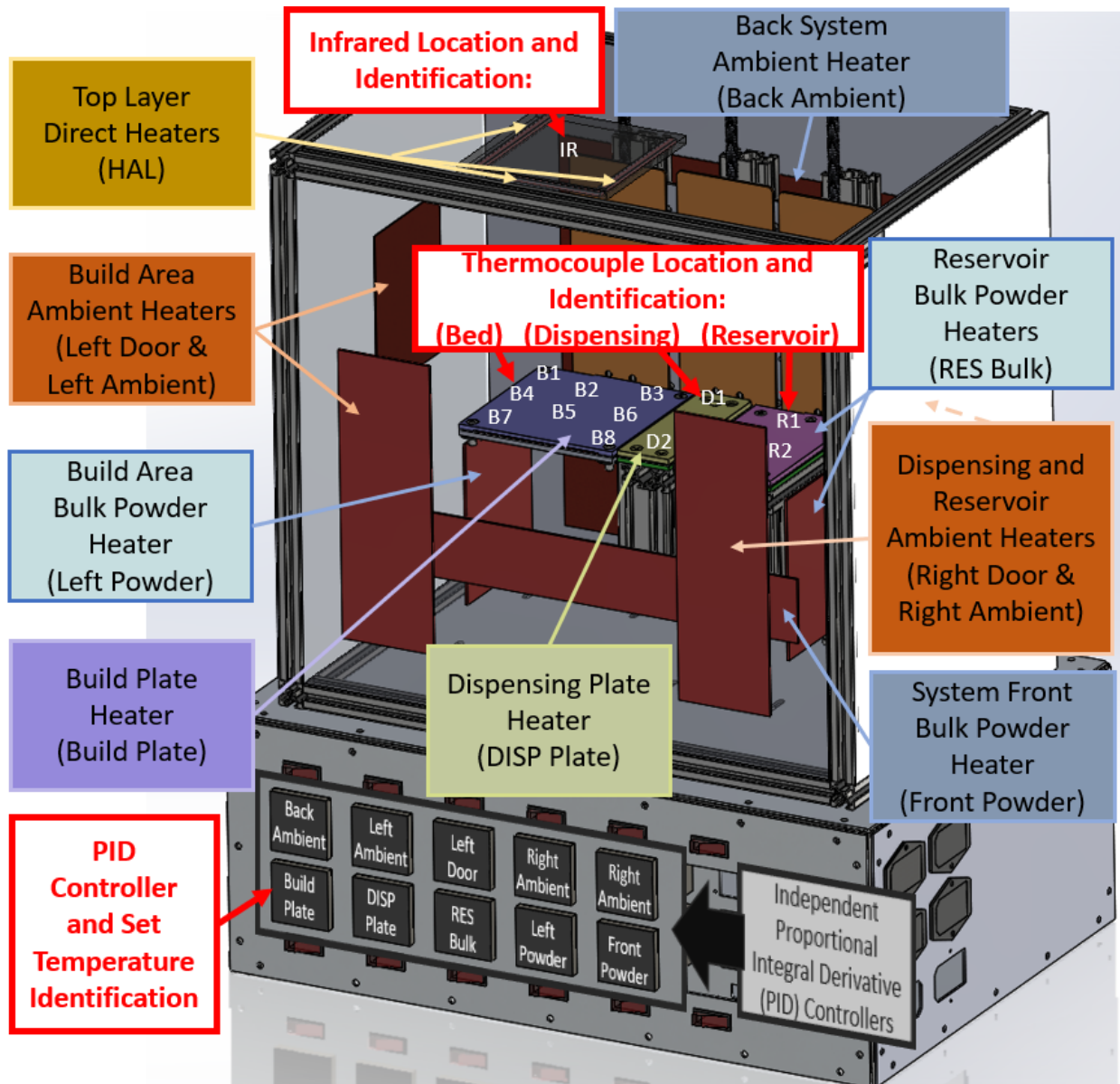


Figure 3.17: Heater, PID Control, and Thermocouple and Identification Corresponding to the Temperature Profile Graphs (Figures 3.18 thru 3.20)

- PID Identification corresponds to heater location and temperature profile graphs.
- Thermocouple Identification labeled in white lettering on plates with “B” = Build Plate, “D” = Dispensing Plate, “R” = Reservoir Plate
- Integrated Infrared Sensor Identified by white “IR” label

### Build Plate Temperature @ Powder Surface

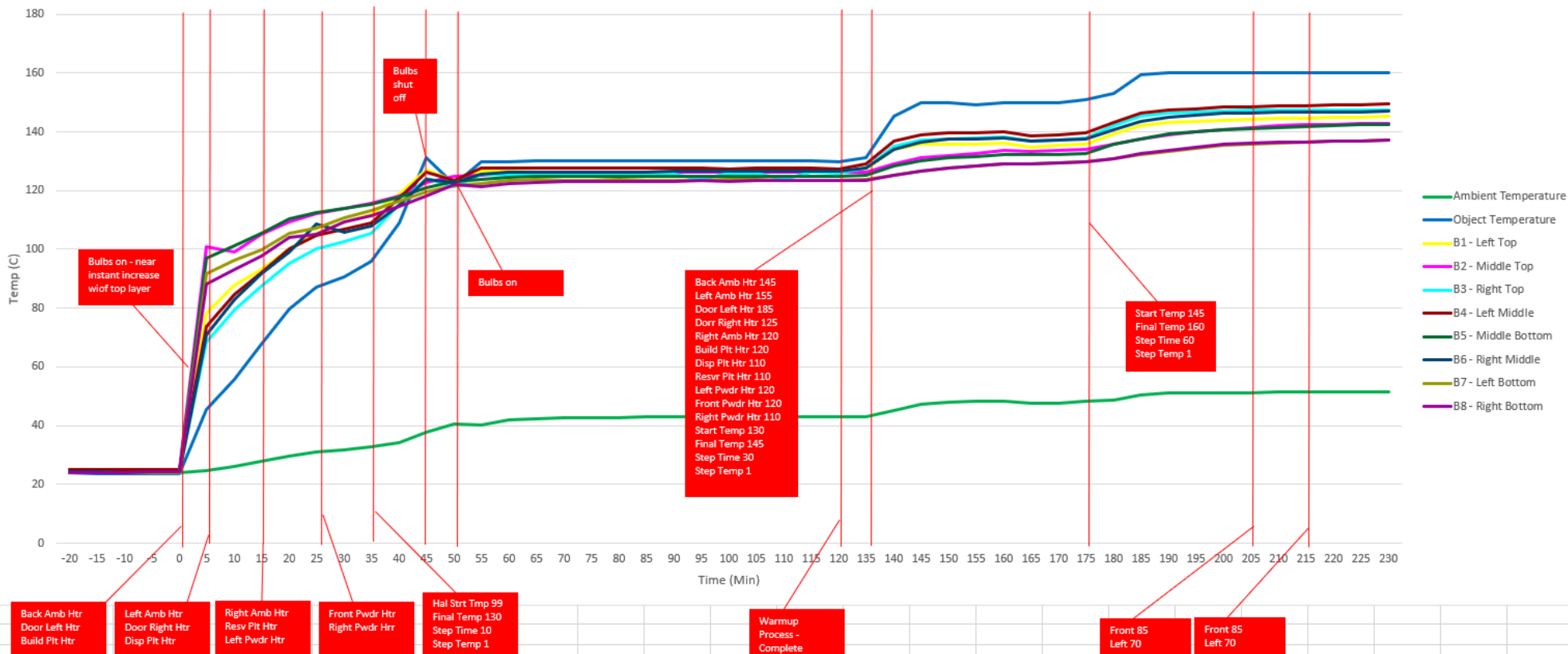


Figure 3.18: Build Area Ambient Thermocouple Data

Dispensing Plate Temperature @ Powder Surface

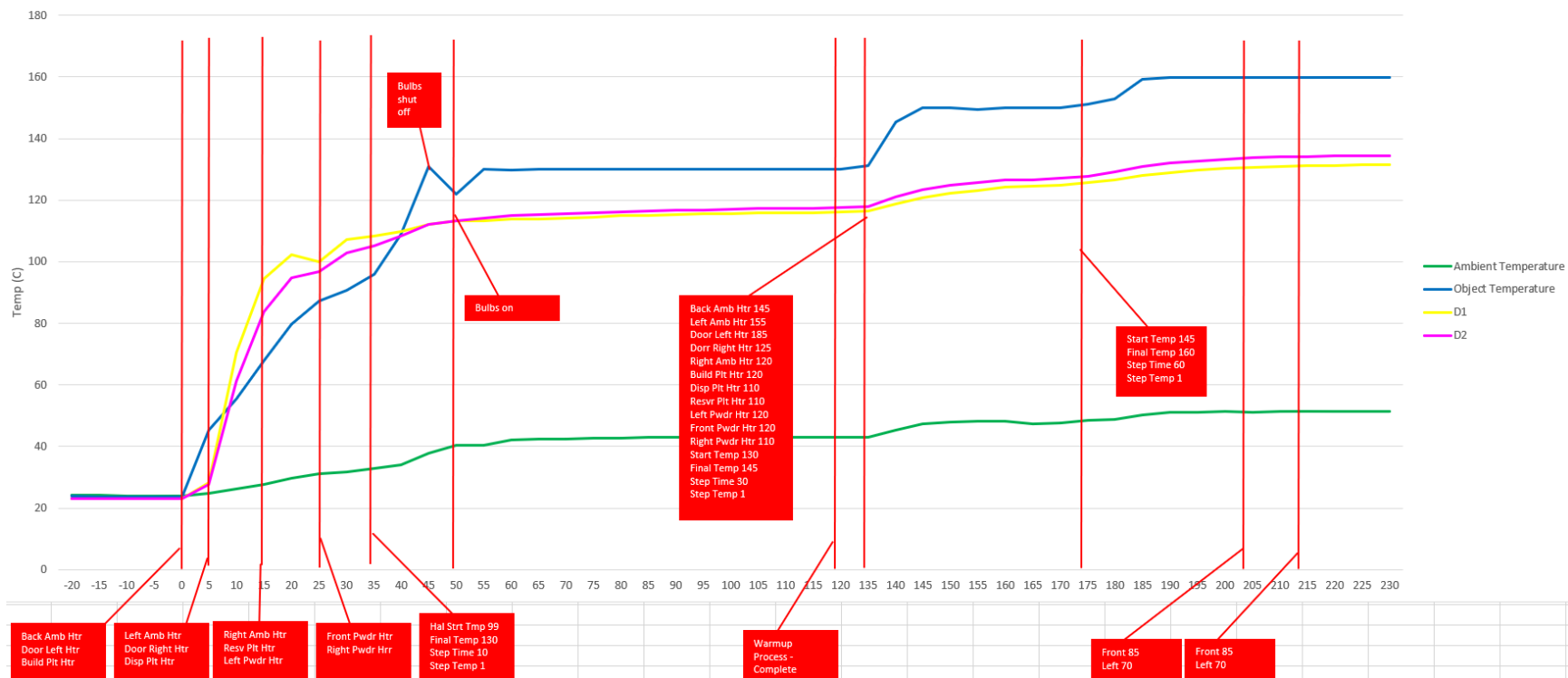


Figure 3.19: Dispensing Ambient Thermocouple Data

### Reservoir Plate Temperature @ Powder Surface

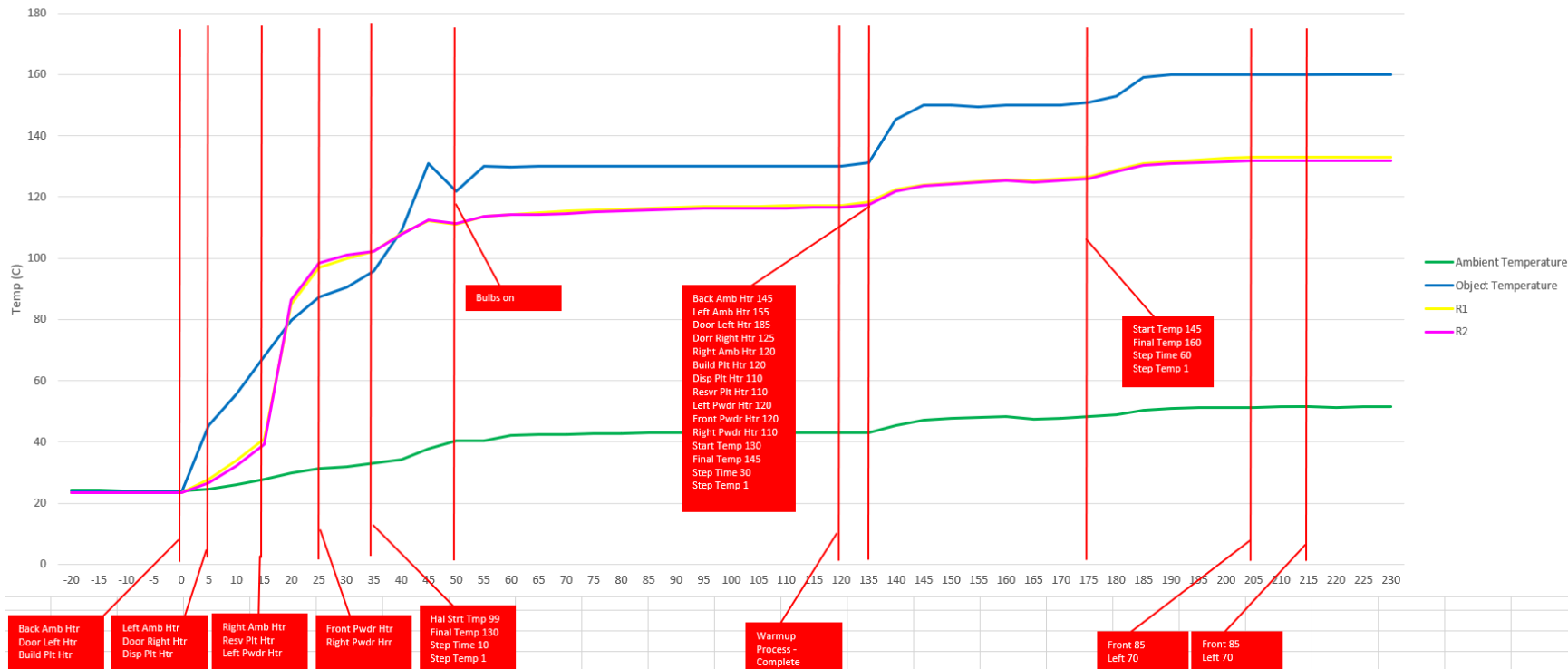


Figure 3.20: Reservoir Ambient Thermocouple Data

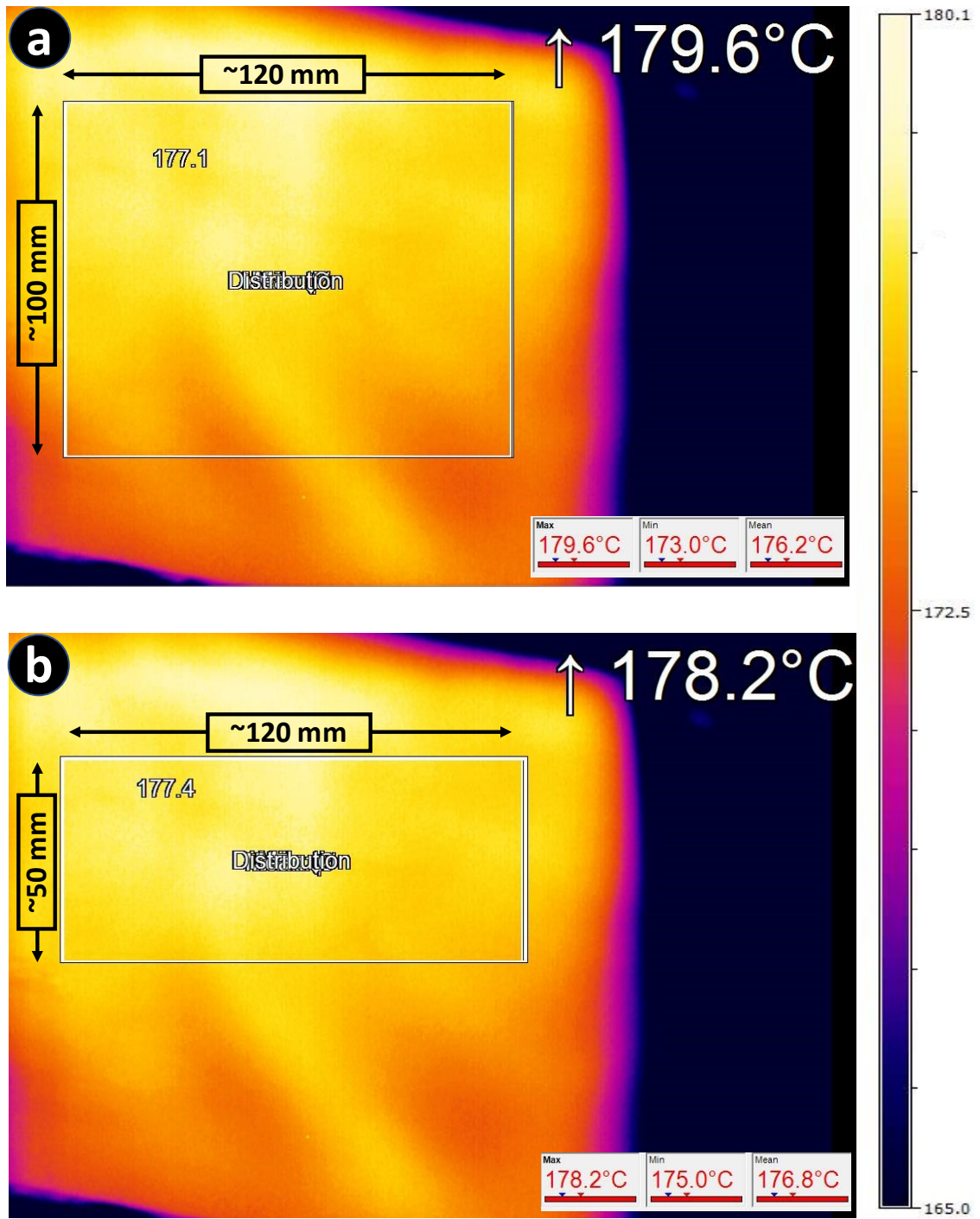


Figure 3.21: Infrared Image of Build Area (Top Layer Direct Heaters set to 165° C and Bulb Weights Set To: Front = 90, Left = 65, Right = 110)  
 (a) Data for a ~120x100 mm area  
 (b) Data for a ~120x50 mm area



Figure 3.22: Tuned PID Setting for PA12 and PA12+CF and Internal Temperatures 13 hours and 15 Minutes into Print

***Material Switch Thermal Management:***

Thermal management testing, tuning, and characterization following a material switch using the same settings used for single material steady state printing (Figure 3.22) resulted in poor layer adhesion between different materials. There were two primary causes of degraded layer adhesion between different blends of material

1. Extended delays when switching materials with an external material through the dispensing port.
2. Difference in required energy density for the new material.

The first multi-material thermal management algorithms were based on material switches took up to 8+ minutes to accomplish (see next section for details). If build area temperatures

were held at steady state sintering temperatures during this delay the material would over-sinter and cause the entire cake around the old material to crack and warp during a material change (Figure 23a). This was combated by lowering the temperature during external material switches, however, a balance had to be experimentally determined or the material around the part would warp and crack the cake from being too cool (Figure 23b). Novel temperature control was developed, and the parameters are given in Figure 3.24, however, this system still had to work in conjunction with subsystem 4 (Multiple Reservoirs with intra-print powder extraction/addition) which minimized powder exchange timing to avoid complete sintering of the cake (Figure 23c)

Tuning the novel temperature control system resulted in multiple temperature settings and strict timing after the material exchange was complete. The initial temperatures during this process yielded ideal M2 adhesion with a 2°C decrease in top layer temperature (Figure 2.24b) during powder extraction and addition followed by a 6°C increase (Figure 2.24C) for the application of the first layer with the new material. Subsequent layers were stepped back down (1-2°C increments, Figure 2.24d) until reaching ideal sintering/build temperature for the new material (Figure 2.24e).

The second multi-material thermal management algorithms were based on changes in required sintering energy density between the first and second material. Energy density had to be balanced between the previous material and the new material during a material switch at the material interface layers. This was a balance between warping and a fully sintered layer could not be consistently achieved with the top layer IR heaters and a single pass of the laser. It was found that running the laser at maximum power (5W) produced the best results, however, even at this power if the laser was slowed enough to sinter the new material to the previous material there would be excessive warping and dimension differences between the two materials resulting

in the materials pulling apart from each other. If the laser was run at a faster speed there would not be sufficient energy to sinter the new material to the previous material. A novel multi-pass laser technique was developed to overcome these issues between varying blends of material. The first pass was done at 2-5 times the speed required to sinter the material which “preheated” the material prior to sintering. This preheat temperature was above an acceptable cake temperature for the top layer but below the sintering temperature. The second pass of the laser was the “sintering” pass. Finally, there was a third pass of the laser to allow the sintered layer to fully bake and coalesce (combine and adhere) to the previous layer before relatively cool powder was spread on top of the sintered part. Speeds were adjusted based on hatch angle to further increase energy density uniformity between layers since windowing (Figure 3.6) was used to increase print efficiency and decrease print time. This multi-pass technique is illustrated in Figure 3.25 and was adopted for most single blend prints as well.

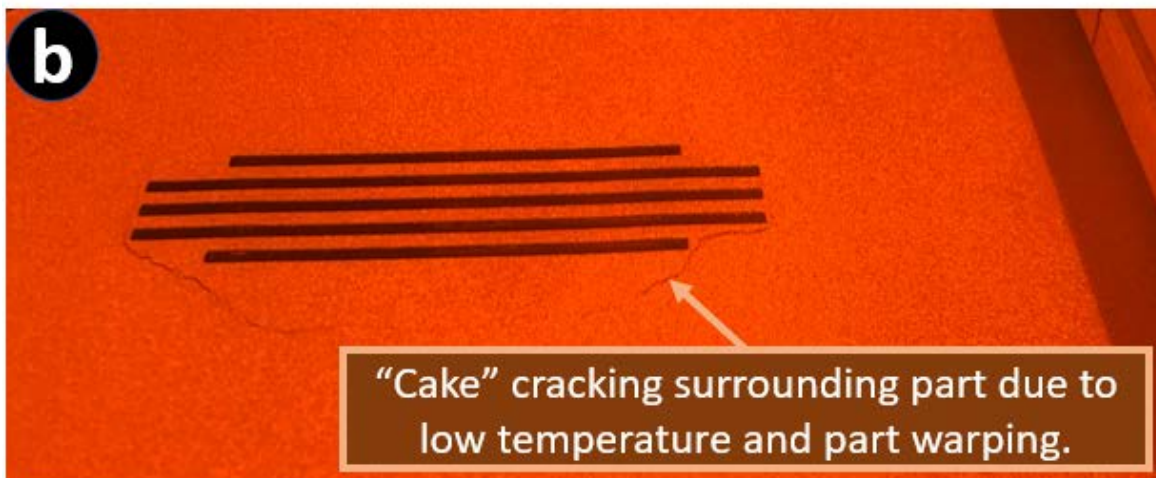
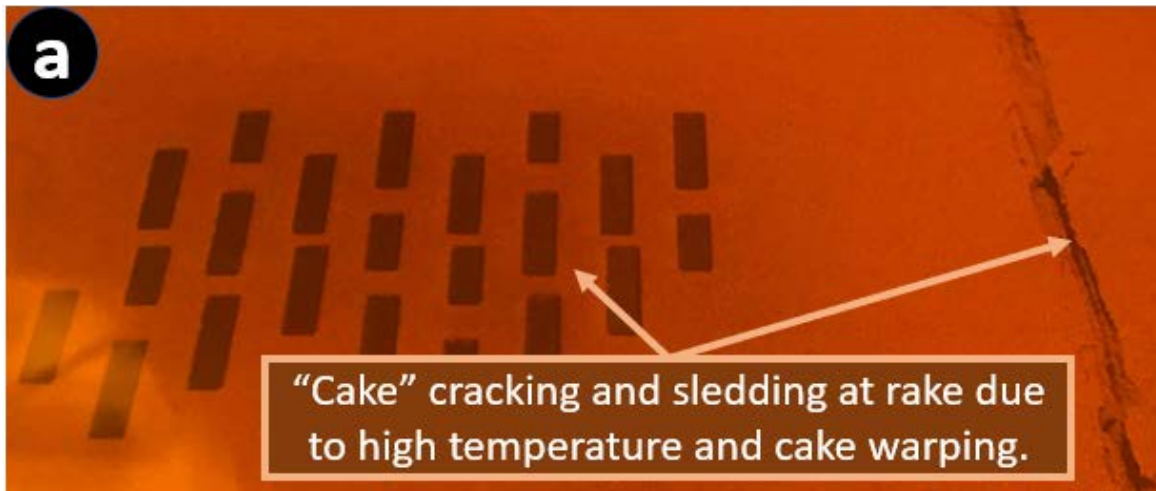


Figure 3.23: a) Over-Sintered Top Layer and Cake After Maintaining Top Layer at Sintering Temperature for 8-10 Minutes. b) Cake Cracking Due to Being Allowed To Cool Too Much External During Material Switch

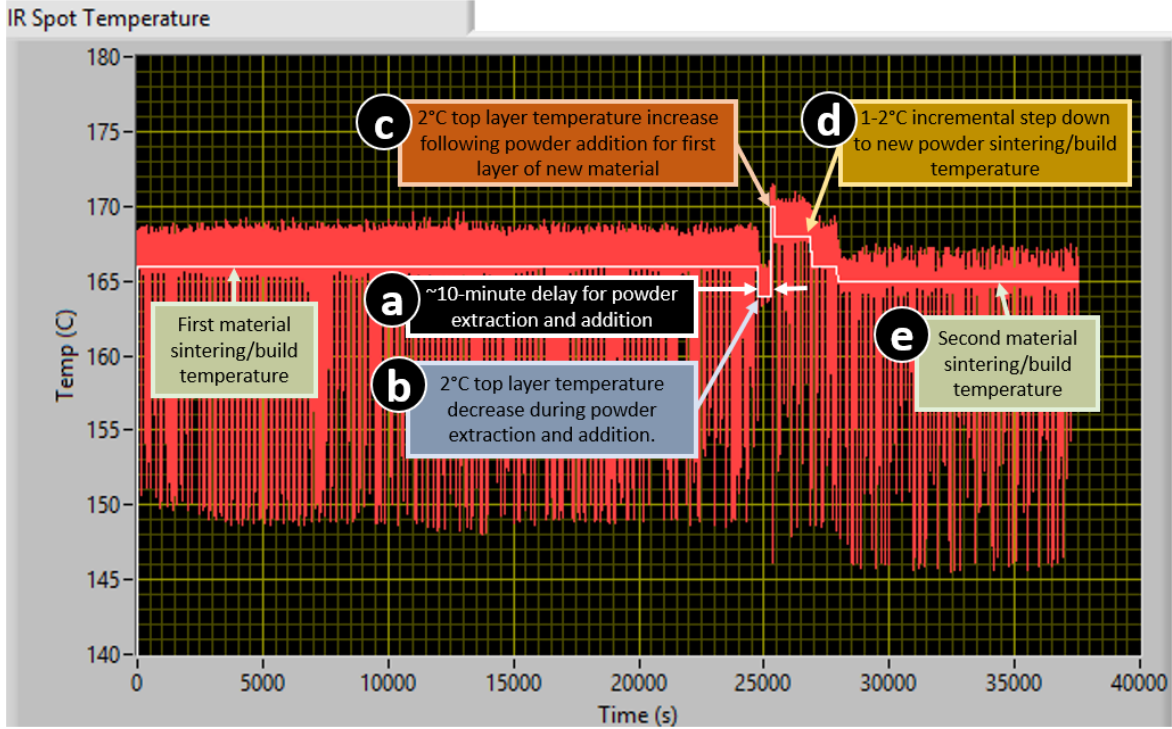


Figure 3.24: Temperature Profile During Powder Extraction and Addition

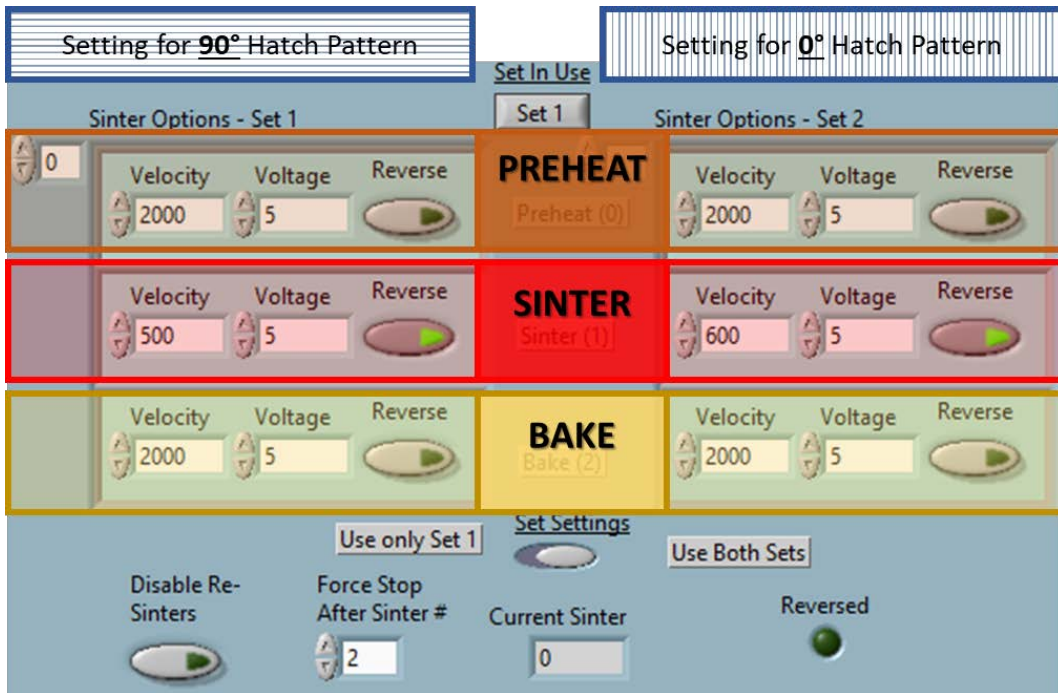


Figure 3.25: Multi-Pass Lasing with “Preheat”, “Sinter”, and “Bake” Lasing Customized for each Hatch Direction

#### **Subsystem 4: Multiple Reservoirs with intra-print powder extraction/addition**

Various hardware and vacuums were tested to accomplish the methods for powder extraction and it was found that a 5.5 peak HP vacuum reduced to a 0.25 inch hose coupled with an extended “spoon” (Figure 3.26) extracted all powder in 1-2 minutes depending on the volume of powder to be extracted. With the rake and shield moved between the dispensing chamber and build area there was  $<1^{\circ}$  C measured temperature fluctuations at the top layer which was included in the temperature setting for external material switches (Discussed in the previous section, Figure 3.24). Hardware was also tested to accomplish the methods for powder addition, and it was found that 1 inch copper tubing worked well for the powder addition because it uniformly preheated the powder and produced uniform powder flow with minimal dust when delivering powder through the powder addition port (Figure 2.26). This process took much longer than the powder extraction and ranged between 4-8 minutes. The combined time required for powder extraction and addition was ~8-10 minutes.

Imaging of the final part during material switches revealed minimal contamination between powders. However, when carbon fiber is used there was evidence of contamination at the first couple layers and can be seen clearly at the surface (Figure 3.27) after the first could layer there was only evidence of 1 or 2 fibers in layers that were intended to be neat/0% CF. Microscopy of fracture surfaces showing material switches is provided in chapter 6.

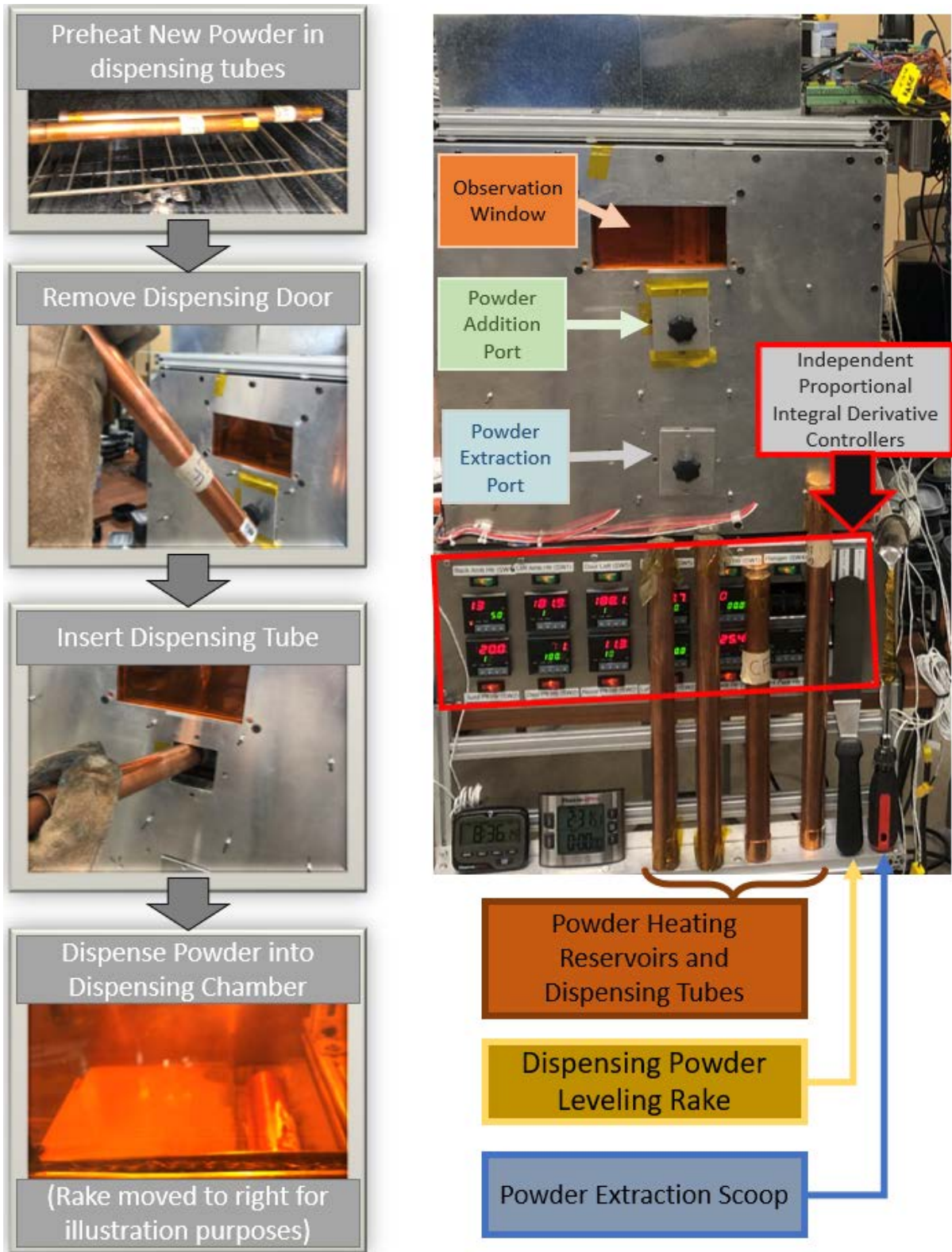


Figure 3.26: Powder Addition with Copper Dispensing Tubes, Leveling Rake, and Scoop

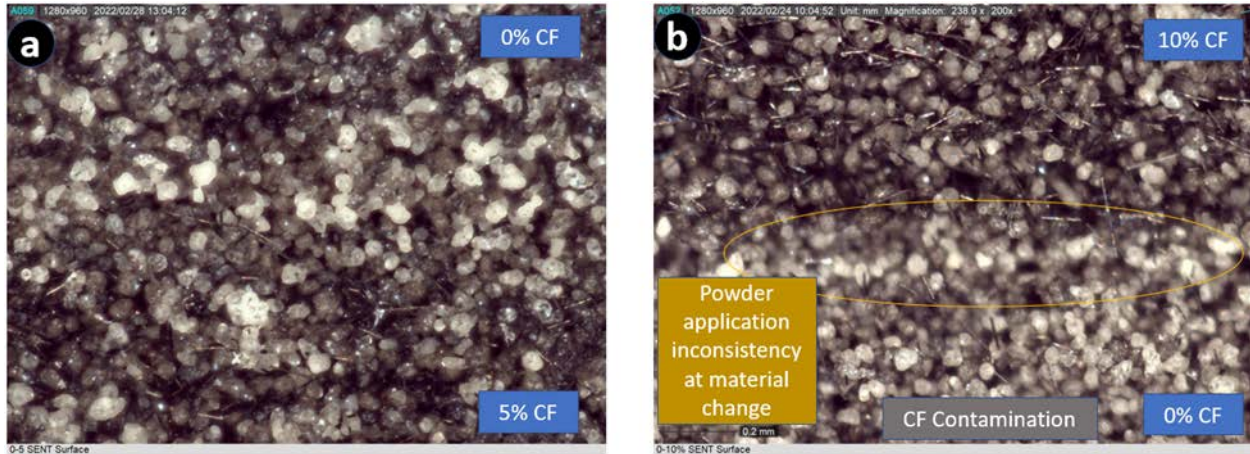


Figure 3.27: Comparison of Homogeneous and Inconsistent Powder Switch and Interface

- Homogeneous powder switch with smooth layer transition and negligible contamination
- Inconsistent powder switch CF Contamination when Switching from 5% CF by Volume to Neat PA12

### Subsystem 5: Multi-Material Layer Application

Multi-Material layer application (switching between the dispensing and reservoir chambers or after adding powder to the dispensing chamber) testing, tuning, and characterization resulted in poor layer adhesion between different materials with single pass powder recoating. Single pass recoating was prone to layer inconsistencies which resulted in voids and low density material at material interfaces (Figure 3.28). To rectify these inconsistencies in powder spreading a novel multi-pass recoating system was developed (Figure 3.29). The multi-pass recoating system was used when spreading powder from both the dispensing and reservoir chambers but only illustrated from the dispensing chamber in Figure 3.29. First the build area was lowered 1.5-2.5 times the distance of a single layer to allow “extra” powder to be delivered (Figure 3.29a). To fill this void the feed plate was raised an appropriate amount above what would be required for a single layer application (Figure 3.29a). Powder was spread (Figure 3.29b) and then the build plate was raised to set a single layer height (Figure 3.29c). Powder was then removed (i.e.

scraped off the top) of the build area with a reverse raking motion and delivered back to the feed chamber (Figure 3.29d). This novel multi-pass recoating system resulted in consistent material changes through all blends tested (Figure 3.30). However, this system also resulted in improved results for single material prints (Figure 3.31)

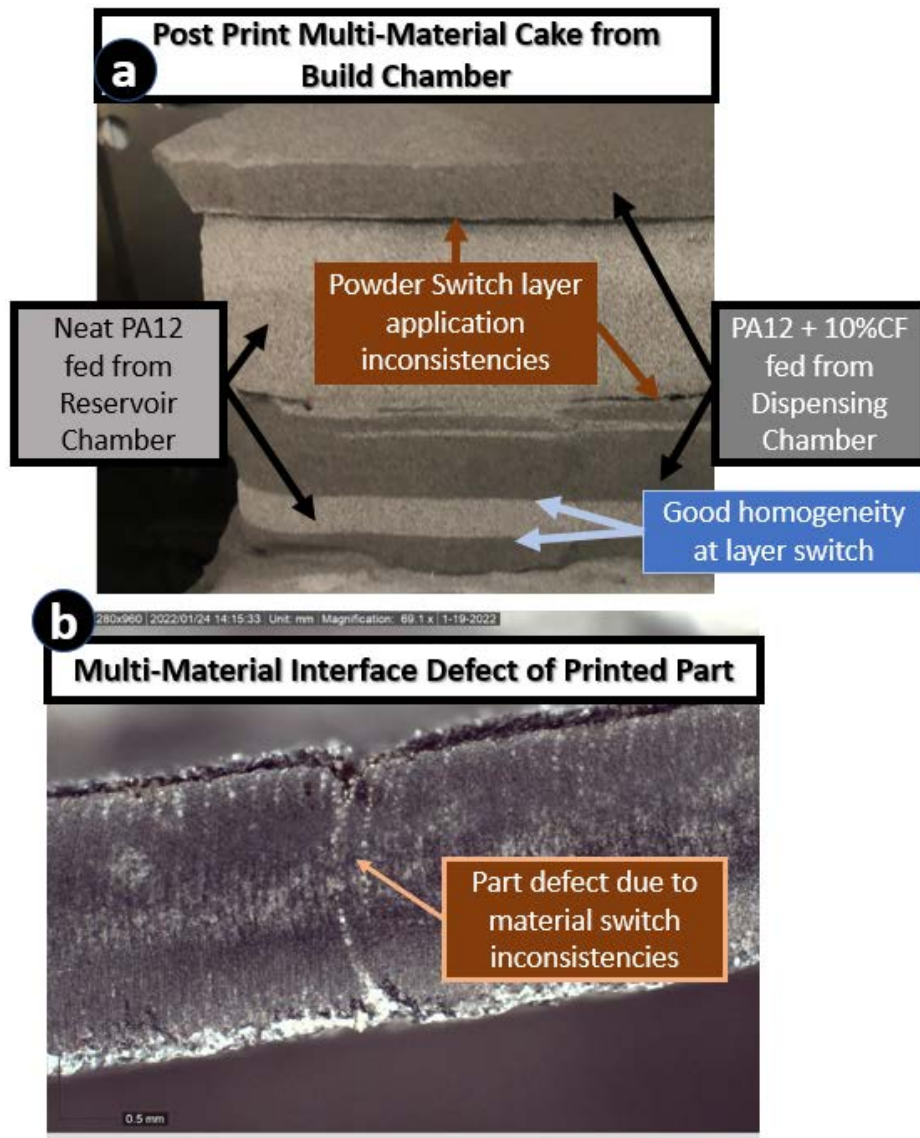


Figure 3.28 Layer Inconsistencies Resulting In:  
a) Voids and low-density material at material interfaces in the build chamber  
b) Part defects at multi-material interface

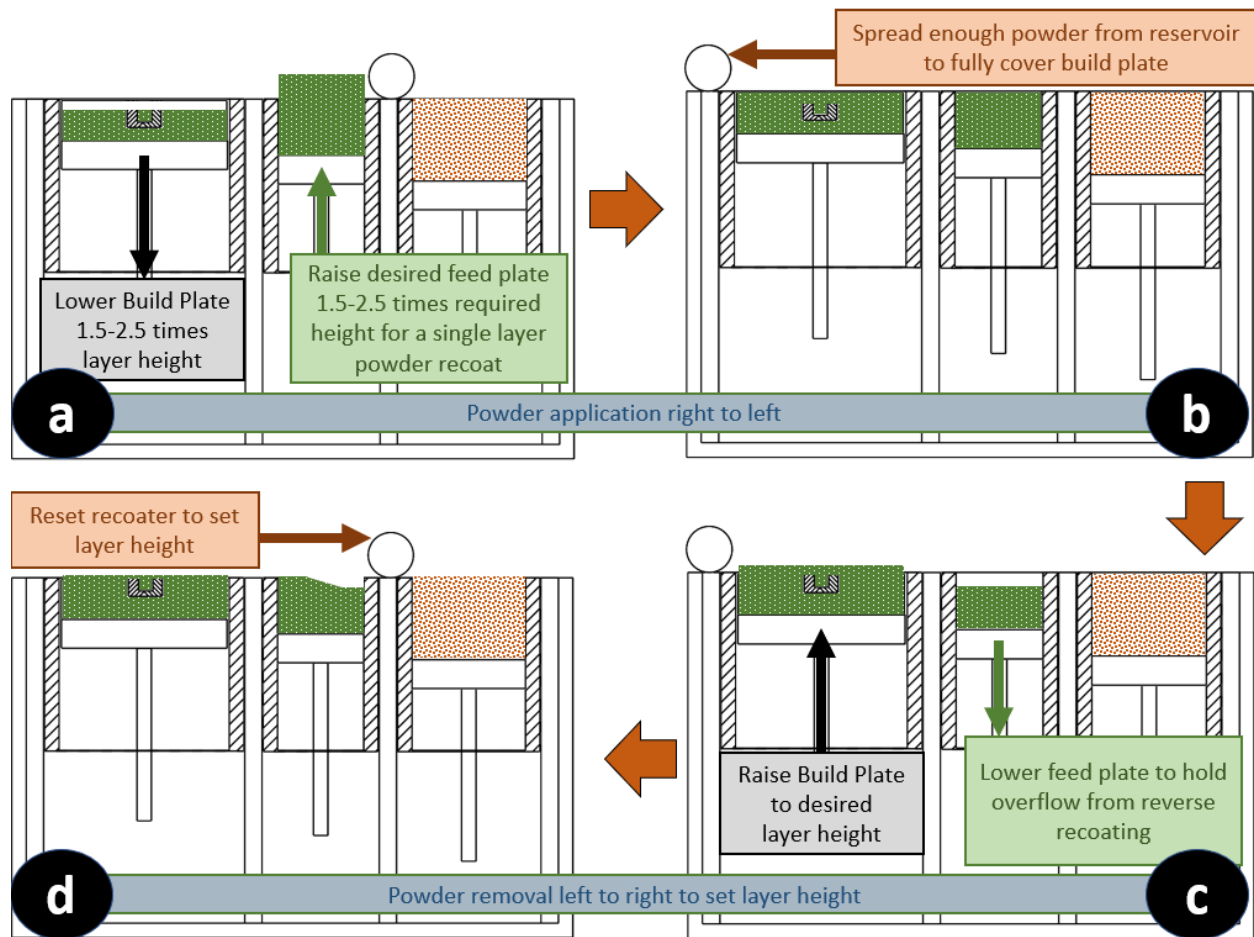


Figure 3.29 novel multi-pass recoating system was developed

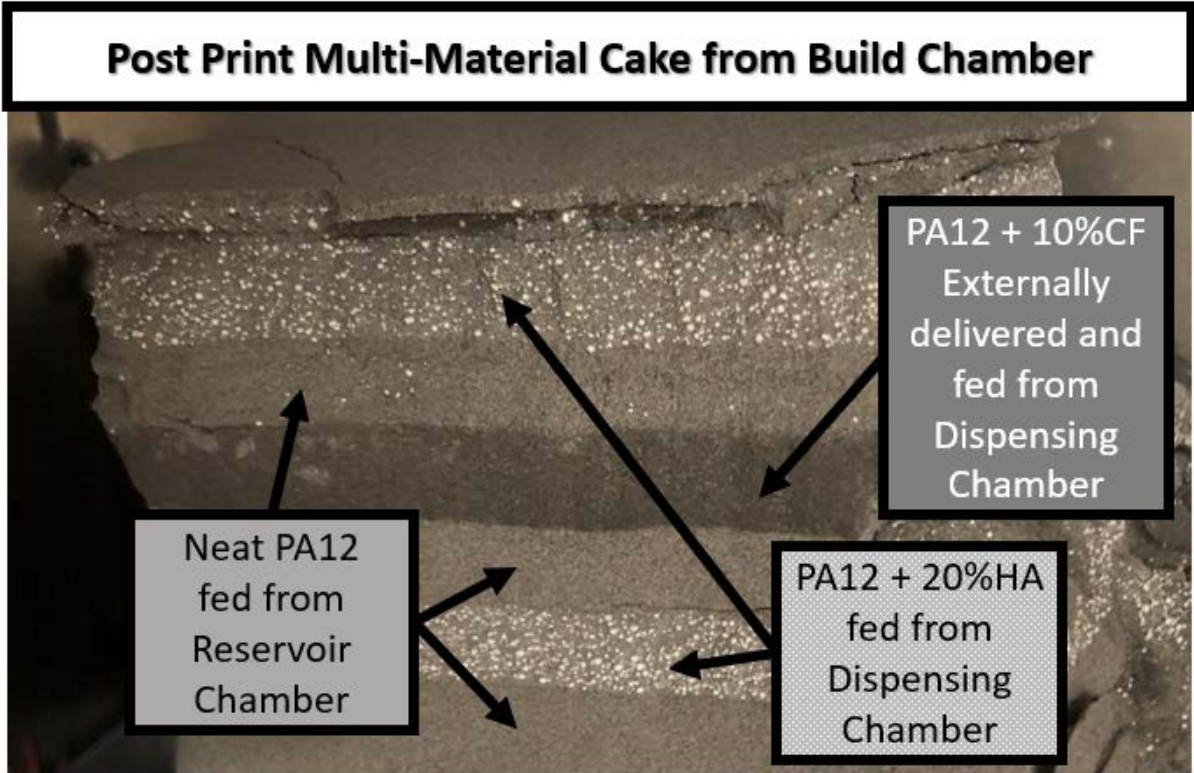


Figure 3.30: Post Print Cake Showing Homogeneous Layer Application at Material Changes Novel Multi-Pass Recoating System

### 0% CF Fracture Surface Comparison

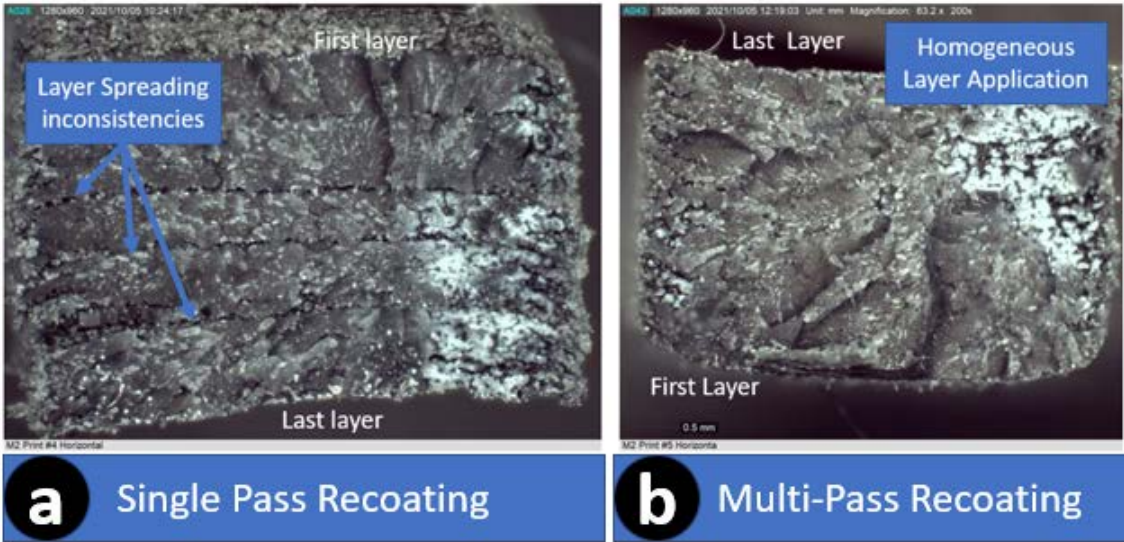


Figure 3.31: Tensile Fracture Surface of Single Material Print Demonstrating Advantages of Novel Multi-Pass Recoating System

## Subsystem 6: Part Anchoring

Multi-Material part anchoring with 10% or 5% CF/PA12 facilitated previously unprintable Single Edge Notch Tensile (SENT) specimens due to warping. The SENT specimens were used for Aim 4 and initial 0% CF layers are illustrated in Figure 3.32 without anchoring (3.32a) and with anchoring (3.32b). Comparison of CF anchoring is shown in Figure 3.33a, with thicker anchors reducing warping over thinner anchors. Quantification of warping is presented in the following chapter (Aim 2). M2 anchors also enabled printing TPE blends with PA12 anchors (Figure 3.33b) and high concentrations of HA with PA12 anchors (Figure 3.33c).

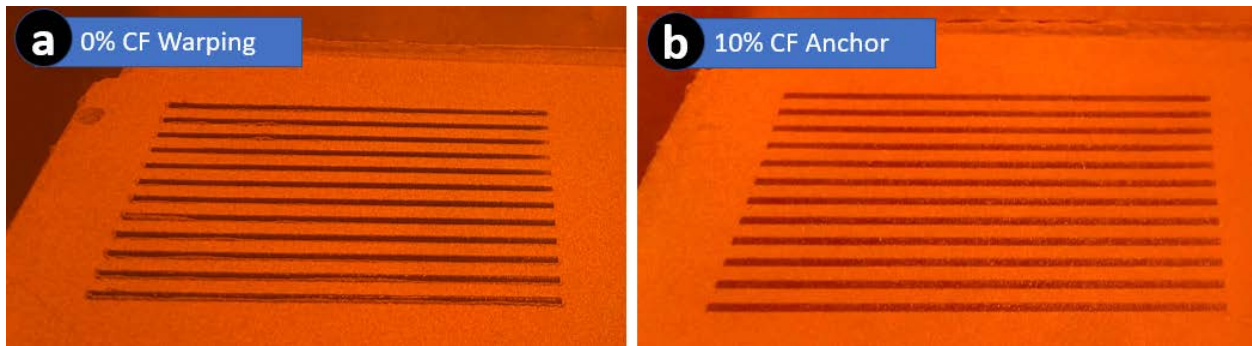


Figure 3.32: PA12 Single Edge Notch Tensile Specimen without Anchoring (a) and with 10% CF anchor (b)

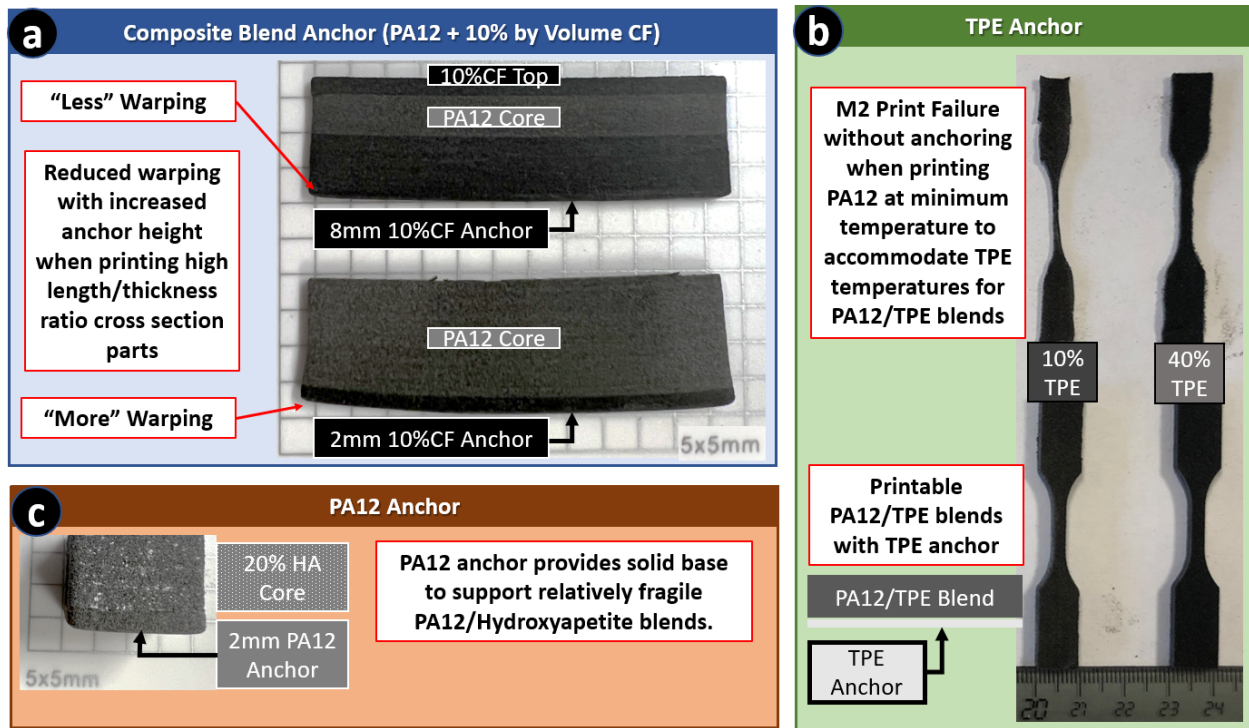


Figure 3.33: Anchoring results with 10% CF anchor (a) and PA12 anchor (b and c)

## Subsystem 7: Multi-Material SLS Host and User Interface

The M2 host was tuned throughout this research and resulted in full print status feedback with real time M2 and thermal control. Limited automation was integrated for material switches and most subsystems had to be manually controlled during material switches. This increased time required, time variation, and possibility for human error between material switches. Final results are depicted in the methods section of this chapter.

## DISCUSSION

All subsystems synchronously demonstrated feasibility of design and have also paved the way for improved efficiency and effectiveness. The developed M2 SLS Prototype was capable of consistently printing bi-material parts using the two internal chambers. Minimizing the time between layers and for the entire print was a critical aspect to the design. Future printers using

this design should incorporate more automation to reduce time during material switches and a higher-powered laser to reduce time while sintering each layer. Integrating automation does not simply reduce the amount of user interaction but decreases delays between layer applications which is critical in reducing layer inconsistencies and adhesion between layers.

Though the two-powder chamber prototype proved the feasibility of M2 PBF, multiple internal chambers would drastically reduce time of 3+ material prints. Multiple internal chambers (Provisional patent Provisional Patent 63/262,580) could be added either in a linear method (Figure 3.34 and 3.36) or a radial method (Figure 3.37 and 3.38) to reduce time between material changes. The most efficient technique would likely be to simply mirror the design of the prototype (Figure 3.34) with removable (i.e., “swappable”) reservoirs (Figure 3.35), allowing four internal materials with very little change to anything else in the current prototype. This mirrored system would also limit when the reduced temperature profile would have to be used since material changes internally between the dispensing and reservoir chambers had similar times as applying single material layers and so the hypothesized acceptance criteria of  $<3^{\circ}\text{C}$  maintained ideal thermal conditions for continues prints between materials.

High performance materials such as PEEK (critical for biomedical applications) will require high temperature capability. This will require a high-powered laser along with high powered ambient and top layer heaters. However, an inert chamber will likely be required to fully test these types of polymers and will increase the complexity of external powder switches.

# 4 Internal Material Design

Linear design with internal removable chambers

- Internal Capacity: 4 material

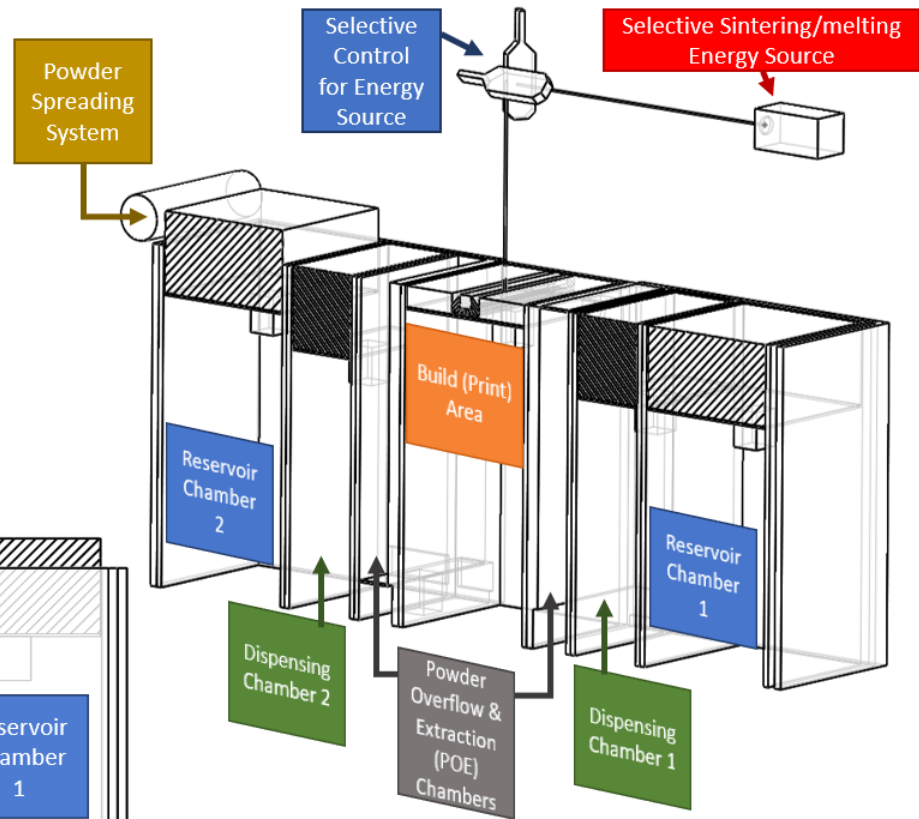
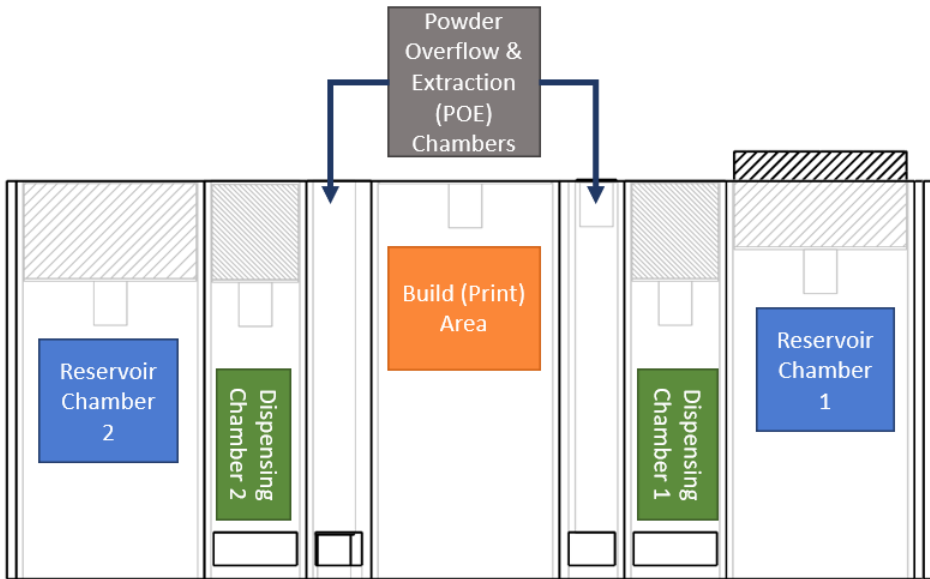


Figure 3.34: M2 SLS Mirrored 4 Chamber Design with Single Recoater

All Chambers are removable to facilitate material exchange with external chambers

Linear design depicted for clarity, however, this feature applies to all designs

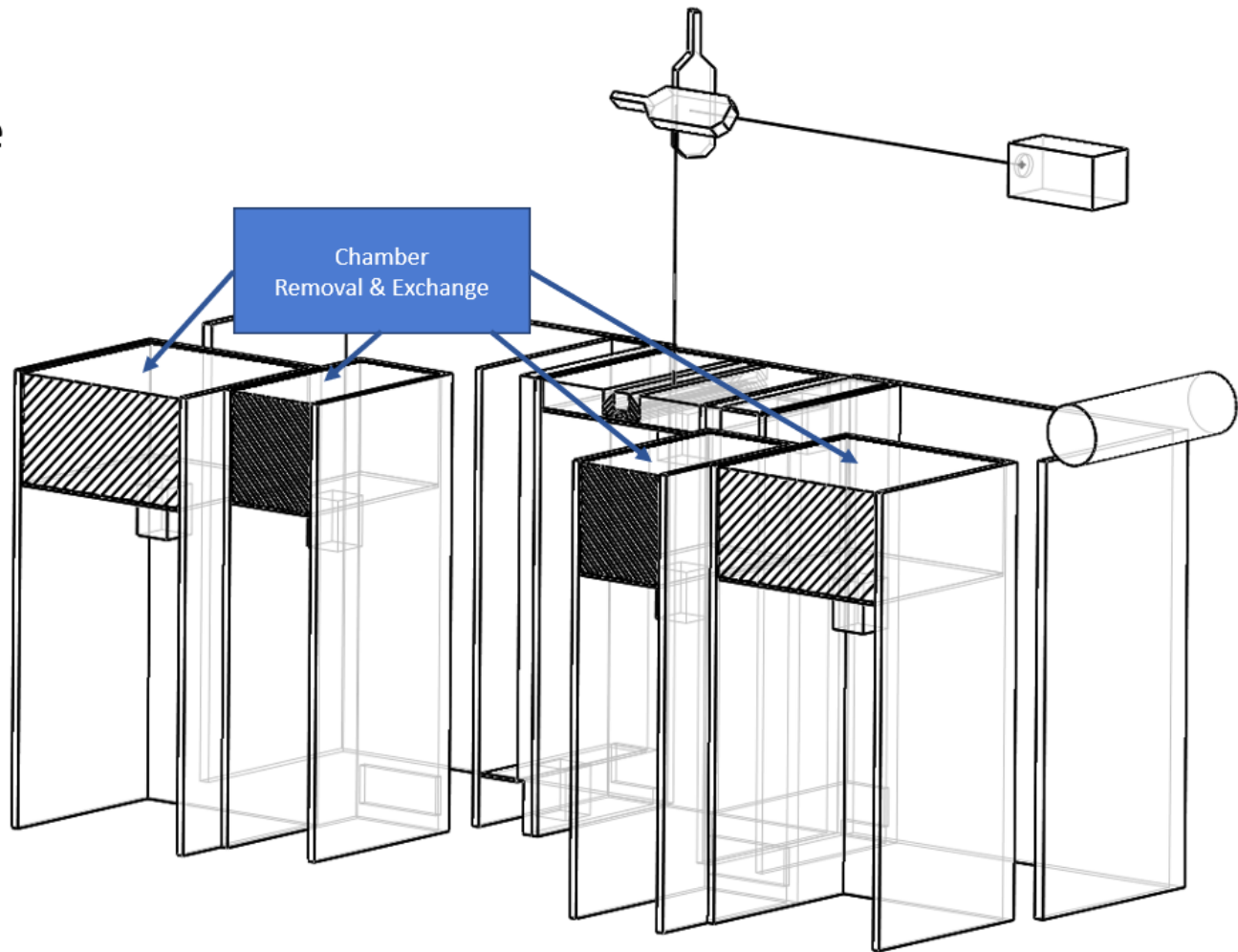


Figure 3.35: M2 SLS Removable (i.e., “Swappable”) 4 Chamber Design with Single Recoater

# 8 Internal Material (chamber) Design

**Rectilinear design with internal removable chambers**

- **Internal Capacity: 8 material**
- **Rotating chamber and/or spreader**

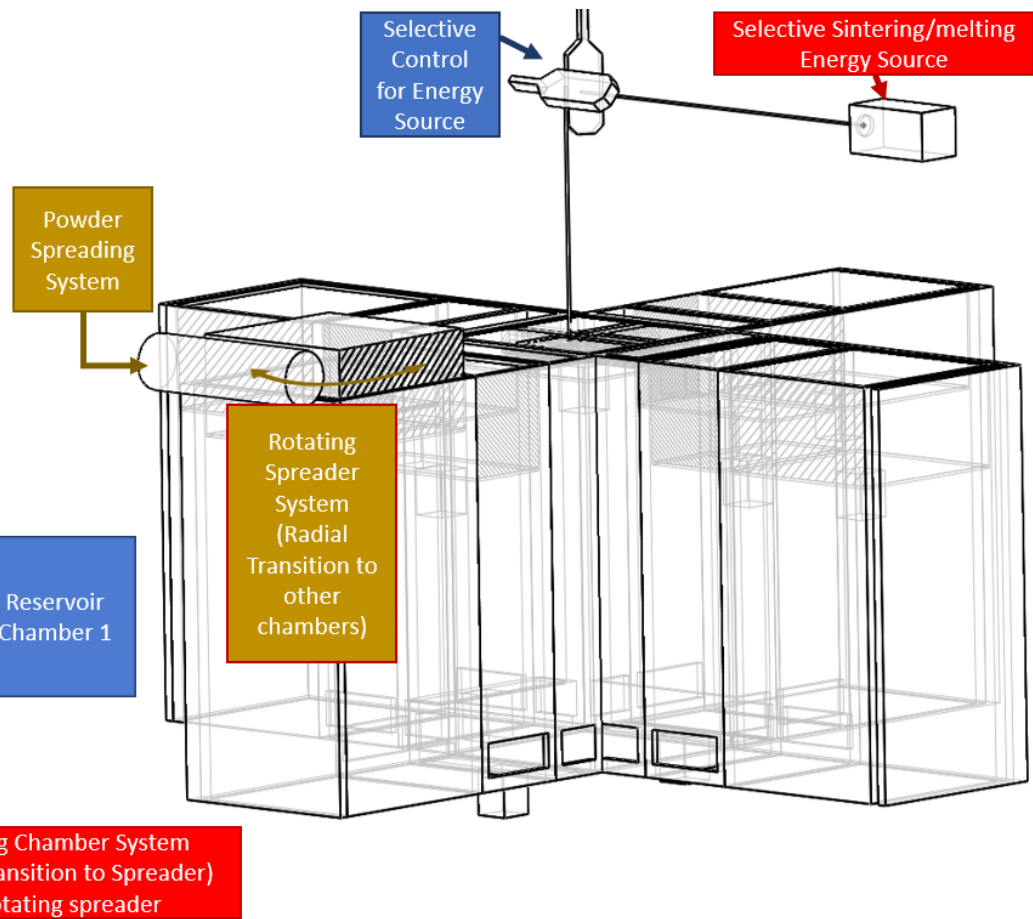
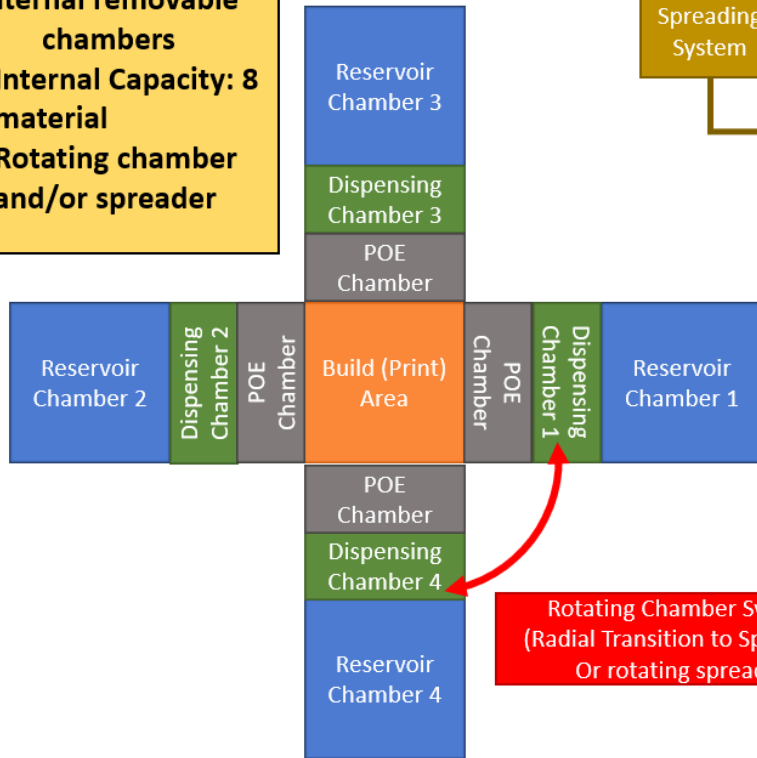


Figure 3.36: M2 SLS Linear 8 Chamber Design

# 8+ Internal Material (chamber) Design

**Radial Design:  
Single Rotating  
spreader or rotating  
powder chambers**

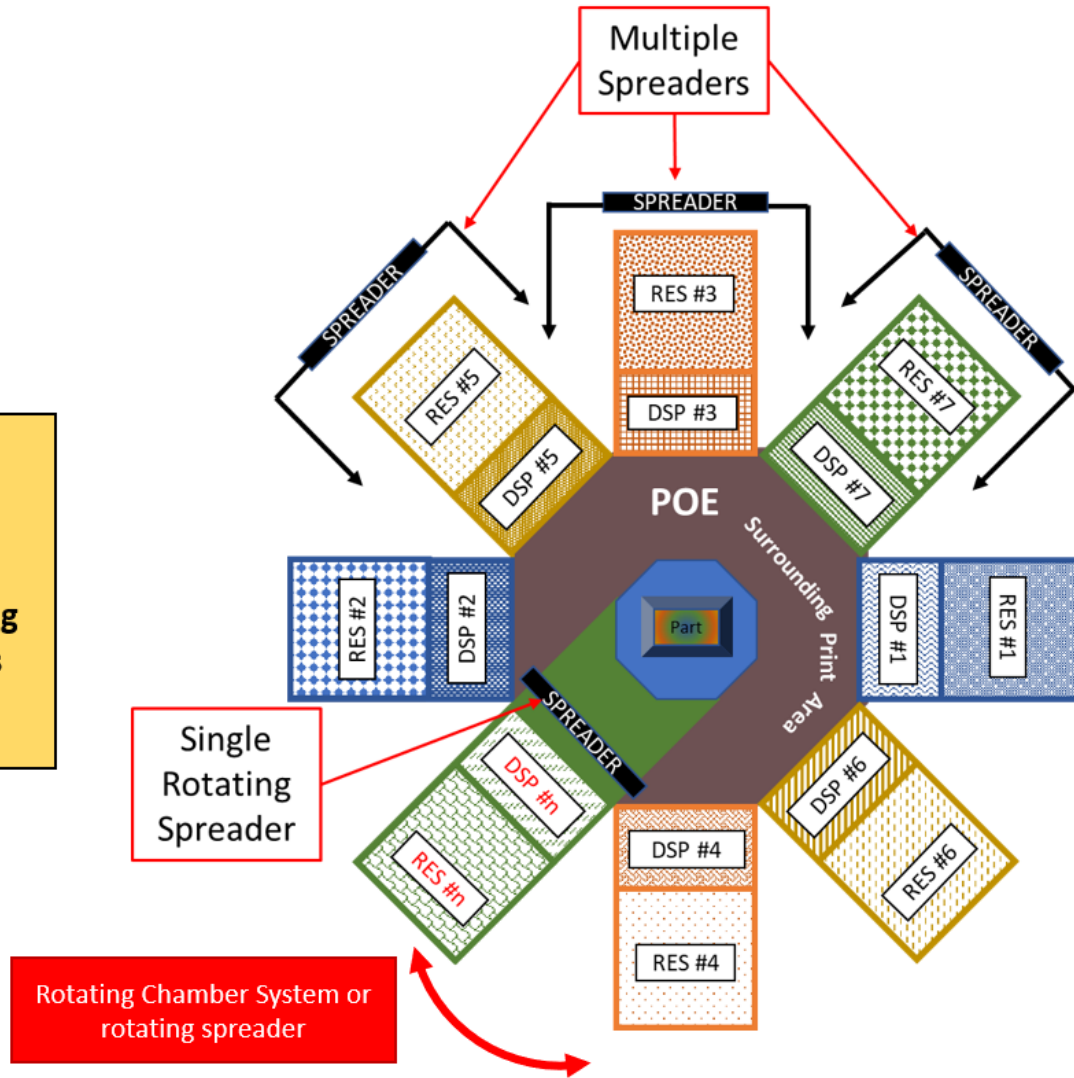


Figure 3.37: M2 SLS Radial 8+ Chamber Design

# 15+ Internal Material (Chamber) Design

**Rectilinear design with internal removable chambers and internal radial chamber system**

- Internal Capacity: 15+ material
- Rotating chamber and/or spreader

**Rotating Chamber System**  
 (Can mirror on other side to double number of internal chambers and combine with removable chamber system)

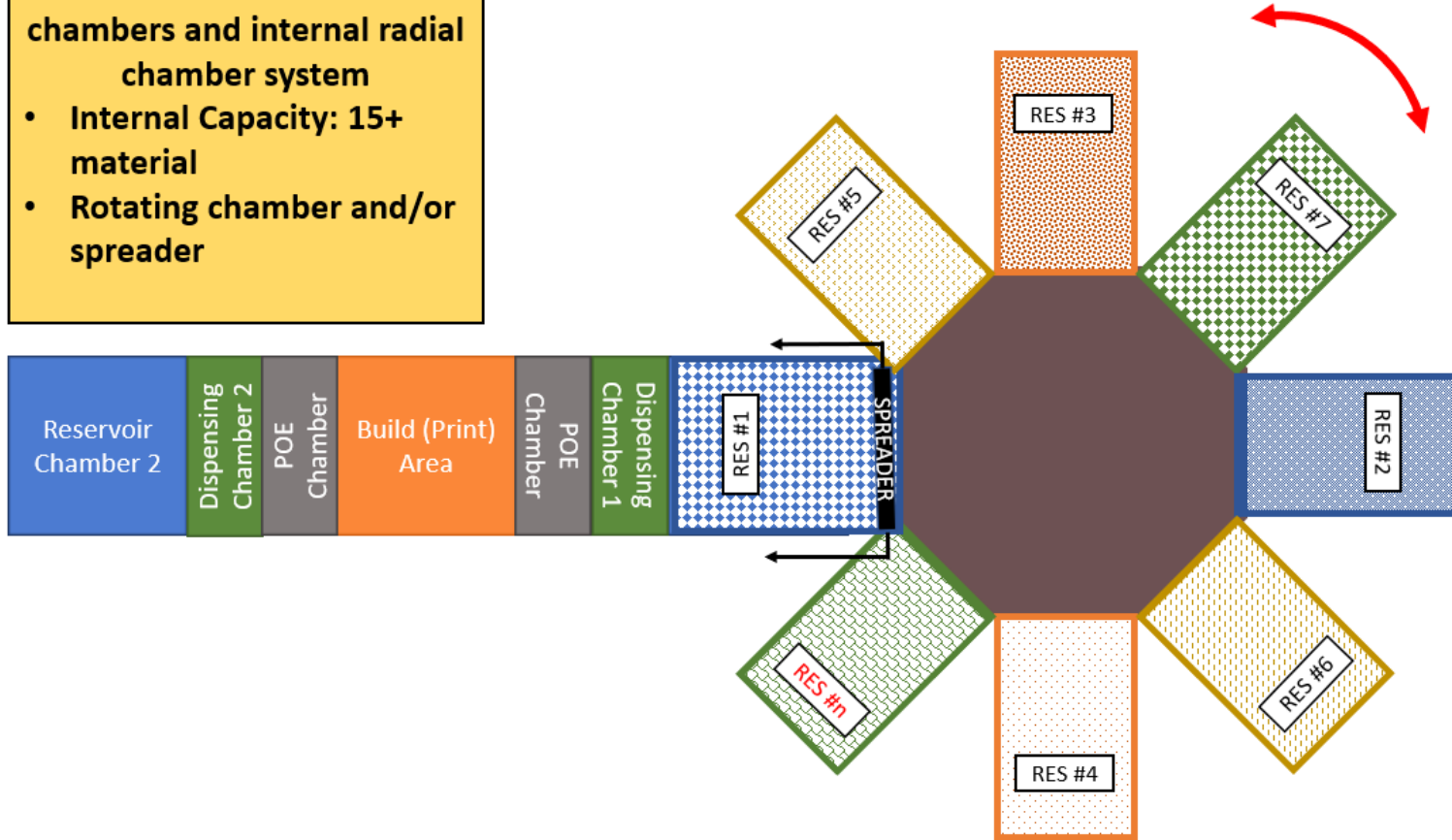


Figure 3.38: M2 SLS Linear 15+ Chamber Design

Much of Aims 1 and 2 testing was conducted concurrently and the research in the remaining aims continued this work and matured the subsystems to provide a fully operational prototype. Much of the discussion in those chapters is applicable to the M2 SLS design but is not repeated in this section.

## **BROADER IMPLICATIONS**

Many of the methods and results presented have been motivated by the goal of building and testing an operation prototype. However, the methods developed have a much broader scope than just low temperature sintering applications. First, the multi-chamber design can be implemented across most PBF systems and can be used to protect materials from the harsh environment of most PBF systems during extended prints. Keeping materials out of the environment required for sintering until needed can be applied to both single material and M2 prints. Second the multi-pass recoating has opened the door to customizing fiber or other composite material orientation. For instance, systems should be tested that still pull material from constant reservoir but have second or third pass recoating from a different direction to change the direction of fibers. This could be particularly helpful in increasing the homogeneity of AM parts if the fiber orientation was changed each layer or in customizing material properties based on load orientation. Third, the multi-pass lasing introduces “real time heat treatment options” that could maintain geometrical accuracy and complexity while fully sintering particles. Lastly, M2 anchoring can be used to sinter two materials together that have marginal sintering window overlap. When combined all these subsystems lead to a manufacturing process that may be developed to possibly produce previously unachievable parts in PBF.

## **CONCLUSION**

Overall, the design of the specific M2 subsystems and their integration into an SLS system worked well and the M2 SLS prototype proved the feasibility of M2 PBF capable of LCC and the manufacturing of functionally graded materials and parts. The lack of automation and robustness of components in the prototype caused substantial issues for the system, which will need to be upgraded before mass producing multi-material parts. In particular, a system with more than two internal powder chambers should be incorporated for parts consisting of more than two materials. Lastly, build area powder extraction should be tested and tuned to facilitate 3-dimensional material control.

## **Chapter 4: Aim 2 - SLS Material, Fiber, and Particulate Compatibility and Sintering Testing**

### **INTRODUCTION**

Aim 2 of the project investigated the feasibility of sintering mechanically blended ratios of thermoplastics (TP), thermoplastic elastomers (TPE), fibers, and particulates. Methodology incorporated materials compatible with low temperature ( $< 170^{\circ}\text{C}$ ), blue diode laser ( $455\text{ nm } \lambda$ ,  $5.0\text{ W}$ ), and ambient air sintering to accommodate testing using the Multi-Material (M2) Selective Laser Sintering (SLS) prototype developed in Aim 1. Though these constraints limited viable polymer powders and material blends to generally dark grey color, low temperature melting, and stable at elevated temperatures in the presence of oxygen; the results are directly applicable to most SLS systems currently available. Mechanical blending feasibility and performance were projected to other powders and materials and applicable to the future impacts discussed in Chapter 1. The results of Aim 2 ultimately added material variability to the M2 SLS prototype and most single material SLS systems.

Pioneering powder blend compatibility to meet the requirements of this research began with investigating neat (virgin) polymer powder flow, thermomechanics, sintering, and final part evaluation to ensure compatibility with the proposed M2 SLS. Commercially available neat powders known to perform well in similar sintering environments as the M2 SLS were tested to find sintering window overlap of the powders. Material blend investigation followed the same evaluation method as the neat polymer investigation. Printed blends were tested for mixture homogeneity, particle coalescence, and layer bonding. Aim 2 initial results led to an in-depth evaluation of Nylon-12 (PA12) as a matrix material and the feasibility of functionalizing final parts with TPE, carbon fiber (CF), and hydroxyapatite (HA). Aim 2 concluded with specific M2

SLS prototype sintering settings for PA12/CF and PA12/HA blend ratios that were used in Aims 3 and 4.

## **BACKGROUND**

Polymers available for SLS are limited by the distinctive and relatively rare material properties required to successfully sinter a polymer powder (Schmid & Wegener, 2016a). Thermal material properties specific to sintering (Figure 4.1) must match the selected sintering energy source. When sintering polymer blends, all materials in the blend are subject to the same energy sources and thermal conditions and at a minimum must be tolerant of the sintering process. Polymer blends with fibers and/or particulates can be susceptible to conglomerating and clumping out of the blend during powder spreading. Avoiding particle conglomeration while assure adhesion between blended particles, laser hatch lines, and layers during sintering is essential to final part integrity.

AM blending in PBF has unique challenges and requirements when compared to M2 fabrication in other AM processes such as Fused Deposition Modeling (FDM) (i.e., FFF – Fused Filament Fabrication) or Polyjet printing. In most other manufacturing methods material blending is done in a molten or liquid state. This inherently requires the blend to flow in a liquid state which becomes problematic for high percentages of fibers or particulates in composite blends. Liquid state blending can be done for PBF applications to the PBF prior to the printing process. In this case the blend material normally requires re-powderization post blend solidification. This may also involve specialized manufacturing methods to adhere or encapsulate different fillers into a single M2 powder mixture (C. Yan et al., 2011a; Yuan et al., 2019). These methods make it difficult to alter blend ratios once a specific ratio is manufactured because the entire process of liquid blending and re-powderization must be done to change a blend. Also, this

blending technique can be limited to liquid flowability which in turn limits the volume of fibers or particulates that can be added to a blend similar to M2 FFF printing.

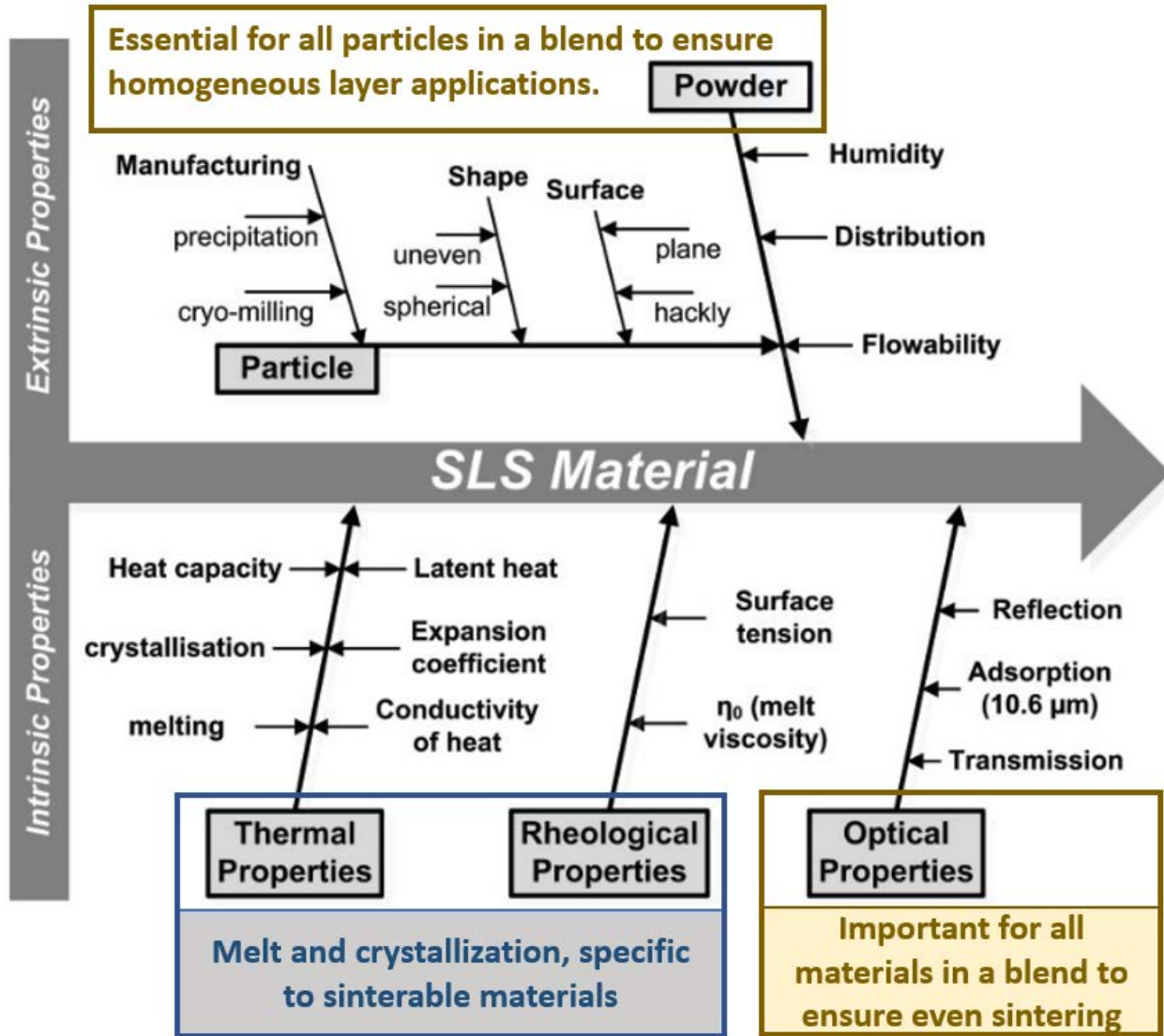


Figure 4.1: Material properties and the effect on sintering (Adapted from Schmid, et al. (Schmid & Wegener, 2016b))

Blended polymer powders generally require intrinsic and extrinsic properties to coincide, while blended composites required some commonality in extrinsic and optical properties between the materials (Figure 4.1). Thermal property overlap was required to achieve polymer

chain blending and bonding during recrystallization of dissimilar mechanically blended polymer powders (Drummer et al., 2012). When blending in fibers and/or particulates the fibers and particulates tested do not melt or recrystallize and are stable at the sintering temperatures (i.e., do not change shape or degrade); however, compatible extrinsic (Figure 4.1) and optical properties are required between all blended particles to ensure homogeneous layer spreading and uniform sintering, respectively.

Sintering mechanisms for polymer PBF require material thermal properties which allow particle coalescence and fusion by selectively softening the powder through heating. Many semi-crystalline thermoplastics (TP) have compatible thermal properties for this process and as such were used for this study. Semi-crystalline TPs begin to soften (rapid decrease in modulus of elasticity) when approaching the material's glass transition ( $T_g$ ) (Tobolsky, 1960). Polymer chains possess enough thermal energy to mobilize at  $T_g$  and shear strength begins to drop, and viscosity becomes dominant. However, substantial softening does not occur until the melting temperature ( $T_m$ ) is reached, at which point the crystalline regions lose their structure (Azom, 2016). Polymer sintering processes are complex, but primary binding mechanisms occur during cooldown. Polymers stiffen at the re-crystallization temperature ( $T_r$ ) when the chains reposition and cross-link. The sharp decrease in specific heat flow at  $T_m$  and sharp increase at  $T_r$  found in many polyamides (PA) make them ideal polymers for sintering (Figure 4.2) (Gibson & Shi, 1997). Many copolymer TPEs have a PA hard link that follows a similar coalescing process as PAs and have an amorphous soft link that remains relatively unaffected during sintering (Figure 4.3) (Yuan et al., 2019). Pesetskii et al. (Pesetskii et al., 1999) mechanically blended polyamide 12 and thermoplastic polyurethanes (TPU) pellets and then extruded the mixture into a single blended material via a twin screw extruder. Pesetskii discovered partial compatibility between the

polyamide 12 with both the soft and hard blocks of the TPU. The similarity of the thermal properties and binding mechanisms of a PA TP and copolymer TPE hard block may result in sintering window overlap for blended ratios which was essential to sinter blends for this research.

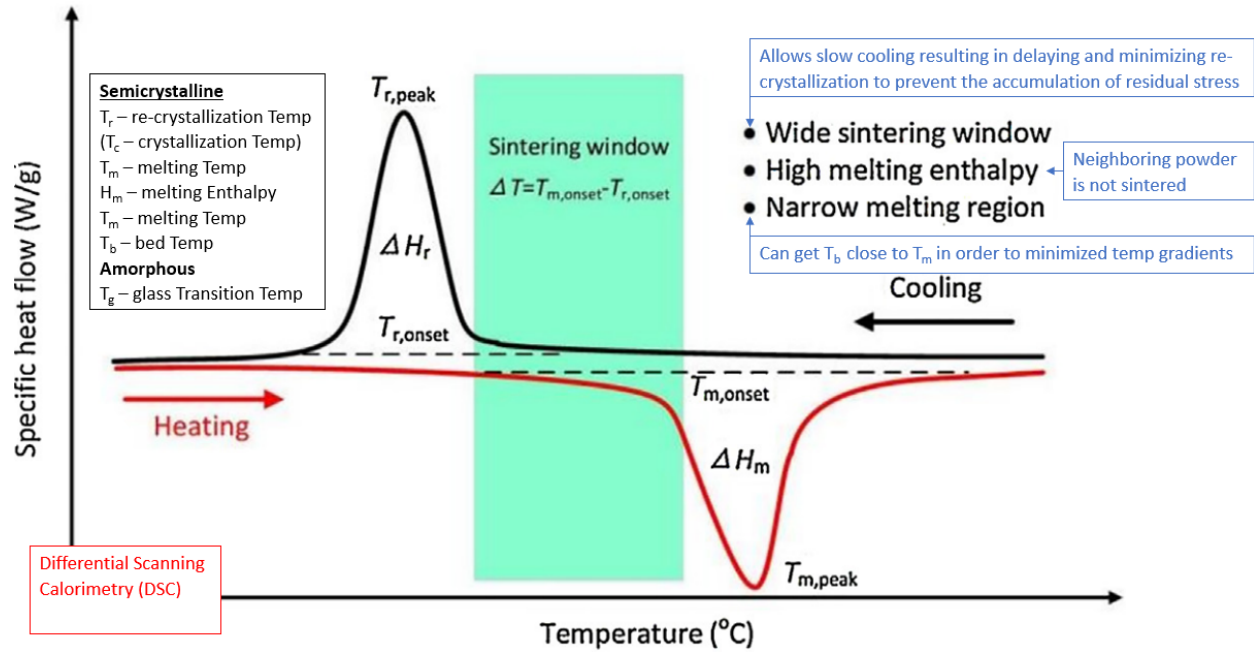


Figure 4.2: Required material properties for sintering. (Adapted from Schmid, et al. (Schmid & Wegener, 2016b))

Polyamide 12 (PA12) TP, also known as Nylon 12, and copolymer TPE powders were selected to provide a sinterable material property overlap criteria discussed above and the capacity to validate possible future synthetic joints. Carbon fiber (CF) and Hydroxyapatite (HA) particulates were selected to enable functionalization of joint implants using CF for wear resistance and HA for osseointegration. Both CF and HA composite testing was done in a PA12 matrix.

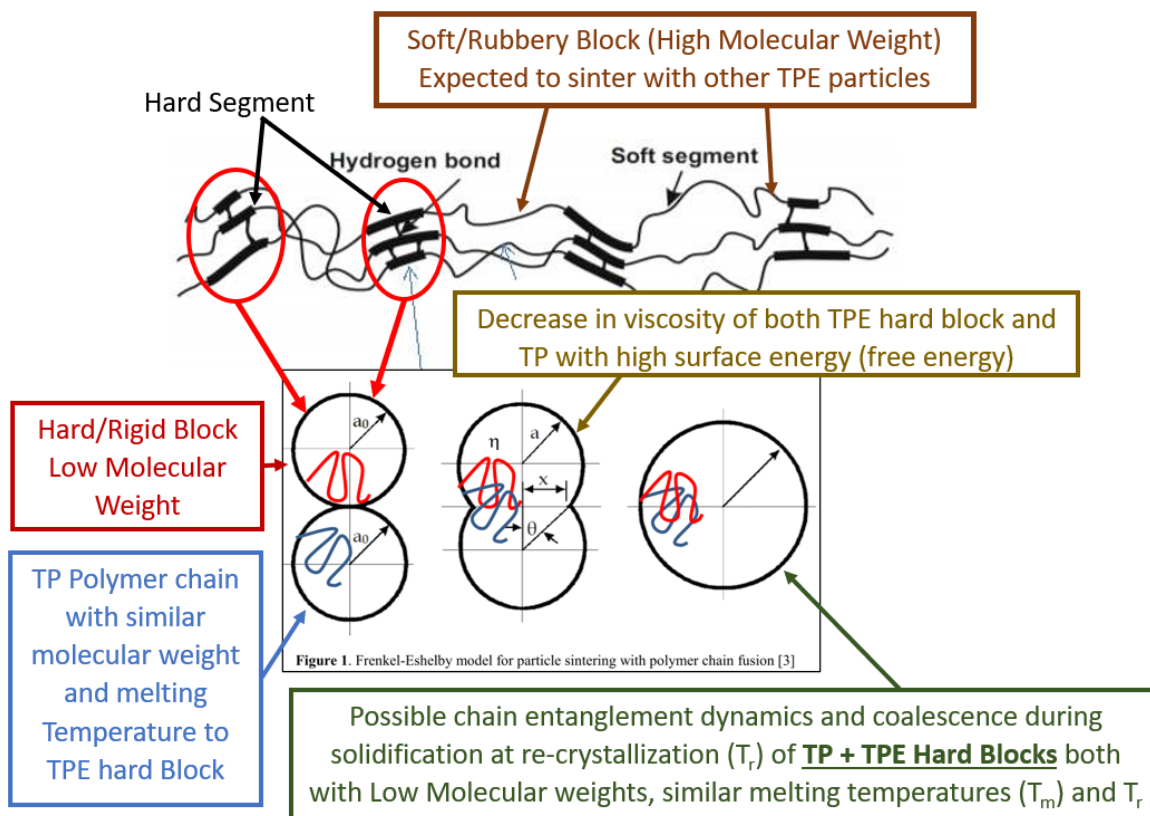


Figure 4.3: Possible chain entanglement dynamics of TP and TPE hard blocks (Adapted from Auhl, et al. (Auhl et al., 2019) )

Research and industry have mechanically blended TP, TPE, fibers and particulates which indicated this combination was likely to work well in the prototype M2 SLS. Below are examples of blends that demonstrated the feasibility and possible outcomes for the selected PA12 matrix blends with TPE, CF, and HA.

### Fiber Blend

PA12/CF blends have been sintered with good bonding between the fibers and thermoplastic by first encapsulating the fiber in a thermoplastic (C. Yan et al., 2011b). Compatibility is established between PA12 and CF with this method but limits CF ratios to  $\leq \sim 10\%$  by volume.

## **Particulate Blend**

HA particles have been mechanically mixed with PEEK pellets and extruded (Rodzeń et al., 2021) and showed promise in different sinterable powder mixtures (K. Li et al., 2012). Chung et al. have successfully mechanically mix and sintered glass bead and silica particles with PA11, also indicating possible success with PA12/HA blends. Carbon particulate (pearl) blending with PA12 has successfully increased the UTS of sintered parts (Espera et al., 2019a), indicating possible improved UTS with PA12/HA blends at low ratios.

## **Material Blend (Polymeric Composite)**

Polyjet additively manufactured polymeric composites have been successfully manufactured and the resultant changes in E and UTS based on material blend ratio has been characterized (Lumpe et al., 2019; Meng et al., 2020). Actively mixing filament during fused filament fabrication (FFF) is also capable of controlling E and UTS (Green, Slager, et al., 2021). Combined, these successes pointed to the feasibility of sintering PA12/TPE blends.

## **Critical Sintering Parameters and Material Properties for Blended Polymer PBF**

Sintering parameters and material properties critical to SLS printing are detailed below and outlined in Figure 4.1-4.3 (definitions given in parenthesis for some parameters to add clarity). These parameters were used to select materials and methods for Aim 2:

### **Sintering Energy Source Properties:**

- **Energy Source Type:** diode laser used in the MS SLS prototype.

1. **Wavelength ( $\lambda$ ):** Had to be compatible with optical properties of any powder selected to ensure sufficient energy absorption to sinter material.
  - Prototype laser wavelength = 455 nm
2. **Power:** Had to match material thermal properties of any selected powder to ensure sufficient energy to sinter material.
  - Prototype maximum laser power = 5 watts (W)
3. **Rate (laser speed):** Had to be balanced to affectively sinter raster to raster and layer to layer. A high laser speed increases the surface temperature and increases raster to raster bonding, but a lower laser speed allows the laser energy to penetrate deeper and increase layer to layer bonding (Drummer et al., 2014).
  - Prototype typical sintering speeds 350-800 mm/sec.

#### **Bulk Material (Intrinsic) Properties:**

- **Thermal Properties:** Dictated sintering window (Figure 4.1).
  1. **Melting Temperature ( $T_m$ ):** (complete softening through de-crystallization or free movement of polymer chains during polymer heating (Gibson & Shi, 1997) which decreases viscosity and allows coalescence through surface energy.)

Melting temperature overlap required between TP and TPE.

    - Blended TP and TPE powders had to have overlapping sintering windows with similar  $T_m$ .
    - CF does not have a defined  $T_m$  and the temperatures and energy densities remained well below HA  $T_m$ .

2. **Re-crystallization Temperature ( $T_r$ ):** (onset of crystallization temperature during cooldown (L. J. Tan et al., 2020).) Re-crystallization overlap was required between TP and TPE in TP/TPE blends.

- Blended TP and TPE powders should have had overlapping sintering windows with similar  $T_r$  to allow crystallization and solidification of entangled polymer chains between TP and TPE
- The amount of crystallization is primarily based on cooling rate. Zhao et al. have shown that PA12 begins to crystallize after 50 minutes during cooling at 168 °C (Zhao et al., 2018).

3. **Sintering Window:** (region between  $T_m$  and  $T_r$ , sintering window magnitude =  $T_m - T_r$ ) Overlap between TP and TPE was ideal.

- PA12 has a sintering window magnitude of approximately 20-30° C (L. J. Tan et al., 2020). It was desired PA12 and TPE sintering windows overlap for TP/TPE blend sintering.
- Clumping can occur by particles coalescing over time at temperatures below the sintering window. This affected TPE during long prints when blended with PA12 and held at elevated temperatures to accommodate PA12 particle sintering.

- **Rheological Properties**

1. **Melt Viscosity:** (viscosity of a polymer above melting temperature) Allowed melted particles to flow in liquid form (Figure 4.4) (Haworth et al., n.d.; Vasquez et al., 2014). Viscosity is also affected by polymer aging at elevated temperatures which can cause viscosity to initially increase due to cross linking followed by a

chain scission and a decrease viscosity (Allen et al., n.d.; Zhao et al., 2018). This can occur during extended prints or when re-using powder and result in an increase in porosity due to an increase in flowability (Wudy et al., 2014; Zhao et al., 2018).

- Melt viscosity had to be low enough to allow melted polymer to encapsulate the blended fibers and particulates for composite blends.

2. **Surface Tension:** (tendency of a fluid to seek a low surface energy state and so occupy the smallest possible surface area) Time to fully coalesce is material dependent and required materials to be held at elevated energy and temperature states for material specific amounts of time. (Figure 4.4) (Hejmady et al., 2019; Vasquez et al., 2014).

- Surface Tension strong enough to

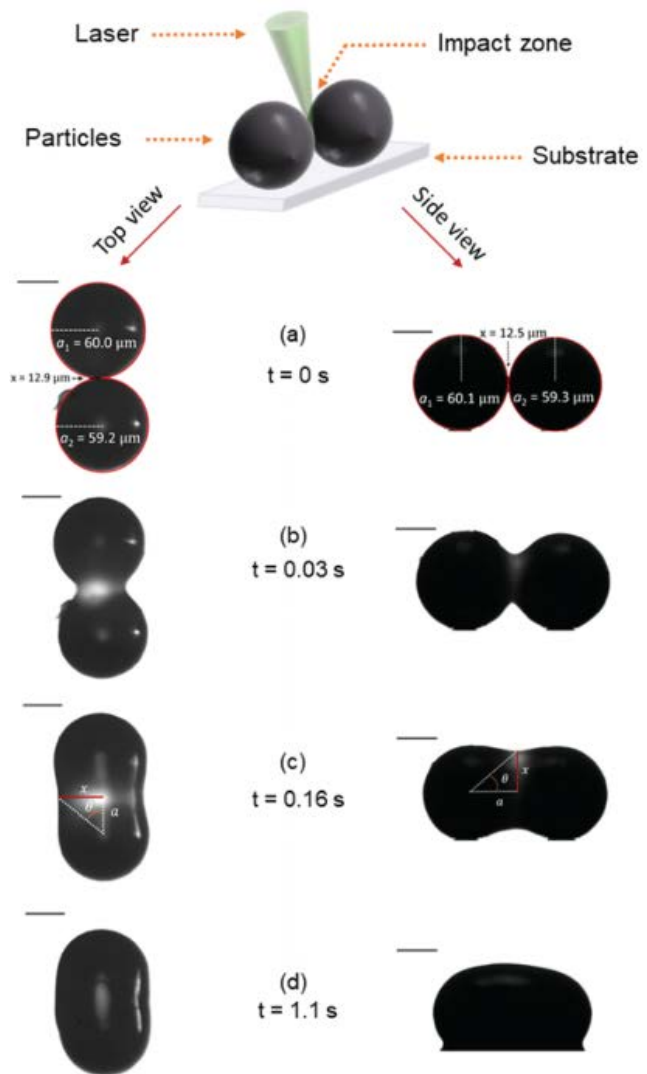


Figure 4.4: Particle coalescence due to surface tension and decrease of viscosity at  $T_m$  (image adapted from Hejmady et al., 2019)

coalesce compatible TP and TPE hard sections for powder blends.

- **Chemical Properties**

1. **Molecular Weight:** increases and deteriorates material properties when held at high temperatures for long periods of time (Cano et al., 2018; Craft et al., 2018; J. Zhang & Adams, 2016).
  - Material change processes described in Aim 1 for the M2 SLS prototype increased print times compared to single material SLS. TP and TPE powders had to be tolerant to these conditions while thermal systems had to minimize bulk powder time at elevated temperatures. This also decreased powder re-useability (see discussion on “powder re-use”).
2. **Chemical Crosslinking:** (Intermolecular joining of two or more molecules, generally through covalent bonding.) Likely to occur when PA12 and TPE are held at elevated temperatures (Craft et al., 2018).
  - Chemical crosslinking considerations were the same as molecular weight affects above.
3. **Chain Scission:** (Breaking of polymer chains). Chain scission will generally result in lower mechanical properties (Czelusniak & Amorim, n.d.; Drummer et al., 2010, 2014).
4. **Oxygen Functional Group Decomposition:** (Oxygen – Carbon bond decomposes). Oxygen functional group decomposition will generally result in lower mechanical properties (Czelusniak & Amorim, 2020).
5. **Crystallization:** (Degree of order or alignment of polymer chains (i.e., chain folding) in some segments of the polymer which can occur due to cooling below

the crystallization temperature or induced by mechanical manipulation such as stressing a part.). Density, melting point, and stiffness generally increase with an increase in crystallinity.

- Density of amorphous PA12 is 0.99 g/cm<sup>3</sup> and is increased to 1.034 g/cm<sup>3</sup> for the  $\alpha$ -phase crystal polymorph and 1.085 g/cm<sup>3</sup> for the  $\gamma$ -phase crystal polymorph (K. Chen et al., 2022; L. Li et al., 2003b).
- During sintering crystallization normally occurs slowly at high temperatures followed by slow cooling to room temperature resulting in  $\gamma$ -phase crystallization (Goodridge et al., 2012; L. Li et al., 2003a; Paolucci et al., 2020).
- Sintered density is generally reported between 0.95-1.02 g/cm<sup>3</sup> for PA12 and up to 1.04 g/cm<sup>3</sup> for compression molded parts (J.-P. Kruth et al., 2006).
- Czelusniak found a decrease in crystal fraction with increasing energy density when sintering PA12/CF composites (Czelusniak & Amorim, 2020).
- X-ray diffraction (XRD), Nuclear Magnetic Resonance (NMR), and Differential Scanning Calorimeter (DSC) are examples of test procedures that can be used to estimate crystallinity (XRD and NMR or compare relative crystallinity (DSC) between different samples (Martynková et al., 2021).

6. **Chemical Groups:** (Specific molecular makeup and polymer chains for TP and TPE (Liu & Ramakrishna, 2019).) Ideally chemical groups would be matched for

blends to facilitate coalescence and chain entanglement between blended powders.

- This information is proprietary for each sintering powder tested was not disclosed by the powder manufacturers.

7. **Thermal Oxidation:** (Oxidation caused by elevated temperatures.) Materials must remain inert in ambient air during sintering process at elevated temperatures (Chatham et al., 2019).

- M2 SLS prototype does not have an inert chamber which required the materials to remain inert in ambient air during the sintering process.

8. **Additives:** (Added materials and chemicals to improve sintering performance and recyclability.) Proprietary blends TP and TPE powders manufactured for SLS can be coated or doped with a binder material to increase flow and sintering effectiveness (J.-P. P. Kruth et al., 2004).

- All tested powders were assumed to not be pure PA12 or TPE and were assumed to have additives to facilitate sintering. Details of these coatings were not disclosed by the manufacturer causing PA12s from different manufactures to produce different results. As a result, sintering parameters were re-tested for each manufacturers variant of powder.

9. **Powder Re-use:** (Reusing unsintered powder from previous prints.) Powder re-use will affect particle coalescence and final part properties (Dadbakhsh et al., 2017; Pavan et al., 2017).

- Fresh powder was used when part material properties were to be measured following a print to ensure consistency and comparability between tests.

10. **Powder Preheating:** (Preheating bulk powder prior to sintering.) Preheating time and temperature affect overall print quality (density, warping, dimensional accuracy) and removal of secondary sintered layers during part removal (C. Yan et al., 2021)

- Preheat parameters were tested for each material and blend to achieve ideal sintering parameters.

- **Optical Properties** (Figure 4.5)

1. **Absorption:** (Laser energy absorbed by the powder or blend.) Laser energy absorption is required to heat and soften powder when sintering material.

- Absorption properties for the M2 SLS prototype diode laser forced TP and TPE powders to be dark grey or black in color.
- Absorption for CF is typically over 70% with minimal reflection at  $\lambda=455$  nm (Weber et al., 2012). High absorption and low reflectance of CF heated surrounding powder and aided coalescence of PA12 matrix and bonding between PA12 and CF.
- Absorption of HA is typically less than 10% at  $\lambda=455$  nm will result in HA gaining very little energy or heat during sintering (Mondal et al., 2017; Shishkovsky et al., n.d.). Low absorption and high reflectance of HA hindered heating neighboring matrix particles and decreased matrix sintering and bonding to HA particles.

2. **Transmission:** (Laser energy transmitted through a material with minimal energy transfer to the material.) Some transmission is desirable during sintering to heat

the previous layer above  $T_m$  to facilitate sintering between layers and aid layer to layer bonding.

- Tested TP and TPE powders were designed for sintering and had adequate transmission properties to sinter layers together. However, CF and HA generally have very low transmission properties, particularly at 5W, which hindered layer to layer bonding in blends with high concentrations of CF and HA [(Adibekyan et al., 2019; Han et al., 2020; Zaami et al., 2021)].
3. **Reflection:** (Laser energy reflected off a material with minimal energy transfer to the material.) All materials used for sintering will have some reflection (based on wavelength and material type) which takes away from the energy being absorbed and transmitted.
- High reflection of HA at  $\lambda=455$  nm is expected decreased heating of HA and caused relative cold spots around HA particles which resulted in degrade matrix sintering and HA/matrix bonding. In contrast, CF absorbed the laser energy with generally strong CF/HA bonding (Kaygili et al., 2013; Khademhosseini & Camci-Unal, 2018).

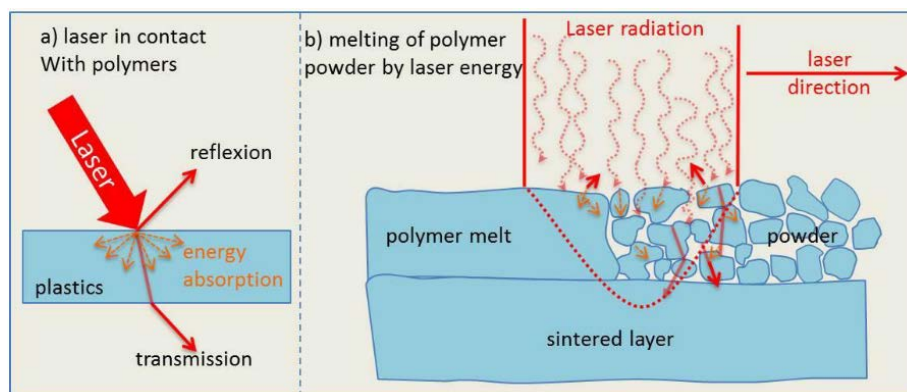


Figure 4.5: Laser/Powder Interaction (image adapter from Schmid et al. (Schmid & Wegener, 2016b))

- **Polymer Matrix and Fiber/Particulate Infill Bonding**

1. **Interfacial bonding** – bonding between the surfaces of the fiber and the matrix.

- Bond strength for interfacial bonding involving polymers is mainly determined by the interdiffusion of the polymer chains across the interface when the temperature is brought above the glass transition or melting temperatures (Bourban et al., 2001). Generally, this describes chain interdiffusion of two polymers (figure 4.3); however, it was hypothesized the same mechanisms applied to polymer/fiber bonding and will be influenced by fiber surface roughness and friction with polymer chain length and crystallinity (Jero et al., 1991; Park & Seo, 2011).
- Liu et al. found sintering untreated CF and PA12 produced good interfacial bonding; however, Yan et al. increased interfacial bonding between PA12 and CF through an oxidation surface treatment.

2. **Interfacial bond strength measurement** – the most common interfacial bond strength measurements are done indirectly by measuring the mechanical properties (e.g., stress-strain or bending) of an entire part. However, direct measurements can be done of individual fibers as well.

- Indirect interfacial bond strength measurement – if the part becomes stiffer with the addition of stiffer material it demonstrates there was bonding between the fiber and matrix. This bonding can be improved through fiber surface modification (C. Yan et al., 2011a).
- Direct interfacial bond strength – can be measured with fiber pullout and pushout tests (DiFrancia et al., 1996; Kerans & Parthasarathy, 1991).

3. **Fracture Mechanics** – Sintered PA12/CF composites most fracture mechanisms occur at the interlayer region or micro-crack bridging formed from the interfaces between CF and PA12 (Czelusniak & Amorim, 2021; Liu et al., n.d.; Tang et al., 2021a). However, for composite blends manufacturing with PBF fiber orientation is normally dictated by the spreading process resulting in fibers generally be orientated along the spreading direction with very few fibers crossing between layers. In fact, Jansson et a. found zero fibers crossing layers in the z-direction (Jansson & Pejryd, 2016).
  - In many cases this mechanism is based on energy density the sintered part tends to fracture along the layer-to-layer interface (low energy density) or along matrix-CF interfaces (high energy density) (Czelusniak & Amorim, 2021).

### **Extrinsic Powder/Particle Properties:**

- **Flow Properties**

1. **Particle Size:** (Size of particles and particle size distribution (PSD)) Both the particle size and PSD affect final part density and layer height (Schmid & Wegener, 2016b).
  - Tested particles were generally < 0.1 mm in any direction and so nominal layer height was set to 0.1 mm. Rod shaped CF crossed layers and were influence and orientated by the raking process.
2. **Particle Shape:** (Particle shape and distribution of shape) Spherical or near spherical particles with varying sizes can help facilitate dense powder layer

application (Amado et al., n.d.; Malekipour & El-Mounayri, n.d.; Schmid & Wegener, 2016a).

- Blended TP/TPE powder had similar particle shapes.
- Adding particulates, especially fibers >5% volume, can increase porosity in powder and during layer spreading resulting in increased porosity compared to neat powder sintered parts.

### 3. Particle Density

- Blended particles should generally have similar size and weight, or heavier particles will have a propensity to fall to the bottom of the reservoir during raking.

### 4. Angle of repose (Steepest surface angle of loose material (powder or blends), Figure 4.6): low angle is ideal for spreading.

- Fiber and particulate blends tend to cause angle of repose to increase because of material clumping.

### 5. Spreading Speed: (Speed of recoater (normally a rake or roller) when moving powder from the reservoir to the build area.) Generally spreading or raking the powder at a slower speed increases powder layer density (Yao et al., 2021).

- Spreading speed was tested for each material and blend with initial rake speed of 10 mm/sec will be used.



Figure 4.6: Angle of Repose (powder image from Sinterit website)

6. **Sintered Powder Density:** (Density of sintered part based on density of top layer powder and sintering energy). Porosity in sintered layer decreases tensile strength layer to layer and raster to raster (Drummer et al., 2014; Wörz & Drummer, 2018b).

- **Environmental and Post Processing Effects**

1. **Hydration:** (Water absorption by polymer typically through humid environment or water immersion). Rajesh et al. found PA12 absorbed only 0.15% weight after 12 hours of being immersed in water and resulted in enhanced tensile strength and hardness (Paolucci et al., 2020; Rajesh et al., 2002). Similarly low absorption rates were found in PA12/CF composites (Kurokawa et al., 2003).
2. **Dehydration:** (Removing water from polymer via oven drying or dehydration). Tanaka found complete reversal of PA12/CF moisture absorption through oven drying (TANAKA et al., 2013).
3. **Post Process Treatment:** (Treating a part post-print to manipulate and improve mechanical properties). Plessis et al. have demonstrated hot isostatic pressing (HIP) can improve density post printing (du Plessis et al., 2021) and Zhu et al. have bonded epoxy resin to PA12/CF sintered parts using post processing heat treatments (Zhu et al., 2016). Post processing treatments can also include non-thermal techniques such as stress treatments (see crystallinity section) and sanding or machining.
  - It was hypothesized that these types of post process treatments would not only be beneficial in decreasing porosity, increasing crystallinity, and increasing bonding between fibers or particulates and matrix material but

also increasing bonding and consistency between M2 interfaces. This is likely particularly true with material changes in a single layer. The effects of post processing treatments specific to M2 PBF should be investigated in future studies which may include machining parts to desired shapes post printing.

### **PBF Material Compatibility Summary**

Solid state particle blending has unique challenges and advantages when compared to liquid or molten state blending. Mechanically blending powders and fillers allows material ratios to be modified at any time through the blending process and shifts flowability requirements from the liquid state to the powder state. However, ensuring a homogeneous mixture is maintained throughout the PBF process can be difficult if the particle properties within the blend are not similar. Mechanically blending powders and filler for AM has had initial success involving Nylon-11 (PA11) with glass or silica particulates, 316 stainless steels with copper alloy, tungsten carbide with Cobalt, and PEEK with HA (Chung & Das, 2006, 2008; Fai Leong et al., 2016; L. R. Jepson et al., 2000; K. H. Tan et al., 2003; Wei et al., 2019). All blends require high powered lasers and inert chambers and none of the technology is capable of LCC. However, the initial success of these projects demonstrates feasibility to incorporate LCC into polymer PBF using mechanically blended powder and fillers.

### **METHODS**

Polymer PBF seeks to sinter powder directly under the laser beam while bonding bordering rasters and layers without coalescing neighboring powder. Aim 2 investigated material compatibility as it pertained to the sinterability utilizing M2 SLS prototype the mechanisms

described in Aim 1. These methods found compatible materials that minimize part defects and increase part functionality.

Feasibility of discrete materials and material blends were tested for powder/blend flowability, spreadability, and sinterability. Modified ASTM D638-14 Type V specimens were printed to evaluate warping, dimensional accuracy, porosity, and sintering. Type V specimens provide several distinct benefits for this type of testing:

1. The orientation during printing changes the cross-sectional area of each layer substantially. This allowed energy density and material compatibility to be tested between blends while evaluating the effects of different anchoring techniques.
2. The thickness offered orientations to be printed with as little as 32 layers. This shortened print times and facilitated testing multiple settings in a single heat up cycle. This orientation also gave a large printed cross-sectional area and stressed the system when evaluating warping and sledding.
3. The geometry had both squared and rounded edges. This allowed simultaneously testing multiple aspects of hatch patterns and galvanometer movements.
4. The geometry covered approximately half of the print area. This allowed single material prints to be simultaneously printed with M2 prints with the novel design of experiments (DOE) discussed in the following section.
5. Type V specimens were used for characterization testing in Aim 3. Testing the same specimen in Aim 2 allowed time to fine tune printing parameters to support repeatable print results for characterization testing in following aims.

Test flow, specimens, methods, and acceptance criteria are outlined in Figure 4.5. Neat material printing was an iterative process (Figure 4.5 – top red arrow) with laser and temperature

parameters adjusted to bracket minimum and maximum parameters and to determine a sintering window (Figure 4.5b - blue). Sintering windows overlap of varying materials was found to determine initial sintering compatibility. Fibers and particulates do not soften and thus did not have a sintering window. Optical properties, laser interaction (Figure 4.5a - orange), and bonding to polymer matrix materials during sintering determined compatibility of fibers and particulates (Figure 4.5c - green). Espera et al. (Espera et al., 2019a) have manually blended up to 10% volume by weight carbon black pearls (~5 microns particle size) with PA12 for sintering which was used as an initial testing point for PA12 and CF.

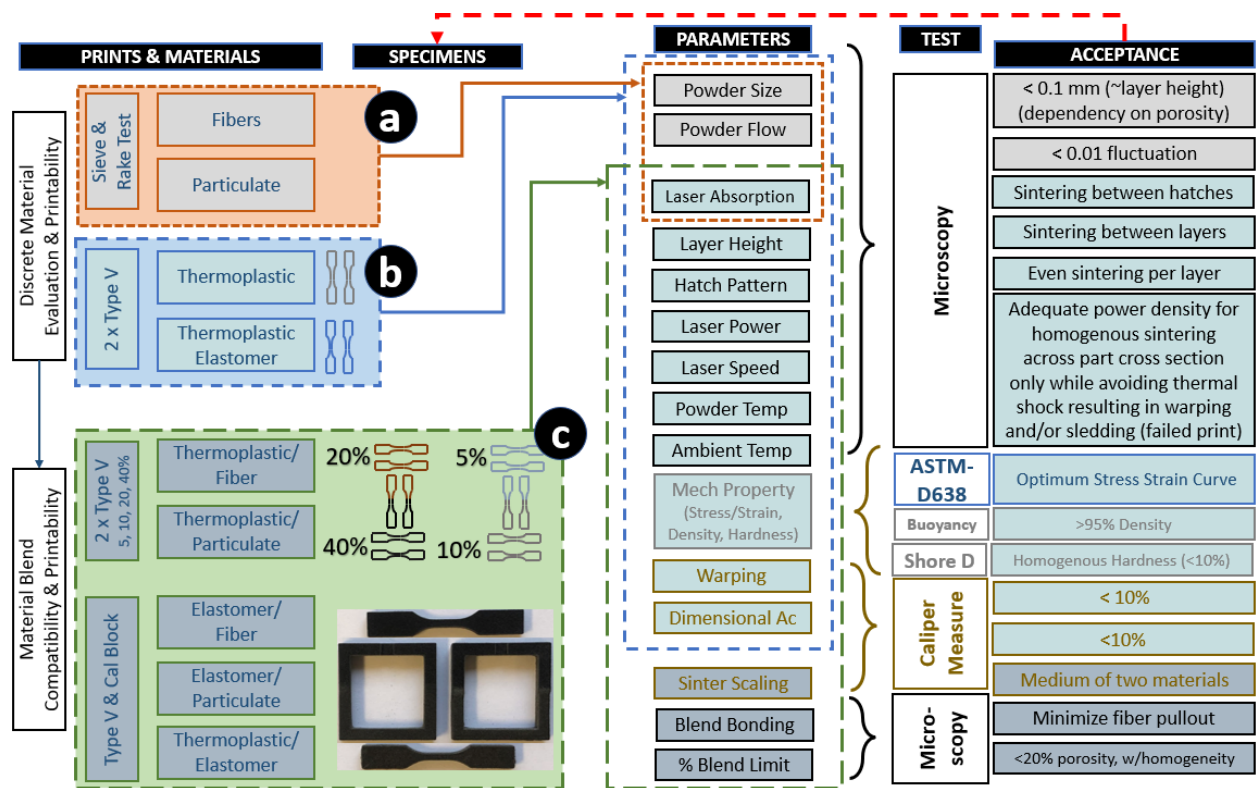


Figure 4.5: Material compatibility test methods and acceptance criteria. (a) Teat particle and fiber evaluation. (b) Neat powder evaluation. (c) Material Blend evaluation.

### ***Material Preparation***

All material was sieved using a #100 SS mesh sieve (ASTME 1, Hogentogler Inc, Columbia, MD).

### ***Bi-Material DOE Specimen Printing***

A novel “Bi-Material” Design of Experiment (DOE) was used for testing M2 interaction during sintering using a single material commercial SLS: two material or material blend powders were positioned side by side in a single reservoir (Figure 4.7). Two different blend ratio specimens and M2 specimens could be concurrently printed (Figure 4.8). Real time and post print side by side evaluation of spreading, thermomechanics, and powder interface in the same thermal and energy density environment enable with this DOE. Printing two blends simultaneously also increased testing efficiently while conserving powder (Figure 4.5c).



Figure 4.6: Bi-Material DOE reservoir preparation.

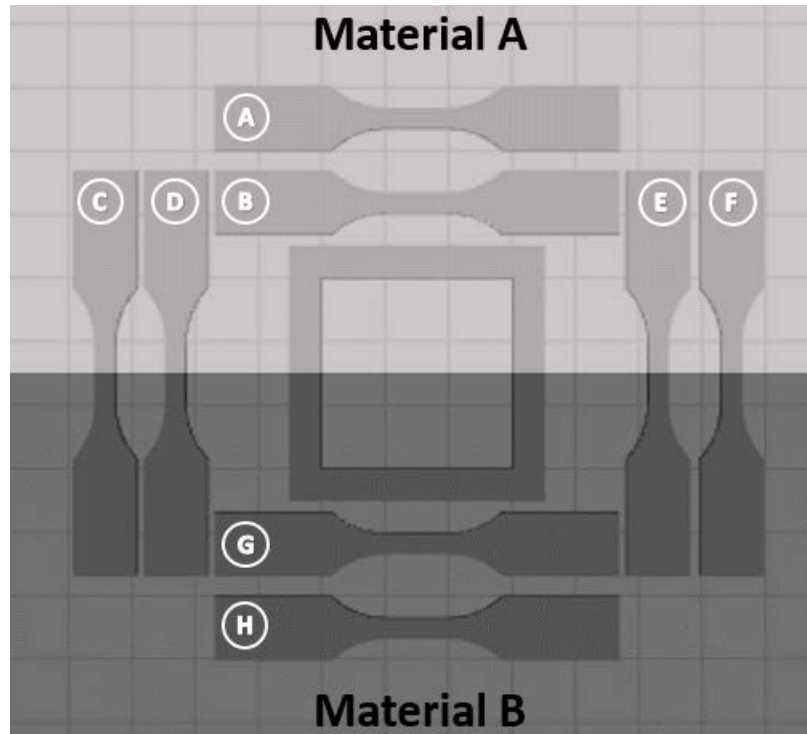


Figure 4.7: Bi-Material DOE Print Planning.

A Sintratec Kit SLS printer with a 1.8 W, 455 nm diode laser (Sintratec AG, Switzerland) modified with two independently controlled build area 200 W heaters (Figure 4.8) was used for initial sintering and material blend tests.

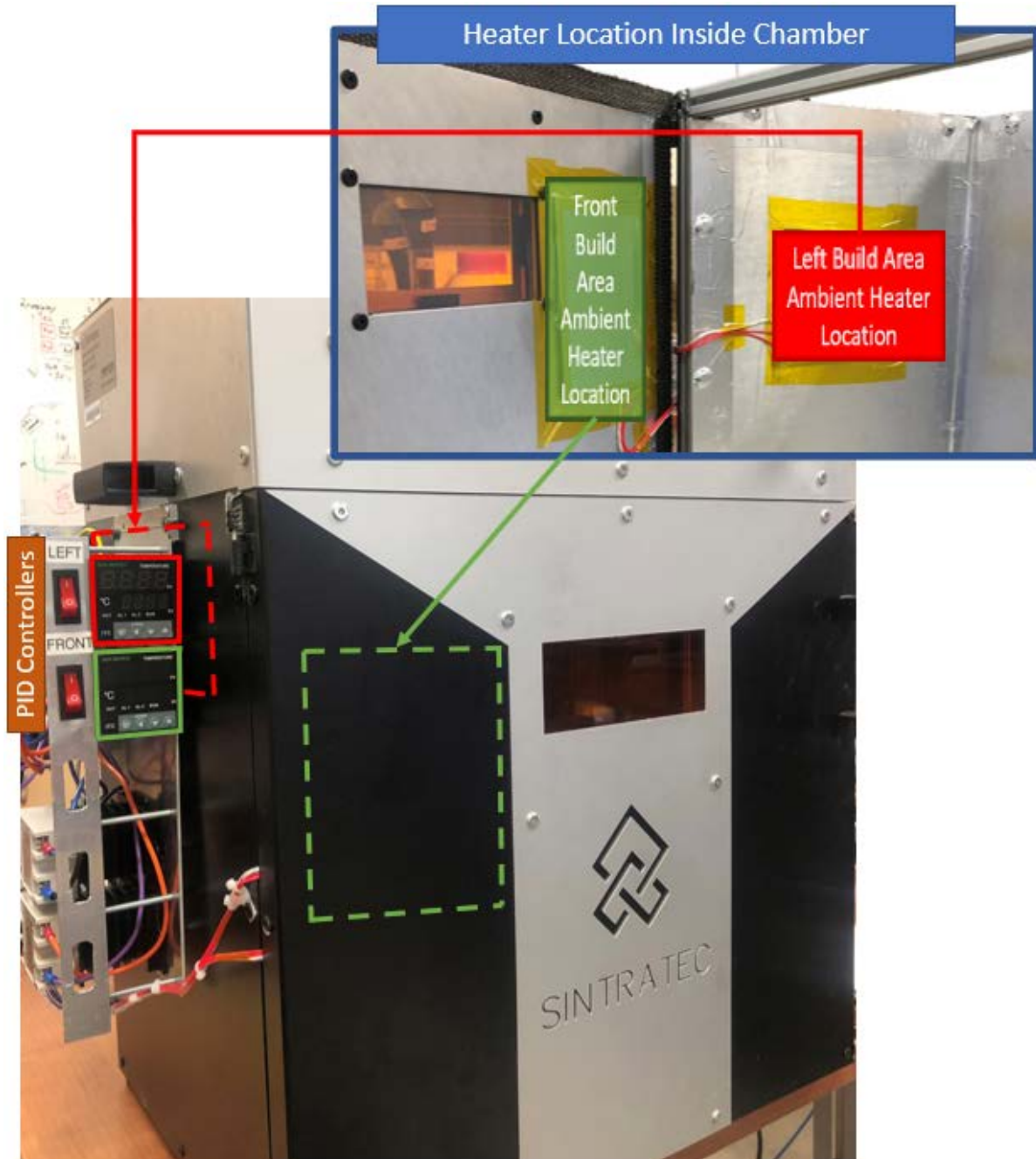


Figure 4.8: Sintratec Kit build area heater modification.

### *Specimen Evaluation*

Specimen testing was done to tune the following print parameters for each material or blend printed:

## 1. Temperatures

- a. Ambient: build area. (~80-150° C)
- b. Ambient: reservoir area. (~70-130° C)
- c. Powder: build. (~120-140° C)
- d. Powder: reservoirs. (~80-120° C)
- e. Powder: top layer. (~140-175° C)

## 2. Laser

- a. Speed. (300-700 mm/sec)
- b. Power (constant 1.8 W for all Sintratec Kit testing, 1-5 W for M2 SLS)

## 3. Spreading

- a. Layer height (0.8-1.2 mm)
- b. Rake speed (20-50 mm/sec)

The effects of the above parameters for each material/blend were evaluated using the following five basic methods: Macroscopic print quality evaluation, specimen dimensional analysis, hardness testing, optical microscopy, and porosity assessment.

1. **Macroscopic print quality evaluation:** this was the most broad and general evaluation looking for sintering and build quality. (Figure 4.9). Overall print defects including sintering completeness, sledding, warping, surface quality, macroscale porosity were evaluated. All other methods went into more detail based on this initial evaluation.

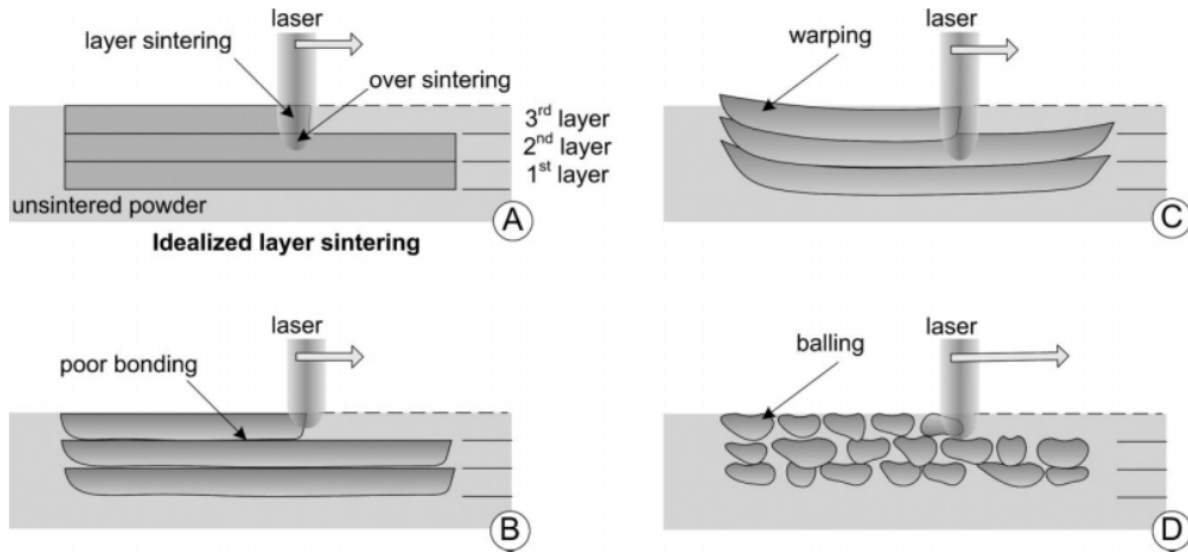


Figure 4.9: Primary defects that will require material and blend specific temperatures and laser parameters (adapted from Beal et al. (Beal et al., 2009)).

2. **Hardness testing:** Hardness was evaluated on a shore hardness scale of A (low modulus of elasticity, TPE prominent material) or D (high modulus of elasticity, TP prominent material) (Figure 4.10)
3. **Specimen dimensional analysis:** This included evaluation of dimensional accuracy and warping. Measurements were done using a digital caliper and optical microscope. Typical measurement locations are found in Figure 4.11
4. **Microscopy:** primary microscope will be a Dino-Lite Edge Plus (AM4917MZT) 1.3MP 20x-220x (Dunwell Tech Inc., Torrance, CA). This microscope was moved into the print chamber to take images of the powder spread or used to image samples (Figure 4.12). Depth of field capability of ~0.5 mm at 220x magnification was used for porosity and fracture imaging (Figure 4.12) (*Dino-Lite Digital Microscope*, n.d.). Maximum magnification is 220x, if more magnification was required for further

analysis Keyence optical microscope used. If greater contrast was required Hitachi TM1000 Scanning electron microscope was used.

- Porosity assessment:** Image contrast analysis using ImageJ software (*ImageJ*, n.d.) was done of the surface and cross section from images taken during the microscopy analysis (Figure 4.14). ImageJ is an open-source image processing program designed for multidimensional images (*ImageJ*, n.d.). The software can calculate material area and features based on contrast between pixels. ImageJ has been used to estimate composite particle size and porosity in PBF composites (Chung & Das, 2006; Khudiakova et al., 2020). However, in this study there was minimal contrast between materials (except HA) and particle distribution using ImageJ did not produce reliable or repeatable porosity and material measurements. As such all porosity and material fraction measurements were done qualitatively.

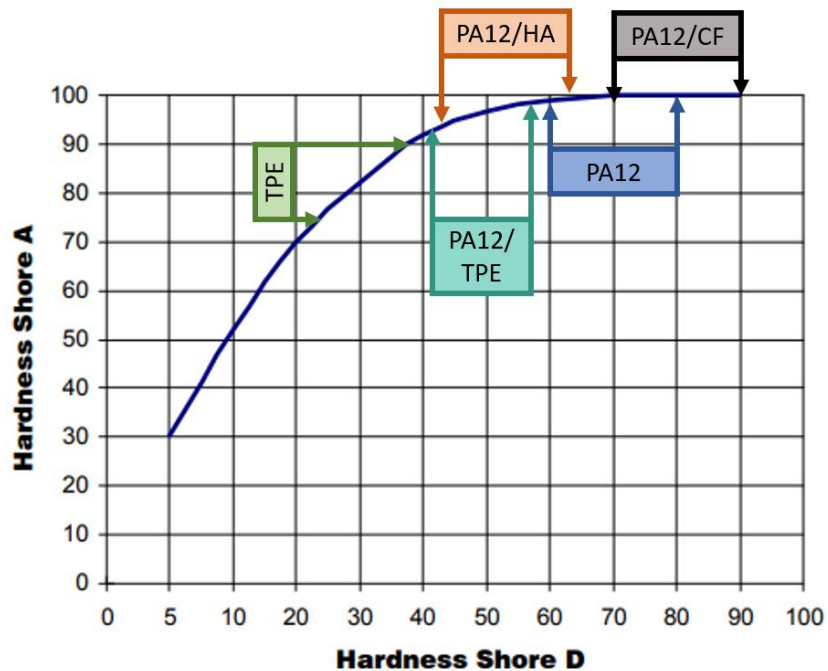


Figure 4.10: Hypothesized Shore Hardness Ranges for Tested Materials and Blends

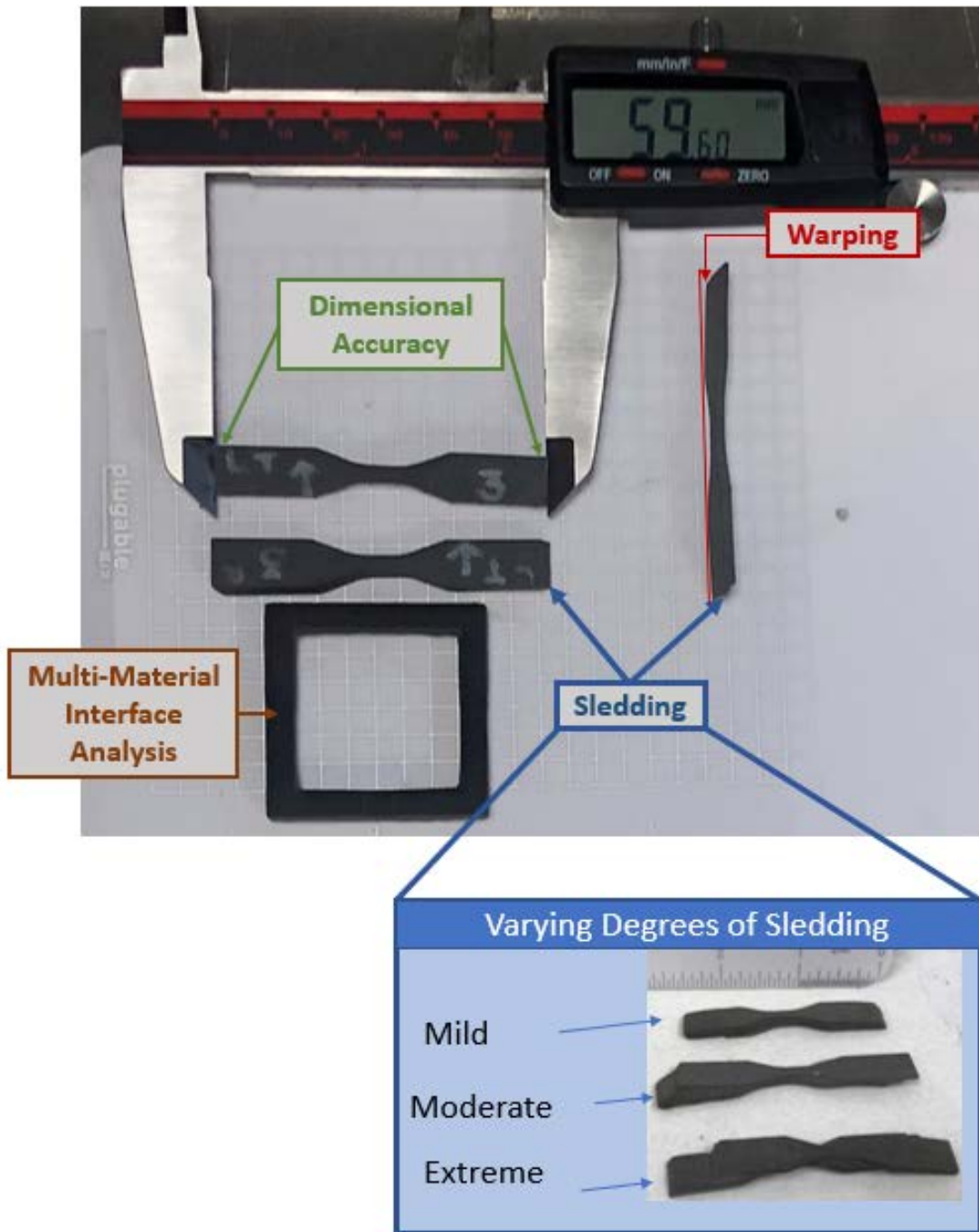


Figure 4.11: Dimensional analysis measurements

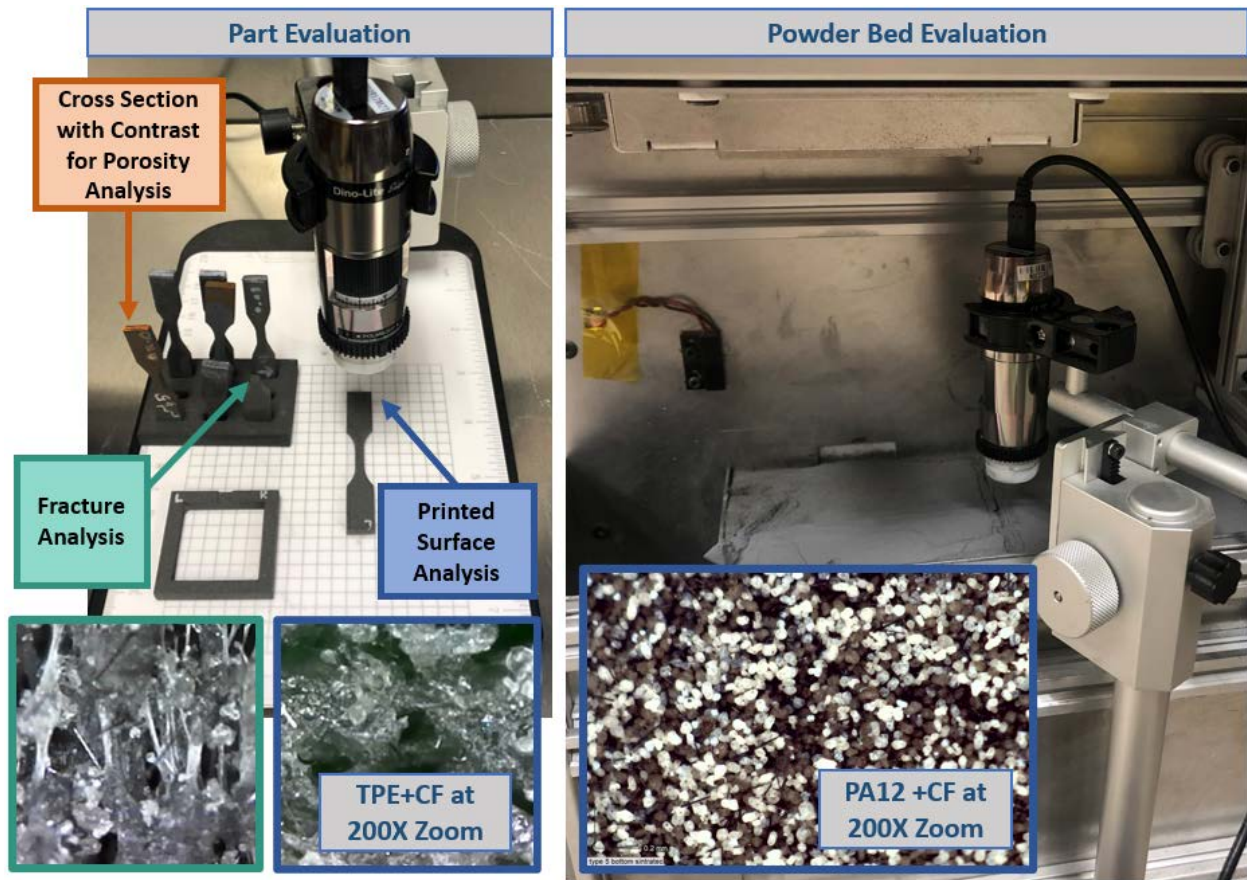


Figure 4.12: Optical Microscopy analysis of printed parts and powder bed using Dino-Lite microscope

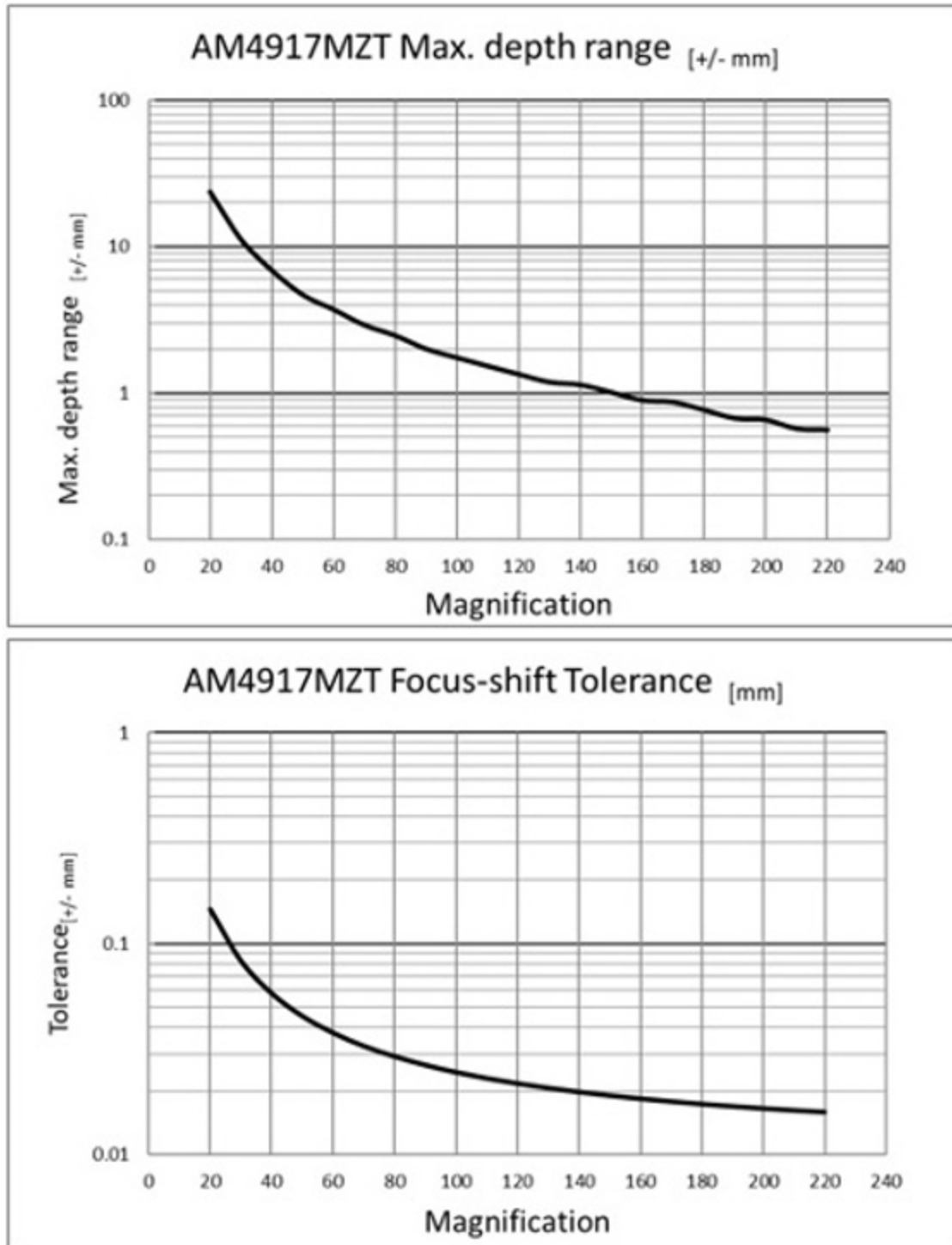


Figure 4.13: Depth of Field (DOF) capability of optical analysis with Dino-Lite AM4917MZT Equipped with DOF capability (Dino-Lite Technical Specifications, (Dino-Lite, 2022))

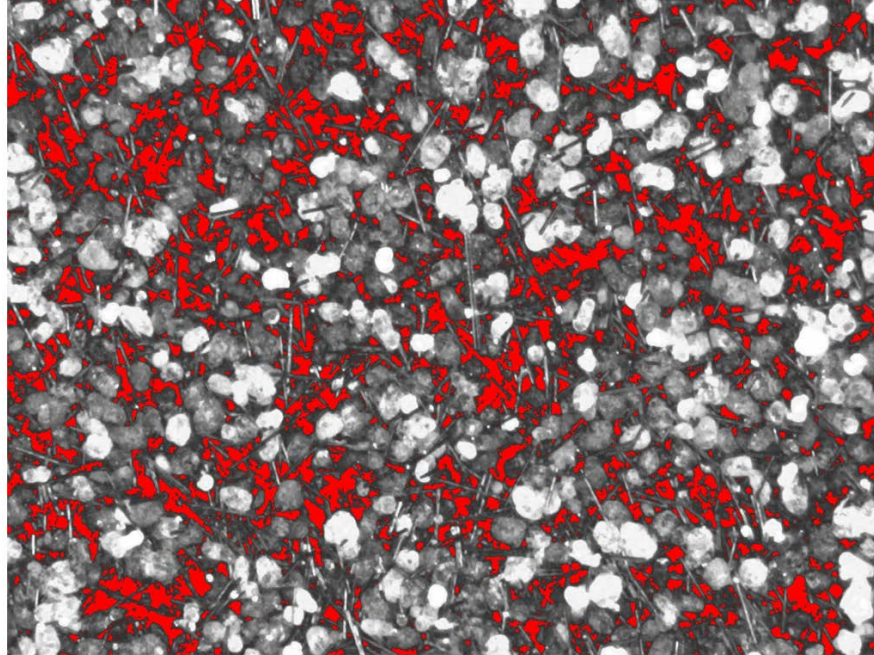


Figure 4.14: Porosity (estimated in red by the ImageJ program) analysis of PA12 mixed with 20% CF using ImageJ image processing program were inconclusive

The sintering window for each material or blend was defined using the print parameters discussed above. Single material TP or TPE sintering window characterization was done prior to blend testing to give a baseline for composite blends and ensure overlap for TP/TPE blends. If there was no overlap in TP and TPE sintering windows, then the materials were not compatible for simultaneous sintering.

### **Single Material Evaluation**

Selecting and evaluating neat materials was based on compatibility with the prototype M2 SLS (temperatures, environment, spreading, laser, etc.). A range of material properties specific to sintering was needed to ensure property overlap between TP and TPE. Thus, the metrics in Table 4.1 were used for selection criteria. Based on the results of the comparison in Table 4.1, two PA12 powders and three TPE powders were selected for blend compatibility

testing (summarized in Table 4.2 and imaged in Figure 4.15). Manufacture data sheets are in Appendix D.

Table 4.1: TP and TPE powder selection criteria and material brand comparison.

Compatibility Criteria				RESULTS
Acceptance Color Code	Good	Acceptable	Poor	
Color (~Absorption)	Dark Colors	N/A	Light Colors	
Percent Elongation TP	x<10%	10≤x≤20%	x>20%	
Percent Elongation TPE	x>300%	150≤x≤300%	x<150	
Ultimate Tensile Strength TP	x>40 MPa	30≤x≤40 Mpa	x<30 MPa	
Ultimate Tensile Strength TPE	x>5 MPa	x≤5 Mpa	N/A	
Melting Temperature	175≤x≤185 C	165≤x≤195 C	x<165, x>190 C	

Material	PA12	TPE	PA12	TPE
BRAND	SINTERIT	SINTERIT	SINTRATEC	SINTRATEC
Color (~Absorption)	Navy Grey	Grey	Grey	Grey
Percent Elongation	10%	196%	8%	438%
UTS (TPE/PA)	32 MPa	6 MPa	40-50 MPa	N/A
Melting Temperature	185 C	190 C	180 C	110 C

TPE	Duraform Flex	Duraform FR1200	DuraForm GF	DuraForm HST	DuraForm PA
SINTERIT	3D Systems	3D Systems	3D Systems	3D Systems	3DSystems
Grey	White	Off-White	Off-White	Off-White	White
137%	110%	5.9%	1.4%	4.5%	14%
14.65 Mpa	1.8 MPa	41 MPa	26 MPa	48 - 51 MPa	48 MPa
160 C	N/A	N/A	N/A	N/A	N/A

DuraForm ProX	Duraform TPU	PA 2200	PA 2201	PA 2241 FR	TPU 1301
3D Systems	3D Systems	EOS	EOS	EOS	EOS
Grey	White	White	Natural Grey	White	White
3%	220%	18%	15%	9%	250%
37 MPa	2.0 MPa	48 MPa	48 MPa	49 MPa	60 MPa
N/A	N/A	176 C	176 C	185 C	138 C

PA12-GFX 2550	PA12-L 1600	PA12-S 1550	STARK 3200	TPU-70A	Ultrasint PA6
Prodways Materials	Prodways Materials	Prodways Materials	Prodways Materials	Prodways Materials	Prodways Materials
Grey	White	Black/Blue/Red/Grey	Black	White	Black
8%	36%	15%	>1.2%	350%	.9-2%
30 MPa	46 MPa	44 MPa	>35 MPa	7 MPa	56 - 91 MPa
181 - 183 C	183 C	181 - 183 C	>199 C	105 - 122 C	>218 C

Multicolor	PA12	Ultrasint TPU 001	PA12	PEBA	Ultrasint TPU 88A
Sculpteo - Colorjet	Sculpteo - HP Jet	Sculpteo - HP Jet	Sculpteo - SLS Tech	Sculpteo - SLS Tech	Sculpteo - SLS Tech
White	Grey	Grey	Grey	White	White
0.25%	20%	220%	20 +/- 5%	200 +/- 70%	270%
9 MPa	48 MPa	9 MPa	45 +/- 3 MPa	7-8 MPa	8 MPa
112 C	187 C	120-150 C	172 - 180 C	150 C	120-150 C

Table 4.2: Manufacturer Data for selected TP, TPE, CF, HA (Blank Cells: data not provided).

Properties	Material						
	Sintratec PA12	Sintratec TPE	Sinterit PA12 SMO	Sinterit TPE	Sinterit FLEXA	Carbiso MF80	HA - SIAL
<b>General Info</b>							
TYPE	Nylon 12	TPE	Nylon 12	TPE	TPU	Carbon Fiber	Hydroxyapatite
Granulation	60 [µm]	60 [µm]	38 [µm]	65 [µm]	50 [µm]		
Granulation - Average			18 - 90 [µm]	50 – 80 [µm]	20 - 105 [µm]		
Fiber Diameter *						7 [µm]	
Fiber Length *						80 [µm]	
Color	Dark Grey	Dark Grey	Navy Grey	Grey	Grey	Black	White
Refresh Ratio	(add 70% new)	(add 50% fresh)	26% (fresh powder)	10% (add 30% fresh)	0%	Varied per print	
<b>Parameters</b>							
UTS			32 MPa	6.0 MPa	3.7 MPa	3470 MPa	
Tensile Stress	47.8 MPa	2 MPa					
Compression					14.65 MPa		
Stiffness	1750 MPa	29.9 MPa				246 GPa	
Elongation (at break)	8%	438%	10%	196%	137%		
Elongation (at break) xy	14.10%	250%					
Elongation (at break) z	4%	63%					
Hardness - Shore A				90	70 / 90		
Hardness - Shore D			74				
<b>Thermal Properties</b>							
Melting Temp	176 C / 185 C nds	95 C	182 / 185 nds	190 C	160 C		
Softening Temp	130 C (stable temp)	80 C	172 C		67.6 C		
Density - Powder	1.0-1.1 g/cm <sup>3</sup>	1.20 g/cm <sup>3</sup>	1.02-1.10 g/cm <sup>3</sup>	0.4-0.5 g/cm <sup>3</sup>	1.22-1.32 g/cm <sup>3</sup>		
Density - Printout			0.92 g/cm <sup>3</sup>		0.80 g/cm <sup>3</sup>		
Density - Relative		1.11-1.20 g/cm <sup>3</sup>					
Density - Fiber						1800 kg/m <sup>3</sup>	
<b>Charpy U- + V-</b>							
<b>Notched Impact Testing</b>							
Impact Resistance (unnotched)			16 KJ/m <sup>2</sup>				
1. U			5.23 KJ/m <sup>2</sup>				
2. V			3.28 KJ/m <sup>2</sup>				
<b>Surface Roughness</b>							
Ra - Side Surface			9.68 [µm]				
Rz - Side Surface			54.184 [µm]				
Ra - Top Surface			6.47 [µm]				
Rz - Top Surface			31.633 [µm]				
<b>Test Standard</b>							
DIN EN ISO 527-1	✓	✓					

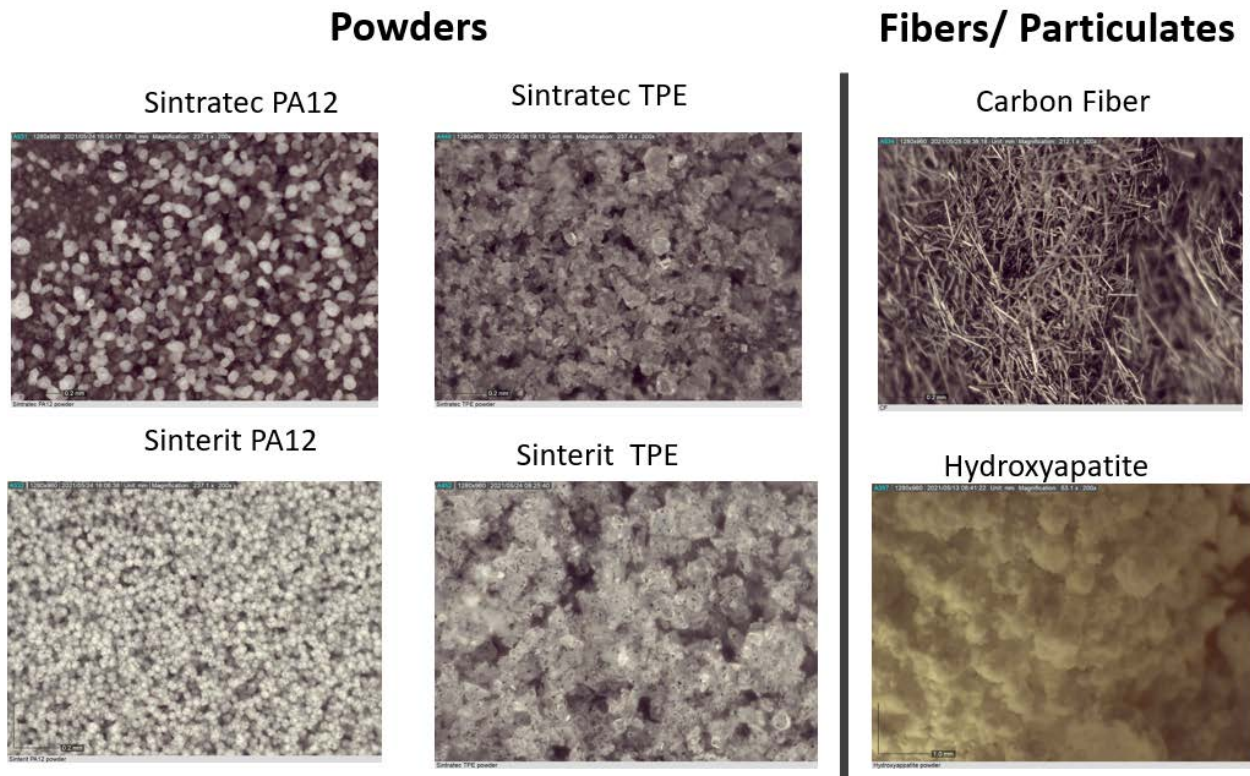


Figure 4.15: Images (200x) of each powder selected for blend testing

### ***Thermoplastics***

Sintratec and Sinterit (Krakow, Poland) brand PA12 sintering powders were the selected TP powders for Aim 2. Molecular structure was assumed to be a standard polyamide-12 structure (Figure 4.14) (Gul et

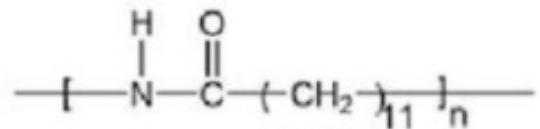


Figure 4.14: PA12 Molecular Structure

al., 2016), However, the chemical makeup and additives are unknown. Manufacturer recommended initial sintering temperatures and energy was also unknown for Sinterit PA12. Testing was done in accordance with Figure 4.5 to determine the sintering window for each powder. The cold side of the sintering window with low ambient and powder temperatures was the focus of testing to determine overlap with the proposed TPE with warping and layer adhesion being the primary obstacles.

### ***Thermoplastic Elastomers***

Sintratec TPE, Sinterit TPE and Sinterit “Flexa Grey” powders were selected. Selection criteria was primarily based on advertised color,  $T_m$ , percent elongation (%EL) at break, and availability. Though the exact polymer chemical group of the TPEs is proprietary to each company, for blend planning, these powders were assumed to be copolymers with a PA hard block with amorphous dominated soft blocks. The hot side of the sintering window with high temperatures and energy density was the focus of testing to find overlap with PA12 powders. Operating at the high end of the sintering window degraded flowability and resulted in zero re-use due to chemical cross linking and thermal oxidation.

### ***Fibers***

Carbiso™ (Coseley, UK) recycled milled M80 CF with a 0.08 mm maximum length and 0.007 mm diameter was selected for fiber testing. This length was hypothesized to be long enough to increase wear and ultimate tensile strength (UTS) but likely to adversely affect spreadability. It was also hypothesized that initially random orientation in the reservoir would occur; however, some orientation is expected to occur along the spreading axis during layer applications. Sintering window of the matrix material was expected to minimally affect as CF is completely stable at PA12 sintering temperatures with good heat absorption and minimal reflection of laser energy.

Espera et al. (Espera et al., 2019b) utilized the sintering parameters in Figure 4.16 for mixtures of up to 10% by weight of carbon black pearls (~5 microns). These setting were used as the initial setting for Sinterit PA12 + CF (<10%) mixtures.

Build parameters (Sintratec Kit)	
Layer height	100 microns
Laser scanning speed	550 mm/s
Printing surface target heating temp.	150°C
Printing surface target printing temp.	165°C
Chamber target heating temp.	140°C
Chamber target printing temp.	145°C
Preheating time	1.75 hours

Figure 4.16: Initial print setting for Sinterit PA12+CF blends (adapted from Espera et al. (Espera et al., 2019a))

Incapsulated fibers are an emerging technology for PBF powders and would likely increase spreadability and sinterability and are available on the market today. However, encapsulated fibers or particulates were not considered for this study as precise and high ratio control is powder specific. Custom powders like this are hypothesized to work well in the M2 SLS for specific applications and could be incorporated into future studies.

### *Particulates*

Sigma-Aldrich (Saint Louis) recycled Hydroxyapatite [ $3\text{Ca}_3(\text{PO}_4)_2 \cdot \text{Ca}(\text{OH})_2$ ] powder was selected for particulate testing. Maximum diameter is not provided from the manufacturer and so sieving was used to ensure a maximum overall length of 0.08 mm. Water absorption could result in clumping during spreading, thus dehydration at 250°C for 24 hours was done prior to sieving.

HA powder is inert at planned sintering temperatures; however, the powder is white with high laser reflectivity which decreases matrix/particulate adhesion and overall sintering effectiveness. This was hypothesized to cause “cold pockets” around HA particles and diminish sintering and particulate/PA12 adhesion at these locations. Increased laser power was tested but

does not increase absorptivity of HA and the area around HA will always be relatively cool compared to the PA matrix.

### **Material Blend Compatibility**

A single TP and single TPE was selected for blend testing based on neat testing results. CF and HA were mixed with the selected TP for fiber and particulate testing. The powder sintering window were the driving factor for all blends being tested. Decreasing cross sectional area and thus amount of area required to be covered with a homogenous mixture and sintered each layer while decreasing overall layer sintering time facilitated sintering with composite blends over 30% filler. Testing type V specimens in different orientations and locations in the build area was used to test layer adhesion and build orientation affects.

Blends loaded into the reservoir were smoothed and de-aerated but not packed. Thus, blend ratios were based on material density and weighed for mixing ratios. Percent volume (% vol) was calculated and used for reporting. Corresponding density was loose bulk density per ASTM D7481 (Chatham et al., 2019). Materials were blended using a Reveo vacuum sealed mechanical tumbler (FeraDyne, Superior, WI ) (Figure 4.17)

The following sequence was used for blend preparation:

1. Sieve
2. Blend
3. Sieve (if required and possible without adverse blending affects).
4. Scoop into desired chamber
5. De-Aerate



Figure 4.17: Mechanical tumbler used for all material blending.

Each blend required a unique set of temperature and laser parameters. Prior to any material testing (Figure 4.5) powder spreading and sintering testing focused on minimizing basic part defects with 1–3-layer tests and real-time parameter adjustments to determine if M2 anchoring would be required. Initial build area arrangement had type V specimens in three orientations with the reservoir loaded per the Bi-Material DOE (Figure 4.6). The hypothesized successes and difficulties below were used to derive initial blend ratios and print parameters and customize each blend to highlight benefits and disadvantages compared to other manufacturing methods while ensuring printability with PBF.

### ***Thermoplastic/Fiber Blend***

Blend consisted of the selected TP blended with up to 60 % vol CF. Matrix crackling, interface debonding, fiber aggregation, fiber pullout, fiber cracking, cavities and cracks were qualitative investigated based on the research done by Wang, S et al. (S. Wang et al., 2021).

#### **Hypothesized Success:**

1. High fiber volume compared to other AM methods
2. Thermal absorption and heating
3. PA12/Fiber bonding
4. Cross layer fibers increase multi-layer adhesion
5. Increase in UTS up to approximately 10-15 % vol CF

#### **Hypothesized Difficulties:**

1. Blend spreading (flowability) and layer density at greater than 20 % vol CF.
2. Increased porosity at all blends and high porosity at blends over 20 % vol CF

### ***Thermoplastic/Particulate Blend***

Blend consisted of the selected TP blended with up to 60 % vol HA. Poor mechanical properties were expected at ratios over 20% HA; however, reporting properties of high HA content is applicable to current osseointegration research.

#### **Hypothesized Successes:**

1. High particulate volumes compared to other manufacturing methods.
2. Complex HA/matrix lattice structures compared to other manufacturing methods.

#### **Hypothesized Difficulties:**

1. Relatively high density compared to TP will cause HA to fall out of solution to the bottom of the blend during spreading.
2. White color and high reflectivity will cause local cooling around HA particles and poor adhesion to TP.
3. Uneven layer heating due to the high reflectivity.
4. Particle shape and hygroscopic properties will cause powder clumping and result in nonhomogeneous mixtures and final part properties.
  - Even though the HA is dehydrated initial testing indicates the HA particles absorb moisture from the air and blended powders during blend preparation and printing.
5. Lower overall strength and mechanical properties compared to neat PA12.

### ***Thermoplastic/Thermoplastic Elastomer Blend***

Blend consisted of the selected TP blended with up to 60 % vol TPE. Ideally this percentage would go to 100 % TPE to maximize property changes; however, at high percentages of TPE the energy density was hypothesized to be too low to accommodate PA12 sintering. At these conditions, the PA12 particles were expected to act more like a particulate in a TPE matrix.

#### **Hypothesized Successes:**

1. Customizable material properties such as modulus of elasticity, UTS, hardness, etc.
2. Up to 1% mixture resolution with TPE remaining evenly dispersed within the powder blends.

3. Homogeneous sintering and cross-material polymer chain bonding resulting in cohesive parts up to approximately 40-60% TPE ratio.

**Hypothesized Difficulties:**

1. Flowability and spreading of high percentages of TPE at the relatively high temperatures required for TP.
2. Part warping at high percentage of TPE
3. Insufficient sintering with high percentages of TP because of the relatively low temperatures for TP.

**RESULTS**

Initially, a baseline was established for the laser and galvanometers used in the M2 SLS prototype. Sintering PEEK was attempted, but sintering light color, high temperature materials, such as PEEK was not possible even by decreasing the laser speed to very low rates. The material transitioned from being under-sintered directly to burning (Figure 4.18). Based on material properties and compatibility with the M2 SLS prototype, Sintratec and Sinterit powders were investigated in depth for this research. Figure 4.19 compares Sinterit and Sintratec powders with the selected carbon fibers and HA particulates at required reservoir temperatures to accommodate sintering. TPE tending to agglomerate and clump at these temperatures which resulted in limiting the blend ratio. HA and CF were also susceptible to clumping, but that was temperature independent and was a factor of the shape and energy between the particles.

Sintering TPE at temperatures high enough to accommodate PA12 resulted in warping of the PA12 due to low ambient temperatures (Figure 4.20). Finding a compatible sintering window for simultaneous sintering of PA12 and TPE was then aided with the use of a TPE base (Figure

4.21). Compatible parameters for Sinterit V1 PA12+CF (up to 30 %vol CF) were achievable with the Bi-Material DOE using the modified Sintratec Kit (Figures 4.8 and 4.22). The sintering parameters found during this compatibility testing were used to test dimensional stability with increasing amounts of CF. Generally, the PA12/CF mixture maintained printed shape (less warping and shrinking) as the ratio increased (Figure 4.23). Binary interfaces at the large cross sections with the M2 SLS resulted in warping, sledding and interface debonding when print setting were held constant between materials with single pass lasing and single pass recoating without anchoring (Figure 4.24)

Spreading was inconsistent above 40-60% infill even with multi-pass recoating (Figure 4.25). Blend spreading up to 30% HA and CF resulted in sinterable layer density and heights. Spreading resulted in HA clumping in mixtures above 30% HA and sintering became less effective with the selected laser wavelength. Sintering blends up to 60% of CF and HA was possible and the matrix material bonded together and to the fibers and particulates enough to form a part but resulted in high porosity and inconsistent mechanical properties.

Matrix/filler bonding indicated good bonding between PA12 and CF and poor bonding between PA12 and HA (Figure 2.26). Some HA particles were completely engulfed/encapsulated in sintered PA12 and thus remained in the matrix; however, much of the HA did not adhere to the PA12 and fell off the part during part removal and cleaning post print (Figure 4.26, and 4.29).

Contrast image processing was attempted with optical images but was not used for quantitative characterization due to difficulty with cross sectioning and color contrast of the used materials. Porosity and filler content had mixed results depending on the blend. Contrast in the images were not satisfactory for porosity calculations using ImageJ software. There may be

enough contrast to determine HA percentages using ImageJ software, however, further testing is required to verify this. There is insufficient contrast between material types for fiber infill calculations (Figure 4.27). Further image processing detail and preliminary results can be found in Appendix C for reference for future research. Qualitative microscopy cross sectioning was used to determine acceptable sintering parameters and blending (examples of CF in Figure 4.28 and HA Figure 4.29). Based on these results PA12/CF was selected for quantitative tensile testing to fine tune sintering parameters for Aims 3 and 4.



Figure 4.18: Laser power and wavelength unable to reach sintering window for PEEK. Laser energy is not sufficiently absorbed into the particles for affective heating and simply burns the top surface.

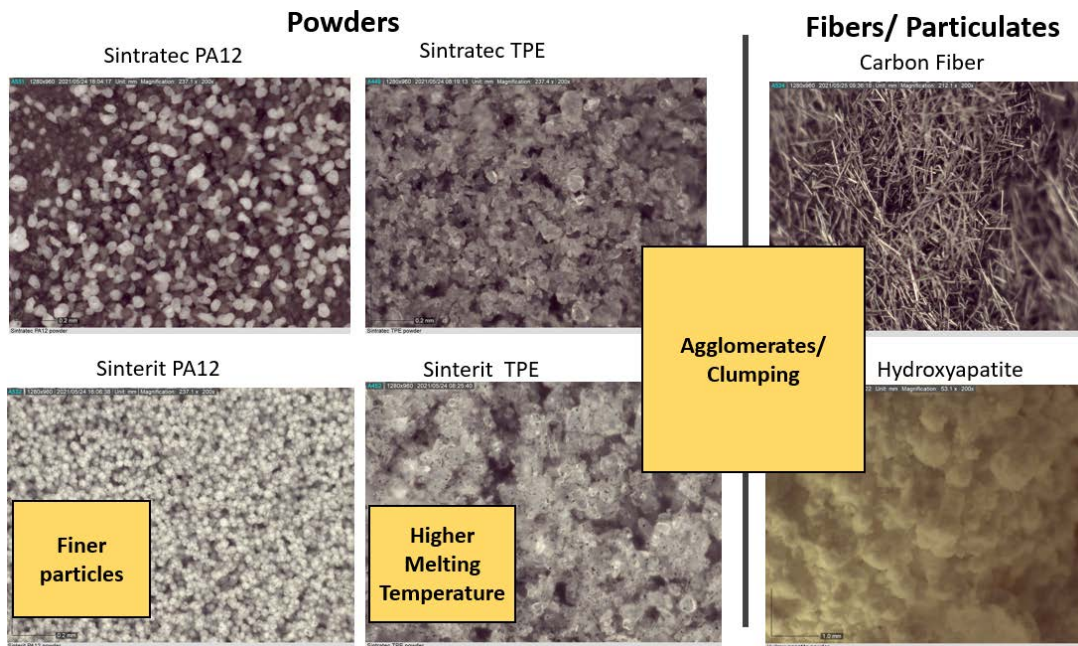


Figure 4.19: Sinterit and Sintratec powders with the selected carbon fibers and HA particulates

**PA12 sintered like an inert “particulate” based on melting Temperature Difference**

- Led to minimal increase in elasticity and greatly reduced mechanical properties.

**Shrinking with TPE/PA12 Mix**

- Led to part edges warping off the cake material resulting in M2 anchoring being used.

**Spreading voids with Sintratec Control**

- Required approximately 2 times the normal amount of material to be dispensed using traditional single pass spreading.

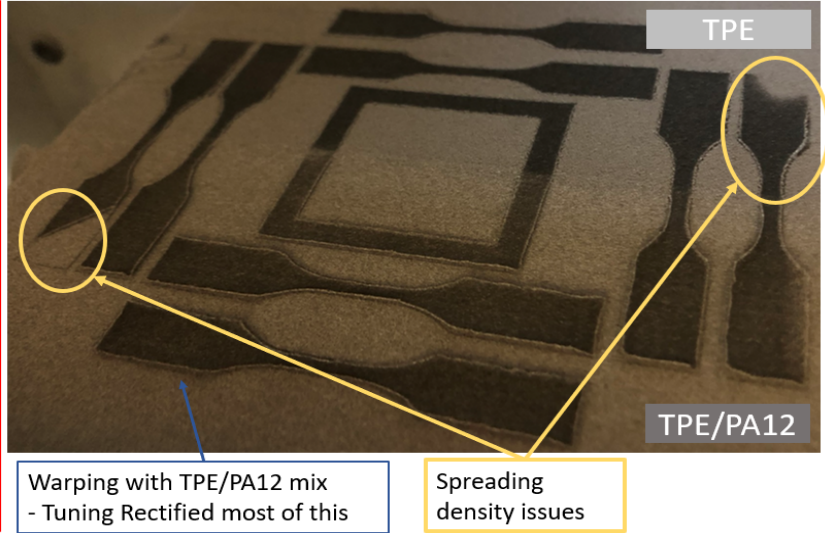


Figure 4.20: Novel DOE and challenges determining overlap in sintering window.

**Multi-Material Part Tuning Parameters and Effects**

- Temperature and laser density tuning to mitigate part defects (right & bottom part) result in ideal part properties (left & top part)

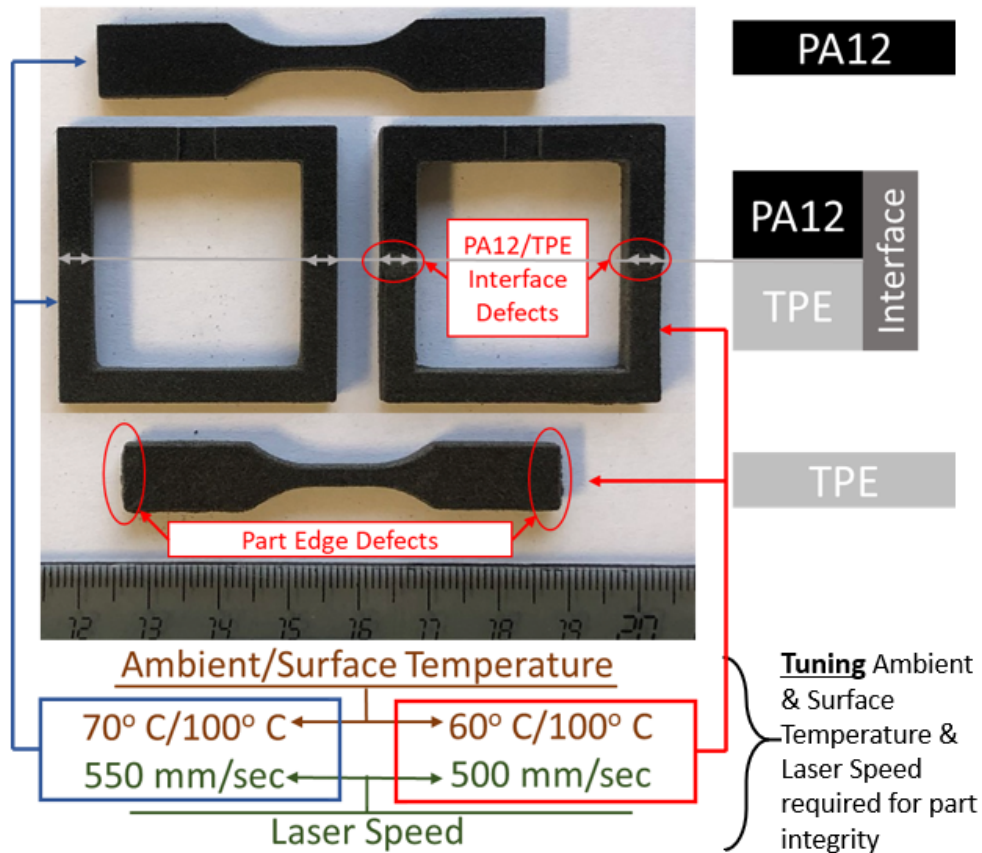


Figure 4.21: Effects of energy density on PA12/TPE Blends anchored on a TPE base.

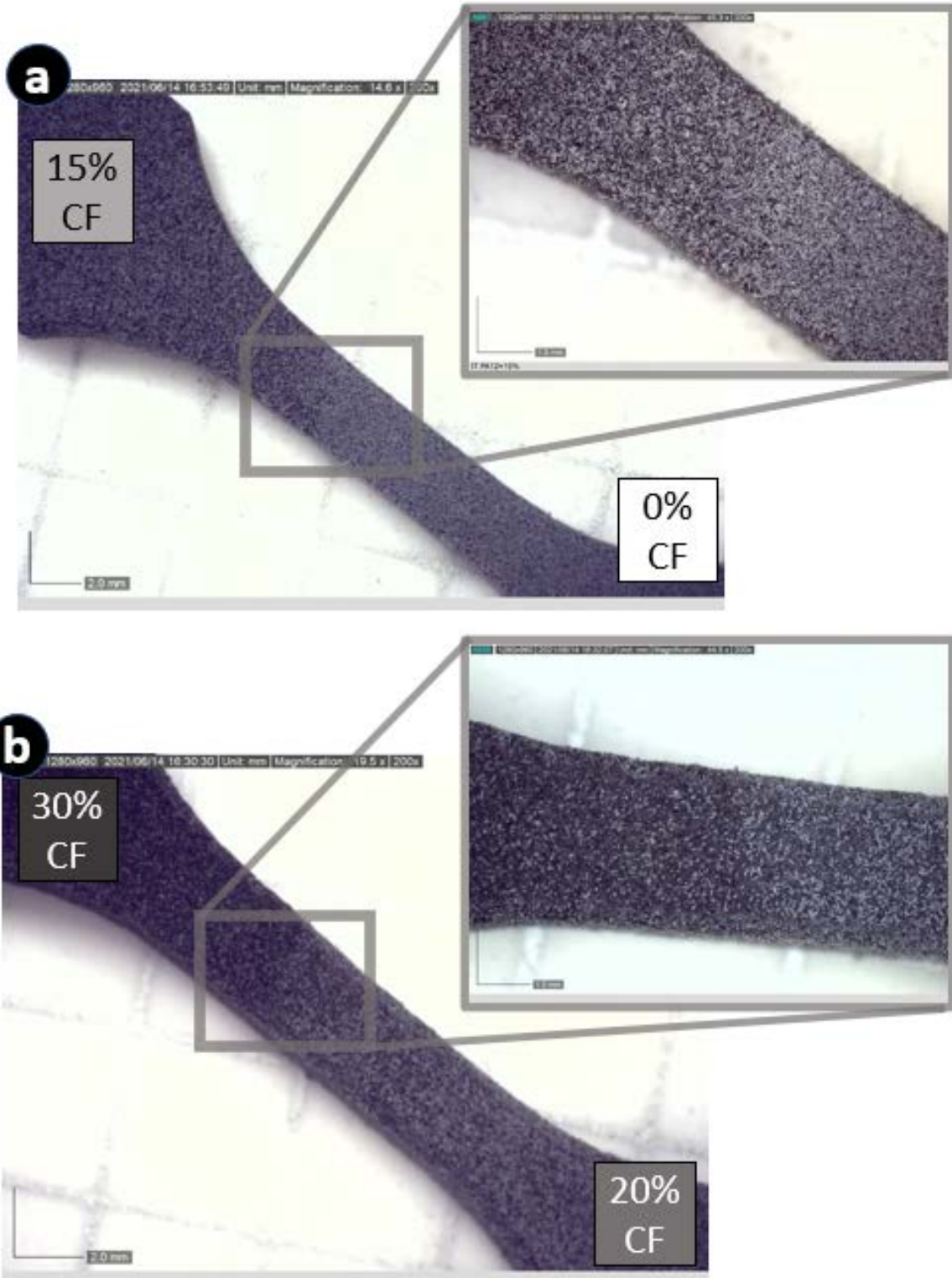


Figure 4.22: Homogeneous Sinterit PA12 + CF prints with the Bi-Material DOE printed on the modified Sintratec Kit. a) Printed at 500 mm/sec, chamber 140° C, powder surface 165° C. b) Printed at 525 mm/sec, chamber 140° C, powder surface 163° C.

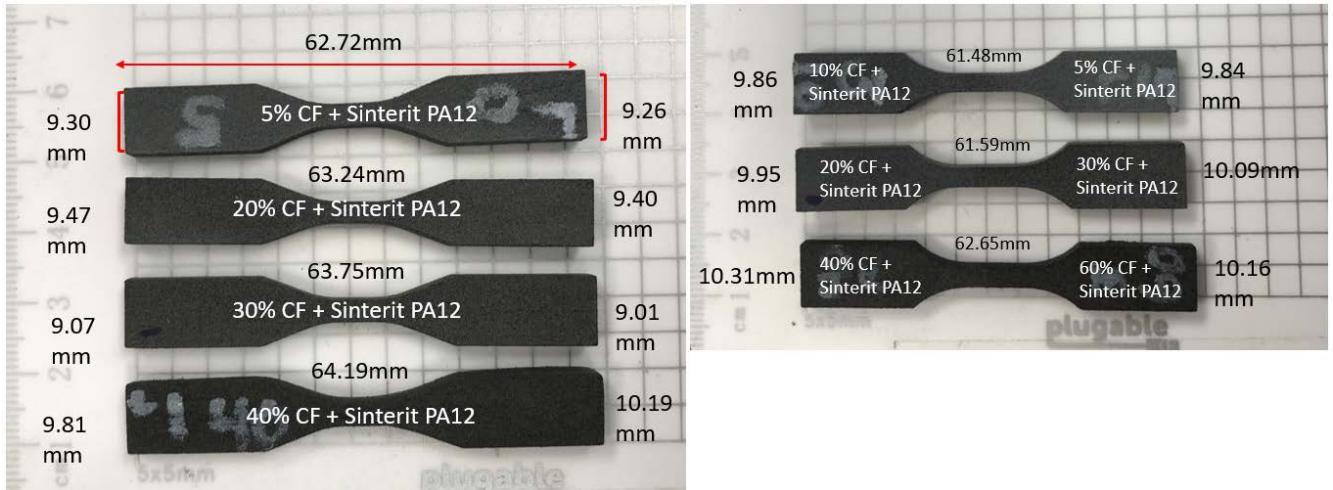


Figure 4.23: Effects of CF infill ratio on dimensional accuracy.

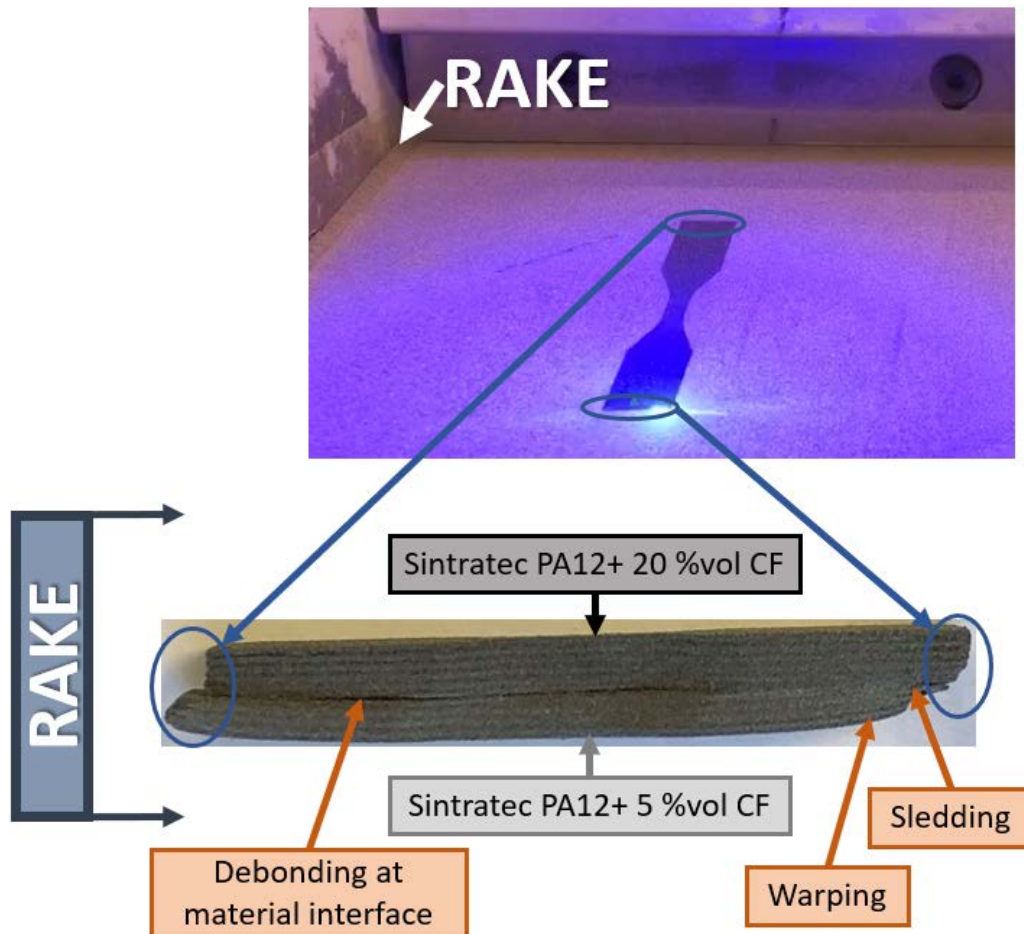


Figure 4.24: Binary interface of Sintratec PA12+5 %vol CF and PA12+20 %vol CF sintered at constant thermal and laser settings for both blends resulting in warping, sledding and debonding at the change in blend interface.

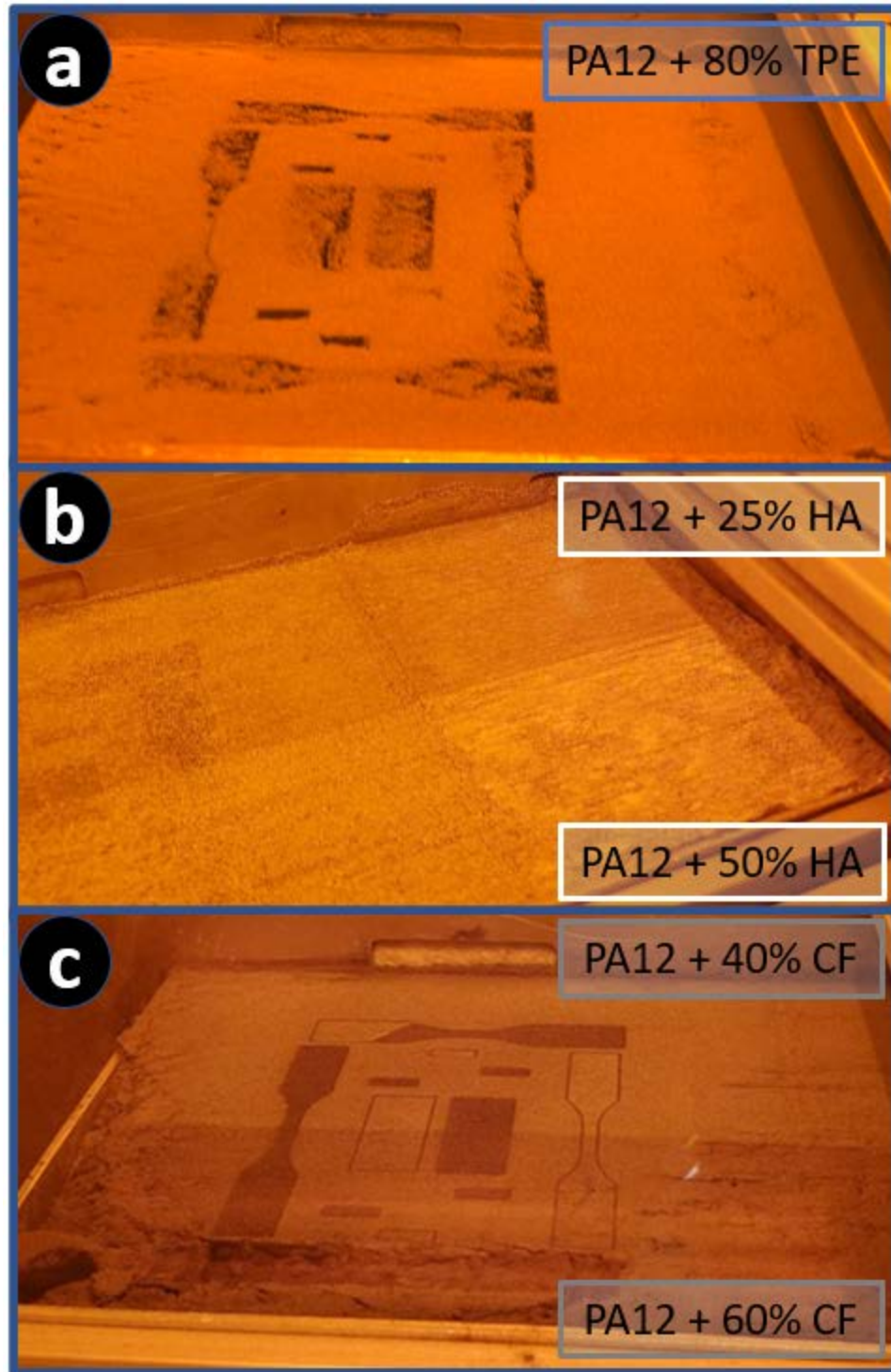


Figure 4.25: Blend spreading difficulties at high infill percentage (a) 80% TPE – clumping of TPE due to partial sintering in high temperature chamber required to sinter PA12 (b) 50% HA – high agglomeration compared to 25% HA in reservoir due to spread mechanisms. (c) 60% CF – poor layer consistency and density with part sledding when compared to 40% CF.

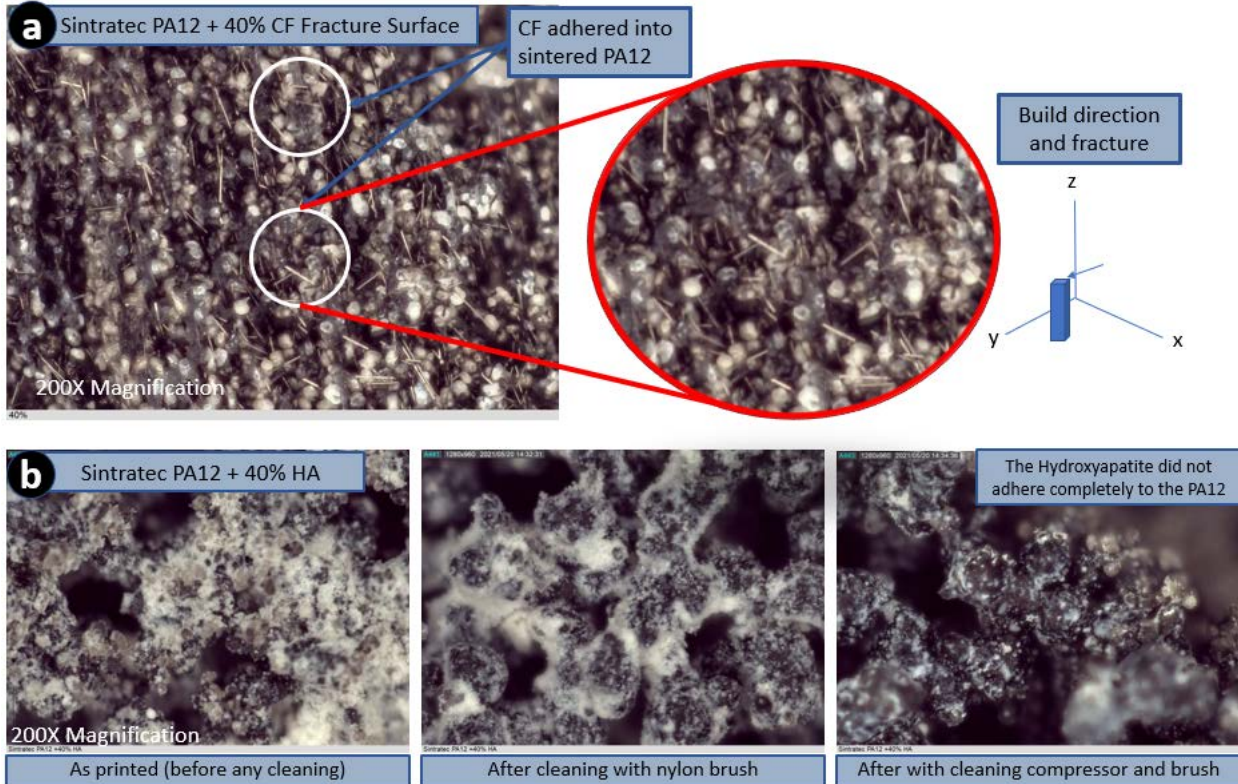


Figure 4.26: Initial PA12 + CF and PA12 + HA microscopy analysis (a) overall success with CF integration and adhesion to PA12 matrix. (b) challenges with HA spreading and adhesion.

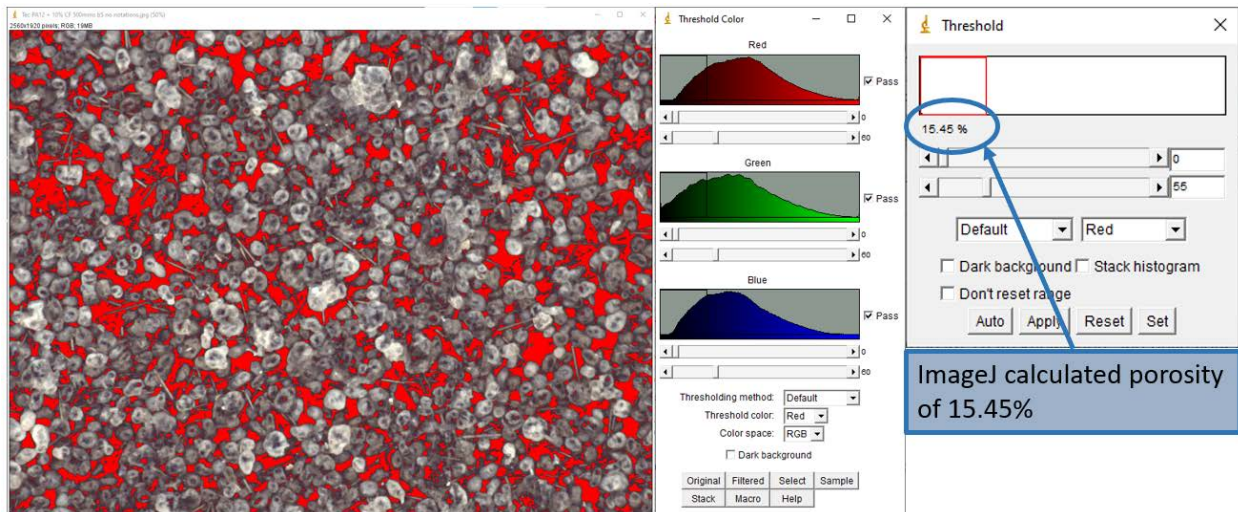


Figure 4.27: Inconclusive porosity calculation using ImageJ with Sintratec PA12 blend and 10% vol CF

## Cut Cross Section Porosity 5%CF

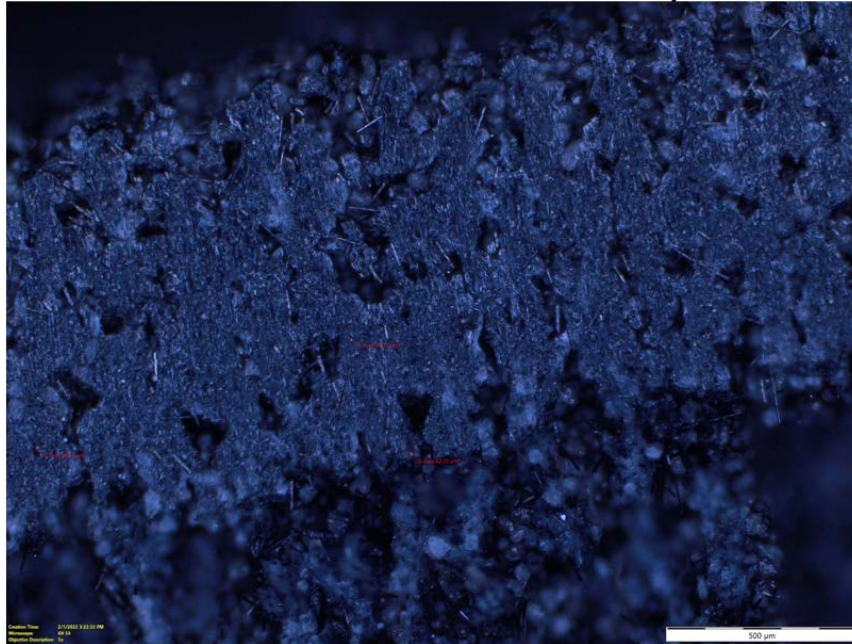


Figure 4.28: PA12/5%CF Qualitative analysis of porosity showing homogeneous CF mixture, but high porosity required sintering parameter adjustment to decrease porosity.

## PA12+25% HA

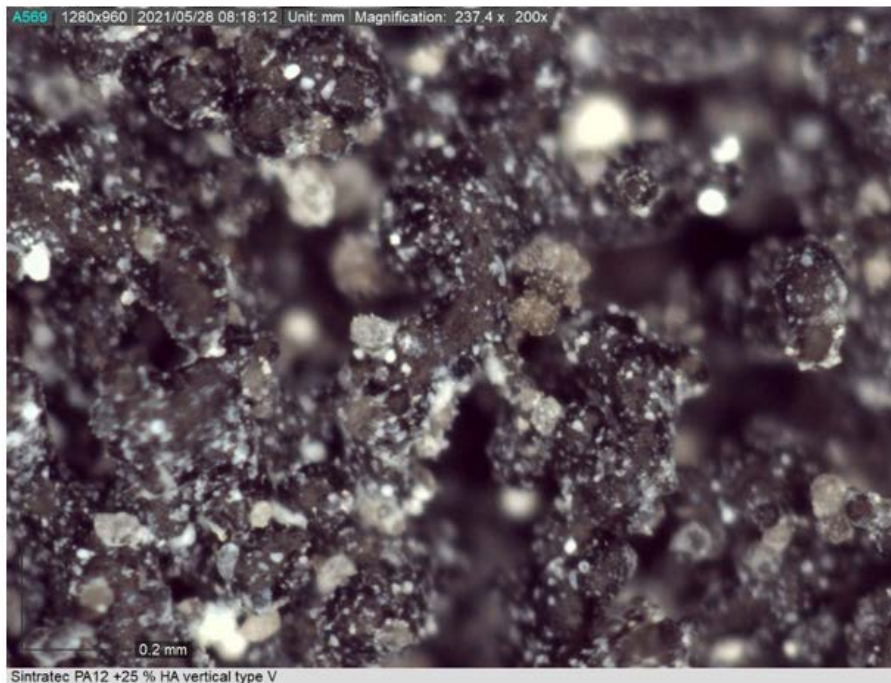


Figure 4.29: PA12/25%HA Qualitative printed surface analysis of porosity showing homogeneous HA mixture but extreme porosity with most of the HA not adhering to PA12 Matrix.

Following the initial testing described above, Sinterit V1 PA12 powder was selected for the matrix material for all subsequent blend testing and characterization. However, Sinterit discontinued the V1 powder and replaced it with a “V2” powder which had very different spreading results compared to the V1 powder. The Sinterit V2 powder did not sieve using the 100# mesh and had considerable clumping and spreading issues which produced unacceptable layer adhesion. As a result, the PA12 matrix for this research was switched to Sintratec powder. Powder comparison clearly showed the Sinterit powder was finer and lighter in color which initially seemed to aid sintering and analysis (Figures 4.30 and 4.31) However, comparison of layer adhesion between Sinterit V2 and Sintratec powders which necessitated the switch in matrix material is listed below and depicted in Figure 4.32.

The following are key differences between the discontinued powder and the Sintratec powder:

1. **Surface Temperature:** Required surface temperature and energy density to sinter the PA12 increased with the Sintratec powder. Sintering temperature window increased from 159-165 to 169-178 degrees Celsius, and the associate laser energy density increased with a similar ratio.
2. **Particle Size:** Powder particle size and distribution increased with the Sintratec powder (Figure 4.31)
3. **Color Contrast:** The color contrast between carbon fiber (CF) and the matrix powder decreased with the Sintratec powder (Figure 4.30).

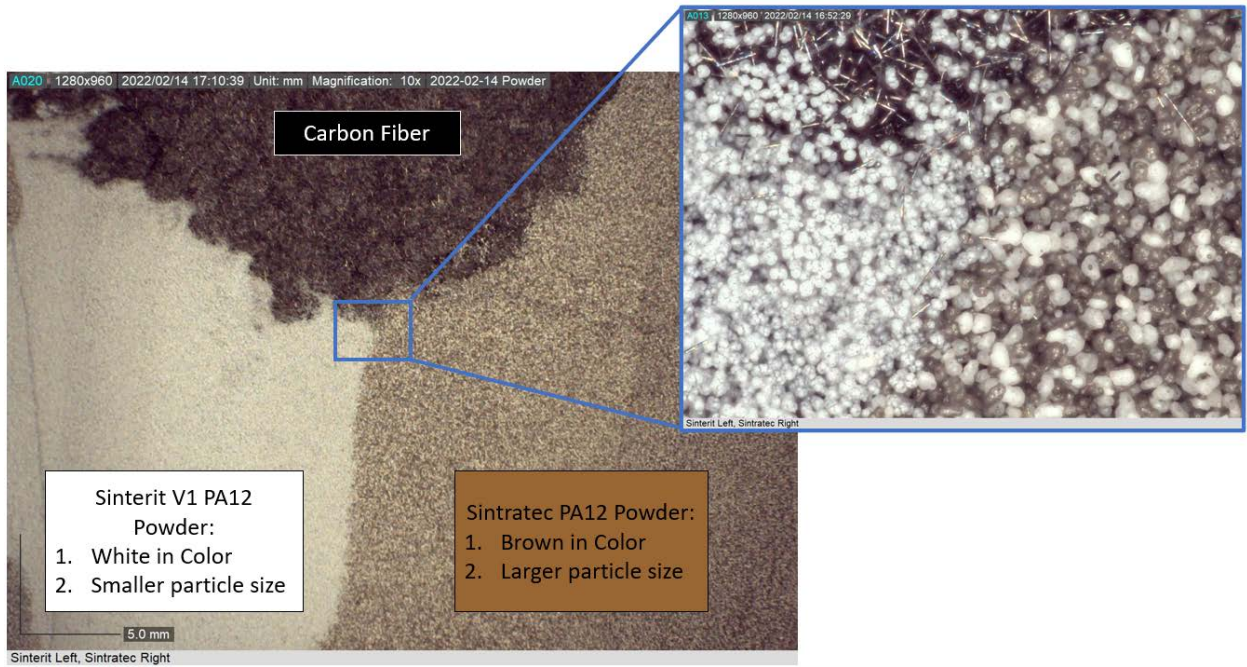


Figure 4.30: Microscopy comparison of Sinterit and Sintratec powder and CF (10x zoom left, 200x zoom right)



Figure 4.31: Microscopy comparison of Sinterit and Sintratec powder and CF at 248x zoom

Sinterit

Sintratec

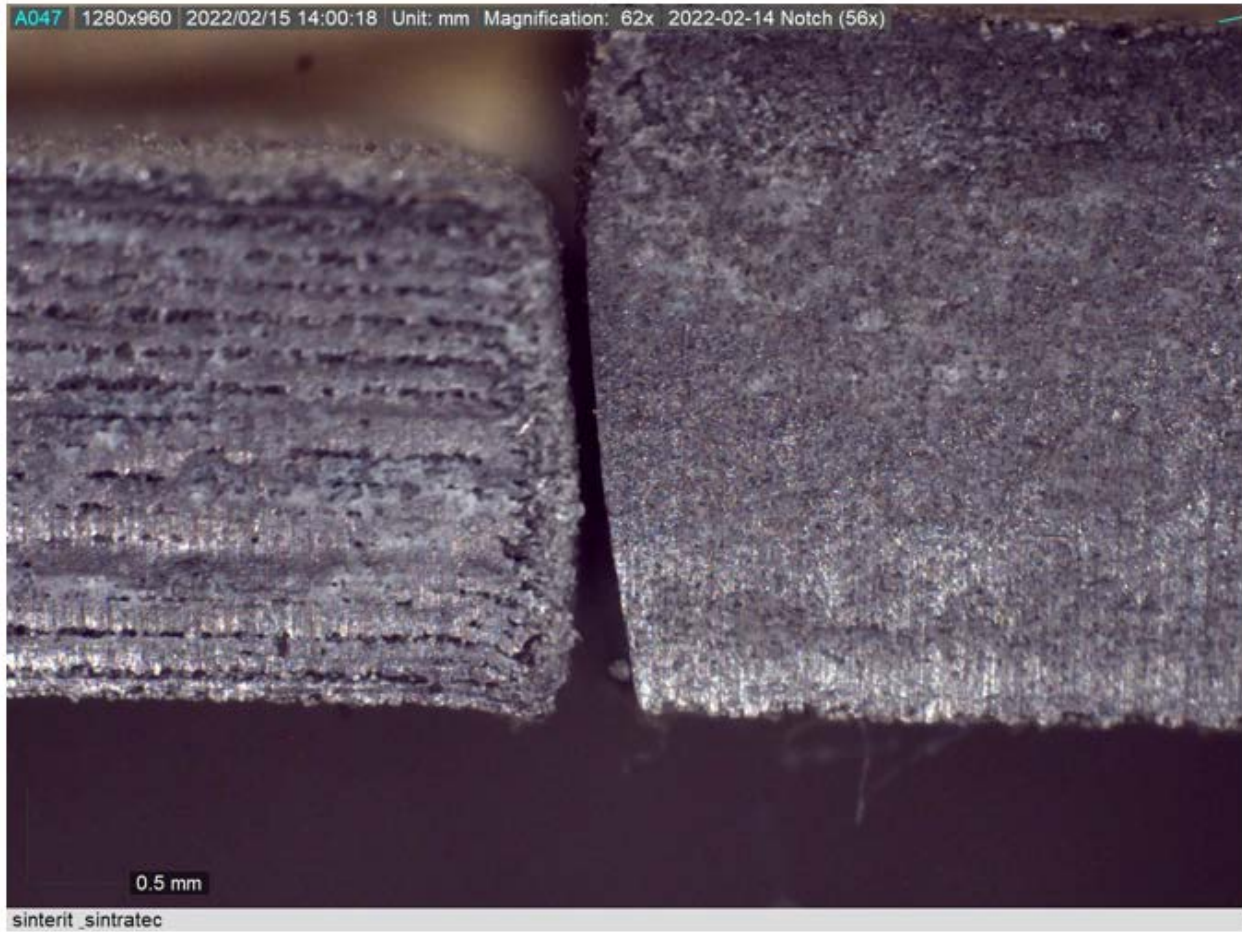


Figure 4.32: Microscopy comparison of Sinterit V2 and Sintratec PA12 layer adhesion with spreading inconsistencies during Sinterit V2 layer application.

Based on the initial results and material selection discussed above quantitative testing was done on various Sintratec PA12 + CF blends to determine ideal sintering parameters using the M2 SLS prototype. Tensile specimens were printed in sets of 3 attached in the grip area (Figure 4.33). This DOE aided in print efficiency, organization, multiple prints per heat up cycle, and stressing the system with a large cross section area (combined grip area) with a relatively small cross section area (gauge). The selected geometry also provided rounded and squared edges to assess varying geometric shapes. Approximately 6-12 of these were printed for each blend to quantitatively analyze.

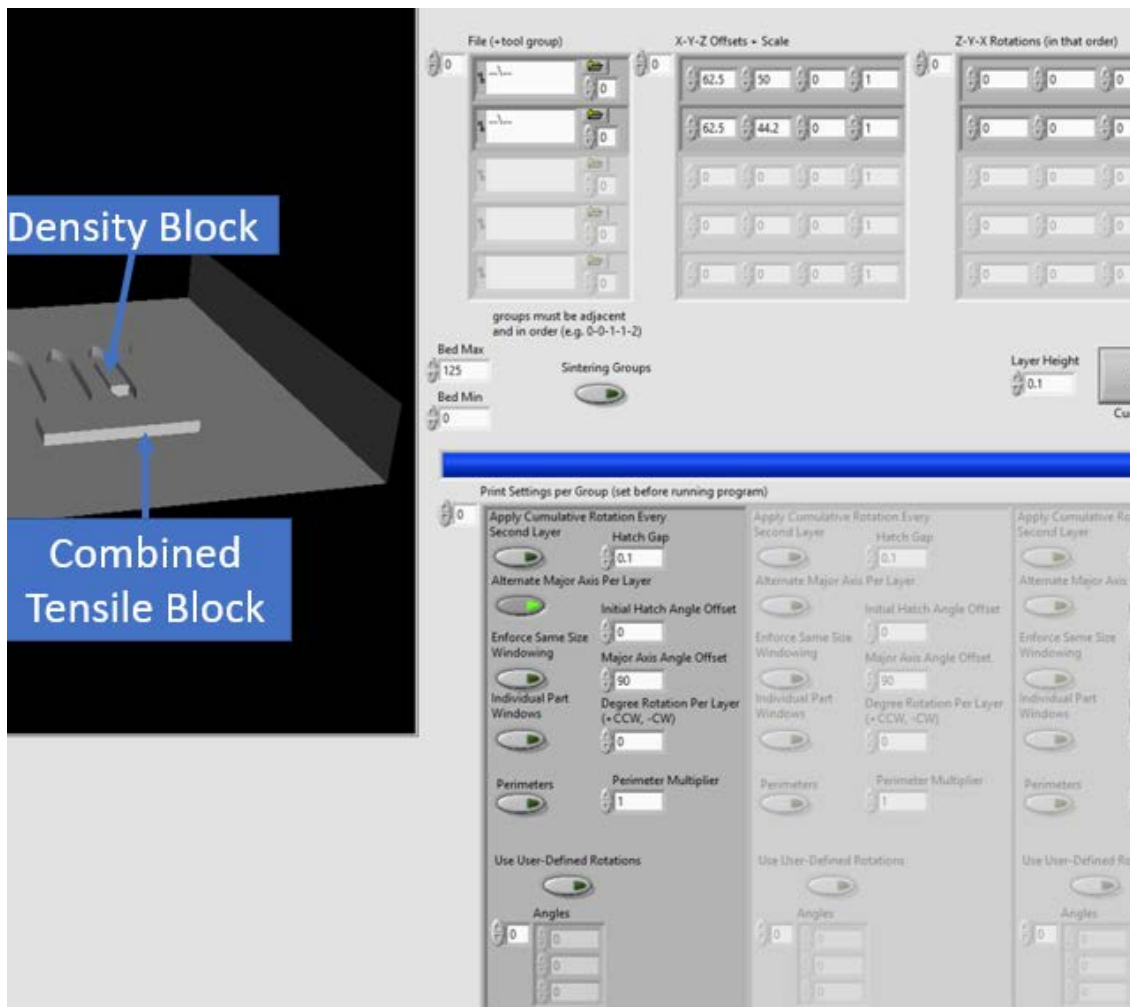


Figure 4.33: M2 SLS print setup and planning for density, hardness, and tensile testing.

Buoyancy density testing was done in accordance to ASTM D-792 on a separate density specimen and shore D hardness testing was done on the grip portion of the tensile testing prior to pulling the tensile specimen. Density testing showed differences between blends but did not have enough difference between sintering parameters to determine optimal energy density (Figure 4.34). Hardness testing also did not provide conclusive differences between sintering energy densities. The only parameters that provided conclusive quantitative results on the differences of energy density and sintering parameters were tensile test results. These results were coupled with qualitative fractography (Examples in Figures 4.35 and 4.36) to select print parameters for Aims 3 and 4. Dimensional and tensile data for the final selected blend sintering parameters are found in Figures 3.37. Data was arranged such that H1-3 were the selected print parameters for each specimen. Laser was at 5W except for 10% H4-6 which had a laser fault resulting in lower-than-expected energy density for this specimen. Tables of density, warping, and hardness with selected print parameters for each blend are found in chapters 5 and 6 (Tables 5.1, 6.1, and 6.2, respectively).

ID	Blend %CF	Laser Speed (mm/sec)	Specimen (SPN)		Measured Density (g/cm <sup>3</sup> )		
			Serial #	Energy	SPN	Mean	SD
P1↑	0% CF	2000 (Pre-Heat)	220115	High Energy Density	1.0232	1.0239	0.0009
P2↑	(Neat	500 (Sinter)			1.0249		
P3↑	PA12)	3000 (Bake)			1.0237		
P1↓	0% CF	3000 (Pre-Heat)	220115	Low Energy Density	1.0219	1.0198	0.0022
P2↓	(Neat	700 (Sinter)			1.0199		
P3↓	PA12)	3000 (Bake)			1.0176		

Figure 4.34: Buoyancy Density comparison of PA12 tensile test specimens printed at high (↑) and low (↓) densities.

### 0% CF Tensile Test Fractography Energy Density Comparison

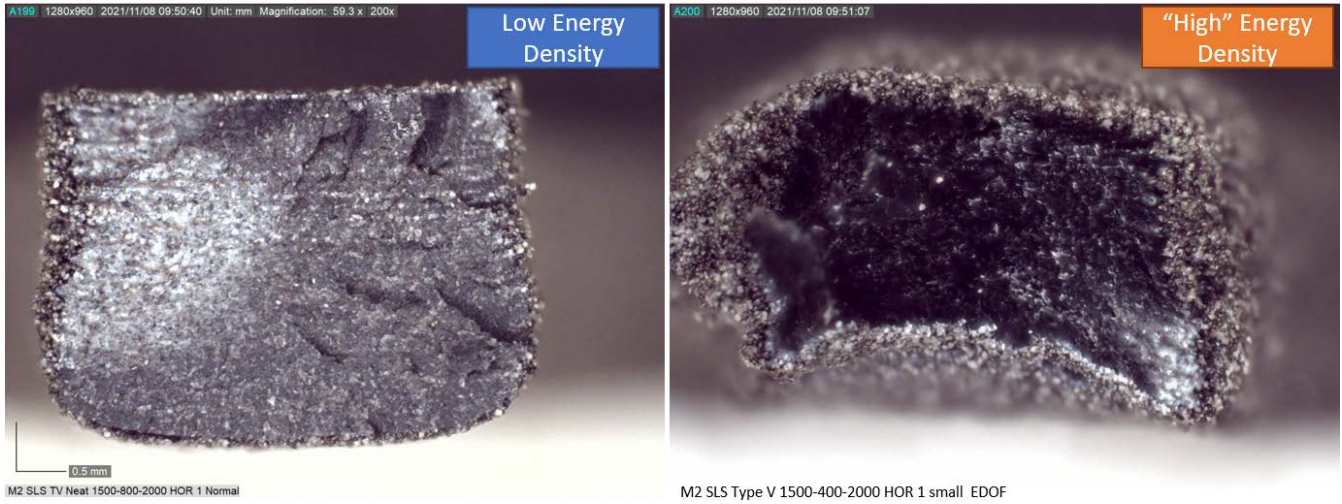


Figure 4.35: 0%CF Tensile Specimen comparing sintering energy densities (Dino-Lite AM4917MZT. Zoom: 59x

### 5% CF Tensile Test Fractography Energy Density Comparison

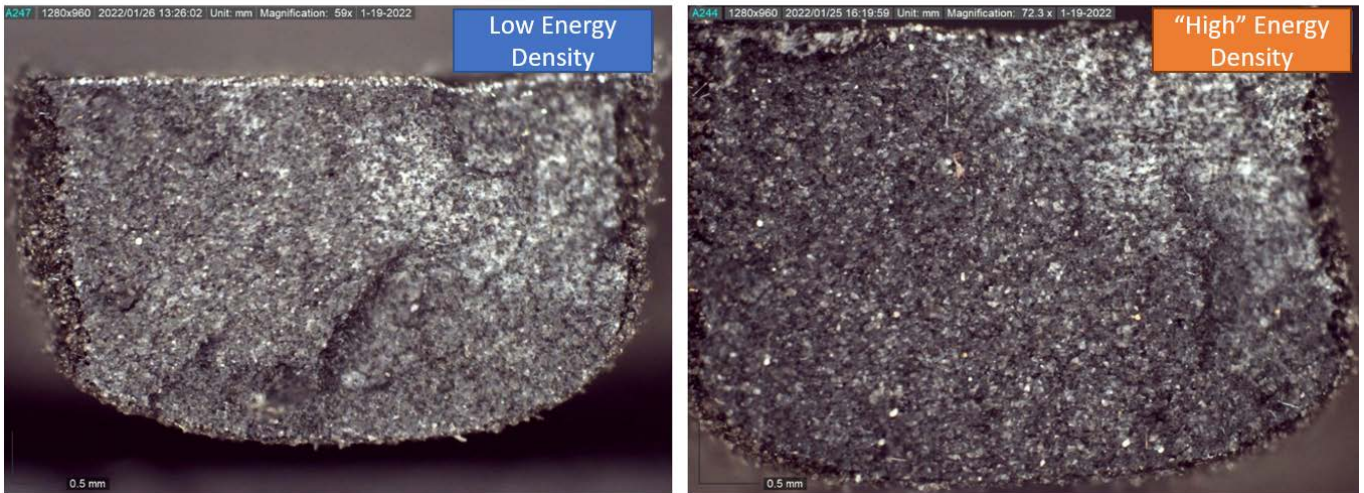
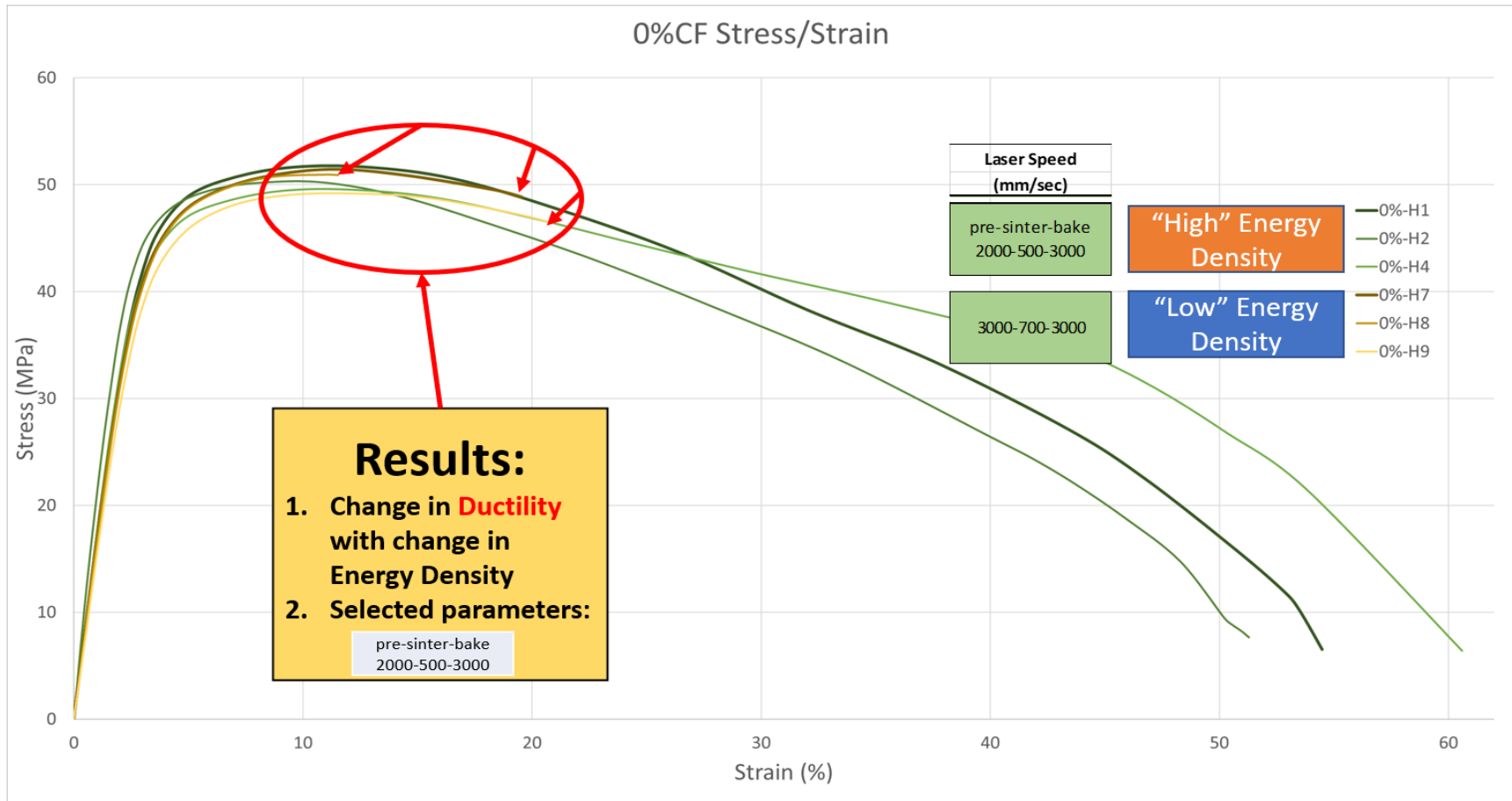


Figure 4.36: 5%CF Tensile Specimen comparing sintering energy densities (Dino-Lite AM4917MZT. Zoom: 59x Left (low density), 72x Right (high density)



Blend %CF	Print Direction	Laser Speed (mm/sec)	Specimen (SPN)		Dimensions (mm)		Cross Section (mm <sup>2</sup> )			Modulus of Elasticity (Mpa)			Ultimate Tensile Stress (Mpa)			Strain at Failure (%)			
			Serial #	ID	Width	Thickness	SPN	Mean	SD	SPN	Mean	SD	SPN	Mean	SD	SPN	Mean	SD	
0% CF (Neat PA12)	Horizontal	pre-sinter-bake 2000-500-3000	220115	H1	5.26	3.68	19.34	19.57	0.48	1711	1832.00	171.12	51.82	51.24	0.75	54.43	52.85	2.23	
				H2	5.40	3.73	20.12			1953			50.39			51.28			
				H3	5.26	3.66	19.25			*			51.52			*			
				3000-700-3000	H4	5.97	3.76	22.45	22.11	0.47	1701	1701.40	*	49.64	49.57	0.81	60.50	60.50	*
					H5	5.81	3.84	22.31			*			48.72			*		
					H6	5.77	3.74	21.58			*			50.35			*		
		1500-800-2000	211103	H7	5.43	3.71	20.15	20.19	0.17	1671	1610.50	81.48	51.48	50.61	1.09	19.47	17.24	5.07	
				H8	5.25	3.88	20.37			1642			50.97			11.43			
				H9	5.22	3.84	20.04			1518			49.39			20.82			

Figure 4.37: 0%CF Final Energy Density Comparison of Dimensional and Tensile Test Data.

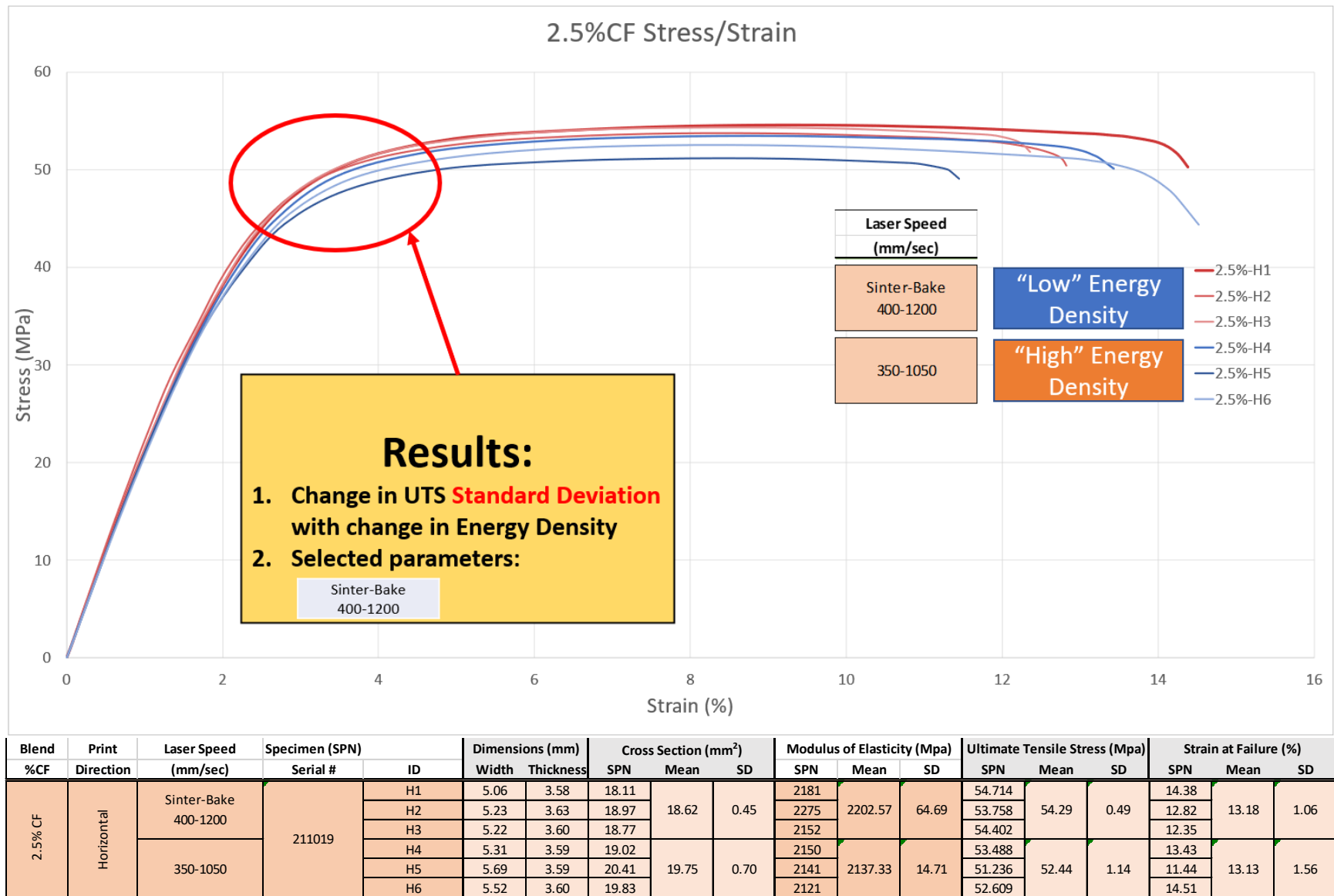
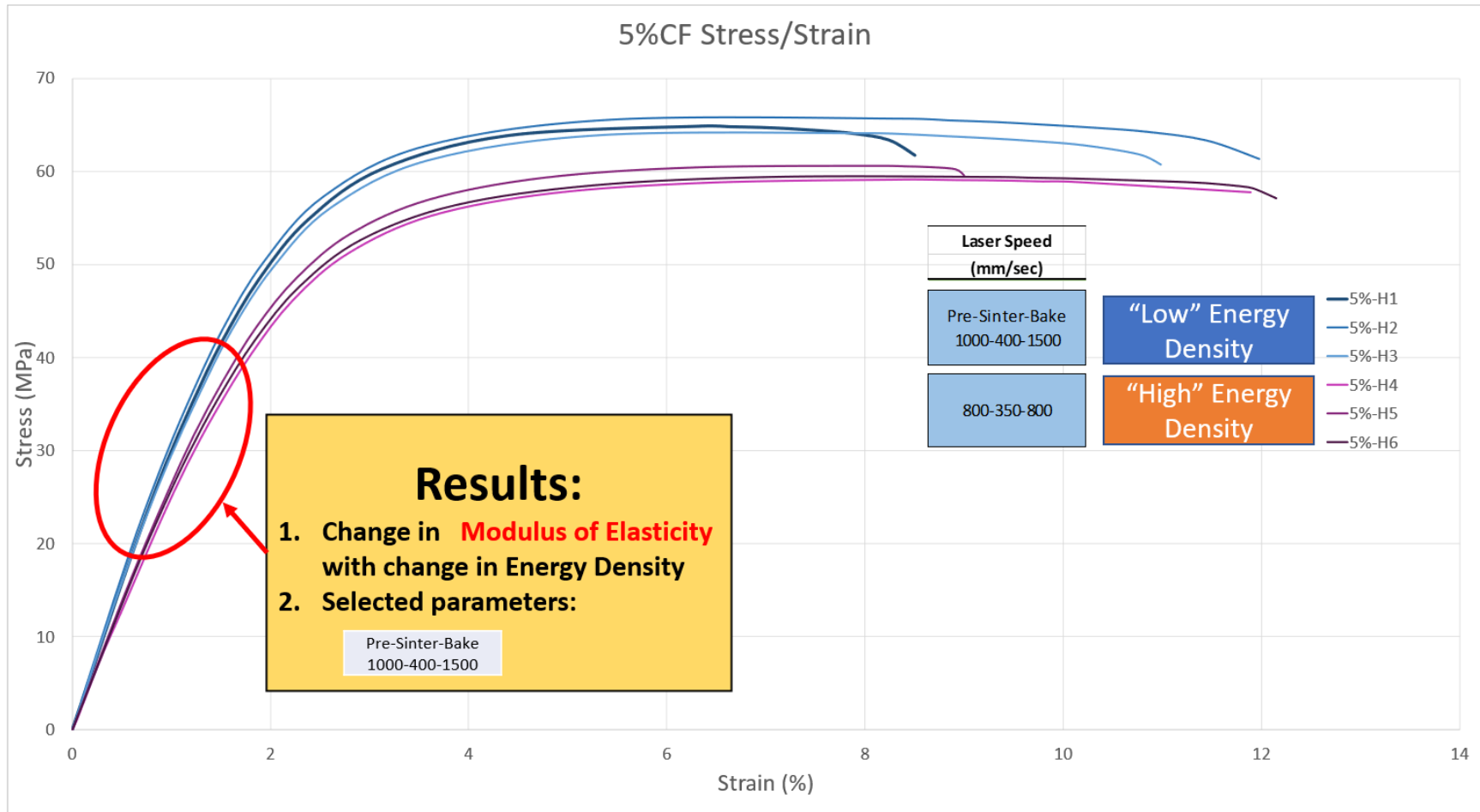


Figure 4.38: 2.5%CF Final Energy Density Comparison of Dimensional and Tensile Test Data.



Blend	Print	Laser Speed	Specimen (SPN)		Dimensions (mm)		Cross Section (mm <sup>2</sup> )			Modulus of Elasticity (Mpa)			Ultimate Tensile Stress (Mpa)			Strain at Failure (%)			
			%CF	Direction	(mm/sec)	Serial #	ID	Width	Thickness	SPN	Mean	SD	SPN	Mean	SD	SPN	Mean	SD	
5% CF	Horizontal	Pre-Sinter-Bake 1000-400-1500	211027	H1	5.49	3.69	20.26	19.90	0.36	3135	3216.53	103.79	64.880	65.05	0.80	8.50	10.49	1.79	
				H2	5.53	3.60	19.91			3333			65.930			11.98			
				H3	5.41	3.61	19.53			3181			64.355			10.98			
		800-350-800	211101	H4	5.87	4.01	23.54	23.82	0.30	2593	2685.37	87.22	59.134	59.77	0.81	11.89	9.00	11.01	1.75
				H5	5.92	4.02	23.80			2767			60.675			9.00			
				H6	5.93	4.07	24.14			2696			59.500			12.15			

Figure 4.39: 5%CF Final Energy Density Comparison of Dimensional and Tensile Test Data.

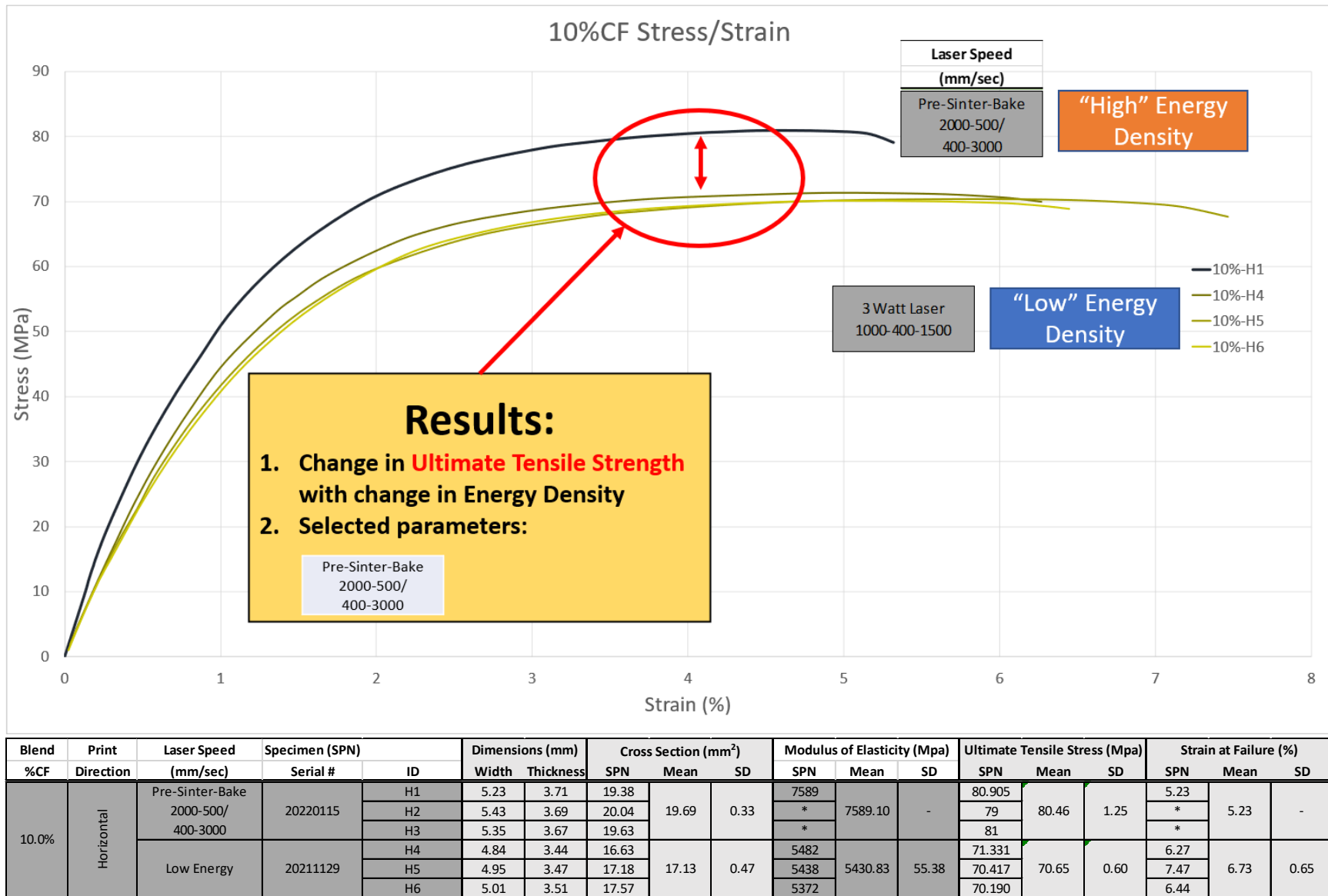


Figure 4.40: 10%CF Final Energy Density Comparison of Dimensional and Tensile Test Data.

## DISCUSSION

The single blend results indicate PA12 mechanically blended with TPE powders, CF, and HA composites can be functionalized via LCC in M2 PBF. It is important to consider the end use of a printed part when selecting temperature and energy density (i.e., laser speed and power) for each material blend. For instance, if the printed part is intended for a form and fit model with high geometric accuracy and resolution requirements as opposed to sintered material properties (e.g., energy absorption or high UTS) a lower energy density combined with faster laser speed and higher power would likely produce the desired results. This is a critical factor when discussing M2 manufacturing as many times the M2 aspect of the manufacturing is intended for an end use part and not simply a form and fit prototype. The material and blend results in this aim provided the techniques, parameters, and initial material properties to design single material and M2 LCC experiments (Aims 3 and 4 respectively). Consequently, the blend characterization in this aim was focused on maximizing the as printed material properties as opposed to geometric accuracy and complexity. However, future work will likely lead to requirements for higher geometric accuracy and resolution and lead to investigations in tuning a specific dimension scaling factor for each direction of each material and investigation post print processing techniques such as heat treatments. It was found the most effective way to quantitatively tune print parameters was via tensile test. Interestingly, each blend had slightly different changes in tensile properties with a change in energy density and so each material was tuned using different tensile metrics. Below each blend is discussed individually as it pertains to SLS tuning and implementation into M2 SLS manufacturing:

## Neat PA12

Neat PA12 was the only material that had a considerable difference in maximum strain (plastic deformation) with a change in energy density. With a relatively high energy density the material was capable of large (>50%) strain values as opposed to 10-20% for lower energy densities, but the modulus of elasticity and UTS stayed relatively consistent between these energy densities. The high energy density with high strain capability did come at the cost of reduced geometric accuracy which will have to be considered in future design planning when using SLS. If high energy absorption is required, the tradeoff may require the part to be machined to size after printing if post heat treatment is unavailable or not desired. However, the multi-pass lasing technique (Aim 1) should also be explored using more than 3 laser passes for “real time heat treatment”. Likely the first step will be to characterize the effects of two “sintering” passes. If “real time heat treatment” techniques like this do not provide the required geometrical and material properties, lower energy density during printing can be used followed by post print heat and/or pressure treatment. Real time and post print heat treatments were not tested during this study and should be characterized in future studies to see if both high strain and geometric requirements can be simultaneously achieved. This will also lay the groundwork for future M2 SLS parts printed with a PA12 matrix. The value of M2 SLS parts with PA12 matrix material should not be underestimated as it is currently the most prolific SLS material with greatly reduced cost and complexity of both the required sintering equipment (i.e., laser and chamber) and the powder. These aspects of PA12 make it an ideal material to further functionalize the M2 SLS design and FGMs developed in this research.

## **PA12/HA Blends**

HA blends highlighted the limitations of the M2 SLS prototype hardware and did not sinter well in the prototype because of the low temperatures (ambient maximum of ~160° C) and laser properties (wavelength of 455 nm and maximum power 5W) of the prototype. Further testing using the blending techniques from this aim is recommend with a different laser properties. Suggest CO2 laser (10.6µm) or Nd:YAG (1.06µm) laser with a minimum power output of 20W and an ambient temperature temperatures of 200°+ C. Nd:YAG lasers are currently still being developed for PBF and will likely require IR-absorbing pigments for this application. However, CO2 lasers are well established and have demonstrated sintering capability with white color PEEK powder (Berretta et al., 2016; Schmidt et al., 2007) and will likely have better results with white HA particulates. Since PEEK is well established as a biomaterial and currently being used for implants (e.g., dental implants) it is recommended to focus on PEEK/HA blending for future HA blend testing and PEEK/HA ratio FGM implants.

## **PA12/TPE Blends**

PA12/TPE blends highlighted the benefits of M2 anchoring when printing materials with marginal sintering window overlap. The TPE was relatively tolerant of temperature swings from the lowest TPE ambient setting of 110 °C all the way to 160 °C for PA12 sintering after being sintered which is ideal for an anchoring material. However, the fresh TPE powder was still susceptible to clumping and inconsistent powder spreading if it was held above 110 °C for even brief periods of time. The removable reservoir design from Aim 1 should be investigated to avoid this clumping by only having the TPE powder in the heated system when it is actively being used and spread. This would avoid the powder degradation over time when using powders

from other reservoirs. With or without removable chambers both the rate and overall percentage of crystallization will be affected for all materials being sintered as temperatures are adjusted from one material to another. These affects should be characterized in the future, but the results of PA12/TPE blends with TPE anchoring in Aim 3 have opened the door to sintering parts that do not necessarily have an overlap in sintering windows. Again, it is likely this will necessitate post sintering heat treatment, but in this case large differences in thermal properties between materials will likely limit the effectiveness of heat treating the entire part at a uniform temperature and will require more creative heat treatment techniques that focus on specific areas of the final part. It is also important to note that sinterable TPE powders are available from numerous manufactures, and all have distinct melting points and sintering parameters. So, unlike PA12, a change in TPE powder from what was studied in this aim could result in a considerable change in performance when blended with PA12.

### **PA12/CF Blends**

PA12/CF blends highlighted the difficulty of spreading non-spherical shaped particles like CF but also highlighted the relatively large changes in material properties (>60% increase in UTS and >300% increase in E) achievable with only small amounts of added CF ( $\leq 10\%$  CF). A large factor in this success was the multi-pass powder spreading developed in Aim 1 and this technique should be investigated using a roller (possibly counter rotating in both directions) and expended to more than only two passes to see if layers resulting in near 100% density can be achieved at greater than 10% CF. Spreading inconsistencies occurred at  $\geq 20\%$  CF resulting in high porosity and poor mechanical properties. However, blends up to 60% CF were sinterable (i.e., material bonded enough to form a part, though extreme unintended porosity existed). This

capability is a distinct advantage over other AM process such as FFF and Polyjet that require liquid flow. Further testing is recommended with encapsulated fibers to investigate powder flowability to included encapsulated fibers mixed with raw fibers to increase overall fiber percentage and manipulate fiber orientation within a part. The encapsulation process should also include studies into increasing the bonding between the matrix and fiber with studies similar to those done by Yan et al. (C. Yan et al., 2011a). However, the blend characterization in this Aim has demonstrated mechanical blending without in depth treatments to increase material bonding can be very advantageous. The simplicity of this method is an important aspect of this research as it allows blend ratios to be quickly adjusted with both new powders and already blended powders by simply adding more matrix or infill material.

Lastly, it is important to consider these results as they apply to biomedical implants and other material applications. CF blends with PEEK are much more suited for orthopedic implant applications and have already been studied for sinterability (B. Chen et al., 2017; M. Yan et al., 2018). PA12 matrix specimens with CF mainly only had a change in UTS with a small change of modulus in elasticity based on a change in energy density and this outcome is not expected with PEEK matrix specimens based on the sintering window and re-crystallization of PEEK. All PA12/CF blends were also fairly tolerant of changes around the optimum energy density with material property differences only perceptible through tensile test. This is indicative of the large PA12 sintering window and is not expected to be true with other high-performance matrix material such as PEEK.

## **TPE/CF Blends**

TPE/CF blends highlighted the effectiveness of the sintered bond between the TPE and CF and customizable changes between tensile and bending properties. Though fiber/matrix bonding, bending, and tensile properties were only qualitatively evaluated it has shown a promising future in biomimicry of soft tissue with a high increase in tensile stiffness coupled with a small increase in bending stiffness when CF is added. Future studies should quantify bending and tensile properties of various ratios of TPE/CF to build a repository for future material selection. Based on the results of the blends tested it is expected tensile tests will provide quantitative data capable of tuning laser parameters similar to PA12/CF. However, unlike PA12 there are numerous proprietary TPE SLS powders with vast differences in properties between different powders. Likely these proprietary blends will bond to CF at varying levels and blends will have to be tested not only for material properties, but also TPE/CF bonding.

## **Material Blending Future Work**

The material blending characterization from this research has provided the initial data showing the feasibility of M2 PBF manufacturing using different blends of materials. SLS material blend future work should be coupled with the recommended future work from Aim 1 to incorporate high temperature capability into the M2 SLS prototype. This will open the door to study blends such as PEEK/HA and PEEK/CF which are appropriate for orthopedic implants. Changing material color and specifically selecting color contrast between different materials will allow image thresholding analysis and allow greater characterization of blend uniformity, porosity, and LCC in M2 specimens. Single blend ratio sintering testing will have to focus on

achieving desired material properties combined sintering window overlap for M2 prints. Geometric accuracy and complexity in parts will also have to be increased to accommodate osseointegration lattice structures as it will be difficult to correct dimensional accuracy in these structures with machining or other traditional manufacturing processes post sintering. It is recommended to incorporate post process heat and/or pressure treatments to investigate both complex geometries and matrix/fiber or matrix/particulate bonding to include specific fiber pullout testing. However, for biomedical research, geometry and material properties are just an initial obstacle. Follow on research will have to include osseointegration of as printed parts and long-term performance of implanted SLS materials.

## **BROADER IMPLICATIONS**

The blend characteristics studied as they pertain to the SLS process established certain methods and results that gave M2 PBF a promising future not only for orthopedic implants and synthetic joints but for numerous other applications as well. Parts could be functionalized to adapt to and achieve multiple end use requirements such as wear resistance, osseointegration, energy absorptions, high strength, low weight, customizable stiffness, etc. based on material blending. This M2 manufacturing reshaping through composite and material blending will also be able to attain the current benefits (i.e. complex geometry, controlled density, interwoven parts, etc.) of PBF. As an example, the center “spine” of an airfoil could be stiffened with relatively high amounts of CF while the wing tips could be allowed to flex with relatively low amounts of CF and top layer airflow could be energized with bleed through ports through the wing at precise locations. Similarly, implants could have complex lattice structure with increasing ratios of HA toward the outside of the implant at the bone/implant interface while customizing the modulus of

elasticity at the core with CF or other stiffening fiber to produce an isoelastic stiffness. Overall, this opens the door to implement M2 technology into other PBF methods such as SLM; ultimately putting M2 PBF within reach for industries requiring high performance functionally graded materials.

## **CONCLUSION**

Mechanical blend testing has demonstrated the feasibility of blending TPE, HA, and CF with a PA12 matrix up to 60% volume for SLS applications. When sintering in the M2 SLS prototype, mechanical properties are degraded with blends above 10% for CF and HA and above 40% for TPE. Bonding between sintered PA12 and CF when mechanically blended established the foundation for Aims 3 and 4 and characterization of functional gradients using PA12/CF blends printed with the M2 SLS prototype. Tensile test was the only quantitative method found that clearly demonstrated the differences in material properties with respect to sintering energy density. Subsequently, printing parameters using tensile data from this aim were used for Aims 3 and 4 printing. However, future work should be considered with other characterization such as microCT, DSC, XRD, burn off, and contrast imaging based on the SLS tuning required for desired material properties.

## **Chapter 5: Aim 3 - Characterization of Stress-Strain and Fracture Data for Polyamide 12 and Carbon Fiber blends.**

### **INTRODUCTION**

Aim 3 characterized stress-strain and fracture data for single material thermoplastic (TP)/fiber blends described in Aim 2. Tensile test specimens were Additively Manufactured (AM), commonly known as “printed” using the multi-material (M2) Selective Laser Sintering (SLS) prototype from Aim 1. Polyamide 12 (PA12) matrix with carbon fiber (CF) infill blend characterization established an initial data repository for material selection in future work. These blends underwent tensile tests to measure printed blend mechanical properties both perpendicular and parallel to the build direction. Modulus of Elasticity (E), yield stress ( $\sigma_y$ ), and Ultimate Tensile Strength (UTS) were determined from tensile test stress-strain data. This characterization provided insight into the mechanical behavior of PA12 powder sintered by the M2 SLS and reinforced with 0%, 2.5%, 5%, and 10% CF. Selection of material blends in Aim 4 was informed by these results ensuring effective investigation into the efficacy of Functionally Graded Materials (FGM) fabricated with the M2 SLS prototype. Tensile performance (stress-strain curves) from vertically and horizontally printed specimens can vary considerably. Tensile properties for both vertical (perpendicular loading) and horizontal (parallel loading) specimens were analyzed in Aim 3. To ensure consistency of data between Aims 3 and 4 horizontal print orientation with intralayer tensile loading (i.e., tensile loading parallel to rake direction) was selected for all tests in Aim 4 and comparison of results between Aim 3 and Aim 4.

## BACKGROUND

The additive nature, both between rasters and layers, of powder bed fusion (PBF) inherently leads to anisotropy in printed parts. Anisotropic tensile properties are influenced by laser, temperature, and hatch print parameters. All of these parameters were primarily determined in Aim 2. However, the greatest impact to tensile properties is generally based on the following two primary loading directions (Figure 5.1) (Cano et al., 2018):

1. **Perpendicular Tensile Loading:** Tensile load along the build direction primarily transmits the tensile load perpendicularly to the printed layers or from layer to layer resulting in **interlayer loading**.
  - **Vertical Print Orientation:** Tensile test specimens printed with interlayer loading are described as being “vertically” printed.
  - **Printing Effects:** Vertically printed tensile specimens inherently minimizes the sintered area for each layer and as a result generally has reduced part warping and sledding as compared to the horizontal print orientation.
2. **Parallel Tensile Loading:** Tensile load parallel to the layers primarily distributes the tensile load within layers or **intralayer loading**.
  - **Horizontal Print Orientation:** Tensile test specimens printed with intralayer loading are described as being “horizontally” printed (Cano et al., 2018).
  - **Printing Effects:** Horizontally printed tensile specimens decrease number of layers from ~635 to ~32 as compared to the vertical print orientation. This significantly decrease the print time and thus the time the reservoir powder remains at elevated temperatures.

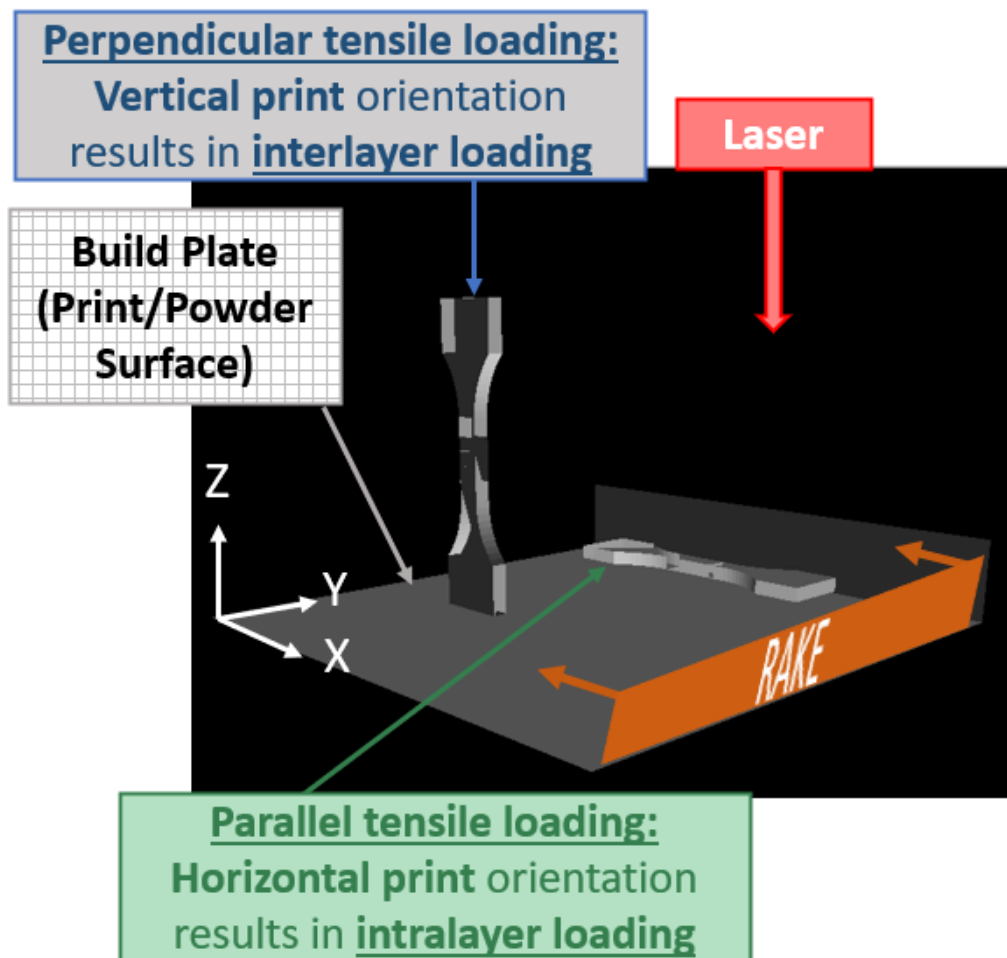


Figure 5.1: Loading and print orientation designations for tensile test specimens

Although Hatch patterns can affect layer to layer adhesion during interlayer loading, particularly in the form of energy uniformity throughout a layer during sintering (Ahrari et al., 2017; Parry et al., 2019). Hatch pattern also tends to become more influential on mechanical properties when substantial plastic or elastic deformation exists during tensile loading (Kiani et al., 2020; Wörz & Drummer, 2018). However, generally layer to layer adhesion is much more dependent on laser settings than hatch pattern (Wörz & Drummer, 2018). As described in this research, perpendicular tensile loading for most thermoplastics will transfer the load from layer

to layer and tensile properties are largely independent of hatch pattern. In contrast, parallel tensile loading will transmit considerable load along or between rasters and tensile properties are highly dependent on the hatch pattern (Wörz & Drummer, 2018). However, these principles affect the entire stress-strain relationship and generally result in a lower ultimate tensile strength (UTS) for perpendicular loading (Figures 5.2a,b, and 5.3). Turk et al. (Türk et al., 2017) did find during elevated temperature testing above 50° C initial modulus of elasticity was slightly lower for horizontal builds in fiber reinforced polymers. However, the dominating factor for the M2 SLS prototype and fiber reinforced blends was layer application (recoating) and laser transmittance through the material (Adibekyan et al., 2019; Zaami et al., 2021).

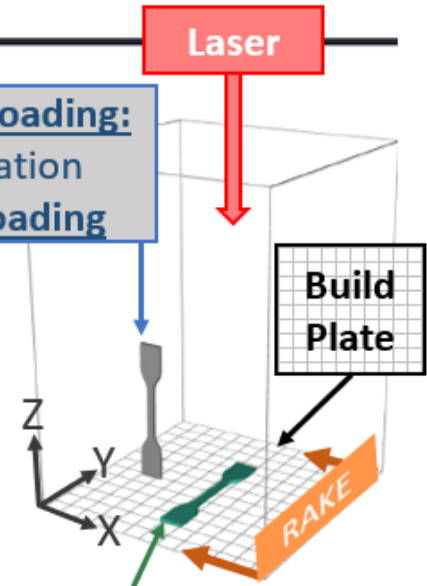
# Tensile test Sintratec PA12

**Test standard**  
DIN EN ISO 527-1

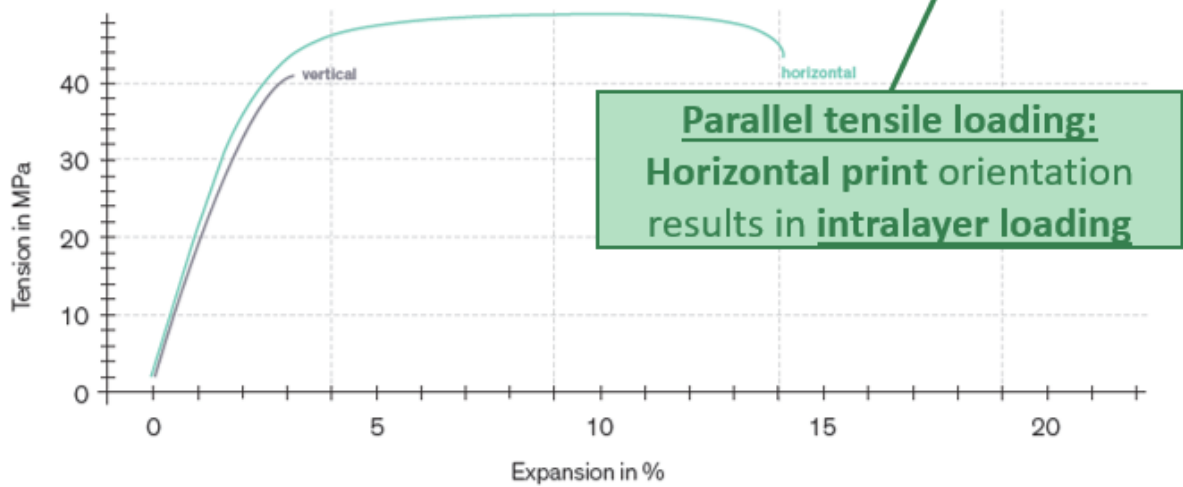
**Test specimen**  
Type 5A printed with the Sintratec S1

**Perpendicular tensile loading:**  
**Vertical print orientation**  
results in **interlayer loading**

	$\epsilon_{tb}$ %	b mm	L h mm
Test object horizontal (XY)	-	4,49	2,39
Test object vertical (Z)	-	4,31	2,26



**Test graphic**



**Parallel tensile loading:**  
**Horizontal print orientation**  
results in **intralayer loading**

**Test results**

	$E_t$ MPa	$\sigma_y$ MPa	$\epsilon_y$ %	$\sigma_m$ MPa	L $\epsilon_m$ %	$\sigma_b$ MPa	$\epsilon_b$ %
Test object horizontal (XY)	1610	47,8	8,9	47,8	8,9	43,1	-
Test object vertical (Z)	1750	-	-	40,8	3,1	40,8	3,1

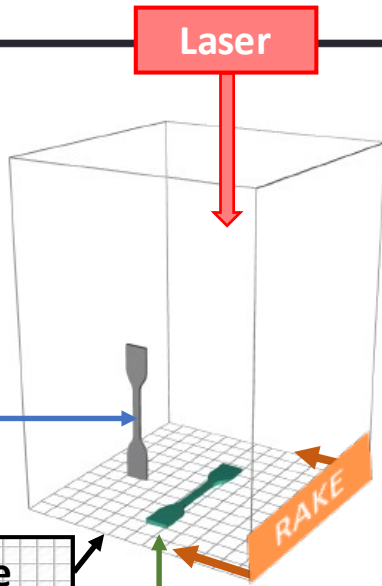
Figure 5.2a: Sintratec reported PA12 tensile test properties based on build direction (Boxed text added) (Sintratec, 2021a).

# Tensile test Sintratec PA12

**Test standard**  
DIN EN ISO 527-1

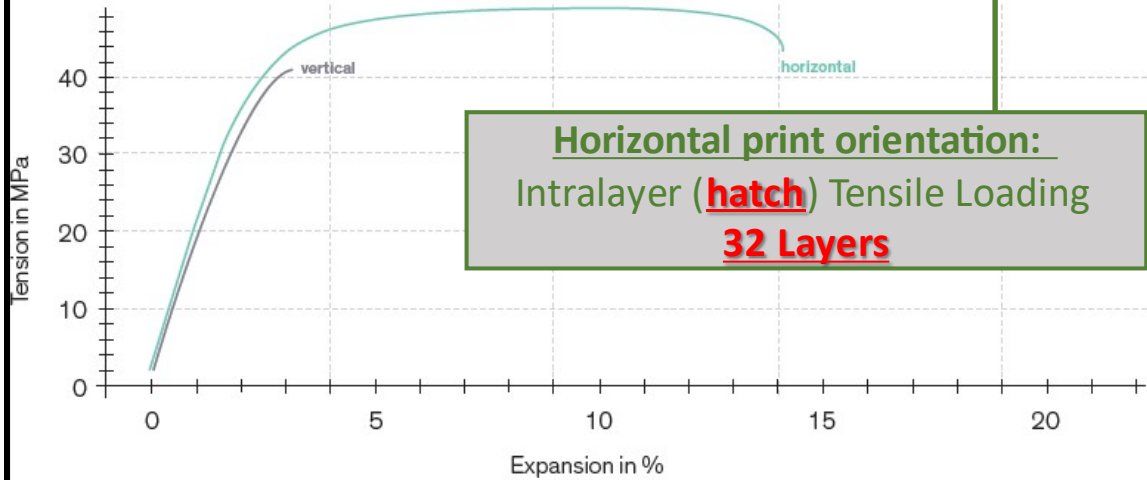
**Test specimen**  
Type 5A printed with the Sintratec S1

**Vertical print orientation:**  
Interlayer (**layer-layer**) Tensile Loading  
**635 Layers**



**Build Plate**

**Test graphic**



**Horizontal print orientation:**  
Intralayer (**hatch**) Tensile Loading  
**32 Layers**

**Test results**

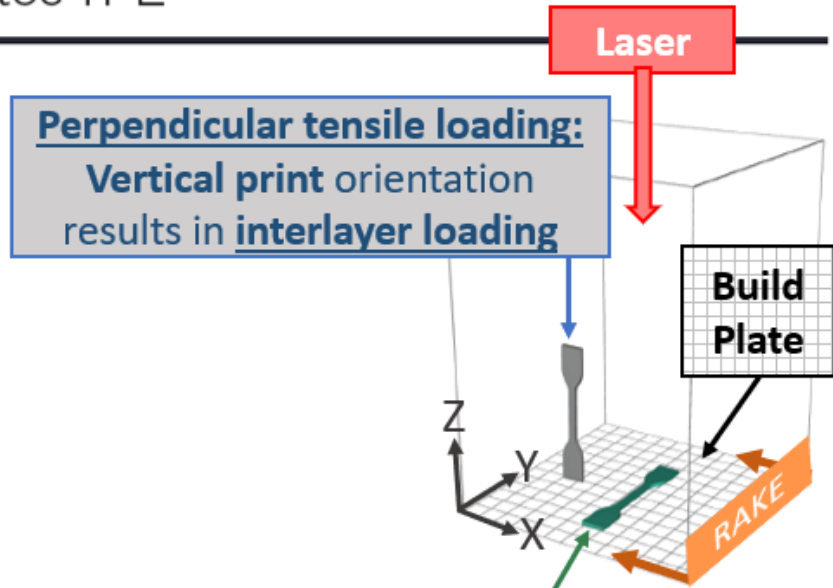
	$E_t$ MPa	$\sigma_y$ MPa	$\epsilon_y$ %	$\sigma_m$ MPa	$L \epsilon_m$ %	$\sigma_b$ MPa	$\epsilon_b$ %
Test object horizontal (XY)	1610	47,8	8,9	47,8	8,9	43,1	–
Test object vertical (Z)	1750	–	–	40,8	3,1	40,8	3,1

Figure 5.2b: Sintratec reported PA12 tensile test properties based on build direction comparing layer count and loading for each print direction (Sintratec, 2021a).

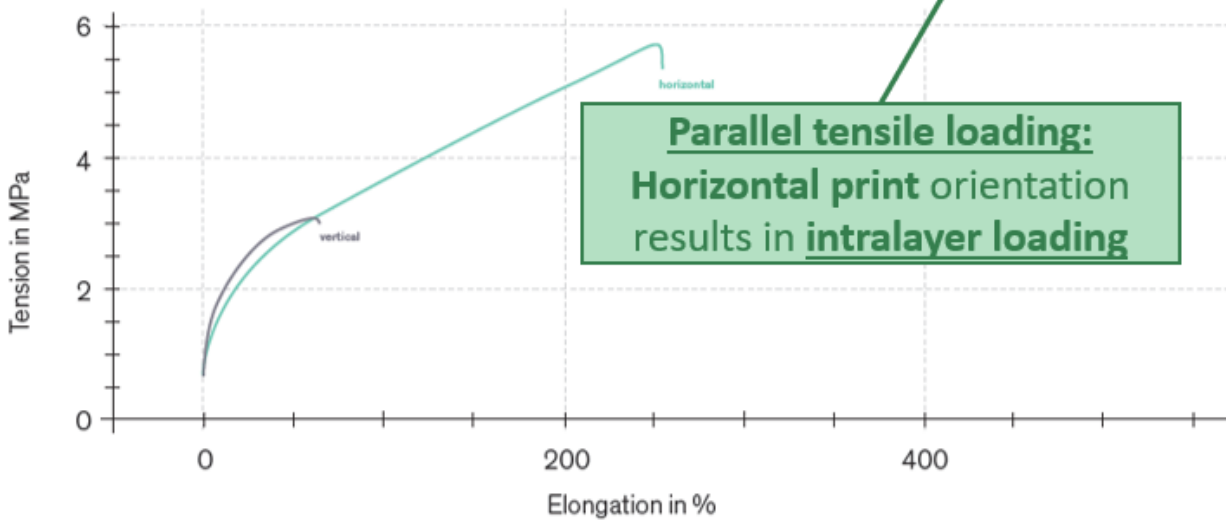
# Tensile Test Sintratec TPE

Test standard  
DIN EN ISO 527-1

Test specimen  
Type 5A printed with the Sintratec S1



## Test graphic



## Test results

	$E_t$ MPa	$\sigma_m$ MPa	$\epsilon_m$ %	$\sigma_b$ MPa	$\epsilon_{tb}$ %	b mm	h mm
Test object horizontal (XY)	29.9	1.82	12	5.28	250	3.62	2.47
Test object vertical (Z)	28	2.00	12	2.98	63	3.78	1.76

Figure 5.3: Sintratec reported TPE tensile test properties based on build direction (Boxed text added) (Sintratec, 2021b).

Tensile and bonding properties at material interfaces can be investigated using one-dimension (1D) gradients under perpendicular loading (normal stress). Mode I tensile opening/failure may occur at interfaces with sharp changes in material properties (Figure 5.4) (Bartlett et al., 2015a, 2015b; “Composites Design in the Real World,” 2003; Fedorov & Matveenکو, 2016; Krueger, 2015). Testing one-dimensional (1D) gradients with additively

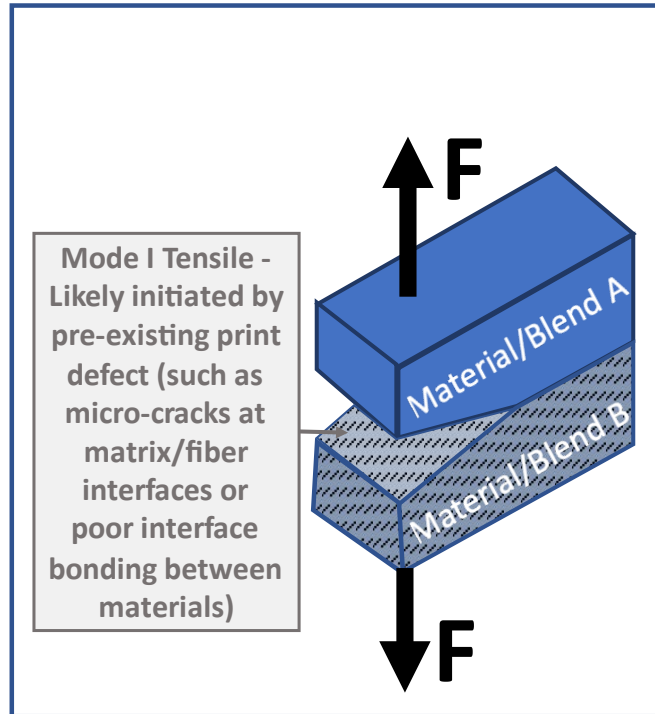


Figure 5.4: Mode I Tensile Failure.

manufactured Type V specimens have been modeled by Ituarte et al. (Ituarte et al., 2019) and experimentally tested by Lumpe et al. (Lumpe et al., 2019). The DOE in Figure 5.5 enables the entire tensile load, prior to specimen deformation, to be transmitted perpendicular to the material interface. However, the interaction of fiber and matrix powder compared to polyjett liquid recoating create a distinct difference between Lumpe’s M2 specimens and M2 specimens manufactured with M2 PBF. Aim 3 studied these affects as they relate to print orientation and tensile properties to establish a specimen type and print direction for M2 testing in Aim 4. This studied also provided an initial repository for mechanically blended PA12/CF tensile data and laid a foundation for future material blend and M2 PBF testing and characterization.

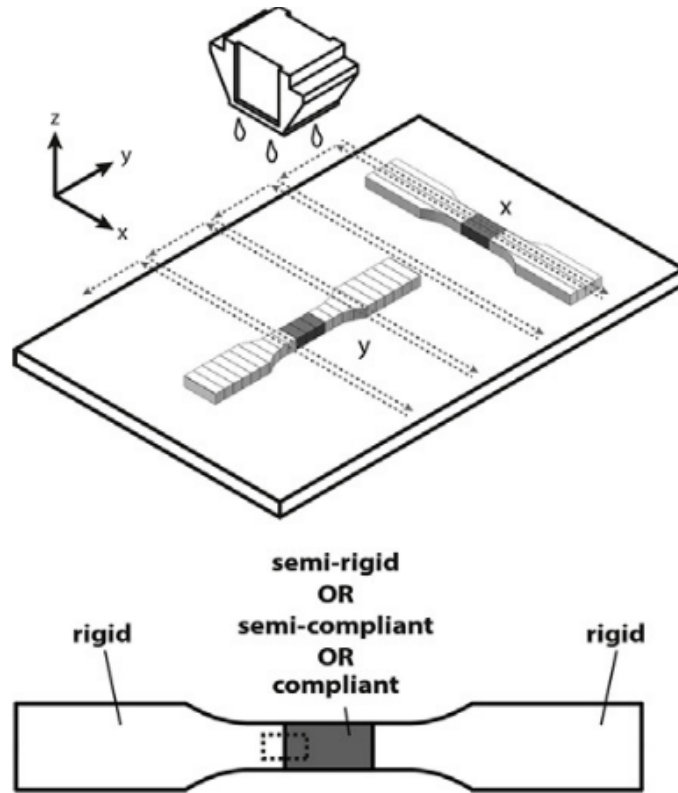


Figure 5.5: Lumpe et al. gradient testing Design of Experiment (DOE) with Type V test specimens additively manufactured using material jetting (Lumpe et al., 2019)

## METHODS

A total of 64 specimens were printed with a minimum of three from each blend used for printed blend characterization including tensile, dimensional, density, porosity, and fracture analysis as described in Figure 5.6 and in accordance with Aim 2 methods. The remaining specimens for each blend were tested as required for print or test anomalies.

Buoyancy density tests were done using ethanol and an electronic balance in accordance with ASTM D-792 test standards. Tensile loading rate and ambient environment impacts tensile data results for both single material and M2 specimens (Lumpe et al., 2019) and so both were held constant for all tests. Grip rate was set to 10 mm/min for tensile specimens and an ambient test temperature of approximately 23 °C was used in accordance with ASTM D638-14 and

similar tests done by Roberson et al., Lumpe et al., and Green et al. (ASTM International, 2006; Carrete et al., 2019; Chávez et al., 2019; Green et al., 2021).

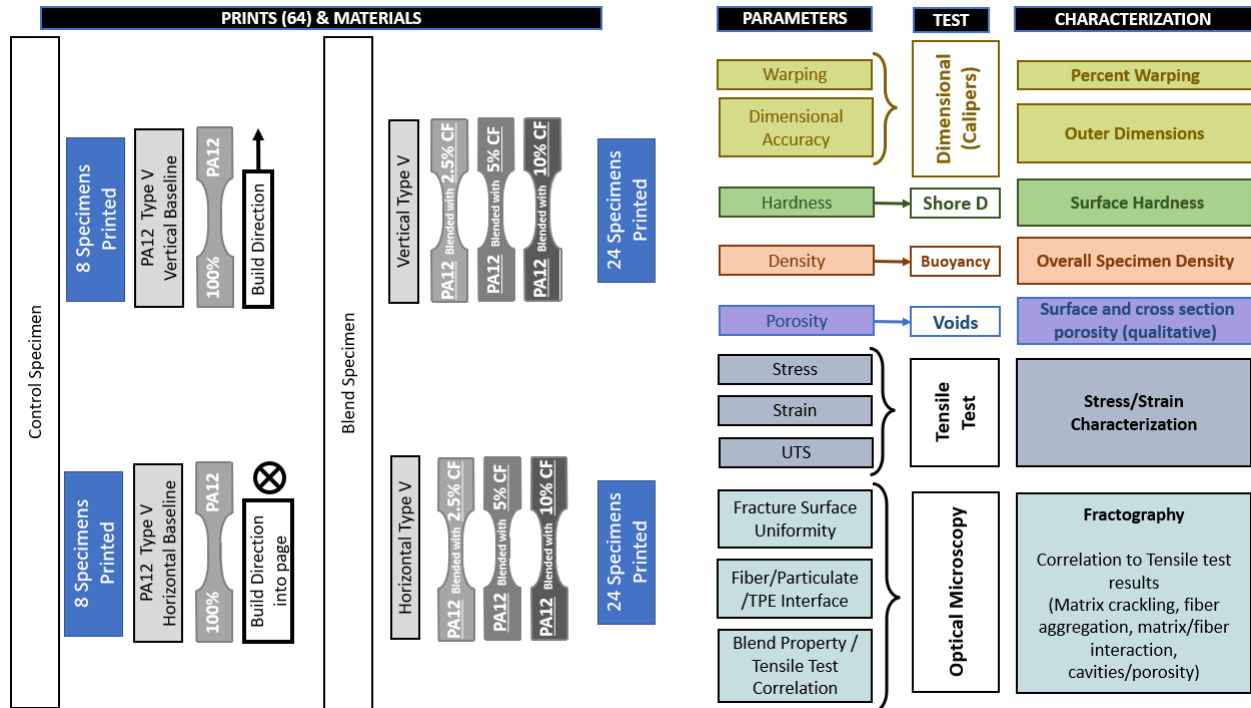


Figure 5.6: Summary of Aim 3 methods including specimens, tests, and characterization. Specimen manufacturing was done in the order listed: neat followed by composite. Analysis was done in the order listed for each control and blend specimen: dimensional, density tensile, optical microscopy analysis.

ASTM D638-14 Type V tensile test specimens (Figure 5.7a) were modified to allow direct comparison with future M2 tensile characterization. Gauge length (G) was increased to allow 3 material testing within the gauge length similar to experiments done by Lumpe et al and Tang et al. (Lumpe et al., 2019; Tang et al., 2021a). Width (W) was proportionally increased to the gauge length. Length overall (LO) was held constant which decreased grip length to accommodate the longer gauge length. Modified tensile test specimen (“3mmP”) dimensions are found in 5.7b. Testing was also done which would allow 5mm for each material and also had the

width increased proportionally. These specimens were referred to as “5mmP”. During comparison testing tensile results between 3mmP and 5mmP were very similar and some of the vertical print tensile tests were done using 5mmP from the comparison testing (Figure 5.7c). Specimens for each blend were printed in sets of 3-6 specimens for horizontal specimens and sets of 6-12 specimens for vertical specimens. Specimens were offset in x and y directions to improve powder flow and spreading uniformity for each part and isolate each specimen from neighboring specimens. Example of a 6-specimen vertical print is depicted in Figure 5.8.

A single window constant time hatch pattern (Figure 3.5) without perimeters and layer rasters oriented at 0 and 90 degrees were used based on the results from Aim 2 to increase print efficiency and printed specimen property consistency. This hatch pattern also aided in consistent comparison between vertical and horizontal specimens though tensile properties were still primarily based on layer-to-layer adhesion for vertical specimens and hatch pattern for horizontal specimens. Minimizing total sintering time was critical for vertical prints to prevent clumping in the reservoir over time based on partial sintering over time, molecular weight and chemical crosslinking (chapter 4).

ASTM D638 – 14

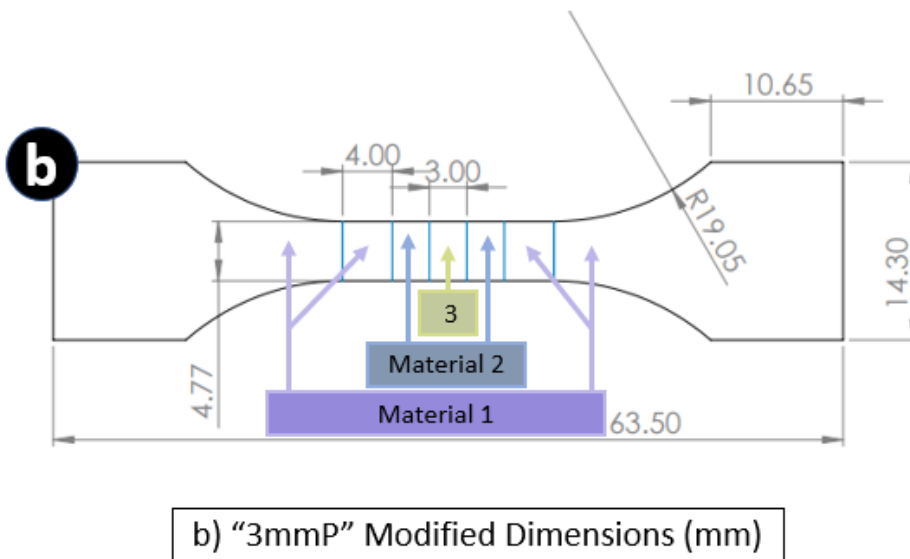
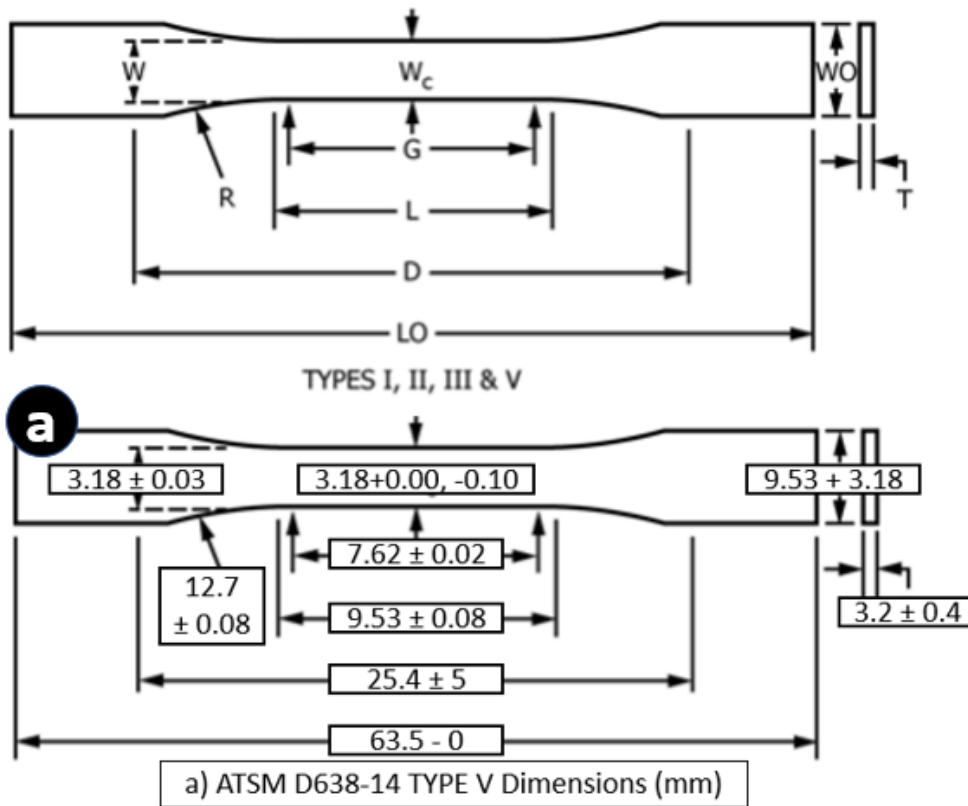


Figure 5.7:  
a) Original tensile test specimen definitions and lengths (ASTM D638-14)  
b) "3mmP" modified tensile test specimen to accommodate tri-material specimen.

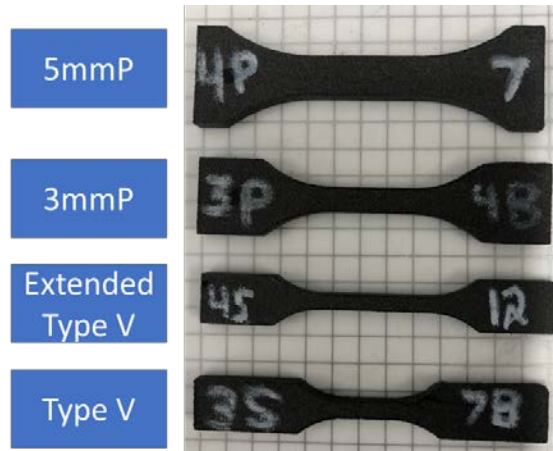


Figure 5.7c: Comparison prints of standard D638 Type V tensile specimen, extended tensile specimen with reduced grip length, 3mmP specimen, and 5mmP specimen.

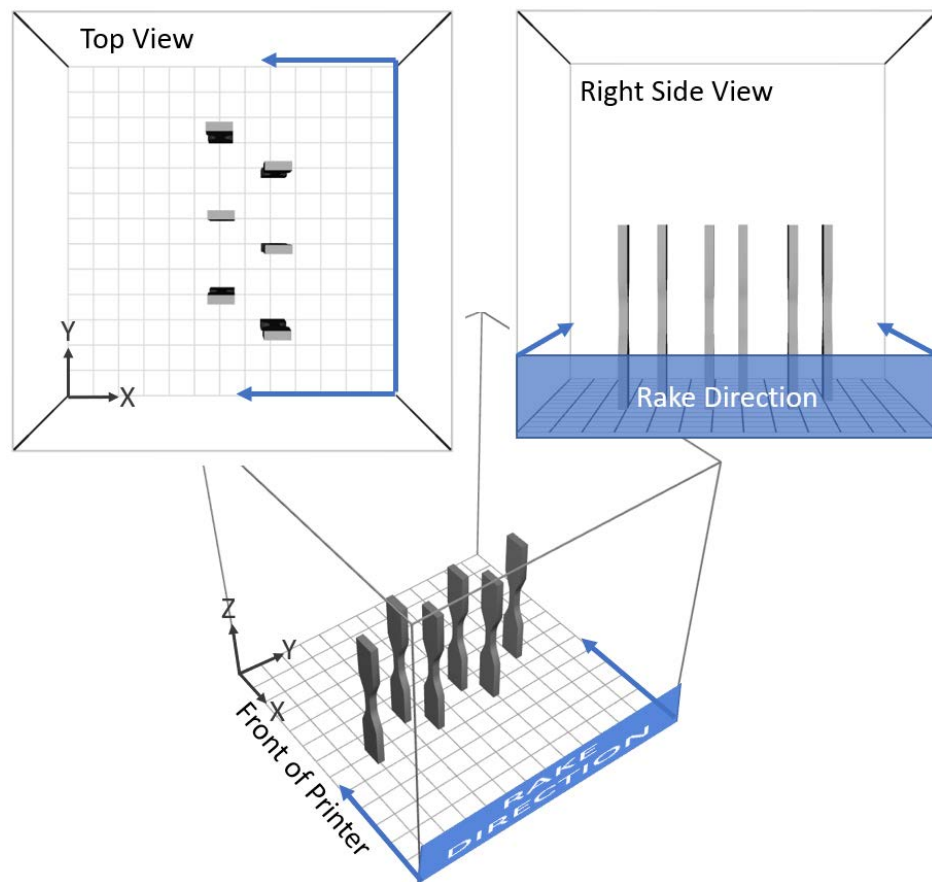


Figure 5.8: Proposed tensile specimen print scheme (Specimen and build area images from Sintratec Central print program).

## RESULTS

Warping was minimal with the selected parameters from Aim 3 and negligible after specimen cleaning post print. For this reason, quantitative warping measurements were not reported for tensile specimens. (Quantitative warping results for Single Edge Notch Tensile (SENT) specimens can be found in chapter 6, table 6.1). Qualitative porosity results remained consistent with Aim 2 results. However, vertically printed specimens with CF had severe layer adhesion inconsistencies. This was partially due to 24-48 hour print times based on the layer count (Figure 5.2b) and on laser speed and number of specimens per print. This extended time periodically resulted in extreme powder degradation (Figure 5.9). Powder degradation to this extent typically resulted in cake clumping, cracking, and warping and eventually led to catastrophic print failure. Cake warping was least prevalent for 10% CF; however, blending clumping resulting in high porosity and poor layer adhesion was most severe with 10% CF. Most vertically printed 10% CF specimens broke along a layer during post print cleaning, though this trend was specimen specific and not layer specific (i.e., not all specimens broke along the same layer (Figure 5.10). Many others broke during grip tightening during tensile testing or withstood minimal extension before fracturing along multiple layers (Figure 5.11). Tensile test data was calculated for specimens that reached at least 0.30% strain. Most 10% CF specimens failed well before 0.30% strain and are not reported. Buoyancy density results are presented in Table 5.1 and further discussed in Table 5.2. Shore D hardness tests for these blends were done on SENT specimens in order to capture hardness along a cross section perpendicular to the layers (hypothesized to be the hardest with lowest variance) and on the surface parallel to the layers (hypothesized to be the softest with highest variance). Hardness results are presented in chapter 6, Figure 6.2. Graphed and tabulated dimension and tensile results for 0, 2.5, 5, and 10% vol CF

tensile specimens are presented in Figures 5.12 thru 5.15 respectively. A figure comparing a representative stress/strain curve from each blend is depicted in Figure 5.16. Vertical specimens for 0% CF and 10% CF had data from 5mmP specimens which had 60% more cross sectional area than 3mmP specimen. In all graphs solid lines represent horizontal print orientation and dashed lines represent vertical print orientation.

Optical fractographic imaging was done for all specimens. Representative images are found in Figures 5.17 thru 5.20. In all specimen, 0% CF (neat PA12) was the only fracture surface that showed a highly ductile fracture mechanism. All horizontally printed specimens blended with CF tended to have 3-dimensional fracture surfaces with the crack propagating parallel (axial) to the load direction. Vertically printed 2.5% and 5.0% CF specimens had greatly reduced crack propagation parallel to the load direction and vertically printed 10% CF specimen had near zero 3-dimensional features and appeared to be flat along a single layer. Optical fractography also depicted the difference in sintering and dimensions between horizontally and vertically printed specimens (Figures 5.19 and 5.20, respectively). Vertically printed specimens had a much smaller area printed each layer and had a larger outer area of partially sintered particles. Horizontally printed specimens had one side with more rounded corners (bottom layer) and the opposite side with more squared off corners (top layer). This same phenomenon was present with the vertical printed specimens but was not evident at the fracture surface and instead was evident at the “bottom” grip (first layer printed) and “top” grip (last layer printed).



Figure 5.9: Example of powder degradation during extended vertical prints.

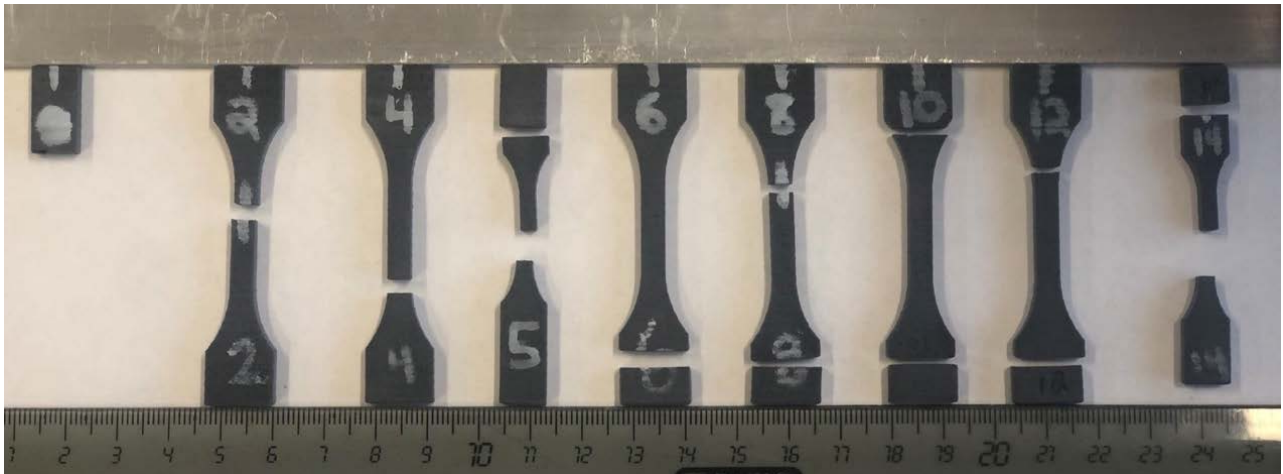


Figure 5.10: Example of specimen condition following post print cleaning of 10% CF vertically printed tensile specimens. Some specimens broke during removal and some broke during cleaning.

## Tensile Test (vertical)



Figure 5.11: 10% CF vertically printed tensile specimen failure during grip insertion and initial pulling.

Table 5.1: PA12/CF Buoyancy Density Results (ASTM D-792 Test Standards)

Blend	Laser Speed	Specimen (SPN)		Measured Density (g/cm <sup>3</sup> )		
		Serial #	ID	SPN	Mean	SD
0% CF (Neat PA12)	2000 (Pre-Heat) 500 (Sinter) 3000 (Bake)	220115	H1	1.0232	1.0239	0.0009
			H2	1.0249		
			H3	1.0237		
5% CF	800 (Pre-Heat) 350 (Sinter) 800 (Bake)	211027	H1	1.0704	1.0758	0.0047
			H2	1.0788		
			H3	1.0782		
10% CF	1000 (Pre-Heat) 400 (Sinter) 1500 (Bake)	20220115	H1	1.0997	1.0998	0.0007
			H2	1.0991		
			H3	1.1005		

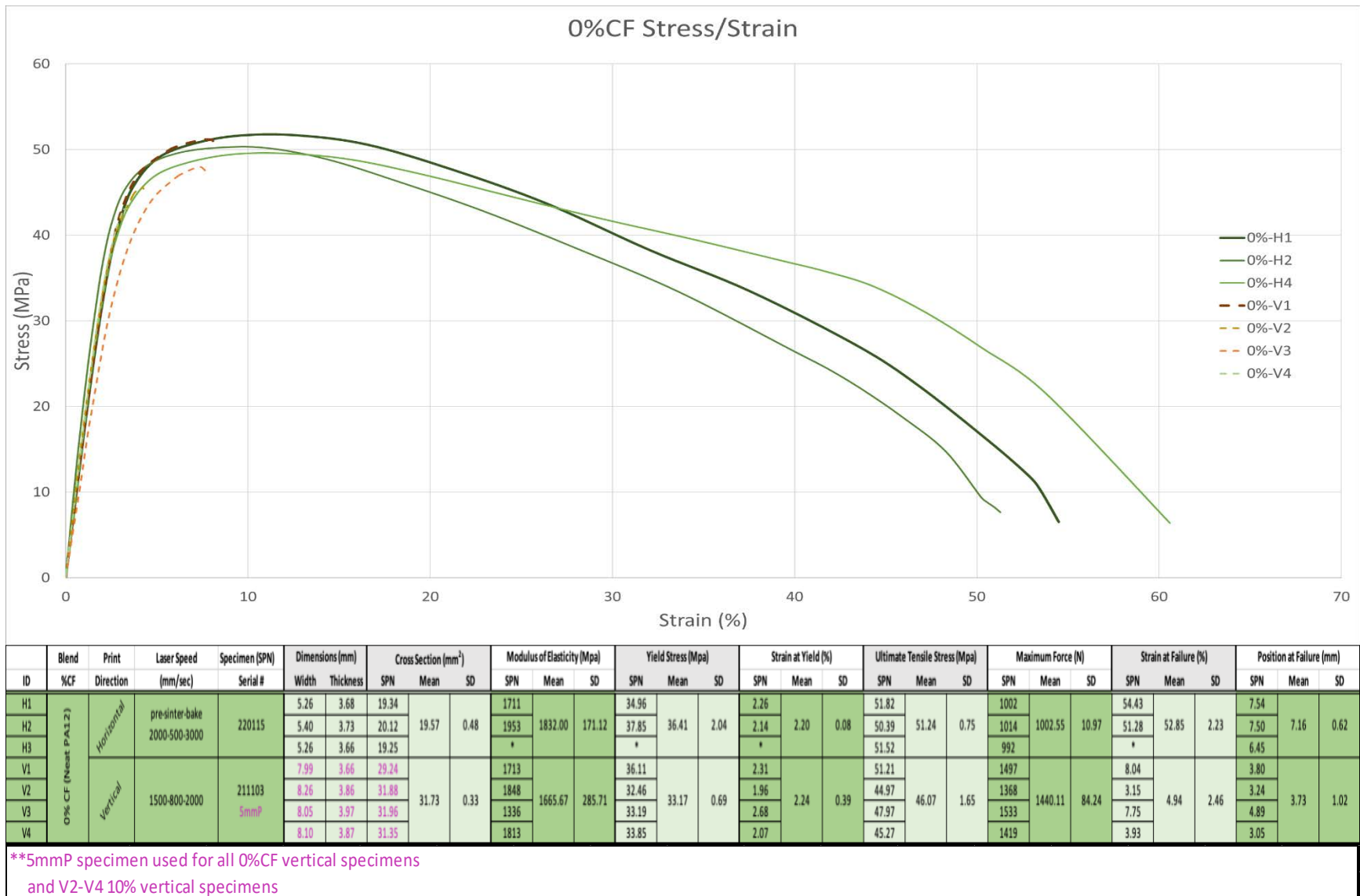


Figure 5.12: 0% CF Vertical and Horizontal Specimen Dimensional and Tensile Test Data.

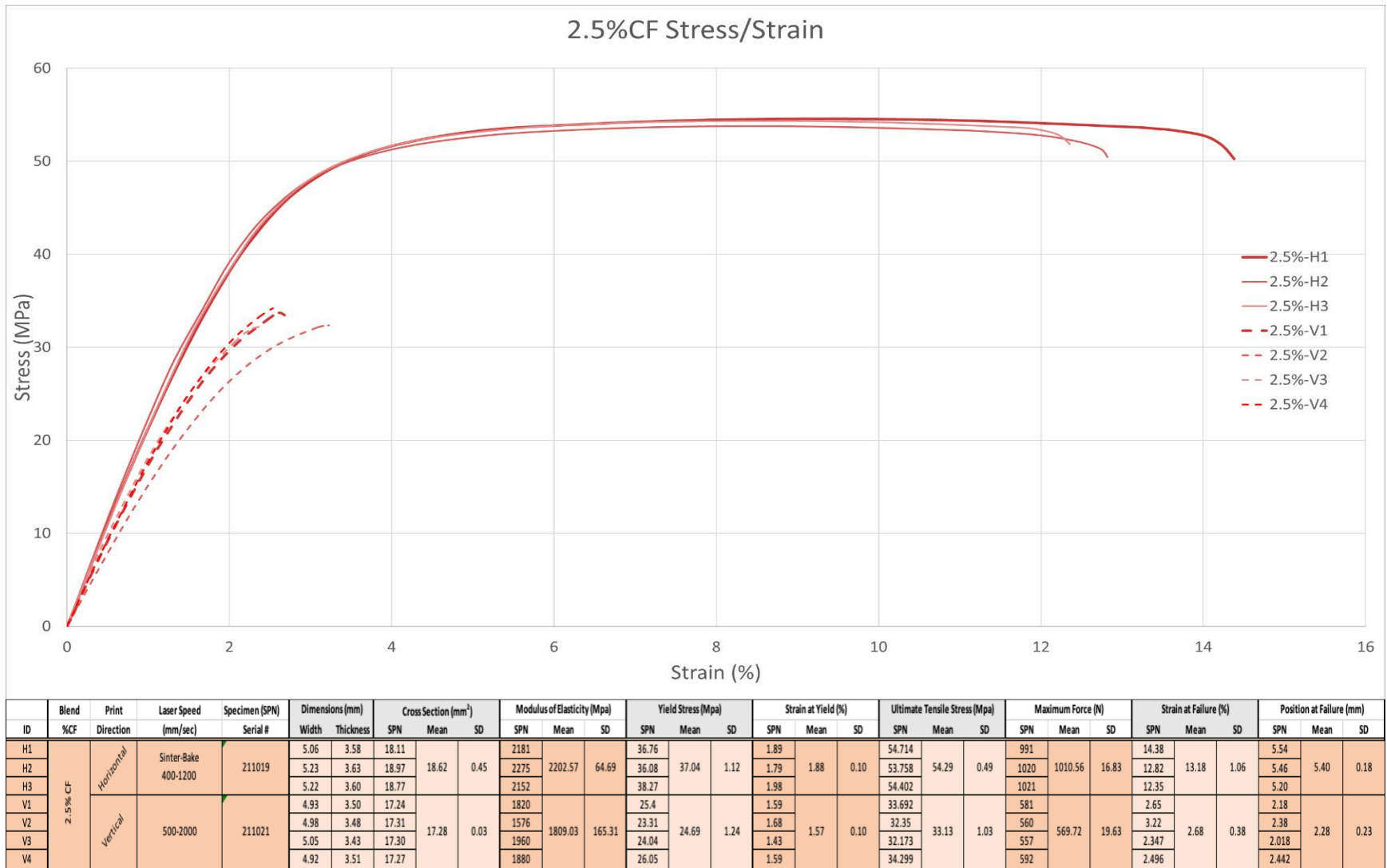


Figure 5.13: 2.5% CF Vertical and Horizontal Specimen Dimensional and Tensile Test Data.

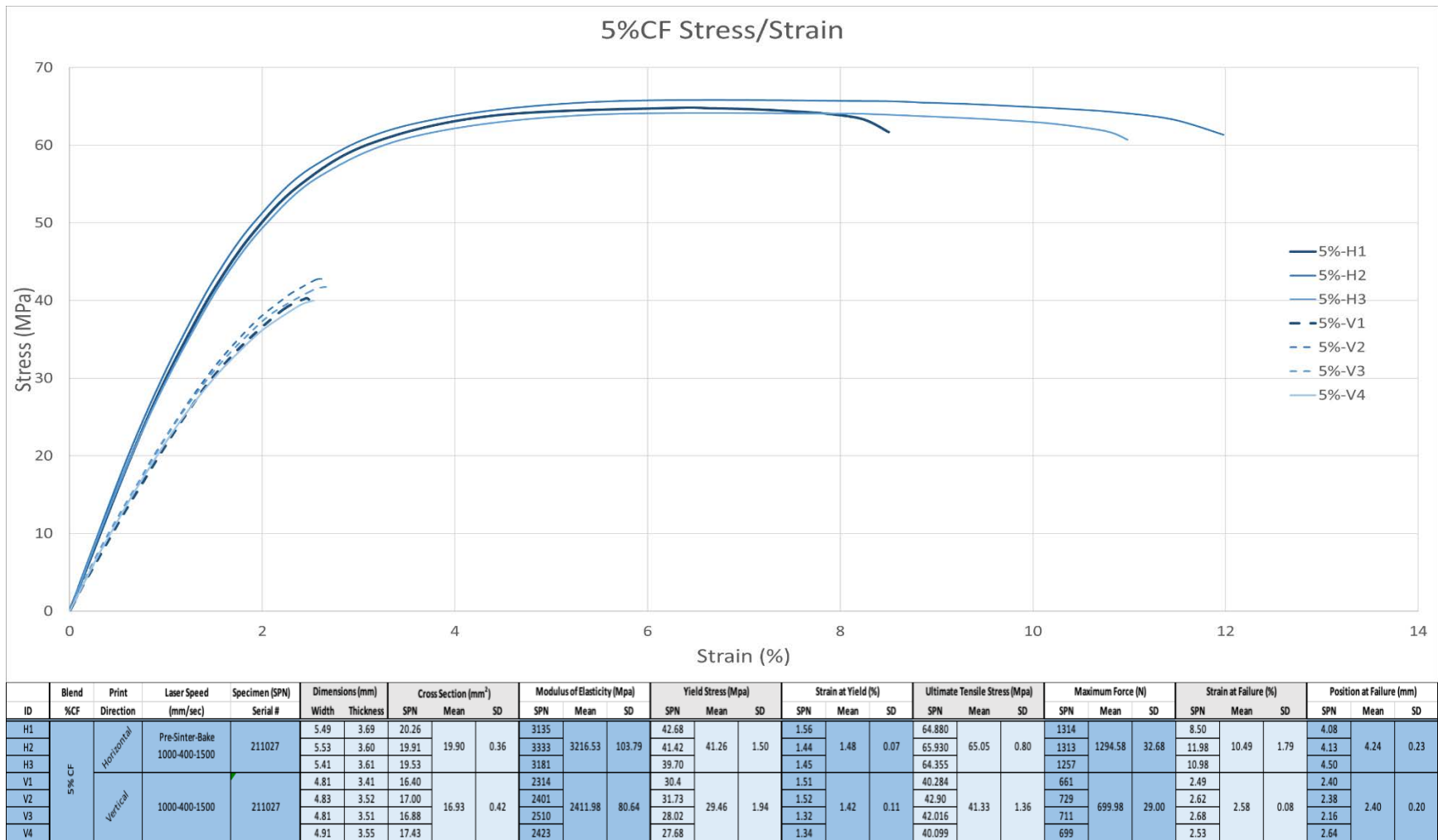
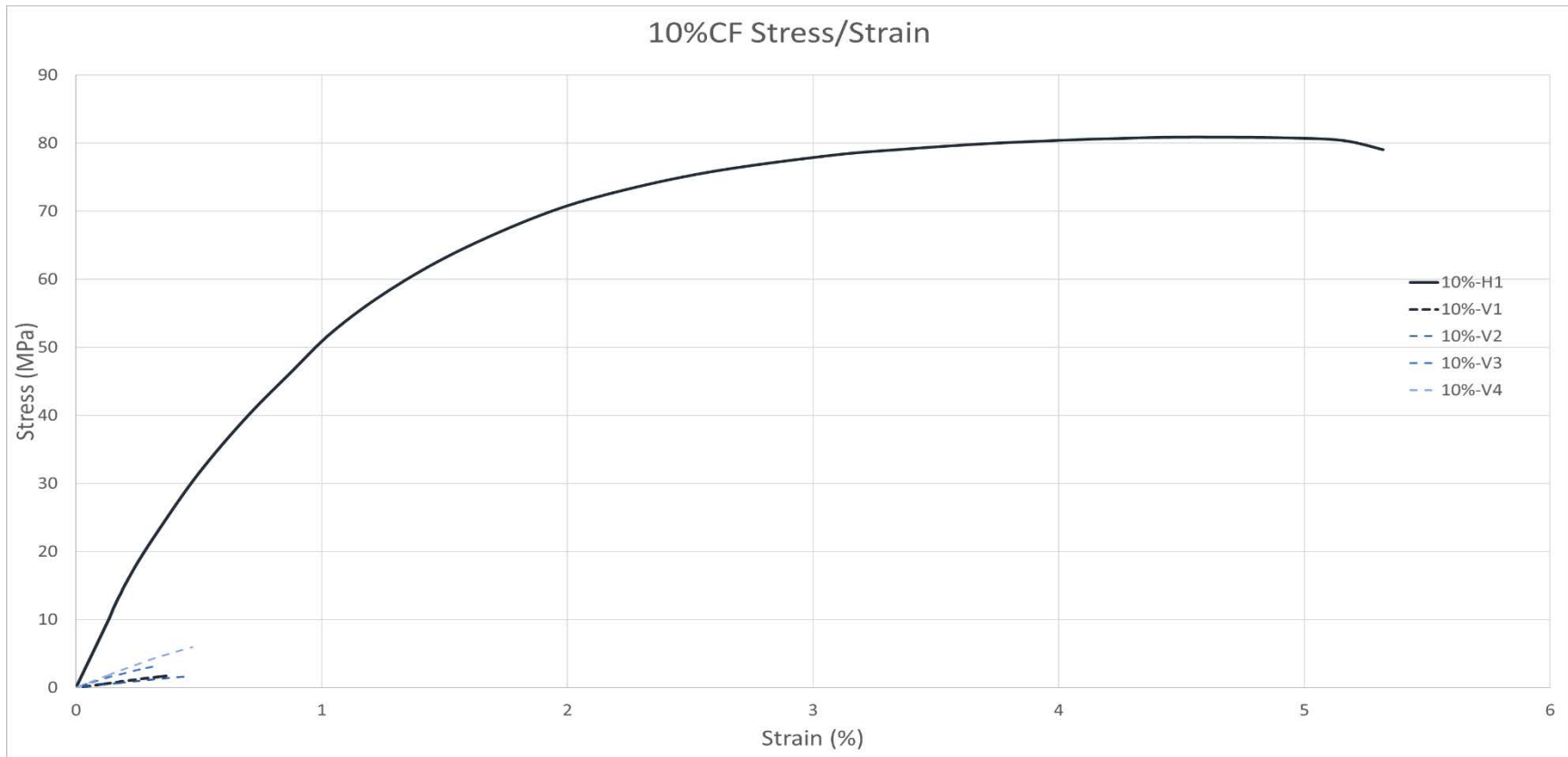


Figure 5.14: 5% CF Vertical and Horizontal Specimen Dimensional and Tensile Test Data.



ID	Blend %CF	Print Direction	Laser Speed (mm/sec)	Specimen (SPN) Serial #	Dimensions (mm)			Cross Section (mm <sup>2</sup> )			Modulus of Elasticity (Mpa)			Yield Stress (Mpa)			Strain at Yield (%)			Ultimate Tensile Stress (Mpa)			Maximum Force (N)			Strain at Failure (%)			Position at Failure (mm)		
					Width	Thickness	SPN	Mean	SD	SPN	Mean	SD	SPN	Mean	SD	SPN	Mean	SD	SPN	Mean	SD	SPN	Mean	SD	SPN	Mean	SD	SPN	Mean	SD	
H1	10.0%	Horizontal	Pre-Sinter-Bake 2000-500/ 400-3000	20220115	5.23	3.71	19.38	19.69	0.33	7589	7589.10	-	42.09	42.09	-	0.75	0.75	-	80.905	80.46	1.25	1570	1584.24	14.52	5.23	5.23	-	4.85	4.74	0.15	
H2					5.43	3.69	20.04			*			*			79			1584			*			4.79						
H3					5.35	3.67	19.63			*			*			81			1599			*			4.57						
V1					4.71	3.30	15.54			-			-			480			NA			NA			NA			1.747			27.14903
V2	Vertical	100-400-1500	20211129	7.71	3.39	26.10	26.07	0.28	399	853.87	483.70	NA	NA	NA	NA	NA	NA	3.271	3.35	2.33	44.80258	84.69	64.90	0.47	0.44	0.10	0.601225				
V3				7.71	3.42	26.33			1145			NA			3.271			94.75411			0.34			0.826671							
V4				7.70	3.35	25.78			1391			NA			6.674			172.0553			0.57			1.334599							

\*Selected all 10%CF vertical specimens that strained >0.30% (all others failed <0.30% strain)    \*\*5mmP specimen used for all 0%CF vertical specimens and V2-V4 10% vertical specimens    - Single data point (i.e., no standard deviation)

Figure 5.15: 10% CF Vertical and Horizontal Specimen Dimensional and Tensile Test Data.

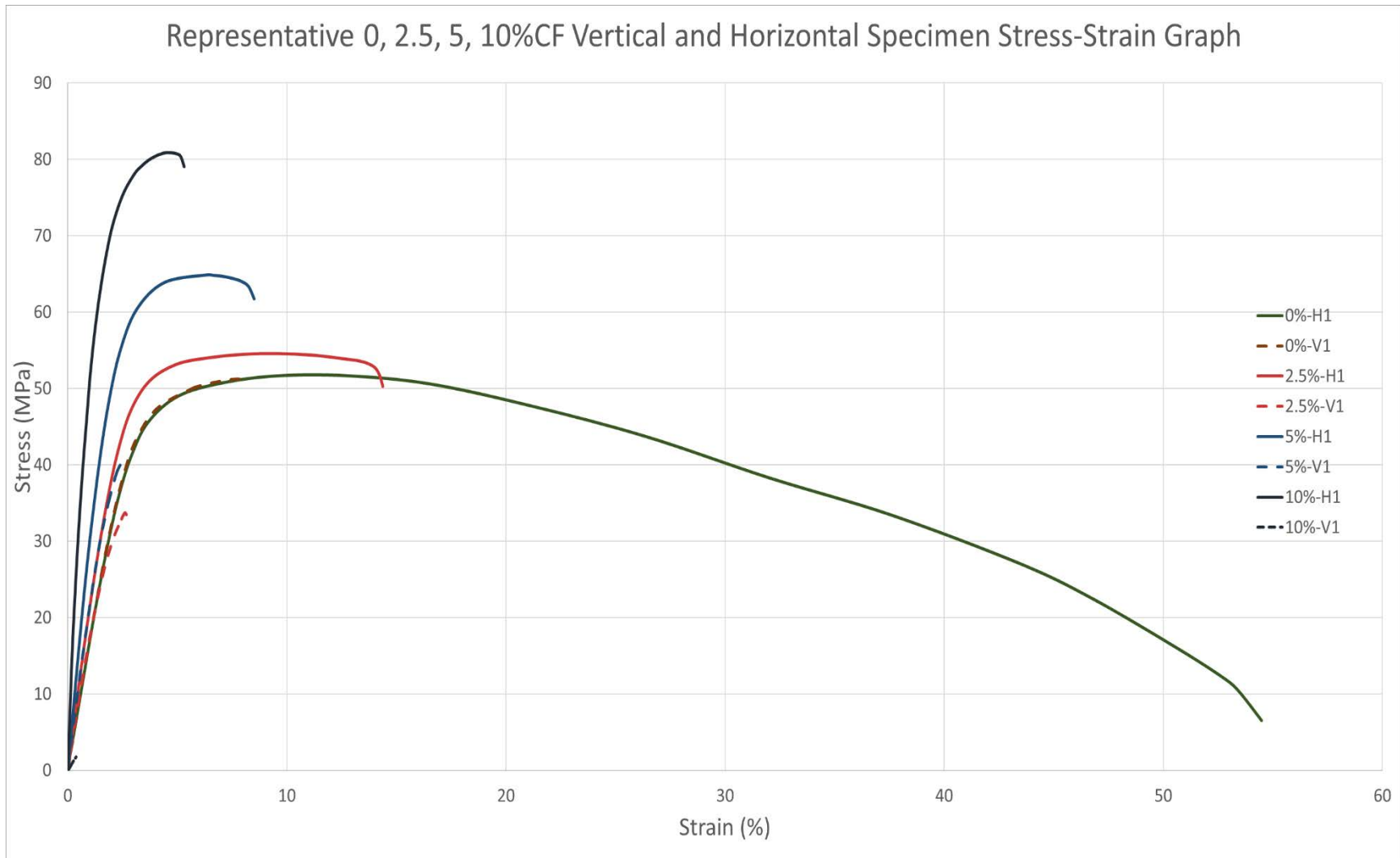


Figure 5.16: Representative 0, 2.5, 5, 10%CF Vertical and Horizontal Specimen Stress-Strain Graph



Figure 5.17: Fracture Surface of Neat PA12 (0% vol CF) Horizontally Printed 3mmP Tensile Specimen



Figure 5.18: Fracture Surface of PA12 + 5% vol Carbon Fiber Horizontally Printed 3mmP Tensile Specimen



Figure 5.19: Fracture Surface of PA12 + 10% vol Carbon Fiber Horizontally Printed 3mmP Tensile Specimen

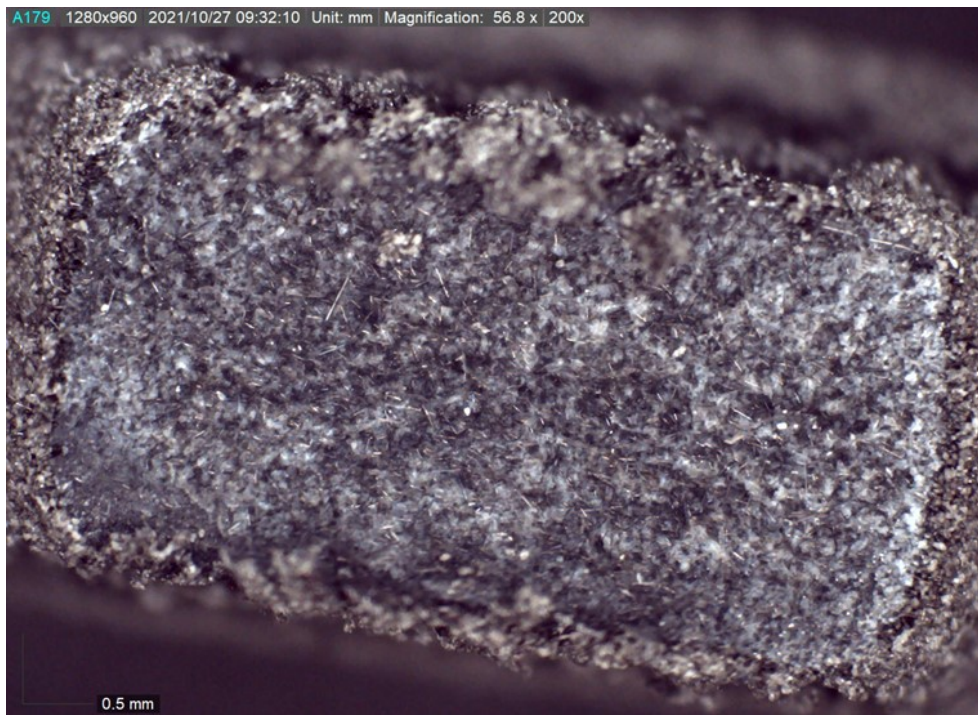


Figure 5.20: Fracture Surface of PA12 + 10% vol Carbon Fiber Vertically Printed 3mmP Tensile Specimen

## **DISCUSSION**

Characterization results of PA12 mechanically blended with CF at 0, 2.5, 5, and 10% ratios by volume demonstrated the ability to customize and tune material properties in SLS through powder blending. Tensile data showed increasing density, modulus of elasticity, and UTS with an increase in CF for horizontally printed specimens. Possibly the most important aspect of this trend is it indicates matrix/fiber bonding was strong enough to influence overall printed part material properties. However, the most obvious result of this aim was the drastic degradation of material properties in vertically printed specimens with the addition of CF. The vertically printed specimens revealed a drastic decrease in layer-to-layer adhesion and consistency with an increase in CF. In contrast to the tensile results, density tests were similar between vertical and horizontal specimens. Differences and similarities between vertical and horizontal prints are discussed in more detail in the following sections.

### **Horizontally Printed Specimen Density, Porosity, and Blend Homogeneity**

Density showed an expected increase with the increase in carbon fiber since sintered PA12 density is  $\sim 0.92\text{-}1.03\text{ g/cm}^3$  (matweb and materialise data sheet, Appendix E) and CF =  $1.8\text{ g/cm}^3$  (Carbisio data sheet, Appendix D). However, it is important to note that the density of sintered PA12 can vary by  $>10\%$  based on sintering energy density. The sintering energy density for these tests was at the upper end of the sintering window to maximize material tensile properties and layer-to-layer adhesion (see Aim 2 discussion). Also, though cross-section and fractographic contrast thresholding quantitative porosity analysis was inconclusive based on limited material contrast, qualitatively there appear to be near zero porosity. Based on these factors, two different calculations were performed to estimate a “theoretical” density (Table 5.2).

In both cases it is assumed the measured density ratio of the blend is the actual blend ratio (perfectly homogeneous blend at measured ratio):

1. Neat PA12 measured density from buoyancy test was assumed to be the actual density of the sintered PA12. This assumes 100% dense (zero porosity) and zero material degradation in the sintering process. This calculation leads to the calculated density being 1.23% below the measured density for 5%, and 0.16% above the measured density for 10%. Around 1% difference for both indicates overall very low porosity and expected ratios of CF for the blends. However, it does show that for 10% there is either slightly less CF than 10% and/or up to 0.16% porosity. This assumes identical PA12 densities between the neat material and the 10% CF blend (identical material degradation). A negative 1.23% density indicates up to a 1.6% difference in actual CF content to measured content (6.6% CF content = zero difference from measured density to calculated density). This could also indicate non-uniform material degradation or crystallinity between the neat PA12 and 5%, which would result in a slight density change of the sintered PA12 matrix between the two blends. Because the calculated 10% blend PA12 matrix density was very close to the calculated sintered neat PA12, and it is most likely the change in density was in the 5% matrix. However, most probable is that it is a combination of all factors involved. Because this method results in an increase in density for one of the blends, calculation #2 was also done, below.
2. Most dense measured PA12 was assumed to be the actual density of the sintered PA12. This assumption leads to the conclusion that a deviation of measured density from calculated density was primarily due to an increase in porosity. This led to the

5% measured density being used to calculate a density of  $1.038 \text{ g/cm}^3$  for the sintered PA12 matrix material. This results in the calculated density being above the measured for both the 0% and 10% CF blends (1.33% above for 0% CF and 1.27% for 10% CF). Overall, this shows similar results to the first calculation method with porosity around 1% or less and near homogenous blend of CF at the measured ratio. Since there is no CF in the neat specimen the change in density would have to be from voids, material degradation, changes in crystallinity, and/or measurement errors. The most likely cause is voids. For the 10% CF blend, an incorrect ratio of CF is added to the list of possible causes. In this case, the mostly likely cause is a combination of both the presence of voids and a slightly lower than expected percentage of CF.

Based on both calculations, the overall density analysis results indicate porosity around 1% or less, possible 2.6% error in the 5% blend ratio, and/or minor differences in material degradation between the samples. Further testing, such as burn-off testing, would be required to further narrow down the possible causes.

Though density testing provides insight to porosity and blend ratio, further testing should be done to characterize these properties. Because the PA12 matrix material had to be grey in color to accommodate sintering with the prototypes 455nm wavelength, there was very little contrast between the PA12, CF, and any pores. There was not enough contrast to use contrast thresholding techniques to quantify percent PA12, CF, and voids. Future study with different lasers should use materials that maximize contrast between different materials. However, there was also considerable mechanical damage to the material during cross-sectioning, which caused both CF and voids to be obscured during cross sectioning. Different matrix material will also

mechanically deform differently during cross-sectioning, and that may help reflect actual material properties in a cross-sectioned specimen.

Table 5.2: PA12/CF Blend Buoyancy Density Results Compared to Calculated Theoretical Values

Blend	Laser Speed	Specimen (SPN)		Measured Density (g/cm <sup>3</sup> )			Theoretical		Theoretical	
							(PA12 Density=1.024 g/cm <sup>3</sup> ) (CF Density=1.8 g/cm <sup>3</sup> )		(PA12 Density=1.038 g/cm <sup>3</sup> ) (CF Density=1.8 g/cm <sup>3</sup> )	
%CF	(mm/sec)	Serial #	ID	SPN	Mean	SD	Density (g/cm <sup>3</sup> )	Difference from Measured	Density (g/cm <sup>3</sup> )	Difference from Measured
0% CF (Neat PA12)	2000 (Pre-Heat)	220115	H1	1.0232	1.0239	0.0009	1.0239	0.00%	1.0377	1.33%
	500 (Sinter)		H2	1.0249						
	3000 (Bake)		H3	1.0237						
5% CF	800 (Pre-Heat)	211027	H1	1.0704	1.0758	0.0047	1.0627	-1.23%	1.0758	0.00%
	350 (Sinter)		H2	1.0788						
	800 (Bake)		H3	1.0782						
10% CF	1000 (Pre-Heat)	20220115	H1	1.0997	1.0998	0.0007	1.1015	0.16%	1.1139	1.27%
	400 (Sinter)		H2	1.0991						
	1500 (Bake)		H3	1.1005						

### Vertical Printed Specimen Tensile Test

Vertically printed specimens had greatly reduced mechanical tensile performance with an increase of CF when compared to horizontally printed specimens. Neat PA12 vertical specimens were the only specimens to have similar modulus of elasticity and UTS as horizontal printed specimens but did have over 10 times the strain at failure for horizontal specimens as compared to vertical specimens. This shows the ductility between rasters is generally much greater than between layers even though other properties are similar (Figures 5.16 thru 5.18). This becomes critical if designing parts for energy absorption which will be explored further in Aim 4 with M2 parts. Vertical specimens with CF always had a lower modulus of elasticity when compared to horizontal specimens. This decrease of stiffness is likely due to the strain relief between closely positioned vertical fibers based on zero bonding between CFs that were in direct contact coupled

with microvoids in these areas. The greatly decreased UTS with an increase in CF can be directly related to a decrease in layer-to-layer adhesion with an increase in CF. This is likely due to the following factors:

1. Increase in layer application inconsistency with an increase in CF.
2. Increase in number of CFs directly in contact with each other in the vertical direction (Compare Figures 5.19 and 5.20). CF in direct contact will have no bonding between the fibers.
3. Very few CFs crossing layer to layer (Figure 5.20) based on the rake and spreading mechanisms. In contrast, fibers almost always cross hatches because based on being oriented along the spreading direction.
4. Extended print times for vertical prints leading to powder degradation and powder clumping.

These findings certainly point to the limitations of loading specimens along the build direction but also point toward the following future studies to better understand and mitigate these limitations:

1. Test other spreading techniques such as a roller and triple pass spreading.
2. Test a high-powered laser to increase lasing speed (decrease overall print time) and increase the melt pool surrounding the CF to increase the melt pool and mobility of the polymer chains at the CF/PA12 interface.
3. Test other matrix materials and characterize the effects and dependencies different materials have on layer-to-layer bonding.

4. Further study on the specific fracture mechanism to determine if different CF geometry and/or PA12 geometry will increase layer-to-layer bonding while keeping the benefits of the CF across hatches.
5. Investigate using all or some encapsulated fibers. Encapsulated fibers will likely improve spreading but limit the maximum number of fibers that can be used and complicate customizing blend ratios.

In summary, vertically printed specimens were not robust enough to test gradients manufactured by the M2 SLS prototype because the marginal and inconsistent layer-to-layer adhesion would mask most effects of LCC in PBF. Further testing is required to increase layer-to-layer adhesion before the benefits of LCC can be realized in specimens subject to a tensile load perpendicular to the build direction.

### **Horizontal Printed Specimen Tensile Test**

Horizontally printed specimens demonstrated consistent and customizable material properties with the addition of CF (Figure 5.16 and Table 5.3). Tabulated data of the percent increase of E, yield stress, and UTS for each blend above neat PA12 is presented in Table 5.4. Modulus of Elasticity vs percent carbon fiber was graphed (Figure 5.21) with a 2<sup>nd</sup> order polynomial curve fit. The fit showed an R<sup>2</sup> value of near 0.9999 and estimated modulus of elasticity equal to  $[59(\%CF)^2 - 16*(\%CF) + 1843]$  MPa (See equation on Figure 5.21). The curve fits indicate the future possibility of using both numerical and analytical analysis to predict and plan for material properties within 0-10% CF. However, a correlation like this did not exist for UTS and Yield stress (Figure 5.22). So, a broader prediction of material properties would require more data to be collected at more ratios (both between 0-10% CF and >10% CF) of CF.

Poisson's ratio should be included in this data collection in order facilitate finite element models. This information would provide a data repository that would not only tune material properties but also predict performance based on CF ratios.

Based on the data, it is hypothesized that PA12-CF interface cause stress concentrators that form micro cracks. Initially these micro cracks effectively relieve stress at the PA-CF interface, but eventually the micro cracks coalesce and form a route for a crack to propagate through the entire cross-section. This fracture mechanism can be seen in the fractography images (Figures 5.17 thru 5.19) and is also supported by the modeling done by Tang et al. (Tang et al., 2021b). Further SEM research and fiber pullout characterization should be done to verify this hypothesis.

Overall, 2.5% CF had a minimal increase between blend ratios compared to the differences between 0, 5, and 10% CF (Table 5.5). The 5% CF blend also split the difference in material properties between 0% and 10% CF better than 2.5%. Therefore, 0%, 5%, and 10% CF blends were used in Aims 4.

Table 5.3: PA12/CF Blend Ratios Comparison of Tensile Data

ID	Blend	Print	Laser Speed	Specimen	XSection (mm <sup>2</sup> )		E (Mpa)		Yld Stress (Mpa)		Yld Strain (%)		UTS (Mpa)		Max Force (N)		Strain @Fail (%)		Pos at Fail (mm)	
	%CF	Direction	(mm/sec)	Serial #	Mean	SD	Mean	SD	Mean	SD	Mean	SD	Mean	SD	Mean	SD	Mean	SD	Mean	SD
H1	0% CF (Neat PA12)	Horizontal	pre-sinter-bake 2000-500-3000	220115	19.57	0.48	1832	171	36.41	2.04	2.20	0.08	51.24	0.75	1003	11	52.85	2.23	7.16	0.62
H2																				
H3																				
V1		Vertical	1500-800-2000	211103 5mmP**	31.73	0.33	1666	286	33.17	0.69	2.24	0.39	46.07	1.65	1440	84	4.94	2.46	3.73	1.02
V2																				
V3																				
V4																				
H1	2.5% CF	Horizontal	Sinter-Bake 400-1200	211019	18.62	0.45	2203	65	37.04	1.12	1.88	0.10	54.29	0.49	1011	17	13.18	1.06	5.40	0.18
H2																				
H3																				
V1		Vertical	500-2000	211021	17.28	0.03	1809	165	24.69	1.24	1.57	0.10	33.13	1.03	570	20	2.68	0.38	2.28	0.23
V2																				
V3																				
V4																				
H1	5% CF	Horizontal	Pre-Sinter-Bake 1000-400-1500	211027	19.90	0.36	3217	104	41.26	1.50	1.48	0.07	65.05	0.80	1295	33	10.49	1.79	4.24	0.23
H2																				
H3																				
V1		Vertical	1000-400-1500	211027	16.93	0.42	2412	81	29.46	1.94	1.42	0.11	41.33	1.36	700	29	2.58	0.08	2.40	0.20
V2																				
V3																				
V4																				
H1	10.0%	Horizontal	Pre-Sinter-Bake 2000-500/ 400-3000	20220115	19.69	0.33	7589	-	42.09	-	0.75	-	80.46	1.25	1584	15	5.23	-	4.74	0.15
H2																				
H3																				
V1*		Vertical	100-400-1500	20211129	15.54	-	854	490	NA	NA	NA	NA	3.35	2.33	85	65	0.44	0.10	0.81	0.38
V2*																				
V3*																				
V4*																				
*Selected all 10%CF vertical specimens that strained >0.30% (all others failed <0.30% strain)				**5mmP specimen used for all 0%CF vertical specimens and V2-V4 10% vertical specimens				- Single data point (i.e., no standard deviation)												

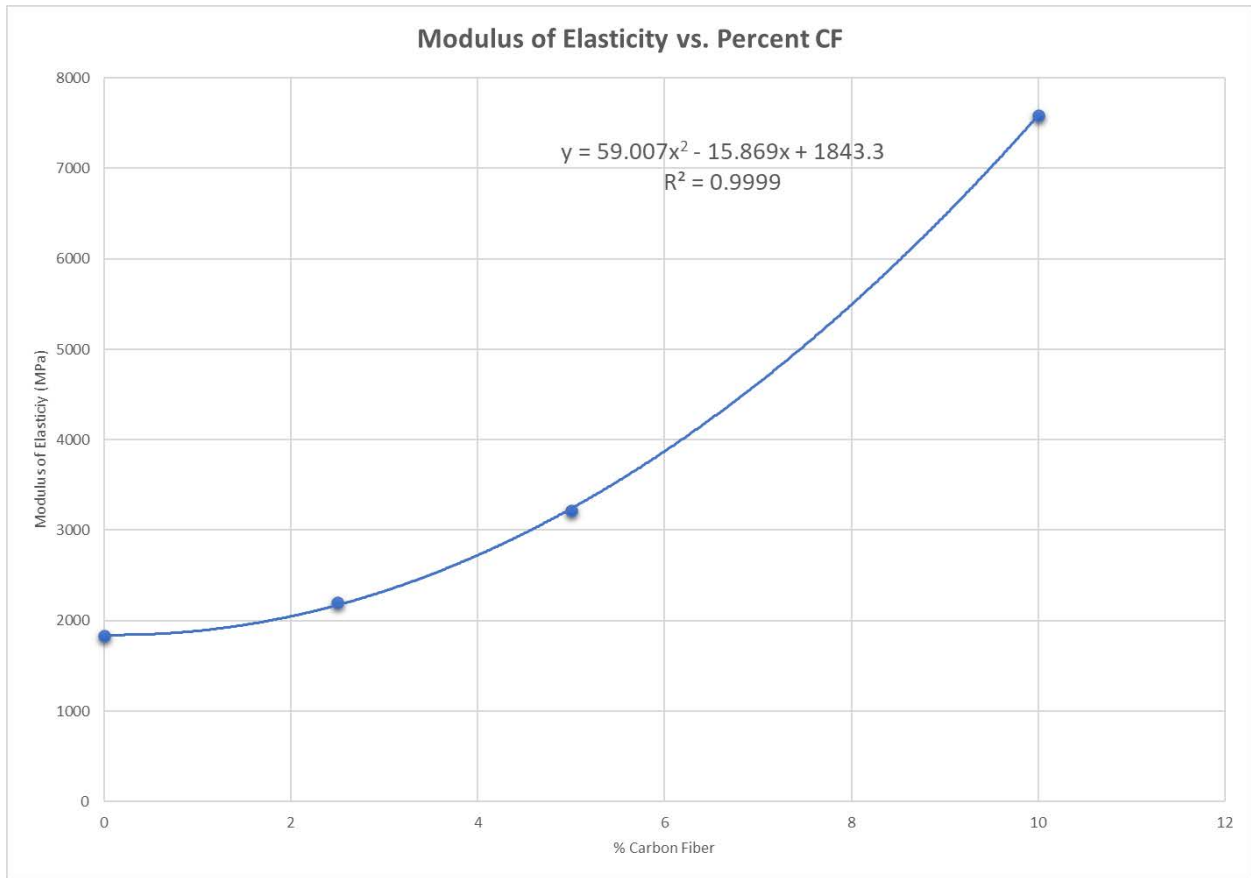


Figure 5.21: Modulus of Elasticity vs Percent CF

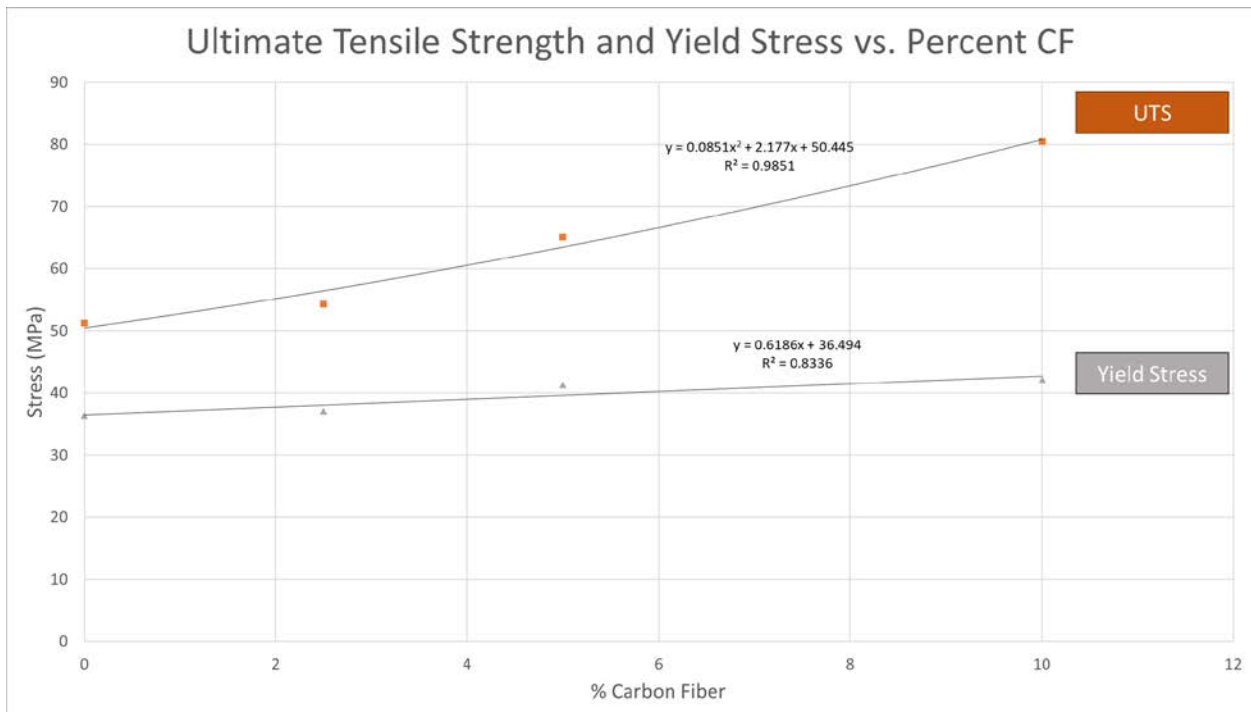


Figure 5.22: Ultimate Tensile Strength (UTS) and Yield Stress vs Percent CF

Table 5.4: PA12/CF Blend Ratios Comparison of Tensile Data

ID	Blend %CF	Modulus of Elasticity (Mpa)			Increase <sup>1</sup> %	Yield Stress (Mpa)			Increase <sup>1</sup> %	Ultimate Tensile Stress (Mpa)			Increase <sup>1</sup> %
		SPN	Mean	SD		SPN	Mean	SD		SPN	Mean	SD	
H1	0% CF (Neat PA12)	1711	1832.00	171.12	0%	34.96	36.41	2.04	0%	52	51.24	0.75	0%
H2		1953				37.85				50			
H3		*				*				52			
H1	2.5% CF	2181	2202.57	64.69	20%	36.76	37.04	1.12	2%	55	54.29	0.49	6%
H2		2275				36.08				54			
H3		2152				38.27				54			
H1	5% CF	3135	3216.53	103.79	76%	42.68	41.26	1.50	13%	65	65.05	0.80	27%
H2		3333				41.42				66			
H3		3181				39.70				64			
H1	10.0%	7589	7589.10	-	314%	42.09	42.09	-	16%	81	80.46	1.25	57%
H2		*				*				79			
H3		*				*				81			
<sup>1</sup> Percent increase from 0% CF specimen				*Strain data not available		- Single data point (i.e., Standard Deviation (SD) does not apply) note: SD is given for Neat PA12 with only 2 data points for comparison purposes but is not applicable to some analysis							

### BROADER IMPLICATIONS

Future work is needed to capitalize on the successes of blending fibers with matrix powders in PBF to tune and customize material properties and to seek out solutions to mitigate the effects fibers have on layer-to-layer adhesion. First, PA12/CF data collected should be added to with additional data points between 0 and 10% CF. The intent is to build repository of data using easily accessible low temperature sintering material to build analytical models verified by experimental data and analytical models used to select blends based on required material performance. (e.g., CF percentage could be selected to match stiffness of bone to form an isoelastic implant core or selected to meet attachment point load requirements on aircraft wings.) This approach will advance the selection of other matrix and/or fibers blends to fill specific performance requirements. Secondly, based on increase of raster-to-raster stiffness and strength with the addition of fibers that cross rasters coupled with the decrease in layer-to-layer adhesion with fibers that generally do not cross layers research should be done to create recoating techniques that promotes fibers crossing layers. Some initial theories on customizing raster orientation have been discussed in Aim 2 using multiple raking directions. However, these

techniques would not promote vertical fiber orientations. Methods involving dropping the fibers onto the build area from above instead of spreading laterally should be testing. This could be done for the fiber only or for the fiber/matrix blend. If it is the fiber only this also could lead to customizing fiber content without pre-mixing the blend. In either case the material could be dropped onto the build area via pipettes and or delivery mechanisms within a recoater. If both a data repository and a method to control multiple fiber orientations are realized the tunability of material properties in PBF and FGMs would be greatly advanced and could fill current material and manufacturing voids.

## **CONCLUSION**

Density results for both print orientations indicated homogeneous PA12/CF mixture through mechanical blending with low porosity for all tested blends. These results suggest a promising future mechanically blending powders, fibers, and particulates for PBF applications. The distinct change in tensile properties (specifically ultimate tensile strength and modulus of elasticity) of horizontally printed specimens between 0%, 2.4%, 5%, 10% vol CF composites demonstrates PA12-CF bond performance capable of customizing material properties by sintering mechanically blended untreated materials. PA12/CF Blends up to 10% appear to have “tunable” material properties for horizontal blends, offering a promising future for mechanical blending and PBF. In contrast, vertically specimens above 5% had very poor tensile properties with extremely long print times in the M2 SLS prototype. The layer-to-layer adhesion deterioration with an increase in CF in these blends indicate that additional research is required prior to realizing the effects of functionalized gradients parallel to the build and load direction. For both vertically and horizontally printed specimens, further research is recommended with

different sintering energy sources and different blends to more thoroughly characterize the tunability of material properties using mechanically blended powders and fibers.

Based on the results from Aim 3, 0%, 5%, and 10% CF ratio Single Edge Notch Tensile (SENT) specimen with the notch parallel to the build direction (e.g., perpendicular or across layers) and the tensile load parallel to the layers (“horizontally printed”, Figure 5.2a) were selected to test M2 characteristics in Aim 4. SENT specimens were selected to produce a more robust characterization of LCC with binary gradients in SLS applications while avoiding results that are dominated by specific material and the M2 SLS prototype characteristics such as laser wavelength, layer application devices, heating methods, and nylon powder.

## **Chapter 6: Aim 4 - Characterization of Local Composition Control with Binary Interfaces and One-Dimensional Gradients**

### **INTRODUCTION**

Aim 4 characterized stress-strain, fracture, and interface bond strength for one-dimensional (1D) binary material interfaces and gradients consisting of polyamide-12 (PA12) and carbon fiber (CF) blends. Modulus of Elasticity from Aim 3 was used to select specific PA12/CF blends for the multi-material (M2) Single Edge Notch Tensile (SENT) specimens. SENT specimens were additively manufactured (AM), commonly known as “printed”, utilizing the local composition control (LCC) capability of the multi-material (M2) Selective Laser Sintering (SLS) prototype from Aim 1. Material interfaces and one-dimensional (1D) gradients were printed in the build direction. SENT test results were analyzed to describe the effects of material interfaces and gradients. Stress, strain, energy, crack propagation, and fracture process zone (FPZ) properties were calculated using digital image correlation (DIC). Optical and scanning electron microscopy were used to analyze fracture and material interface characteristics. Results have established an initial data repository for future work including gradient selection to functionalize SLS printed parts with LCC in the build direction.

### **BACKGROUND**

Functionally graded materials (FGM) with large physical property changes at the interfaces are susceptible to stress concentrations and premature failure at these interfaces (Bartlett et al., 2015a). A gradual change in material properties can reduce overall stress and stress concentrations resulting in increased strength and toughness of functionally graded M2 tensile and SENT parts (Y. Li et al., 2020; Mirzaali et al., 2019; Parihar et al., 2018; Saleh et al.,

2020). Fracture characteristics become more difficult to predict with the addition of Discontinuous Fiber Composites (DFC) (El-Sagheer et al., 2021; Ko et al., 2019).

A shallow gradient in material properties is especially important when transitioning between materials with relatively large differences in E or Poisson's ratio ( $\nu$ ) (Chowdhuri & Xia, 2013; El-Wazery & El-Desouky, 2015; Erdogan, 1995; Gayen et al., 2019). Lumpe et al. have experimentally characterized this in material jetted AM specimens (Figure 6.1) (Lumpe et al., 2019). Generally a three-dimensional (3D) transition in material properties is superior to 1D gradients in reducing stress concentration due to stress singularities and edge effects at 1D interfaces (Lauke, 2007; Sedmak et al., 2018). These effects can be minimized by implementing a 3D component to the material interface (Green, 2018; Lauke et al., 2003).

Nonetheless, one-dimensional gradients are an effective alternative to 3D interfaces in reducing stress concentrations in M2 parts (Bartlett et al., 2015a). AM can achieve 1D gradients in the build direction through layer-by-layer composition control (Chung, 2008; Chung & Das, 2006; Peng, 2008; Wei et al., 2019). The resolution and slope of the gradient using layer by layer composition control is determined by the layer height and properties of the material for each layer. Maximum resolution is dictated by minimum achievable layer height and change in material properties. Consecutive layers can be applied with the same material to spread out a gradient. Though this technique may benefit final M2 part performance and increase UTS, this will not increase the resolution of the gradient.

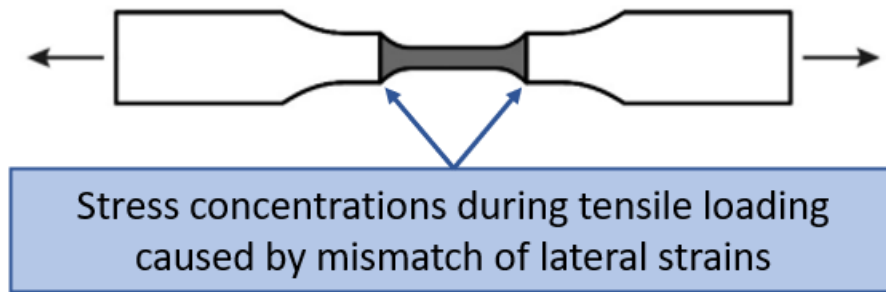


Figure 6.1: Stress concentration at material interface with dissimilar material properties due to differences in lateral strains between materials. (Adapted from Lumpe et al. (Lumpe et al., 2019)).

Tensile and failure characteristics in 1D binary material interfaces have also been studied by Lumpe et al. using material jetting manufactured specimens (Lumpe et al., 2019). A key difference between 1D gradient manufacturing in Aim 1 and Lumpe's work is gradients using the PBF techniques pioneered in Aim 1 required the gradient to be along the build direction (Figure 3.9) whereas in material jetting the gradient can be perpendicular to the build direction (Figure 6.2). Much of the focus was decrease stress concentrations due to changes in lateral strains (often due to mismatch in poisson's ratio between materials). One dimensional binary Material gradients based on E to decrease stress concentrations have also been studied both analytically and experimentally (using material jetting) by Bartlett et al. (Bartlett et al., 2015b) (Figure 6.3). This method can functionalize materials that have drastically different material properties by decreasing stress concentrations found at binary material interfaces with large variations in E. One-dimension LCC is used to integrate gradients along expected tensile loading paths within M2 parts to decrease failures at material interfaces by alleviating stress concentrations while, in many cases, increasing interface bond strength.

One dimensional binary gradients can also be manufactured through layer by layer LCC in PBF by incorporating a powder change at specific layers can create gradual transitions in

material properties. Selecting the powder blend for each layer in a vertically printed M2 tensile specimen (Figure 5.1) to facilitate a gradual transition in E is hypothesized to be an effective method to define local compositions in FGM structure to increase the strength of the material interface. This method of LCC was used to functionalize materials that have drastically different material properties by decreasing stress concentrations found in binary material interfaces. In order to build on the tensile, bending, and torsional research discussed above Aim 4 investigated the effects of crack propagation through binary gradients. To further investigate unique capabilities of PBF when compared to the liquid flow requirements of polyjetting Aim 4 focused on varying CF ratios (CF cannot be brought to a liquid state) in a PA12 matrix.

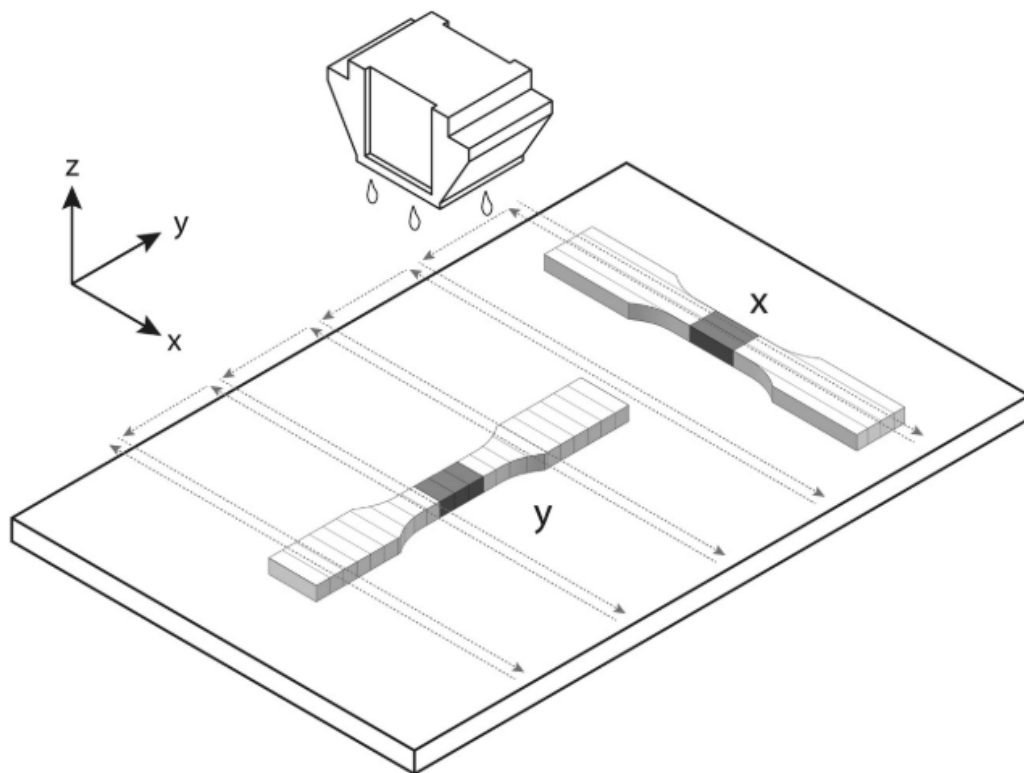


Figure 6.2: Material Jetting additively manufactured layout of binary material interface tensile test specimens with gradients perpendicular to build direction. (Adapted from Lumpe et al. (Lumpe et al., 2019)).

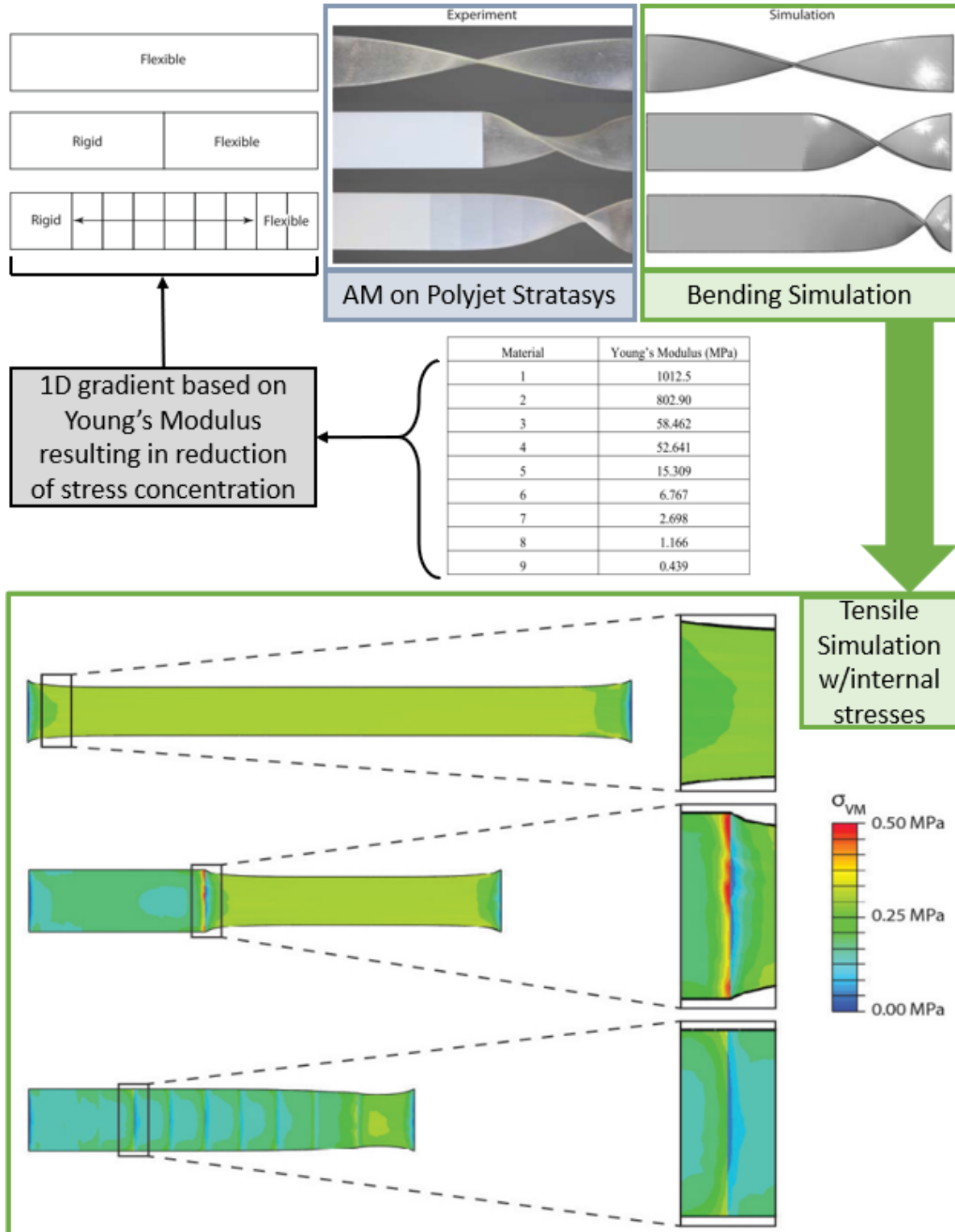


Figure 6.3: Stress concentrations reduction example using 1D gradients. Simulation with experimental results using material jetting done by Bartlett et al. (adapted from Bartlett et al. Figures 2, S2, and Table S1 (Bartlett et al., 2015a, 2015b))

Single Edge Notch Tension (SENT) specimens were selected to characterize 1D gradients and M2 properties in PBF based on the consistency and accuracy of quantitative tensile tests that clearly demonstrate a change in tensile properties for horizontal specimens. Vertical specimens that were loaded perpendicular to the layers were plagued by inconsistencies with that addition of fiber. It appears this was primarily due to powder spreading inconsistencies, extended print times, and near zero transmittance of CF. Collectively these factors decreased layer-to-layer adhesion resulting in inconsistent and reduced tensile properties along the build direction. As compared to Type V specimens, SENT specimens will not draw direct correlations to interface bond strength, but mitigate these effects through the following two mechanisms:

a. Testing Orientation: M2 SENT tests load the specimen perpendicular to the build direction which mitigates the effects of poor and/or inconsistent layer-to-layer adhesion.

b. Build Orientation: M2 SENT specimens have a build direction along the width as opposed to the length which requires approximately 1/3 of the layers and print time as compared to M2 Type V specimens often found in research. The reduced print time decreases nylon degradation during printing resulting in more consistent layer application and adhesion.

## **METHODS**

A total of 52 SENT specimens and 9 tensile specimens were printed to evaluate multi-material (M2) printing with local composition control (LCC) in the M2 Selective Laser System (SLS) prototype build in Aim 1. The 9 tensile specimens were used to verify tensile properties from the exact laser settings and blended material used for the SENT specimen. 24 single material SENT specimens were printed as a baseline for M2 Specimens (a group of 0% CF, a group of 5% CF, and a group of 10% CF, Figure 6.4). 24 bi-material M2 specimens and 8

gradient specimens were printed for M2 and LCC testing. (Figure 6.4). Four Specimens from each specimen type were initially tested to verify both the M2 properties and the test methods (e.g. specimen dimensions, load rate, notch technique, effects of DIC speckle, etc.) and this Test is labeled “Test 1” or “T1” throughout the results and discussion. After a complete analysis of the data from “Test 1”, the second set of specimens were evaluated, and this evaluation is discussed in Appendix F and labeled “Test 2” or “T2”. A comparison of Test 1 and Test 2 is also found in Appendix F. It is important to emphasize all 8 specimens for each set of specimens were printed at the same time. Optical and scanning electron microscopy, porosity, material interface, and fracture analysis as described in Figure 6.4 were analyzed. This testing was intended to demonstrate the value of LCC in PBF by decreasing material interface failures and increasing UTS and consistency of FGM parts, particularly with specimens consisting of 10% CF.

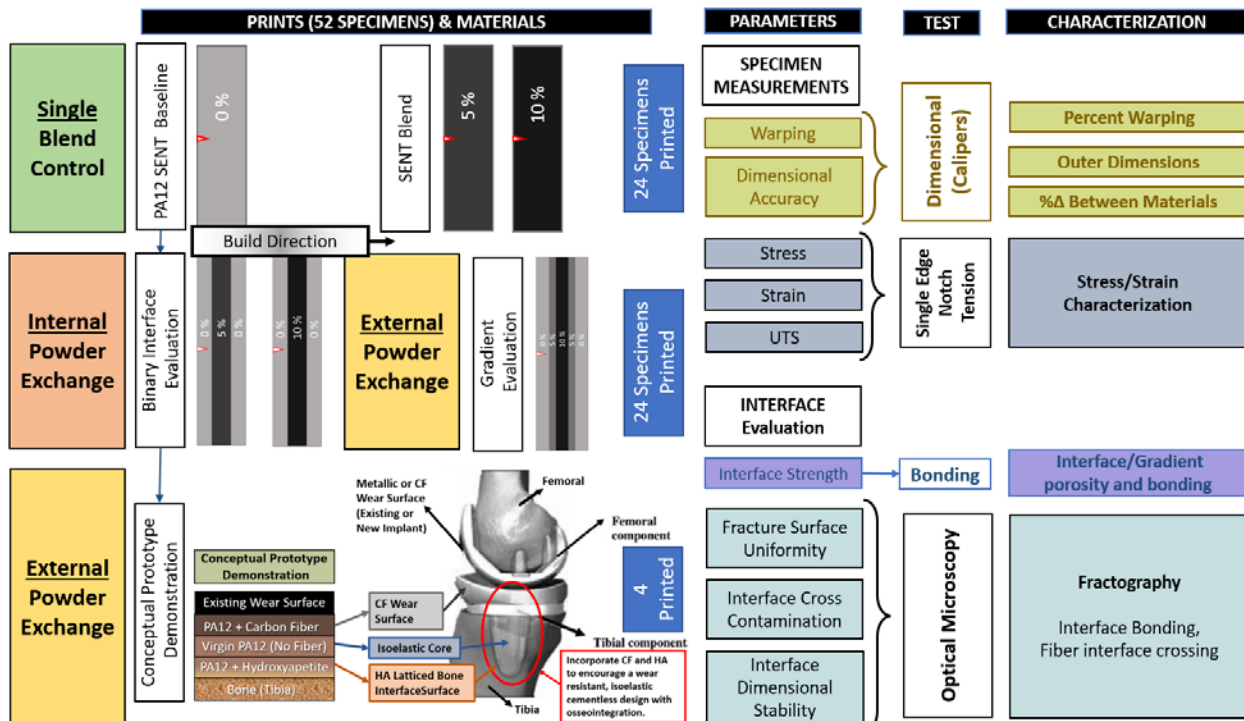


Figure 6.4: Aim 4 SENT and Conceptual Prototype Print Scheme.

A single implant prototype demonstration was printed as described in Figure 6.4. with compositions informed by Aim 2. The goal of the conceptual prototype was to demonstrate the feasibility of LCC in PBF to functionalize future implants with fully dense CF wear surfaces, latticed HA bone interfaces, and patient specific core for isoelastic designs.

### **SENT Specimen Evaluation**

SENT Specimens were designed and printed in accordance with the specifications in Figure 6.5. Prints were “stacked” to facilitate printing two sets of M2 SENT specimens in a single print cycle with the top and bottom (first and last) parts of the print containing horizontal tensile specimens (Figure 6.6) so that tensile properties of each print could be tested. These horizontal specimens also allowed print parameters to be adjusted prior to starting the SENT printing. SENT specimens starting with 0%CF were printed with a CF anchor (Figure 6.7) which was machined off prior after warping measurements were taken but prior to any testing testing. Following machining hardness testing was done in the grip section of the SENT specimen. Hardness testing was done on both the sintered surface (“surface” hardness) and along the machined width (“cross section” hardness). Notching followed the hardness testing and was done with a custom jig (Figure 6.8) and each specimen was checked prior to testing to ensure consistency in notching (Figure 6.9). Digital Image Correlation (DIC) analysis was done to determine tensile properties, fracture energy, and fracture process zone (FPZ) characteristics. Tensile rate was 0.8 mm/min (2% of gauge length) and DIC pictures were taken at 20 frames per second for most tests. Warping was also evaluated based on the dimensions and calculations described in 6.10. All warping measurements were done with as printed specimens (prior to

machining). These measurements did include the printed M2 anchor if applicable and as such the effects of anchoring were included in the calculations.

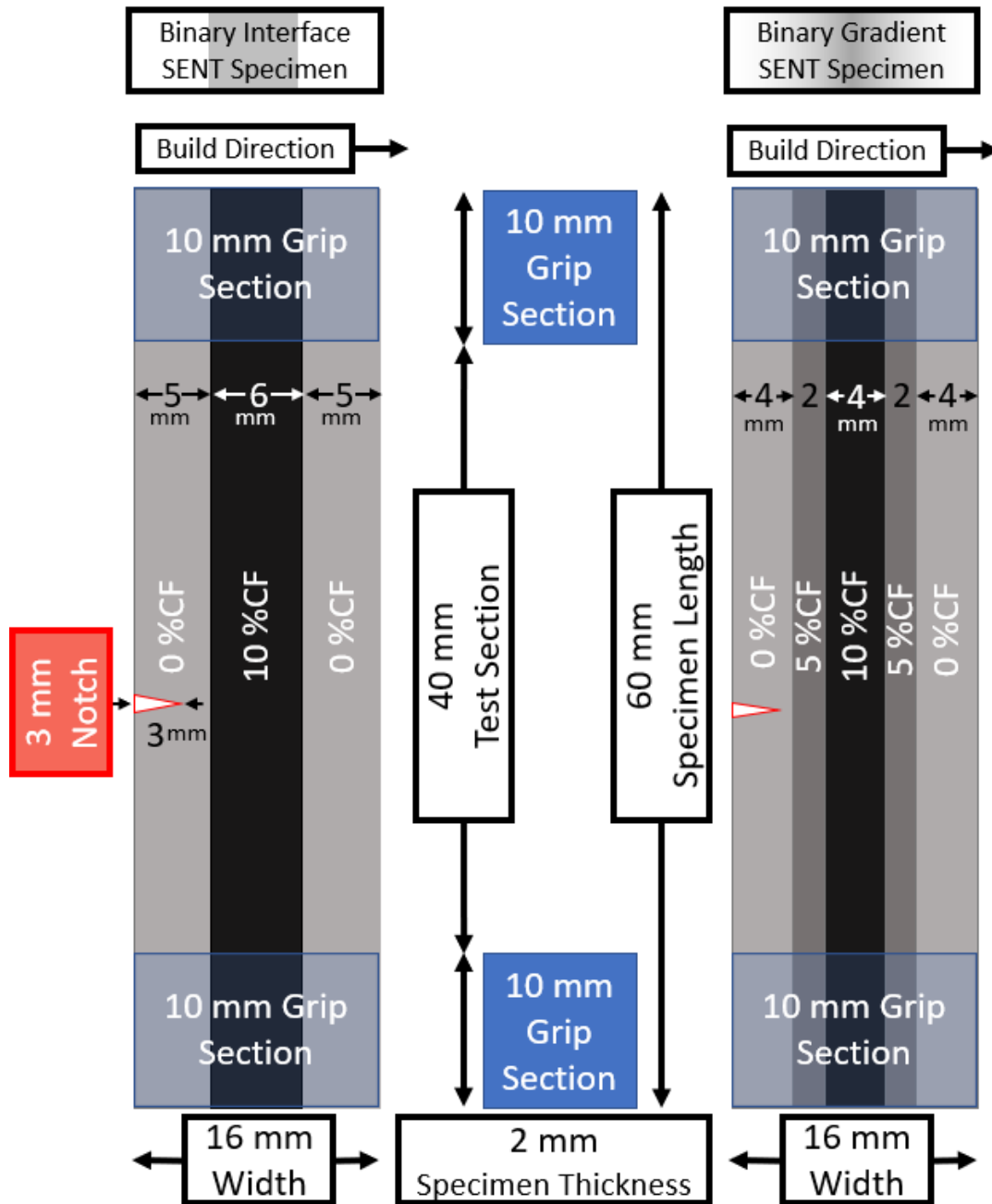


Figure 6.5: Single Edge Notch Tensile Specimen Design and Dimensions

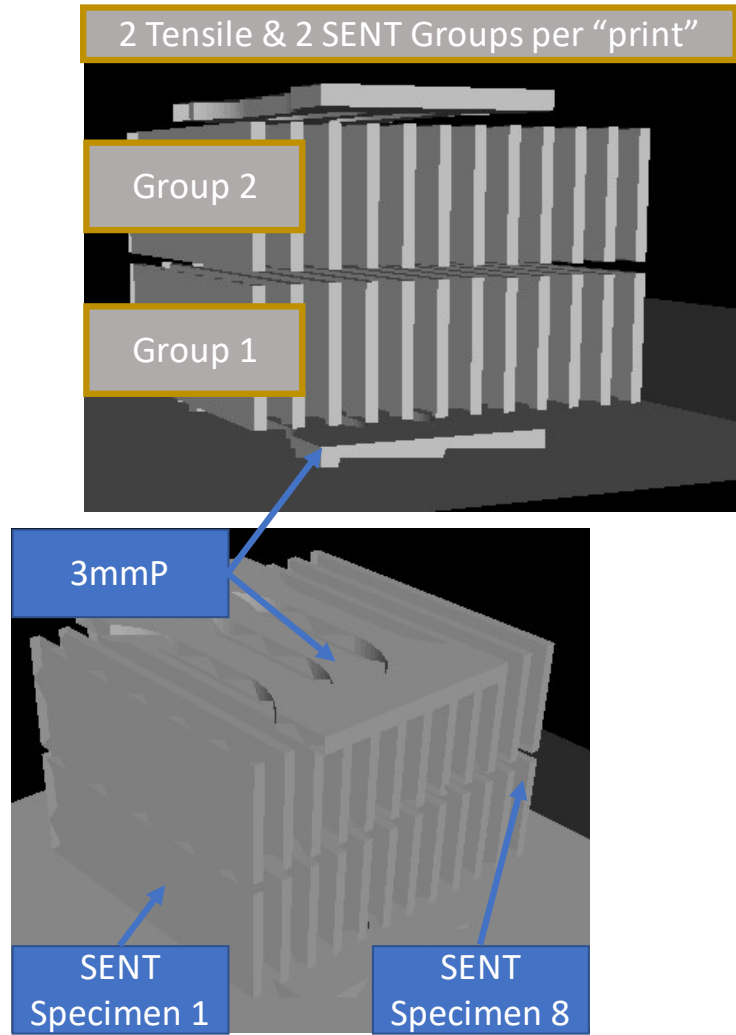


Figure 6.6: Single Edge Notch Tensile Specimen Print Planning (Specimens labeled 1-8 front to back to track specimen characteristics based on location in print area)

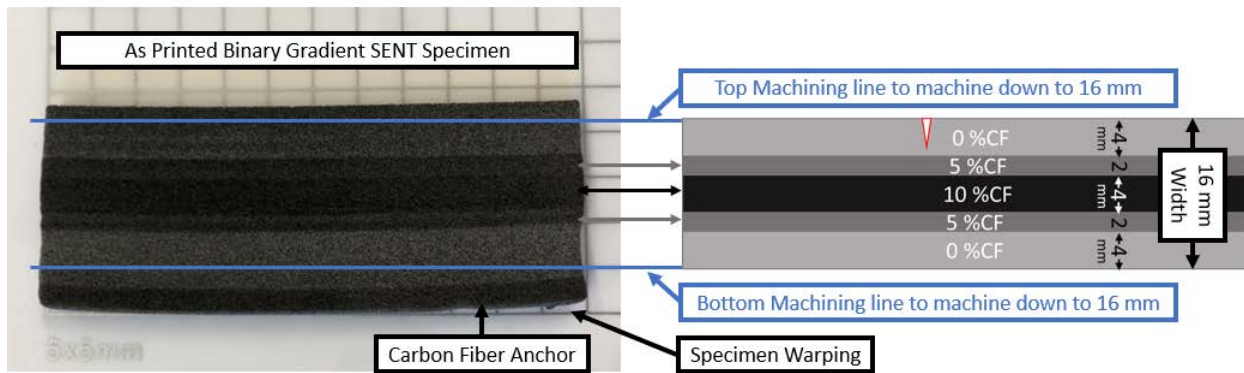


Figure 6.7: SENT Specimen Post Print Machining

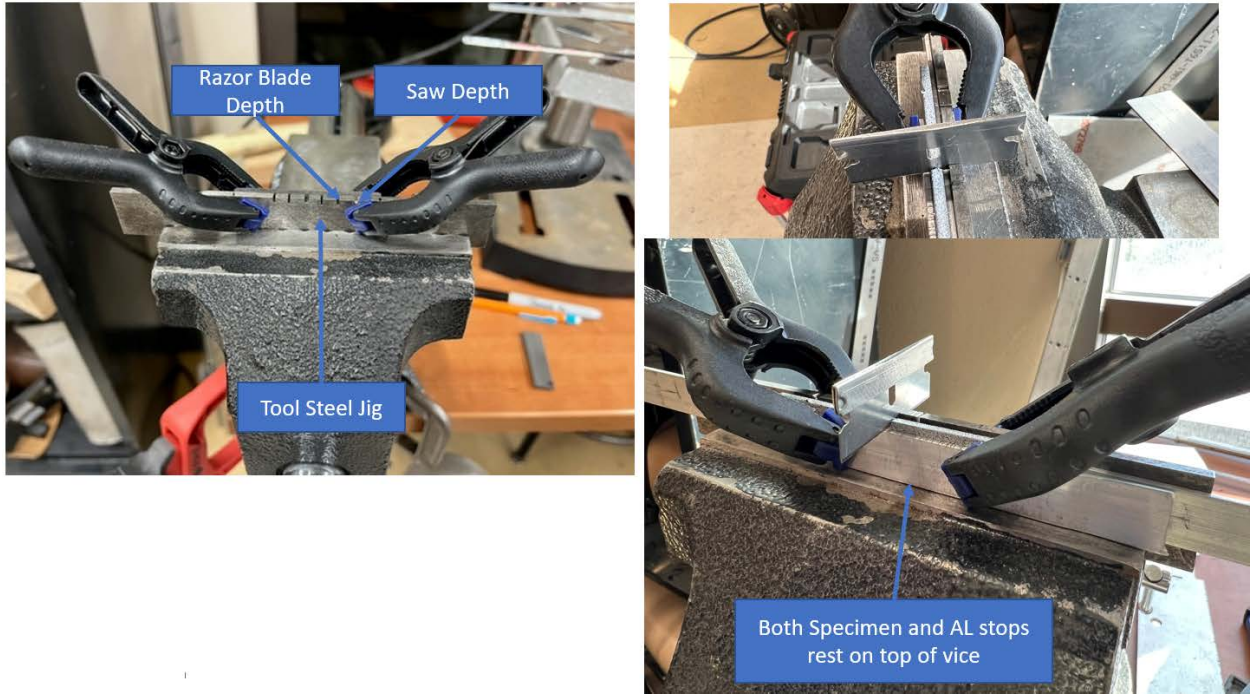


Figure 6.8: SENT Specimen Notching Jig

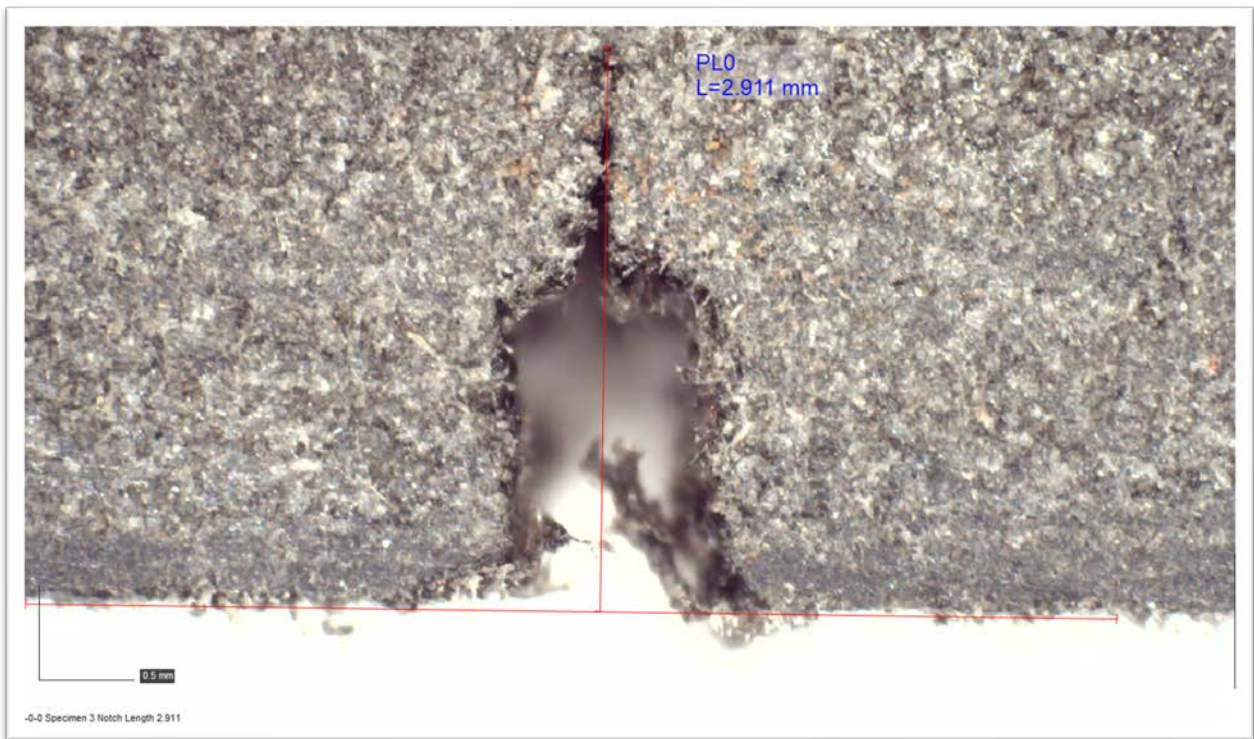


Figure 6.9: SENT Specimen Notch Analysis

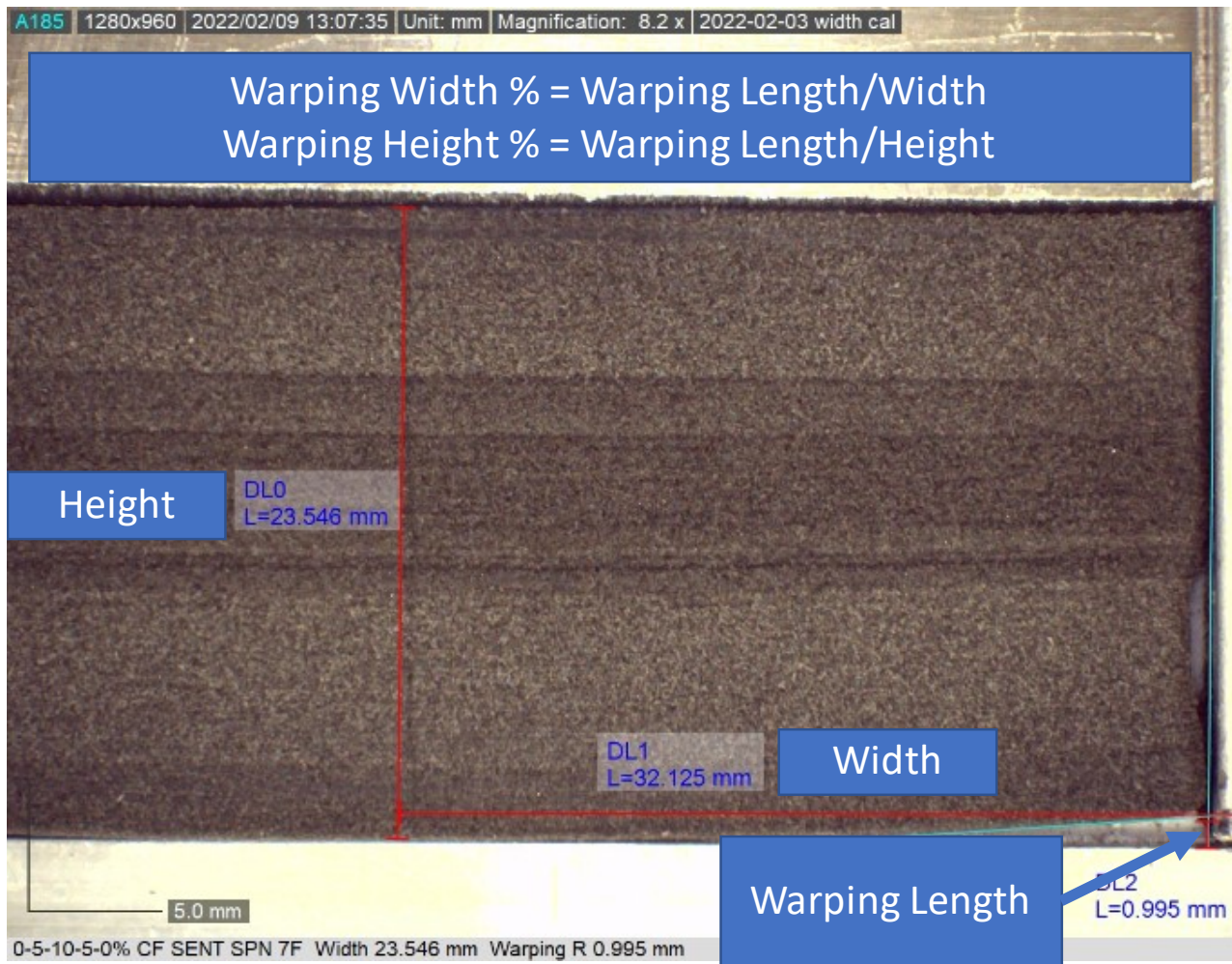


Figure 6.10: SENT Specimen Warping Analysis

### Multi-Material Prototype Demonstration

A conceptual prototype demonstration for an implant design (Figure 6.10) was printed with the top surface incorporating CF to simulate a wear resistant surface, the middle section incorporating purely PA12 to simulate patient specific isoelastic feasibility, and the bottom surface incorporating HA to simulate osseointegration capability. Overall goal was to demonstrate the value and feasibility of LCC implants using polymer PBF for future joint implants.

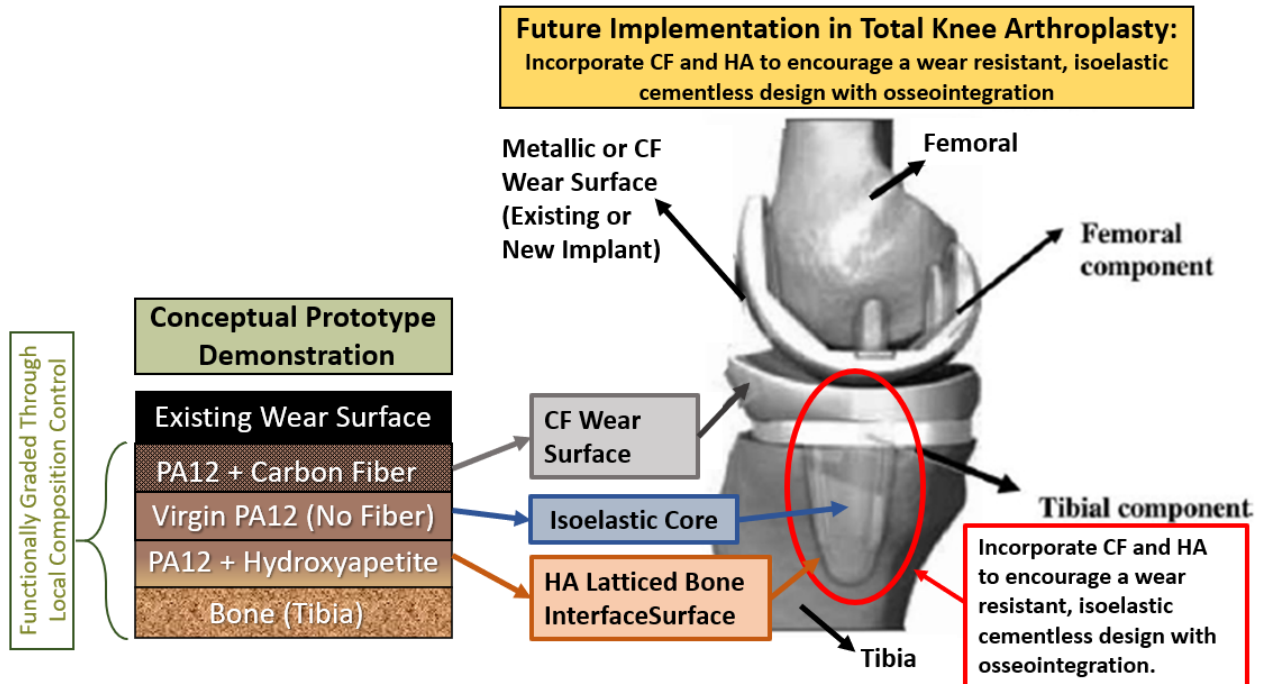


Figure 6.11: One-dimensional LCC joint implant conceptual prototype design

## RESULTS

Warping data was the first data collected post print. Quantitative warping data is found in Table 6.1 below. For the single material specimens there was a decrease in warping with an increase in CF content even with the 0% CF specimens having a 2 mm (20 layer) 10% CF anchor. Among the M2 specimens, the 10-0-10% CF specimens had the least amount of warping.

After the warping measurements were collected the specimens were machined and hardness data was the second set of data collected hardness data was collected in the grip length. Cross section hardness was consistently slightly higher than surface hardness but both cross section and surface hardness had similarly low variance between measurement locations (Table 6.2). There was also a consistent increase in hardness with an increase in CF (Table 6.2).

After machining and hardness data collection the specimens were notched and speckled to collect stress, strain, and fracture data. Notch analysis was done for each specimen (as depicted in Figure 6.9) and all notches were within  $\pm 0.1$  mm of the intended notch length of

3.0mm. Most of the notches were within  $\pm 0.03$  mm of the intended notch depth. Energy (U) ( $\text{MJ}/\text{mm}^3$ ) was calculated at Crack initiation (Ci), max force (Fmax), and failure for each specimen (Figure 6.12). Tabulated data of the results is presented in Tables 6.3 and 6.4. Energy data is only given for a single representative specimen for each specimen type. In Tables 6.3 and 6.4 maximum values are highlighted with a blue cell and second highest values are highlighted with a red outlined cell. If two specimens were within 1% both specimen cells are highlighted the same (blue infill or red outline). These highlights show a trend that the gradient specimens normally outperformed all other specimens and specimens containing the 5% CF blend also performed well. 0-5-0% CF specimen T1-5 performed similar to the other 0-5-0% CF in terms of stress but strained about twice as much as the other specimen (Figure 6.15). To clearly show the strain difference, T1-5 data is presented along with the more representative specimen T1-4 for 0-5-0% CF specimens (Figures 6.18e and 6.18f respectively).

DIC calculated strain fields at crack initiation, maximum force, and failure are presented in Figures 6.12a thru 6.12g. These figures highlight crack arrestment at a material change followed by a sudden failure as opposed to the relatively ductile response of the single material specimens (clearly evident in Figure 6.12). Figure 6.13 compares Aim 3 tensile data to Aim 4 SENT tensile data. (Note: cross section area calculations for SENT stress was based on the cross section prior to notching.) Figure 6.14 compares the single material stress-strain curves and Figure 6.15 compares the M2 specimen stress strain curves. Figure 6.16 has a representative curve from each specimen on a single plot and Figure 6.17 has the same plot with the addition of the crack initiation lines. These data (Figures 6.12 thru 6.17) are the plotted data giving the background to the tabulated in Tables 6.3 and 6.4 with amplifying energy data in (6.18a thru 6.18i). FPZ DIC eye mapping is highlighted in Figures 6.25 and 6.26. In these figures “T”

designates the test number and “-x” designates specimen number. (e.g. 0CF T1-2 = 0%CF Test 1, Specimen 2). Figure 6.18a specifically depicts the effect of crack propagation through material interfaces. In the DIC strain field crack dissipation (with a correlated change in stress and strain) can be seen in the form of multiple cracks opening at the 0-10% CF interface.

Post tensile testing the fracture surfaces were imaged and characterized using SEM microscopy. Figures 6.19 thru 6.30 are SEM fractography images focusing on ratio transitions and PA12/CF bonding and interfaces. All fractures began with a ductile portion at the notch to crack initiation sections. This ductile portion varied based on CF content with the more CF ratios having less of a ductile portion. All fractography showed a smooth transition between CF ratios with no perceptible break or imperfection in the PA12 matrix material. Brittle fracture tended to have 3 dimensional aspects with axial fracture propagation. Overall, these images also showed good bonding between the PA12 matrix and carbon fibers.

Joint implant conceptual prototypes were the final prints of this research and is presented in Figure 6.31. The conceptual prototypes were optically imaged and show smooth transitions between material blends with both HA and CF infill. Mechanical testing and fractography were not done on the conceptual prototypes.

Table 6.1 SENT Specimen Warping Results  
 (Percent warping definitions and description found in Figure 6.10)

Blend %CF	Test	ID	Warping Total	
			Mean	SD
0% CF	Height	2	5.26%	0.87%
		4		
		6		
	Width	4	2.95%	1.04%
		5		
5% CF	Height	2	2.32%	1.66%
		4		
		6		
		8		
	Width	2	1.65%	1.20%
		4		
		6		
10% CF	Height	2	1.42%	0.57%
		4		
		6		
		8		
	Width	2	0.91%	0.36%
		4		
		6		
		8		
0-5-0% CF	Height	2	4.16%	1.78%
		3		
	Width	2	1.77%	0.78%
		3		
0-10-0% CF	Height	2	4.75%	1.78%
		5		
		6		
	Width	2	3.09%	1.17%
		5		
10-0-10% CF	Height	2	1.57%	0.61%
		4		
		6		
		8		
	Width	2	0.94%	0.36%
		4		
		6		
		8		
0-5-10-5-0% CF Gradient	Height	3	3.42%	0.98%
		6		
		7		
		8		
	Width	3	2.59%	0.74%
		6		
		7		
		8		

Decreased Warping

Decreased warping with increased CF content

Decreased warping with CF printed first  
 (Same trend when M2 anchor number of layers is increased)

Table 6.2: SENT Specimen Shore D Hardness Results

Blend	Laser	Serial #	ID	Point	Shore D Hardness			Total		
					SPN	Mean	SD	Mean	SD	
0% CF (Neat PA12)	2000 (Pre-Heat) 500 ( Sinter ) 3000 ( Bake )	220115	Surface	H1	P1	74.5	73.07	1.25	73.47	1.31
					P2	72.5				
					P3	72.2				
				H2	P1	73.0	72.50	0.50		
					P2	72.0				
					P3	72.5				
				H3	P1	74.0	74.83	0.76		
					P2	75.5				
					P3	75.0				
			Cross Section	H1	P1	73.5	74.83	1.53	74.67	1.48
					P2	74.5				
					P3	76.5				
				H2	P1	75.0	74.00	1.73		
					P2	75.0				
					P3	72.0				
				H3	P1	75.5	75.17	1.53		
					P2	76.5				
					P3	73.5				
5% CF (Neat PA12)	800 (Pre-Heat) 300 ( Sinter ) 800 ( Bake )	211027	Surface	H1	P1	74.5	74.67	0.76	75.39	1.08
					P2	75.5				
					P3	74.0				
				H2	P1	76.0	75.83	0.76		
					P2	75.0				
					P3	76.5				
				H3	P1	77.0	75.67	1.53		
					P2	76.0				
					P3	74.0				
			Cross Section	H1	P1	77.0	77.67	1.15	77.89	0.86
					P2	79.0				
					P3	77.0				
				H2	P1	77.5	77.67	0.76		
					P2	78.5				
					P3	77.0				
				H3	P1	79.0	78.33	0.76		
					P2	78.5				
					P3	77.5				
10% CF (Neat PA12)	1000 (Pre-Heat) 400 ( Sinter ) 1500 ( Bake )	20220115	Surface	H1	P1	79.5	78.83	0.58	78.67	0.79
					P2	78.5				
					P3	78.5				
				H2	P1	77.5	77.83	0.29		
					P2	78.0				
					P3	78.0				
				H3	P1	80.0	79.33	0.58		
					P2	79.0				
					P3	79.0				
			Cross Section	H1	P1	81.0	81.33	0.29	81.17	0.66
					P2	81.5				
					P3	81.5				
				H2	P1	80.0	81.33	1.15		
					P2	82.0				
					P3	82.0				
				H3	P1	81.0	80.83	0.29		
					P2	80.5				
					P3	81.0				

Table 6.3: Test 1 SENT Analysis Data (Crack Initiation Data for Highlighted Yellow Specimens).

ID	Blend %CF	Dimensions (mm)		Cross Section (mm <sup>2</sup> )			Maximum Force			Maximum Stress (Mpa)			Frame Count	Force (N)	Stress (Mpa)	Energy MJ/mm <sup>3</sup>	Crack Initiation				
		Width	Thickness	SPN	Mean	SD	SPN	Mean	SD	SPN	Mean	SD					Ext <sub>0</sub> 30mm (%)	ε <sub>yy_max</sub> (%)	ε <sub>xx_max</sub> (%)	ε <sub>xy_max</sub> (%)	VM (%)
1	0% CF (Notch PA12)	16.13	2.61	42.10	42.90	1.52	796.62	903.45	72.54	18.92	21.07	1.76	2111	636.28	15.11	0.24	2.78	6.08	6.58	2.05	4.73
3		16.02	2.81	45.02			923.44			20.51											
7		15.96	2.69	42.93			936.74			21.82											
8		15.86	2.62	41.55			956.99			23.03											
1	5% CF	16.07	2.94	47.25	50.98	2.58	1341.64	1173.18	113.06	28.40	23.14	3.51	2841	1095.29	21.05	0.27	2.17	7.73	1.05	3.69	6.26
3		16.06	3.24	52.03			1100.74			21.15											
5		16.15	3.29	53.13			1132.55			21.32											
7		15.99	3.22	51.49			1117.79			21.71											
1	10% CF	16.02	2.53	40.53	41.64	0.91	1111.20	814.05	270.91	27.42	19.58	6.68	2021	621.52	14.83	0.11	1.23	7.15	1.01	2.25	5.50
2		16.06	2.61	41.92			636.28			15.18											
7		16.05	2.58	41.41			538.55			13.01											
8		16.05	2.66	42.69			970.19			22.72											
4	0-5-0% CF	16.00	2.38	38.08	38.94	0.76	1122.52	1196.85	81.78	29.48	30.70	1.36	2401	796.07	20.91	0.27	2.19	4.14	0.63	1.66	3.33
5		15.73	2.47	38.85			1183.57			30.46											
6		16.01	2.43	38.90			*FG			*FG											
8		16.04	2.49	39.94			1284.46			32.16											
1	0-10-0% CF	16.01	2.62	41.95	43.19	1.04	1034.82	1086.20	111.04	24.67	25.13	2.13	1871	616.79	14.70	0.14	1.65	4.83	0.94	1.80	3.46
3		16.07	2.67	42.91			1056.89			24.63											
4		15.98	2.78	44.42			1249.49			28.13											
7		15.93	2.73	43.49			1003.58			23.08											
1	10-0-10% CF	16.11	2.87	46.24	45.56	0.95	1041.27	1082.29	60.58	22.52	23.75	1.12	2121	841.50	18.47	0.15	1.17	4.40	0.92	2.79	3.80
3		16.22	2.85	46.23			1147.17			24.82											
5		16.16	2.82	45.57			1119.51			24.57											
7		16.02	2.76	44.22			1021.20			23.10											
1	0-5-10-5-0% CF Gradient	16.05	2.69	43.17	44.75	1.29	1302.66	1389.04	71.69	30.17	31.03	1.04	3591	1350.38	30.54	0.70	3.68	9.22	2.45	4.33	7.56
2		16.08	2.75	44.22			1388.79			31.41											
4		16.04	2.85	45.71			1478.21			32.34											
5		16.04	2.86	45.87			1386.50			30.22											

Note: blue cells indication max values and red boarded cells indicate second highest value.

\*FG = Failure at grip instead of notch and so maximum force was not included in material property calculations

Table 6.4: Test 1 SENT Data at Maximum Stress and Failure for Highlighted Yellow Specimens

ID	Blend %CF	Maximum Stress									Failure								
		Frame Count	Force (N)	Stress (Mpa)	Energy MJ/mm <sup>3</sup>	Exto <sub>30mm</sub> (%)	ε <sub>yy_max</sub> (%)	ε <sub>xx_max</sub> (%)	ε <sub>xy_max</sub> (%)	VM (%)	Frame Count	Force (N)	Stress (Mpa)	Energy MJ/mm <sup>3</sup>	Exto <sub>30mm</sub> (%)	ε <sub>yy_max</sub> (%)	ε <sub>xx_max</sub> (%)	ε <sub>xy_max</sub> (%)	VM (%)
1	0% CF (Neat PA12)	3061	785.32	18.65	0.68	5.23	11.83	0.84	3.36	8.55	4401	142.88	3.93	1.61	12.36	23.44	0.77	4.02	16.85
3																			
7																			
8																			
1	5% CF	2881	1098.88	21.12	0.30	2.69	8.35	1.09	3.76	6.70	3391	294.92	5.67	0.77	5.32	15.32	0.80	2.51	11.40
3																			
5																			
7																			
1	10% CF	2086	635.71	15.17	0.13	1.36	8.34	1.01	2.49	6.15	2539	149.33	0.23	0.37	8.79	0.30	0.30	1.94	6.68
2																			
7																			
8																			
4	0-5-0% CF	3627	1121.95	29.46	0.90	4.58	13.83	1.59	5.32	10.68	3754	1065.92	27.99	1.04	5.16	14.60	1.13	6.19	11.86
5				30.43									2.35						
6		5020	1182.28	30.43	1.90	9.23	29.06	5.61	14.46	24.42	5300	1106.62	28.48	2.35	10.45	26	5.12	13.96	23.68
8																			
1	0-10-0% CF	3601	1036.25	24.70	0.40	4.70	10.65	4.04	4.31	8.31	3741	990.25	23.61	0.40	5.19	12.15	1.51	3.84	9.88
3																			
4																			
7																			
1	10-0-10% CF	3251	1119.37	24.56	0.67	3.94	9.16	2.72	4.39	7.62	4161	947.26	20.79	1.50	7.46	20.98	1.77	4.26	15.35
3																			
5																			
7																			
1	0-5-10-5-0% CF Gradient	3764	1390.94	31.45	0.83	4.04	10.16	2.51	4.67	8.31	3819	1392.71	30.82	0.86	4.23	12.06	0.52	1.92	9.42
2																			
4																			
5																			

Note: blue cells indication max values and red boarded cells indicate second highest value.

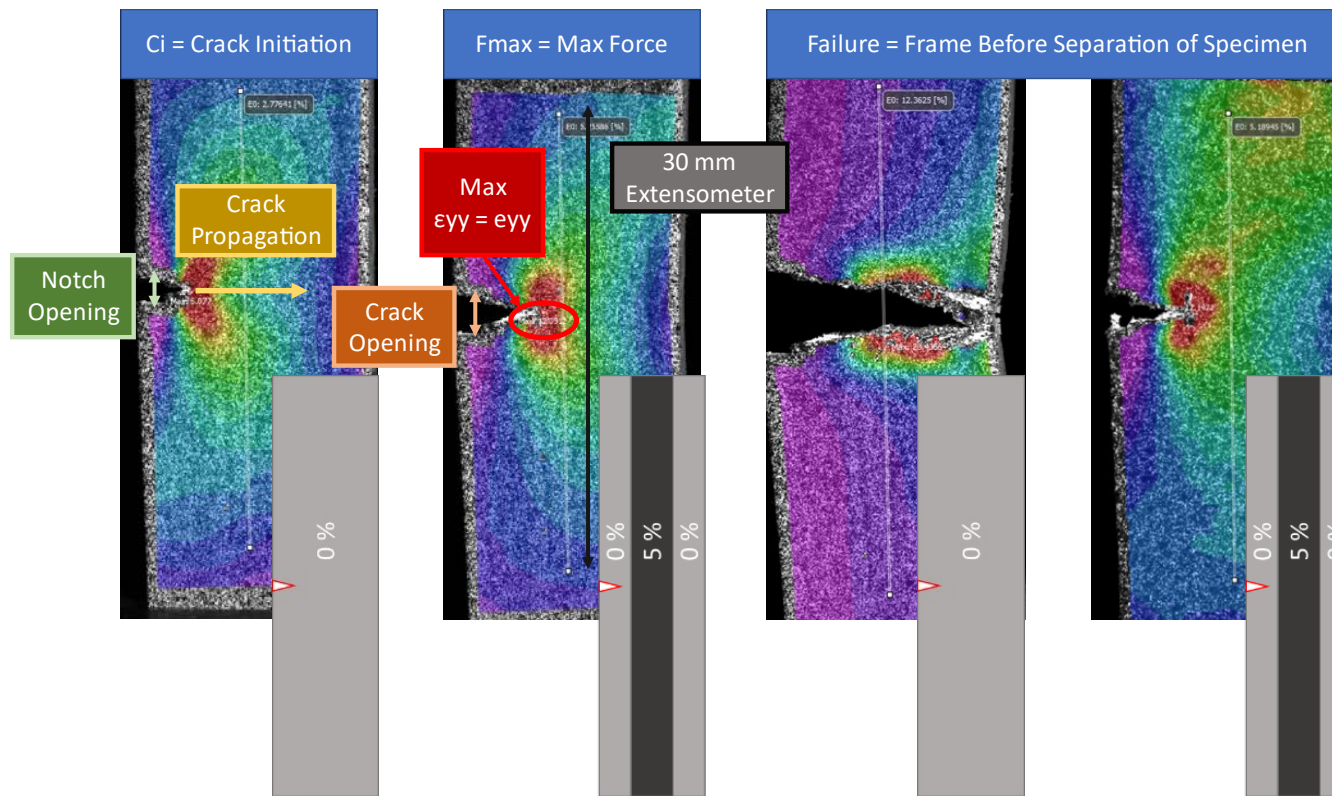


Figure 6.12: Depiction of SENT Test DIC Results Definitions and Terms:

**Crack Initiation Frame (Ci)** = the frame at which the notch transitions to a crack and begins to propagate into the specimen.

**Max Force Frame (Fmax)** = the frame at which maximum force was achieved.

**Failure Frame** = the frame prior to complete separation of the SENT Specimen.

**Energy (MJ/mm<sup>3</sup>)** = The area under the stress / 30mm extensometer strain curve at anyone one of the above frames.

**Strains:** All given in percent (“Exto” = 30mm Extensometer Strain,  $\epsilon_{yy}$  = max strain on specimen as calculated by DIC).

**Stress (MPA):** Current Stress for the current frame based on the original (before notch) cross section of the specimen

**Scaling** = All sets of DIC images are either scaled to each specimen (strain field color is scaled to each specific specimen and not constant across all specimens) or a constant scale for all specimens (scale bar is given in image and applies to all specimen in the image)

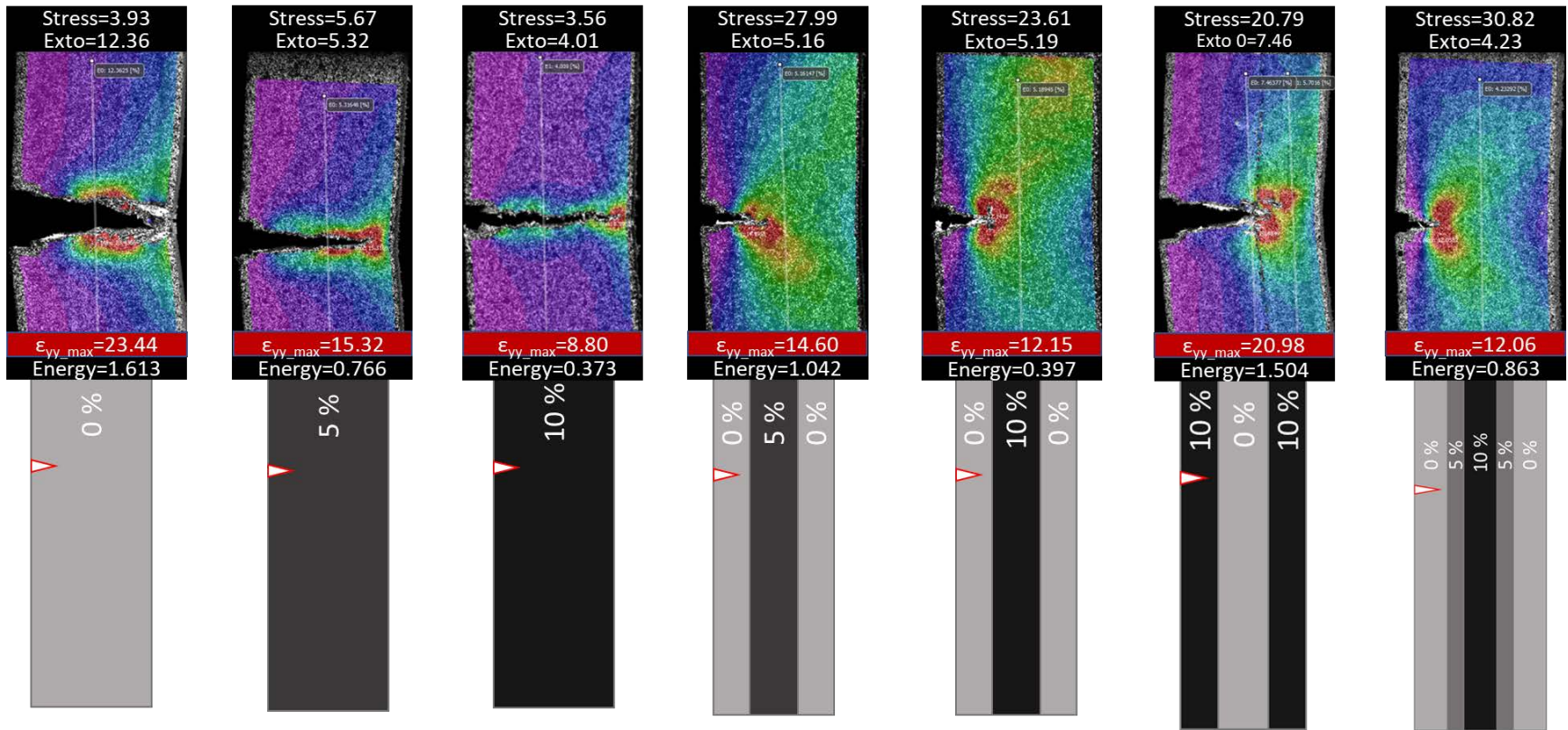


Figure 6.12a: SENT Test DIC Results the Frame Before Specimen Failure scaled to each specimen frame with stress and energy data

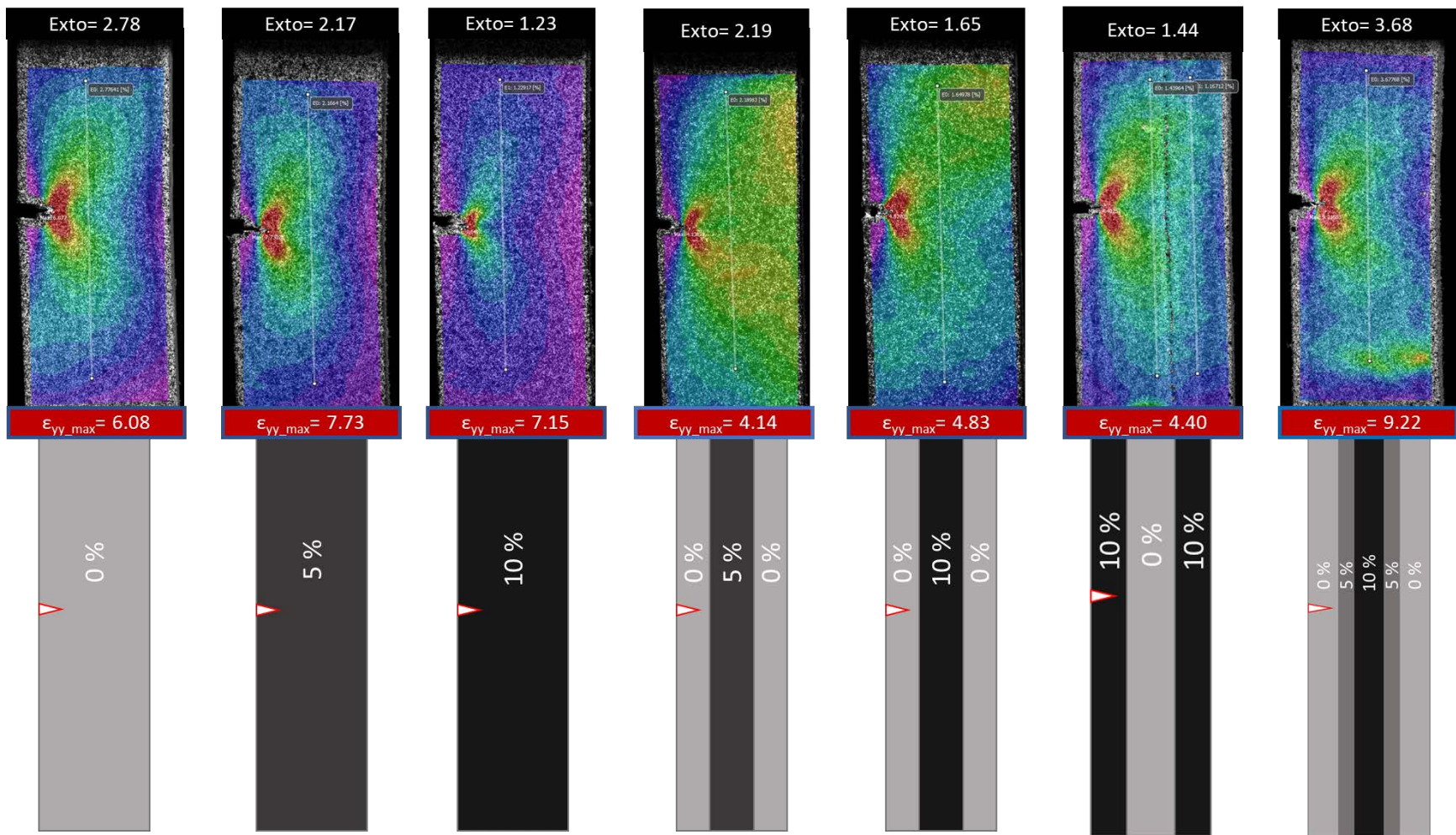


Figure 6.12b: SENT Test DIC Results at the Frame of Specimen Crack Initiation (Ci) scaled to each specimen frame

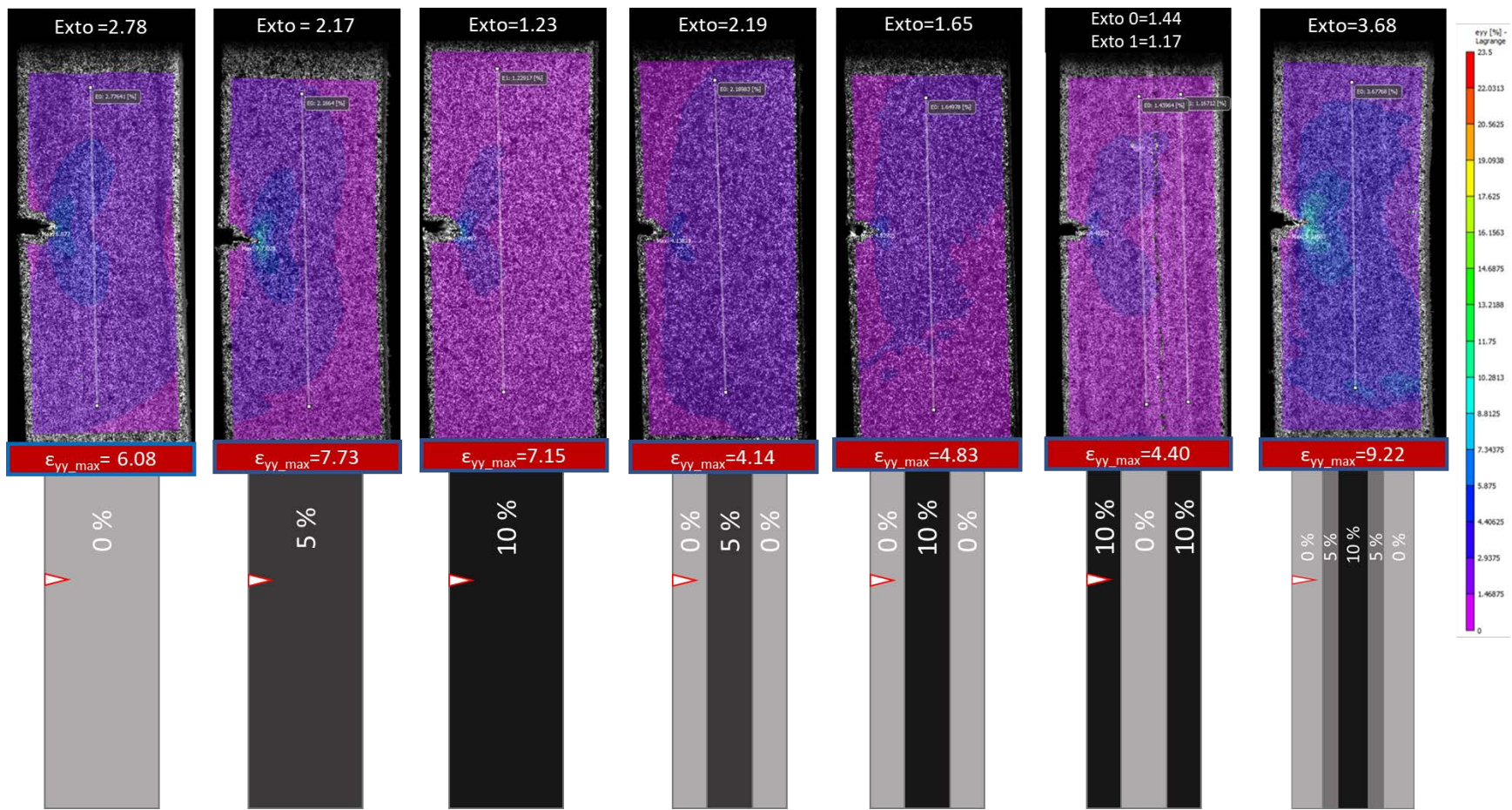


Figure 6.12c: Test 1 SENT Test DIC Results at the Frame of Specimen Crack Initiation (Ci), scaled to ALL

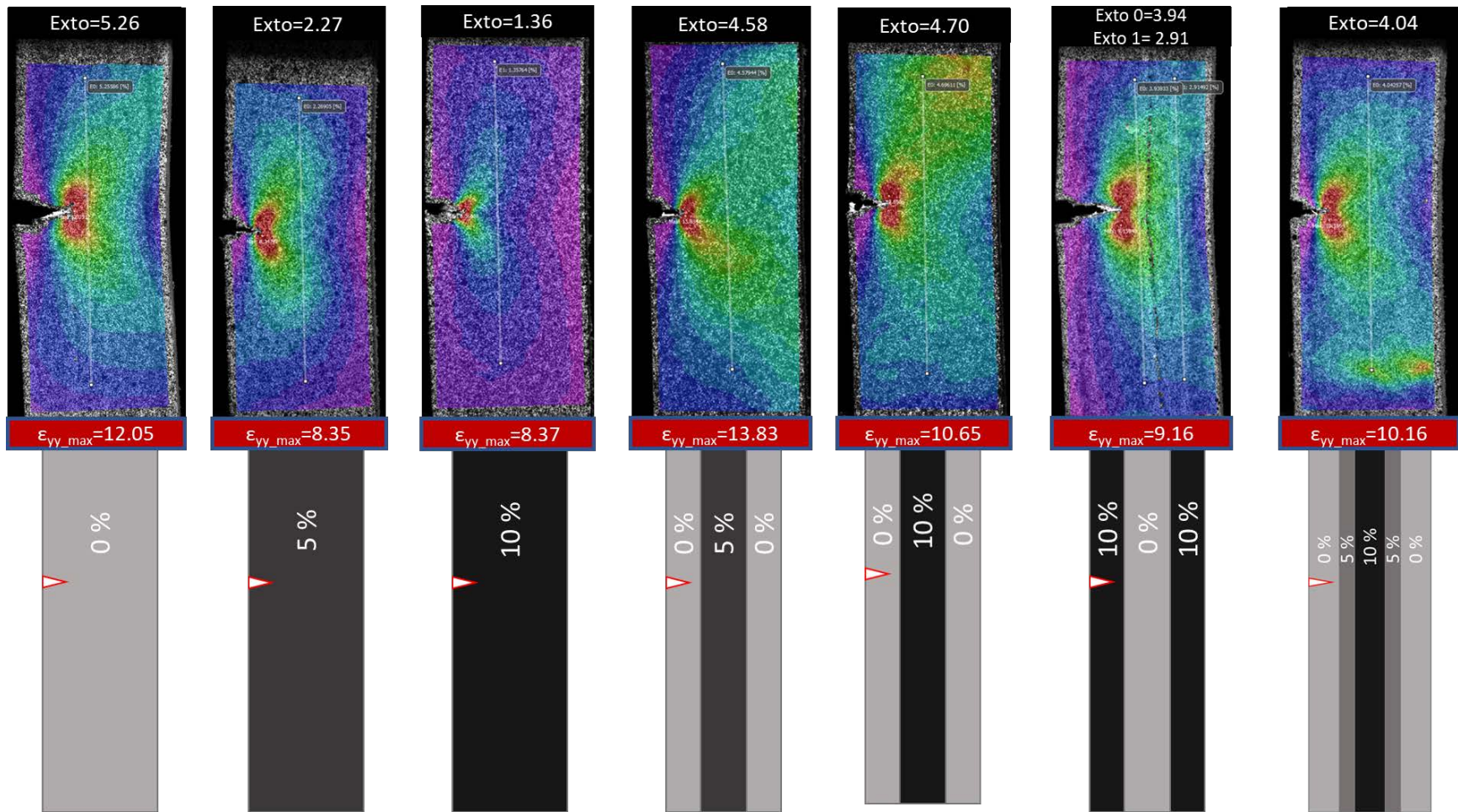


Figure 6.12d: Test1 SENT Test DIC Results the Frame at Specimen Max Force (MF) scaled to each specimen

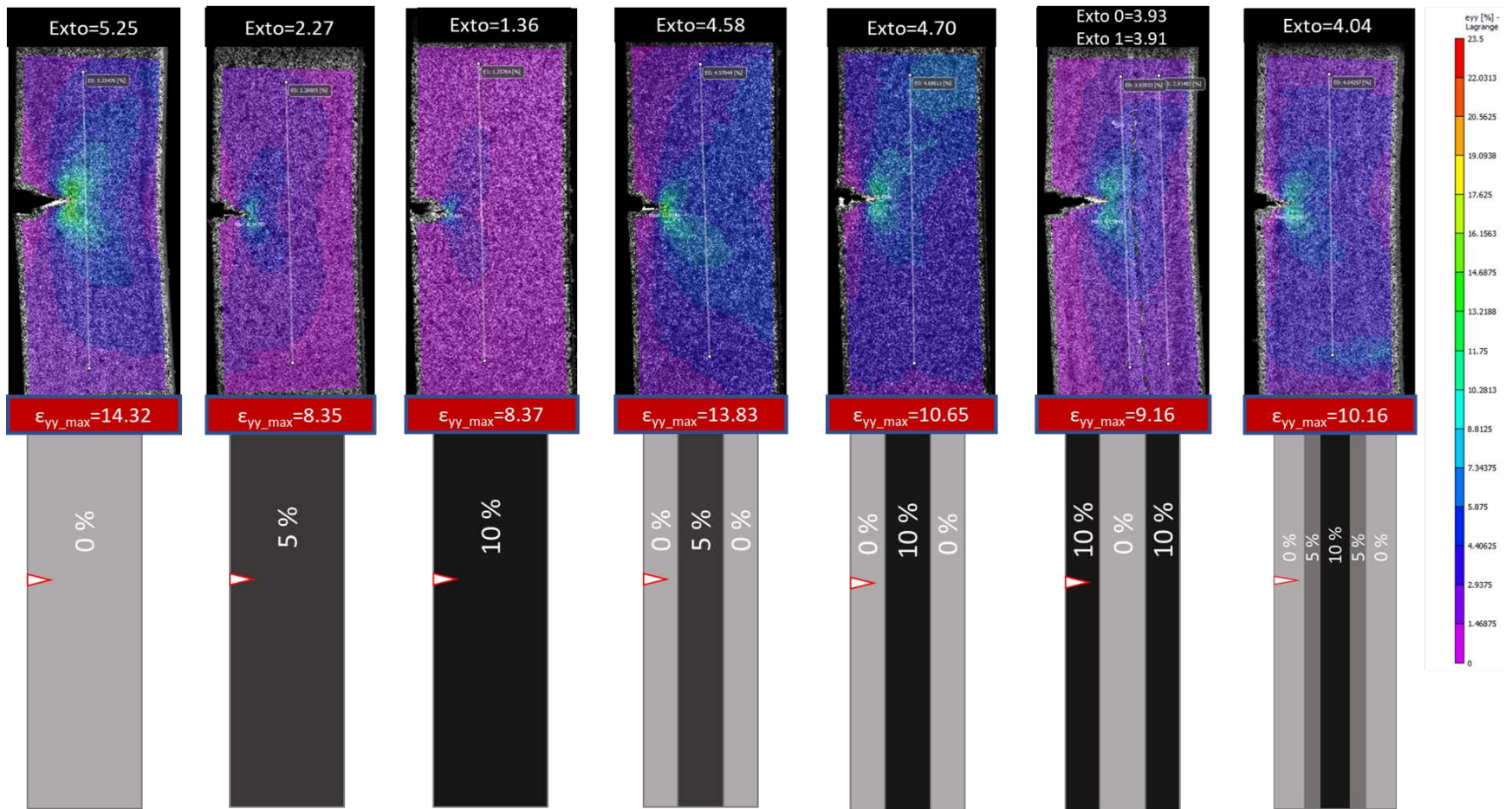


Figure 6.12e: SENT Test DIC Results the Frame Before Specimen Max Force (MF) scaled to ALL

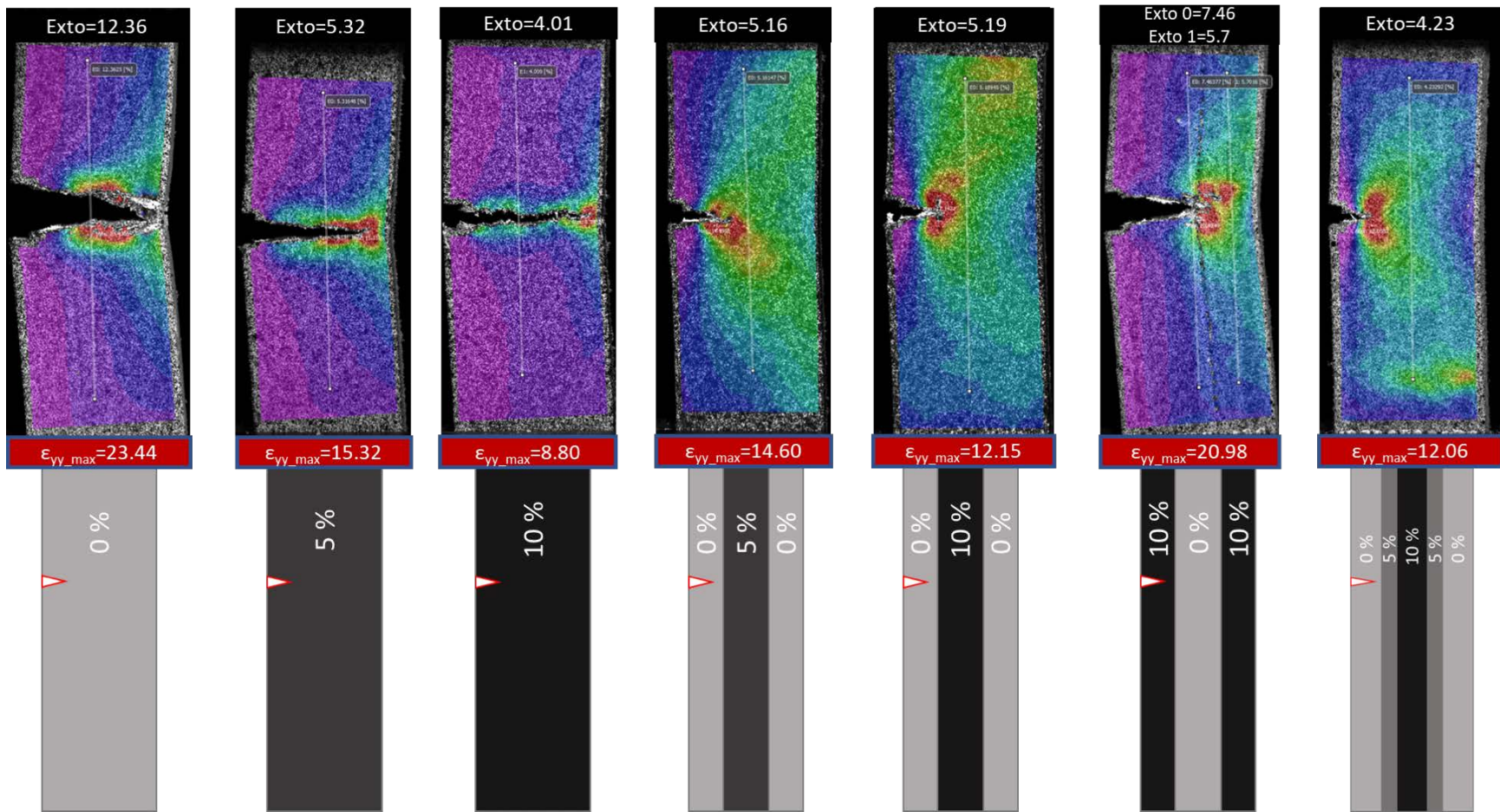


Figure 6.12f: SENT Test DIC Results the Frame Before Specimen Failure scaled to each specimen frame

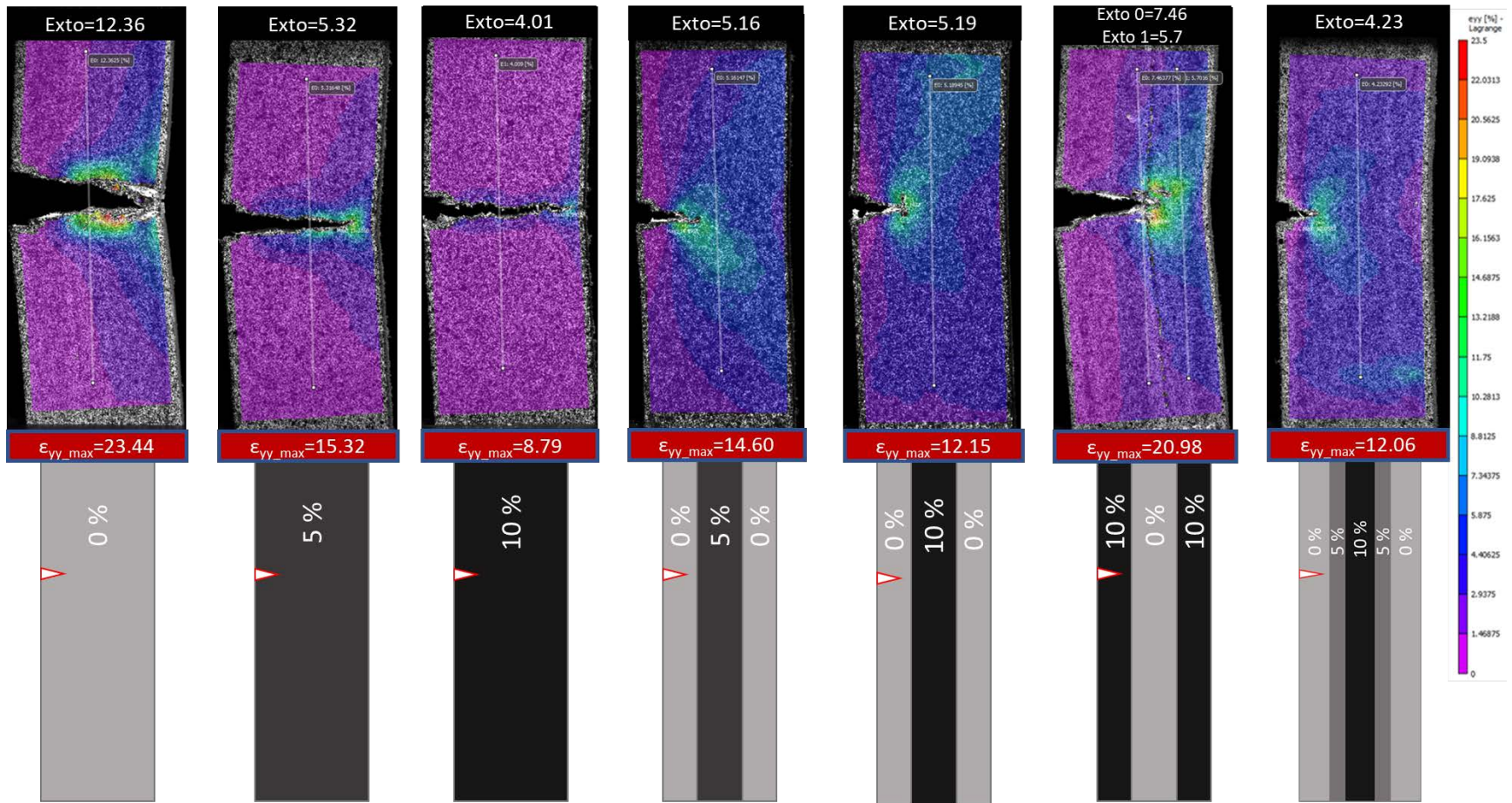


Figure 6.12g: SENT Test DIC Results the Frame Before Specimen Failure scaled to ALL

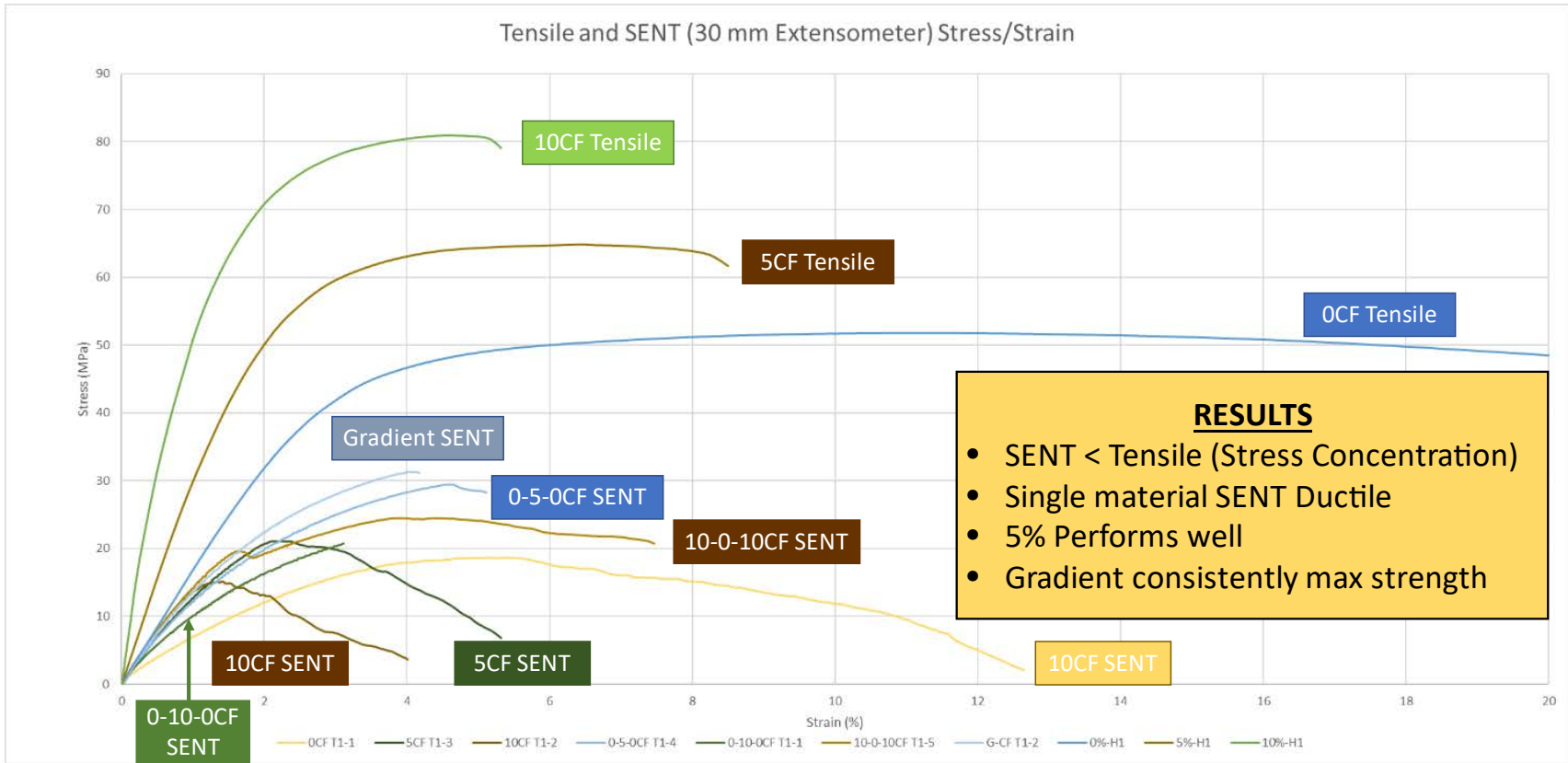
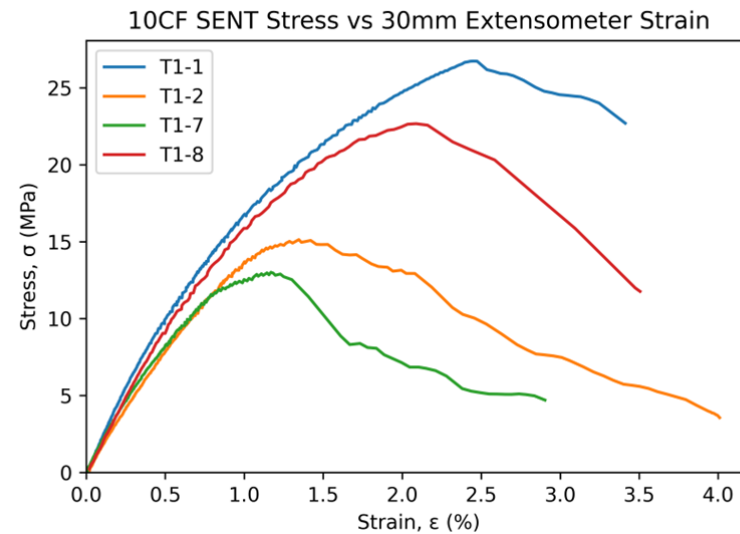
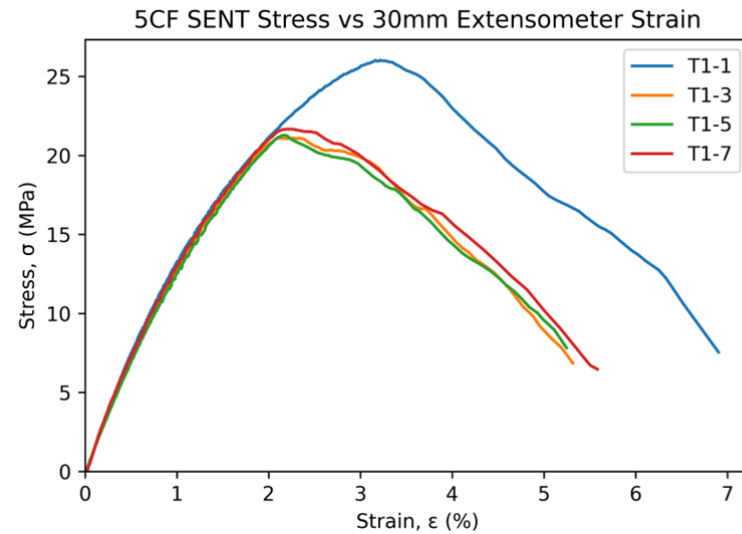
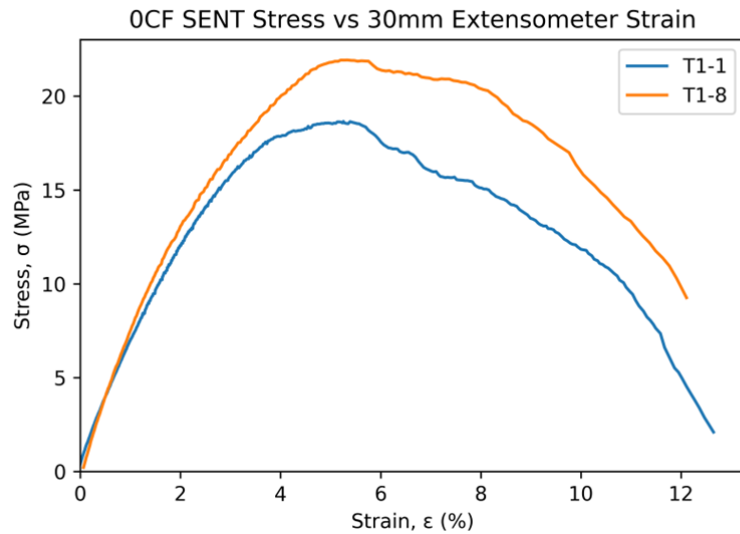


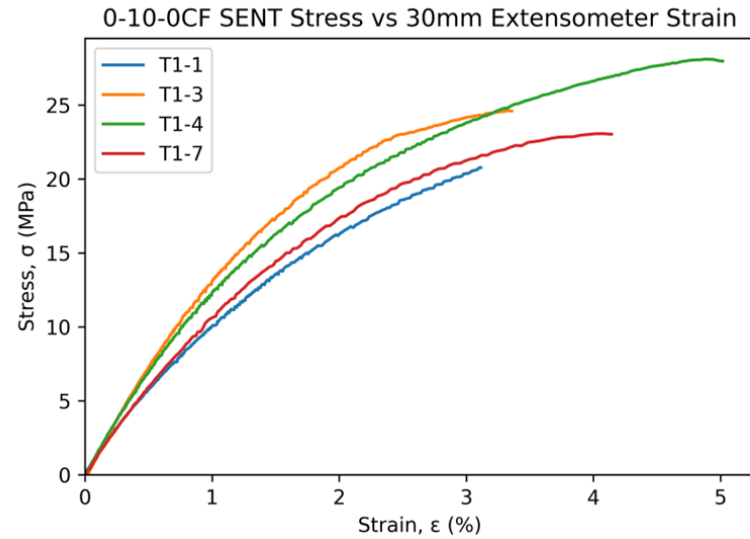
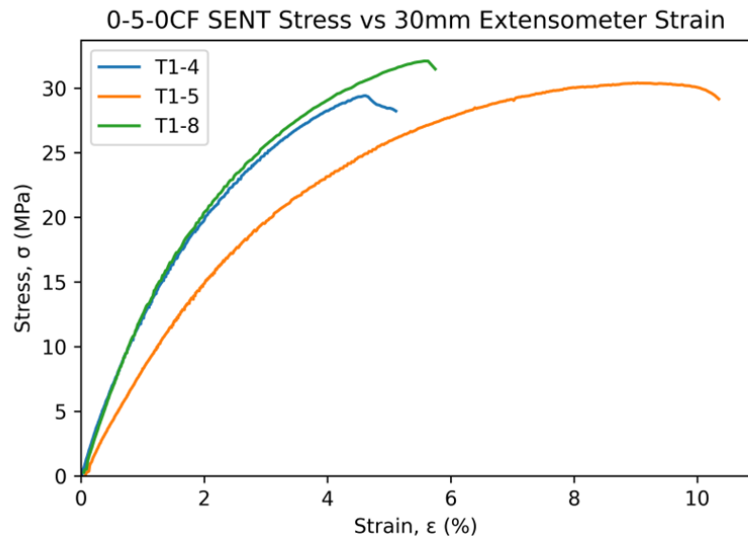
Figure 6.13: Comparison of 3mmP Horizontally Printed Tensile Test (Aim 3) and 30mm Extensometer SENT Stress/Strain



**RESULTS**

- High variance and unpredictability with 10CF
- High predictability and low deviation with 5CF

Figure 6.14: Single Material SENT Results Overview (T1 = Test 1, -x = Specimen Number)



**RESULTS**

- Multi-Material makes 10CF materials more predictable.
- Gradient is most predictable with both Stress and strain.

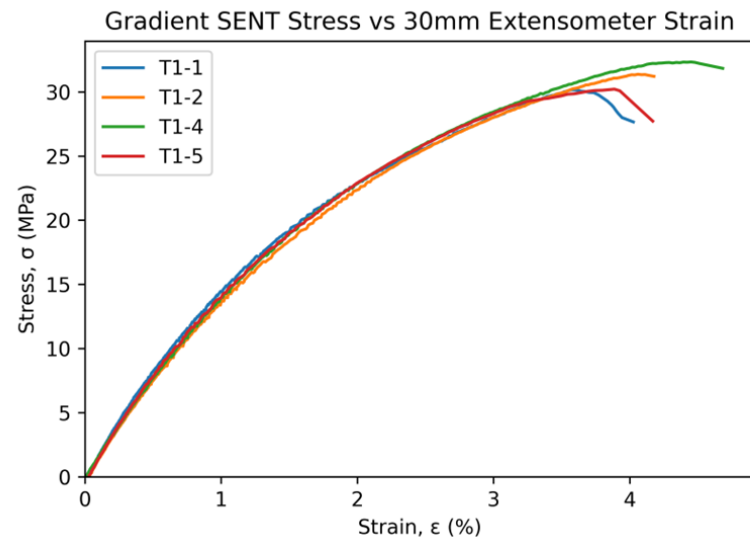


Figure 6.15: Bi-Material and Binary Gradient SENT Results Overview (T1 = Test 1, -x = Specimen Number)

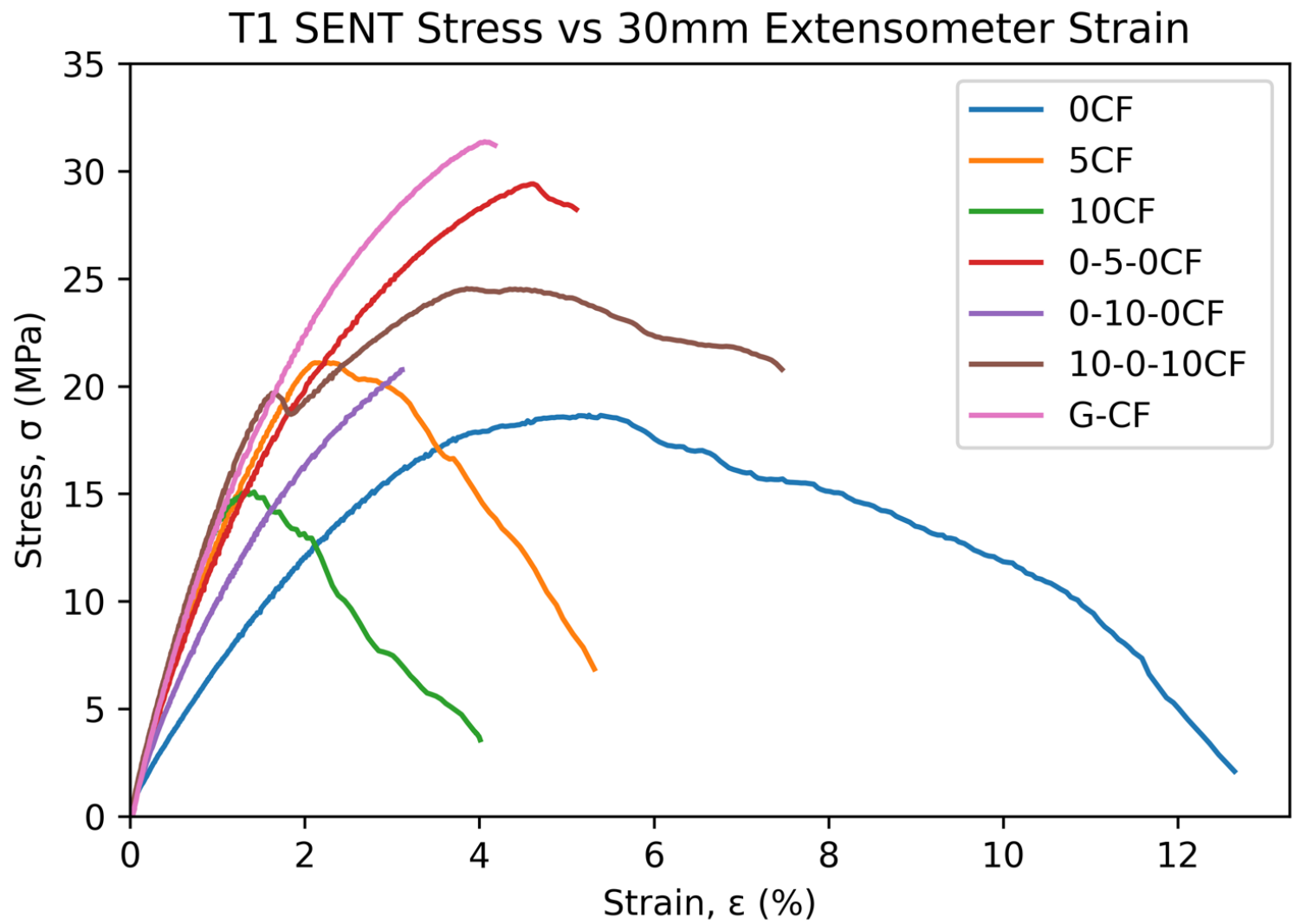


Figure 6.16: SENT 30mm Extensometer Stress/Strain Comparison of Representative Specimen from Each Test

## T1 SENT Stress vs 30mm Extensometer Strain

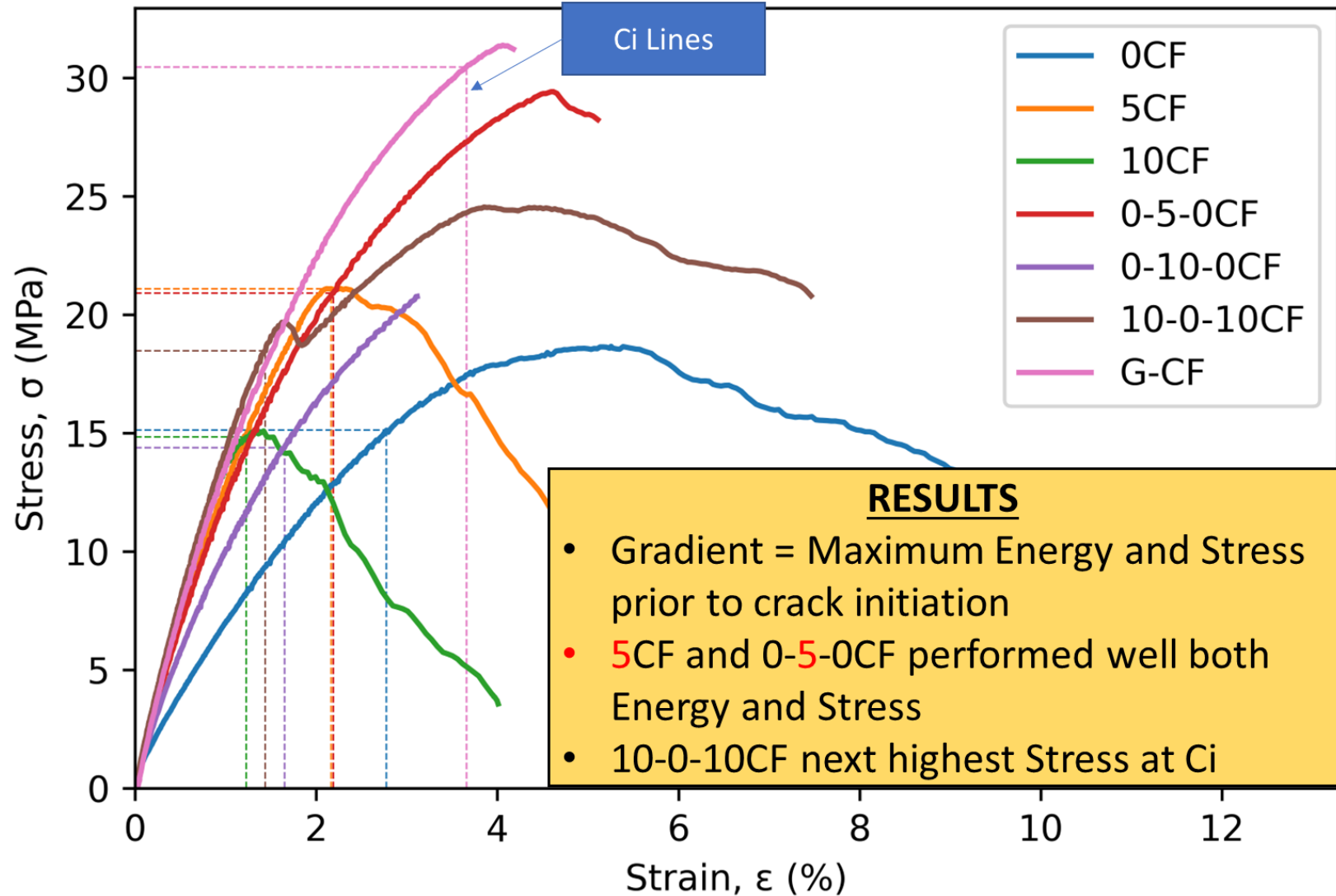


Figure 6.17: SENT 30mm Extensometer Stress/Strain Comparison of Representative Specimen from Each Test with Crack Initiation Lines (dotted) for each Specimen.

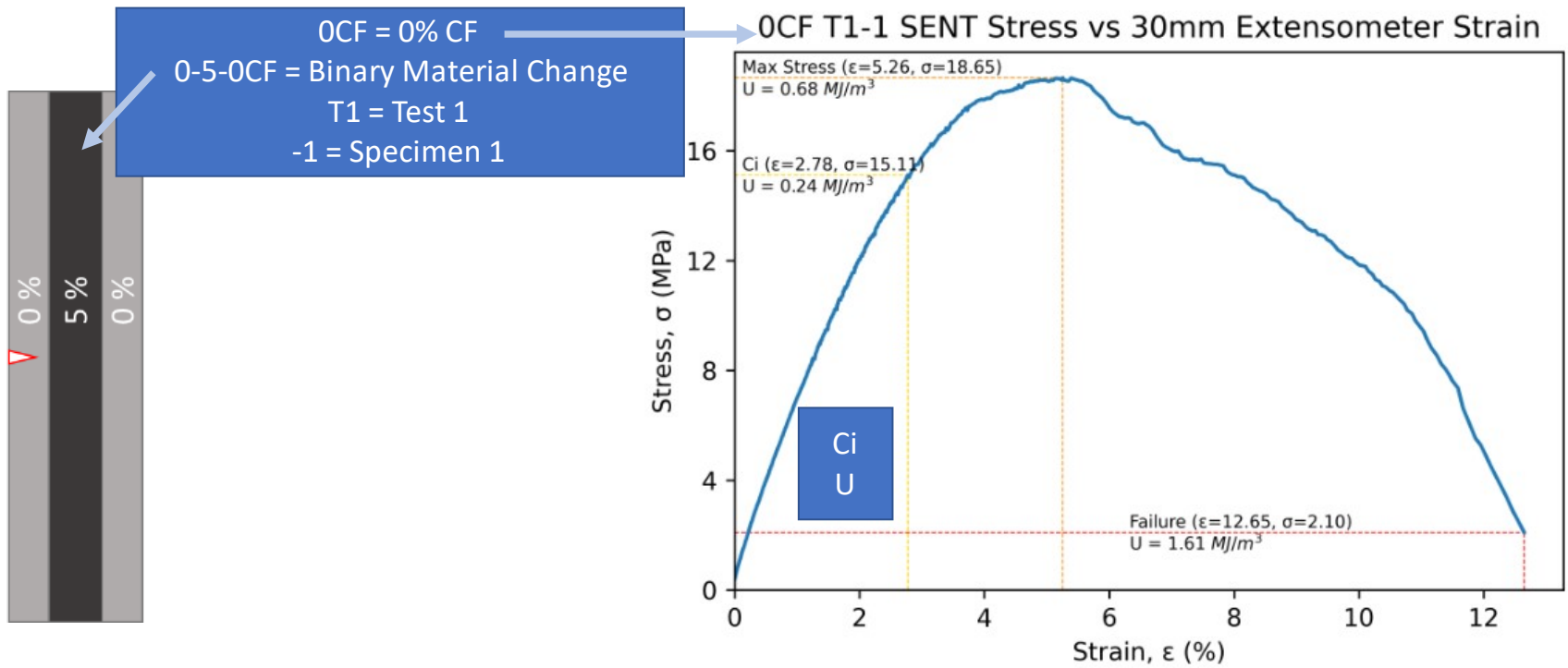


Figure 6.18: Depiction of SENT Test DIC Results Energy Calculation Definitions and Terms:

# 10-0-10CF T1-5 SENT Stress vs 30mm Extensometer Strain

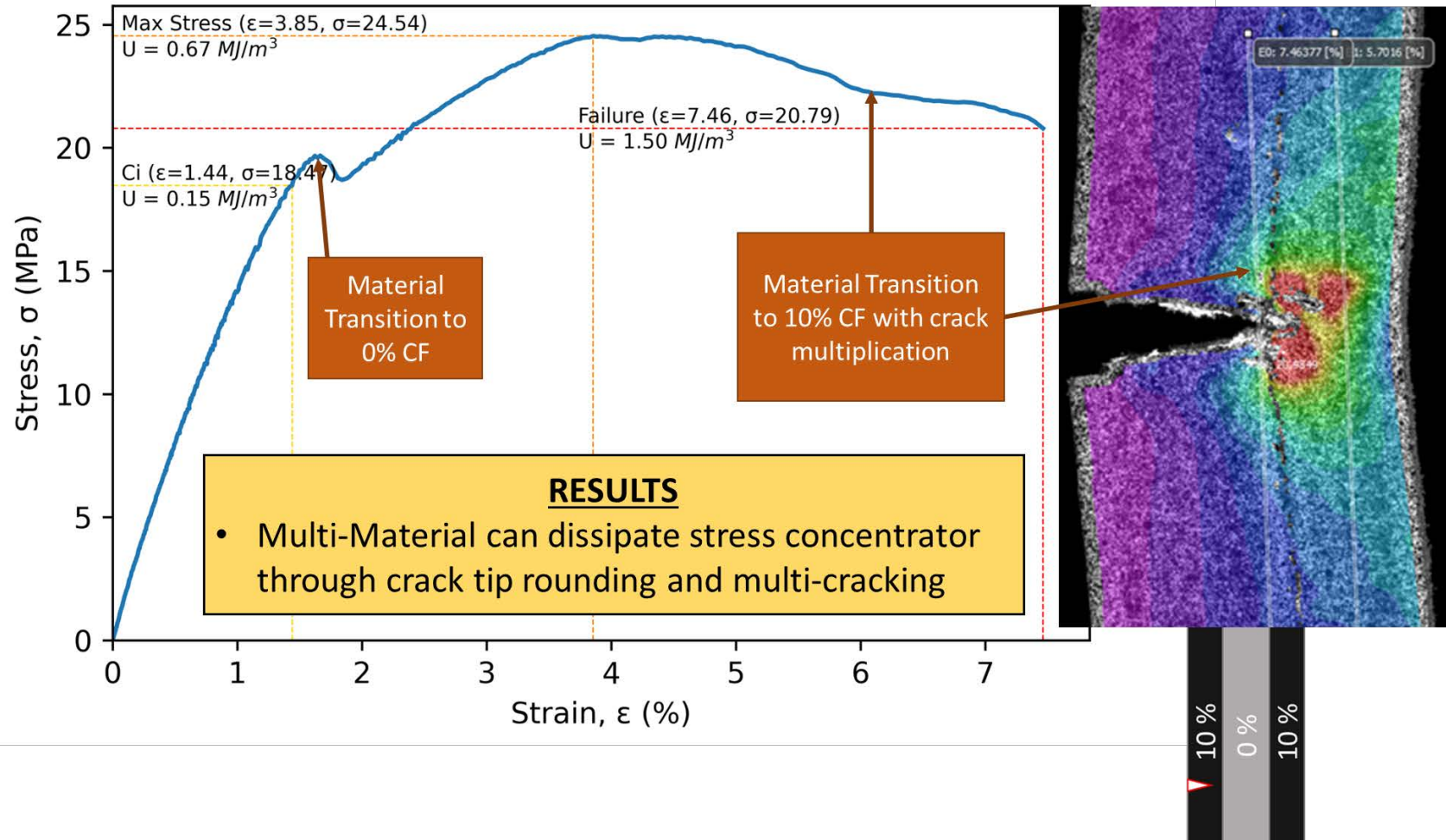


Figure 6.18a: 10-0-10% CF SENT Test Results with DIC Strain Mapping and Stress-Strain Curve with Energy Data

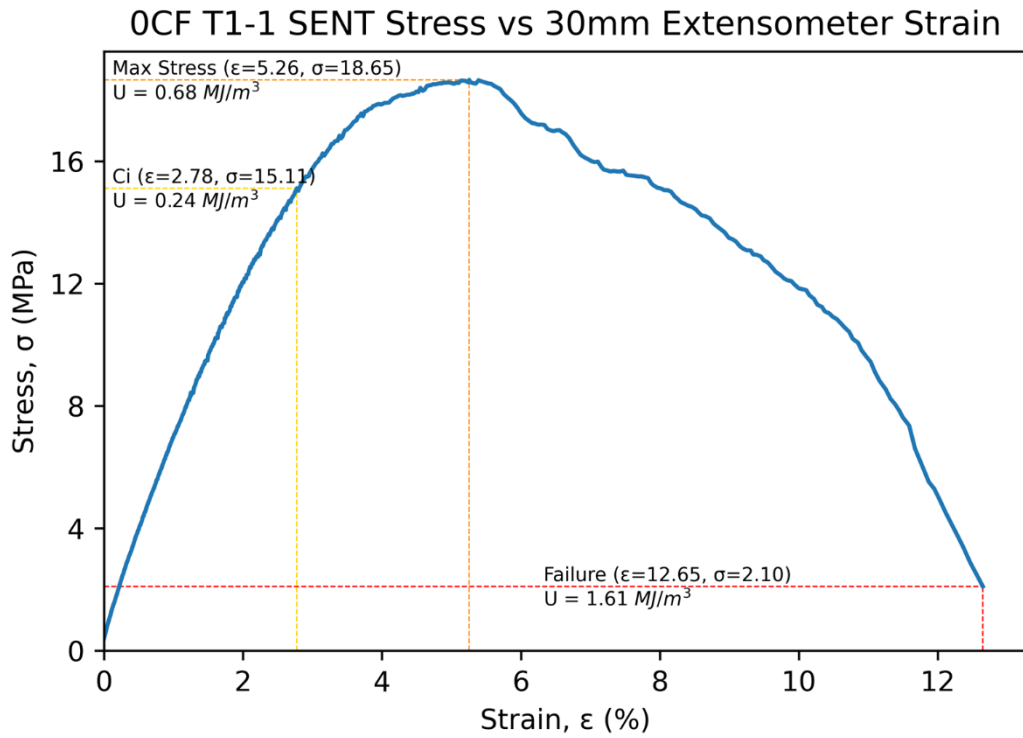


Figure 6.18b: 0%CF Single Material SENT Energy Data

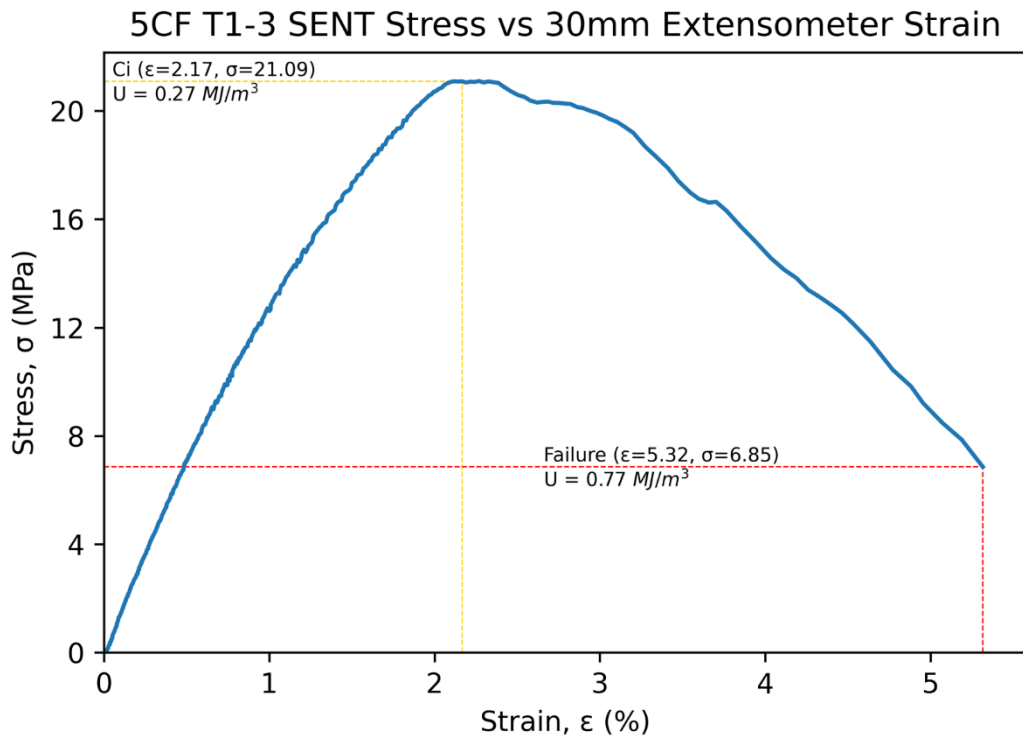


Figure 6.18c: 5%CF Single Material SENT Energy Data.

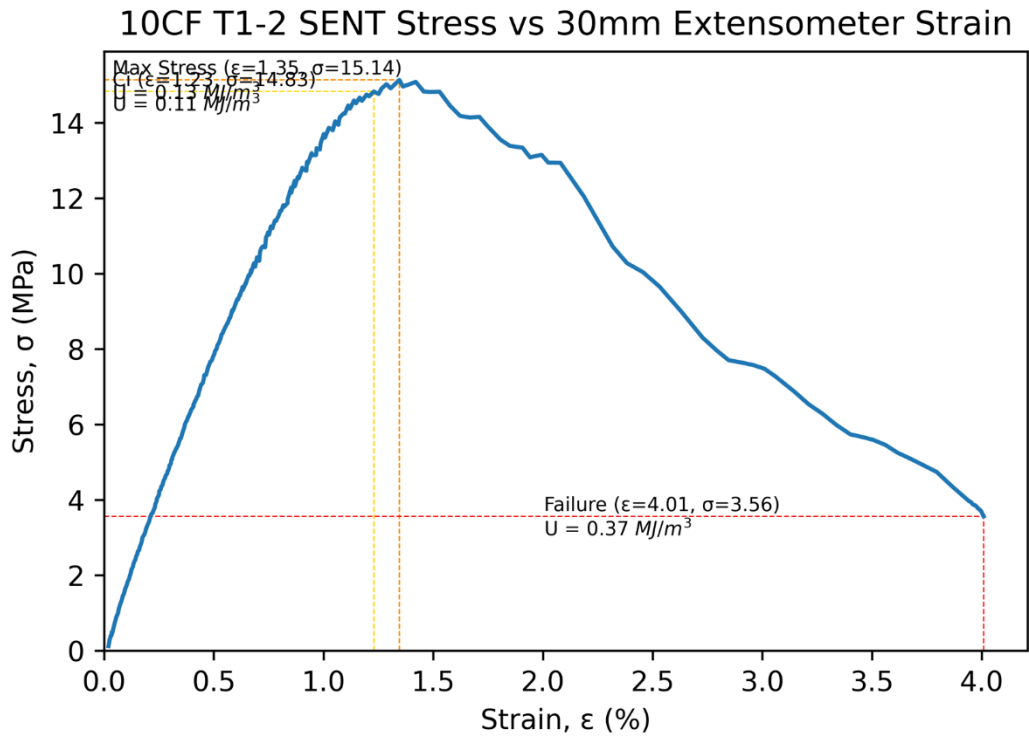


Figure 6.18d: 10%CF Single Material SENT Energy Data.

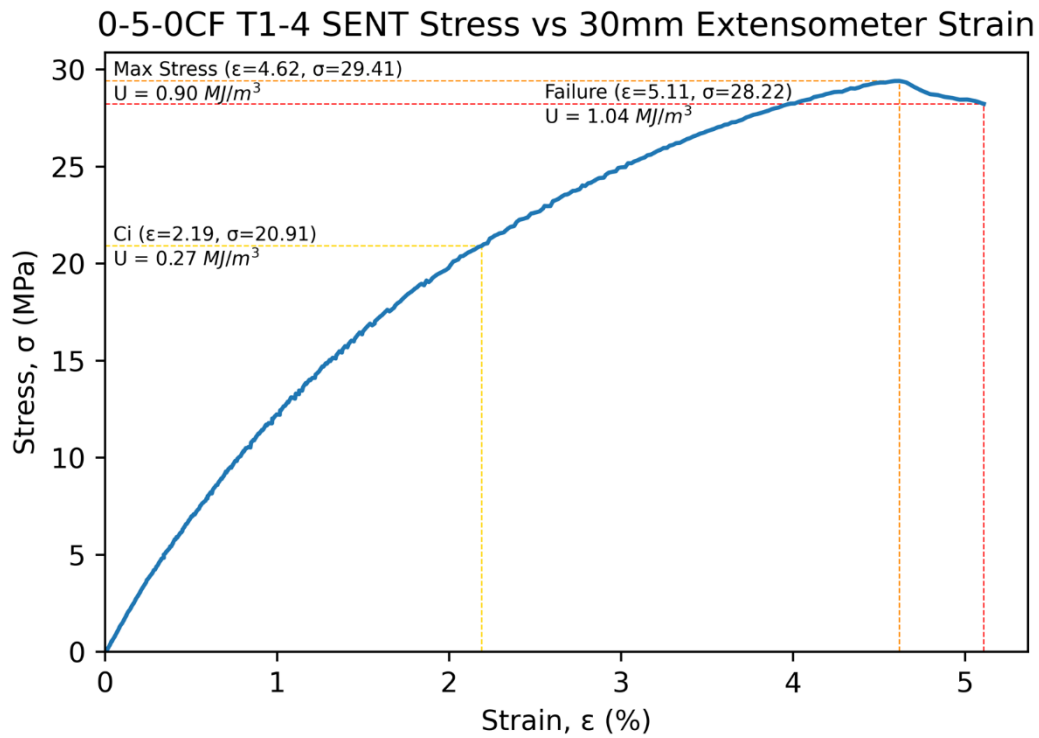


Figure 6.18e: 0-5-0%CF Binary Material SENT Energy Data.

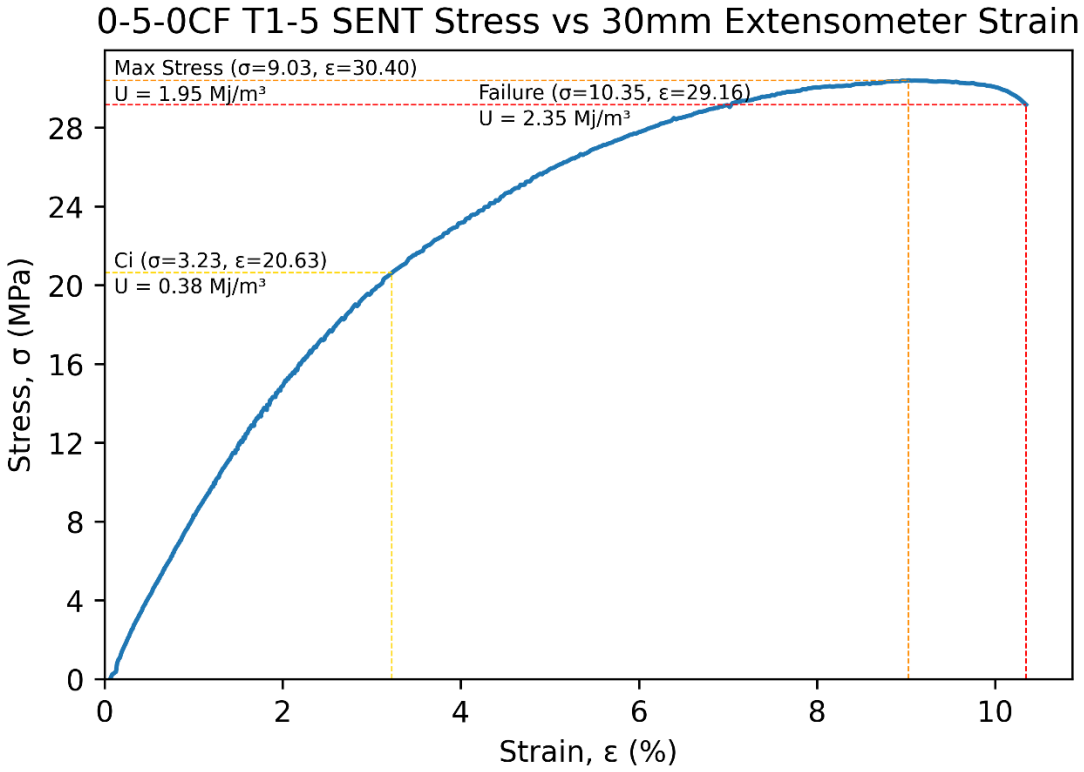


Figure 6.18f: 0-5-0%CF Binary Material SENT Energy Data.

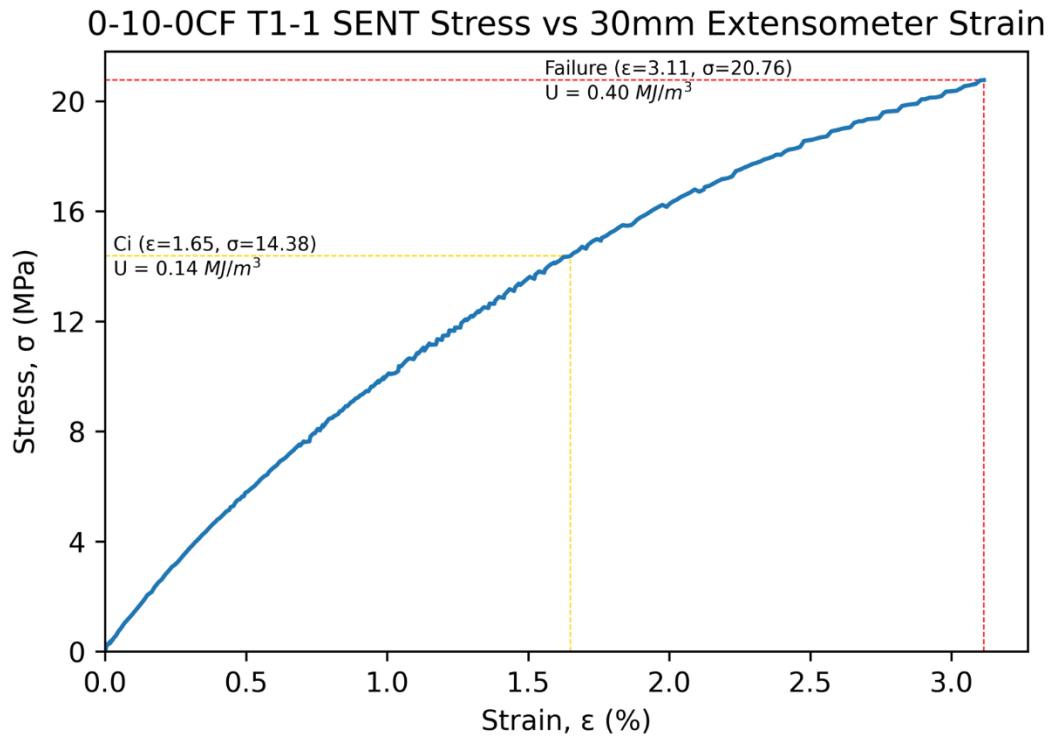


Figure 6.18g: 0-10-0%CF Binary Material SENT Energy Data.

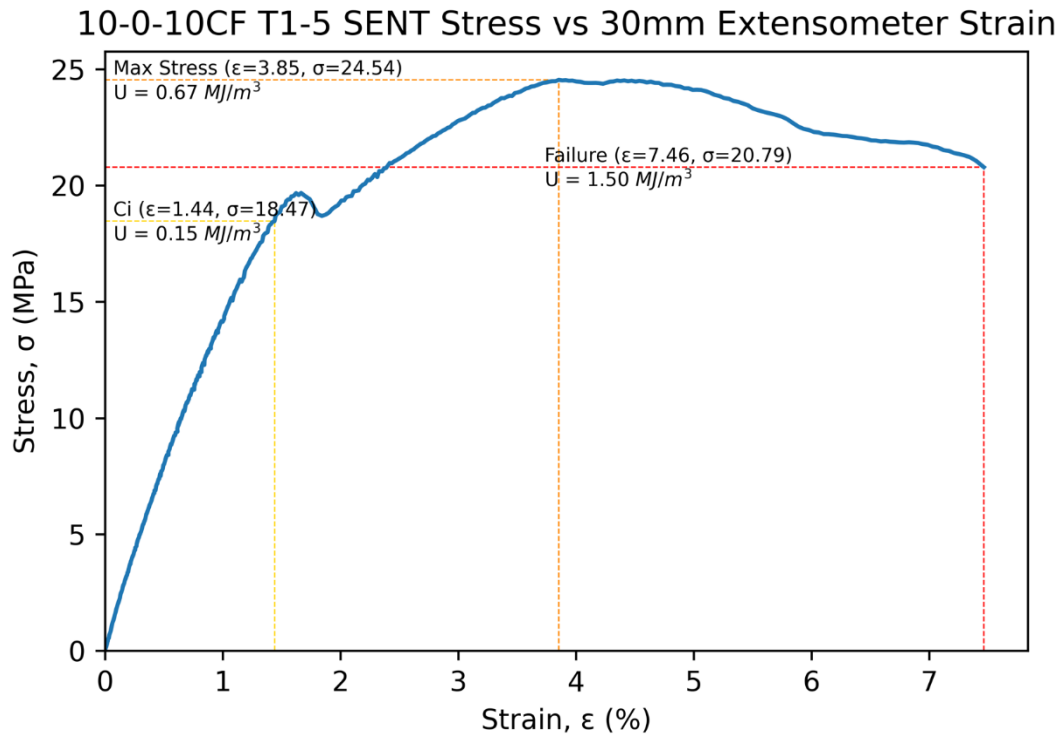


Figure 6.18h: 10-0-10%CF Binary Material SENT Energy Data

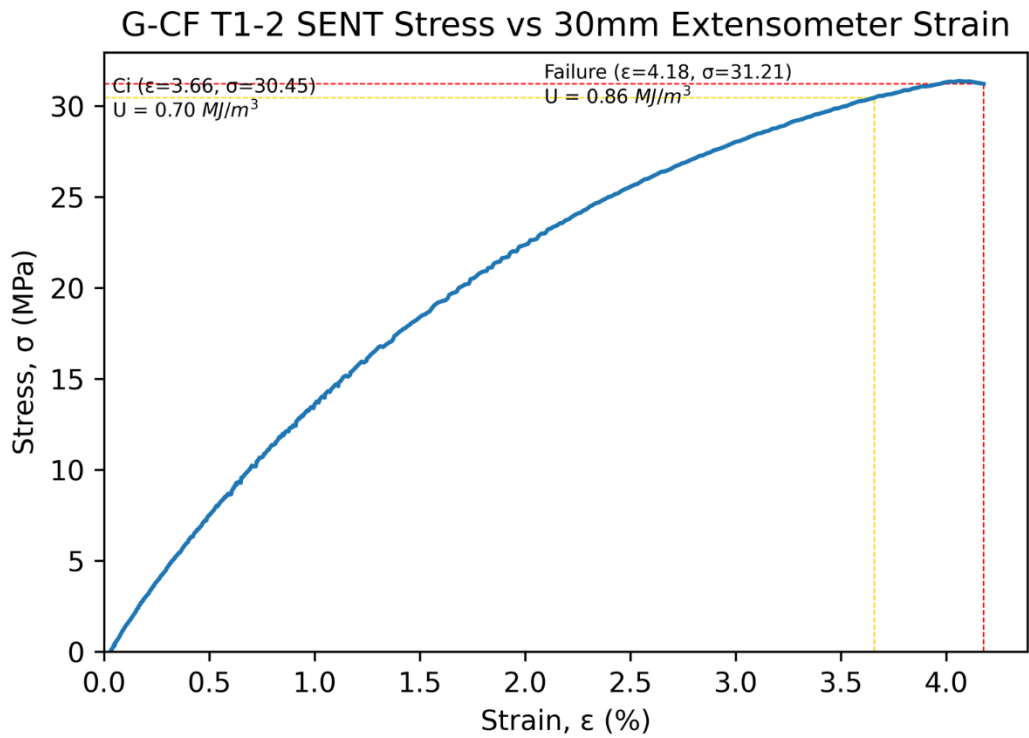


Figure 6.18i: 0-5-10-5-0%CF Gradient SENT Energy Data.

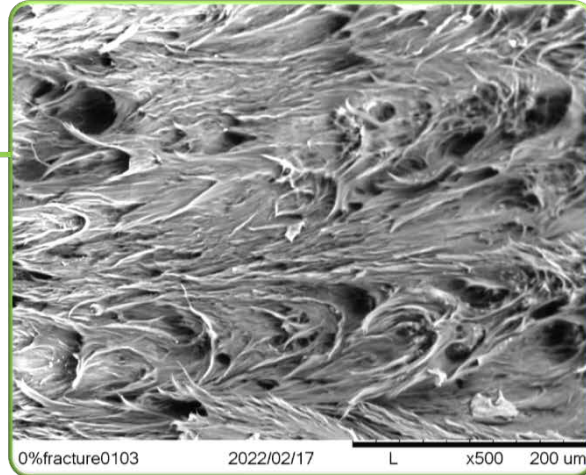
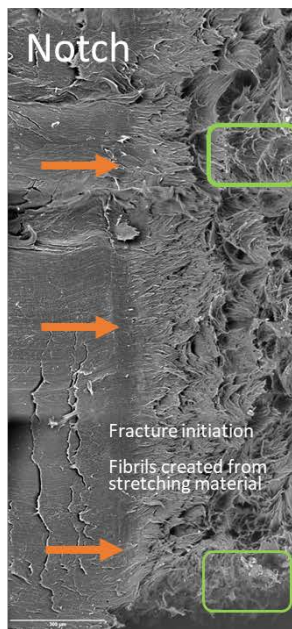
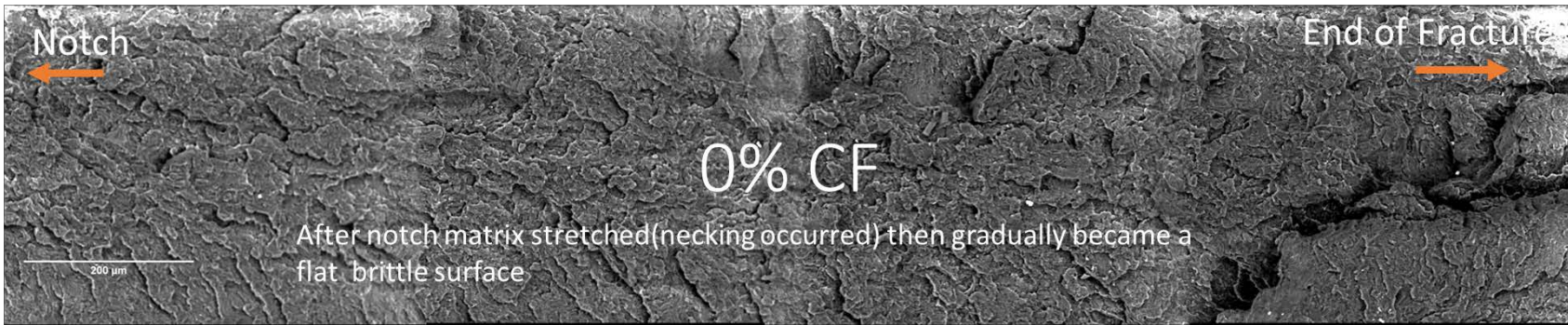


Figure 6.19: 0% SENT SEM Fractography

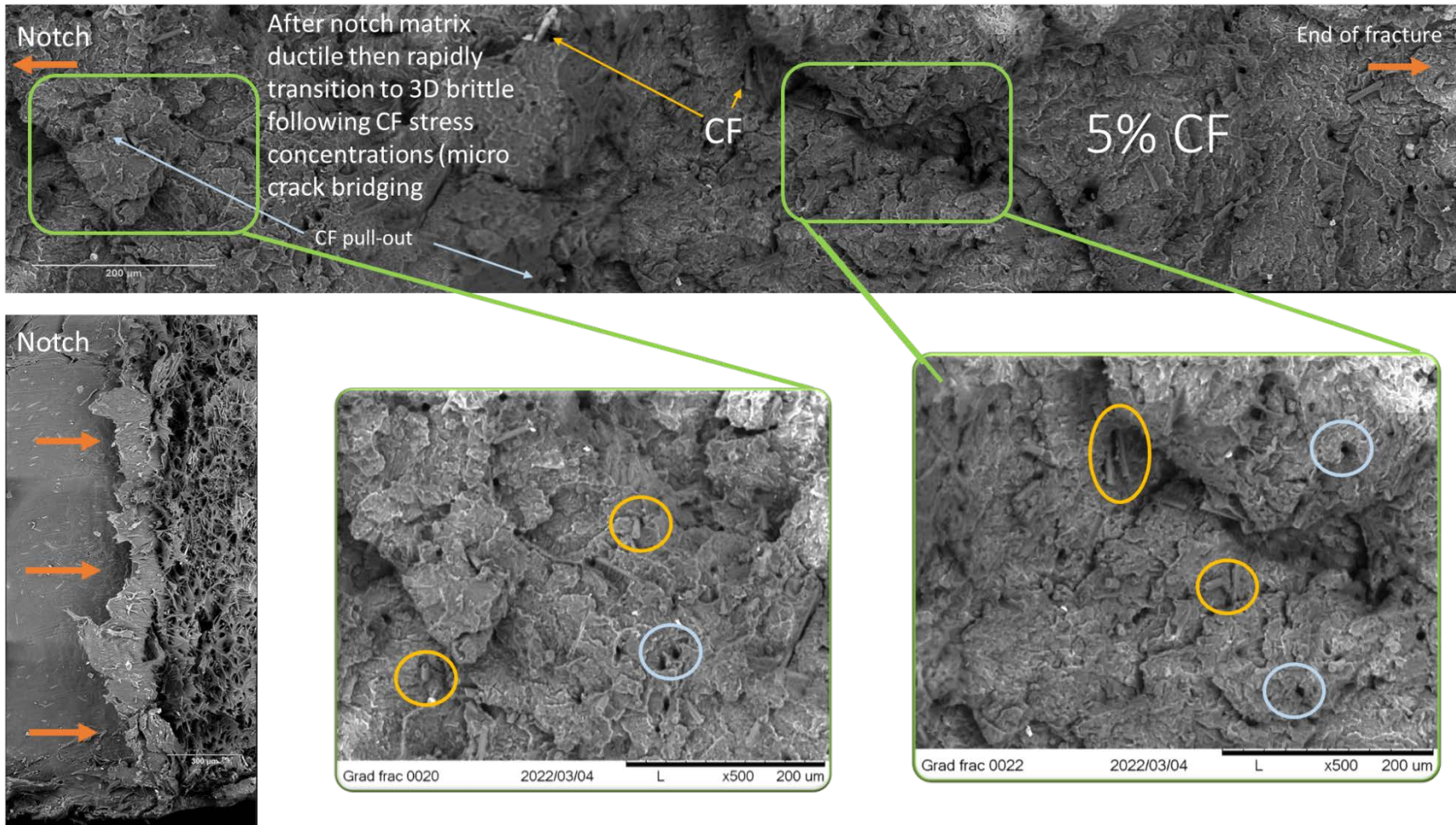


Figure 6.20: 5% SENT SEM Fractography

Note: Orange circles indicate examples of fiber and blue circles indicate examples of voids left by fiber pullout

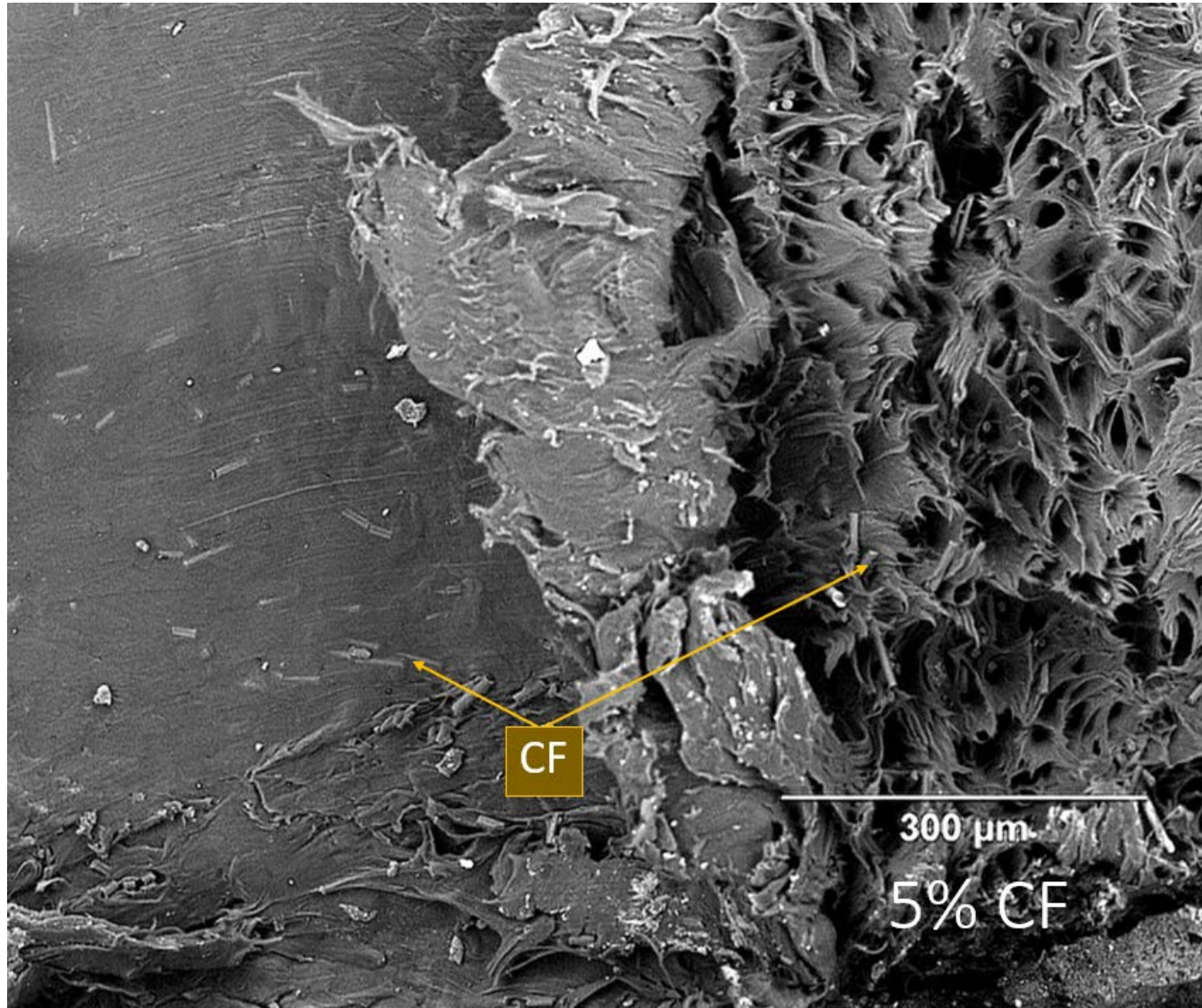


Figure 6.21: 5% SENT SEM Notch Fractography

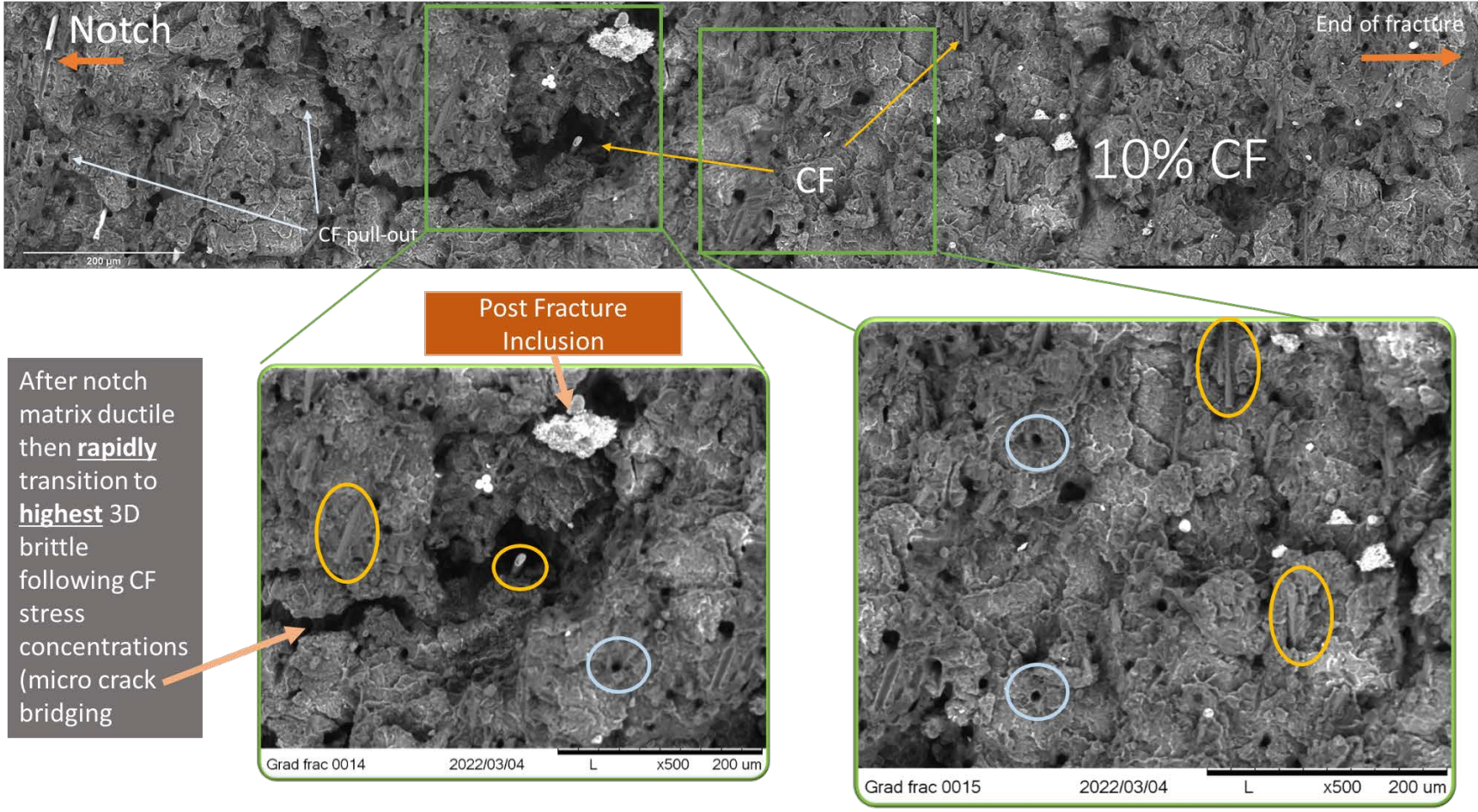


Figure 6.22: 10% SENT SEM Fractography  
 Note: Orange circles indicate examples of fiber and blue circles indicate examples of voids left by fiber pullout

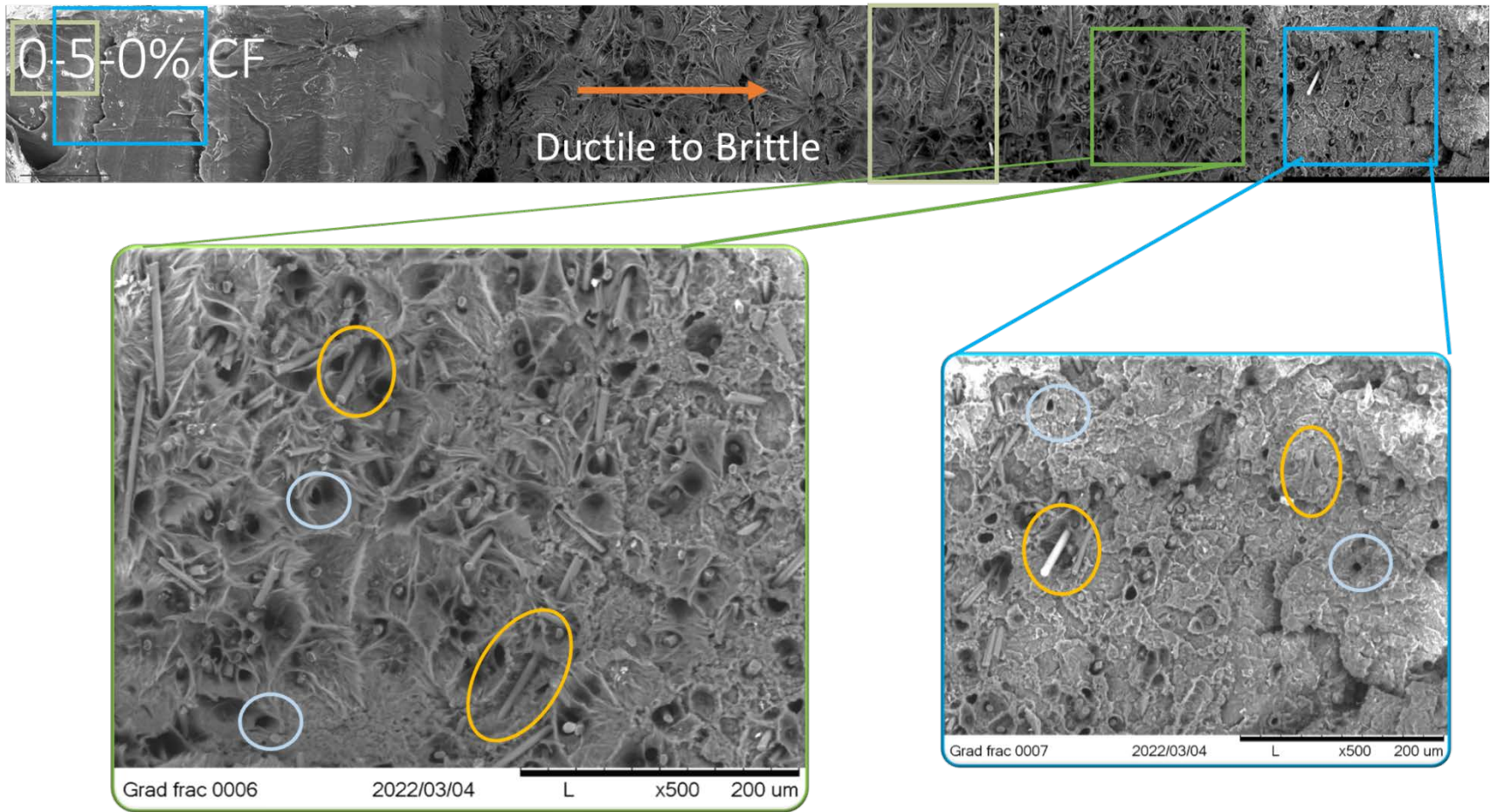


Figure 6.23: 0-5-0% SENT SEM Fractography

Note: Orange circles indicate examples of fiber and blue circles indicate examples of voids left by fiber pullout

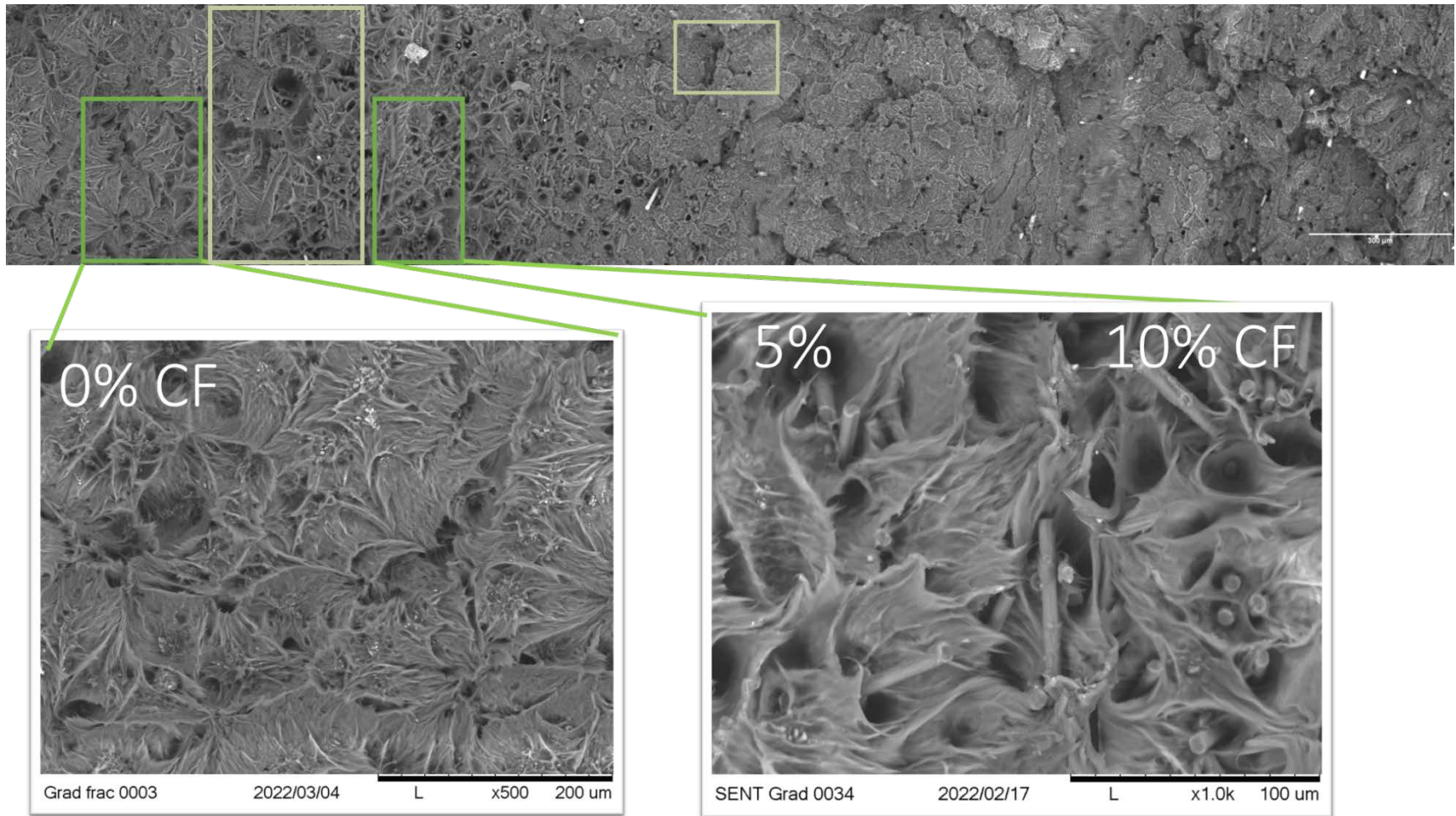
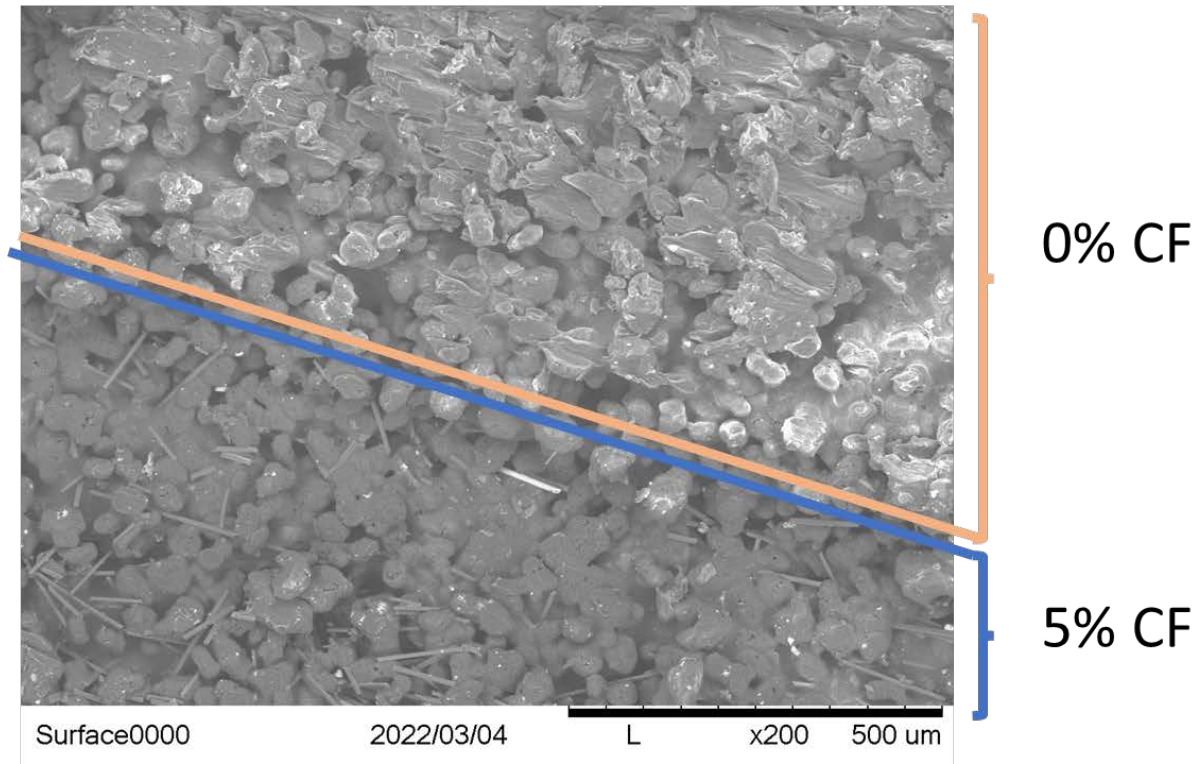


Figure 6.24: SENT SEM Fractography of CF Gradient Transitions

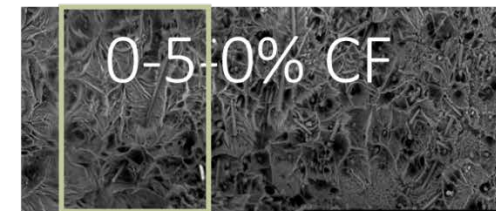
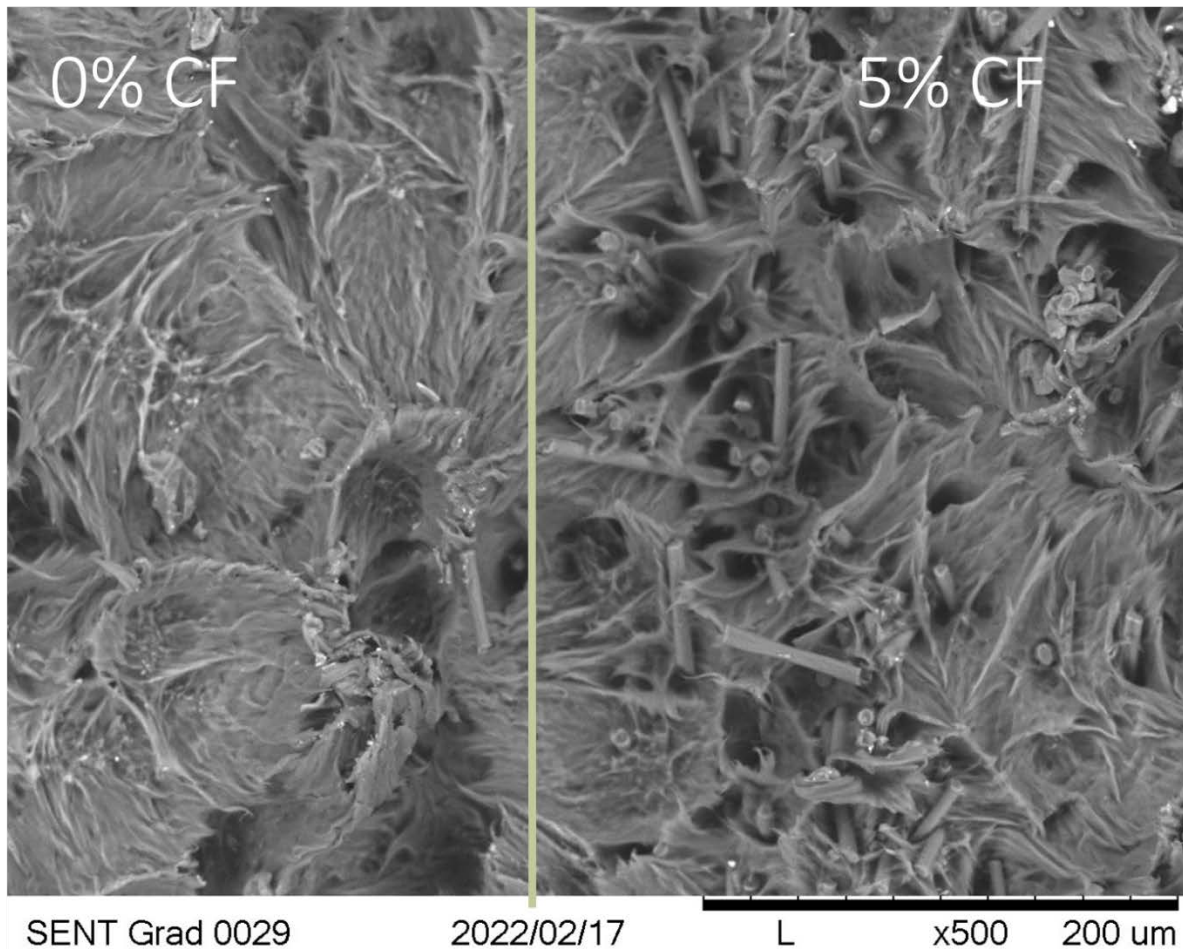
0-5-0% CF



**RESULTS**

- Homogeneous PA12 Matrix sintering at CF binary interface (0-5CF)
- Sharp binary interface with minimal CF contamination at 0CF fracture

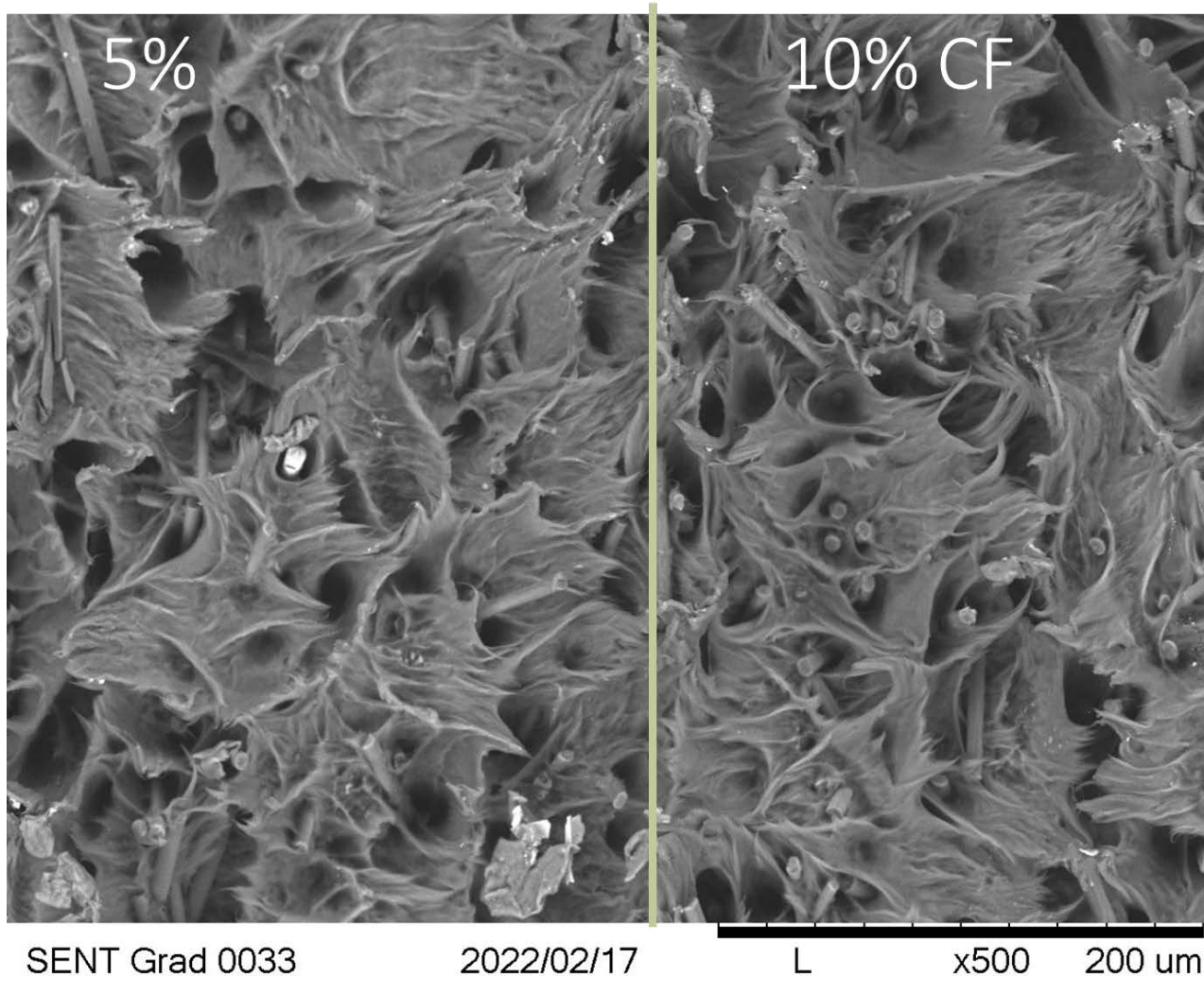
Figure 6.25: 0-5% SENT SEM Sanded Surface of CF Gradient Transition (estimated with 0% blue line, 5% orange line).



### **RESULTS**

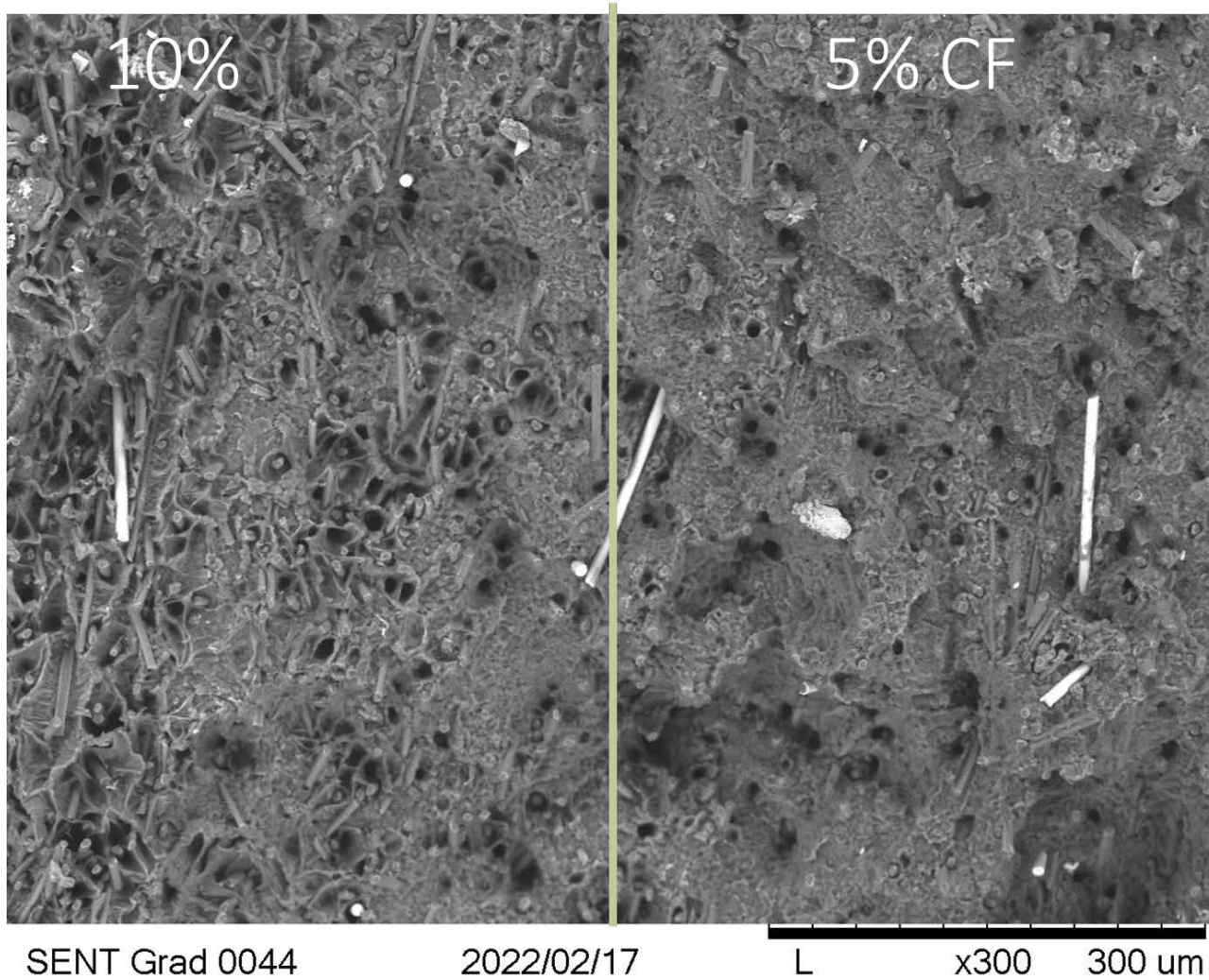
- Homogeneous PA12 Matrix sintering at CF binary interface (0-5CF)
- Sharp binary interface with minimal CF contamination at 0CF fracture

Figure 6.26: 0-5% SENT SEM Fractography of CF Gradient Transition (estimated with green line)



- RESULTS**
- Homogeneous PA12 Matrix sintering at CF binary interface
  - Sharp binary interface with minimal CF contamination at OCF fracture

Figure 6.27: 5-10% SENT SEM Fractography of CF Ductile Gradient Transition (estimated with green line)



- RESULTS**
- Homogeneous PA12 Matrix sintering at CF binary interface
  - Sharp binary interface with minimal CF contamination at OCF fracture
  - Sharp white color indicates charging on surface from SEM

Figure 6.28: 10-5% SENT SEM Fractography of CF Gradient Brittle Transition (estimated with green line)

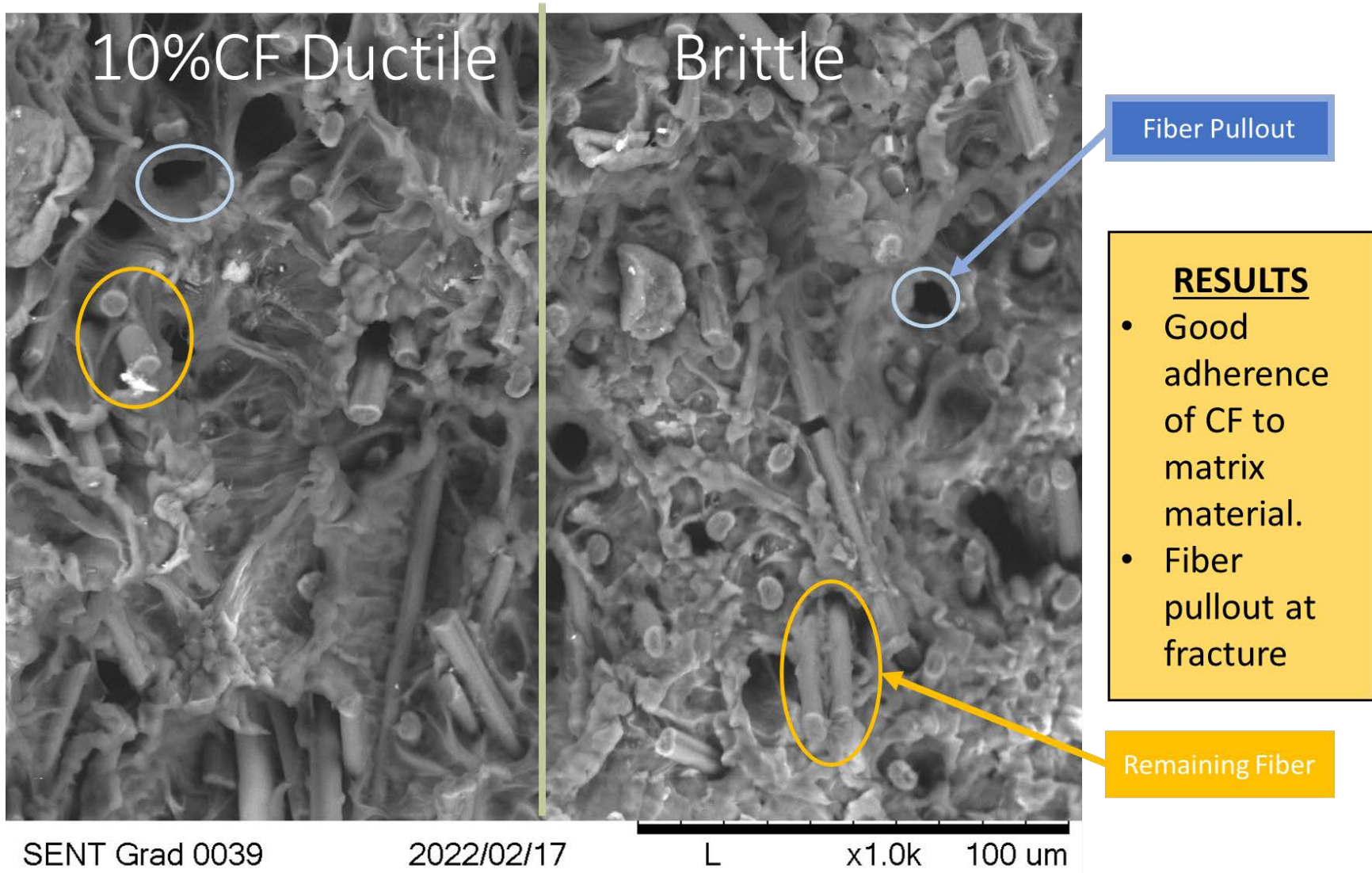


Figure 6.29: 10% SENT SEM Fractography of CF Ductile to Brittle Transition (estimated with green line)

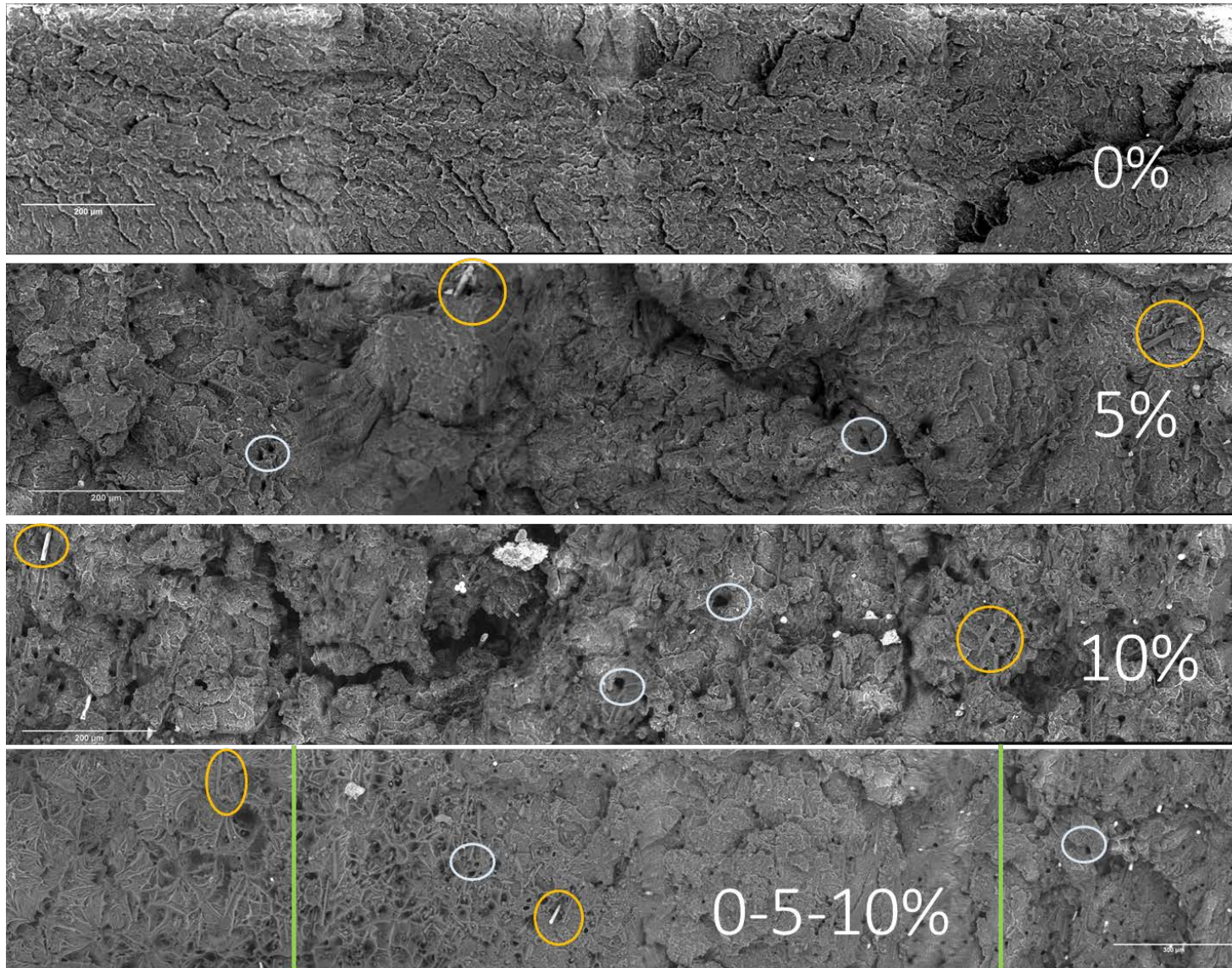


Figure 6.30: 0%, 5%, 10%, Binary Gradient SENT SEM Fractography comparison (gradient transition estimated with green line)

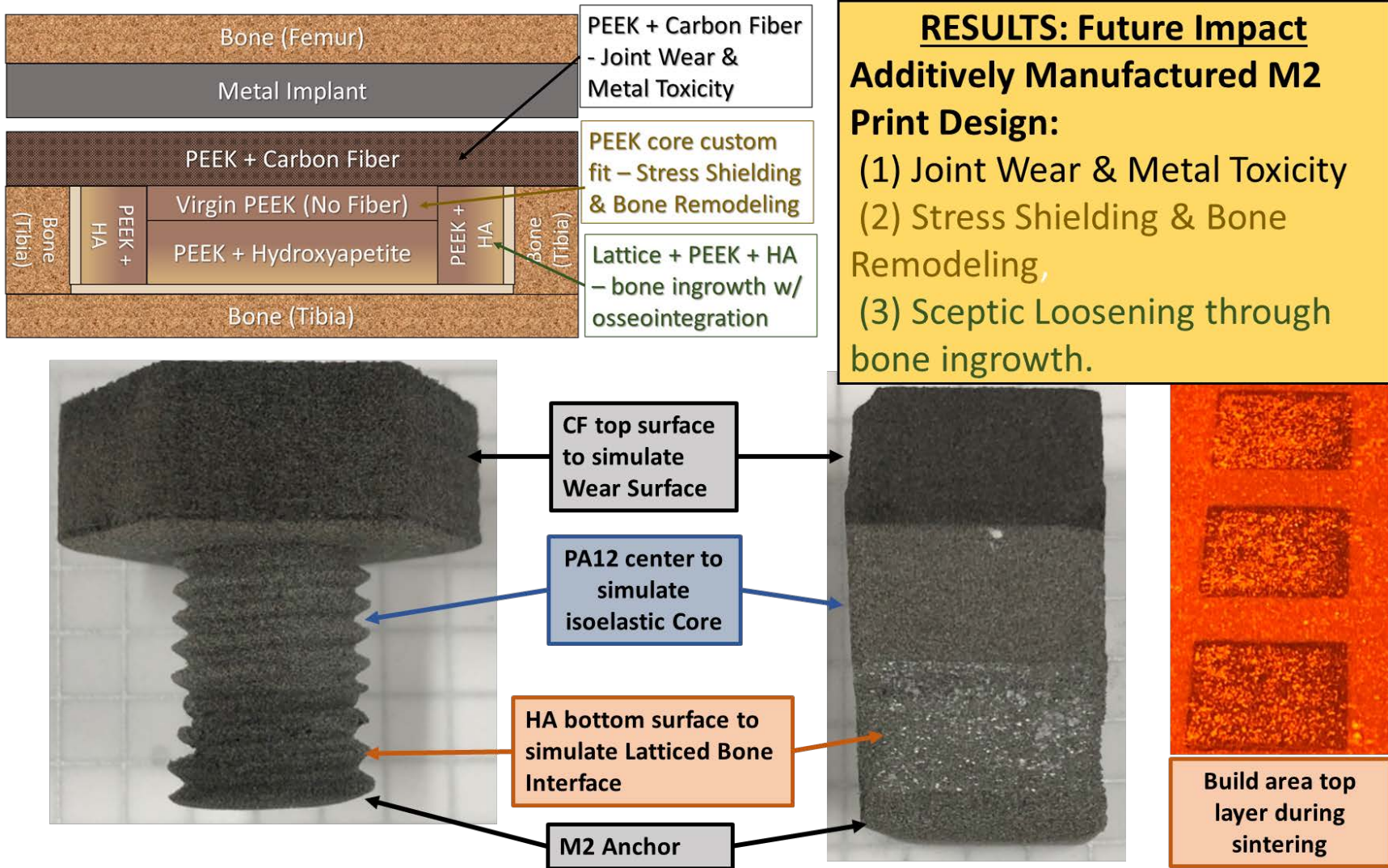


Figure 6.31: Joint implant conceptual prototype

## DISCUSSION

M2 SENT and warping test results exemplify how M2 PBF can alter part characteristics through LCC and FGM for *both* (a) binary changes in fiber content and (b) binary gradients of fiber content. Hardness and fractographic results indicated fully sintered PA12 matrix material throughout the specimen including across CF ratio transitions. These tests also pointed toward homogenous CF mixtures with good PA12/CF bonding.

Warping, hardness, and tensile data DOE had a specific order of testing which is important to consider when doing follow on testing. Testing was done in the following order: Warping – hardness – tensile and changing the order could change the results. An obvious example is warping measurements: if the specimen was first machined to gather cross section hardness data the machining process would “square” the sample and warping measurements would indicate zero or near zero warping for all specimens because the machining process would be analyzed instead of warping. More subtle changes would occur for hardness testing based on tensile rig grip effects on the surface of the specimens. Regardless of the exact impact on results, the DOE must be carefully considered not only for accuracy of results but also comparability of results from other tests.

The DOE order described above was performed on four of the eight specimens printed for each SENT specimen type (i.e., four from 0% Cf, 5% CF, 10% CF, 0-5-0% CF, 0-10-0% CF, 10-0-10% CF, and 0-5-10-5-0% CF SENT Specimens) and the results analyzed to fully analyze the DOE and determine if changes should be made prior to testing the second half of the specimen. The testing done on the first four specimens was labeled “Test 1”. Analysis of Test 1 results showed reliability in the DOE and DOE order and so the second half of the specimen

were test approximately one month after Test 1. The testing done on the second half of the specimens was labeled “Test 2”. Test 2 results tended to indicate more “brittle” material properties than Test 1. The differences between Test 1 and Test 2 are significant and are reviewed in the last section of this discussion and thoroughly investigated in Appendix F. The following sections describe warping, hardness, and tensile results and the difference of Test 1 and Test 2 as they apply to binary changes and gradients of CF in SENT specimen:

### **Warping and Anchoring during SLS process**

Warping results show PA12/CF dimensional stability and the effectiveness of M2 PA12/CF anchoring. The 5% and 10% CF parts have approximately half the warping as the neat PA12 part even with a 2mm 10% CF anchor on the neat PA12 specimen. 10% CF specimen also had slightly less warping than the 5% CF specimen and so warping decreased with both an increase in CF and increase in anchor thickness for the ratios tested. This shows the importance of a balance between both the CF content in anchoring and the number of layers (thickness) of the anchor. CF anchor up to 10% CF was tested and these results cannot be project beyond 10% CF. In fact, the results show 5% CF is a good balance between spreading, sintering, warping, and mechanical strength. As such it is recommend future tests with similar materials use between 5-10% CF for anchoring as an initial setting. However, it is likely other anchoring geometries will be more effective other than simply extending the first layer geometry and then machining off the extra material as done in this test. For this test machining off the excess material worked exceptionally well because the parts were already designed to be machined to size based on required specimen shape and size regardless of warping. However, many parts will not be able to be easily machined based on final part geometry and so different anchoring points and

geometries should be investigated. When exploring anchoring options, it is critical to consider that SLS anchoring generally is not required to dissipate heat as it is in most SLM manufacturing. As such, geometries and methods that are not common in SLM may work well for M2 SLS anchoring. For instance, anchoring geometries with minimal attachment points and area may work well for SLS and facilitate anchor removal. However, in SLM this is likely a poor choice because it will limit heat removal from the part. In SLM heat conduction of the anchor material will also have to be considered when selecting the M2 anchor. Lastly, material properties other than dimensional stability are also important for SLS anchoring. This was seen in Aim 2 when TPE was used as an anchor because of sintered TPE's tolerance to large temperatures fluctuations during the sintering process and not specifically selected based on a dimensional stability during sintering. For HA composites, anchoring was selected based on maximum adhesion to the matrix material to prevent damage to the delicate composite structure designed for osseointegration. In all cases, M2 anchoring has been shown to enable otherwise unworkable geometries and material combination to manufacture via SLS by reducing warping and stabilizing the part enough to prevent sledding and subsequent print failure during the powder application process.

### **Hardness of Sintered Parts**

Both surface and cross section hardness had low variance between tests which indicates uniform sintering with very few voids (if the needle from the hardness test would have hit an unsintered portion or a void the reported hardness would have been notably lower than when the needle hit fully sintered material). The surface hardness similarity to the cross-section hardness coupled with the low standard deviation of the surface hardness results show that nearly all the

loose particles post print were removed from the surface. The uniformity in surface hardness also points to minimal imperfections in layer adhesion otherwise the needle from the hardness testing would have at times penetrated between loose particles on the surface or between the layers and resulted in much lower hardness than when fully sintered particles were encountered. It is also important to note that some of the increase in cross section hardness as compared to the surface hardness is likely from mechanical and heat damage during machining; however, some of this same type of damage would have occurred during the post print sanding process likely to a lesser extent than machining. Lastly, an increase in hardness with an increase in CF is expected as CF is a lot harder than sintered PA12; however, the low standard deviation in these measurements' points to a homogeneous mixture of PA12 and CF (i.e., if the mixture was not homogenous the hardness when the needle hit CF would be much higher than when the needle only hit PA12 matrix material). In total, the consistency and low standard deviation of the hardness tests for each material indicated a well sintered homogeneous blend for each CF ratio tested.

### **Single Edge Notch Tensile Test Single Material, Binary Material, and Binary Gradient Material Comparison**

The comparison in Figure 6.13 between 3mmP tensile results in Aim 3 and SENT results in this Aim. Reduced UTS for the SENT specimen should be expected since all SENT specimen cross sectional area was the area before the notch (with a 3mm notch in a 16mm specimen the load bearing cross section was reduced by nearly 20%). Also, the stress concentrators from the notch would normally decrease tensile properties when compared to a specimen that was not notched. Similarities between the tensile specimens in Aim 3 and the notched specimens are hypothesized to be the PA12/CF interface bonding, microcracking, and stress concentration

along with overall specimen porosity and layer-to-layer adhesion. Further testing may become necessary in the future to quantify this hypothesis.

The tabulated SENT data (Table 6.3 and 6.4) indicate a clear trend that the gradient specimen outperform the other specimen in maximum stress, crack resistance, consistent performance (i.e., small standard deviation), and still had enough plastic deformation to absorb relatively large amounts of energy prior to crack initiation. Generally, implementation of FGM into a system would be governed by UTS, E, wear, and other material properties. An important property concerning crack propagation as tested in the SENT test would be  $C_i$ . Normally if a part is going to stay in service with a defect (simulated by the notch) it would stay in service until the crack began to propagate. As such,  $C_i$  would often be used as the design criteria for the energy test results presented. If this is the case, the differences between the 0-5-0%CF specimen 4 and specimen 5 become much less critical since UTS, E, and  $C_i$  are similar. Overall, the gradient specimen still outperformed the binary specimens in most cases. However, further testing to build a much more robust data repository is required prior to implementing any of these printed material into operational systems.

Crack initiation data for the gradient specimen could have been skewed by the crack being twice as close to the first material change as compared to other specimens. Further testing should be done with the notch equally spaced from the first material change for the gradient and binary materials. 5% CF did appear to be the best compromise with the most consistent results and improvements in material properties when compared to 10% CF specimen performance. 10%CF specimens continued to have sporadic properties like the tensile specimens. 10% inconsistencies were based on similar difficulties during manufacturing discussed in previous aims. However, M2 specimens with 10CF became very consistent with greatly increased

maximum stress and in all cases the gradient specimens with 10% at the core could withstand the highest stress before failure. Possibly the most important aspect of these results is the ability to benefit from the properties of the 10% CF while curtailing the inconsistencies of the 10% CF performance.

10-0-10%CF specimen clearly portrayed many of the benefits of the M2 tests (Figure 6.26) and absorbed nearly the same amount of energy as the very ductile 0% CF SENT specimen. This is especially noteworthy considering over half of the 10-0-10%CF specimen contained the 10% CF blend. When under load, the 10% portion furthest from the crack of the 10-0-10% CF specimen acted like a stiff “backbone” and also dissipated crack energy by multiplying a single crack into multiple cracks when the crack approached this stiff “backbone”. These specimens also had very consistent performance which continued to be a stark contrast to the single material 10%CF composites throughout this research.

Compared to the single material specimen, M2 SENT Specimen also redefined the strain fields at failure. At failure the M2 SENT specimens had dissipated the strain field throughout the entire specimen more than the single material specimens and achieved higher strengths (Figure 6.12a). This was particularly obvious when comparing 10% to gradient specimens, which also indirectly shows a strong matrix bond through CF ratio transitions.

Scanning electron microscopy (Figures 6.19 thru 6.30) directly showed seamless transitions between CF ratios and between ductile to brittle transitions along the fracture. The SEM images showed no perceptible defects or change in the PA12 matrix material when transitioning between CF ratios or changes in fracture mechanics (i.e., ductile to brittle fracture). CF also appeared to be evenly distributed and generally aligned with the raking and fracture direction with strong adherence to the matrix material. All of this pointed to the effectiveness of

the M2 PBF design to change materials (to include changes in fiber concentration) throughout a printed part.

The conceptual implant prototype (Figure 6.31) brought all the discussed M2 PBF techniques together into a single tri-material specimen. The tri-material specimen was anchored with a PA12 base then seamlessly transitioned into HA composite section (simulate osteointegration portions of an implant) into a core of PA12 (simulate an isoelastic structure) and finally blended into a 10% CF blend (simulate a high wear surface). This gives strong evidence to the feasibility of using this technology for future orthopedic implants along with other industries that will benefit from FGMs.

### **SENT Test 1 and Test 2 Differences**

To conclude Aim 4, a second test (“Test 2”) was done approximately 3 weeks after printing and finishing the first test (“Test 1”). Test 2 was performed on the remaining 4 specimens from each printed group after the DOE and results from Test 1 were analyzed. Test 2 specimen sets were stored in ambient air and out of direct sunlight in the “as printed” state (i.e., no post print cleaning or processing was done prior to storage). No changes to the DOE were made and all Test 2 specimens were sanded, machined, notched, and speckled according to Test 1 DOE *shortly prior* to performing Test 2 SENT analysis. Overall, Test 2 results had more brittle characteristics than Test 1 (Figure F.4a).

An initial comparison between the two tests was done by re-notching and “re-pulling” (“Test 3”) the top half and bottom half of the fractured SENT specimens from Test 1 and Test 2. Test 3 results from the “re-pulled” half specimens are NOT directly comparable to the initial tests. Specimen size, strain rate proportionality to specimen dimension, possible strain hardening,

plastic deformation, and other factors between the initial tests and Test 3 make the results of these two tests distinctly different. However, by using the exact specimens that were initially printed at the same time and tested during the original tests helped ensure consistency between the original tests and the “re-pull” test based on blending and print parameters. Test 3 specimens were also subjected to three different environments to test the effect of moisture on the specimens. One set was soaked in water for 24 hours and pulled wet, a second set was dried for 24 hours and pulled directly out of the dryer, and a third set remained in the same storage environment used for Test 1 and Test 2 specimens. Generally, the results of Test 3 showed minimal differences between the wet, dried, and ambient specimens as compared to the differences between Test 1 and Test 2 (Figure F.5). Complete test results of Test 3 are in Appendix F with a discussion of possible reasons for the differences between Test 1 and Test 2. However, a conclusive reason was not found, and further testing is required to investigate the differences between Test 1 and Test 2.

Overall, Test 2 results show material properties are affected by a combination of environmental conditions, storage, preparation, and time since printing. Test 3 results were more representative of Test 1 than Test 2 and the results and discussion of Aim 4 focused on Test 1 results with the same discussion for Test 2 presented in Appendix F. However, most of the trends from Test 1 concerning single material, binary material, and binary gradient material specimens are consistent between Test 1 and Test 2. The previous SENT discussion in this section (“*Single Edge Notch Tensile Test Single Material, Binary Material, and Binary Gradient Material Comparison*”) applies to both Test 1 and Test 2 results. Both tests indicate some clear advantages to FGM manufactured using PBF and the “*Broader Implications*” discussed below apply to both tests.

## **BROADER IMPLICATIONS**

The SENT results point to a promising future for M2 PBF. Binary gradients have demonstrated the ability to increase reliability, delay crack initiation, absorb additional energy, increase tensile strength, dissipate fracture process zone energy, and delay part failure. The implications of this could be far reaching across multiple industries if this technology is matured. The increased reliability would allow the benefits (e.g. high stiffness and low weight) of a material to be used in a FGM which otherwise would not be reliable enough to be implemented into a system based on failure rates. Delayed crack initiation and high energy absorption combat print inconsistencies often found in AM (especially with CF composites) that could allow AM to be used in application requiring strict quality control that was previously unattainable (e.g. medical implants). Dissipating fracture process zone energy and delaying part failure could allow enough time between system damage detection and system failure to shut system down (e.g. land an aircraft after a bird strike) prior to catastrophic failure. All of these implications are in addition to the inherent capability of FGM to functionalize parts based on the capability to implement material LCC (i.e. the implant discussed with CF functionalized for wear and HA functionalize for osseointegration in a single implant).

## **CONCLUSION**

PA12/CF M2 SENT specimen consistently had improved material properties and crack growth resistance when compared to single material specimen. The gradient specimen withstood the most stress and the 10-0-10CF specimen absorbed nearly as much fracture energy as the 0% CF SENT specimen. Fractography results showed seamless transition between CF ratios with the

subsystems designed and implemented in the M2 SLS prototype. Fractography and hardness testing also showed a homogenous CF mixture with consistent sintering of the PA12 matrix. The printed joint implant conceptual prototype consisting of PA12 with functionalized sections of neat PA12, CF blends, and HA blends demonstrated the future impact of this technology as it relates to joint implants. Ultimately, the combination of all these results confirmed this type of M2 manufacturing has a promising future and impact as it relates to joint implants and other areas of industry seeking FGMs.

## Chapter 7: Conclusion

Multi-material manufacturing with functional gradients and local composition control (LCC) is an emerging technology with high demand in numerous industries. This research investigated multi-material (M2) technology with potential applications to joint implants and synthetic joints along with applications aircraft design. Novel manufacturing subsystems combined with established selective laser sintering (SLS) additive manufacturing (AM) processes was pioneered to enable printing M2 parts with LCC and functionally graded materials (FGM). Powder bed fusion (PBF) material blends consisting of low temperature thermoplastics (TP), low temperature thermoplastic elastomers (TPE), carbon fibers (CF), and hydroxyapatite (HA) particulates were explored to match the M2 SLS prototype designed and built.

Aim 1 (M2 SLS invention) and Aim 2 (material compatibility testing) have established feasibility of mechanically blending powders and composites for M2 PBF manufacturing. Aim 3 demonstrated modulus of elasticity can be planned and tuned with the addition of CF in a PA12 matrix by sintering blends with different ratios of CF. Aim 4 characterized fracture resistance and a change in material properties across single material, binary material, and binary gradient material single edge notch tensile (SENT) specimens. An increase in the stability and maximum tensile strength was realized with the addition of binary gradients.

M2 SLS manufacturing, material blending, and M2 composite parts have demonstrated the feasibility of sintering material gradients with 1D gradients and LCC along the build direction with a matrix material mechanically blended with TPE, CF, and HA. Various PA12/CF blends were characterized via ASTM D638-14 modified Type V tensile tests. Printing and characterization of SENT specimens with binary and gradient material interfaces validate the novel M2 PBF subsystems. A M2 printed joint implant conceptual prototype consisting of a

PA12 matrix functionalized with binary changes of CF and HA demonstrated this type of M2 manufacturing has a promising future for joint implants.

## References

- Adibekyan, A., Kononogova, E., Monte, C., & Hollandt, J. (2019). Review of PTB Measurements on Emissivity, Reflectivity and Transmissivity of Semitransparent Fiber-Reinforced Plastic Composites. *International Journal of Thermophysics*, 40(4). <https://doi.org/10.1007/s10765-019-2498-0>
- Ahrari, A., Deb, K., Mohanty, S., & Hattel, J. H. (2017). *Multi-Objective Optimization of Cellular Scanning Strategy in Selective Laser Melting*. <https://doi.org/10.1109/CEC.2017.7969639>
- Alhonkoski, M., Salminen, L., Pakarinen, A., & Veermans, M. (2021). 3D technology to support teaching and learning in health care education – A scoping review. *International Journal of Educational Research*, 105. <https://doi.org/10.1016/j.ijer.2020.101699>
- Allen, N. S., Harrison, M. J., Follows, G. W., & Matthews, V. (n.d.). *Thermal and Photochemical Degradation of Nylon 6,6 Polymer: Part 1 Influence of Amine-Carboxyl End Group Balance on Luminescent Species*.
- Amado, A., Schmid, M., Levy, G., & Wegener, K. (n.d.). *ADVANCES IN SLS POWDER CHARACTERIZATION*.
- American Joint Replacement Registry. (2019). *Annual Report*.
- Anand, S., & Gerner, F. (2014). *Ratnadeep Paul Center for Global Design and Manufacturing Effect of Thermal Deformation on Part Errors in Metal Powder Based Additive Manufacturing Processes*. <https://doi.org/10.1115/1.4026524>
- Arnholt, C. M., White, J. B., Lowell, J. A., Perkins, M. R., Mihalko, W. M., & Kurtz, S. M. (2019). Postmortem Retrieval Analysis of Metallosis and Periprosthetic Tissue Metal Concentrations in Total Knee Arthroplasty. *The Journal of Arthroplasty*. <https://doi.org/10.1016/j.arth.2019.08.038>
- ASTM International. (2006). *Standard Test Method for Tensile Properties of Plastics 1 D638-1. January 2004*, 1–15. <https://doi.org/10.1520/D0638-14.1>
- Auhl, D., Rohnstock, F., Lösckke, O., Schäfer, K., Wang, P., & Wagner, M. H. (2019). 3D-printing quality in relation to melt flow and fusion behavior of polymer materials. *AIP Conference Proceedings*, 2107. <https://doi.org/10.1063/1.5109498>
- Azom. (2016). *Thermoplastics An Introduction*. 1–4.
- Bandyopadhyay, A., & Heer, B. (2018). Additive manufacturing of multi-material structures. In *Materials Science and Engineering R: Reports* (Vol. 129, pp. 1–16). Elsevier Ltd. <https://doi.org/10.1016/j.mser.2018.04.001>
- Bartlett, N. W., Tolley, M. T., Overvelde, J. T. B., Weaver, J. C., Mosadegh, B., Bertoldi, K., Whitesides, G. M., & Wood, R. J. (2015a). A 3D-printed, functionally graded soft robot powered by combustion. *Science*, 349(6244), 161–165. <https://doi.org/10.1126/science.aab0129>
- Bartlett, N. W., Tolley, M. T., Overvelde, J. T. B., Weaver, J. C., Mosadegh, B., Bertoldi, K., Whitesides, G. M., & Wood, R. J. (2015b). A 3D-printed, functionally graded soft robot powered by combustion. *Science*, 349(6244), 161–165. <https://doi.org/10.1126/science.aab0129>
- Bartsch, K., Lange, F., Gralow, M., & Emmelmann, C. (2019). Novel approach to optimized support structures in laser beam melting by combining process simulation with topology

- optimization. *Journal of Laser Applications*, 31(2), 022302.  
<https://doi.org/10.2351/1.5096096>
- Beal, V. E., Paggi, R. A., Salmoria, G. V., & Lago, A. (2009). Statistical evaluation of laser energy density effect on mechanical properties of polyamide parts manufactured by selective laser sintering. *Journal of Applied Polymer Science*, 113(5), 2910–2919.  
<https://doi.org/10.1002/app.30329>
- Berretta, S., Wang, Y., Davies, R., & Ghita, O. R. (2016). Polymer viscosity, particle coalescence and mechanical performance in high-temperature laser sintering. *Journal of Materials Science*, 51(10), 4778–4794. <https://doi.org/10.1007/S10853-016-9761-6>
- Bonnheim, N., Ansari, F., Regis, M., Bracco, P., & Pruitt, L. (2019). Effect of carbon fiber type on monotonic and fatigue properties of orthopedic grade PEEK. *Journal of the Mechanical Behavior of Biomedical Materials*, 90(November 2018), 484–492.  
<https://doi.org/10.1016/j.jmbbm.2018.10.033>
- Bourban, P., Bernet, N., Zanetto, J., Chawla, K., Mortensen, A., & Manson, J. (2001). *Part A: applied science and manufacturing Processing of Fibers and Composites*.
- Bruck, G. J. (2017). *LASER ADDITIVE MANUFACTURE OF THREE - DIMENSIONAL COMPONENTS CONTAINING MULTIPLE MATERIALS FORMED AS INTEGRATED SYSTEMS*.
- Byrne, D. P., Lacroix, D., Planell, J. A., Kelly, D. J., & Prendergast, P. J. (2007). Simulation of tissue differentiation in a scaffold as a function of porosity, Young's modulus and dissolution rate: Application of mechanobiological models in tissue engineering. *Biomaterials*, 28(36), 5544–5554. <https://doi.org/10.1016/j.biomaterials.2007.09.003>
- Cano, A. J., Salazar, A., & Rodríguez, J. (2018). Effect of temperature on the fracture behavior of polyamide 12 and glass-filled polyamide 12 processed by selective laser sintering. *Engineering Fracture Mechanics*, 203(July), 66–80.  
<https://doi.org/10.1016/j.engfracmech.2018.07.035>
- Carrete, I. A., Bermudez, D., Aguirre, C., Alvarez-Primo, F. A., Anil-Kumar, S., Chinolla, P., Gamboa, M., Gonzalez, S. A., Heredia, H. E., Hernandez, A. M., Levario, E., Lindquist, J. R., Luna, V. C., Martinez, L. M., Mendez, V. E., Slager, J. J., Ugarte-Sanchez, L., Urquidi, Y. A., Zamora, A., & Roberson, D. A. (2019). Failure Analysis of Additively Manufactured Polyester Test Specimens Exposed to Various Liquid Media. *Journal of Failure Analysis and Prevention*, 19(2), 418–430. <https://doi.org/10.1007/s11668-019-00614-0>
- Chatham, C. A., Long, T. E., & Williams, C. B. (2019). A review of the process physics and material screening methods for polymer powder bed fusion additive manufacturing. *Progress in Polymer Science*, 93, 68–95.  
<https://doi.org/10.1016/j.progpolymsci.2019.03.003>
- Chávez, F. A., Quiñonez, P. A., & Roberson, D. A. (2019). Hybrid metal/thermoplastic composites for FDM-type additive manufacturing. *Journal of Thermoplastic Composite Materials*, 1–20. <https://doi.org/10.1177/0892705719864150>
- Chen, B., Wang, Y., Berretta, S., & Ghita, O. (2017). Poly Aryl Ether Ketones (PAEKs) and carbon-reinforced PAEK powders for laser sintering. *Journal of Materials Science*, 52(10), 6004–6019. <https://doi.org/10.1007/S10853-017-0840-0>
- Chen, K., Koh, Z. H., Le, K. Q., Teo, H. W. B., Zheng, H., Zeng, J., Zhou, K., & Du, H. (2022). Effects of build positions on the thermal history, crystallization, and mechanical properties of polyamide 12 parts printed by Multi Jet Fusion. *Virtual and Physical Prototyping*, 17(3), 631–648. <https://doi.org/10.1080/17452759.2022.2046478/FORMAT/EPUB>

- Chen, Q., Guillemot, G., Gandin, C.-A., & Bellet, M. (2017a). Three-dimensional finite element thermomechanical modeling of additive manufacturing by selective laser melting for ceramic materials. *Additive Manufacturing*, *16*, 124–137. <https://doi.org/10.1016/j.addma.2017.02.005>
- Chen, Q., Guillemot, G., Gandin, C.-A., & Bellet, M. (2017b). Three-dimensional finite element thermomechanical modeling of additive manufacturing by selective laser melting for ceramic materials. *Additive Manufacturing*, *16*, 124–137. <https://doi.org/10.1016/j.addma.2017.02.005>
- Chianrabutra, S., Mellor, B. G., & Yang, S. (2015). A Dry Powder Material Delivery Device for Multiple Material Additive Manufacturing. *Solid Freeform Fabrication Symposium*, 36–48.
- Chivel, Y. (2017). *Selective laser sintering/melting of multi-material parts*.
- Chowdhuri, M. A. K., & Xia, Z. (2013). Interface bonding strength measurement of a joint between elastic and viscoelastic materials. *Composites Part B: Engineering*, *44*(1), 253–259. <https://doi.org/10.1016/j.compositesb.2012.05.027>
- Chueh, Y. H., Wei, C., Zhang, X., & Li, L. (2020). Integrated laser-based powder bed fusion and fused filament fabrication for three-dimensional printing of hybrid metal/polymer objects. *Additive Manufacturing*, *31*(October 2019), 100928. <https://doi.org/10.1016/j.addma.2019.100928>
- Chung, H. (2008). Processing and properties of functionally graded polymer composites produced by selective laser sintering. In *Itinerario*.
- Chung, H., & Das, S. (2006). Processing and properties of glass bead particulate-filled functionally graded Nylon-11 composites produced by selective laser sintering. *Materials Science and Engineering: A*, *437*(2), 226–234. <https://doi.org/10.1016/J.MSEA.2006.07.112>
- Chung, H., & Das, S. (2008). Functionally graded Nylon-11/silica nanocomposites produced by selective laser sintering. *Materials Science and Engineering: A*, *487*(1–2), 251–257. <https://doi.org/10.1016/J.MSEA.2007.10.082>
- Composites design in the real world. (2003). *Reinforced Plastics*, *47*(8), 50–53. [https://doi.org/10.1016/s0034-3617\(03\)00843-9](https://doi.org/10.1016/s0034-3617(03)00843-9)
- Craft, G., Nussbaum, J., Crane, N., & Harmon, J. P. (2018). Impact of extended sintering times on mechanical properties in PA-12 parts produced by powderbed fusion processes. *Additive Manufacturing*, *22*(July), 800–806. <https://doi.org/10.1016/j.addma.2018.06.028>
- Czelusniak, T., & Amorim, F. L. (n.d.). *Influence of energy density on polyamide 12 processed by SLS: from physical and mechanical properties to microstructural and crystallization evolution*. <https://doi.org/10.1108/RPJ-02-2020-0027>
- Czelusniak, T., & Amorim, F. L. (2020). Influence of energy density on selective laser sintering of carbon fiber-reinforced PA12. *International Journal of Advanced Manufacturing Technology*, *111*(7–8), 2361–2376. <https://doi.org/10.1007/S00170-020-06261-2/FIGURES/12>
- Czelusniak, T., & Amorim, F. L. (2021). Influence of energy density on polyamide 12 processed by SLS: from physical and mechanical properties to microstructural and crystallization evolution. *Rapid Prototyping Journal*, *27*(6), 1189–1205. <https://doi.org/10.1108/RPJ-02-2020-0027>
- Dadbakhsh, S., Verbelen, L., Leuven, K. U., Verkinderen, O., Strobbe, D., Van Puyvelde, P., & Kruth, J.-P. (2017). Effect of PA12 powder reuse on coalescence behaviour and microstructure of SLS parts Special Issue “Trends and Prospects of Biomedical Alloys in Additive Manufacturing” in applied sciences with impact factor of 2.474 View project

- Dimensional Metrology CMM View project Effect of PA12 powder reuse on coalescence behaviour and microstructure of SLS parts. *Article in European Polymer Journal*. <https://doi.org/10.1016/j.eurpolymj.2017.05.014>
- DebRoy, T., Wei, H. L., Zuback, J. S., Mukherjee, T., Elmer, J. W., Milewski, J. O., Beese, A. M., Wilson-Heid, A., De, A., & Zhang, W. (2018a). Additive manufacturing of metallic components – Process, structure and properties. *Progress in Materials Science*, 92, 112–224. <https://doi.org/10.1016/j.pmatsci.2017.10.001>
- DebRoy, T., Wei, H. L., Zuback, J. S., Mukherjee, T., Elmer, J. W., Milewski, J. O., Beese, A. M., Wilson-Heid, A., De, A., & Zhang, W. (2018b). Additive manufacturing of metallic components – Process, structure and properties. *Progress in Materials Science*, 92, 112–224. <https://doi.org/10.1016/j.pmatsci.2017.10.001>
- DiFrancia, C., Ward, T. C., & Claus, R. O. (1996). The single-fibre pull-out test. 1: Review and interpretation. *Composites Part A: Applied Science and Manufacturing*, 27(8), 597–612. [https://doi.org/10.1016/1359-835X\(95\)00069-E](https://doi.org/10.1016/1359-835X(95)00069-E)
- Dino-Lite. (2022). *How to acquire depth information with EdgePLUS AM4917*. Web Page. <https://www.dinolite.us/en/support/dpq>
- Dino-Lite Digital Microscope*. (n.d.). Retrieved June 7, 2021, from [https://www.dinolite.com/faq\\_detail.php?index\\_id=34](https://www.dinolite.com/faq_detail.php?index_id=34)
- Drummer, D., Drexler, M., & Wudy, K. (2014). Impact of heating rate during exposure of laser molten parts on the processing window of PA12 powder. *Physics Procedia*, 56(C), 184–192. <https://doi.org/10.1016/J.PHPRO.2014.08.162>
- Drummer, D., Rietzel, D., & Kühnlein, F. (2010). Development of a characterization approach for the sintering behavior of new thermoplastics for selective laser sintering. *Physics Procedia*, 5(PART 2), 533–542. <https://doi.org/10.1016/j.phpro.2010.08.081>
- Drummer, D., Wudy, K., Kühnlein, F., & Drexler, M. (2012). Polymer Blends for Selective Laser Sintering: Material and Process Requirements. *Physics Procedia*, 39, 509–517. <https://doi.org/10.1016/j.phpro.2012.10.067>
- du Plessis, A., Yelamanchi, B., Fischer, C., Miller, J., Beamer, C., Rogers, K., Cortes, P., Els, J., & MacDonald, E. (2021). Productivity enhancement of laser powder bed fusion using compensated shelled geometries and hot isostatic pressing. *Advances in Industrial and Manufacturing Engineering*, 2, 100031. <https://doi.org/10.1016/j.aime.2021.100031>
- El-Sagheer, I., Abd-Elhady, A. A., El-Din, H., Sallam, M., Naga, S. A. R., Sallam, A. A. ;, Naga, E.-D. M. ;, & Eg, A. A. A. (2021). An Assessment of ASTM E1922 for Measuring the Translaminar Fracture Toughness of Laminated Polymer Matrix Composite Materials. *Polymers 2021, Vol. 13, Page 3129, 13(18)*, 3129. <https://doi.org/10.3390/POLYM13183129>
- El-Wazery, M. S., & El-Desouky, A. R. (2015). A review on Functionally Graded Ceramic-Metal Materials. *Environ. Sci*, 6(5), 1369–1376.
- Erdogan, F. (1995). Fracture mechanics of functionally graded materials. *Composites Engineering*, 5(7), 753–770. [https://doi.org/10.1016/0961-9526\(95\)00029-M](https://doi.org/10.1016/0961-9526(95)00029-M)
- Espera, A. H., Valino, A. D., Palaganas, J. O., Souza, L., Chen, Q., & Advincula, R. C. (2019a). 3D Printing of a Robust Polyamide-12-Carbon Black Composite via Selective Laser Sintering: Thermal and Electrical Conductivity. *Macromolecular Materials and Engineering*, 304(4). <https://doi.org/10.1002/mame.201800718>
- Espera, A. H., Valino, A. D., Palaganas, J. O., Souza, L., Chen, Q., & Advincula, R. C. (2019b). 3D Printing of a Robust Polyamide-12-Carbon Black Composite via Selective Laser

- Sintering: Thermal and Electrical Conductivity. *Macromolecular Materials and Engineering*, 304(4). <https://doi.org/10.1002/mame.201800718>
- Ester, F. J., Larrea, A., & Merino, R. I. (2011). Processing and microstructural study of surface laser remelted Al<sub>2</sub>O<sub>3</sub>–YSZ–YAG eutectic plates. *Journal of the European Ceramic Society*, 31(7), 1257–1268. <https://doi.org/10.1016/j.jeurceramsoc.2010.08.016>
- Fai Leong, K., Tan, K., Chua, C., Leong, K., Cheah, C., Cheang, P., Abu Bakar, M., & Cha, S. (2016). Scaffold development using selective laser sintering of polyetheretherketone-hydroxyapatite biocomposite blends. *Biomater.* 24: 3115-3123 Scaffold development using selective laser sintering of polyetheretherketone-hydroxyapatite biocomposite blends. *Biomaterials*, 24, 3115–3123. [https://doi.org/10.1016/S0142-9612\(03\)00131-5](https://doi.org/10.1016/S0142-9612(03)00131-5)
- Fedorov, A. Y., & Matveenko, V. P. (2016). *Optimization of the mechanical properties of functionally graded materials in the vicinity of singular points. 1785*, 20001. <https://doi.org/10.1063/1.4967030>
- Fleming, C., Sadaghiani, M. S., Stellon, M. A., & Javan, R. (2020). Effectiveness of Three-Dimensionally Printed Models in Anatomy Education for Medical Students and Resident Physicians: Systematic Review and Meta-Analysis. *Journal of the American College of Radiology*, 17(10), 1220–1229. <https://doi.org/10.1016/j.jacr.2020.05.030>
- Forderhase, P., & Deckard, C. (1993). Multiple Powder Delivery For Selective Laser Sintering. In *International Patent WO93/08928*.
- Ganguli, A., Pagan-Diaz, G. J., Grant, L., Cvetkovic, C., Bramlet, M., Vozenilek, J., Kesavadas, T., & Bashir, R. (2018). 3D printing for preoperative planning and surgical training: a review. In *Biomedical Microdevices* (Vol. 20, Issue 3, pp. 1–24). Springer New York LLC. <https://doi.org/10.1007/s10544-018-0301-9>
- Gao, J., Xing, D., Dong, S., & Lin, J. (2020). The primary total knee arthroplasty: A global analysis. *Journal of Orthopaedic Surgery and Research*, 15(1). <https://doi.org/10.1186/s13018-020-01707-5>
- Gayen, D., Tiwari, R., & Chakraborty, D. (2019). Static and dynamic analyses of cracked functionally graded structural components: A review. In *Composites Part B: Engineering* (Vol. 173, p. 106982). Elsevier Ltd. <https://doi.org/10.1016/j.compositesb.2019.106982>
- Gibson, I., & Shi, D. (1997). Material properties and fabrication parameters in selective laser sintering process. *Rapid Prototyping Journal*, 3(4), 129–136. <https://doi.org/10.1108/13552549710191836>
- Gonzalez, R. V., & Green, J. T. (2019). *Hotend for additive manufacturing with an actuated rod in a heated chamber*.
- Goodridge, R. D., Tuck, C. J., & Hague, R. J. M. (2012). Laser sintering of polyamides and other polymers. *Progress in Materials Science*, 57(2), 229–267. <https://doi.org/10.1016/J.PMATSCI.2011.04.001>
- Green, J. T. (2018). *a New Approach To Multiplanar , Real-Time Simulation of Physiological Knee Loads and Synthetic Knee Components Augmented By Local Composition*.
- Green, J. T., Asme, M., Hale, R. F., Hausselle, J., & Gonzalez, R. V. (2017). *A Reconfigurable Multiplanar In Vitro Simulator for Real-Time Absolute Motion With External and Musculotendon Forces*. <https://doi.org/10.1115/1.4037853>
- Green, J. T., Ph, D., Green, J. T., Ph, D., Green, J. T., Ph, D., Slager, J. J., Stewart, C. M., Gonzalez, R. V., & Lopez, M. (2021). Additive Manufacturing Synthetic tissue development using local composition control to biomimic functional gradients and simulate physiological load response (submitted). *Submitted to Additive Manufacturing*.

- Green, J. T., Slager, J. J., Lopez, M., Chanoi, Z., Stewart, C. M., & Gonzalez, R. V. (2021). Local control of mechanical properties through multi-material blending in fused filament fabrication with an active-mixing hotend (submitted). *Submitted to Additive Manufacturing*.
- Greiner, S., Wudy, K., Lanzl, L., & Drummer, D. (2017). *Selective laser sintering of polymer blends: Bulk properties and process behavior*.  
<https://doi.org/10.1016/j.polymertesting.2017.09.039>
- Gul, S., Kausar, A., Mehmood, M., Muhammad, B., & Jabeen, S. (2016). Progress on Epoxy/Polyamide and Inorganic Nanofiller-Based Hybrids: Introduction, Application, and Future Potential. In *Polymer - Plastics Technology and Engineering* (Vol. 55, Issue 17, pp. 1842–1862). Taylor and Francis Inc. <https://doi.org/10.1080/03602559.2016.1185628>
- Gusarov, A. V., Pavlov, M., & Smurov, I. (2011a). Residual Stresses at Laser Surface Remelting and Additive Manufacturing. *Physics Procedia*, 12, 248–254.  
<https://doi.org/10.1016/j.phpro.2011.03.032>
- Gusarov, A. V., Pavlov, M., & Smurov, I. (2011b). Residual Stresses at Laser Surface Remelting and Additive Manufacturing. *Physics Procedia*, 12, 248–254.  
<https://doi.org/10.1016/j.phpro.2011.03.032>
- Hale, R. (2016). *Validation Of An Error Sonification Auditory Feedback Training Validation Of An Error Sonification Auditory Feedback Training Program On Proper Sagittal Plane Squat Technique Program On Proper Sagittal Plane Squat Technique*.
- Hale, R., Green, J., Hausselle, J., Saxby, D., & Gonzalez, R. V. (2018). Quantified in vitro tibiofemoral contact during bodyweight back squats. *Journal of Biomechanics*, 79, 21–30.  
<https://doi.org/10.1016/j.jbiomech.2018.07.002>
- Han, Y. H., Gao, R., Bajpai, I., Kim, B. N., Yoshida, H., Nieto, A., Son, H. W., Yun, J., Jang, B. K., Jung, S., Jingming, Z., Hwang, K. H., Chen, F., Shackelford, J. F., & Kim, S. (2020). Spark plasma sintered bioceramics—from transparent hydroxyapatite to graphene nanocomposites: a review. In *Advances in Applied Ceramics* (Vol. 119, Issue 2, pp. 57–74). Taylor and Francis Ltd. <https://doi.org/10.1080/17436753.2019.1691871>
- Haworth, B., Hopkinson, N., Hitt, D., & Zhong, X. (n.d.). *Shear viscosity measurements on Polyamide-12 polymers for laser sintering*. <https://doi.org/10.1108/13552541311292709>
- Hejmady, P., Van Breemen, L. C. A., Anderson, P. D., & Cardinaels, R. (2019). Laser sintering of polymer particle pairs studied by in situ visualization. *Soft Matter*, 15(6), 1373–1387.  
<https://doi.org/10.1039/c8sm02081g>
- How multi-powder deposition will transform industrial 3D printing*. (n.d.). Retrieved June 10, 2019, from <https://medium.com/@aerosint/how-multi-powder-deposition-will-transform-industrial-3d-printing-fa7c83631091>
- Huiskes, R., Weinans, H., & van Rietbergen, B. (1992). The relationship between stress shielding and bone resorption around total hip stems and the effects of flexible materials. *Clinical Orthopaedics and Related Research*, 124–134.
- ImageJ*. (n.d.). Retrieved June 7, 2021, from <https://imagej.net/>
- Ituarte, I. F., Boddetti, N., Hassani, V., Dunn, M. L., & Rosen, D. W. (2019). Design and additive manufacture of functionally graded structures based on digital materials. *Additive Manufacturing*, 30(July), 100839. <https://doi.org/10.1016/j.addma.2019.100839>
- Jansson, A., & Pejryd, L. (2016). Characterisation of carbon fibre-reinforced polyamide manufactured by selective laser sintering. *Additive Manufacturing*, 9, 7–13.  
<https://doi.org/10.1016/J.ADDMA.2015.12.003>

- Jepson, L., Beaman, J., Bourell, D. L., & Wood, K. (1997). SLS processing of functionally gradient materials. *Solid Freeform Fabrication Symposium*, 67–80.
- Jepson, L. R. (2002). *Multiple Material Selective Laser Sintering*.
- Jepson, L. R., Beaman, J. J., Bourell, D. L., & Wood, K. L. (2000). Multi-Material Selective Laser Sintering : Empirical Studies and Hardware Development. *NSF Design and Manufacturing Grantees Conference, February 2017*, 2–5.
- Jero, P. D., Kerans, R. J., & Parthasarathy, T. A. (1991). Effect of Interfacial Roughness on the Frictional Stress Measured Using Pushout Tests. *Journal of the American Ceramic Society*, 74(11), 2793–2801. <https://doi.org/10.1111/J.1151-2916.1991.TB06845.X>
- Jones, D. B., Sung, R., Weinberg, C., Korelitz, T., & Andrews, R. (2016). Three-Dimensional Modeling May Improve Surgical Education and Clinical Practice. *Surgical Innovation*, 23(2), 189–195. <https://doi.org/10.1177/1553350615607641>
- Kang, K.-T., Son, J., Suh, D.-S., Kwon, S. K., Kwon, O.-R., & Koh, Y.-G. (2018). Patient-specific medial unicompartamental knee arthroplasty has a greater protective effect on articular cartilage in the lateral compartment. *Bone and Joint Research*, 7(1), 20–27. <https://doi.org/10.1302/2046-3758.71.BJR-2017-0115.R2>
- Kaygili, O., Keser, S., Ates, T., Al-Ghamdi, A. A., & Yakuphanoglu, F. (2013). Controlling of dielectrical and optical properties of hydroxyapatite based bioceramics by Cd content. *Powder Technology*, 245, 1–6. <https://doi.org/10.1016/j.powtec.2013.04.012>
- Kennedy, Z. C., & Christ, J. F. (2020). Printing polymer blends through in situ active mixing during fused filament fabrication. *Additive Manufacturing*, 36, 101233. <https://doi.org/10.1016/j.addma.2020.101233>
- Kerans, R. J., & Parthasarathy, T. A. (1991). Theoretical Analysis of the Fiber Pullout and Pushout Tests. *Journal of the American Ceramic Society*, 74(7), 1585–1596. <https://doi.org/10.1111/J.1151-2916.1991.TB07144.X>
- Khademhosseini, A., & Camci-Unal, G. (2018). *3D Bioprinting in Regenerative Engineering: Principles and Applications*.
- Khudiakova, A., Berer, M., Niedermair, S., Plank, B., Truszkiewicz, E., Meier, G., Stepanovsky, H., Wolfahrt, M., Pinter, G., & Lackner, J. (2020). Systematic analysis of the mechanical anisotropy of fibre-reinforced polymer specimens produced by laser sintering. *Additive Manufacturing*, xxx, 101671. <https://doi.org/10.1016/j.addma.2020.101671>
- Kiani, A., Khazaei, S., Badrossamay, M., Foroozmehr, E., & Karevan, M. (2020). An Investigation into Thermal History and Its Correlation with Mechanical Properties of PA12 Parts Produced by Selective Laser Sintering Process. *Journal of Materials Engineering and Performance*, 29(2), 832–840. <https://doi.org/10.1007/S11665-020-04640-0/FIGURES/8>
- Ko, S., Davey, J., Douglass, S., Yang, J., Tuttle, M. E., & Salviato, M. (2019). Effect of the thickness on the fracturing behavior of discontinuous fiber composite structures. *Composites Part A: Applied Science and Manufacturing*, 125, 105520. <https://doi.org/10.1016/J.COMPOSITESA.2019.105520>
- Kontinen, Y. T., Xu, J. W., Pätäälä, H., Imai, S., Waris, V., Li, T. F., Goodman, S. B., Nordsletten, L., & Santavirta, S. (1997). Cytokines in aseptic loosening of total hip replacement. *Current Orthopaedics*, 11(1), 40–47. [https://doi.org/10.1016/S0268-0890\(97\)90050-5](https://doi.org/10.1016/S0268-0890(97)90050-5)
- Krueger, R. (2015). The virtual crack closure technique for modeling interlaminar failure and delamination in advanced composite materials. In *Numerical Modelling of Failure in*

- Advanced Composite Materials* (pp. 3–53). Elsevier Inc. <https://doi.org/10.1016/B978-0-08-100332-9.00001-3>
- Kruth, J.-P., Levy, G., Schindel, R., Craeghs, T., & Yasa, E. (2006). Consolidation of polymer powders by selective laser sintering. *PhD Research Additive Manufacturing - University of Leuven*. [https://d1wqtxts1xzle7.cloudfront.net/34699316/PMI08\\_Kruth\\_Levy\\_Keynote-libre.pdf?1410431321=&response-content-disposition=inline%3B+filename%3DPMI08\\_Kruth\\_Levy\\_Keynote.pdf&Expires=1653019640&Signature=DVzfgV1Omw5XJKwmU5SO-QfJ6WaYHXBjwTBcZv653RtKmbJiWVGv3wEoinCFjVTw7zjdh061~ymxkaBuAmd5F47NKAAaTszXGc08xX9Fs4IFPPfpxxQH~-bFyuJwXwIy7ahjkhCBYK1q4OT6wjeoD8E0SS32z7HyAqDXTG6TBMEcisEyQb8KN-NSX2N6nTTuVy4xaos4zg1xuiuUk0F0N9asbfaqES-ZGeMmYZAunFYbu8nI93kp2Ia4mc4O9SXQ8dseikhDeTQLKqOdcYGt6n3owjT8W9YQuQjD4n6TprZi9WAPT6-pNG5FpeWGR-alk2X8H3wAzfoMzg5vHLwUNw\\_\\_&Key-Pair-Id=APKAJLOHF5GGSLRBV4ZA](https://d1wqtxts1xzle7.cloudfront.net/34699316/PMI08_Kruth_Levy_Keynote-libre.pdf?1410431321=&response-content-disposition=inline%3B+filename%3DPMI08_Kruth_Levy_Keynote.pdf&Expires=1653019640&Signature=DVzfgV1Omw5XJKwmU5SO-QfJ6WaYHXBjwTBcZv653RtKmbJiWVGv3wEoinCFjVTw7zjdh061~ymxkaBuAmd5F47NKAAaTszXGc08xX9Fs4IFPPfpxxQH~-bFyuJwXwIy7ahjkhCBYK1q4OT6wjeoD8E0SS32z7HyAqDXTG6TBMEcisEyQb8KN-NSX2N6nTTuVy4xaos4zg1xuiuUk0F0N9asbfaqES-ZGeMmYZAunFYbu8nI93kp2Ia4mc4O9SXQ8dseikhDeTQLKqOdcYGt6n3owjT8W9YQuQjD4n6TprZi9WAPT6-pNG5FpeWGR-alk2X8H3wAzfoMzg5vHLwUNw__&Key-Pair-Id=APKAJLOHF5GGSLRBV4ZA)
- Kruth, J.-P. P., Mercelis, P., Froyen, L., Rombouts, M., Wang, X., Laoui, T., & Froyen, L. (2004). Binding Mechanisms in Selective Laser Sintering and Selective Laser Melting Reference : *Solid Freeform Fabrication Proceedings*, 2315(5), 357–371. <https://doi.org/10.1108/01445150310698652>
- Kurokawa, M., Uchiyama, Y., Iwai, T., & Nagai, S. (2003). Performance of plastic gear made of carbon fiber reinforced polyamide 12. *Wear*, 254(5–6), 468–473. [https://doi.org/10.1016/S0043-1648\(03\)00020-6](https://doi.org/10.1016/S0043-1648(03)00020-6)
- Kurtz. (2019a). Index. In *PEEK Biomaterials Handbook*. <https://doi.org/10.1016/B978-0-12-812524-3.09991-9>
- Kurtz, S. M. (2011). *PEEK biomaterials handbook*. William Andrew.
- Kurtz, S. M. (2012). An Overview of PEEK Biomaterials. In *PEEK Biomaterials Handbook* (pp. 1–7). William Andrew Publishing. <https://doi.org/10.1016/B978-1-4377-4463-7.10001-6>
- Kurtz, S. M. (2019b). Foreword. *PEEK Biomaterials Handbook*, ix–x. <https://doi.org/10.1016/B978-0-12-812524-3.09987-7>
- Kurtz, S. M., & Devine, J. N. (2007). PEEK biomaterials in trauma, orthopedic, and spinal implants. *Biomaterials*, 28(32), 4845–4869. <https://doi.org/10.1016/J.BIOMATERIALS.2007.07.013>
- Langridge, B., Momin, S., Coumbe, B., Woin, E., Griffin, M., & Butler, P. (2018). Systematic Review of the Use of 3-Dimensional Printing in Surgical Teaching and Assessment. *Journal of Surgical Education*, 75(1), 209–221. <https://doi.org/10.1016/j.jsurg.2017.06.033>
- Langton, D. J., Jameson, S. S., Joyce, T. J., Hallab, N. J., Natu, S., & Nargol, A. V. F. (2009). Early failure of metal-on-metal bearings in hip resurfacing and large-diameter total hip replacement A CONSEQUENCE OF EXCESS WEAR. *THE JOURNAL OF BONE AND JOINT SURGERY*. <https://doi.org/10.1302/0301-620X.92B1>
- Lauke, B. (2007). Stress concentration along curved interfaces as basis for adhesion tests. *Composite Interfaces*, 14(4), 307–320. <https://doi.org/10.1163/156855407780452887>
- Lauke, B., Schüller, T., & Schneider, K. (2003). Determination of interface strength between two polymer materials by a new curved interface tensile test. *Composite Interfaces*, 10(1), 1–15. <https://doi.org/10.1163/156855403763586765>

- Laumer, T., Stichel, T., Raths, M., & Schmidt, M. (2016). Analysis of the influence of different flowability on part characteristics regarding the simultaneous laser beam melting of polymers. *Physics Procedia*, 83, 937–946. <https://doi.org/10.1016/j.phpro.2016.08.098>
- LeBel, M. E., Haverstock, J., Cristancho, S., van Eimeren, L., & Buckingham, G. (2018). Observational Learning During Simulation-Based Training in Arthroscopy: Is It Useful to Novices? *Journal of Surgical Education*, 75(1), 222–230. <https://doi.org/10.1016/j.jsurg.2017.06.005>
- Leu, M. C., Deuser, B. K., Tang, L., Landers, R. G., Hilmas, G. E., & Watts, J. L. (2012). Freeze-form extrusion fabrication of functionally graded materials. *CIRP Annals - Manufacturing Technology*, 61(1), 223–226. <https://doi.org/10.1016/j.cirp.2012.03.050>
- Li, C., Liu, Z. Y., Fang, X. Y., & Guo, Y. B. (2018a). Residual Stress in Metal Additive Manufacturing. *Procedia CIRP*, 71, 348–353. <https://doi.org/10.1016/j.procir.2018.05.039>
- Li, C., Liu, Z. Y., Fang, X. Y., & Guo, Y. B. (2018b). On the Simulation Scalability of Predicting Residual Stress and Distortion in Selective Laser Melting. *Journal of Manufacturing Science and Engineering, Transactions of the ASME*, 140(4). <https://doi.org/10.1115/1.4038893>
- Li, K., Yeung, C. Y., Yeung, K. W. K., & Tjong, S. C. (2012). Sintered hydroxyapatite/polyetheretherketone nanocomposites: Mechanical behavior and biocompatibility. *Advanced Engineering Materials*, 14(4), B155–B165. <https://doi.org/10.1002/adem.201080145>
- Li, L., Koch, M. H. J., & de Jeu, W. H. (2003a). *Crystalline Structure and Morphology in Nylon-12: A Small-and Wide-Angle X-ray Scattering Study*. <https://doi.org/10.1021/ma025732l>
- Li, L., Koch, M. H. J., & de Jeu, W. H. (2003b). Crystalline Structure and Morphology in Nylon-12: A Small- and Wide-Angle X-ray Scattering Study. *Macromolecules*, 36(5), 1626–1632. <https://doi.org/10.1021/MA025732L>
- Li, Y., Feng, Z., Hao, L., Huang, L., Xin, C., Wang, Y., Bilotti, E., Essa, K., Zhang, H., Li, Z., Yan, F., & Peijs, T. (2020). A Review on Functionally Graded Materials and Structures via Additive Manufacturing: From Multi-Scale Design to Versatile Functional Properties. *Advanced Materials Technologies*, 5(6). <https://doi.org/10.1002/admt.201900981>
- Liew, Y., Beveridge, E., Demetriades, A. K., & Hughes, M. A. (2015). 3D printing of patient-specific anatomy: A tool to improve patient consent and enhance imaging interpretation by trainees. *British Journal of Neurosurgery*, 29(5), 712–714. <https://doi.org/10.3109/02688697.2015.1026799>
- Lim, K. H. A., Loo, Z. Y., Goldie, S. J., Adams, J. W., & McMenamin, P. G. (2016). Use of 3D printed models in medical education: A randomized control trial comparing 3D prints versus cadaveric materials for learning external cardiac anatomy. *Anatomical Sciences Education*, 9(3), 213–221. <https://doi.org/10.1002/ase.1573>
- Liu, Y., & Ramakrishna, S. (2019). *Molecular Chain - an overview | ScienceDirect Topics*. <https://www.sciencedirect.com/topics/engineering/molecular-chain>
- Liu, Y., Zhu, L., Zhou, L., & Li, Y. (n.d.). *Microstructure and mechanical properties of reinforced polyamide 12 composites prepared by laser additive manufacturing*. <https://doi.org/10.1108/RPJ-08-2018-0220>
- Lumpe, T. S., Mueller, J., & Shea, K. (2019). Tensile properties of multi-material interfaces in 3D printed parts. *Materials and Design*, 162, 1–9. <https://doi.org/10.1016/j.matdes.2018.11.024>

- Mahamood, R. M., & Akinlabi, E. T. (2017). Types of Functionally Graded Materials and Their Areas of Application. In *Topics in Mining, Metallurgy and Materials Engineering* (pp. 9–21). Springer Science and Business Media Deutschland GmbH. [https://doi.org/10.1007/978-3-319-53756-6\\_2](https://doi.org/10.1007/978-3-319-53756-6_2)
- Mahamood, R. M., Akinlabi, E. T., Shukla, M., & Pityana, S. (2012). Functionally graded material: An overview. *Proceedings of the World Congress on Engineering*, 3, 1593–1597.
- Malekipour, E., & El-Mounayri, H. (n.d.). *Common defects and contributing parameters in powder bed fusion AM process and their classification for online monitoring and control: a review*. <https://doi.org/10.1007/s00170-017-1172-6>
- Martynková, G. S., Slíva, A., Kratošová, G., Barabaszová, K. Č., Študentová, S., Klusák, J., Brožová, S., Dokoupil, T., & Holešová, S. (2021). Polyamide 12 Materials Study of Morpho-Structural Changes during Laser Sintering of 3D Printing. *Polymers 2021, Vol. 13, Page 810*, 13(5), 810. <https://doi.org/10.3390/POLYM13050810>
- Meng, L., Yang, X., Salcedo, E., Baek, D. C., Ryu, J. E., Lu, Z., & Zhang, J. (2020). A Combined Modeling and Experimental Study of Tensile Properties of Additively Manufactured Polymeric Composite Materials. *Journal of Materials Engineering and Performance*, 29(4), 2597–2604. <https://doi.org/10.1007/s11665-020-04746-5>
- Mercelis, P., & Kruth, J.-P. (2006a). Residual stresses in selective laser sintering and selective laser melting. *Rapid Prototyping Journal*, 12/5, 254–265. <https://doi.org/10.1108/13552540610707013>
- Mercelis, P., & Kruth, J.-P. (2006b). Residual stresses in selective laser sintering and selective laser melting. *Rapid Prototyping Journal*, 12/5, 254–265. <https://doi.org/10.1108/13552540610707013>
- Miao, X., & Sun, D. (2010). Graded/gradient porous biomaterials. *Materials*, 3(1), 26–47. <https://doi.org/10.3390/ma3010026>
- Mirzaali, M. J., de la Nava, A. H., Gunashekar, D., Nouri-Goushki, M., Doubrovski, E. L., & Zadpoor, A. A. (2019). Fracture behavior of bio-inspired functionally graded soft-hard composites made by multi-material 3D printing: The case of colinear cracks. *Materials*, 12(7). <https://doi.org/10.3390/MA12172735>
- Mondal, S., De Anda Reyes, M. E., & Pal, U. (2017). Plasmon induced enhanced photocatalytic activity of gold loaded hydroxyapatite nanoparticles for methylene blue degradation under visible light. *RSC Advances*, 7(14), 8633–8645. <https://doi.org/10.1039/C6RA28640B>
- Mumtaz, K., Vora, P., & Hopkinson, N. (2011). A method to eliminate anchors/supports from directly laser melted metal powder bed processes. *22nd Annual International Solid Freeform Fabrication Symposium - An Additive Manufacturing Conference, SFF 2011, August 2011*, 55–64.
- Murr, L. E., Gaytan, S. M., Martinez, E., Medina, F., & Wicker, R. B. (2012). Next generation orthopaedic implants by additive manufacturing using electron beam melting. *International Journal of Biomaterials*, 2012. <https://doi.org/10.1155/2012/245727>
- Naebe, M., & Shirvanimoghaddam, K. (2016). Functionally graded materials: A review of fabrication and properties. In *Applied Materials Today* (Vol. 5, pp. 223–245). Elsevier Ltd. <https://doi.org/10.1016/j.apmt.2016.10.001>
- NIINO, M., HIRAI, T., & WATANABE, R. (1987). Functionally gradient materials. In pursuit of super heat resisting materials for spacecraft. *Journal of the Japan Society for Composite Materials*, 13(6), 257–264. <https://doi.org/10.6089/jscm.13.257>

- Ollivere, B., Darrah, C., Barker, T., Nolan, J., & Porteous, M. J. (2009). Early clinical failure of the Birmingham metal-on-metal hip resurfacing is associated with metallosis and soft-tissue necrosis. *J Bone Joint Surg [Br]*, *8*, 91–1025. <https://doi.org/10.1302/0301-620X.91B8>
- Pandit, H., Glyn-Jones, S., McLardy-Smith, P., Gundle, R., Whitwell, D., Gibbons, C. L. M., Ostlere, S., Athanasou, N., Gill, H. S., & Murray, D. W. (2008). *Pseudotumours associated with metal-on-metal hip resurfacings*. *90*(7). <https://doi.org/10.1302/0301-620X.90B7>
- Paolucci, F., Peters, G. W. M., & Govaert, L. E. (2020). Plasticity-controlled failure of sintered and molded polyamide 12: Influence of temperature and water absorption. *Journal of Applied Polymer Science*, *137*(14), 48525. <https://doi.org/10.1002/APP.48525>
- Parihar, R. S., Setti, S. G., & Sahu, R. K. (2018). Recent advances in the manufacturing processes of functionally graded materials: A review. *IEEE Journal of Selected Topics in Quantum Electronics*, *25*(2), 309–336. <https://doi.org/10.1515/secm-2015-0395>
- Park, S. J., & Seo, M. K. (2011). Modeling of Fiber-Matrix Interface in Composite Materials. *Interface Science and Technology*, *18*, 739–776. <https://doi.org/10.1016/B978-0-12-375049-5.00009-8>
- Parry, L. A., Ashcroft, I. A., & Wildman, R. D. (2019). Geometrical effects on residual stress in selective laser melting. *Additive Manufacturing*, *25*, 166–175. <https://doi.org/10.1016/J.ADDMA.2018.09.026>
- Pavan, M., Faes, M., Strobbe, D., Van Hooreweder, B., Craeghs, T., Moens, D., & Dewulf, W. (2017). On the influence of inter-layer time and energy density on selected critical-to-quality properties of PA12 parts produced via laser sintering. *Polymer Testing*, *61*, 386–395. <https://doi.org/10.1016/j.polymertesting.2017.05.027>
- Pelclova, D., Sklensky, M., Janicek, P., & Lach, K. (2012). *Clinical Toxicology Severe cobalt intoxication following hip replacement revision: Clinical features and outcome Severe cobalt intoxication following hip replacement revision: Clinical features and outcome*. <https://doi.org/10.3109/15563650.2012.670244>
- Peng, S.-Y. (2008). Processing and properties of functionally graded polymer composites produced by selective laser sintering. In *Itinerario*.
- Pesetskii, S. S., Fedorov, V. D., Jurkowski, B., & Polosmak, N. D. (1999). Blends of thermoplastic polyurethanes and polyamide 12: Structure, molecular interactions, relaxation, and mechanical properties. *Journal of Applied Polymer Science*, *74*(5), 1054–1070. [https://doi.org/10.1002/\(SICI\)1097-4628\(19991031\)74:5<1054::AID-APP3>3.0.CO;2-M](https://doi.org/10.1002/(SICI)1097-4628(19991031)74:5<1054::AID-APP3>3.0.CO;2-M)
- Pinkerton, A. J. (2016). [INVITED] Lasers in additive manufacturing. *Optics and Laser Technology*, *78*, 25–32. <https://doi.org/10.1016/j.optlastec.2015.09.025>
- Pitkin, M. (2008). One lesson from arthroplasty to osseointegration in search for better fixation of in-bone implanted prosthesis. In *Journal of Rehabilitation Research and Development* (Vol. 45, Issue 4, p. vii). NIH Public Access. <https://doi.org/10.1682/JRRD.2007.11.0192>
- Rajesh, J. J., Bijwe, J., & Venkataraman, B. (2002). Effect of water absorption on erosive wear behaviour of polyamides. *Journal of Material Science*.
- Revell, P. A., Al-Saffar, N., & Kobayashi, A. (1997). Biological reaction to debris in relation to joint prostheses. *Proceedings of the Institution of Mechanical Engineers, Part H: Journal of Engineering in Medicine*, *211*(2), 187–197. <https://doi.org/10.1243/0954411971534304>
- Roberts, I. A. (2012a). Investigation of Residual Stresses in the Laser Melting of Metal Powders in Additive Layer Manufacturing. *Journal of Materials Processing Technology*, *68*(11–12), 849–869. <https://doi.org/10.1007/s00170-007-1181-y>

- Roberts, I. A. (2012b). Investigation of Residual Stresses in the Laser Melting of Metal Powders in Additive Layer Manufacturing. *Journal of Materials Processing Technology*, 68(11–12), 849–869. <https://doi.org/10.1007/s00170-007-1181-y>
- Roberts, V. I., Esler, C. N. A., & Harper, W. M. (2007). A 15-year follow-up study of 4606 primary total knee replacements. *The Journal of Bone and Joint Surgery. British Volume*, 89-B(11), 1452–1456. <https://doi.org/10.1302/0301-620x.89b11.19783>
- Rodzeń, K., Sharma, P. K., McIlhagger, A., Mokhtari, M., Dave, F., Tormey, D., Sherlock, R., Meenan, B. J., & Boyd, A. (2021). The direct 3D printing of functional PEEK/hydroxyapatite composites via a fused filament fabrication approach. *Polymers*, 13(4), 1–18. <https://doi.org/10.3390/polym13040545>
- Saleh, B., Jiang, J., Fathi, R., Al-hababi, T., Xu, Q., Wang, L., Song, D., & Ma, A. (2020). 30 Years of functionally graded materials: An overview of manufacturing methods, Applications and Future Challenges. *Composites Part B: Engineering*, 201(August), 108376. <https://doi.org/10.1016/j.compositesb.2020.108376>
- Sames, W. J., List, F. A., Pannala, S., Dehoff, R. R., & Babu, S. S. (2016). *The metallurgy and processing science of metal additive manufacturing FULL CRITICAL REVIEW The metallurgy and processing science of metal additive manufacturing*. <https://doi.org/10.1080/09506608.2015.1116649>
- Santosa, J., Jing, D., & Das, S. (n.d.). *EXPERIMENTAL AND NUMERICAL STUDY ON THE FLOW OF FINE POWDERS FROM SMALL-SCALE HOPPERS APPLIED TO SLS MULTI-MATERIAL DEPOSITION-PART I*.
- Schmid, M., & Wegener, K. (2016a). Additive Manufacturing: Polymers applicable for laser sintering (LS). *Procedia Engineering*, 149(June), 457–464. <https://doi.org/10.1016/j.proeng.2016.06.692>
- Schmid, M., & Wegener, K. (2016b). Additive Manufacturing: Polymers applicable for laser sintering (LS). *Procedia Engineering*, 149, 457–464. <https://doi.org/10.1016/j.proeng.2016.06.692>
- Schmidt, M., Pohle, D., & Rechtenwald, T. (2007). Selective Laser Sintering of PEEK. *CIRP Annals*, 56(1), 205–208. <https://doi.org/10.1016/J.CIRP.2007.05.097>
- Scholes, S. C., & Unsworth, A. (2007). The wear properties of CFR-PEEK-OPTIMA articulating against ceramic assessed on a multidirectional pin-on-plate machine. *Proceedings of the Institution of Mechanical Engineers, Part H: Journal of Engineering in Medicine*, 221(3), 281–289. <https://doi.org/10.1243/09544119JEIM224>
- Scholes, S. C., & Unsworth, A. (2009). Wear studies on the likely performance of CFR-PEEK/CoCrMo for use as artificial joint bearing materials. *Journal of Materials Science: Materials in Medicine*, 20(1), 163–170. <https://doi.org/10.1007/s10856-008-3558-3>
- Sedmak, S. A., Golubović, Z. Z., Murariu, A. C., & Sedmak, A. S. (2018). Numerical simulation of tensile testing of PE 80 polymer specimens. *Thermal Science*, 22(1), 641–649. <https://doi.org/10.2298/TSCI170219203S>
- Shishkovsky, I., Nagulin, K., & Sherbakov, V. (n.d.). *Laser sinterability and characterization of oxide nano ceramics reinforced to biopolymer matrix*. <https://doi.org/10.1007/s00170-014-6633-6>
- Singh, J. A., Yu, S., Chen, L., & Cleveland, J. D. (2019). Rates of total joint replacement in the United States: Future projections to 2020–2040 using the national inpatient sample. *Journal of Rheumatology*, 46(9), 1134–1140. <https://doi.org/10.3899/jrheum.170990>

- Sintratec. (2021a). Sintratec PA12 Material and Tensile Data Sheet. In *Sintratec Test Data*.  
[https://cdn.shopify.com/s/files/1/2574/6810/files/Factsheet\\_Tensile\\_Test\\_Sintratec\\_TPE\\_EN.pdf?6692680011026805216](https://cdn.shopify.com/s/files/1/2574/6810/files/Factsheet_Tensile_Test_Sintratec_TPE_EN.pdf?6692680011026805216)
- Sintratec. (2021b). Sintratec TPE Material and Tensile Data Sheet. In *Sintratec Test Data*.  
[https://cdn.shopify.com/s/files/1/2574/6810/files/Factsheet\\_Tensile\\_Test\\_Sintratec\\_PA12\\_EN.pdf?2563564693558467541](https://cdn.shopify.com/s/files/1/2574/6810/files/Factsheet_Tensile_Test_Sintratec_PA12_EN.pdf?2563564693558467541)
- Sloan, M., Premkumar, A., & Sheth, N. P. (2018). Projected volume of primary total joint arthroplasty in the u.s., 2014 to 2030. *Journal of Bone and Joint Surgery - American Volume*, 100(17), 1455–1460. <https://doi.org/10.2106/JBJS.17.01617>
- Sola, A., Bellucci, D., & Cannillo, V. (2016). Functionally graded materials for orthopedic applications – an update on design and manufacturing. In *Biotechnology Advances* (Vol. 34, Issue 5, pp. 504–531). Elsevier Inc. <https://doi.org/10.1016/j.biotechadv.2015.12.013>
- Song, J., Xiang, D., Wang, S., Liao, Z., Lu, J., Liu, Y., Liu, W., & Peng, Z. (2018). In vitro wear study of PEEK and CFRPEEK against UHMWPE for artificial cervical disc application. *Tribology International*, 122(February), 218–227.  
<https://doi.org/10.1016/j.triboint.2018.02.034>
- Steuben, J. C., Iliopoulos, A. P., & Michopoulos, J. G. (2016a). Discrete element modeling of particle-based additive manufacturing processes. *Computer Methods in Applied Mechanics and Engineering*, 305, 537–561. <https://doi.org/10.1016/j.cma.2016.02.023>
- Steuben, J. C., Iliopoulos, A. P., & Michopoulos, J. G. (2016b). Implicit slicing for functionally tailored additive manufacturing. *CAD Computer Aided Design*, 77, 107–119.  
<https://doi.org/10.1016/j.cad.2016.04.003>
- Stucker, B., L.Starr, T., & J.Gornet, T. (2014). Powdered bed fusion systems, apparatus and processes for multi-material part production. In *United States Patent Application Publication*.
- Tampieri, A., Celotti, G., Sprio, S., Delcogliano, A., & Franzese, S. (2001). Porosity-graded hydroxyapatite ceramics to replace natural bone. *Biomaterials*, 22(11), 1365–1370.  
[https://doi.org/10.1016/S0142-9612\(00\)00290-8](https://doi.org/10.1016/S0142-9612(00)00290-8)
- Tan, K. H., Chua, C. K., Leong, K. F., Cheah, C. M., Cheang, P., Abu Bakar, M. S., & Cha, S. W. (2003). Scaffold development using selective laser sintering of polyetheretherketone-hydroxyapatite biocomposite blends. *Biomaterials*, 24(18), 3115–3123.  
[https://doi.org/10.1016/S0142-9612\(03\)00131-5](https://doi.org/10.1016/S0142-9612(03)00131-5)
- Tan, L. J., Zhu, W., & Zhou, K. (2020). Recent Progress on Polymer Materials for Additive Manufacturing. *Advanced Functional Materials*, August.  
<https://doi.org/10.1002/adfm.202003062>
- TANAKA, K., MIZUNO, S., HONDA, H., KATAYAMA, T., & ENOKI, S. (2013). Effect of Water Absorption on the Mechanical Properties of Carbon Fiber/Polyamide Composites. *Journal of Solid Mechanics and Materials Engineering*, 7(5), 520–529.  
<https://doi.org/10.1299/JMMP.7.520>
- Tang, H., Chen, H., Sun, Q., Chen, Z., & Yan, W. (2021a). Experimental and computational analysis of structure-property relationship in carbon fiber reinforced polymer composites fabricated by selective laser sintering. *Composites Part B: Engineering*, 204(October 2020).  
<https://doi.org/10.1016/j.compositesb.2020.108499>
- Tang, H., Chen, H., Sun, Q., Chen, Z., & Yan, W. (2021b). Experimental and computational analysis of structure-property relationship in carbon fiber reinforced polymer composites

- fabricated by selective laser sintering. *Composites Part B: Engineering*, 204(October 2020). <https://doi.org/10.1016/j.compositesb.2020.108499>
- Taylor Green, J., & Taylor, J. (2018). *A New Approach To Multiplanar, Real-Time Simulation Of Physiological Knee Loads And Synthetic Knee Components Augmented By Local Composition Control In Fused Filament Fabrication*.
- Tobolsky, A. V. (1960). *Properties and structure of polymers*.
- Tofail, S. A. M., Koumoulos, E. P., Bandyopadhyay, A., Bose, S., O'Donoghue, L., & Charitidis, C. (2018). Additive manufacturing: scientific and technological challenges, market uptake and opportunities. *Materials Today*, 21(1), 22–37. <https://doi.org/10.1016/J.MATTOD.2017.07.001>
- Türk, D.-A., Brenni, F., Zogg, M., & Meboldt, M. (2017). Mechanical characterization of 3D printed polymers for fiber reinforced polymers processing. *Materials & Design*, 118, 256–265. <https://doi.org/10.1016/J.MATDES.2017.01.050>
- Udupa, G., Rao, S. S., & Gangadharan, K. V. (2014). Functionally Graded Composite Materials: An Overview. *Procedia Materials Science*, 5, 1291–1299. <https://doi.org/10.1016/J.MSPRO.2014.07.442>
- Valsamis, E. M., Golubic, R., Glover, T. E., Husband, H., Hussain, A., & Jenabzadeh, A. R. (2018). Modeling Learning in Surgical Practice. *Journal of Surgical Education*, 75(1), 78–87. <https://doi.org/10.1016/j.jsurg.2017.06.015>
- Vasquez, G. M., Majewski, C. E., Haworth, B., & Hopkinson, N. (2014). A targeted material selection process for polymers in laser sintering. *Additive Manufacturing*, 1, 127–138. <https://doi.org/10.1016/j.addma.2014.09.003>
- Veruva, S. Y., Lanman, T. H., Isaza, J. E., Freeman, T. A., Kurtz, S. M., & Steinbeck, M. J. (2017). Periprosthetic UHMWPE Wear Debris Induces Inflammation, Vascularization, and Innervation After Total Disc Replacement in the Lumbar Spine. *Clinical Orthopaedics and Related Research®*, 475(5), 1369–1381. <https://doi.org/10.1007/s11999-016-4996-8>
- Wang, A., Lin, R., Stark, C., & Dumbleton, J. H. (1999). Suitability and limitations of carbon fiber reinforced PEEK composites as bearing surfaces for total joint replacements. *Wear*, 225–229, 724–727. [https://doi.org/10.1016/S0043-1648\(99\)00026-5](https://doi.org/10.1016/S0043-1648(99)00026-5)
- Wang, S., Yao, Y., Tang, C., Li, G., & Cui, J. (2021). Mechanical characteristics, constitutive models and fracture behaviors of short basalt fiber reinforced thermoplastic composites under varying strain rates. *Composites Part B: Engineering*, 218, 108933. <https://doi.org/10.1016/j.compositesb.2021.108933>
- Wang, X., Jiang, M., Zhou, Z., Gou, J., & Hui, D. (2017a). 3D printing of polymer matrix composites: A review and prospective. *Composites Part B: Engineering*, 110, 442–458. <https://doi.org/10.1016/J.COMPOSITESB.2016.11.034>
- Wang, X., Jiang, M., Zhou, Z., Gou, J., & Hui, D. (2017b). 3D printing of polymer matrix composites: A review and prospective. *Composites Part B: Engineering*, 110, 442–458. <https://doi.org/10.1016/J.COMPOSITESB.2016.11.034>
- Weber, R., Hafner, M., Michalowksi, A., Graf, T., & Emmelmann, C. (2012). Influence of laser cutting parameters on CFRP part quality. *J. Mach. Tools Manuf*, 39(2), 253–258. <https://doi.org/10.1364/OE.22.001474>
- Wei, C., Sun, Z., Chen, Q., Liu, Z., & Li, L. (2019). *Additive Manufacturing of Horizontal and 3D Functionally Graded 316L/Cu10Sn Components via Multiple Material Selective Laser Melting*. <https://doi.org/10.1115/1.4043983>

- Whitehead, J., & Lipson, H. (2020). Inverted multi-material laser sintering. *Additive Manufacturing*, *36*, 101440. <https://doi.org/10.1016/j.addma.2020.101440>
- Witzleb, W.-C., Ziegler, J., Krummenauer, F., Neumeister, V., Guenther, K.-P., & Witzleb, C. (2006). Acta Orthopaedica Exposure to chromium, cobalt and molybdenum from metal-on-metal total hip replacement and hip resurfacing arthroplasty Exposure to chromium, cobalt and molybdenum from metal-on-metal total hip replacement and hip resurfacing arthroplast. *Acta Orthopaedica*, *77*(5), 697–705. <https://doi.org/10.1080/17453670610012863>
- Wolford, M. L., Palso, K., & Bercovitz, A. (2015). Hospitalization for total hip replacement among inpatients aged 45 and over: United States, 2000-2010. *NCHS Data Brief*, *186*, 1–8.
- Woodfield, T. B. F., Van Blitterswijk, C. A., De Wijn, J., Sims, T. J., Hollander, A. P., & Riesle, J. (2005). Polymer scaffolds fabricated with pore-size gradients as a model for studying the zonal organization within tissue-engineered cartilage constructs. *Tissue Engineering*, *11*(9–10), 1297–1311. <https://doi.org/10.1089/ten.2005.11.1297>
- Wörz, A., & Drummer, D. (2018a). *Understanding Hatch-Dependent Part Properties in SLS*.
- Wörz, A., & Drummer, D. (2018b). *Understanding Hatch-Dependent Part Properties in SLS*.
- Wudy, K., Drummer, D., Kühnlein, F., & Drexler, M. (2014). Influence of degradation behavior of polyamide 12 powders in laser sintering process on produced parts. *AIP Conference Proceedings*, *1593*, 691–695. <https://doi.org/10.1063/1.4873873>
- Yadroitsev, I., Gusarov, A., Yadroitsava, I., & Smurov, I. (2010). Single track formation in selective laser melting of metal powders. *Journal of Materials Processing Technology*, *210*(12), 1624–1631. <https://doi.org/10.1016/j.jmatprotec.2010.05.010>
- Yan, C., Hao, L., Xu, L., & Shi, Y. (2011a). Preparation, characterisation and processing of carbon fibre/polyamide-12 composites for selective laser sintering. *Composites Science and Technology*, *71*(16), 1834–1841. <https://doi.org/10.1016/j.compscitech.2011.08.013>
- Yan, C., Hao, L., Xu, L., & Shi, Y. (2011b). Preparation, characterisation and processing of carbon fibre/polyamide-12 composites for selective laser sintering. *Composites Science and Technology*, *71*(16), 1834–1841. <https://doi.org/10.1016/j.compscitech.2011.08.013>
- Yan, C., Shi, Y., Li, Z., Wen, S., & Wei, Q. (2021). Selective laser sintering forming accuracy control. In *Selective Laser Sintering Additive Manufacturing Technology* (pp. 671–716). Elsevier. <https://doi.org/10.1016/b978-0-08-102993-0.00005-9>
- Yan, M., Tian, X., Peng, G., Li, D., & Zhang, X. (2018). High temperature rheological behavior and sintering kinetics of CF/PEEK composites during selective laser sintering. *Composites Science and Technology*, *165*, 140–147. <https://doi.org/10.1016/J.COMPSCITECH.2018.06.023>
- Yao, D., An, X., Fu, H., Zhang, H., Yang, X., Zou, Q., & Dong, K. (2021). Dynamic investigation on the powder spreading during selective laser melting additive manufacturing. *Additive Manufacturing*, *37*(November 2020), 101707. <https://doi.org/10.1016/j.addma.2020.101707>
- Yuan, S., Shen, F., Chua, C. K., & Zhou, K. (2019). Polymeric composites for powder-based additive manufacturing: Materials and applications. *Progress in Polymer Science*, *91*(December), 141–168. <https://doi.org/10.1016/j.progpolymsci.2018.11.001>
- Zaami, A., Baran, I., Bor, T. C., & Akkerman, R. (2021). Optical characterization of fiber-reinforced thermoplastic tapes for laser-based composite manufacturing. *Composites Part A: Applied Science and Manufacturing*, *146*. <https://doi.org/10.1016/j.compositesa.2021.106402>

- Zaeh, M. F., & Branner, G. (2010). Investigations on residual stresses and deformations in selective laser melting. *Production Engineering*, 4(1), 35–45. <https://doi.org/10.1007/s11740-009-0192-y>
- Zhang, J., & Adams, A. (2016). Understanding thermal aging of non-stabilized and stabilized polyamide 12 using 1H solid-state NMR. *Polymer Degradation and Stability*, 134, 169–178. <https://doi.org/10.1016/j.polymdegradstab.2016.10.006>
- Zhang, Y., Guillemot, G., Bernacki, M., & Bellet, M. (2018). Macroscopic thermal finite element modeling of additive metal manufacturing by selective laser melting process. *Computer Methods in Applied Mechanics and Engineering*, 331, 514–535. <https://doi.org/10.1016/j.cma.2017.12.003>
- Zhao, M., Wudy, K., & Drummer, D. (2018). Crystallization kinetics of polyamide 12 during Selective laser sintering. *Polymers*, 10(2). <https://doi.org/10.3390/POLYM10020168>
- Zheng, Y. X., Yu, D. F., Zhao, J. G., Wu, Y. L., & Zheng, B. (2016). 3D Printout Models vs. 3D-Rendered Images: Which Is Better for Preoperative Planning? *Journal of Surgical Education*, 73(3), 518–523. <https://doi.org/10.1016/j.jsurg.2016.01.003>
- Zhu, W., Yan, C., Shi, Y., Wen, S., Liu, J., Wei, Q., & Shi, Y. (2016). A novel method based on selective laser sintering for preparing high-performance carbon fibres/polyamide12/epoxy ternary composites. *Scientific Reports*, 6. <https://doi.org/10.1038/SREP33780>

## Acronyms

ACL – Anterior Cruciate Ligament

C – Celsius

CF – Carbon Fiber

E – Modulus of Elasticity

FGM – Functionally Graded Material

FPZ – Fracture Process Zone

HA – Hydroxyapatite

HIP – Hot Isostatic Pressing

LCC – Local Composition Control

LEFM – Linear Elastic Mechanics

PA11 – Polyamide 11 (Nylon-11)

PA12 – Polyamide 12 (Nylon-12)

PBF – Powder Bed Fusion

PID – Proportional Integral Controller (PID)

SLA - Stereolithography

SLM – Selective Laser Melting

SLS – Selective Laser Sintering

STL – Standard Triangle/Tessellation Language

$T_m$  – Melting Temperature

$T_r$  – Recrystallization Temperature

TP – Thermoplastic

TPE – Thermoplastic Elastomer

TPU – Thermoplastic Polyurethane

U – Fracture Energy (typical units MJ/mm<sup>3</sup>)

UHMWPE – Ultra-high-molecular-weight polyethylene (UHMWPE)

UTJLS – University of Texas Joint Load Simulator

UTS – Ultimate Tensile Strength

FATC – Femoral ACL Tibial Complex

VM – Von Misses Stress

W – watt

$\epsilon_{xx}$  (also  $e_{xx}$ ) – Transverse/Lateral Strain

$\epsilon_{xy}$  (also  $e_{xy}$ ) – Shear Strain

$\epsilon_{yy}$  (also  $e_{yy}$ ) – Axial/Normal Strain

$\lambda$  – wavelength

$\nu$  – Poisson's ratio

**Appendix A: UTEP Disclosure D2020-0015**

Appendix A contains University of Texas at El Paso Disclosure D2020-0015 originally submitted on July 24<sup>th</sup> 2020.

The University of Texas at El Paso  
Disclosure D2020-0015

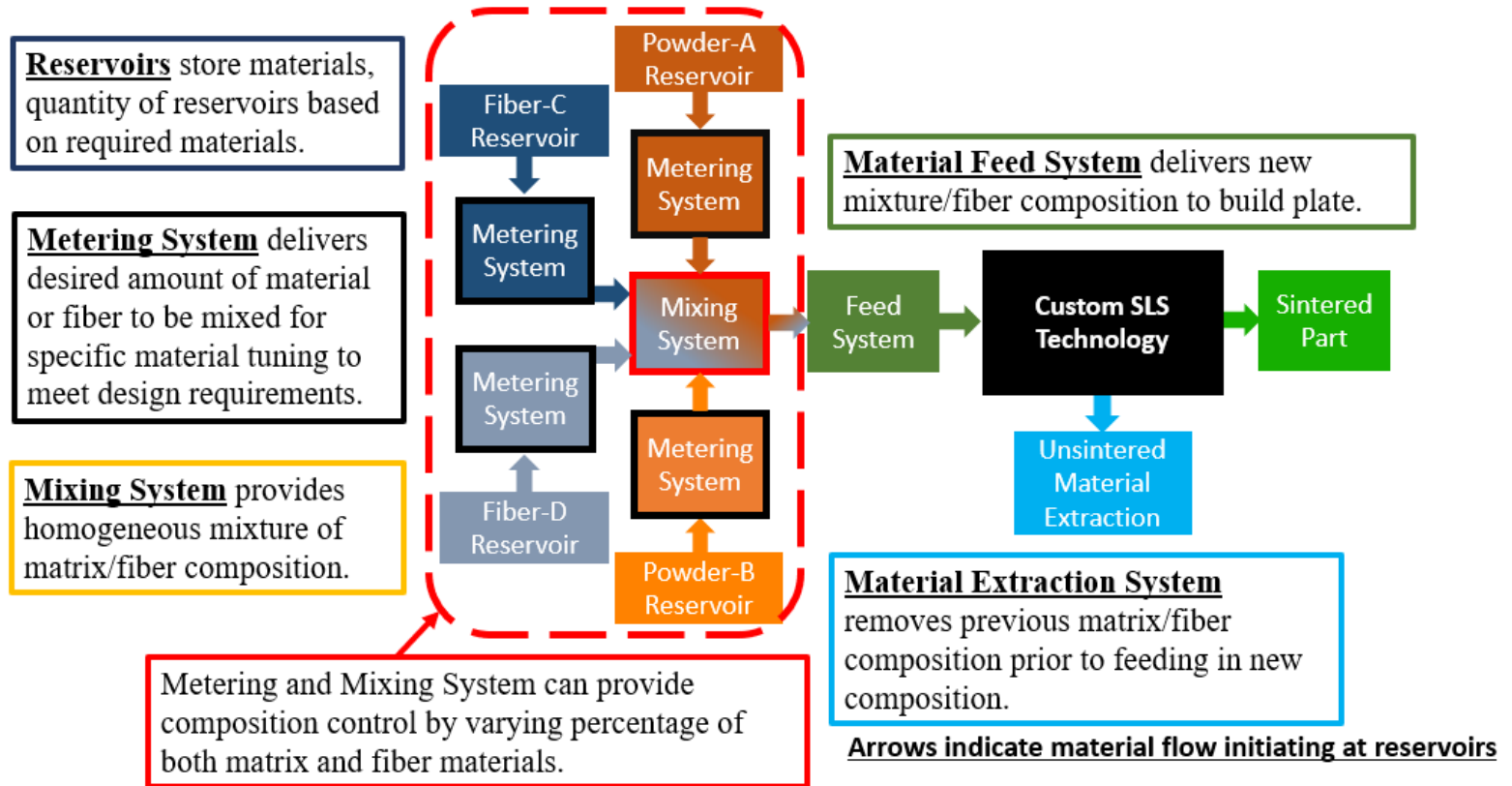
“Multiple Material Local Composition  
Control Selective Laser Sintering System”

Author: Jonathan Slager

[jjslager@miners.utep.edu](mailto:jjslager@miners.utep.edu)

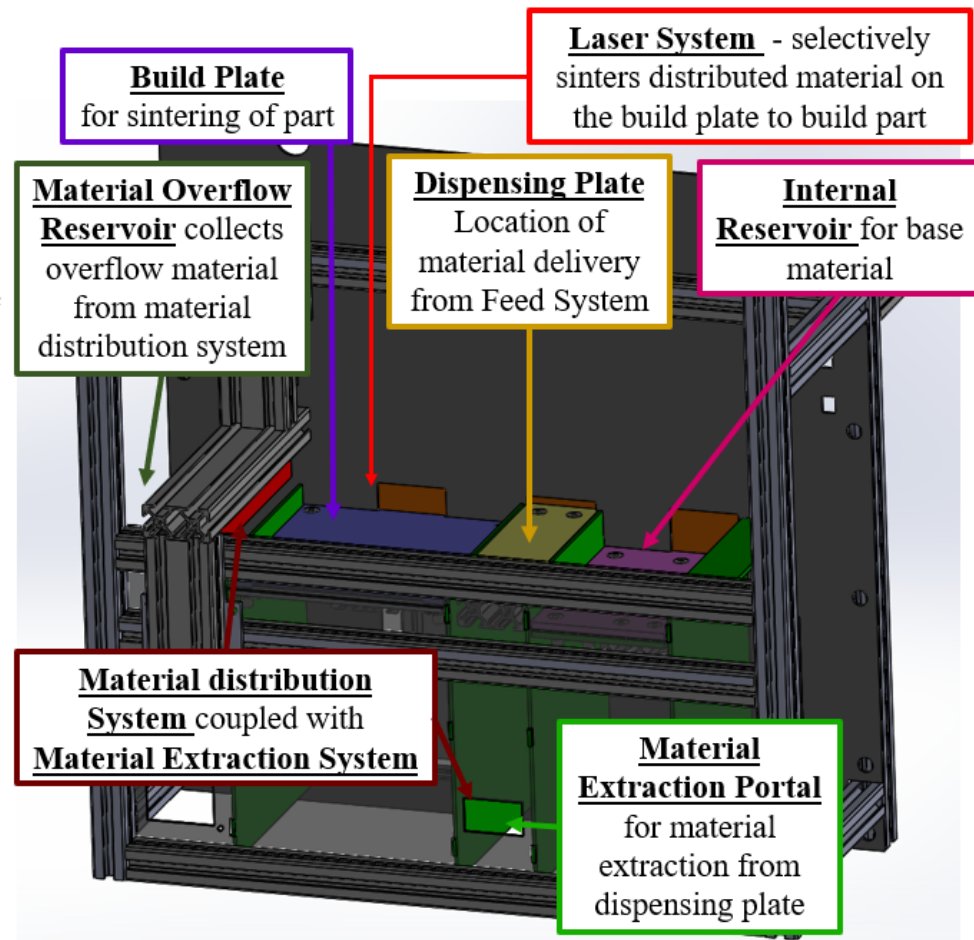
Version 2020-07-24

# Multiple Material LCC SLS System Block Diagram



# Custom SLS Design

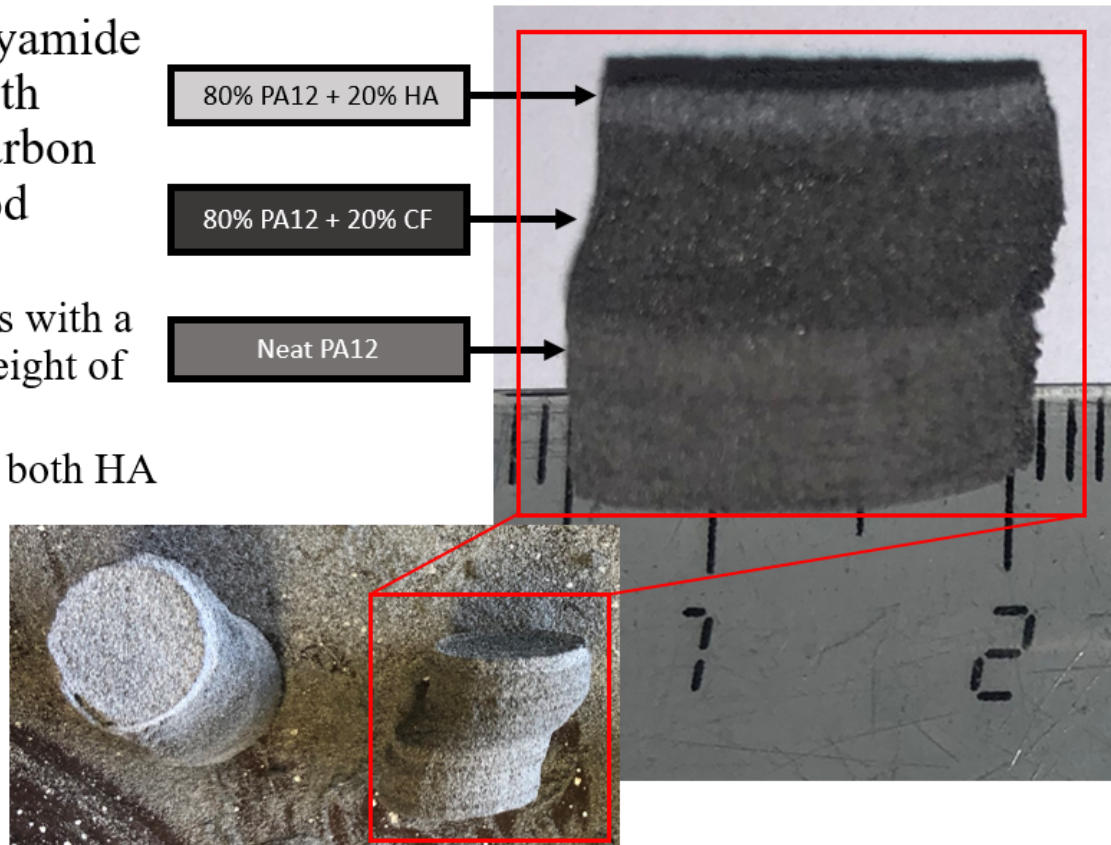
- **Internal Reservoir** mixture remains in the system at all times and can be dispensed anytime.
- **Dispensing Plate** accepts new material from feed system and can be cleaned through material extraction portal prior to delivery of the next material.
- **Part Anchoring** part may be anchored to build plate to secure part during material extraction.
- **Material distribution System** spreads material over build plate/part and sets layer height.
- **Material Extraction System** removes material to prevent contamination with new material delivery.



# Material Testing Preliminary Results

- Preliminary results with Polyamide 12 (PA12) powder mixed with Hydroxyapatite (HA) and carbon fiber (CF) demonstrated good bonding between mixtures.

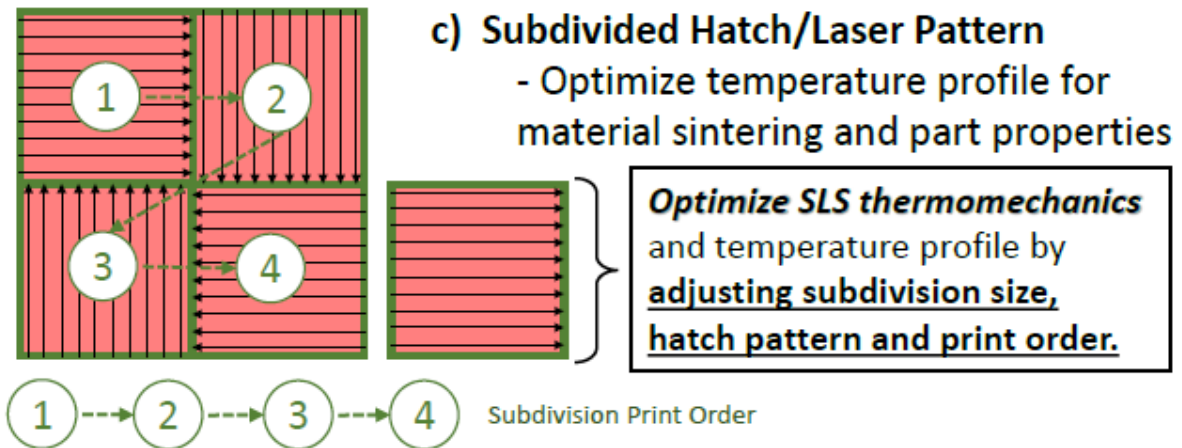
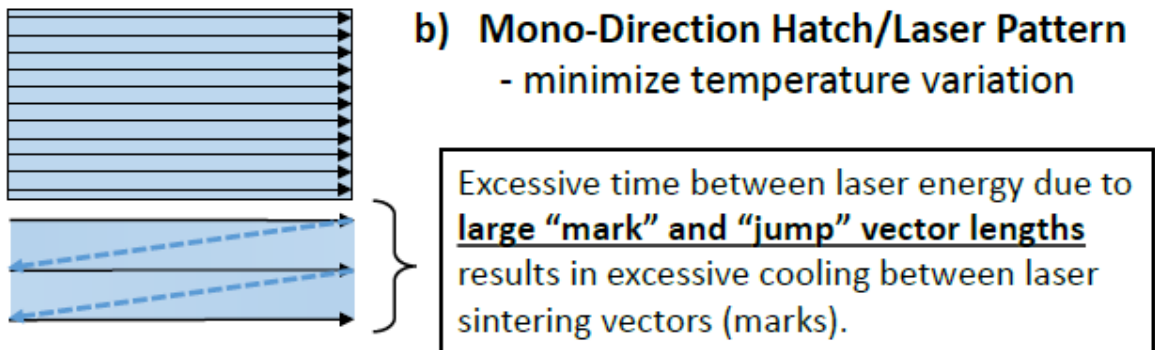
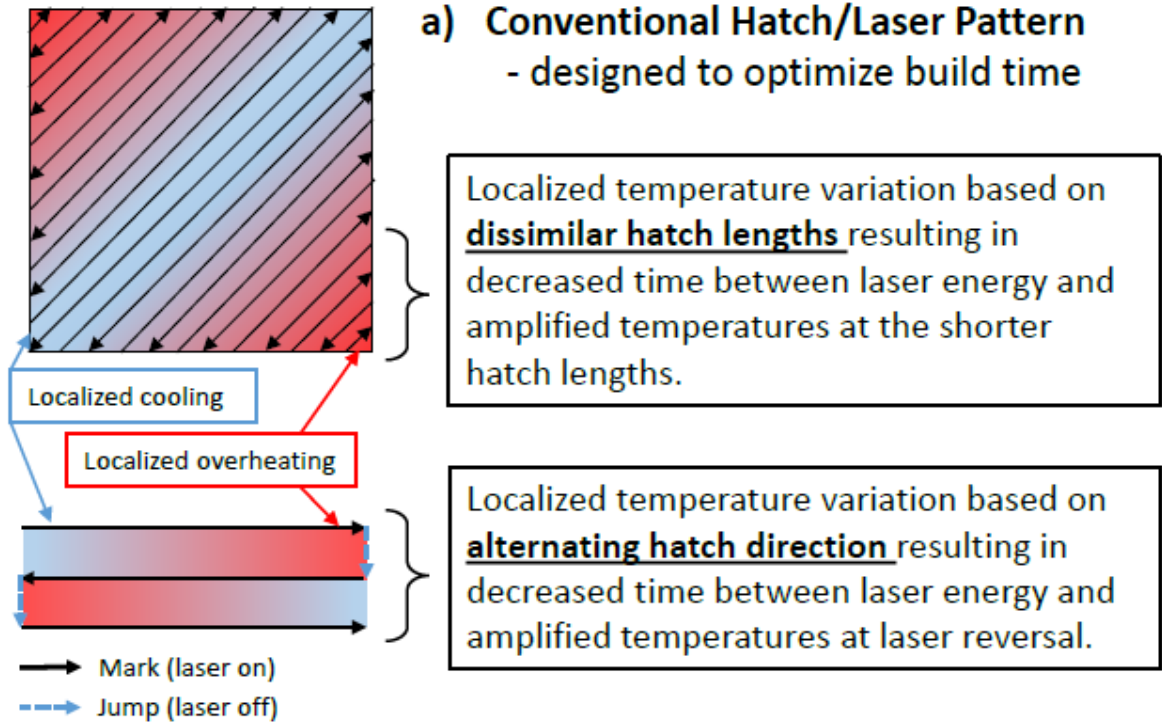
- The specimens were cylinders with a diameter of 12.7 mm and a height of 25.4 mm.
- 20% by volume was used for both HA and CF.
- Material change was done between layers.
- There were complications with printer tuning which caused significant sledding.



## **Appendix B: Alternate Hatch Patterns**

Appendix B contains the hypothesized effects on energy density and heat of varying hatch patterns. These patterns were experimentally tested but were not fully quantitatively characterized. Future work is recommended to experimentally verify the effectiveness of these hatch patterns with different materials and material blends. It is likely different hatch patterns will be required for different materials and will have to be set in the M2 SLS host or a M2 PBF system to match the material.

**Figure 1: Impact of SLS Hatch Pattern on Thermomechanics**



## **Appendix C: Initial Blend Microscopy Contrast Imaging Results**

Appendix C contains figures demonstrating the inconsistencies encountered with image contrast analysis. This data is given to give a reference point for the difficulties encountered with the low contrast between the material used. This was particularly evident between CF and PA12 powders tested. However, depending on the manufacturer, each powder had white particles mixed blended in to aid with sintering using a diode laser. Future work with these materials is required to find accurate ratios of matrix, infill, and pores.

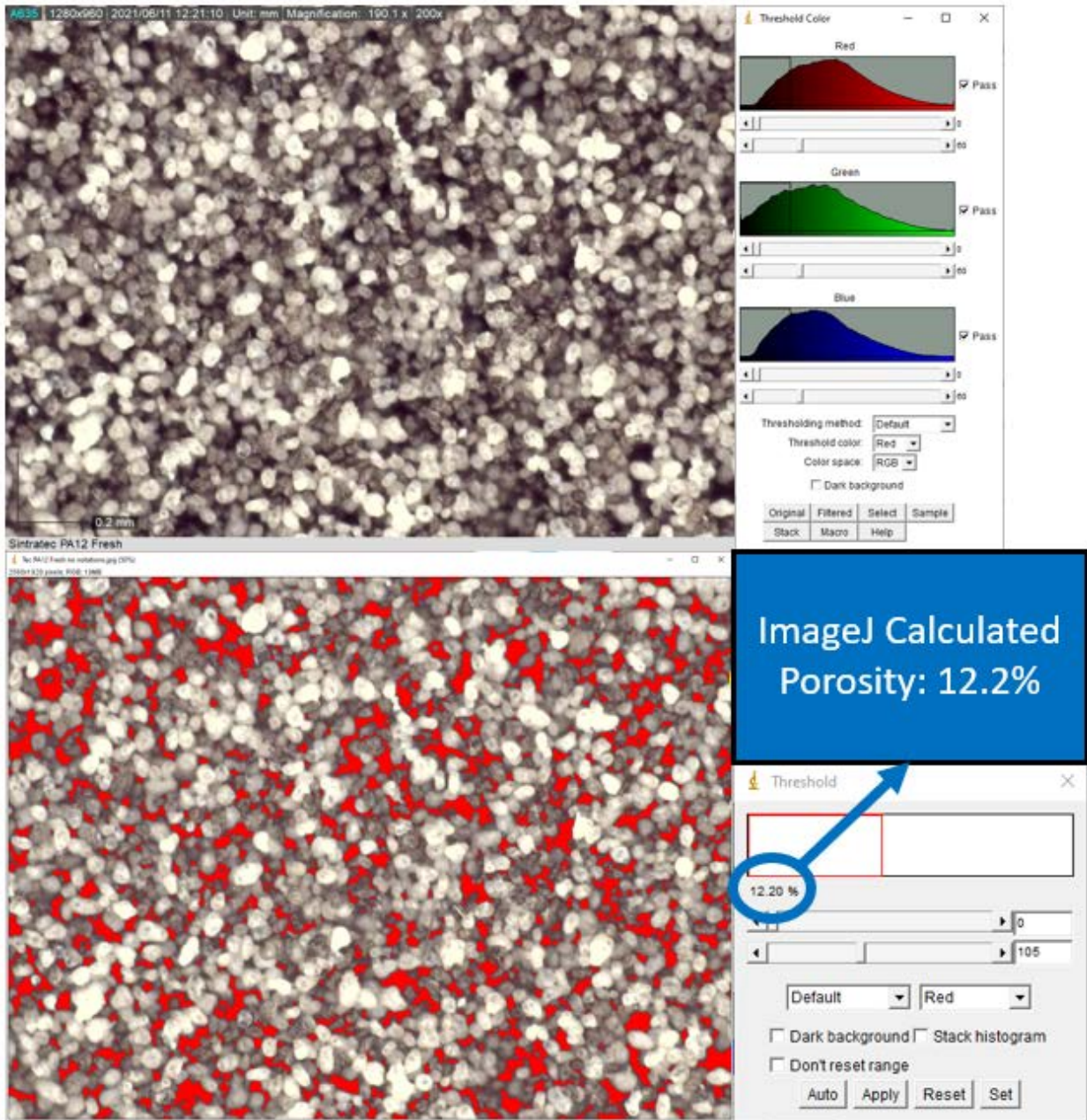


Figure C1: Neat Sintratec PA12 Contrast Imaging (Porosity Calculation).

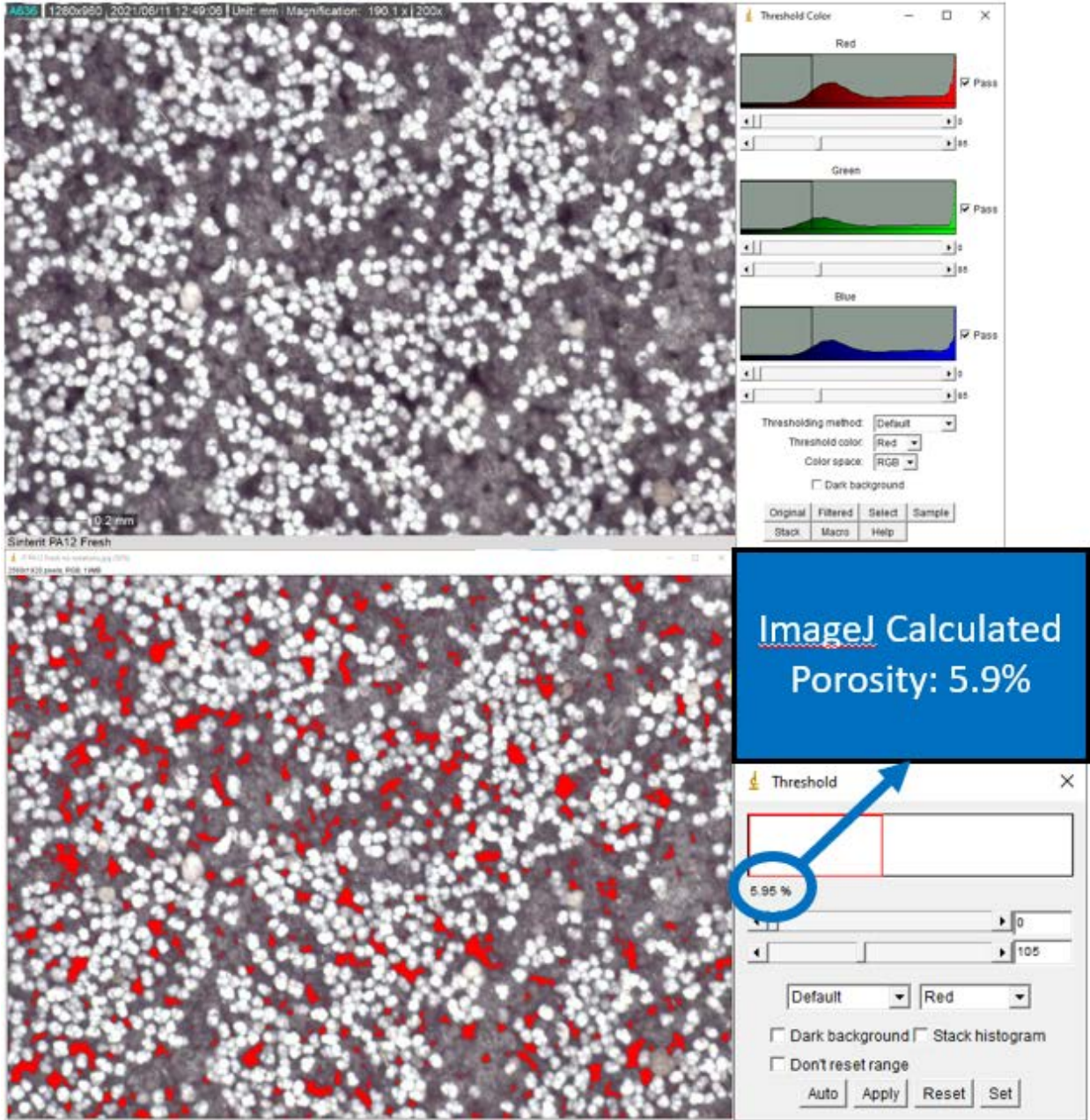


Figure C2: Neat Sinterit V1 PA12 Contrast Imaging (Porosity Calculation).

# Sintratec PA12 + 10% CF

## D3 – Porosity Analysis

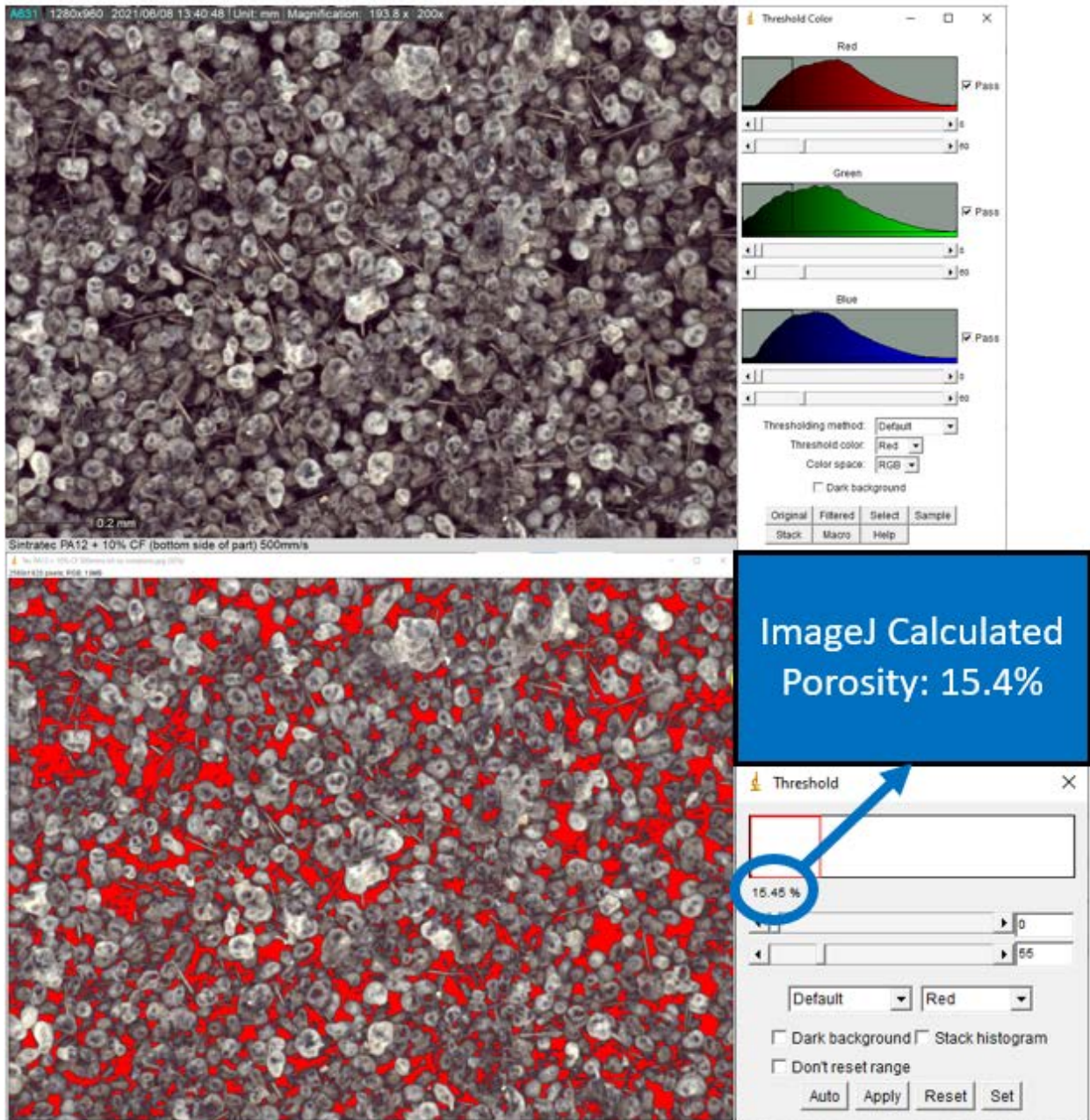


Figure C3: Sintratec PA12 + 10%CF vol Contrast Imaging (Porosity Calculation).

# Sinterit PA12 + 40% CF

## D4.1 – Porosity Analysis

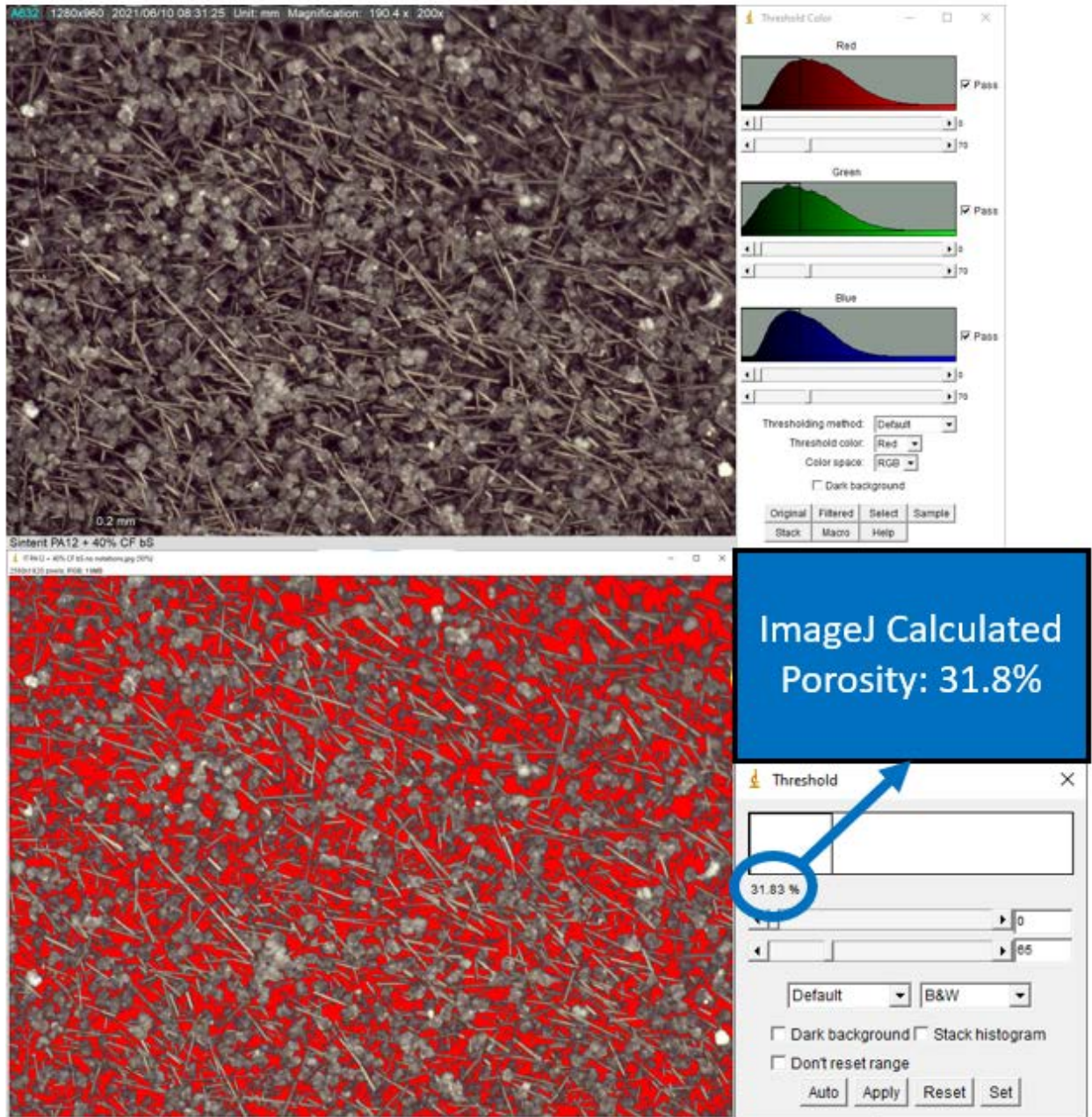


Figure C4: Sinterit PA12 + 40%CF vol Contrast Imaging (Porosity Calculation).

# Sinterit PA12 + 40% CF

## D 4.2 – CF %vol Analysis

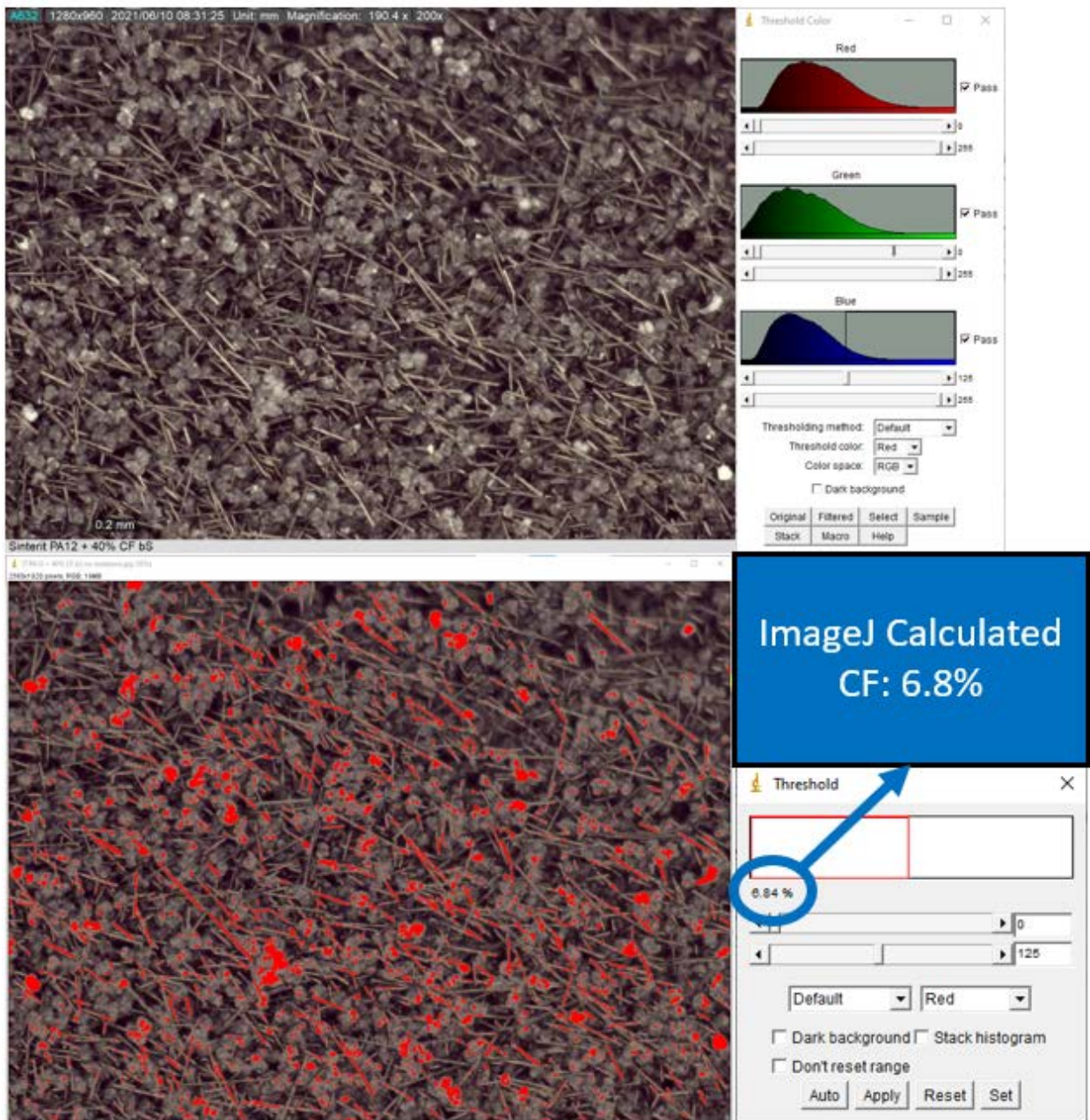


Figure C5: Sinterit PA12 + 40%CF vol Contrast Imaging (CF Calculation).

# Sinterit PA12 + 5% HA

## D5.1 – Porosity Analysis

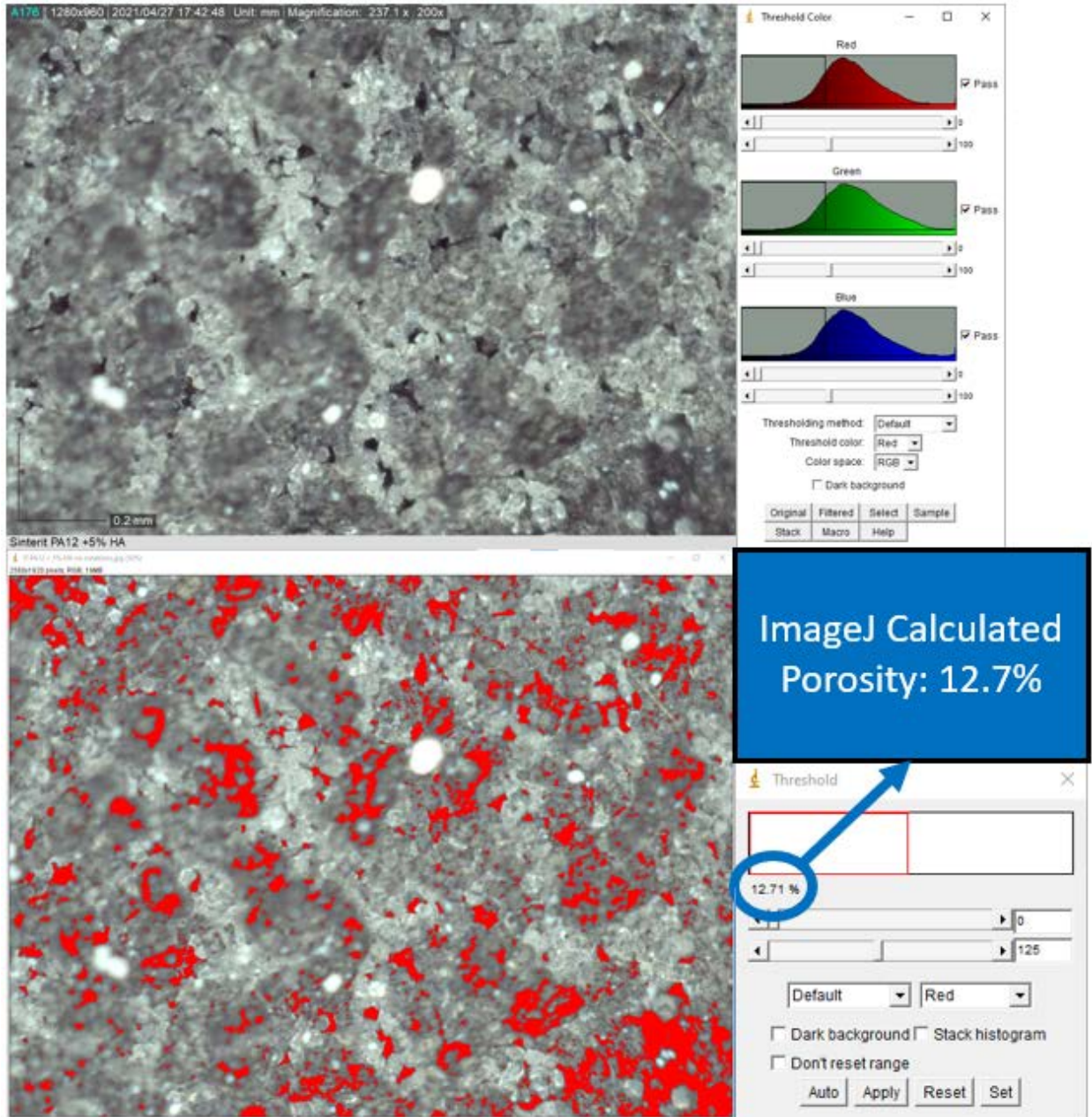


Figure C6: Sinterit PA12 + 5%HA vol Contrast Imaging (Porosity Calculation).

# Sinterit PA12 + 5% HA

## D5.2 – HA %vol Analysis

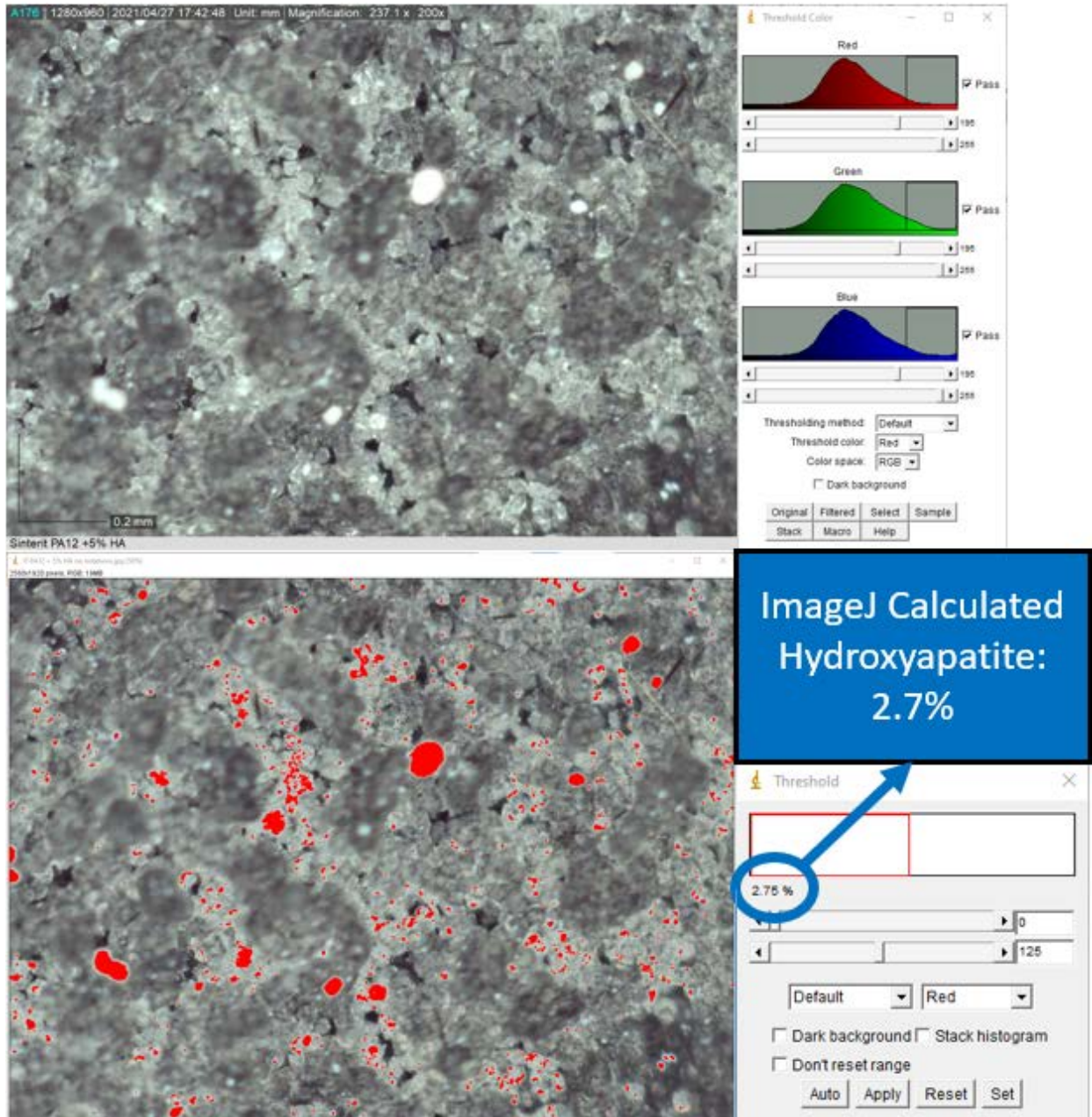


Figure C7: Sinterit PA12 + 5%HA vol Contrast Imaging (HA Calculation).

# Sintratec PA12 + 40% HA

## D6.1 – Porosity Analysis

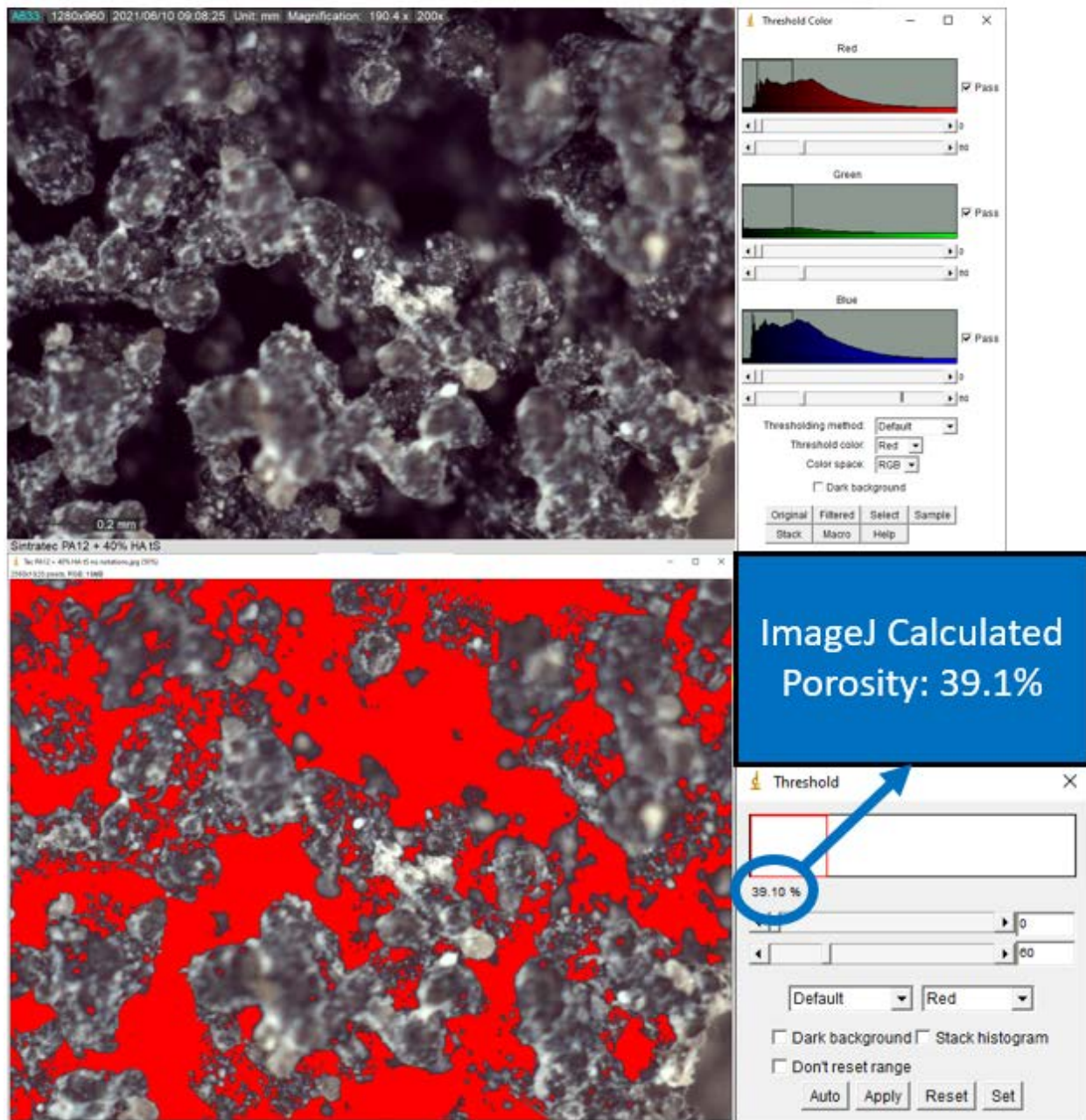


Figure C8: Sintratec PA12 + 40%HA vol Contrast Imaging (Porosity Calculation).

# Sintratec PA12 + 40% HA

## A6.2 – HA %vol Analysis

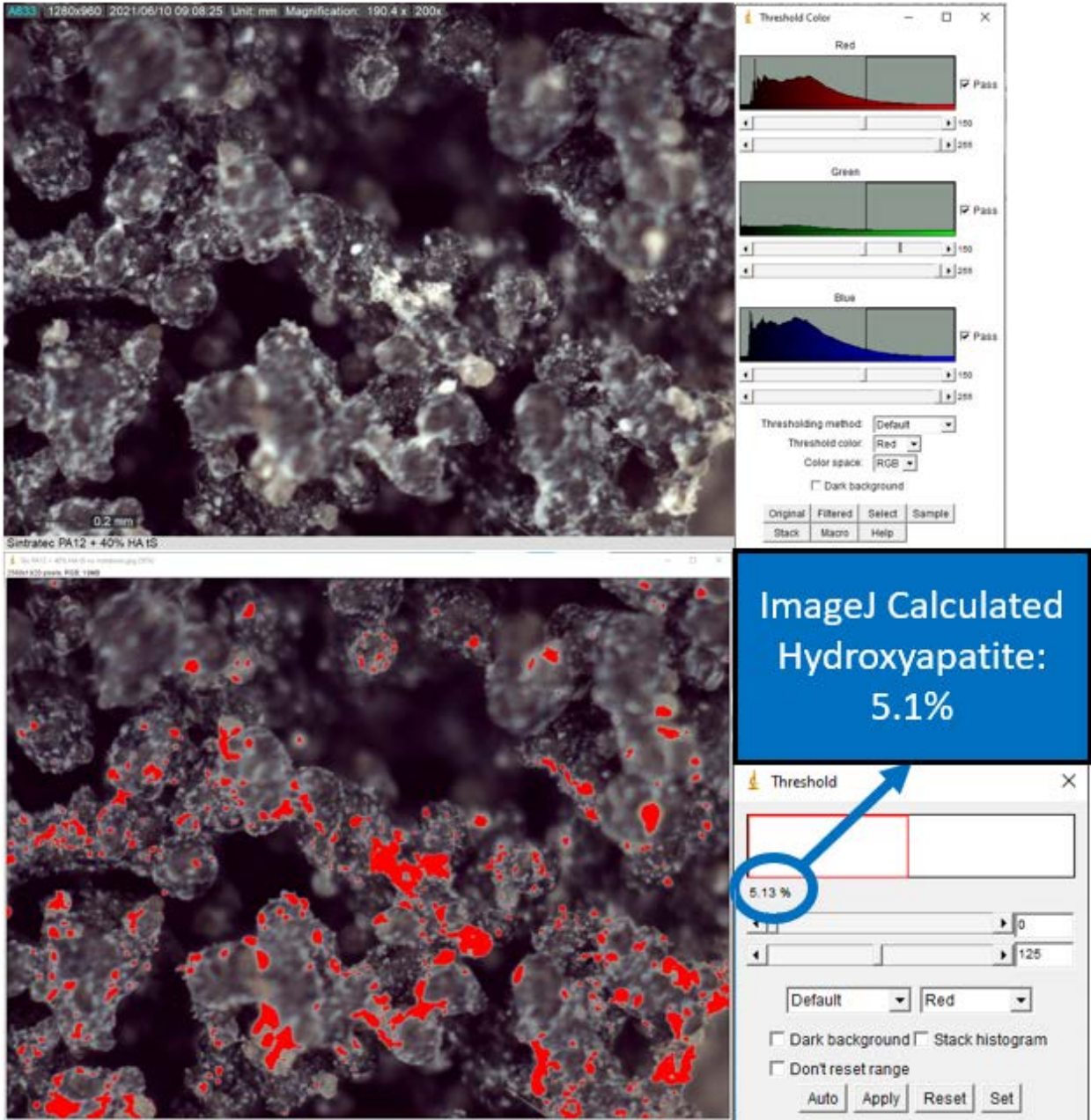


Figure C9: Sintratec PA12 + 40%HA vol Contrast Imaging (HA Calculation).

# Sintratec PA12 + 50% TPE

## A7 – Porosity Analysis

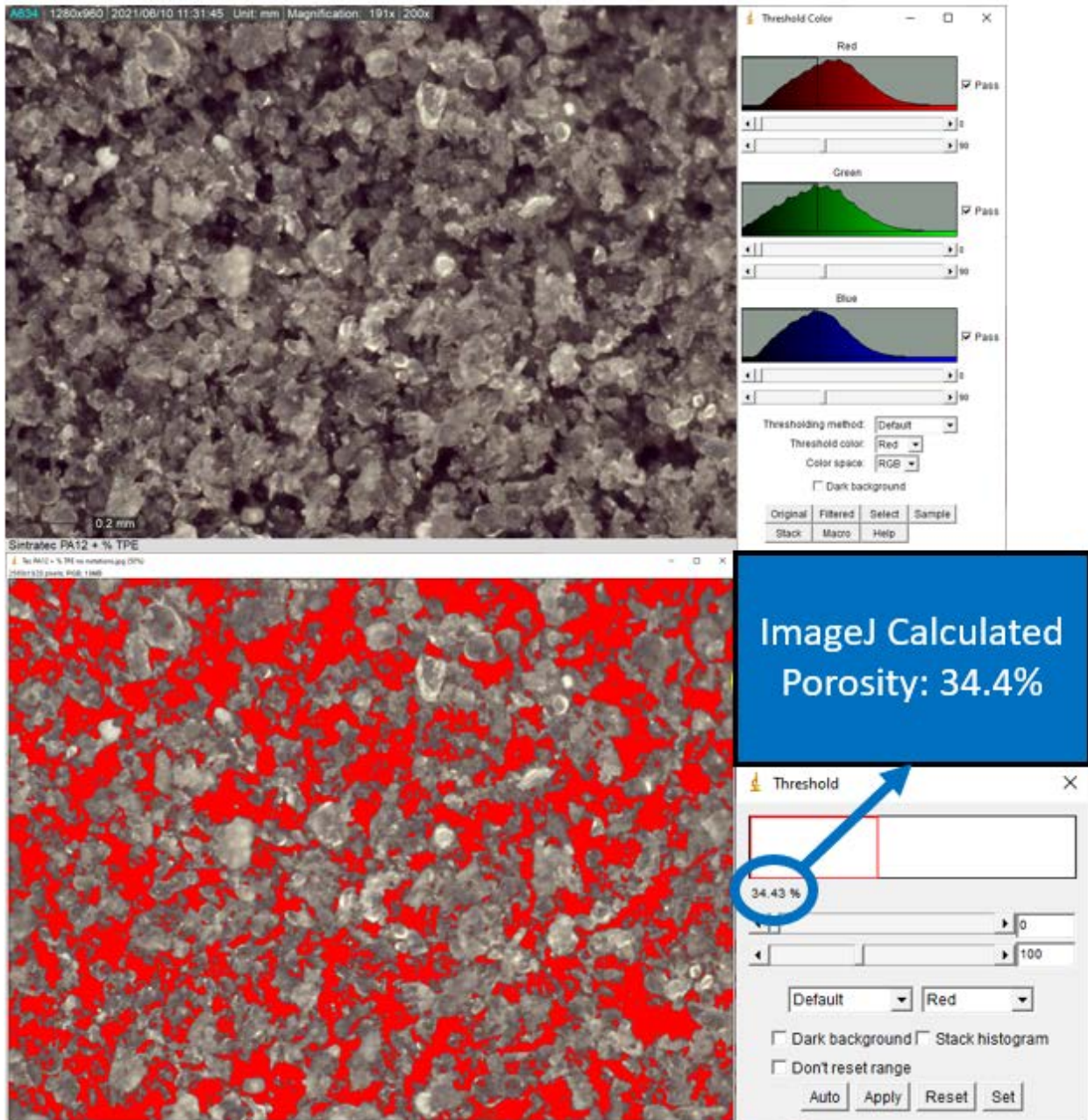


Figure C10: Sintratec PA12 + 50%TPE (Sintratec) vol Contrast Imaging (Porosity Calculation).

# Sinterit PA12 + 50% TPE

## A8 – Porosity Analysis

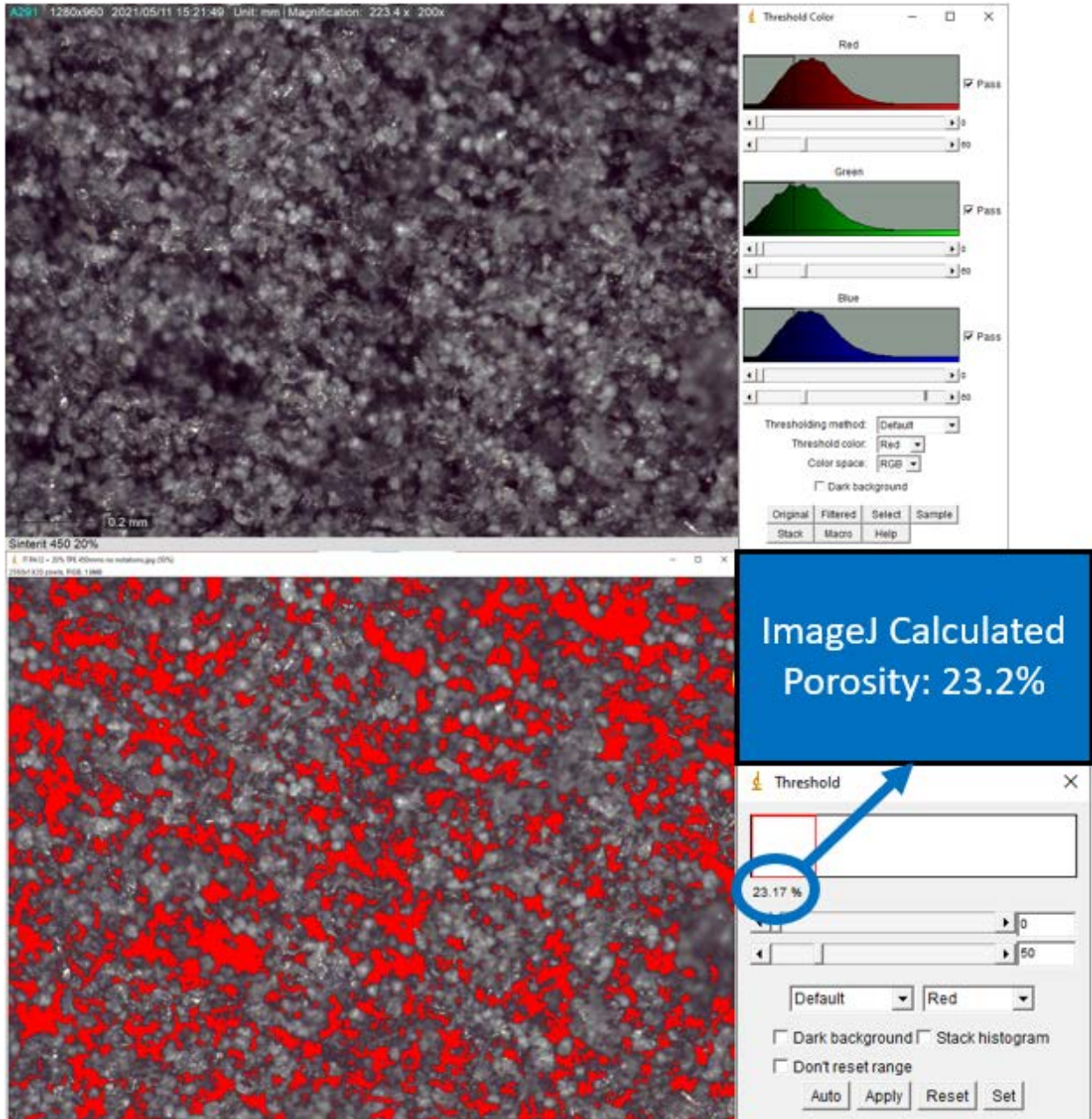


Figure C11: Sinterit PA12 + 50%TPE (Sinterit) vol Contrast Imaging (Porosity Calculation).

## **Appendix D: Manufacture Material Data Sheet.**

Appendix D contains manufacturer material data sheets that were current at the time of testing. All data sheets were available on the manufacture website at time of testing and copied here for future reference in the event manufacturers change material products and remove historical data sheets of previously available products



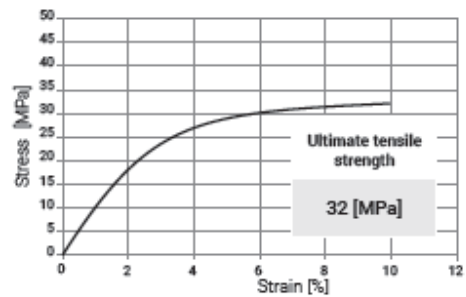
# PA12 Smooth <sup>v2</sup>

High surface quality

Good quality to price ratio | Excellent surface quality and high level of recreated details | High chemical resistance



### Tensile testing



General information		Method
Material type	Nylon 12	
Granulation	18 - 90 [µm]	
Color	Navy Grey	
Material refreshing ratio <sup>1</sup>	26 [%]	
Compatible with <sup>2</sup>	Lisa & Lisa Pro	
Parameters		
Tensile Strength	32 [MPa]	PN-EN ISO 527-2:2012
Elongation at Break	10 [%]	PN-EN ISO 527-2:2012
Impact resistance (Charpy test / unnotched)	16 [KJ/m²]	PN-EN ISO 179-1/1eU:2010
Shore hardness in type D scale	74	PN-EN ISO 868:2005
Thermal properties		
Softening point (Vicat method type A50 / B50)	172 / 155 [°C]	PN-EN ISO 306:2014-02
Melting point	185 [°C]	Internal procedure
Printout density	0.92 [g/cm³]	PN-EN ISO 845:2010

### Applications

Detailed printouts, structural or mechanical (with complicated internal geometry) elements, functional prototypes or final parts.

### Charpy U- and V-notched impact testing

Nº	notch	KJ/m²
1.	U	5.23
2.	V	3.28

Charpy impact test results for specimens tested using pendulum of maximum energy of 50 [J], weight of 6.8 [kg] and length of 380 [mm].

### Surface roughness

Roughness parameter	side surface	top surface
Ra	9.680 [µm]	6.470 [µm]
Rz	54.184 [µm]	31.633 [µm]

Roughness of test specimens surfaces printed with layer thickness of 100 [µm].

Figure D1: Sinterit PA12 Manufacturer Data Sheet.

# Sinterit TPE Powder

Sinterit Powder

In stock

TPE Powder – 2 kg

With TPE it is possible to print functional prototypes such as pumps, bellows, gaskets and other elastic solutions dedicated to work in difficult conditions

FEATURES:

- Elastic
- Durable
- Dense
- After sealer covering – watertight & airtight

APPLICATIONS:

- shoes/insoles parts (wear resistance)
- watertight/airtight items
- gaskets
- skin-touch applications for rubbers
- footwear prototypes,
- hoses and tubes – it's water/air tight
- shock absorbers

Material type: **TPE**

Shore hardness type A scale: **90**

Tensile Strength: **6.0 [MPa]**

Elongation at break: **196%**

Melting point: **190°C**

**Print Ready is suitable ONLY for first printing with TPE.**

\$440.00

1

Add to cart

Add to compare Added to comparison table

SKU	FZ051
Category	Powder for SLS printing
Material type	Thermoplastic Elastomers (TPE)
Packaging	Plastic bottle
Weight	2 [kg] / 4 [l]
Granulation	50 – 80 [µm]
Colour	Grey
Elongation at Break	196 [%]
Tensile Strength	6 [MPa]
Shore Hardness in scale A	90
Material refreshing ratio	10 [%] – to reuse leftover TPE powder add 30% of FRESH powder
Dedicated for	Lisa / Lisa PRO



Figure D2: Sinterit TPE Manufacturer Data Sheet.



Flexible prints with increased extensibility | Adjustable hardness | 100% reusable



General information	Method
Material type	TPU
Granulation	20 - 105 [µm]
Color	Grey
Material refreshing ratio <sup>1</sup>	0 [%]
Compatible with <sup>2</sup>	Lisa & Lisa Pro

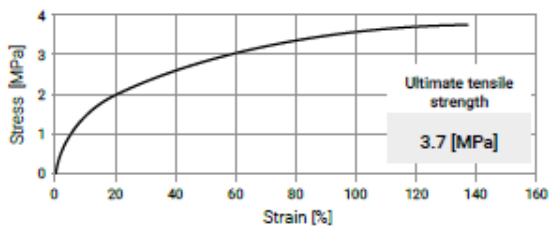
Parameters		
Tensile Strength	3.7 [MPa]	PN-EN ISO 37:2007
Elongation at Break	137 [%]	PN-EN ISO 37:2007
Shore hardness in type A scale	70 / 90 <sup>3</sup>	PN-EN ISO 868:2005

Thermal properties		
Softening point (Vicat method type A50)	67.6 [°C]	PN-EN ISO 306:2014-02
Melting point	160 [°C]	Internal procedure
Printout density	0.80 [g/cm <sup>3</sup> ]	PN-EN ISO 845:2010
Printout water absorption	9.1 [%]	PN-EN ISO 62:2008

### Applications

Standard rubber items, prototypes and design, shock and vibration absorbers, protectors.

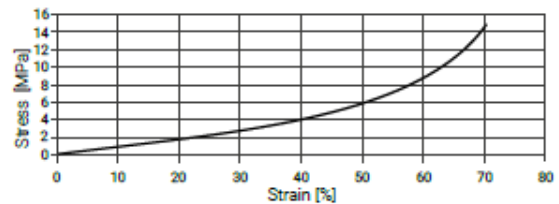
### Tensile testing



While the tensile stress does not exceed 1.8 [MPa], after load release, the test specimens retain their shape, with no external damage observed (e.g. fractures). The test specimens fracture when max tensile stress of 3.7 [MPa] is applied.



### Compression testing



While the compressive stress does not exceed 3.5 [MPa], after load release, the test specimens retain their shape, with no external damage observed (e.g. fractures).

After applying max compressive stress of 14.65 [MPa] and releasing the compressive load, the test specimens irreversibly change their volume from: 14.50 [mm] x 14.50 [mm] x 15.30 [mm] to: 14.85 [mm] x 14.85 [mm] x 14.85 [mm].



<sup>1</sup> Material refreshing ratio - percent of Fresh powder which has to be mixed with Used (unsintered) powder - to be reused during next print. FLEXA has 100 [%] of usability.

<sup>2</sup> Available as part of the appropriate profile purchased.

<sup>3</sup> Depending on printing settings.

Figure D3: Sinterit Flexa Grey Manufacturer Data Sheet.

## Specifications:

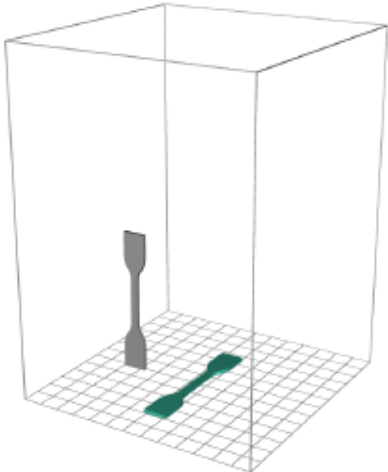
<b>Color</b>	Grey
<b>Melt Point</b>	176 C, 348.8F
<b>Stable Temp (Max)</b>	130C, 266F
<b>Bending Stress (Max)</b>	43.1 MPa
<b>Tensile Stress (Max)</b>	47.8 MPa
<b>Tensile Modulus (Max)</b>	1750 MPa
<b>Particle Size</b>	0.06mm (60 micron)
<b>Volume (1kg)</b>	2L, 2000cm <sup>3</sup> , 122in <sup>3</sup>
<b>Volume (20kg)</b>	40L, 40000cm <sup>3</sup> , 2440in <sup>3</sup>
<b>Cost / Volume (1kg)</b>	\$0.08/cm <sup>3</sup> , \$1.30/in <sup>3</sup>
<b>Cost / Volume (20kg)</b>	\$0.07/cm <sup>3</sup> , \$1.22/in <sup>3</sup>
<b>Reuse Ratio (Sintratec Kit)</b>	70% new / 30% used
<b>Reuse Ratio (Sintratec S2)</b>	30% new / 70% used

Figure D4: Sintratec PA12 Manufacturer Data Sheet.

# Tensile test Sintratec PA12

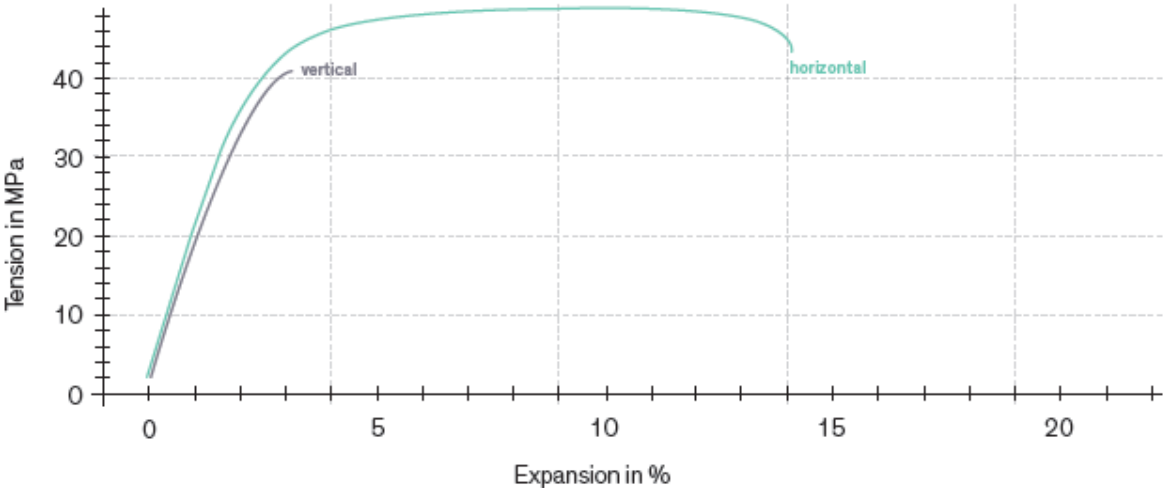
**Test standard**  
DIN EN ISO 527-1

**Test specimen**  
Type 5A printed with the Sintratec S1



	$\epsilon_{tb}$ %	b mm	l h mm
<b>Test object horizontal (XY)</b>	–	4,49	2,39
<b>Test object vertical (Z)</b>	–	4,31	2,26

**Test graphic**



**Test results**

	$E_t$ MPa	$\sigma_y$ MPa	$\epsilon_y$ %	$\sigma_m$ MPa	l $\epsilon_m$ %	$\sigma_b$ MPa	$\epsilon_b$ %
<b>Test object horizontal (XY)</b>	1610	47,8	8,9	47,8	8,9	43,1	–
<b>Test object vertical (Z)</b>	1750	–	–	40,8	3,1	40,8	3,1

Disclaimer: The illustrated results are an average of different tests using the type 5A test specimen. The results are not to be compared with results from tensile tests that were carried out using a type 1A test specimen. Individual results are not guaranteed and can deviate from these values. Unless it has been explicitly agreed, Sintratec does not guarantee any properties or suitability for a particular purpose.

© Sintratec AG 2018. All rights reserved. Any use or reproduction of the contents of this document, in full or in part, requires the written permission of Sintratec AG.

Figure D5: Sintratec PA12 Manufacturer Tensile Data Sheet.

## SPECIFICATIONS:

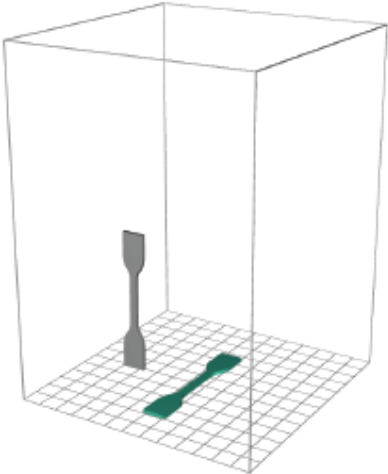
<b>Color</b>	Grey
<b>Melt Point</b>	110C, 230F
<b>Bending Stress (Max)</b>	5.28 MPa
<b>Tensile Stress (Max)</b>	2 MPa
<b>Tensile Modulus (Max)</b>	29.9 MPa
<b>Tension Strain (Max)</b>	250%
<b>Particle Size</b>	0.06mm (60 micron)
<b>Volume (2L)</b>	2L, 2000cm <sup>3</sup> , 122in <sup>3</sup>
<b>Cost / Volume</b>	\$0.07 / cm <sup>3</sup> , \$1.22 / in <sup>3</sup>
<b>Approx Weight (2L)</b>	1.05kg, 2.31lb
<b>Reuse Ratio</b>	50% new / 50% used

Figure D6: Sintratec TPE Manufacturer Data Sheet.

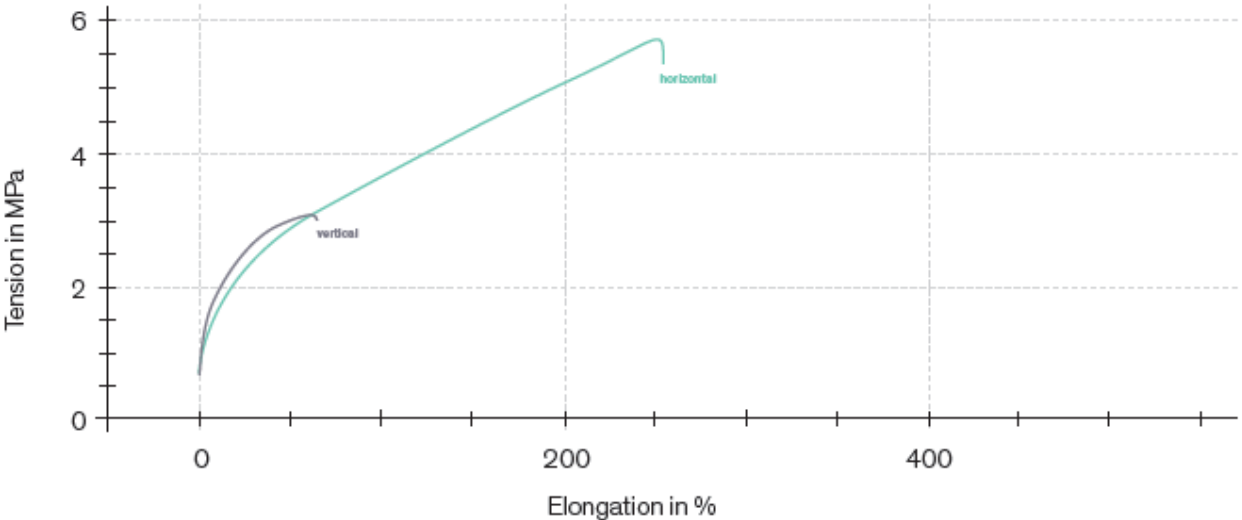
# Tensile Test Sintratec TPE

**Test standard**  
DIN EN ISO 527-1

**Test specimen**  
Type 5A printed with the Sintratec S1



**Test graphic**



**Test results**

	$E_t$ MPa	$\sigma_m$ MPa	$\epsilon_m$ %	$\sigma_b$ MPa	$\epsilon_{tb}$ %	b mm	h mm
<b>Test object horizontal (XY)</b>	29.9	1.82	12	5.28	250	3.62	2.47
<b>Test object vertical (Z)</b>	28	2.00	12	2.98	63	3.78	1.76

Disclaimer: The illustrated results are an average of different tests using the type 5A test specimen. The results are not to be compared with results from tensile tests that were carried out using a type 1A test specimen. Individual results are not guaranteed and can deviate from these values. Unless it has been explicitly agreed, Sintratec does not guarantee any properties or suitability for a particular purpose.

© Sintratec AG 2018. All rights reserved. Any use or reproduction of the contents of this document, in full or in part, requires the written permission of Sintratec AG.

Figure D7: Sintratec TPE Manufacturer Tensile Data Sheet.



**ELG Carbon Fibre Ltd.**  
**RECYCLED CARBON FIBRE**

**CARBISO™** **MF** Milled Fibre



**Carbiso™ MF is recycled carbon fibre milled to 80µm or 100µm.**

Milled fibres are used in demanding applications to increase mechanical properties and provide tailored electrical and thermal conductivity of the chosen matrix.

The milled carbon fibres have excellent dispersibility as the fibres are unsized and are compatible with most thermoset and thermoplastic matrices.

Figure D8a: Carbiso MF100 CF Manufacturer Data Sheet.



Material data of Carbiso™ MF100

Typical properties	Units	Values
Carbon fibre content	%	>95
Other fibre content	%	<5
Fibre diameter	µm	7
Fibre length	µm	100
Sizing content	%	0
Bulk density	g/l	400
Metal contamination *		<0.5g / 1000g
Packaging (Pillow bag)	kg	17.5

\* Our milled fibres have passed through our metal detection and separation systems, metal contamination figures are a guide.

Fibre length distribution of Carbiso™ MF100

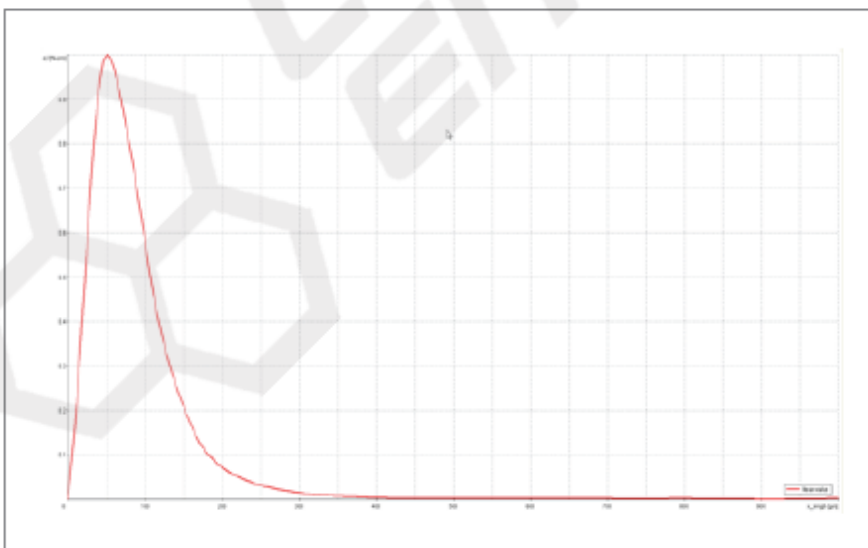


Figure D8b: Carbiso MF100 CF Manufacturer Data Sheet (cont.).



### Mechanical properties of Carbiso™ MF

Typical properties	Units	Values
Tensile strength **	MPa	3470
Tensile modulus	GPa	246
Fibre density	kg/m <sup>3</sup>	1800

\*\* Single filament tests, typically 700MPa lower than impregnated strand testing.

The information presented in this document is provided in good faith, but no warranty is given or is to be implied regarding its accuracy or relevance to any particular application. Users must satisfy themselves regarding the suitability and safety of their use of the information and products in the application concerned.

**ELG Carbon Fibre Ltd.** Cannon Business Park, Gough Road, Coseley, West Midlands, WV14 8XQ  
+44 1902 406010 [www.ELGCF.com](http://www.ELGCF.com)

Figure D8c: Carbiso MF100 CF Manufacturer Data Sheet (cont.).

## Appendix E: Industry Standard Nylon 12 Sintered Properties.

Appendix E contains current (at the time of testing) comparison of two industry data on sintered PA12 parts. Data is available as a reference and for comparison purposes to the results in Aim 4 since Sintratec does not provide such data. All data were available on the manufacture website at time of testing and copied here for future reference in the event manufacturers change material products and remove historical data sheets of previously available products. Data from Matweb on ALM PA 650 PA12 and from Materialise is presented below:

**ALM PA 650 Nylon 12 SLS Prototyping Polymer**

**Categories:** [Polymer](#); [Rapid Prototyping Polymer](#); [Thermoplastic](#); [Nylon \(Polyamide PA\)](#); [Nylon 12 \(PA12\)](#)

**Material Notes:** Combines strength, durability (high impact) and chemical resistance and produces strong, durable, end use prototype parts. SL parts are less porous, more precise and have less noticeable build lines than FDM (Fused Deposition Modeling) parts. LS systems build in 0.004-0.006 inch layers.

Information provided by Axis Prototypes.

**Vendors:**

[Proto3000](#) – Rapid Prototyping Engineering Solutions – Polyjet, FDM, SLA, SLS, DDM. Send us your 3D CAD Drawings for instant quotes, quality service, and fast delivery. For more info, contact us at 1-888-88-PROTO, info@proto3000.com or visit us at [www.proto3000.com](http://www.proto3000.com)

[Axis Proto Inc.](#) Innovative leaders in producing high quality Rapid Prototyping and Rapid Manufacturing solutions using all major 3D printing systems including [Stereolithography](#) technology. Free online quotes at [www.axisproto.com](http://www.axisproto.com)

[Click here](#) to view all available suppliers for this material.

Please [click here](#) if you are a supplier and would like information on how to add your listing to this material.

Physical Properties	Metric	English	Comments
Bulk Density	<a href="#">0.460</a> g/cc	<a href="#">0.0166</a> lb/in <sup>3</sup>	ASTM D1895
Density	<a href="#">1.02</a> g/cc	<a href="#">0.0368</a> lb/in <sup>3</sup>	Sintered Part; ASTM D792
Particle Size	<a href="#">55</a> µm	<a href="#">55</a> µm	Average D50; Laser Diffraction
Melt Flow	<a href="#">30 - 100</a> µm	<a href="#">30 - 100</a> µm	Range (D10 to D90); Laser Diffraction
	<a href="#">50</a> g/10 min @Load 5.00 kg, Temperature 235 °C	<a href="#">50</a> g/10 min @Load 11.0 lb, Temperature 455 °F	ASTM D1238

Mechanical Properties	Metric	English	Comments
Tensile Strength at Break	<a href="#">48.0</a> MPa	<a href="#">6960</a> psi	XY direction; ASTM D638
Elongation at Break	24 %	24 %	XY direction; ASTM D638
Tensile Modulus	<a href="#">1.70</a> GPa	<a href="#">247</a> ksi	XY direction; ASTM D638
Flexural Modulus	<a href="#">1.50</a> GPa	<a href="#">218</a> ksi	XY direction; ASTM D790
Izod Impact, Notched	<a href="#">2.20</a> J/cm	<a href="#">4.12</a> ft-lb/in	ASTM D256
Izod Impact, Unnotched	<a href="#">4.40</a> J/cm	<a href="#">8.24</a> ft-lb/in	ASTM D256

Electrical Properties	Metric	English	Comments
Volume Resistivity	<a href="#">3.10e+14</a> ohm-cm	<a href="#">3.10e+14</a> ohm-cm	50% RH; 500V; ASTM D257
Surface Resistance	<a href="#">3.00e+14</a> ohm	<a href="#">3.00e+14</a> ohm	50% RH; 500V; ASTM D257
Dielectric Constant	2.9	2.9	50% RH; 500V; ASTM D150

Thermal Properties	Metric	English	Comments
Melting Point	<a href="#">181</a> °C	<a href="#">358</a> °F	ASTM D3418
Deflection Temperature at 0.46 MPa (66 psi)	<a href="#">177</a> °C	<a href="#">351</a> °F	ASTM D648
Deflection Temperature at 1.8 MPa (264 psi)	<a href="#">86.0</a> °C	<a href="#">187</a> °F	ASTM D648

Figure E1: Matweb Sintered PA12 Data on ALM PA 650 Nylon 12.

## PA 12 (SLS)

Being a solid material, polyamide powder has the attractive feature of being self-supporting for the generated product sections. This makes support structure redundant. Polyamide allows the production of fully functional prototypes or end-use parts with high mechanical and thermal resistance. Polyamide parts have excellent long-term stability and are resistant against most chemicals. They can be made watertight by impregnation. The PA material used by Materialise is certified as biocompatible and food-safe under certain conditions.

MEASUREMENT	VALUE	STANDARD
Density	0.95 ±0.03 g/cm <sup>3</sup>	
Tensile Strength	48 ±3 MPa	DIN EN ISO527
Tensile Modulus	1650 MPa	DIN EN ISO527
Flexural Strength	41 MPa	D790
Elongation at Break	20 ±5%	DIN EN ISO527
Flexural Modulus	1500 N/mm <sup>2</sup>	DIN EN ISO178
Charpy – Impact strength	53 ±3.8 kJ/m <sup>2</sup>	DIN EN ISO179
Charpy – Notched Impact Strength	4.8 ±0.3 kJ/m <sup>2</sup>	DIN EN ISO179
Izod - Notched Impact Strength	4.4 ±0.4 kJ/m <sup>2</sup>	DIN EN ISO180
Ball Indentation Hardness	77.6 ±2	DIN EN ISO2039
Shore D/A-hardness	D75 ±2	DIN 53505
Heat Deflection Temperature	86 °C	ASTM D648 @ 1.82 MPa

Actual values may vary with build condition

For more information on this material, please visit [mtls.me/pa-12-sls](https://mtls.me/pa-12-sls).

The information and values included in these datasheets, although based on Materialise's knowledge and experience and thus presented in good faith and believed to be accurate, is provided for your guidance only. This information does not release a third party from conducting his own procedures and tests to determine suitability. All guarantees with respect to the information contained herein are explicitly denied. This document was last updated on June 2021.



Figure E2: Materialise Manufacturing Sintered PA12 Manufacturer Data Sheet.

## **Appendix F: Differences between SENT Test 1 and Test 2**

### **INTRODUCTION**

All SENT Specimens for each material blend were printed at the same time as described in Chapter 6. However, 4 specimens (generally the odd numbered specimens for even spacing across the print area, Figure 6.6) were tested on February 4<sup>th</sup> (“Test 1”). This was done to evaluate the DOE prior to testing all the specimen. No modifications were required to the SENT DOE so the last 4 specimens were tested on February 25<sup>th</sup> (“Test 2”) using identical procedures (DOE) as Test 1. Results from Test 2 results were generally more brittle than results from Test 1.

### **METHODS**

All specimens for Test 1 and Test 2 were printed at the same time with the same powder blend and printer settings (i.e., laser, hatch, layer, temperature, recoating, etc.). The preparation and testing were done in accordance with the methods presented in Aim 4. See Chapter 6 (Aim 4) for a description of the methods used.

To further investigate the difference between Test 1 and Test 2 a DOE to tensile test the exact same specimens from Test 1 and Test 2 was created. A third test (“Test 3”) was done by “re-notching” the top half and bottom half of the fractured specimens from Test 1 and Test 2. All other aspects of Test 3 specimen preparation were done in accordance with the methods presented in Aim 4. However, after specimen SENT preparation, specimens were subjected to three different environments to test the effect of moisture on the specimens. One set was soaked in water for 24 hours and pulled directly from the water bath, a second set was dried for 24 hours and pulled directly from the dryer, and a third set was stored in a similar manner (same environment) as all the specimens from Test 1 and Test 2. SENT testing procedures, to include testing rate (0.8 mm/min), were held constant across all three tests even though the specimen were approximately half the length for Test 3.

## RESULTS

Test 2 was compared to Test 1 using the same data flow presented in Chapter 6, Aim 4. Tabulated data comparing the two tests are found in Tables F.1 thru F.2c. DIC calculated 2D strain fields for Test 2 are presented in Figures F.1a thru F.1d. A comparison of the 2D strain fields between Test 1 and Test 2 is found in Figures F.2a thru F.2c. Representative SENT data from each specimen type for Test 2 are presented in Figure F.3. A comparison between Test 1 and Test 2 of representative curves from each test is found in Figures F.4a and F.4b (F.4b has crack initiation lines depicted on the graph.). The results of Test 3 (re-pulling the fractured half specimens from Test 1 and Test 2) are presented in Figure F.5. Figures F.6a thru F.6g individually compare each specimen type from Test 1 and Test 2. Figures F.7a thru F.7g have the individual calculations of fracture energy for each Test 2 representative specimen (calculations for tabulated data in Tables F.2a thru F.2c).

## DISCUSSION

Test 3 data differences between soaked, dried, and ambient specimens did not show similar differences to data differences between Test 1 and Test 2 (Figure F.5). Wetted vs dried specimen results showed relatively small difference in notched tensile properties as compared to the differences between Test 1 and Test 2. It is critical to note that the results from the “re-pulled” half specimens in Test 3 are NOT directly comparable to the initial tests. Specimen size, strain rate proportionality to specimen dimension, possible strain hardening, plastic deformation, and many other factors between the initial tests and Test 3 make the results of these two tests distinctly different. However, by using the exact specimens that were initially printed at the same time and tested during the original tests aided in ensuring consistency between the original tests and the “re-pull” test based on blending and print parameters (i.e., laser, hatch, layer, temperature, recoating, etc.). Test 3 half specimen results were generally like the more ductile Test 1 results. These results suggest moisture was not the reason for the large change in SENT

characteristics between Test 1 and Test 2. Fracture energy, strain fields, and fracture point calculations shown in the DIC data also point toward the second test specimens being much more brittle than the first test but a clear cause was also not evident in this data.

Possible causes for the differences between Test 1 and Test 2 were considered and presented below ( – considerations why it is unlikely the cause listed influenced the difference between Test 1 and Test 2):

1. Print settings – Not only were the print settings the same, but the specimens were all printed at the same time with the powder and same ambient conditions prior to, during, and after printing.
2. Placement in build area – The specimens between the two tests were generally evenly dispersed throughout the build area. With only a few exceptions, Test 1 tested the odd numbered specimens and test 2 tested the even numbered specimens (specimens labeled 1 thru 8, front to back respectively, Figure. 6.6). There were also no trends noted between print locations and specimen results.
3. Error in the load cell between tests – Load cell was checked before and after each test and appeared to have been correct for both tests. Load cell was also thoroughly evaluated after Test 3 and all readings were normal with accurate load measurements within calibration standards.
4. Error in strain rate between tests – Strain rates were checked for both tests and appeared to have been correct. Also, orders of magnitude difference in strain rate were tested and the results all remained similar to Test 1. None of the differences in results between different strain rates were similar to the difference between Test 1 and Test 2
5. Differences in sanding and post print cleaning – Test 2 specimens were sanded more thoroughly than Test 1 specimens to remove excess unsintered powder post print. However, when the Test 2 specimen halves were re-notched and pulled the results tended to resemble Test 1 and not Test 2. The fact that the re-notched Test 2 specimens tend to have properties

like the original Test 1 also indicates machining was not the cause of the difference in tensile data.

6. Difference in speckling – The same methods, exact same can of spray paint, and the same person (i.e., same human factors in technique) speckled all specimens so it is unlikely speckling made the difference. It also appears speckling is not at the cause of the difference because the specimens were relatively unchanged with changes in moisture during Test 3.
7. Notching Technique – There were 3 specimens that broke at the grips from Test 2 and so the original notch from Test 2 was used for Test 3 for the re-pull SENT test. These three specimens DID have similar results to Test 2. Similarity in results pointed to the notch or notching technique being the difference between the tests. However, different notches were tested to see if notching techniques could cause substantial changes ductility behavior and the notch variation results still resembled Test 1. The notches were also all done with the same equipment and same technique, so if something happened to the equipment (i.e., a dull razor blade) during Test 2 then the follow-on Test 3 with the same equipment would likely resemble Test 2 and not Test 1 results. All notch dimensions and physical attributes were also analyzed after each notch formation before SENT testing (“post-notch” microscopy) and there were no differences noted as a whole between Test 1 notches and Test 2 notches. Lastly, SEM microscopy was done on Test 1 and Test 2 notches following SENT testing and no significant differences were found between the two notches.
8. Notch “fusing” together between notching and testing – Post-notch microscopy did not indicate any fusing and no mechanisms for fusing were found. Also, specimens for both tests were notched and speckled 24 hours before testing and so one set of specimens did not have more time than the other to fuse together prior to SENT testing.
9. Fracture mechanics – Fracture surfaces were compared between the two tests and Test 2 fracture surfaces had brittle fracture mechanics properties. However, this is expected to be a result of the brittle properties and not a cause. Fiber pullout, matrix material, and layer bonding all looked similar between the two tests for the brittle and ductile fracture zones.

10. Different levels of specimen slippage in the tensile grips between tests – Test 2 did slip more in the grips than Test 1 during testing which would affect the load distribution during testing. However, the results indicate the specimen slipping in the grips was a result of the higher loads during the second test and not a cause of the higher loads.
11. Change in crystallinity – A change in crystallinity between the two tests is certainly possible. Further testing would be required to verify crystallinity changes over time for the sintered composite blends. However, it is not expected crystallinity would change enough at room temperature in a 3-week period to cause the change in magnitude in ductility between Test 1 and Test 2. Possibly more telling is the crystallinity would have had to revert back to Test 1 properties between Test 2 and Test 3 since Test 3 ductility resembled Test 1. Similar reasoning applies to the following possible reasons for the changes from Test 1 to Test 2 to Test 3:
  - a. Oxidation over time
  - b. Aging
  - c. Chain scission
  - d. Change in bonding between the PA12 and CF

None of the above plausible causes or the analyzed data pointed to a clear reason for the difference in SENT results between Test 1 and Test 2. Further testing should be done to investigate other possible causes for the difference. It is likely that there was not a single cause but a combination of multiple factors.

## **BROADER IMPLICATIONS**

Test 1 and Test 2 have the same broader implications when considered separately (i.e., UTS, E, and fracture energy comparisons between single, binary, and gradient specimens). Test 2 broader implications are the same for Test 1 (see Aim 4 discussion in chapter 6) except for one key difference at crack initiation for the 0-5-0% CF specimens: The 0-5-0% CF specimens were

so brittle that crack initiation occurred at maximum force (Figure F.7d) which is a unique property that prevented crack propagation until right before specimen failure. While this certainly could prolong service life of parts with defects it could also give little to no time to remove a part from service before catastrophic failure of the part occurred. (e.g., if an aircraft has a bird strike and damage propagation is seen it may have time to reduce airspeed and stress on the wing and land prior to catastrophic damage with properties similar to the first test 0-5-0% CF properties. However, this may not be the case with a wing section that possess material properties resembling the second test 0-5-0% CF properties).

The differences between the two tests show the severity of changes in material behavior with a seemingly inconsequential change in material preparation, storage, or in-service conditions. The implications are equally severe as the differences of this could lead to unexpected material performance in-service and possible catastrophic. For instance, if a part was designed for the energy absorption seen in Test 1 gradient specimen but performed like specimen in Test 2 (Table F.2a), catastrophic failure would likely occur in service if any part defects existed. However, Test 1 specimen did not simply perform “better” than Test 2. For example, if a gradient part was designed with a factor of safety based on Test 2 UTS but then performed like a specimen from Test 1 (Table F.2a), again catastrophic failure could occur. These two examples point out the importance of continued research and testing under numerous environments and damaged states to fully understand sintered PA12/CF composites and PA12/CF FGM before “as printed” parts can be used in most applications.

## **CONCLUSION**

A definite source or cause for the difference between Test 1 and Test 2 results is still unclear. Future research and testing should be done to investigate the root factors effecting these changes. It is hypothesized that it is a combination of multiple factors to include storage conditions (humidity, temperature, and lighting), notch formation (different sharpness of the

blade used and possible different rates in notch propagation during creation), alignment on tensile machine, and painting technique for DIC speckle. Future simulations looking at other material properties of LCC M2 SLS parts would likely help characterize the effects of the above items. Wear, fatigue, and bending tests are recommended as starting points to characterize discussed effects more fully on M2 SLS parts with varying ratios of CF. Regardless of future testing, the most important conclusion of these two tests is continued research and testing of sintered PA12/CF composites and PA12/CF FGM is likely required before “as printed” parts can be used in most applications.

Table F.1: Comparison of Test 1 and Test 2 Dimensions and Tensile Data

\*FG = Failure at grip instead of notch and so data not included

ID	Blend	Specimen	Dimensions (mm)		Cross Section (mm <sup>2</sup> )			Maximum Force			Maximum Stress (Mpa)										
	%CF	Test	Width	Thickness	SPN	Mean	SD	SPN	Mean	SD	SPN	Mean	SD								
1	0% CF (Neat PA12)	Test 1	16.13	2.61	42.10	42.90	1.52	796.62	903.45	72.54	18.92	21.07	1.76								
3			16.02	2.81	45.02			923.44			20.51										
7			15.96	2.69	42.93			936.74			21.82										
8			15.86	2.62	41.55			956.99			23.03										
2		Test 2	15.90	2.54	40.39	39.82	0.96	1107.64	1217.77	98.06	27.43	30.62	3.03								
4			15.92	2.52	40.12			1165.09			29.04										
5			16.09	2.51	40.39			1280.66			31.71										
6			16.00	2.40	38.40			1317.71			34.32										
1		5% CF	Test 1	16.07	2.94	47.25	50.98	2.58	1341.64	1173.18	113.06	28.40	23.14	3.51							
3				16.06	3.24	52.03			1100.74			21.15									
5				16.15	3.29	53.13			1132.55			21.32									
7				15.99	3.22	51.49			1117.79			21.71									
2	Test 2		16.04	2.67	42.83	42.45	0.67	1481.37	1604.29	156.69	34.59	37.78	3.49								
4			15.98	2.69	42.99			1678.13			39.04										
6			15.96	2.60	41.50			1467.75			35.37										
8			15.91	2.67	42.48			1789.91			42.14										
1	10% CF		Test 1	16.02	2.53	40.53	41.64	0.91	1111.20	814.05	270.91	27.42	19.58	6.68							
2				16.06	2.61	41.92			636.28			15.18									
7				16.05	2.58	41.41			538.55			13.01									
8				16.05	2.66	42.69			970.19			22.72									
3		Test 2	15.76	2.60	40.98	40.20	0.53	860.56	1052.84	242.65	21.00	26.22	6.19								
4			15.70	2.55	40.04			1404.70			35.09										
5			15.71	2.53	39.75			1012.61			25.48										
6			15.77	2.54	40.06			933.50			23.30										
4		0-5-0% CF	Test 1	16.00	2.38	38.08	38.94	0.76	1122.52	1196.85	81.78	29.48	30.70	1.36							
5				15.73	2.47	38.85			1183.57			30.46									
6				16.01	2.43	38.90			FG			FG									
8				16.04	2.49	39.94			1284.46			32.16									
2	Test 2		15.88	2.17	34.46	35.54	1.53	1436.51	1465.89	41.55	41.69	41.26	0.61								
3			15.65	2.34	36.62			1495.27			40.83										
1			0-10-0% CF	Test 1	16.01			2.62			41.95			43.19	1.04	1034.82	1086.20	111.04	24.67	25.13	2.13
3					16.07			2.67			42.91					1056.89			24.63		
4	15.98	2.78			44.42	1249.49	28.13														
7	15.93	2.73			43.49	1003.58	23.08														
2	Test 2	16.00		2.28	36.48	35.94	0.74	1127.40	1281.69	133.64	30.90	35.68	4.23								
5		16.01		2.24	35.86			FG			FG										
6		16.02		2.18	34.92			1360.99			38.97										
8		16.01		2.28	36.50			1356.69			37.17										
1	10-0-10% CF	Test 1		16.11	2.87	46.24	45.56	0.95	1041.27	1082.29	60.58	22.52	23.75	1.12							
3				16.22	2.85	46.23			1147.17			24.82									
5				16.16	2.82	45.57			1119.51			24.57									
7				16.02	2.76	44.22			1021.20			23.10									
2		Test 2	16.01	2.21	35.38	34.17	1.71	1268.27	1271.14	4.05	35.84	39.05	2.94								
4			16.00	2.06	32.96			1274.00			38.65										
6			15.41	1.52	23.42			1006.73			42.98										
8			16.03	1.62	25.97			1005.44			38.72										
1		0-5-10-5-0% CF Gradient	Test 1	16.05	2.69	43.17	44.75	1.29	1302.66	1389.04	71.69	30.17	31.03	1.04							
2				16.08	2.75	44.22			1388.79			31.41									
4				16.04	2.85	45.71			1478.21			32.34									
5				16.04	2.86	45.87			1386.50			30.22									
3	Test 2		16.00	2.55	40.80	40.56	0.96	1907.28	1849.46	44.67	46.75	45.60	0.92								
6			16.00	2.61	41.76			1862.00			44.59										
7			16.00	2.47	39.52			1811.98			45.85										
8			16.00	2.51	40.16			1816.57			45.23										

Table F.2a: Comparison of Test 1 and Test 2 Fracture Energy Data at Crack Initiation (Ci)

ID	Blend %CF	Specimen Test	Crack Initiation								
			Frame Count	Force (N)	Stress (Mpa)	Energy MJ/mm <sup>3</sup>	Exto <sub>30mm</sub> (%)	$\epsilon_{yy\_max}$ (%)	$\epsilon_{xx\_max}$ (%)	$\epsilon_{xy\_max}$ (%)	VM (%)
1	0% CF (Neat PA12)	Test 1	2111	636.28	15.11	0.24	2.78	6.08	6.58	2.05	4.73
3											
7											
8											
2		Test 2	1161	881.77	21.83	0.23	1.68	3.79	0.31	0.73	2.19
4											
5											
6											
1	5% CF	Test 1	2841	1095.29	21.05	0.27	2.17	7.73	1.05	3.69	6.26
3											
5											
7											
2		Test 2	1481	1462.88	35.25	0.24	1.42	6.52	1.93	3.35	5.37
4											
6											
8											
1	10% CF	Test 1	2021	621.52	14.83	0.11	1.23	7.15	1.01	2.25	5.50
2											
7											
8											
3		Test 2	1111	930.92	23.24	0.12	0.89	5.88	0.48	1.28	3.99
4											
5											
6											
4	0-5-0% CF	Test 1	2401	796.07	20.91	0.27	2.19	4.14	0.63	1.66	3.33
5											
6				2621	801.51	20.63	0.38	3.23	7.31	1.44	3.11
8											
2		Test 2	2031	1492.69	40.76	1.07	3.85	13.14	2.07	3.93	10.22
3											
1	0-10-0% CF	Test 1	1871	616.79	14.70	0.14	1.65	4.83	0.94	1.80	3.46
3											
4											
7											
2		Test 2	1501	1359.99	38.94	0.51	2.11	8.55	0.90	2.77	6.04
5											
6											
8											
1	10-0-10% CF	Test 1	2121	841.50	18.47	0.15	1.17	4.40	0.92	2.79	3.80
3											
5											
7											
2		Test 2	1481	975.20	29.59	0.18	1.27	4.05	0.29	0.62	2.76
4											
6											
8											
1	0-5-10-5-0% CF Gradient	Test 1	3591	1350.38	30.54	0.70	3.68	9.22	2.45	4.33	7.56
2											
4											
5											
3		Test 2	1801	1654.63	41.87	0.49	1.96	7.81	1.34	1.96	5.75
6											
7											
8											

Table F.2b: Comparison of Test 1 and Test 2 Fracture Energy Data at Maximum Stress

ID	Blend %CF	Specimen Test	Maximum Stress								
			Frame Count	Force (N)	Stress (Mpa)	Energy MJ/mm <sup>3</sup>	Exto <sub>30mm</sub> (%)	$\epsilon_{yy\_max}$ (%)	$\epsilon_{xx\_max}$ (%)	$\epsilon_{xy\_max}$ (%)	VM (%)
1	0% CF (Neat PA12)	Test 1	3061	785.32	18.65	0.68	5.23	11.83	0.84	3.36	8.55
3											
7											
8		Test 2	1511	1090.28	37.41	0.23	2.76	11.62	0.73	1.90	8.38
2											
4											
5	5% CF	Test 1	2881	1098.88	21.12	0.30	2.69	8.35	1.09	3.76	6.70
3											
5											
7		Test 2	Failure 170	1464.60	35.29	0.38	1.82	10.03	2.43	4.41	7.39
2											
4											
6	10% CF	Test 1	2086	635.71	15.17	0.13	1.36	8.34	1.01	2.49	6.15
1											
2											
7		Test 2	1111	930.92	23.24	0.12	0.89	5.88	0.48	1.28	3.99
8											
3											
4	0-5-0% CF	Test 1	3627	1121.95	29.46	0.90	4.58	13.83	1.59	5.32	10.68
5											
6											
8		Test 2	5020	1182.28	30.43	1.90	9.23	29.06	5.61	14.46	24.42
2											
3											
3	0-10-0% CF	Test 1	3601	1036.25	24.70	0.40	4.70	10.65	4.04	4.31	8.31
1											
3											
4		Test 2	1511	1361.56	38.99	0.51	2.16	9.63	0.90	2.89	6.76
7											
2											
5	10-0-10% CF	Test 1	3251	1119.37	24.56	0.67	3.94	9.16	2.72	4.39	7.62
6											
8											
2		Test 2	2001	1275.15	38.69	0.67	2.47	7.76	0.45	2.37	5.68
4											
6											
8	0-5-10-5-0% CF Gradient	Test 1	3764	1390.94	31.45	0.83	4.04	10.16	2.51	4.67	8.31
1											
2											
4											
5		Test 2	2034	1810.98	45.82	0.71	3.46	11.95	1.56	3.46	8.56
3											
6											
7											
8											

Table F.2c: Comparison of Test 1 and Test 2 Fracture Energy Failure

ID	Blend Specimen		Failure								
	%CF	Test	Frame Count	Force (N)	Stress (Mpa)	Energy MJ/mm <sup>3</sup>	Exto <sub>30mm</sub> (%)	ε <sub>yy_max</sub> (%)	ε <sub>xx_max</sub> (%)	ε <sub>xy_max</sub> (%)	VM (%)
1	0% CF (Neat PA12)	Test 1	4401	142.88	3.93	1.61	12.36	23.44	0.77	4.02	16.85
3			4401	142.88	3.93	1.61	12.36	23.44	0.77	4.02	16.85
7			4401	142.88	3.93	1.61	12.36	23.44	0.77	4.02	16.85
8			4401	142.88	3.93	1.61	12.36	23.44	0.77	4.02	16.85
2		Test 2	1637	373.46	9.25	0.61	5.14	11.91	0.31	2.00	9.51
4			1637	373.46	9.25	0.61	5.14	11.91	0.31	2.00	9.51
5			1637	373.46	9.25	0.61	5.14	11.91	0.31	2.00	9.51
6			1637	373.46	9.25	0.61	5.14	11.91	0.31	2.00	9.51
1	5% CF	Test 1	3391	294.92	5.67	0.77	5.32	15.32	0.80	2.51	11.40
3			3391	294.92	5.67	0.77	5.32	15.32	0.80	2.51	11.40
5			3391	294.92	5.67	0.77	5.32	15.32	0.80	2.51	11.40
7			3391	294.92	5.67	0.77	5.32	15.32	0.80	2.51	11.40
2		Test 2	1701	1451.13	34.97	0.38	1.82	10.03	2.23	4.41	7.39
4			1701	1451.13	34.97	0.38	1.82	10.03	2.23	4.41	7.39
6			1701	1451.13	34.97	0.38	1.82	10.03	2.23	4.41	7.39
8			1701	1451.13	34.97	0.38	1.82	10.03	2.23	4.41	7.39
1	10% CF	Test 1	2539	149.33	0.23	0.37	8.79	0.30	0.30	1.94	6.68
2			2539	149.33	0.23	0.37	8.79	0.30	0.30	1.94	6.68
7			2539	149.33	0.23	0.37	8.79	0.30	0.30	1.94	6.68
8			2539	149.33	0.23	0.37	8.79	0.30	0.30	1.94	6.68
3		Test 2	1121	900.11	22.47	0.15	5.51	0.59	0.59	0.90	3.63
4			1121	900.11	22.47	0.15	5.51	0.59	0.59	0.90	3.63
5			1121	900.11	22.47	0.15	5.51	0.59	0.59	0.90	3.63
6			1121	900.11	22.47	0.15	5.51	0.59	0.59	0.90	3.63
4	0-5-0% CF	Test 1	3754	1065.92	27.99	1.04	5.16	14.60	1.13	6.19	11.86
5			3754	1065.92	27.99	1.04	5.16	14.60	1.13	6.19	11.86
6		Test 2	5300	1106.62	28.48	2	10.45	26	5.12	13.96	23.68
8			5300	1106.62	28.48	2	10.45	26	5.12	13.96	23.68
2			2071	1335.34	36.46	1.28	4.35	14.56			10.35
3			2071	1335.34	36.46	1.28	4.35	14.56			10.35
1	0-10-0% CF	Test 1	3741	990.25	23.61	0.40	5.19	12.15	1.51	3.84	9.88
3			3741	990.25	23.61	0.40	5.19	12.15	1.51	3.84	9.88
4			3741	990.25	23.61	0.40	5.19	12.15	1.51	3.84	9.88
7		Test 2	1531	1330.03	38.08	0.59	2.32	9.68	0.82	2.94	7.08
2			1531	1330.03	38.08	0.59	2.32	9.68	0.82	2.94	7.08
5			1531	1330.03	38.08	0.59	2.32	9.68	0.82	2.94	7.08
6	10-0-10% CF	Test 1	4161	947.26	20.79	1.50	7.46	20.98	1.77	4.26	15.35
3			4161	947.26	20.79	1.50	7.46	20.98	1.77	4.26	15.35
5			4161	947.26	20.79	1.50	7.46	20.98	1.77	4.26	15.35
7		Test 2	2281	1093.58	33.18	1.41	4.50	11.72	1.36	3.07	8.68
2			2281	1093.58	33.18	1.41	4.50	11.72	1.36	3.07	8.68
4			2281	1093.58	33.18	1.41	4.50	11.72	1.36	3.07	8.68
6	0-5-10-5-0% CF Gradient	Test 1	3819	1392.71	30.82	0.86	4.23	12.06	0.52	1.92	9.42
1			3819	1392.71	30.82	0.86	4.23	12.06	0.52	1.92	9.42
2			3819	1392.71	30.82	0.86	4.23	12.06	0.52	1.92	9.42
4		Test 2	2039	1809.40	45.78	0.71	2.52	12.56	1.51	3.62	8.95
5			2039	1809.40	45.78	0.71	2.52	12.56	1.51	3.62	8.95
3			2039	1809.40	45.78	0.71	2.52	12.56	1.51	3.62	8.95
6	2039	1809.40	45.78	0.71	2.52	12.56	1.51	3.62	8.95		
7	2039	1809.40	45.78	0.71	2.52	12.56	1.51	3.62	8.95		
8	2039	1809.40	45.78	0.71	2.52	12.56	1.51	3.62	8.95		

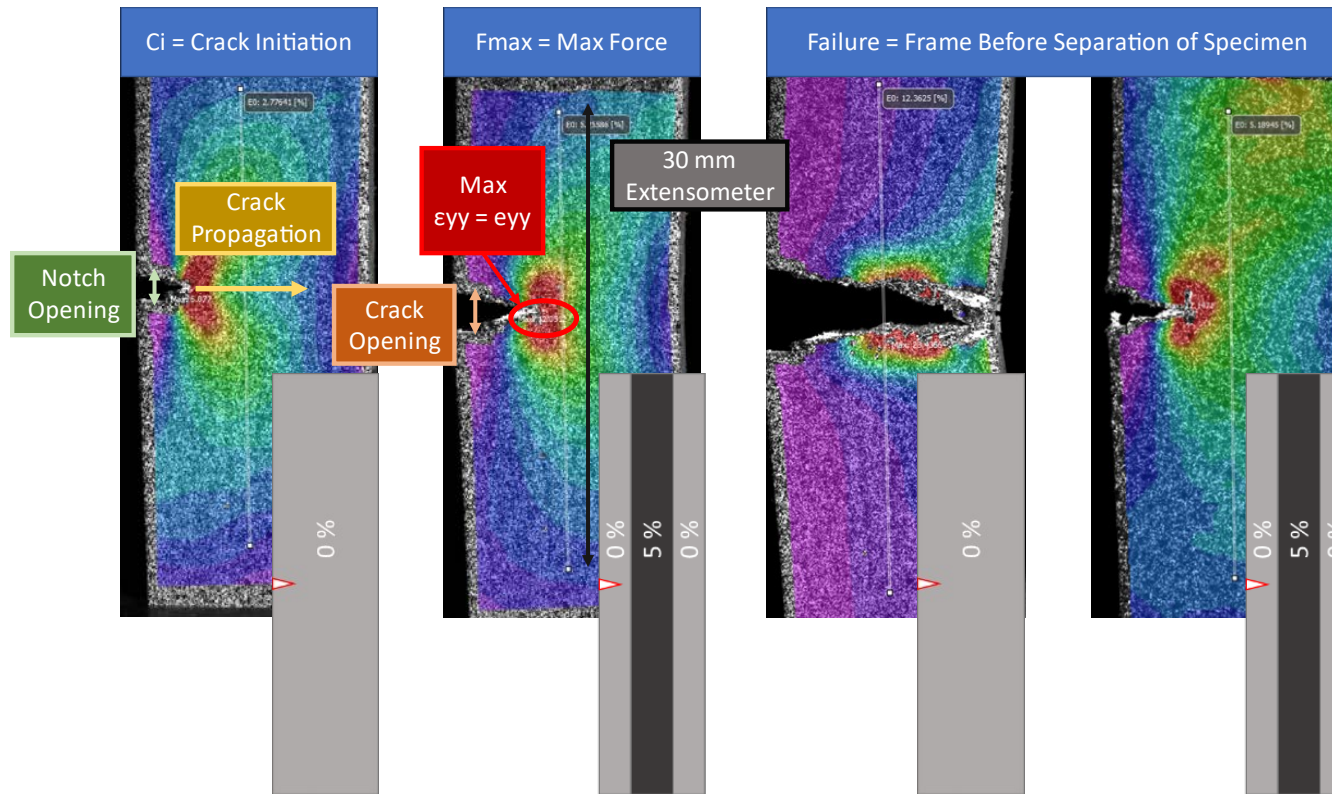


Figure F.1: Depiction of SENT Test DIC Results Definitions and Terms:

**Crack Initiation Frame (Ci)** = the frame at which the notch transitions to a crack and begins to propagate into the specimen.

**Max Force Frame (Fmax)** = the frame at which maximum force was achieved.

**Failure Frame** = the frame prior to complete separation of the SENT Specimen.

**Energy (MJ/mm<sup>3</sup>)** = The area under the stress / 30mm extensometer strain curve at anyone one of the above frames.

**Strains:** All given in percent (“Exto” = 30mm Extensometer Strain,  $\epsilon_{yy}$  = max strain on specimen as calculated by DIC).

**Stress (MPa):** Current Stress for the current frame based on the original (before notch) cross section of the specimen

**Scaling** = All sets of DIC images are either scaled to each specimen (strain field color is scaled to each specific specimen and not constant across all specimens) or a constant scale for all specimens (scale bar is given in image and applies to all specimen in the image)

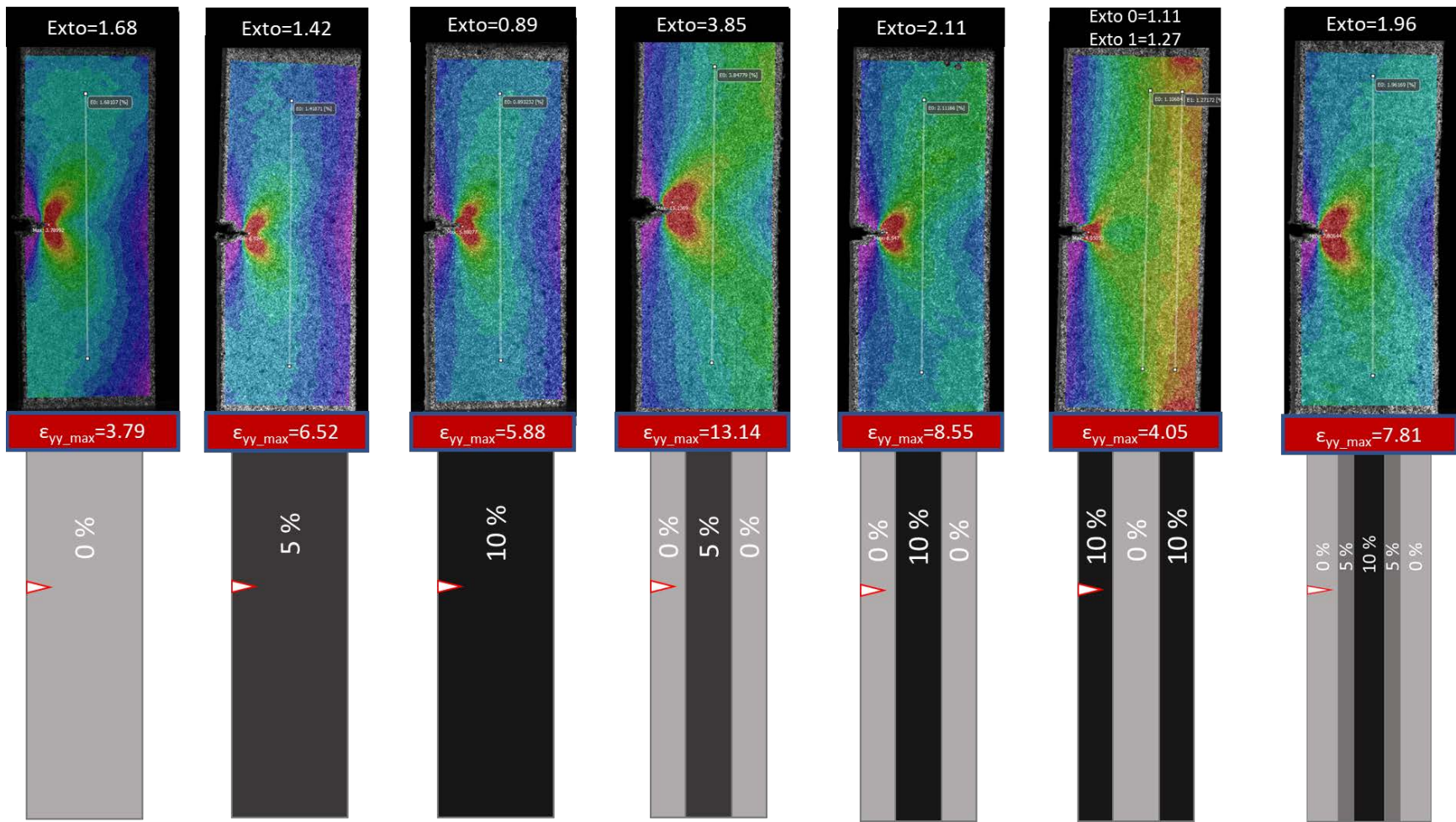


Figure F.1a: Test 2 Crack Initiation (Ci) scaled to each specimen frame

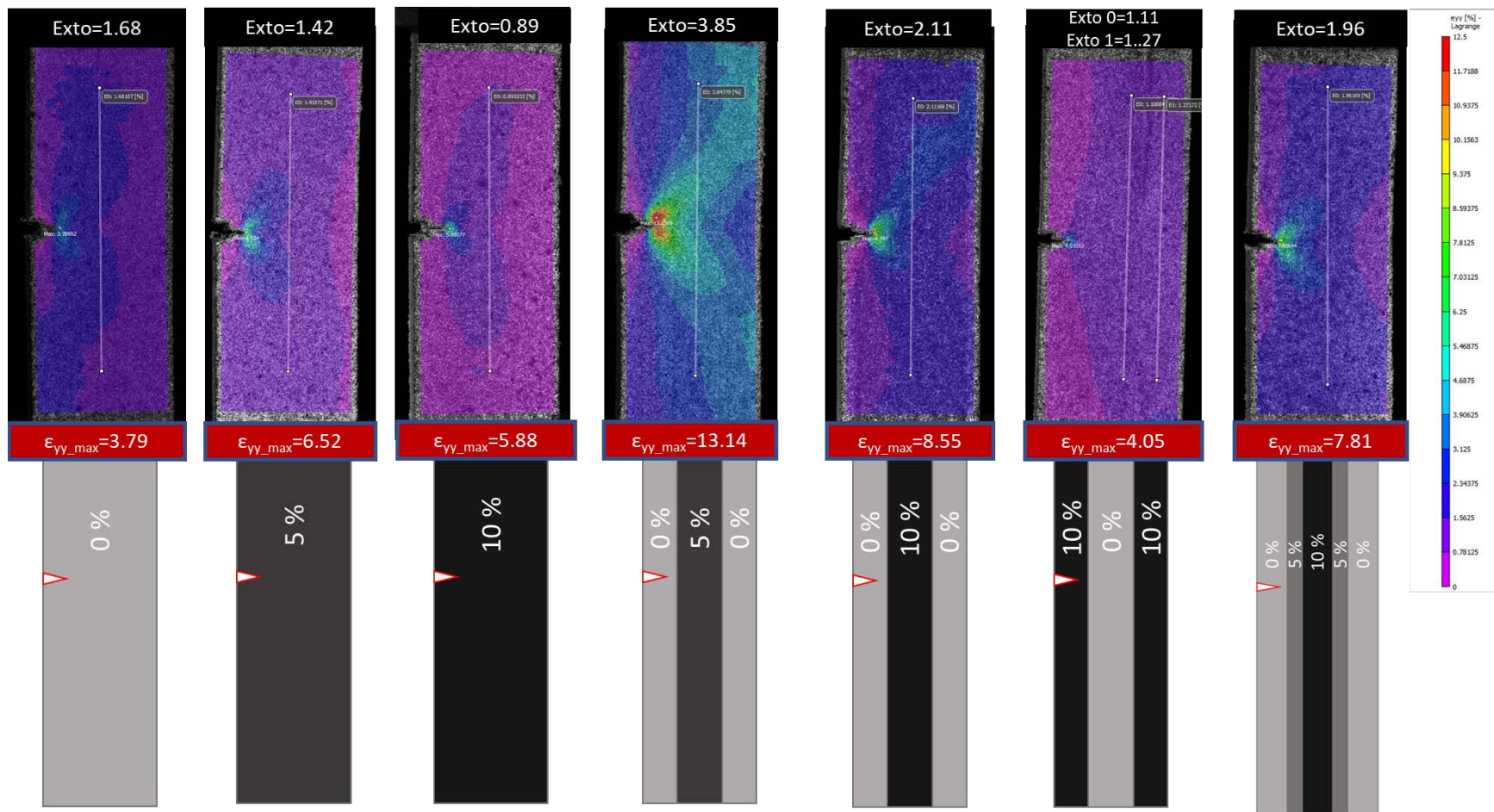


Figure F.1b: Test 2 Crack Initiation (C<sub>i</sub>) scaled to ALL

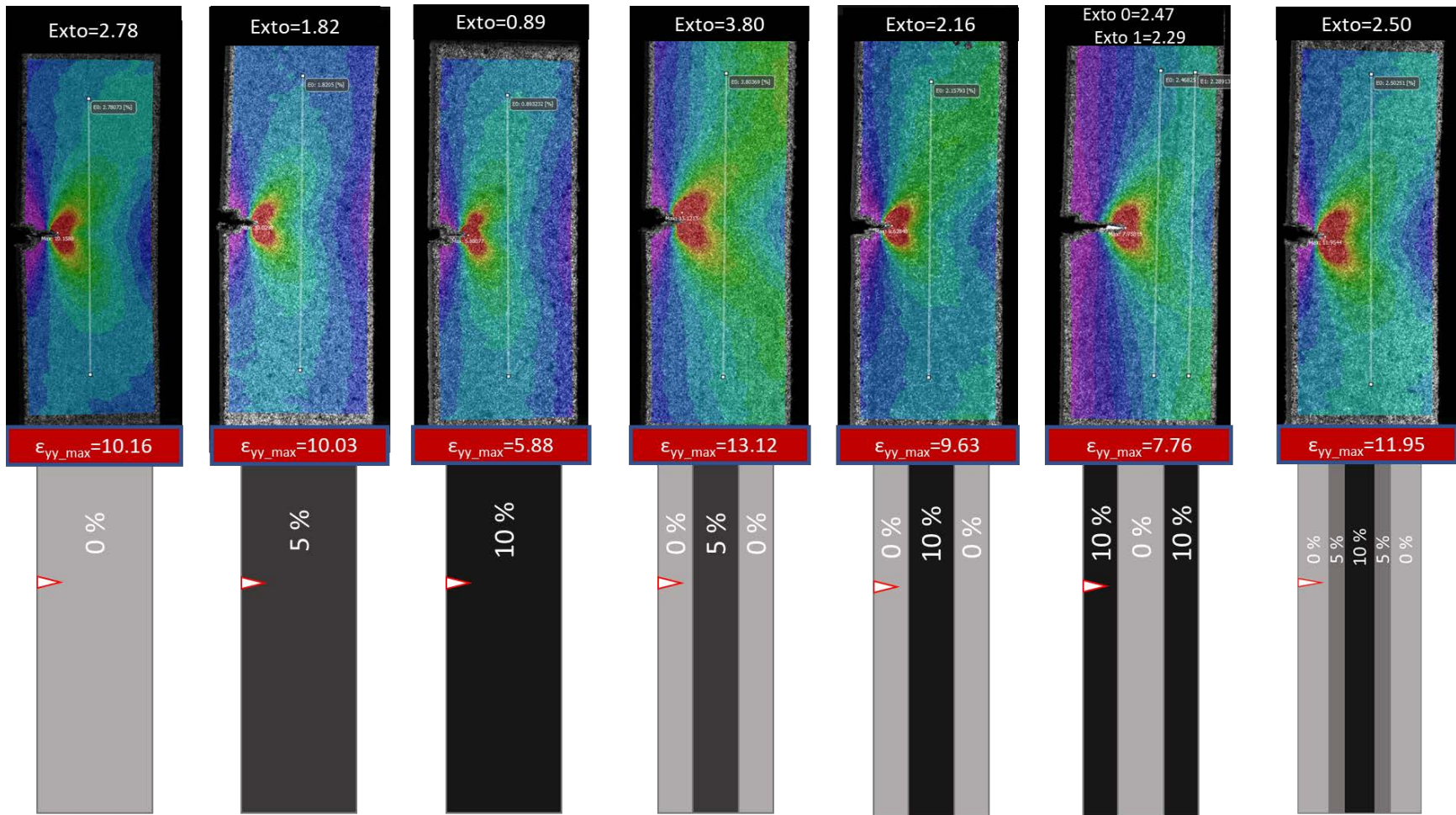


Figure F.1c: Test 2 Max Force (MF) scaled to each specimen frame

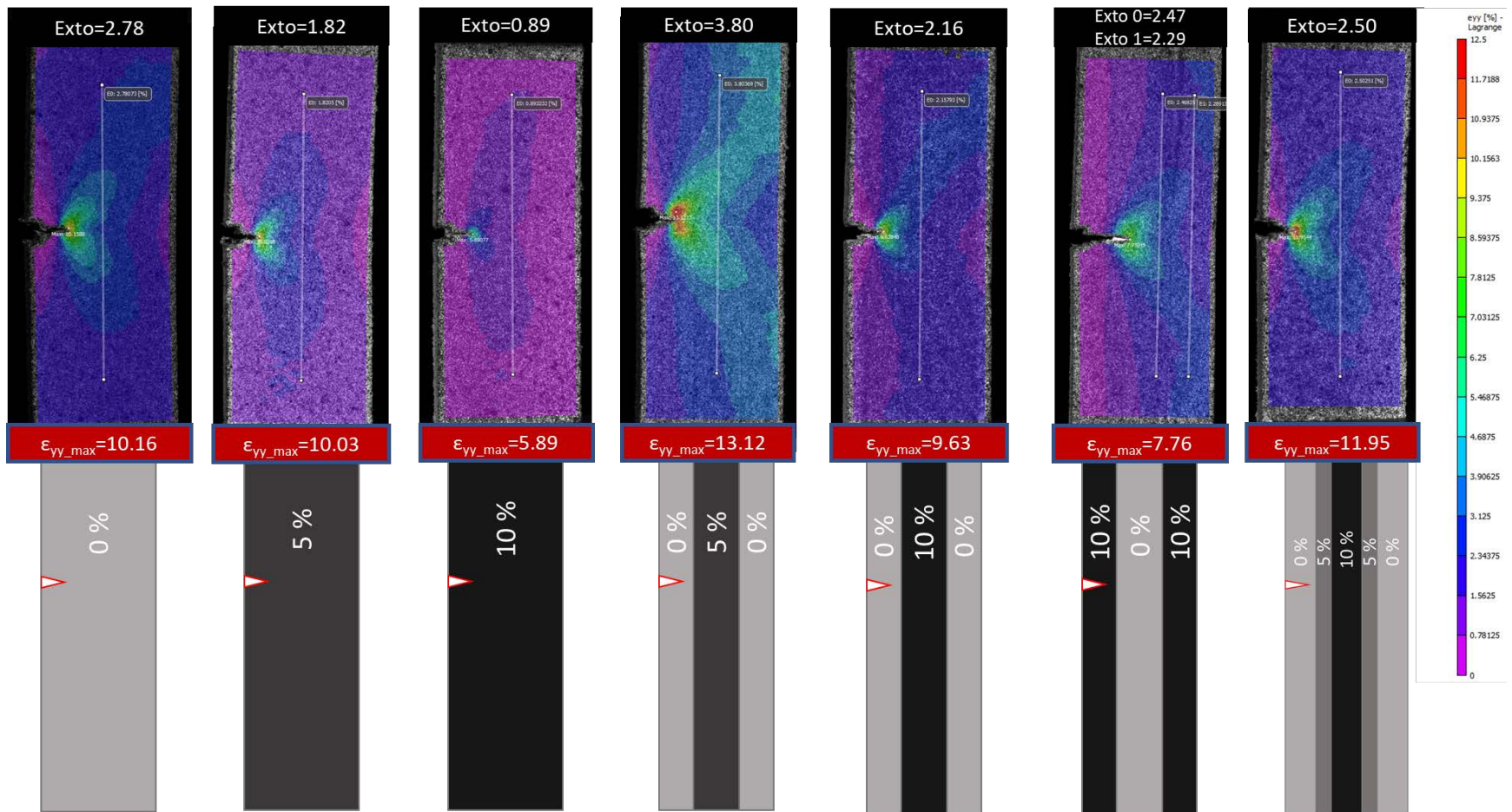


Figure F.1d: Test 2 Max Force (MF) scaled to ALL

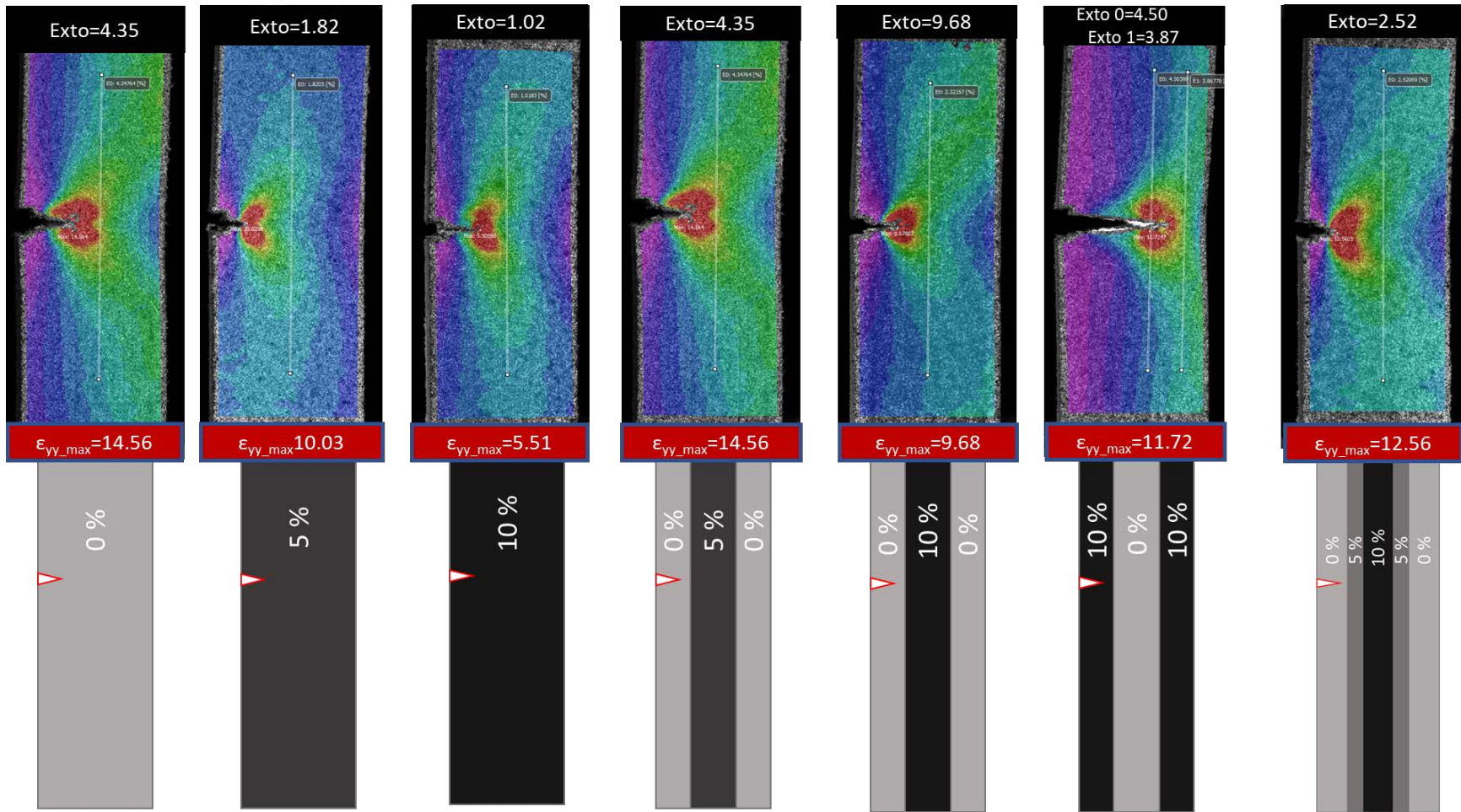


Figure F.1e: Test 2 Failure scaled to each specimen frame

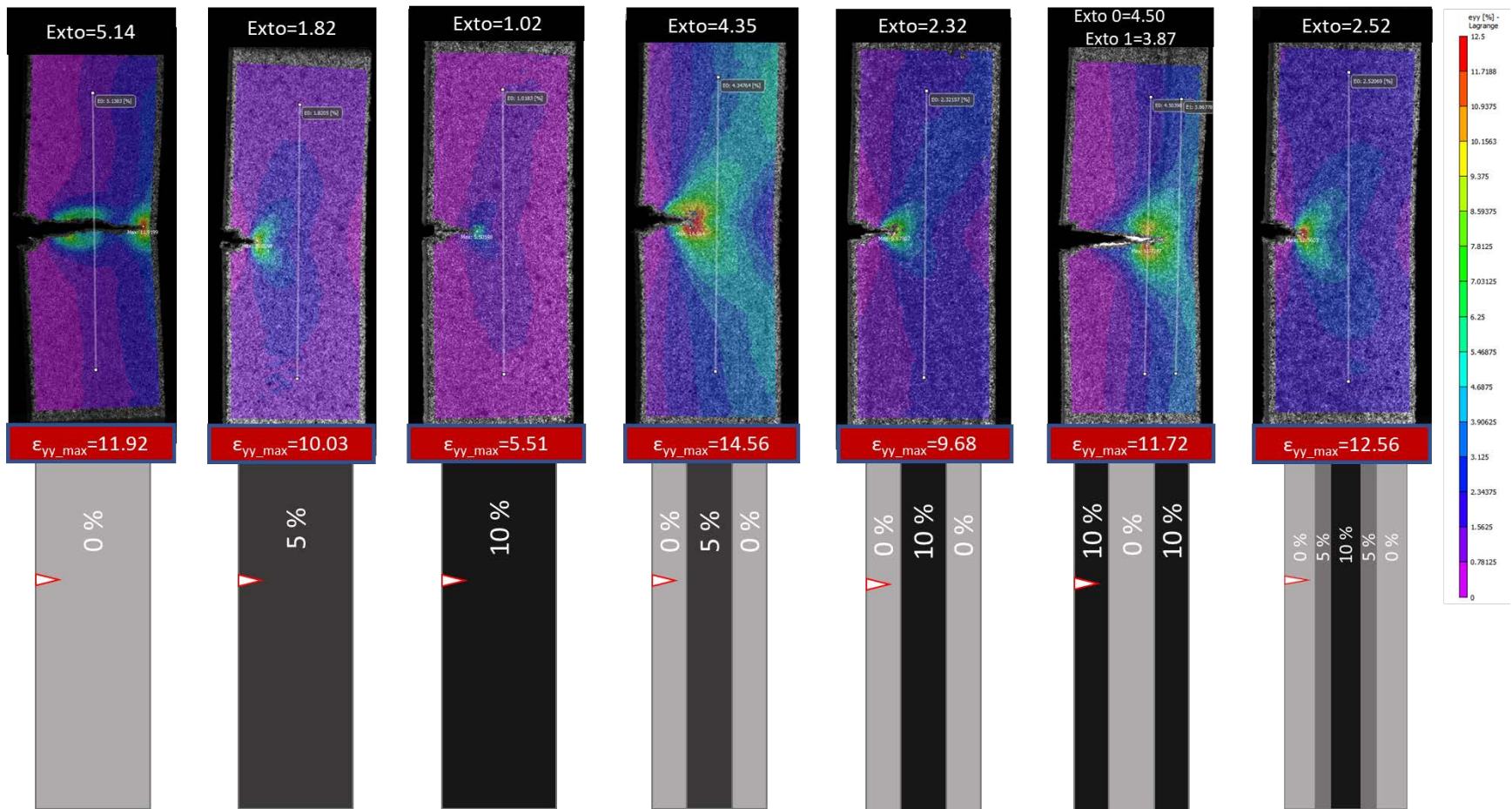


Figure F.1d: Test 2 Failure scaled to ALL

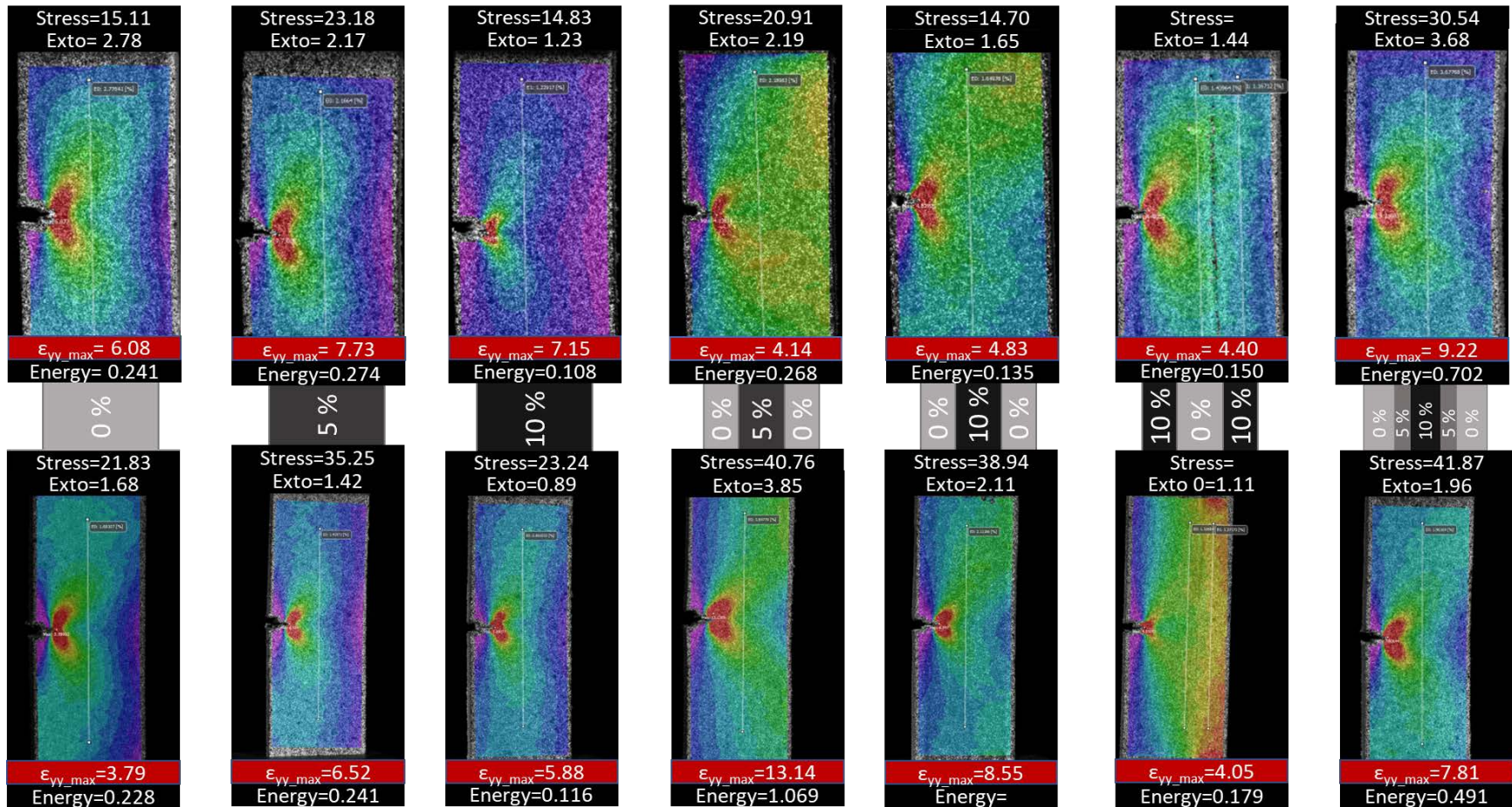


Figure F.2a: Test 1 (top images) and Test 2 (bottom images) Crack Initiation (Ci) scaled to each specimen frame.

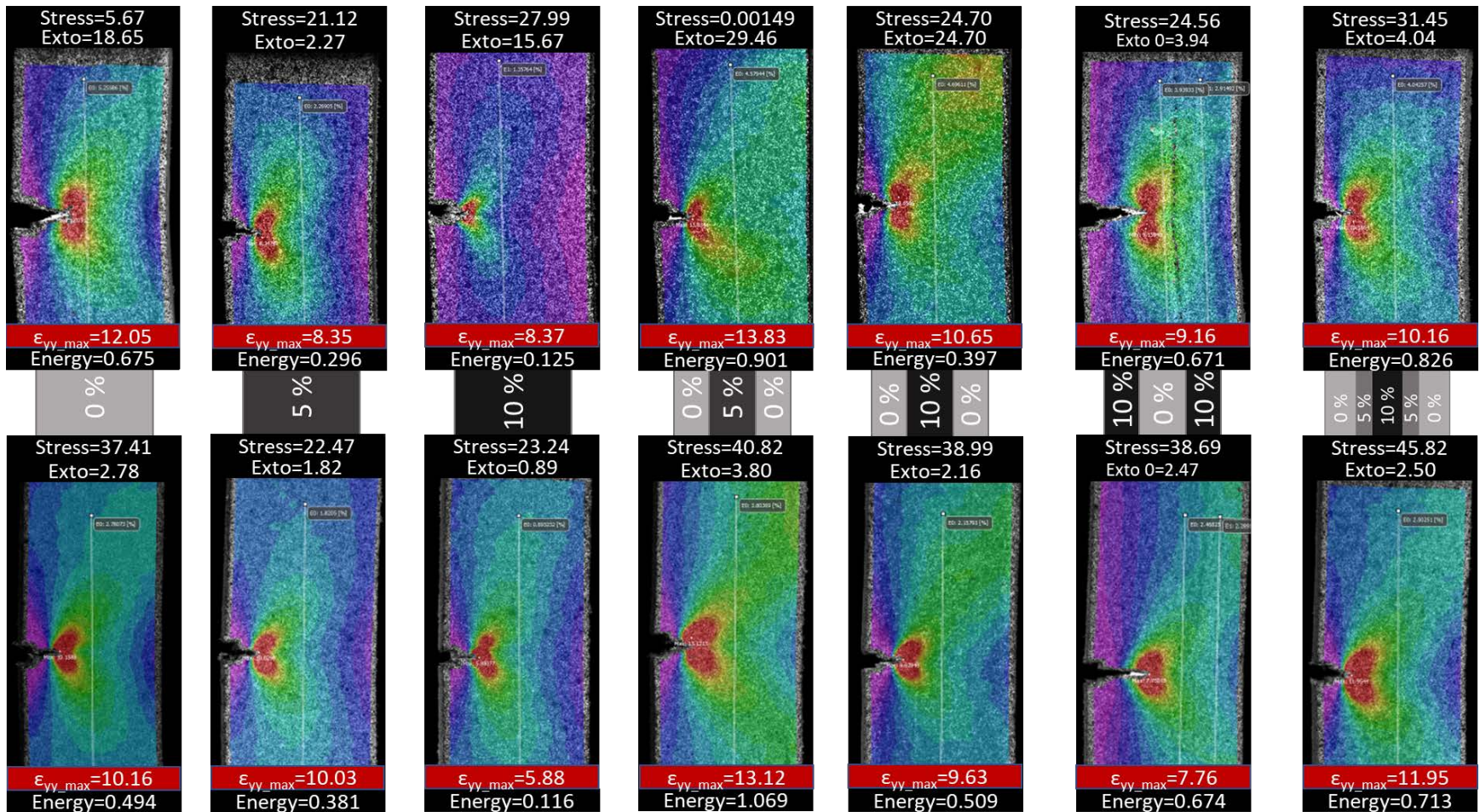


Figure F.2b: Test 1 (top images) and Test 2 (bottom images) Max Force (MF) scaled to each specimen.

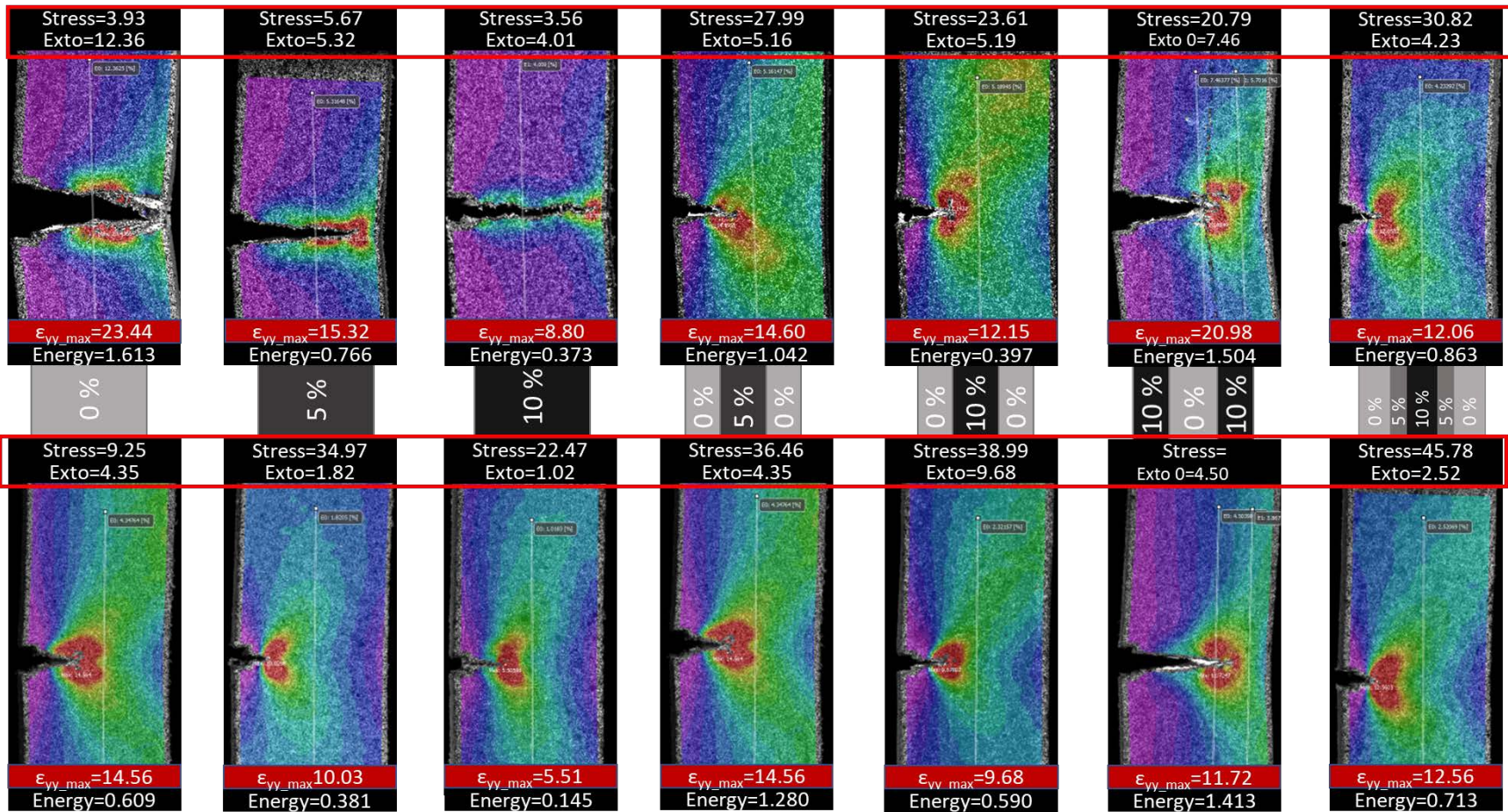


Figure F.2c: Test 1 (top images) and Test 2 (bottom images) Failure scaled to each specimen frame.

### T2 SENT Stress vs 30mm Extensometer Strain

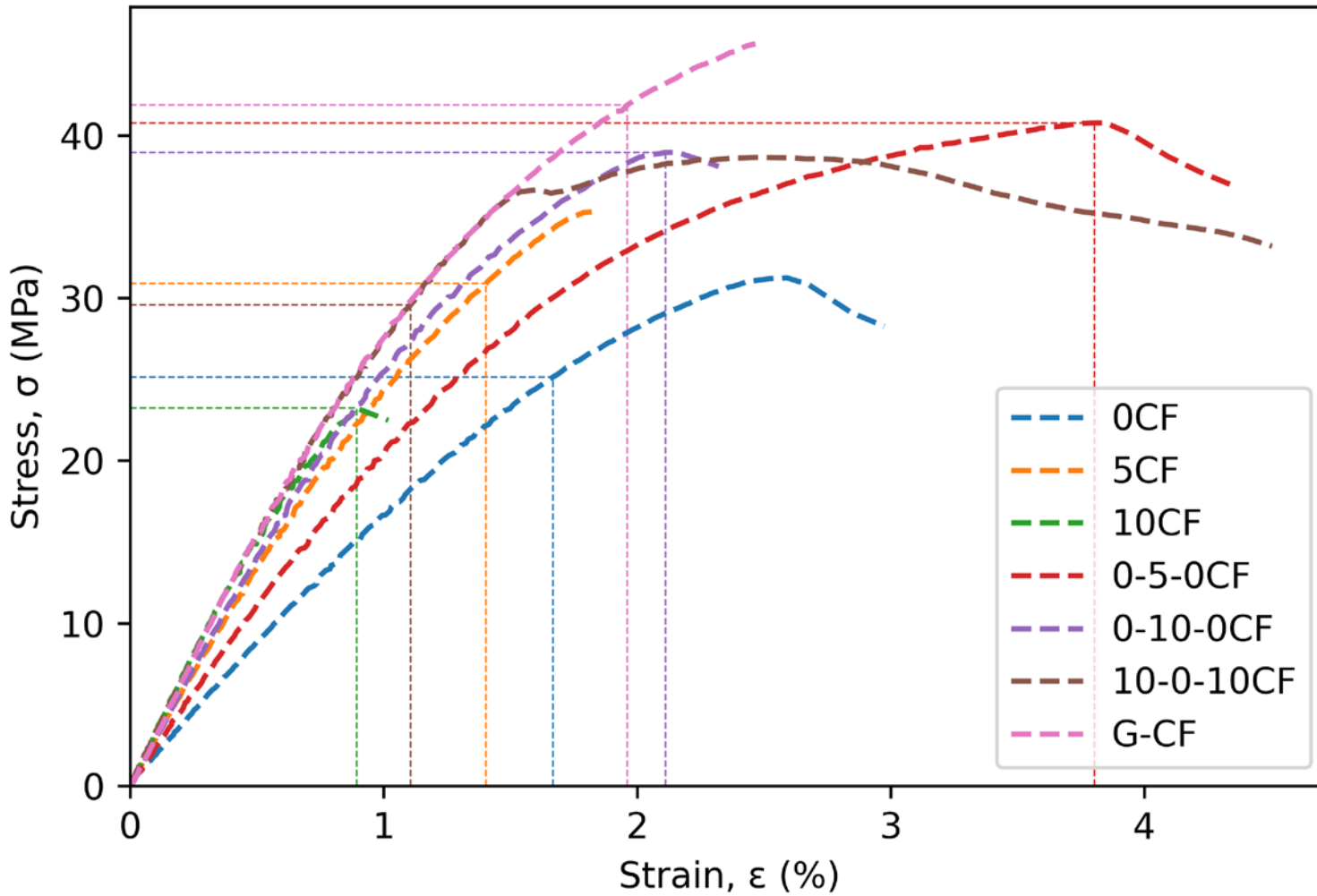
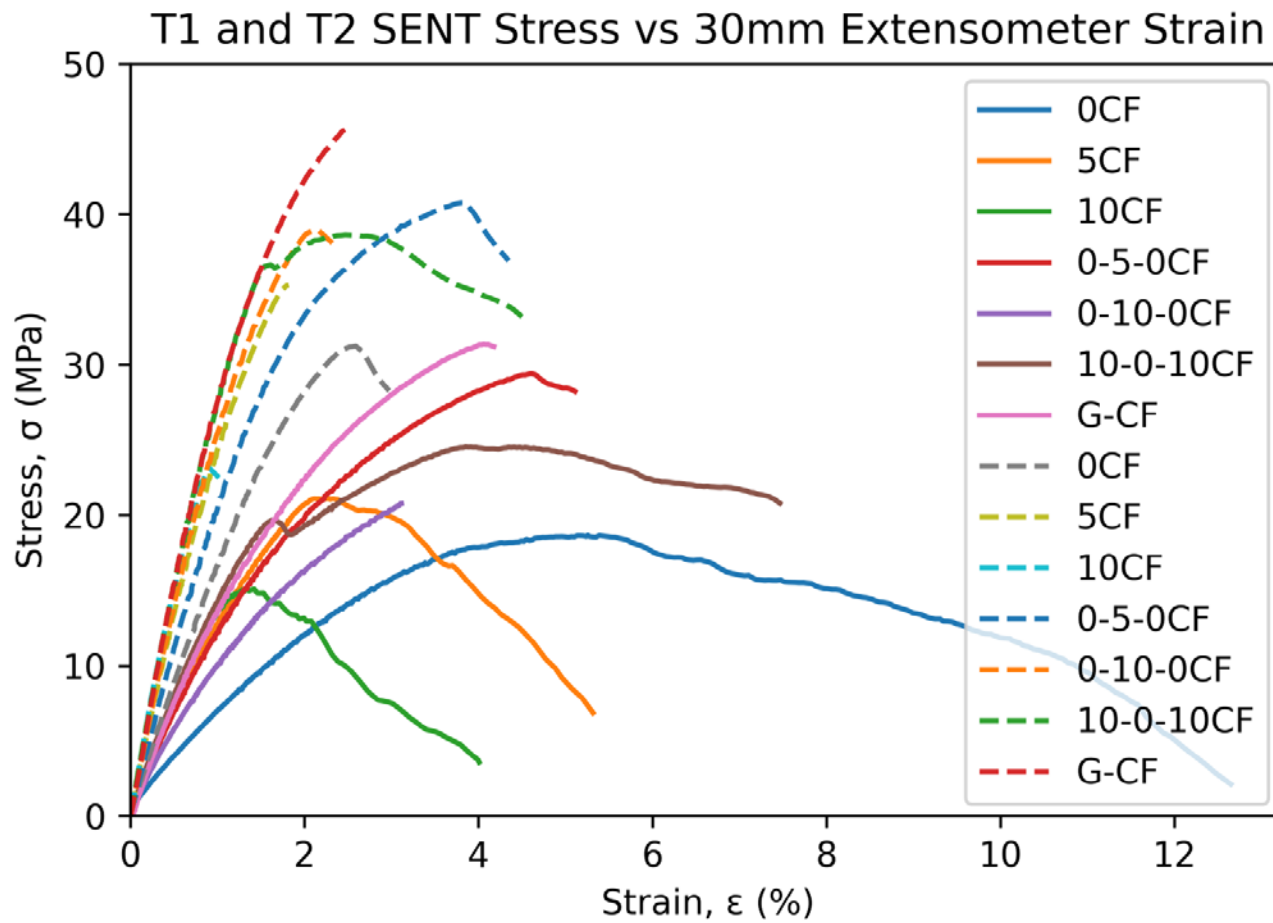


Figure F.3: Test 2 Representative Stress Strain Curve of Each Specimen Type with Crack Initiation Lines  
 (Note: G-CF = 0-5-10-5-0CF Binary Gradient Specimen)



**RESULTS**

- Test 2 more “brittle” than Test 1
  - $\uparrow$  “UTS”
  - $\uparrow$  “Modulus”
- $\downarrow$  Strain
- $\downarrow$  Energy

Figure F.4a: Comparison Test 1 and Test 2 of 30mm Stress-Strain Curves  
 (Note: G-CF = 0-5-10-5-0CF Binary Gradient Specimen)

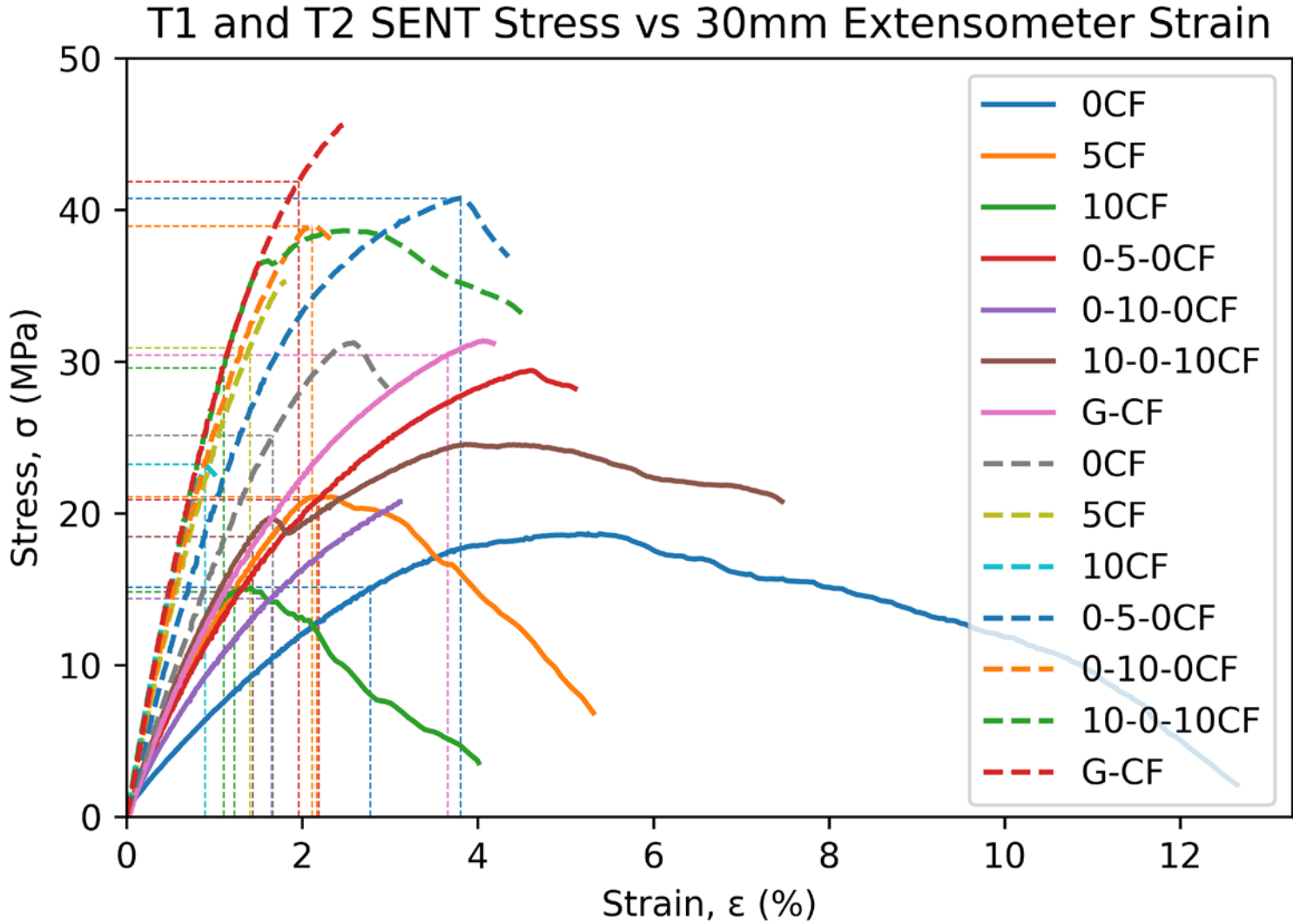
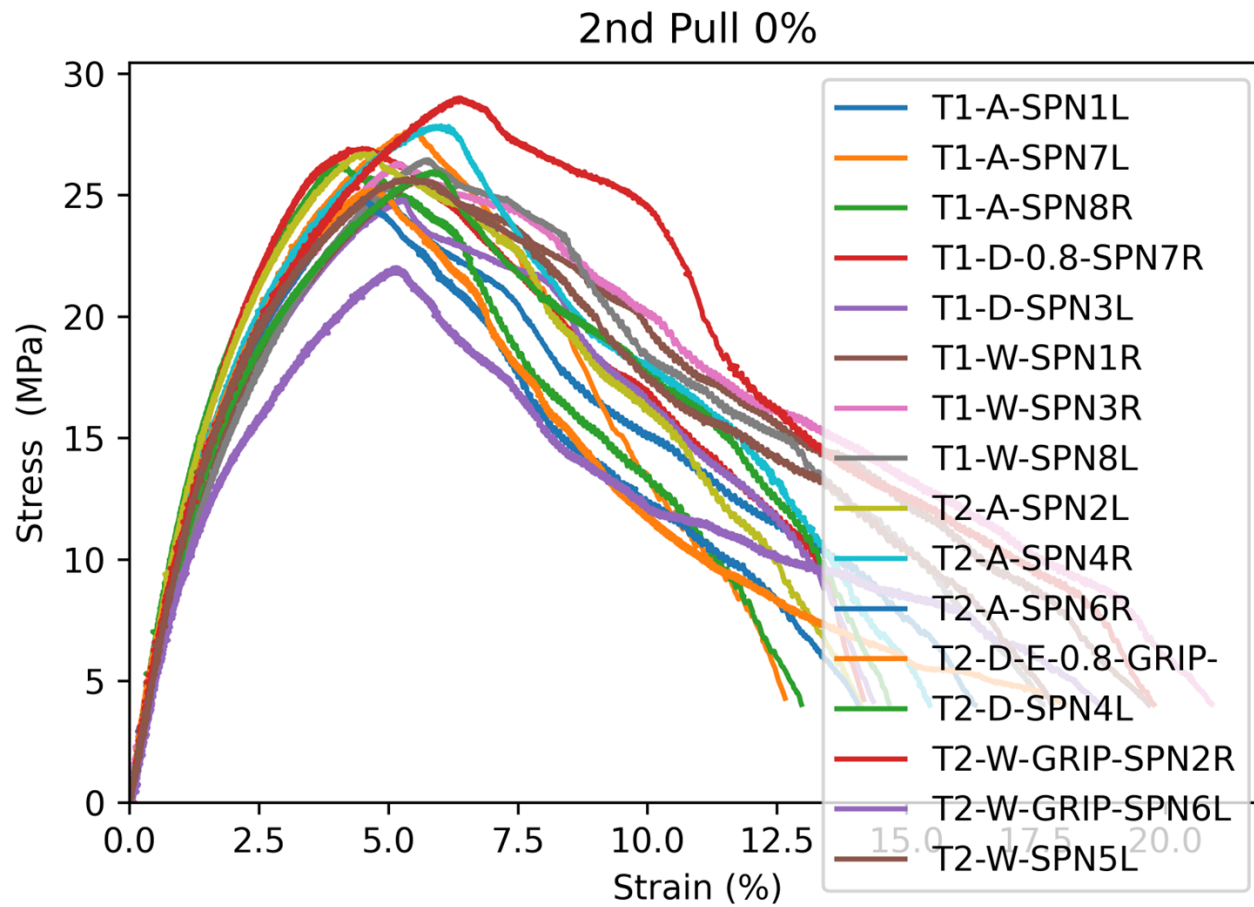


Figure F.4b: Comparison Test 1 and Test 2 of 30mm Stress-Strain Curves with Crick Initiation Lines  
 (Note: G-CF = 0-5-10-5-0CF Binary Gradient Specimen)



**RESULTS**

- Little change between
  - W – wet
  - D – Dried
  - A – Ambient

Figure F.5: Comparison of Wet, Dried, and Ambient Specimen 30mm Stress-Strain Curves

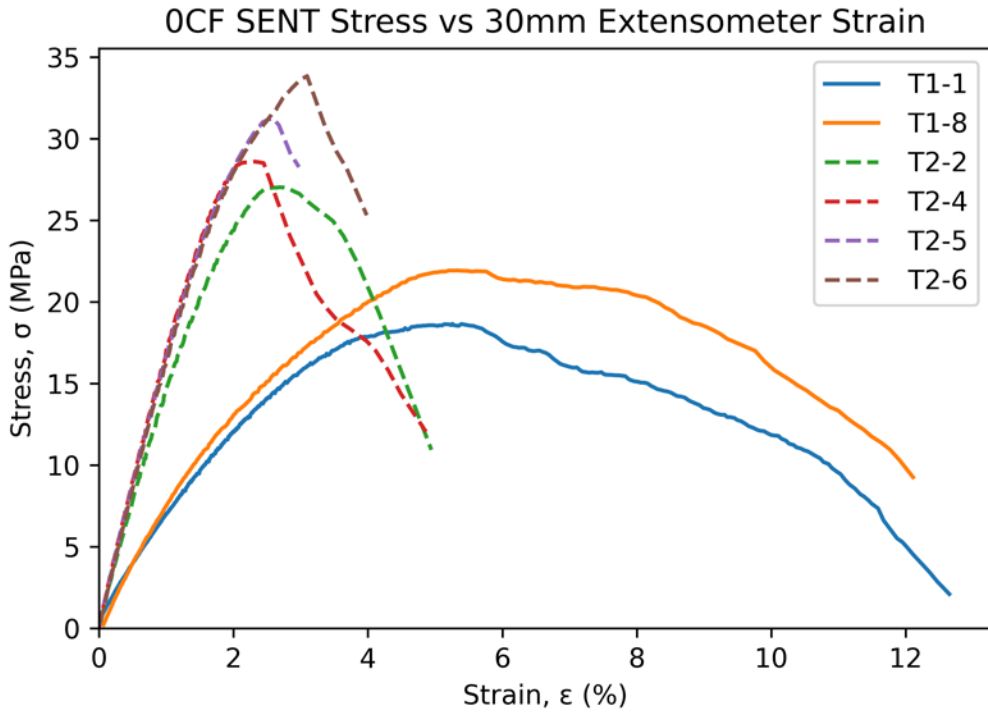


Figure F.6a: 0%CF Single Material SENT 30mm Extensometer Tensile Data Comparison.

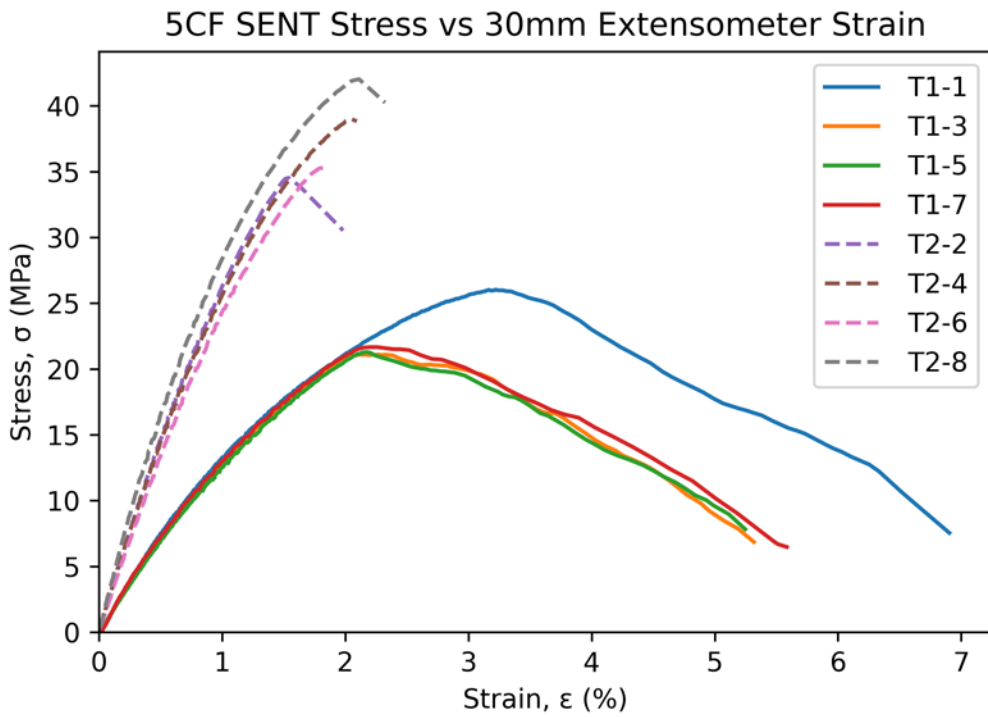


Figure F.6b: 5%CF Single Material SENT 30mm Extensometer Tensile Data Comparison.

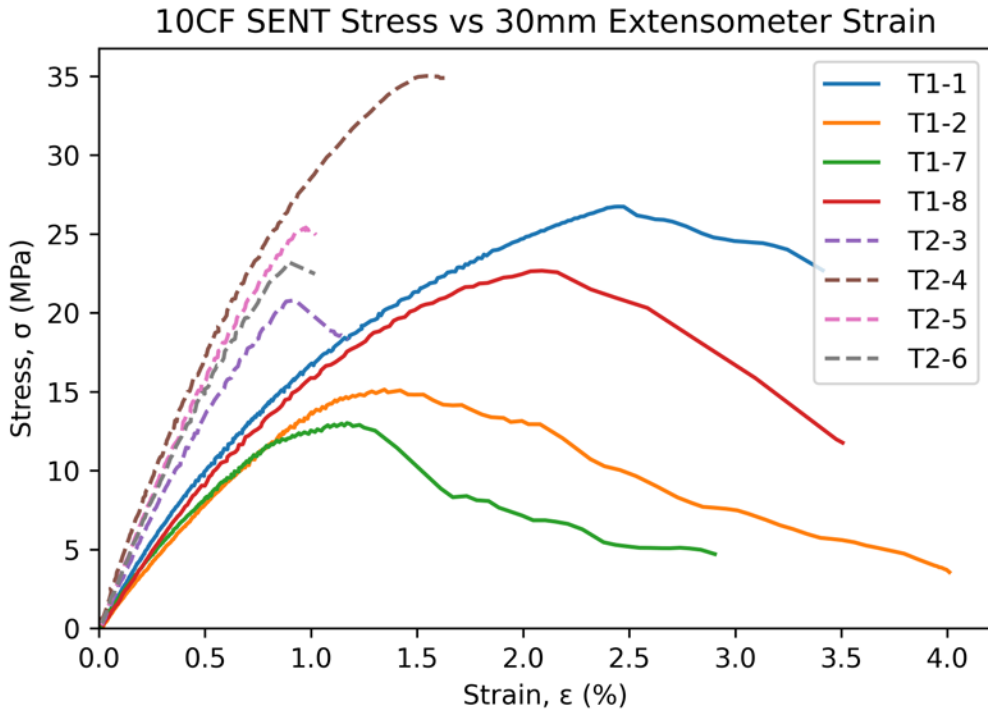


Figure F.6c: 10%CF Single Material SENT 30mm Extensometer Tensile Data Comparison.

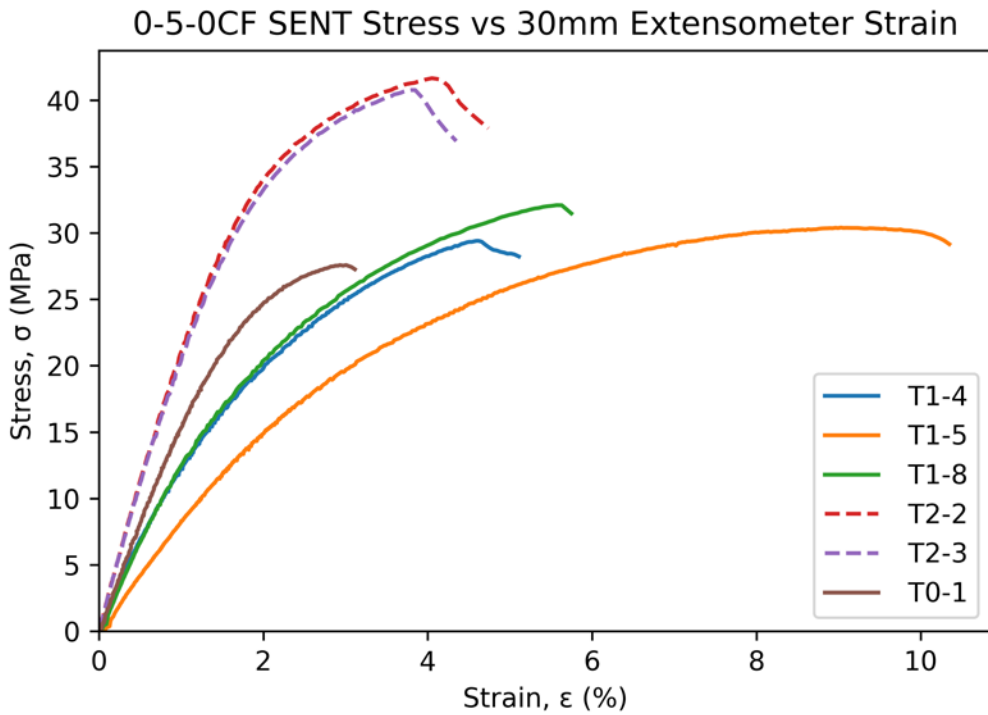


Figure F.6d: 0-5-0%CF Binary Material SENT 30mm Extensometer Tensile Data Comparison.

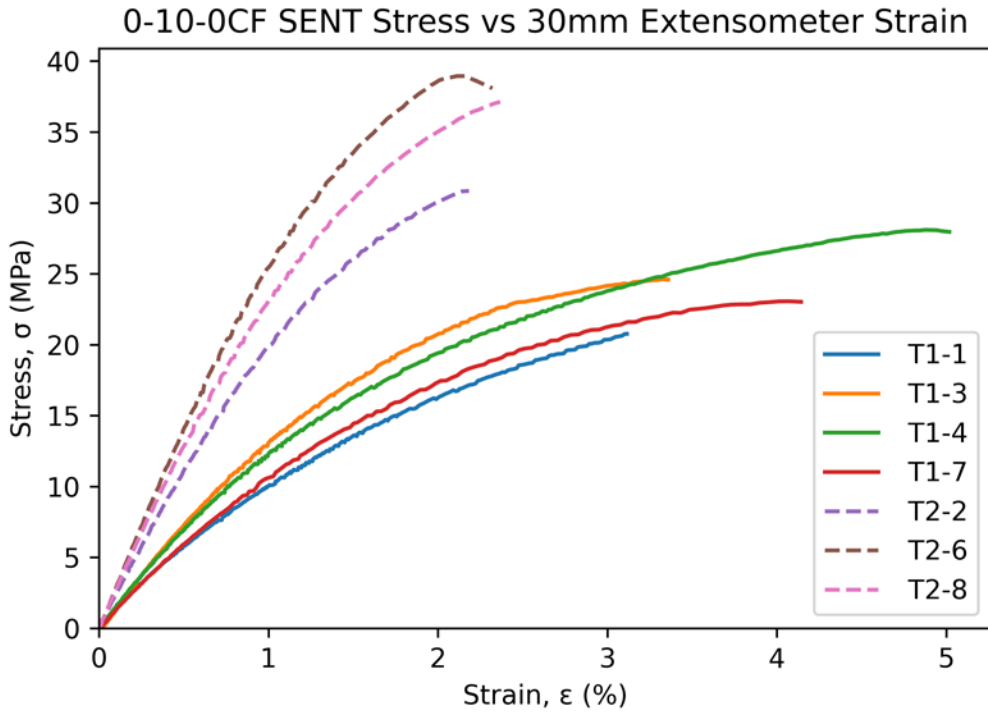


Figure F.6e: 0-10-0%CF Binary Material SENT 30mm Extensometer Tensile Data Comparison.

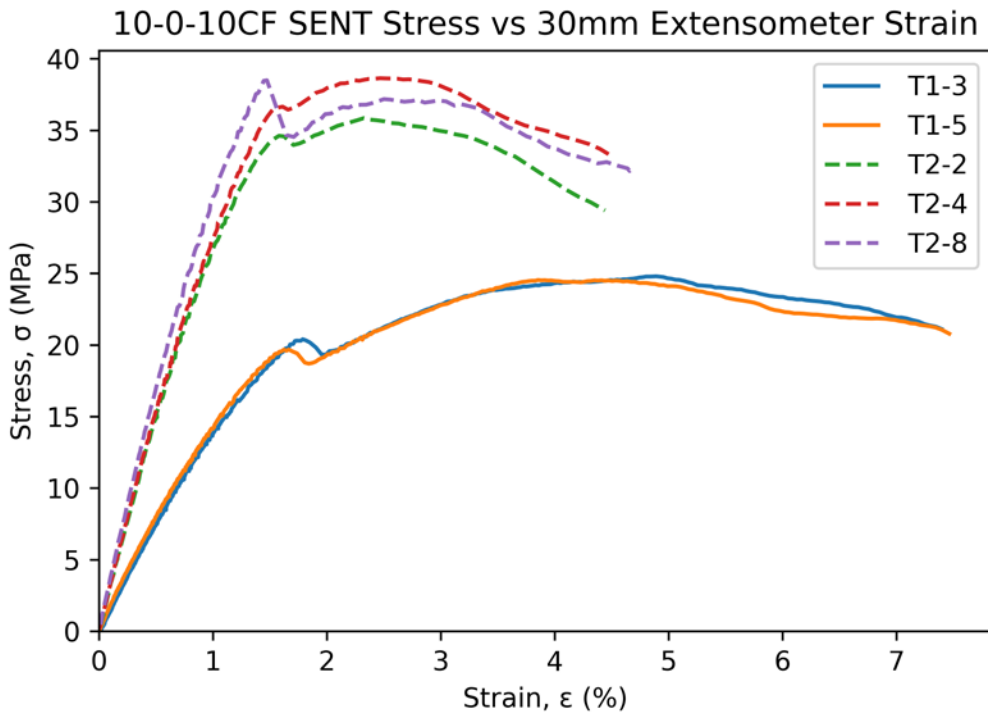


Figure F.6f: 10-0-10%CF Binary Material SENT 30mm Extensometer Tensile Data Comparison.

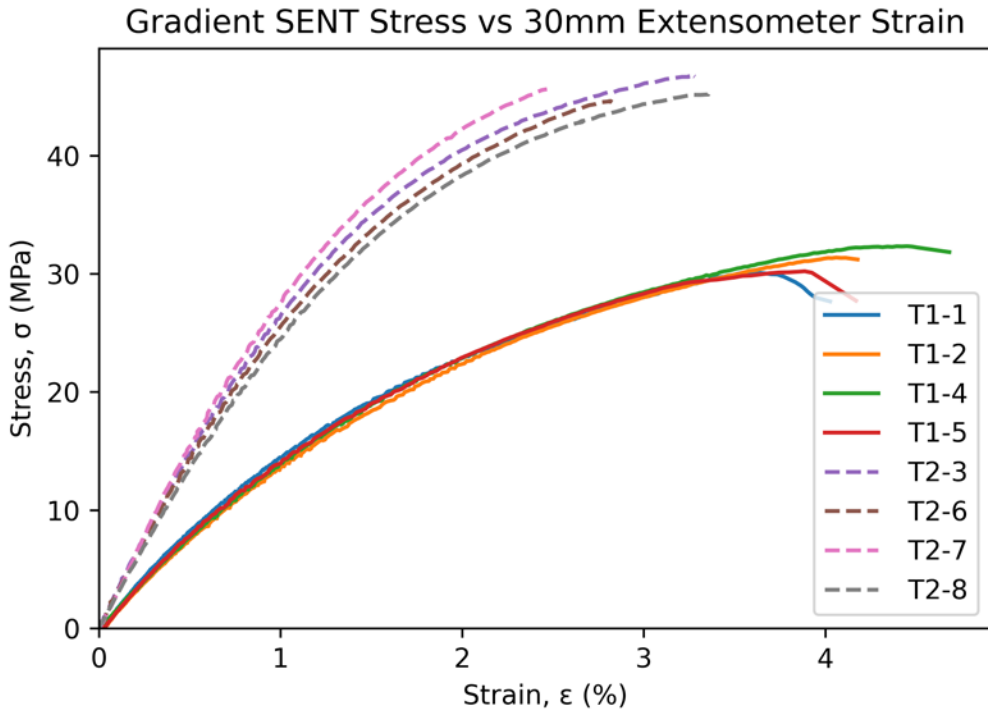


Figure F.6g: 0-5-10-5-0%CF Binary Gradient SENT 30mm Extensometer Tensile Data Comparison.

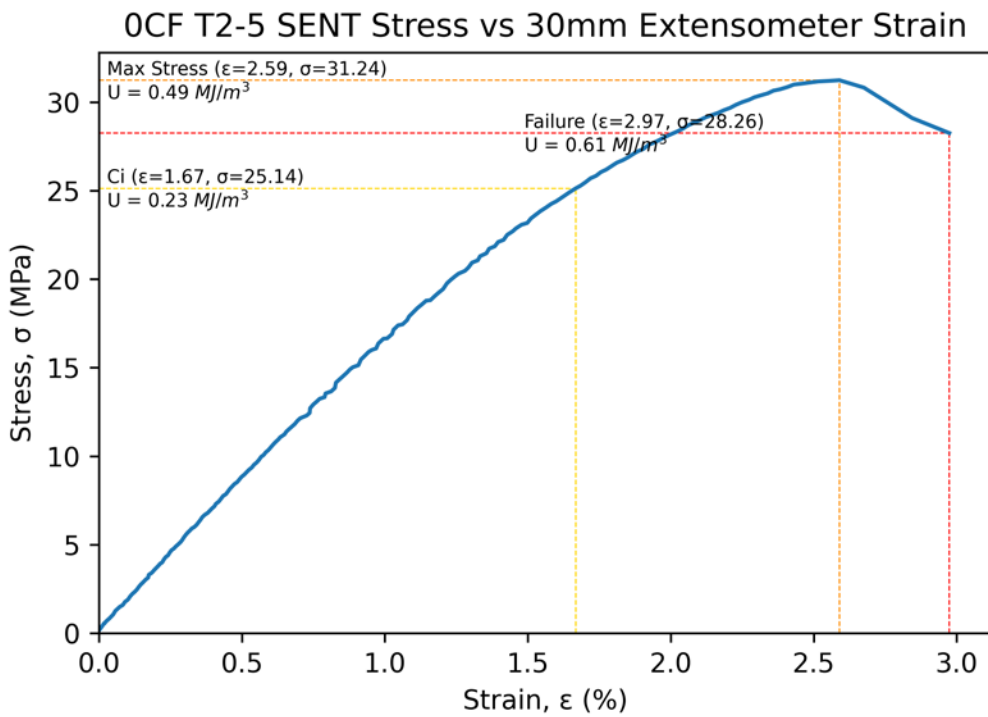


Figure F.7a: 0%CF Single Material SENT Test 2.

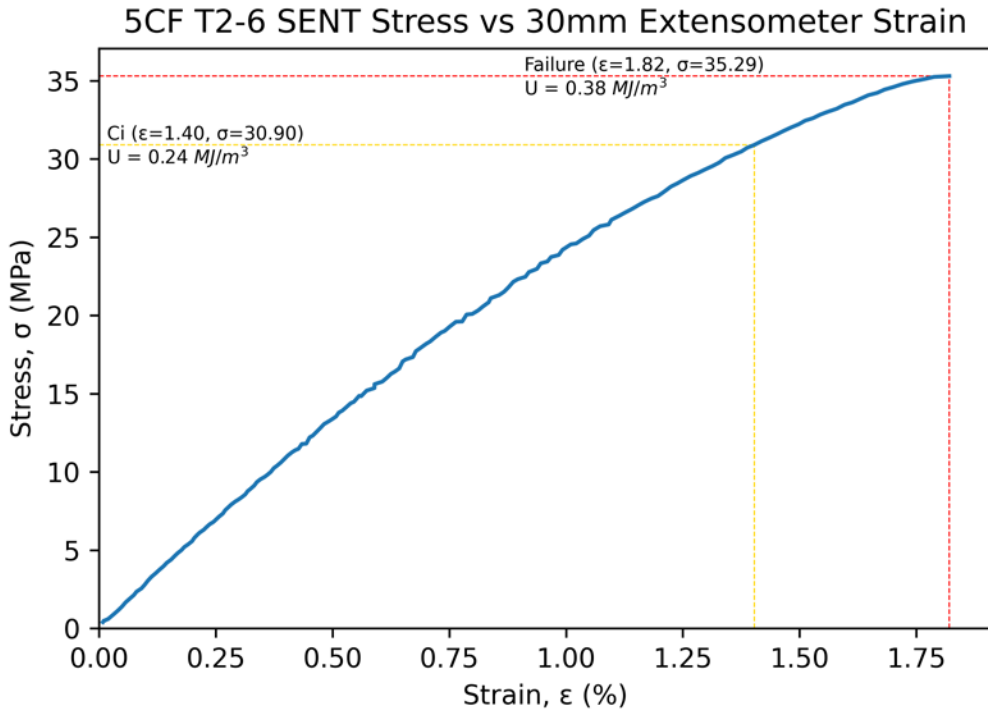


Figure F.7b: 5%CF Single Material SENT Test 2.

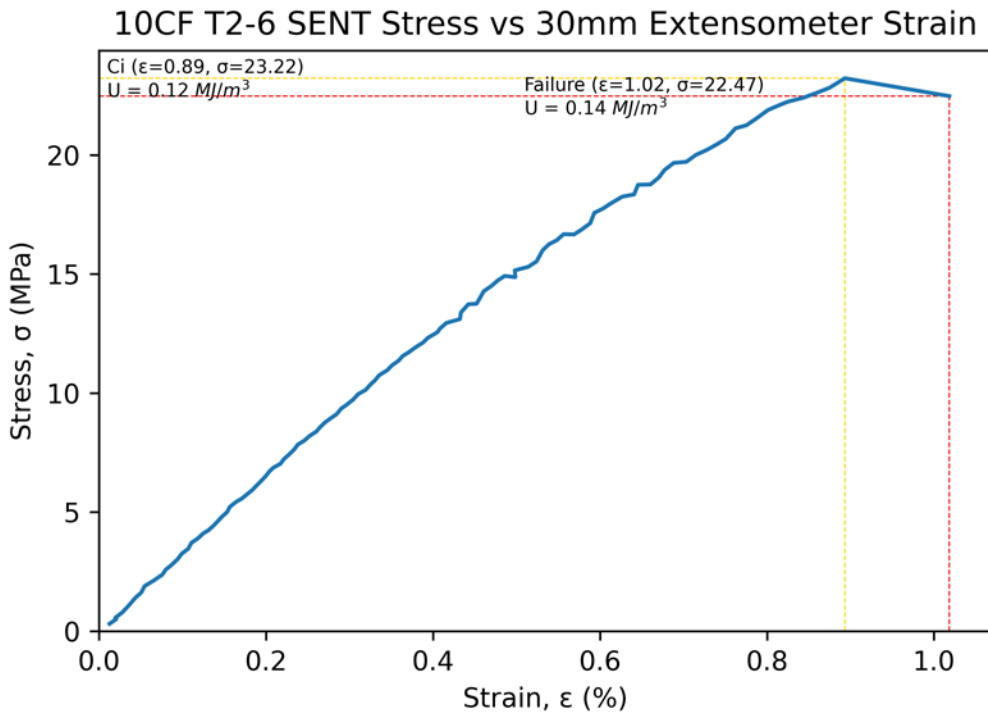


Figure F.7c: 10%CF Single Material SENT Test 2.

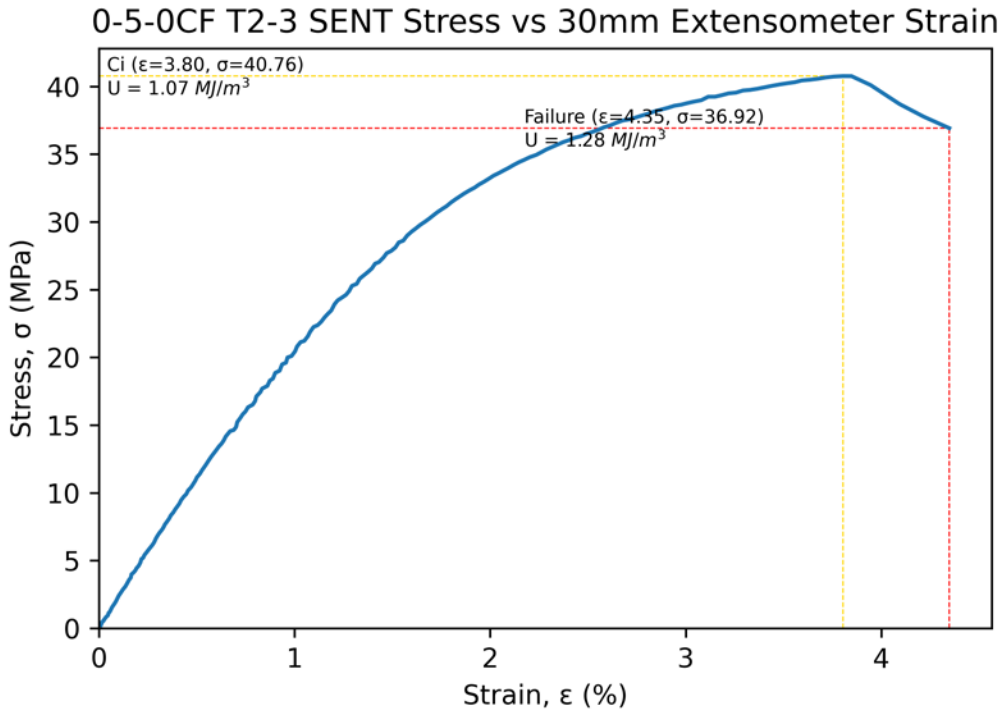


Figure F.7d: 0-5-0%CF Binary Material SENT Test 2.

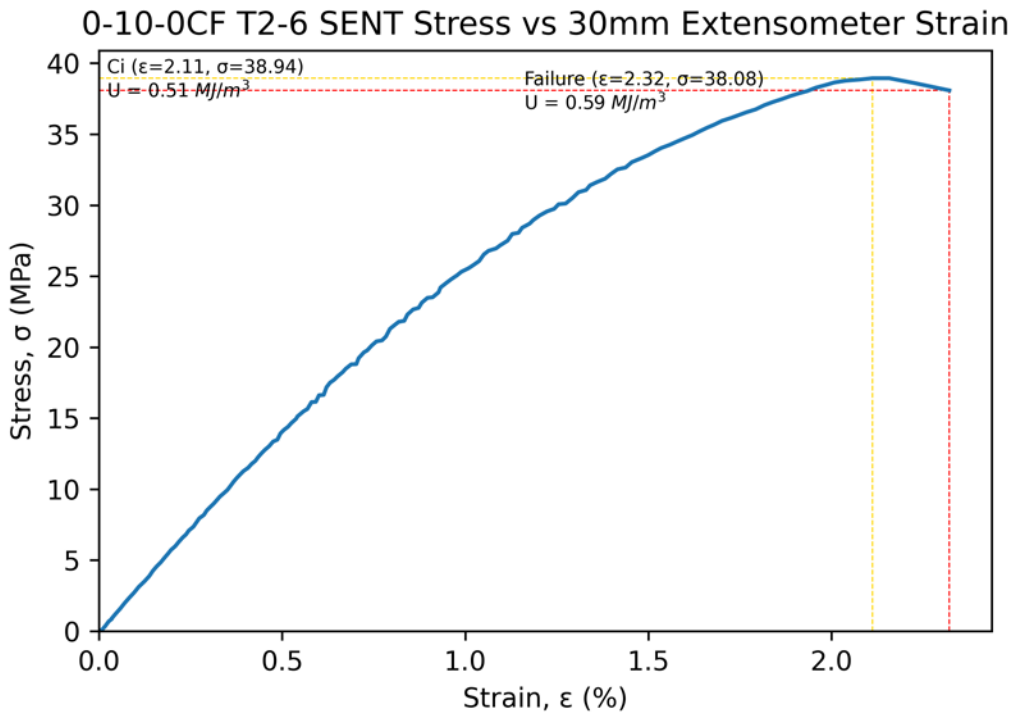


Figure F.7e: 0-10-0%CF Binary Material SENT Test 2.

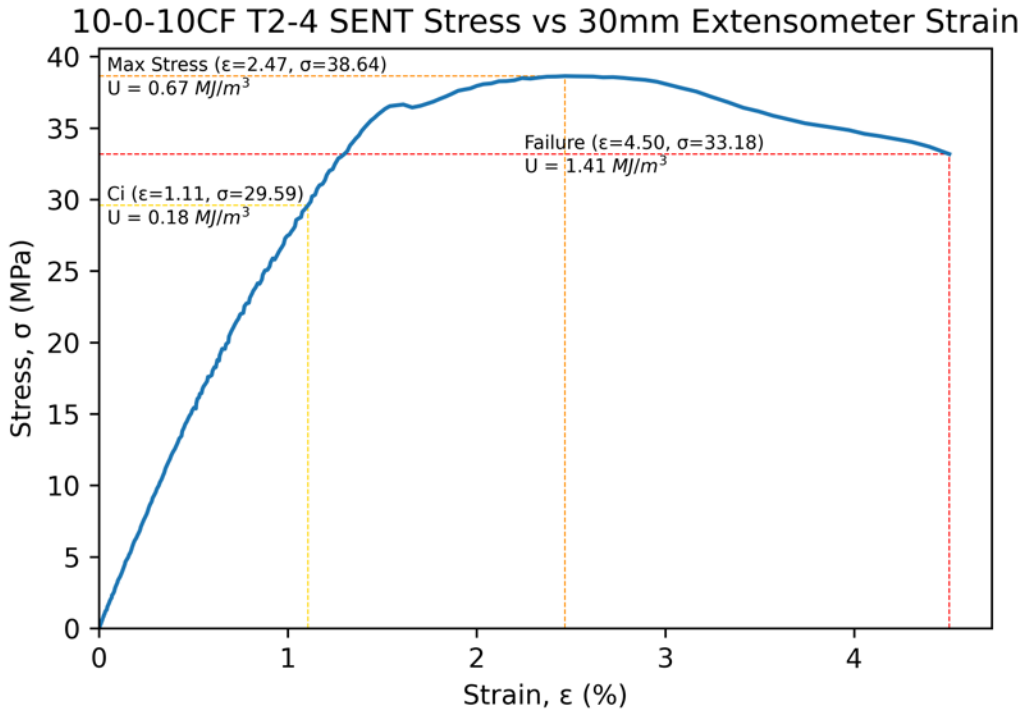


Figure F.7f: 10-0-10%CF Binary Material SENT Test 2.

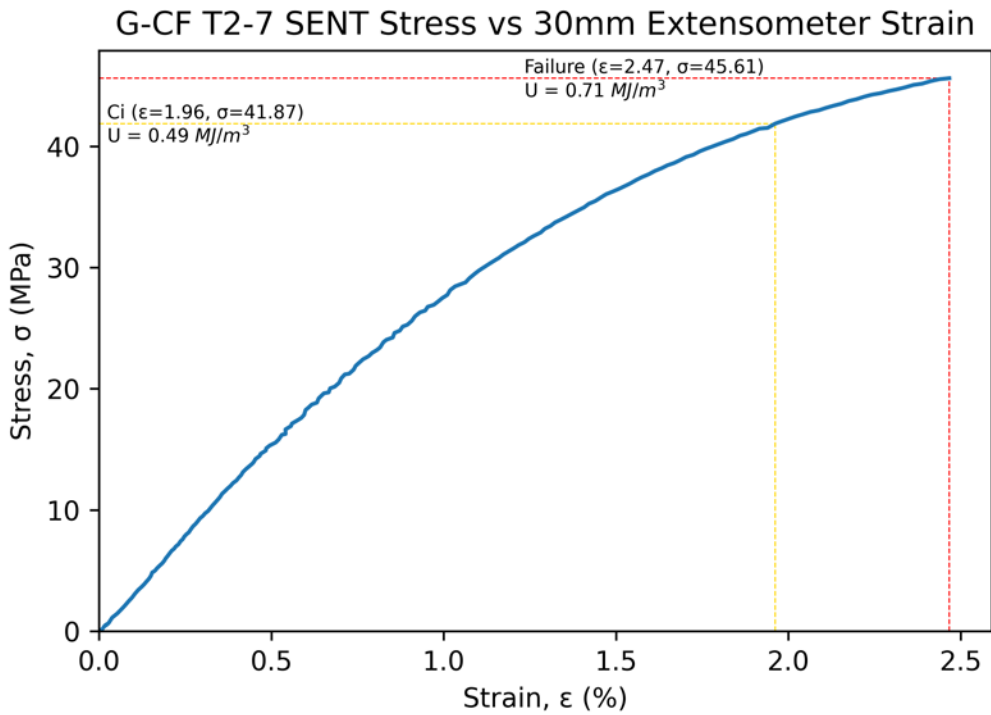


Figure F.7g: 0-5-10-5-0%CF Gradient SENT Test 2

## Vita

Jonathan James Slager is the firstborn son of Donald and Martha Slager. He is the husband of Angel Slager and father to their four children. He grew up with his parents and brother in West Africa until returning to the US for high school where he graduated from Beaver Dam High School, WI. He earned his Bachelor of Science in Engineering with a Mechanical concentration in 2001 from LeTourneau University where he joined the US Navy. He earned a Master of Science degree in Engineering with an Aeronautical concentration from the Air Force Institute of Technology in Dayton, OH and a Test Pilot degree from the United States Naval Test Pilot School in Patuxent River, MD. He has served in the US Navy as a pilot and instructor and is currently transitioning to the United States Naval Academy as an active-duty professor.

Jonathan has 579 carrier arrested landings and over 2,000 hours in the F/A-18 Hornet and Super Hornet along with hours in 33 different types of aircraft as a Test Pilot and Test Pilot Instructor and is a lifetime member of the Society of Experimental Test Pilots (SETP). He has been stationed around the world and at sea and has led numerous training, test, and combat missions including missions in support of Operation Inherent Resolve. At Air Test and Evaluation Squadron 23 (VX-23) he directed and executed both manned and unmanned carrier suitability testing along with system integration, weapon separation, and stability and control testing. He has instructed at the US Naval Test Pilot School and has co-authored "*Failure Analysis of Additively Manufactured Polyester Test Specimens Exposed to Various Liquid Media.*" Published by the *Journal of Failure Analysis and Prevention*. He is currently on the LIMBS International Board of Directors and serving as the West Africa Outreach director for LIMBS while working alongside their team at UTEP on new ultra low-cost prosthetic designs.

Contact Information: [j.j.slager@gmail.com](mailto:j.j.slager@gmail.com)